



Université
de Toulouse

THÈSE

En vue de l'obtention du

DOCTORAT DE L'UNIVERSITÉ DE TOULOUSE

Délivré par : *l'Université Toulouse 3 Paul Sabatier (UT3 Paul Sabatier)*

Présentée et soutenue le 18/09/2023 par :

Léo Vacher

Vers une meilleure compréhension du signal Galactique polarisé en quête de nouvelle physique fondamentale dans le fond diffus cosmologique.

Understanding the Galactic polarized signal in the quest for new fundamental physics in the Cosmic Microwave Background

JURY

ALAIN BLANCHARD	Président du jury	Professeur
MARC-ANTOINE MIVILLE-DESCHÈNES	Rapporteur	Directeur de recherche
JEAN-PHILIPPE UZAN	Rapporteur	Directeur de recherche
CARLO BACCIGALUPI	Examinateur	Professor
NICOLETTA KRACHMALNICOFF	Examinateuse	Assistant professor
JONATHAN AUMONT	Directeur de thèse	Chargé de recherche
LUDOVIC MONTIER	Co-directeur de thèse	Ingénieur de recherche

École doctorale et spécialité :

SDU2E : Astrophysique, Sciences de l'Espace, Planétologie

Unité de Recherche :

Institut de Recherche en Astrophysique et Planétologie (UMR 5277)

Directeur(s) de Thèse :

Jonathan Aumont et Ludovic Montier

Rapporteurs :

Marc-Antoine Miville-Deschênes et Jean-Philippe Uzan

Supposons que nous nous perdions à contempler l'infinité du monde dans le temps et dans l'espace, soit que nous réfléchissions à la multitude des siècles passés et futurs, soit que pendant la nuit le ciel nous révèle dans leur réalité des mondes sans nombre, ou que l'immensité de l'univers comprime pour ainsi dire notre conscience : dans ce cas nous nous sentons amoindris jusqu'au néant ; comme individu, comme corps animé, comme phénomène passager de la volonté, nous avons la conscience de n'être plus qu'une goutte dans l'Océan, c'est-à-dire de nous évanouir et de nous écouler dans le néant. Mais en même temps, contre l'illusion de notre néant, contre ce mensonge impossible, s'élève en nous la conscience immédiate qui nous révèle que tous ces mondes n'existent que dans notre représentation ; ils ne sont que des modifications du sujet éternel de la pure connaissance ; ils ne sont que ce que nous sentons en nous-mêmes, dès que nous oublions l'individualité ; bref, c'est en nous que réside ce qui constitue le support nécessaire et indispensable de tous les mondes et de tous les temps. La grandeur du monde tout à l'heure nous épouvantait, maintenant elle réside sereine en nous-mêmes : notre dépendance à son égard est désormais supprimée ; car c'est elle à présent qui dépend de nous. – Cependant nous ne faisons point effectivement toutes ces réflexions ; nous nous bornons à sentir, d'une manière tout irréfléchie, que, dans un certain sens (la philosophie seule peut le préciser), nous ne faisons qu'un avec le monde, et que par suite son infinité nous relève, bien loin de nous écraser. C'est cette conscience encore toute sentimentale que les Oupanischads des Védas répètent sous tant de formes variées, et surtout dans cette sentence que nous avons citée plus haut : « Hæ omnes creaturæ in totum ego sum, et prætev me aliud ens non est. » [C'est moi qui suis toutes ces créatures dans leur totalité, et il n'y a pas d'autre être en dehors de moi.] (Oupnek'hat, vol. I, p. 122.) Il y a là un ravissement qui dépasse notre propre individualité ; c'est le sentiment du sublime.

ARTHUR SCHOPENHAUER - Le monde comme volonté et comme représentation (p.313).

Remerciements

Mes premiers remerciements vont sans hésitation à mes superviseurs Jonathan et Ludo, pour leur patience, leur bienveillance et leur complicité. Ils n'ont pas seulement été des mentors incroyables, mais ils sont également devenus des amis. Il est difficile d'écrire à quel point je leur suis reconnaissant. Bien qu'éprouvante, cette thèse fut très certainement l'expérience la plus enrichissante de ma vie et c'est entièrement à eux que je le dois. Ils m'ont également enseigné des compétences indispensables que je chérirai toute ma vie : Jonathan m'a appris les règles de la coinche lors d'un trajet en train alors que je n'y ai encore jamais joué et Ludo m'a permis de perfectionner ma technique du chasse-neige en ski, m'évitant une mort certaine.

Plus largement, je remercie tous les enseignants et superviseurs passés (physiciens ou pas), qui ont accepté de prendre de leur temps pour guider l'étudiant perdu mais passionné que j'étais et auprès de qui j'ai eu la chance d'apprendre. A ce sujet, je remercie également tous les étudiants à qui j'ai eu le plaisir d'enseigner à l'Université Paul Sabatier. Ils m'ont aidé à garder la passion qui m'anime même dans les moments les plus difficiles. Je leur souhaite à tous du bonheur et la réussite qu'ils souhaitent.

Pour leur soutien et leur nombreux conseils, je remercie François Boulanger et Vincent Guillet, c'est à eux que je dois ma compréhension de la poussière Galactique. Merci à Vincent également pour ses retours sur la thèse. Je remercie aussi Bruno Regaldo-Saint-Blancard qui m'a donné beaucoup de son temps pour me faire découvrir le monde merveilleux des scattering transform et Erwan Allys grâce à qui je dis scattering transform et plus wavelets, ainsi que Constant Auclair pour son calme à toute épreuve.

Special thanks to my mentors Jens Chluba and Aditya Rotti, who showed me all the secrets of the moment expansion and shared my excitement for the complex moments, all these thrilling new developments would have been impossible without them. Thanks also to Susan Clark and Brandon Hensley who always supported my work and with whom I shared enriching discussions.

From the side of the varying constant, my first thanks go to Nils Schöneberg who took a tremendous amount of his time to support my projects, without him, going so far would simply not have been possible. I would also like to thank Julien Lesgourgues, Alain Blanchard and Brahim Lamine who made our encounter possible. I also thank Carlos Martins who mentored me for more than five years now, regardless of the regularity of my confusing and over-enthusiastic interventions in the meetings. Thanks to my friend João, partner in crime, with whom I could share my passion for physics and music, and his family who hosted me in Porto as well as André, Patricia and Chris who made me discover this wonderful city

years ago. More generally, thanks to all the Φ in the sky student I had the chance to interact with : Catarina, Célia, Chloé, Francisco, Martim, Samuel and many more. Special thanks to Axel Lapel, the king of surf, and all the Euclid summer surfing school. Thanks also to Elsa and Richard and all the good friends of the Azores.

Regarding my work in *LiteBIRD*, I would like to thanks Hirokazu Ishino, Guillaume Patañchon and Giuseppe Puglisi for their supervision and guidance through the whole thesis. "Cimer bro" to my friend and task force duo Yusuke Takase. Overall, thanks to all the students of the Ishino lab for their hospitality, as well as Wang Wang and our discovery of Ume Shu. For all the good times and the great jokes I also thanks Samantha Stever and Eirik "Aradhya" Gjerløw.

Cette thèse n'aurait également pas pu aboutir sans mes incroyables co-bureaux : Jean-Sébastien, Louise, Audrey et Constant Fils-de-Rajon. Je m'excuse pour mes longues absences et les remercie du fond du cœur pour leur soutien. Pensée toute particulière pour Jean-Sébastien son amitié et nos soirées Halo et pizza (je pourrai dire que j'ai partagé le bureau de l'homme le plus stylé du monde). Plus largement merci à toute l'équipe MICMAC de m'avoir chaleureusement accueilli et en particulier à Isabelle Ristorcelli pour toute sa bienveillance et ses encouragements. De plus, merci à Isabelle et Josquin Errard d'avoir bien voulu assurer mon comité de suivi de thèse et à Sandrine Bottinelli d'avoir accepté d'être ma tutrice d'enseignements. De manière générale, j'ai pu trouver à l'IRAP des conditions de travail stimulantes dans lesquelles j'ai pu librement explorer tous mes projets en ne recevant que des encouragements bienveillants et des conseils avisés. Merci également aux stars du JWST : Oliver Bernstein pour son humour et ses conseils de Block theory et Ilane pour son café qui a nourri mon âme. Puisse le groupe des jeunes espoirs d'escalade de l'IRAP perdurer pour toujours. Je remercie également mon macbook, qui malgré toutes les épreuves que nous avons rencontré ensemble, a fait l'effort de ne pas mourir pendant la rédaction.

Many thanks to my rapporteurs Jean-Philippe Uzan and Marc-Antoine Miville-Deschénes who accepted to review this thesis and gave precious feedbacks to improve it. Thanks also to Nico and Carlo for trusting me and welcoming me to SISSA where I will be able to pursue this great adventure.

Je remercie bien sur tous mes amis, sans qui cette aventure n'aurait eu aucun sens. En particulier, merci à Bastien avec qui j'ai pu partager mon enthousiasme, qui a pu parfois frôler la folie. Il m'a apporté un soutien continu et indispensable pendant ces trois ans. Merci également à Robin pour tout ce que nous avons partagé, pour nos discussions interminables, les bons repas qu'il a cuisiné, les randonnées et surtout pour sa patience. Merci à tous les amis que je n'ai plus la chance d'avoir près de moi et avec qui j'ai quand même pu partager de très forts moments pendant ces trois ans : Adrien, Alexis, Arnaud, Babou, Djé, Ian et Emilie, Lou-Anne, Maxime, Momo, Mickaël, Tintin, Yann et Zoé. Merci également aux voisins ainsi qu'à Christophe et Virginie pour les nombreuses soirées et repas qui étaient autant de séances de réanimations pour ma coquille vide et épuisée. Merci également à mon cousin Benjamin et à sa compagne Carole.

A mes parents : Je vous aime du plus profond de mon coeur et cette thèse vous est dédiée. Elle représente l'accomplissement des 25 ans d'amour, de soutien et de richesse que vous m'avez apporté. Vous m'avez permis d'aller au bout de mes rêves et de devenir la personne que je voulais être. Merci plus que tout.

REMERCIEMENTS

Enfin, merci évidemment à ma petite Loona avec qui je partage ma vie depuis plus d'un an maintenant et qui accepte de me suivre à l'autre bout de l'Europe. Tu as toujours su me comprendre, nourrir ma curiosité et me soutenir dans les moments difficiles.

Je dédie également cette thèse à tous ceux qui ne sont plus là pour y assister, mais ont gardé une place privilégiée dans mon cœur : mon ami Miguel et mes grand-parents Rosine, Ginette et Roger.

Abstract

This thesis covers instrumental to theoretical considerations through data analysis revolving around the cosmic microwave background (CMB), on which our current understanding of modern cosmology is largely built. Contemporary challenges focus on its polarization signal, containing precious information about the very early phases of our Universe's history. However, the detection of this extremely faint signal requires the building of highly sensitive instruments as well as an unprecedented characterization of the polarized foreground signal from our Galaxy. In this direction, I contributed to the design optimisation of the future *LiteBIRD* satellite mission targeting the primordial B -modes, putatively induced by gravitational waves in the primordial plasma, signature of an inflationary phase in the first fractions of second after the birth of our Universe. As an active member of this collaboration, I contributed to the production and test of instrumental simulations and I investigated the optimization of its scanning strategy in order to mitigate the impact of far side lobe asymmetry on the science goal. Based on the challenge represented by such a sensitive mission, I strongly committed to the problem of component separation, investigating how to distinguish the CMB signal from the Galactic foregrounds. I investigated in great detail the *moment expansion* method, which allows to grasp the spectral complexity arising from the spatial variation of the physical conditions of emission within our Galaxy. I applied this method to the *LiteBIRD* mission, proving that moments provide a viable path in order to recover an unbiased value for the amplitude of the primordial B -modes, facing the challenge represented by the high sensitivity of the experiment. Furthermore, I developed the first formal generalization of the moment expansion to polarized signal: the *spin-moment* expansion, allowing for a novel and proper treatment of the geometrical properties of polarization. This new development is rich in physical insights and allows to connect the distribution of spectral parameters and magnetic field orientations to the consequences of averaging, as the spectral rotation of the total polarization angle. Following this direction at the E - and B -modes level, I further showed that new observable consequences can be derived and modeled by the spin-moment expansion as the frequency dependence of the foreground E/B ratio and distortions of the EB signal. These effects – signature of the variation of the physical conditions throughout our Galaxy – will have to be properly modeled in the quest for inflation or a non zero primordial EB correlation, induced by the presence of parity violating mechanism in the early Universe, known as cosmic birefringence. In addition to this main contribution, I also briefly explored the possibility to use *scattering transform* to grasp together the spatial and the spectral statistical properties of polarized dust emission and produce multi-frequency synthesis and denoising. In parallel, I led other significant developments related to the most fundamental aspects of our physical theories which can be probed using cosmological observables such as the CMB. By investigating the stability of our

fundamental constants on cosmological time scales, I provided the latest to date constraints on the phenomenological *Bekenstein* models and the string inspired *runaway dilaton* models in which the fine structure constant – quantifying the strength of the electromagnetic interaction – varies through cosmic history. In both models, the constraints are so tight that the expected values for the parameters are excluded. Any theory beyond our standard model of particle physics will have to account for the observed stability of the fundamental constants. These works led to the development of a version of the CLASS Boltzmann solver publicly available which allows for time variations of the fine structure constant.

Résumé

Cette thèse couvre des aspects instrumentaux et théoriques en passant par l'analyse de données, tous liés au fond diffus cosmologique (CMB), sur lequel notre compréhension moderne de la cosmologie est largement fondée. Les défis contemporains se concentrent sur son signal polarisé, contenant des informations précieuses sur les premières phases de l'histoire de notre Univers. Cependant, la détection de ce signal de faible intensité demande la construction d'instruments extrêmement sensibles ainsi qu'une caractérisation sans précédent des émissions polarisées d'avant-plans de notre Galaxie. J'ai ainsi contribué à l'optimisation de la future mission satellite *LiteBIRD* ciblant les modes-*B* primordiaux, signature de la présence d'ondes gravitationnelles dans le plasma primordial laissées par une phase d'inflation dans les premières fractions de seconde suivant la naissance de notre Univers. En tant que membre actif de la collaboration, j'ai contribué à la production et au test de simulations instrumentales ainsi qu'à l'optimisation de la scanning strategy afin de mitiger l'impact de l'asymétrie des far side lobes sur les objectifs scientifiques.

Basé sur le défi représenté par une mission si sensible, je me suis fortement investi sur la problématique visant à séparer le signal du CMB de celui de notre Galaxie. J'ai exploré en grand détail *l'expansion en moments*, une méthode permettant de modéliser la complexité spectrale émergeant de la variation spatiale des propriétés physiques à l'origine de l'émission du signal émis par notre Galaxie. J'ai appliqué cette méthode à *LiteBIRD*, prouvant que l'expansion en moments fournit une direction viable pour retrouver une valeur non biaisée de l'amplitude des modes-*B* primordiaux. J'ai ensuite développé la première généralisation formelle de cette méthode pour le signal polarisé : l'expansion en *spin-moments*, permettant un traitement des propriétés géométriques uniques à la polarisation. Ce nouveau développement est riche en interprétations physiques et relie les distributions des paramètres spectraux et des orientations du champ magnétique avec les conséquences obtenues lorsqu'on les moyenne telle que la dépendance spectrale de l'angle total de polarisation. Poursuivant cette direction au niveau des modes-*E* et -*B*, je montre que de nouvelles conséquences observables peuvent être prédites et modélisées par l'expansion en spin-moments, telles que la dépendance en fréquence du rapport *E/B* et les distorsions du signal *EB* des avant-plans Galactiques. Ces effets devront être proprement traités en quête des signaux laissés par l'inflation ou par la biréfringence cosmique, induite par la présence de mécanisme violent la parité dans l'Univers primordial. En plus de cette contribution principale, j'explore brièvement la possibilité d'utiliser le *scattering transform* pour modéliser conjointement la complexité statistique fréquentielle et spatiale de l'émission polarisée de la poussière pour produire des synthèses et des débruitages multifréquences.

En parallèle, j'ai mené d'autres développements concernant les aspects les plus fondamentaux

de nos théories physiques pouvant être sondés par les observables cosmologiques telles que le CMB. En investiguant la stabilité des constantes fondamentales sur les échelles de temps cosmologiques, je dérive les dernières contraintes en date sur les modèles de *Bekenstein* et du *runaway dilaton* dans lesquels la constante de structure fine – quantifiant la force de l’interaction électromagnétique – peut varier au cours de l’évolution cosmique. Pour les deux modèles, les contraintes sont si resserrées que les valeurs attendues pour les paramètres sont exclues. Toute théorie au-delà du modèle standard de la physique des particules devra alors pouvoir rendre compte de la stabilité observée des constantes fondamentales. Ces travaux ont conduit au développement d’une version publique du Boltzmann solver code CLASS incluant la variation temporelle de la constante de structure fine.

Publications associated to this thesis

1. Schöneberg et al. (2023). News from the Swampland – Constraining string theory with astrophysics and cosmology. *JCAP* 2023(10):039. Preprint available at [arXiv:2307.15060](https://arxiv.org/abs/2307.15060).
2. Fuskeland et al. (2023). Tensor-to-scalar ratio forecasts for extended LiteBIRD frequency configurations. *A&A* 676 A42. Preprint available at [arXiv:2302.05228](https://arxiv.org/abs/2302.05228).
3. Vacher et al. (2023c). Runaway dilaton models: improved constraints from the full cosmological evolution. *Phys.Rev. D* 107.104002. Preprint available at [arXiv:2301.13500](https://arxiv.org/abs/2301.13500).
4. Vacher et al. (2023a). Frequency dependence of the thermal dust E/B ratio and EB correlation: insights from the spin-moment expansion. *A&A* 672, A146. Preprint available at [arXiv:2210.14768](https://arxiv.org/abs/2210.14768).
5. Régaldo-Saint Blancard et al. (2023). Generative Models of Multi-channel Data from a Single Example – Application to Dust Emission. *ApJ*:10.3847/1538-4357/aca538. Preprint available at [arXiv:2208.03538](https://arxiv.org/abs/2208.03538).
6. Ritacco et al. (2023). Dust polarization spectral dependence from Planck HFI data. Turning point on CMB polarization foregrounds modelling. *A&A* 660 A163. Preprint available at [arXiv:2206.07671](https://arxiv.org/abs/2206.07671).
7. LiteBIRD Collaboration et al. (2023). Probing Cosmic Inflation with the LiteBIRD Cosmic Microwave Background Polarization Survey. *PTEP* Issue 4, 042F01. Preprint available at [arXiv:2202.02773](https://arxiv.org/abs/2202.02773).
8. Hubmayr et al. (2022). Optical Characterization of OMT-Coupled TES Bolometers for LiteBIRD. *Journal of Low Temperature Physics*.
9. Vacher et al. (2023b). High precision modeling of polarized signals: Moment expansion method generalized to spin-2 fields. *A&A* 669, A5. Preprint available at [arXiv:2205.01049](https://arxiv.org/abs/2205.01049).
10. Vacher et al. (2022b). Constraints on extended Bekenstein models from cosmological, astrophysical, and local data. *Phys.Rev. D* 106,083522. Preprint available at [arXiv:2207.03258](https://arxiv.org/abs/2207.03258).
11. Hasebe et al. (2022). Sensitivity Modeling for LiteBIRD. *Journal of Low Temperature Physics*.
12. Vacher et al. (2022a). Moment expansion of polarized dust SED: a new path towards

- capturing the CMB B -modes with LiteBIRD. A&A 660, A111. Preprint available at [arXiv:2111.07742](https://arxiv.org/abs/2111.07742).
- 13. Vielva et al. (2022). Polarization angle requirements for CMB B -mode experiments. Application to the LiteBIRD satellite. JCAP 2022(04):029. Preprint available at [arXiv:2202.01324](https://arxiv.org/abs/2202.01324).
 - 14. Krachmalnicoff et al. (2022). In-flight polarization angle calibration for LiteBIRD: blind challenge and cosmological implications. JCAP 2022(01):039. Preprint available at [arXiv:2111.09140](https://arxiv.org/abs/2111.09140).
 - 15. Martins & Vacher (2019). Astrophysical and local constraints on string theory: runaway dilaton models. Phys.Rev. D 100, 123514. Preprint available at [arXiv:1911.10821](https://arxiv.org/abs/1911.10821).

Contents

Remerciements	iii
Abstract	vii
Résumé	ix
Publications associated to this thesis	xi
Table of Contents	xvii
1 Avant-propos (Français)	1
2 Foreword	5
I General introduction	
From the theoretical building blocks to the CMB and its foregrounds	9
3 Modern cosmology: the Standard models	11
3.1 Introduction	11
3.2 Building our standard models from Geometry and symmetries	12
3.2.1 Gravitation and general relativity	13
3.2.2 Gauge theories: the geometrization of particle physics	20
3.3 The Λ -CDM model	22
3.3.1 Cosmological principle and the FLRW metric (i)	23
3.3.2 The components of the Universe (ii)	25
3.3.3 Fundamental equations of cosmology (iii)	27
3.3.4 Perturbation theory in a nutshell	27
3.4 6 parameters to describe the Universe.	29
3.4.1 Cosmological probes	29
3.4.2 The picture so far	31
3.5 A brief history of the Universe as we know it	31
4 Puzzles and missing pieces of our standard models	35
4.1 Late and early tensions	35
4.1.1 Puzzles in the late universe: the dark sides	35
4.1.2 Puzzles in the early Universe	37

4.2	Are there new entities awaiting out there to be discovered?	40
4.2.1	Going beyond GR and Λ -CDM	40
4.2.2	Scalar fields	42
4.3	A scalar field for each puzzle	44
4.3.1	Quintessence and dynamical dark energy	44
4.3.2	Parity violating scalar field, axions and the dark side	44
4.3.3	The inflaton	45
5	Signal from the cosmic origin: the cosmic microwave background	51
5.1	The CMB radiation	51
5.1.1	Historical context of discovery	52
5.1.2	Recombination and the last scattering surface	52
5.1.3	The CMB: Overview of spectral and statistical properties	53
5.2	The physical origin of the CMB anisotropies	56
5.2.1	The Dipole: an open window on our location in the local Universe .	56
5.2.2	Primordial temperature anisotropies	56
5.2.3	Polarization anisotropies	57
5.2.4	Secondary anisotropies	62
5.3	Statistical properties of the CMB anisotropies	64
5.3.1	TT spectrum	65
5.3.2	Polarization spectra	66
5.4	Measuring the CMB	70
5.4.1	CMB science so far: the era of precision cosmology	70
5.4.2	Contemporary and future missions	70
5.5	CMB and the cosmological parameters	72
5.5.1	Probing Λ -CDM on the last scattering surface	72
6	Polarized light from the interstellar medium	75
6.1	Impact of polarized foregrounds on CMB studies	75
6.2	The interstellar medium	78
6.3	The polarized signals of the ISM in Microwave	80
6.3.1	Tools to describe the polarized light of the ISM	80
6.3.2	Synchrotron emission	81
6.3.3	Cosmic dust	83
6.4	Component separation methods	90
6.5	The PySM models	91
II	Personal contributions	
	From the instrument to the fundamental physics through our Galaxy	93
7	Optimizing the design of the <i>LiteBIRD</i> satellite	95
7.1	The <i>LiteBIRD</i> satellite	95
7.1.1	Scientific objectives	96
7.1.2	The instrumental design	98
7.2	The Scanning strategy	100
7.3	From side lobe asymmetry to scanning optimization	101

7.4	Additional personal contribution to the <i>LiteBIRD</i> collaboration	106
8	Towards an accurate modeling of the spectral and spatial properties of complex foreground polarized light	109
8.1	Spatially varying spectral parameters and the problem of SED distortions .	110
8.2	Beyond canonical SEDs: Moment expansion for intensity signal	112
8.2.1	A pedagogical introduction: summing two power laws	112
8.2.2	Moments expansion in intensity in their full glory	115
8.3	Applying moment for component separation: application to <i>LiteBIRD</i> . . .	117
8.3.1	Context: The challenge of component separation with <i>LiteBIRD</i>	117
8.3.2	The paper: Objectives and results	118
8.3.3	Impact, limits and outlooks	123
8.4	Generalization to polarization: Spin-moments expansion	124
8.4.1	Context: A second pedagogical introduction: summing two power laws, again	124
8.4.2	The paper: Objectives and results (in their full glory)	128
8.4.3	Impact, limits and and outlooks	131
8.5	Applying the spin-moments at the <i>E</i> - and <i>B</i> -modes level	132
8.5.1	Context: The indispensable <i>E</i> - and <i>B</i> -modes and their distortions .	132
8.5.2	The paper: Objectives and results	133
8.5.3	Impact, limits and outlooks	138
8.6	Beyond Gaussianity: The Wavelets	138
8.6.1	Coupling between scales and the problem of non gaussianities	138
8.6.2	The scattering transform and non-Gaussian signals	139
8.6.3	Synthesis, denoising and wavelet phase harmonics	142
8.6.4	Personal contribution	144
9	Explaining the values of our standard models' fundamental constants	147
9.1	The fundamental constants and their possible variations	148
9.1.1	What is a fundamental constant?	148
9.1.2	Dimensional and dimensionless constants	151
9.1.3	Gauge couplings and structure constants	154
9.1.4	Phenomenology of varying gauge couplings	157
9.1.5	Varying couplings and gravity	159
9.2	The fine structure constant, its astrophysical impacts and the corresponding observables	161
9.3	Building a modified Boltzmann solver to quantify the impact of varying α cosmology	166
9.3.1	The need and the development of a new tool	166
9.3.2	An illustration: the impact of varying constants on recombination and the CMB	167
9.4	Constraining the Bekenstein model(s)	169
9.4.1	Context: Zoology of the Bekenstein model(s)	169
9.4.2	The paper: Objectives and results	171
9.5	String theories and varying coupling	174
9.5.1	Overview of string theory	174
9.5.2	Dilaton field, coupling to gravity and varying couplings	177

9.6	Constraining the runaway dilaton model	179
9.6.1	Context: The runaway dilaton model(s)	180
9.6.2	The paper: Objectives and results	182
9.6.3	Impact, limits and outlooks	184
9.7	Varying alpha, late and early dark energy	185
9.7.1	Is dark energy related to varying α ?	185
9.7.2	Personal contributions on this topic	186
10 Conclusion and perspectives		189
10.1	Systematic effects for the <i>LiteBIRD</i> mission	189
10.2	Polarized foregrounds	190
10.2.1	The moment expansion	190
10.2.2	Wavelets Scattering transform	191
10.3	Varying constants	191
10.4	A final word	192
11 Conclusion et perspectives (Français)		193
11.1	Effets systématiques pour la mission <i>LiteBIRD</i>	193
11.2	Avant-plans polarisés	194
11.2.1	L'expansion en moments	194
11.2.2	Wavelets Scattering transform	195
11.3	Variation des constantes	195
11.4	Le mot de la fin	196
A A differential geometric overview of the standard models		199
A.1	General relativity	199
A.1.1	Preliminary definitions and motivation	199
A.1.2	The geometrization of gravity II	201
A.2	High energies: particle physics and gauge theories	202
A.2.1	Preliminary definitions and motivation	202
A.2.2	Gauge theories	204
B The mathematical description of polarized light		209
B.1	The challenge of polarized light	209
B.2	The local description of polarized light	210
B.2.1	The power of the Helmholtz decomposition	210
B.2.2	The light wave	210
B.2.3	The Stokes parameters, polarization spinor and polarization tensor .	211
B.3	The polarized signal over the flat sky	214
B.4	The polarized signal over the curved sky	215
B.4.1	The spherical harmonics	215
B.4.2	E - and B -modes on curved sky	216
B.5	E - and B - modes from ladder operators	217
B.6	The Power spectra	219
C Quantifying the asymmetry of the scanning strategy: first attempts		221
C.1	Kolmogorov-Smirnov (KS) test	221

CONTENTS

C.2 Hit-matrix	224
C.3 Beam smoothing power	225
List of Figures	233
List of Tables	235
Main abbreviations and mathematical notations	237
Bibliography	275
D Papers	277
D.1 A&A 660, A111	278
D.2 A&A 669, A5	301
D.3 A&A 672, A146	317
D.4 PhysRevD.106.083522	331
D.5 PhysRevD.107.104002	346

A mes parents

1

Avant-propos (Français)

La présente thèse reflète le travail que j'ai réalisé ces trois dernières années. J'ai eu la chance de couvrir une variété de sujets allant de la physique des particules à la science Galactique, faisant appel à des considérations théoriques et observationnelles demandant une large gamme d'expertises. Tous ces sujets orbitent autour d'une observable commune : le fond diffus cosmologique (ou cosmic microwave background (CMB)), qui représente la plus ancienne lumière observable dans notre Univers, fenêtre ouverte sur l'ensemble du ciel donnant sur nos origines cosmiques. Cette lumière primordiale n'est pas uniquement caractérisée par une intensité en chaque point de la sphère céleste, mais également par une direction d'oscillation privilégiée : sa polarisation. Alors que les propriétés statistiques du CMB ont désormais été cartographiées en intensité avec une grande précision, la majorité de l'information cachée dans sa polarisation – plus délicate à mesurer – représente aujourd'hui un territoire inconnu. Les enjeux d'une telle mesure sont élevés, car une caractérisation fine de ce signal polarisé pourrait permettre de mieux comprendre les premières fractions de seconde suivant la naissance de notre Univers ainsi que la physique des particules impliquée dans les conditions d'énergies extrêmes en jeu à cette époque, bien au-delà de la portée de nos meilleurs accélérateurs de particules. En particulier, la détection d'un motif spécifique dans la polarisation du CMB, connu sous le nom de modes-*B* primordiaux, indiquerait la présence d'un fond d'ondes gravitationnelles baignant l'entièreté du plasma primordial lors de l'émission du CMB. De telles ondes gravitationnelles pourraient être le reliquat d'une phase d'expansion extrêmement violente, *l'inflation cosmique*, induite par un nouveau champ fondamental à l'origine de toutes les particules présentes dans notre Univers. De plus, la détection du signal connu sous le nom de corrélation *EB* dans le CMB serait la signature directe de l'existence d'un mécanisme brisant la symétrie de parité dans l'Univers jeune : la *biréfringence cosmique*. Comme l'inflation, ce mécanisme pourrait être induit par un nouveau champ fondamental, *l'axion*, apparaissant naturellement des propriétés de l'interaction nucléaire forte et/ou en tant que membre des théories alternatives au-delà de notre modèle standard, comme la théorie des cordes.

Cependant, cartographier la polarisation du CMB sur l'ensemble du ciel s'accompagne de défis techniques et instrumentaux majeurs et sans précédent. *LiteBIRD* est une mission satellite japonaise ambitieuse pensée pour faire face à ces défis. Pour cet instrument, chaque aspect technique doit être contrôlé et optimisé pour maximiser la précision à laquelle les

1. AVANT-PROPOS (FRANÇAIS)

modes-*B* primordiaux peuvent être mesurés. Comme les télescopes seront embarqués dans un satellite, il ne sera plus possible d'interagir avec eux après le début de la mission, rendant cette tâche particulièrement délicate. En tant que membre de la collaboration *LiteBIRD*, j'ai contribué à la production et au test de simulations pour l'instrument. Je me suis de plus concentré sur l'optimisation de la *scanning strategy*, choisissant l'ordre et le rythme auxquels les différents télescopes observeront différentes régions du ciel. Ce travail est crucial, car un choix optimal de la scanning strategy apporte la redondance et la symétrie nécessaire à la réduction majeure de certains effets systématiques tout en augmentant le temps accordé à la calibration instrumentale.

Néanmoins, une mission sensible et optimisée pour détecter le signal du CMB sera également sensible à la complexité des autres signaux micro-ondes du ciel. A cause de la position inextricable de notre système solaire dans un bras spiral de la Voie Lactée, toute observation du CMB contiendra inévitablement le signal astrophysique produit par notre propre Galaxie, surimposé à celui-ci. Ainsi, il ne sera pas possible d'extraire les précieuses informations cosmologiques du CMB sans une compréhension fine des émissions d'avant-plans Galactiques. L'émission polarisée complexe du milieu interstellaire (interstellar medium (ISM)) de notre propre Galaxie est largement dominante sur le faible signal du CMB et elle possède un comportement complexe émergeant de la riche intrication de nombreux processus physiques sous-jacents. Le couplage entre turbulence et champs magnétiques donne une dynamique très complexe aux fluides astrophysiques, conduisant à la formation des étoiles et permettant une chimie complexe, probablement nécessaire à l'émergence de la vie organique. Des particules chargées légères et de grains de poussière dans l'ISM influencent cette dynamique tout en étant entraînés par celle-ci et émettent de la lumière hautement polarisée dans le domaine micro-onde. Comprendre ce signal et fournir des moyens pour le modéliser est ainsi conjointement crucial pour la cosmologie et la science Galactique, représentant l'enjeu principal de la présente thèse. En particulier, je me concentrerai sur la complexité émergente de l'inévitable effet de moyenne sur différentes conditions d'émissions. En effet, de part la physique complexe de l'ISM, les propriétés locales comme la composition, la température ou l'orientation des champs magnétiques changent en 3 dimension à travers la Galaxie. Toute observation astrophysique se présentera alors comme un mélange complexe de signaux venant de régions différentes, associés à des propriétés différentes, phénomène que j'appelle le *mixing*. J'explorerai en grand détails la méthode de *l'expansion en moments*, qui permet de capturer minimalement et efficacement les effets du mixing. J'appliquerai cette méthode au satellite *LiteBIRD* ciblant les modes-*B* primordiaux et je démontrerai que les moments fournis sont une direction viable pour affronter le défi représenté par les avant-plans Galactiques. Je présenterai ensuite la première généralisation formelle de l'expansion en moment à la polarisation. Ce nouveau formalisme, que j'ai appelé l'expansion en *spin-moments*, se révèlera puissante, permettant de connecter les propriétés de la poussière (paramètres spectraux et champs magnétiques) aux conséquences du mixing, comme la dépendance en fréquence de l'angle de polarisation. Propageant cette expansion au niveau des modes-*E* et -*B*, j'utiliserai l'expansion en spin-moments pour inférer et modéliser de nouvelles conséquences du mixing comme la dépendance en fréquence du ratio *E/B* des avant-plans et les différents comportements spectraux des spectres en puissance angulaire *EE*, *BB* et *EB*. Ces conséquences auront des implications lourdes pour l'observation du CMB en quête des modes-*B* primordiaux ou de la biréfringence cosmique. Cependant, la complexité des avant-plans n'est pas seulement spectrale, mais présente aussi des caractéristiques spatiales complexes émergeant

de la turbulence, comme les filaments. Pour capturer ces propriétés statistiques, je vais présenter le *scattering transform*, une nouvelle approche prometteuse inspirée de l'analyse de données, qui permet de prendre une description puissante de la complexité spatiale des signaux d'avant-plans. Pendant cette thèse, j'ai contribué aux extensions pionnières de ce formalisme aux observations multifréquences. Ce développement ambitieux pourrait permettre de capturer simultanément la complexité spectrale et spatiale des avant-plans dans un cadre unifié. Dans le futur, une synergie de ce formalisme avec les spin-moments pourrait certainement être profitable.

Il est ainsi urgent de faire face aux défis représentés par les instruments et les avant-plans afin de pouvoir lever le voile sur nos origines cosmiques. Cependant, les enjeux d'une telle enquête vont bien au-delà de l'Univers primordial et rayonnent sur la cosmologie et la physique fondamentale dans son ensemble. Aujourd'hui, le CMB représente la plus précieuse source d'information sur la dynamique de notre Univers. Aussi loin que nous le sachions, cette dynamique est directement dictée par le contenu en particules de l'Univers et les interactions entre ces particules. Le CMB fournit alors une rare sonde de la physique fondamentale et de ses limites. En conjonction avec d'autres sondes, il peut être utilisé pour contraindre une variété de modèles physiques au-delà de nos modèles canoniques de la gravité et de la physique des particules. Dans cette thèse, je vais remettre en question ces modèles au plus près de leurs fondations, en étudiant si la valeur des constantes fondamentales de la nature telle qu'elles sont mesurées sur Terre reste la même dans les régions les plus distantes de l'espace et dans les époques les plus jeunes de l'histoire de notre Univers. Alors que nos théories contemporaines ne peuvent pas expliquer la valeur de ces constantes, détecter leurs variations serait une signature directe de nouvelle physique à l'origine de ces variations, ouvrant une porte vers une possible explication. Je me concerterai sur la constante de structure fine, quantifiant la force de l'interaction électromagnétique. J'explorerai deux modèles de champ scalaires dans lesquels cette constante devient une entité dynamique : un modèle phénoménologique construit à partir de considérations de symétries, le *modèle de Bekenstein* et un modèle émergent de la théorie des cordes, le *runaway dilaton*. En confrontant ces modèles avec une grande diversité de données indépendantes, je dériverai les dernières contraintes en date sur leurs espaces de paramètres, excluant leurs valeurs naturelles. D'après ces résultats, il apparaît que n'importe quel modèle cherchant à unifier la physique, comme la théorie des cordes, devra pouvoir justifier comment la constante de structure fine peut rester si stable à travers l'histoire cosmique.

L'ensemble de ces sujets seront abordés dans l'ordre suivant : la partie I donne une introduction générale aux sujets principaux de cette thèse. Je les présenterais en cherchant à mettre en avant le contexte sous-jacent à mes intérêts de recherche, les incroyables accomplissements déjà effectués ainsi que les nombreux défis devant encore être surmontés. Dans le chapitre 3, je donnerai une revue brève de notre compréhension des lois les plus fondamentales de la physique. Je présenterai ensuite comment inférer l'histoire de notre Univers avec une précision saisissante à partir de ces lois. Dans le chapitre 4, je discuterai certains des puzzles et problèmes observationnels et théoriques contemporains de nos modèles standards. Cette présentation soulignera le besoin de nouveaux phénomènes physiques et/ou de nouvelles entités, encore non découvertes, afin de construire une image cohérente des observations cosmologiques. Dans le chapitre 5, je présenterai le CMB, ses propriétés et la possibilité d'en extraire des informations sur la cosmologique et la nouvelle physique.

1. AVANT-PROPOS (FRANÇAIS)

Dans le chapitre 6, j'introduirai la physique complexe et riche des avant-plans Galactiques polarisés et les procédures standards pour les modeler et les retirer du CMB.

La partie II sera dédiée à mes contributions à ces sujets variés. Partant de ce qui a été achevé en partie I, j'irai de l'instrument jusqu'aux théories qu'il permet de tester, à travers l'émission complexe de notre Galaxie. M'appuyant sur les informations présentées dans l'introduction générale, chaque chapitre est auto-suffisant et largement indépendant des autres. Dans le chapitre 7, je présenterai la mission satellite *LiteBIRD*, offrant l'opportunité pour discuter les défis instrumentaux auquel elle doit faire face afin de cartographier les anisotropies polarisées les plus fines du CMB. Je présenterai ma contribution à la collaboration durant ces trois dernières années, avec un accent particulier sur l'optimisation de la scanning strategy. Dans le chapitre 8, j'introduirai la modélisation de la dépendance en fréquence des avant-plans Galactiques polarisés donnée par l'expansion en moments. Cette méthode apparaissant souvent comme technique et difficile d'approche, j'apporterai une intérêt tout particulier à sa démystification à l'aide d'exemples pédagogiques. Je présenterai ensuite son application réussie pour la séparation de composante paramétrique avec le satellite *LiteBIRD*, discutant ses forces et ses faiblesses. De plus, je présenterai l'expansion en spin-moments. Pour cela, je bâtirai sur notre compréhension de l'expansion en moments en intensité, donnant à nouveau la priorité à la pédagogie. A la suite de cette présentation, je propagerai cette expansion aux modes-*E* et -*B* et en discuterai les conséquences. Pour conclure ce chapitre, je présenterai brièvement ma contribution à l'extension du scattering transform aux observations multifréquences. Dans le chapitre 9, je montrerai que les valeurs des constantes fondamentales de nos modèles standards représentent les "maillons faibles" de nos théories physiques et fournissent ainsi des observables favorables à la recherche de nouvelle physique. Après une revue de l'origine théorique, de l'impact et des conséquences observationnelles de la constante de structure fine, je présenterai mes contributions fournissant les dernières contraintes en date sur les modèles de Bekenstein et du runaway dilaton. Je conclurai par une présentation de mes autres contributions liées à ces sujets, principalement en lien avec l'énergie noire.

Enfin, je présenterai un résumé et mes conclusions dans le chapitre 10. Les perspectives ouvertes pour de futures recherches y seront également discutées.

En compléments, une brève présentation technique de la relativité générale et de notre modèle de la physique des particules est donnée en Appendice A, désirable afin de mieux comprendre les conséquences d'une variation des constantes fondamentales. Une présentation des outils mathématiques permettant la description de la lumière polarisée est donnée en Appendice B, détaillant les fondations théoriques et les interprétations physiques des paramètres de Stokes, de la décomposition en modes-*E* et -*B* et de la décomposition en harmoniques sphériques. Enfin, un complément présentant certains outils utilisés pour optimiser la scanning strategy de l'instrument *LiteBIRD* est donné en Appendice C. Ces annexes sont suivies d'une liste des figures, tables et abréviations. Les papiers écrits en premier auteur durant cette thèse ont été reproduits à la toute fin du manuscrit, en Appendice D.

2

Foreword

The present thesis reflects my work during the past three years. I had the chance to cover a variety of topics ranging from particle physics to Galactic science, involving theoretical to observational considerations and requiring different expertise. These topics are revolving around a common observable given by the cosmic microwave background (CMB), which represents the oldest observable light in our Universe and is thus an open window on our cosmic origins over the entire sky. This primordial light is not only characterized by an intensity given at every point of the celestial sphere, but also by a preferred direction of oscillation: a polarization. While the statistical properties of the CMB have now been mapped in intensity with great accuracy, most of the information hidden in its polarization – more delicate to measure – remains today an uncharted territory. The stakes of such a measurement are high, as an accurate characterization of this polarized signal would shed some light on the very first fractions of second after the birth of our Universe and the particle physics involved in the extreme energy conditions at play during this epoch, far beyond the reach of our best particle accelerators. In particular, the detection of a specific polarization pattern in the CMB, the primordial *B*-modes, would indicate the presence of a significant gravitational wave background bathing the entire primeval plasma at the time of the CMB emission. Such gravitational waves would be the leftover of an extreme phase of primordial expansion, *cosmic inflation*, induced by a new fundamental field at the origin of all the particles present in our Universe. Additionally, the detection of a so-called *EB* correlation in the CMB signal would be the direct signature of a mechanism breaking parity symmetry in the early Universe: *cosmic birefringence*. As inflation, this mechanism could also be induced by a new fundamental field, the *axion*, naturally arising from properties of the strong nuclear force or as members of alternative theories beyond our standard models, as string theory.

However mapping the CMB polarization over the whole sky comes with major and unprecedented technical and instrumental challenges. *LiteBIRD* is an ambitious Japanese satellite mission designed to overcome these challenges. For this instrument, every single technical aspect must be controlled and optimized in order to maximize the accuracy at which the primordial *B*-mode signal can be recovered. As the telescopes will be boarded on a satellite, it will not be possible to interact with them anymore after the start of the mission, making this task especially delicate. As a member of the *LiteBIRD* collaboration, I contributed to the production and test of simulations for the instrument. I further focused on the optimiza-

2. FOREWORD

tion of the *scanning strategy*, choosing in which order and at which pace the telescopes will observe the different regions of the sky. This work is crucial, as an optimal choice of scanning strategy can bring redundancy and symmetry which greatly suppress some systematic effects and increase the time allowed for instrumental calibration.

Nevertheless, the more sensitive and optimized a mission will be to detect the CMB signal, the more it will also be sensitive to the complexity of the other microwave signals in the sky. Due to the inextricable location of our solar system within the spiral arm of the Milky way, any CMB observation will also unavoidably contain the superimposed astrophysical signal produced by our own Galaxy. As such, it is simply not possible to extract the precious cosmological information from the CMB signal without a fine understanding of this Galactic foreground emission. Indeed, the complex polarized emission of the interstellar medium (ISM) of our Galaxy is largely dominant over the faint CMB and it possesses a rich behavior emerging from an intricate underlying physics. The coupling between turbulence and magnetic fields within our Galaxy indeed induces a very complex dynamics, giving birth to stars and allowing for complex chemistry, most certainly at the origin of organic life. Light charged particles and dust grains drive and are carried by this dynamics and emit strongly polarized light in the microwave domain. Understanding this signal and providing ways to model it is hence crucial both for cosmology and for Galactic science and it will represent the main development of this thesis. In particular, I will focus on the complexity arising from the unavoidable averaging over different physical conditions of emission. Indeed, from the complex physics of the ISM, local properties as composition, temperature or magnetic field orientations are expected to change across the 3D Galaxy. Any astrophysical observation will hence present itself as a complex mixture of signals coming from different regions and associated with different properties. I refer to this phenomenon as *mixing*. I will explore in great details the *moment expansion* method, which allows to grasp minimally and powerfully the effects of mixing. I will apply this method to the incoming *LiteBIRD* satellite mission, designed to target the primordial *B*-modes, showing that the moments provide a viable path to face the foregrounds challenge. I will then present the first formal generalization of the moment expansion formalism to polarization. This new formalism, which I named the *spin-moment* expansion, will reveal itself to be powerful as it allows to connect the dust properties (spectral parameters and magnetic fields) to the consequences of the mixing, as the frequency dependence of the polarization angle. Propagating this expansion at the *E*- and *B*-modes level, I will use the spin-moment expansion to infer and model new consequences of mixing as the frequency dependence of the foreground *E/B* ratio and the different behavior of the *EE*, *BB* and *EB* angular power-spectra. These consequences will have heavy implications for CMB observation in the quest for primordial *B*-modes and cosmic birefringence. However, the complexity of foregrounds is not only spectral, but also presents complicated spatial features emerging from turbulence, as filaments. In order to grasp these statistical properties, I will present the *scattering transform*, a promising new approach inspired from data analysis, which can powerfully tackle the spatial complexity of the foreground signal. During this thesis, I contributed to the pioneering extensions of this formalism in order to deal with multi-frequency observations. This ambitious development could make it possible to tackle both spectral and spatial complexity of the foregrounds within the same framework. In the future, a synergy of this formalism with the spin-moments might very well be profitable.

Facing the instrumental and the foreground challenges are thus urgent matters to be tackled

in order to investigate our cosmic origins. However, the stakes of such an inquiry goes way beyond the primordial Universe and radiate on cosmology and fundamental physics as a whole. Today, the CMB represents the most precious source of information about our Universe's dynamics. As far as we know, this dynamics is directly dictated by the Universe's particle content and the interaction between these particles, such that the CMB also provides a rare probe of this fundamental physics and its limits. In conjunction with other probes, it can be used to constrain a variety of physical models beyond our canonical models of gravity and particle physics. In this thesis, I will question these models at their very basis, by investigating whether the values of the fundamental constants of nature as we measure them on Earth remain unchanged in the most distant regions of space and in the earliest epochs of our Universe's history. While our current theories can not explain the values of these constants, detecting their variation would be a direct signature for new physics driving their dynamics and a door open towards a possible explanation of their values. I will focus on the fine structure constant, quantifying the strength of the electromagnetic force and promote it to a dynamical entity in two models of scalar fields: a phenomenological model built from symmetry considerations, the *Bekenstein model* and a model emerging from string theory, the *runaway dilaton* model. By confronting them with a large variety of independent datasets, I will derive the latest to date constraints on the parameter spaces of these models, excluding their natural values. From these results, it appears that any model attempting a unification of physics, as string theory, will have to justify how the fine structure constant can remain so stable throughout cosmic history.

All these topics will be discussed as follows: Part. I provides a general introduction of the main topics covered in this thesis. I will present them with a particular care on providing the big picture lying behind my research interests, the incredible accomplishments already achieved as well as the numerous challenges remaining to be faced. In Chap. 3, I will briefly review our current understanding of the most fundamental laws of physics. I will further present how to infer our Universe's history with an outstanding accuracy from these laws. In Chap. 4, I will highlight some of the contemporary observational and theoretical puzzles of our standard models. They will stress the need for new physical phenomena and/or new entities, undiscovered yet, in order to build a consistent picture of the cosmological observations. In Chap. 5, I will present the CMB radiation, its properties and the possibilities to extract cosmological information and new physics from it. In Chap. 6, I will introduce the complex and rich physics of the Galactic polarized foregrounds to the CMB and the standard procedures in order to model and remove them.

Part II will be dedicated to my contributions on these various topics. Starting from what has been achieved in Part I, I will then go from the instrument back to the theories that can be tested with it, observed through our complex Galaxy. Relying on the information presented in the general introduction, all the chapters are self-contained and largely independent from one another. In Chap. 7, I will present the *LiteBIRD* satellite mission. This will be the opportunity to discuss the instrumental challenges it has to face in order to map the faintest anisotropies of the polarized CMB signal. I will present my contribution to the collaboration in this regard in the past three years, with a focus on the optimization of the scanning strategy. In Chap. 8, I introduce the modeling of the frequency dependence of the Galactic polarized foregrounds given by the moment expansion. As this method often appears as technical and difficult to approach, I will give a special care to demystify it through

2. FOREWORD

pedagogical examples. I will then present the successful application of this formalism for parametric component separation with the *LiteBIRD* satellite, as well as its strength and drawbacks. Furthermore I will introduce the spin-moment expansion. To do so, I will built from our understanding of the intensity moment expansion and special care will again be given to pedagogy. Following this presentation, I will propagate this expansion at the *E*- and *B*-modes level and further discuss its consequences. To conclude this chapter, I will present briefly my contribution to the extension of scattering transform to multi-frequency observations. In Chap. 9, I will show that the values of the fundamental constants of our standard models represent some "weak links" of our physical theories and as such are favored observables in order to seek for this new physics. After reviewing the theoretical origin, impact and observables consequences of a varying fine structure constant, I will present my contributions giving the latest to date constraints on the Bekenstein and the runaway dilaton models. I will conclude with a presentation of my other contribution on this topics, mainly related to dark energy.

Finally, I will present a summary and the conclusions of this thesis in Chap. 10. Perspective for future research will also be discussed.

As complements, a brief technical presentation of general relativity and our standard model of particle physics will be given in Appendix A, desirable for a better understanding of the problematic underlying the variation of the fundamental constants. A presentation of the required mathematical tools for the description of polarized light is given in Appendix B, giving the theoretical foundations and physical interpretation of the Stokes parameters, the *E*- and *B*-mode splitting and the spherical harmonics decomposition. A brief presentation of the scanning strategy optimization tools is given in Appendix C, followed by lists of the figures, tables and abbreviations. All the papers wrote in first author during this thesis can be found at the very end of the manuscript, in Appendix D.

Part I

General introduction

From the theoretical building blocks to the CMB and its foregrounds

3

Modern cosmology: the Standard models

Les choses tombent à cause qu'elles recèlent en elles une humeur maligne, une propension intime, intrinsèque et première, en un mot un principe tombant et qui les fait tomber: La Tombomanie. Or ne croyez pas que cette tombomanie soit l'effet d'une soit-disant loi Universelle; non ! C'est le fruit de la coupable industrie d'un microbe ou virus appelé Le Tombovirus, vous l'aurez deviné. Alors voyez, mordus par le tombovirus, l'objet contaminé est pris au cerveau et saisi de l'envie irrésistible de se précipiter par terre. Il tombe, et, de préférence, là où il faudrait pas. Selon que la chose est plus ou moins contaminée, elle est douée d'une force tombique plus ou moins contondante. Ca dépend de la gravité. De la gravité de la maladie, je veux dire.

– Professeur Shadoko

Contents

3.1	Introduction	11
3.2	Building our standard models from Geometry and symmetries	12
3.3	The Λ -CDM model	22
3.4	6 parameters to describe the Universe.	29
3.5	A brief history of the Universe as we know it	31

3.1 Introduction

Cosmology is the branch of modern physics having the Universe as a whole for object of study. Its acceptance as part of natural sciences was triggered by groundbreaking experimental discoveries in the XXth century – the so-called *observational pillars* of the hot Big-Bang model – setting the stage for theoretical constructions in which the geometry and the matter content of the Universe are thought as interconnected dynamical entities, the behavior of which can be postdicted and predicted.

Past 1926, Edwin Hubble and Milton Humason put forward the increasing radial velocity v of observed nearby galaxies with distance d from spectroscopic observations at Mount Palomar (Hubble, 1926; Hubble & Humason, 1931), modeled by the *Hubble-Lemaître law* $v = H_0 d$ (with proportionality factor H_0 called the "Hubble constant"). After decades of debates, this discovery was later understood as resulting from the *expansion* of the Universe (Lemaître, 1927; Hubble & Tolman, 1935). The further accidental discovery of the *cosmic microwave background* (CMB) in 1964 by the two radio-astronomers Penzias and Wilson – already anticipated by Gamow (1948); Alpher et al. (1948) – allowed to understand that our Universe had emerged from a hot and dense phase at thermodynamic equilibrium (Penzias & Wilson, 1965), providing a strong argument in favor of the "Hot big bang" model¹, defended notably by Friedmann (1922) and Lemaître (1927), who found dynamical solutions to the Einstein equations applied at a spatially homogeneous and isotropic space-time, thought to be a good approximation of the Universe smoothed on large scales. Going in the same direction, some physicists, as George Gamow, figured that *primordial nucleosynthesis* in a hot early Universe could explain the present Helium and Lithium fraction – considering that the contribution of stellar nucleosynthesis alone is not enough to explain the observed abundances (Alpher et al., 1948). Almost 60 years after the discovery of the CMB, our modern picture now builds on these observational pillars to provide a minimal and consistent theory of cosmology in which the dynamics of the Universe can be interpreted in term of the physical entities it contains and of the properties of the interactions between them within general relativity. We can only be astonished by the consistency of such an edifice, in which some connections can be established between the subatomic and the cosmic realms. As such, cosmology now provides a bridge at the interface between particle physics and astrophysics, using the empirical methods of the second discipline in order to tests theories from the first as quantum field theories.

3.2 Building our standard models from Geometry and symmetries

As mentioned above, our understanding of the cosmic evolution heavily relies on the theories used to model it. We will hence first introduce the theoretical frameworks from which our standard model of cosmology can be constructed: general relativity (GR), describing the gravitational field as geometry of space-time and purely gravitational motion as geodesics on this curved space-time and the standard model of particle physics described in the language of gauge theories². GR will be necessary in order to model the behavior of the Universe as a whole while the content and nature of our theories of particle physics can be hoped to be probed with cosmological observations. The framework of GR and particle physics will also provide a powerful guide in order to investigate the possible extensions of our current models which will be discussed in Chap. 4. This discussion will be at the interface between

¹The name, was coined by Fred Hoyle in 1949 to describe the idea that the Universe could have originated in an explosion. He was himself in favor of the concurring "steady state model" combining expansion of the Universe and continuous matter creation in order to interpret the Hubble law (for further discussion, see Sec. 5.1.1).

²Note here that GR is also described using the geometrical tools of gauge theories. However, some subtle differences exist and it remains unclear in what exact sense one could claim that GR is indeed a gauge theory. For a discussion see Appendix A and the references therein.

particle physics and gravity, and hence requires a proper understanding of both theories. This understanding will also be indispensable in order to investigate the possible variations of the fundamental constants of nature, which will be the primary concern of Chap. 9. Indeed, in order to consistently implement such variations, it is crucial to properly understand how these various constants appear within the intricate theoretical architectures of our standard models and the role they have to play in them.

GR and particle physics can both be understood in geometrical terms in the language of differential geometry³. While this formulation is not systematically used, I spent a consequent amount of my time to study it, and I personally believe that it provides a richer and more complete picture of the state of the art in cosmology and fundamental physics. With differential geometry, both GR and particle physics become somehow unified within the same language, in which the concepts of symmetry and invariance are central, and curvature drives the forces and motions shaping the Universe on all scales. As detailed in Appendix B, these tools also reveal themselves to be powerful in order to develop the language used to describe the polarized light of astrophysical and cosmological origin. We will only briefly review the key concepts in the following sections, leaving a more detailed discussion in Appendix A. For accessible introductions, I refer the reader to [Baez & Muniain \(1994\)](#), [Coquereaux \(2002\)](#) and [Faure \(2021a\)](#).

3.2.1 Gravitation and general relativity

Modern cosmology models the evolution of a dynamical Universe and thus a dynamical space-time. Let us first clarify how this notion is made possible, in the context of a geometrical understanding of gravity given by GR.

Special relativity and Poincaré covariance

The *principle of relativity* – already proposed by Galileo ([Galileo Galilei, 1632](#)) – can be stated as follows: *No physical experiment can distinguish immobility from uniform linear motion*. As such, the laws of physics must be expressed in the same way in all frames related to one another by a constant velocity shift (called a *boost*). The class of such frames are called *inertial*. The theory of *special relativity* generalizes this principle of relativity, in order to include Maxwell equations, leading to the straightforward consequence that the speed of light c must be invariant for all inertial observers⁴. A surprising outcome of this exercise is that space and time are better treated together, as the dimensions of a single 4-dimensional space-time in which all free particles are moving on Euclidian straight lines⁵. Formally, space-time can be modeled by a manifold equipped with a flat metric, called the Minkowski metric η , which can be understood as a 4-dimensional surface on which it is

³Disregarding the quantization of the particle fields which involves specific mathematics. We will note cover these details here.

⁴Note that we are reasoning backward from the historical reasoning. Experiments as the interferometric one of [Michelson & Morley \(1887\)](#) forced physicists to conclude that the speed of light must be invariant in all inertial frames, such that the transformation group (Lorentz transformation) must be the one leaving Maxwell equations invariant ([Lorentz, 1895](#)). These transformations were further extensively studied by [Poincaré \(1901, 1905\)](#) and interpreted by [Einstein \(1905\)](#).

⁵In the sense of Euclidian geometry, that is, in a chart $(x^0 = t, x^i)$ defined by 4D orthonormal frames with respect to η (Minkowski frames), the curve $x(\tau)$ satisfies $d^2x^\mu / d\tau^2 = 0$.

possible to compute lengths. For a detailed explanation of these notions, see Appendix A. In this framework, boosts can be understood as (hyperbolic) rotations in space-time planes relating inertial frames to one another. Overall, the laws of physics must remain *covariant* (keeping the same expressions) under rotations and boosts (forming the Lorentz group) as well as space-time translations. The Lorentz group and space-time translations form together the *Poincaré group*, containing all the transformations relating inertial frames.

In the absence of gravity, the Minkowski metric η fixes the geometry of space-time and allows one to define an invariant scalar product between two 4-dimensional vectors everywhere in space-time, from which one can build a notion of length and angles. Considering two events A and B labelled by space-time coordinates (t_A, x_A, y_A, z_A) and (t_B, x_B, y_B, z_B) in an inertial orthonormal frame, a generalization of the Pythagorean theorem in 4 dimensions allows to define the space-time interval⁶ $\Delta s^2 = -c^2\Delta t^2 + \Delta d^2$ with $\Delta t^2 = (t_B - t_A)^2$ and $\Delta d^2 = (x_B - x_A)^2 + (y_B - y_A)^2 + (z_B - z_A)^2$. This quantity is invariant for all inertial observers i.e. under transformations of the Poincaré group, while the notion of simultaneity as well as the values of space and time intervals are relative to the choice of inertial frames.

The principle of general covariance: equivalence of all frames

In order to include gravity and accelerated motion⁷, the principle of relativity must be generalized to any possible frames beyond the inertial ones with orthonormal coordinates, asking that "all systems of reference are equivalent with respect to the formulation of the fundamental laws of physics" (in [Møller 1960](#), p. 220).

To proceed in that direction, the fundamental entities of physical theories must be geometrical objects living in space-time, as vectors, which coordinates transform in a way that keep their geometrical properties invariant. Indeed, a vector seen as an arrow remains the same no matter what frame is chosen to express its components. The formal way to proceed is to ask for *general covariance* i.e. that the equations must be written in terms of geometrical objects⁸, ensuring the invariance of their structure under any choice of frames and coordinate transformations, even non-linear (all diffeomorphisms)⁹.

However, our daily experience is enough to convince us that it is possible to distinguish accelerated motion or gravity from immobility and uniform linear motion. It will thus not be possible to ask for the strict equivalence of all frames. Another type of equivalence however, the one between gravity and acceleration or equivalently between free-fall and inertial motion, allows one to treat all the observers within a unique framework, in which the geometry of space-time becomes dynamical.

⁶In this work, we choose the signature $(-, +, +, +)$, more often used in Gravity theory.

⁷For a treatment of accelerated frames in Minkowski space-time using the framework of differential geometry, see Chap. 5 of ([Nathalie Deruelle, 2018](#)).

⁸As vectors, tensors or spinors as well as p -forms (see Appendix A) which can alternatively be understood as multi-vectors of the space-time algebra (for a pedagogical introduction see e.g. [Chris Doran \(2003\)](#)).

⁹In principle, one should distinguish active and passive diffeomorphisms ([Rovelli & Gaul, 2000](#); [Norton, 2022](#)). Whether or not general covariance is one of the fundamental principles of general relativity, as thought by Einstein himself, is still debated today. On this subject, see e.g. [Norton \(1993\)](#). While general covariance might not be a necessary building principle ("axiom") of GR, there is however no doubt that it played a great role in the history of the ideas leading to it.

Einstein equivalence principle

Consider the following assertion:

- **Universality of free fall (UFF):** In the presence of no other force, all point-like bodies fall identically independently of their mass and composition. Or in Newtonian terms: the inertial mass of point like bodies is exactly equal to their gravitational mass.

UFF is an empirical statement, which validity can be tested experimentally. As we will further discuss quantitatively in Sec. 9.1.5, satellites experiments as MICROSCOPE can provide extremely low bounds on the possible violations of the UFF (Touboul et al., 2022).

The Einstein equivalence principle (EEP) is built from the following consequence of this empirical fact: if the UFF is valid, all objects must fall in the same way (independently of their mass and composition) such that frames in free fall within a gravitational field are indistinguishable from the inertial frames of special relativity. On the other hand, a frame at rest experiencing Earth's gravity is equivalent to a frame in vacuum, in which the ground is linearly accelerated upward with respect to the inertial free falling frames. In other words: gravity and acceleration are (locally¹⁰) equivalent.

As discussed in Di Casola et al. (2015), equivalence principles provide powerful tools to probe the nature of gravity (and fundamental physics in general) and they can be defined in multiple ways. Following Will (2014, 2018), we define the EEP formally by the fulfillment of the three following conditions:

- **Local Lorentz invariance (LLI):** the outcome of any local non-gravitational experiment (i.e. any "small scale" experiment in an inertial/free falling frame) is independent of the velocity of the reference frame in which it is performed. Thus, inertial frames are all equivalent.
- **Local position invariance (LPI):** the outcome of any local non-gravitational experiment is independent of where and when in the Universe it is performed i.e. there is no "preferred" place in the Universe in which laws of physics would be different.
- **Weak equivalence principle (WEP)¹¹:** UFF is exactly valid i.e. the trajectory of a freely falling "test"¹² body is independent of its internal structure and composition. In the simplest case of dropping two different bodies in a gravitational field (in vacuum), WEP states that they should experience the same acceleration.

These three points are not independent according to the so called *Schiff's conjecture* stating that "any complete, self-consistent theory of gravity that embodies WEP necessarily embodies EEP" (Will, 2014). While proven in many simple cases, the validity of Schiff's conjecture is still debated today (Ni, 1977, 2011; Tino et al., 2020)¹³. Note also that a stronger version of the EEP, the strong equivalence principle (SEP) exists. It can be stated identically to

¹⁰When tidal forces can be neglected.

¹¹UFF and WEP are generally used interchangeably. For clarity, we distinguish the empirical statement of the UFF, from the WEP as a theoretical foundation of GR.

¹²With size and mass small enough that tidal forces and self-gravitational effects can be neglected.

¹³In fact, Ni (1977) showed that Schiff's conjecture was not verified in the case of a pseudo-scalar field coupled to electromagnetism presented in Sec. 4.3.2, unless a broader definition is used for WEP.

3. MODERN COSMOLOGY: THE STANDARD MODELS

the EEP but including gravitational interactions in its definition (and hence embodies the EEP). SEP might only be satisfied within GR ([Bertotti & Grishchuk, 1990](#)).

As we will further see, a theory embodying the EEP allows one to interpret gravity as a geometrical consequence of space-time. It is referred to as *metric theory* of gravity.

The validity of the EEP and the SEP can be tested experimentally using a variety of independent measurements, local (e.g. in orbit or laboratory) or astrophysical. To do so, one can assert the validity of each of the principle sub-parts:

- **LLI** can be tested locally using numerous experiments, as descendants of the Michelson-Morley interferometer like cavity experiments using rotating oscillators ([Stanwix et al., 2005](#)) or spectroscopy on laser-cooled trapped atoms and ions [Prestage et al. \(1985\)](#); [Lamoreaux et al. \(1986\)](#); [Chupp et al. \(1989\)](#); [Dreissen et al. \(2022\)](#), which provides the tightest bounds on the LLI to date. Novel methods using entangled pairs of atoms can also provide independent constraints on LLI ([Megidish et al., 2019](#)). Astrophysical observations, as the independence of the speed of light with the source ([Brecher, 1977](#)) or quest for birefringence using the polarized light of distant Galaxies ([Carroll et al., 1990](#)) or within the CMB (see Sec. 4.3.2 and Sec. 5.3.2) can be used to test special relativity as well as the dispersion relation of high energy cosmic rays using experiments as the Pierre Auger observatory ([The Pierre Auger Collaboration et al., 2021](#)). More recently, the validity of the LLI was constrained using gravitational waves ([Kostelecký & Mewes, 2016](#)). For a review of the modern tests of LLI see e.g. [Mattingly \(2005\)](#).
- **LPI** can be mainly tested using gravitational redshift. This is done through spectroscopic measurements of the solar spectra ([Lopresto et al., 1991](#)) and using clocks as maser clocks onboard spacecrafts like Gravity probe A ([Vessot et al., 1980](#)) or fountain atomic clocks in laboratory which provide the sharpest to date constraints on LPI [Lange et al. \(2021\)](#). Conjointly, tests of the stability of fundamental constants can be used to test the LPI on cosmological space and time scales. This last point will represent the main topic of Chap. 9.
- **WEP** can be tested using torsion balances measurements ([Wagner et al., 2012](#)) or lunar laser ranging measurement testing the validity of the UFF between the Earth and the moon ([Williams et al., 2009](#)). As stated above, the latest to date constraint is given by direct comparison of the trajectory of test bodies in orbit as done by the MICROSCOPE mission ([Touboul et al., 2022](#)).
- **SEP** can be tested by looking at perturbations in the Earth-Moon orbit as the Nordtvedt effect using Lunar ranging experiments ([Williams et al., 2009](#)), looking at the behavior of self-gravitating bodies as binary pulsars ([Stairs et al., 2005](#)). The SEP has also been constrained using gravitational waves ([Unnikrishnan & Gillies, 2020](#)).

The above list is far from exhaustive and simply present a brief overview of the experimental landscape. For a complete review on the experimental tests of gravity theories see [Will \(2018\)](#). Despite the ever increasing accuracy of the proposed tests, none of these principles has yet been jeopardized.

The geometrization of gravity

Let us now investigate the consequences of the EEP thus defined. Strikingly, most of the astonishing predictions of GR, as gravitational redshift/time dilatation and deviation of light rays can be derived solely from the EEP i.e. from the local identification of gravity with an upward acceleration. Formally, LLI implies that there must exist inertial frames at each point of space-time, thus related to one another by transformations of the Poincaré group. In these frames the structure of space-time must be given locally by the Minkowski metric η and the laws of physics must be those of special relativity as described in Sec. 3.2.1. From the EEP, we know that the free falling frames provide realizations of such inertial frames. However, the theory must be able to describe more general frames related by general non-linear transformation laws in order to deal with acceleration and gravity (as well as non-orthonormal frames). In these frames, the invariant scalar product $g(v, w)$ between two 4-dimensional vectors v and w , and hence the geometry of space-time must take a more general form than $\eta(v, w)$ and is expressed by a space-time dependent metric tensor $g(x)$, where x labels the points of space-time¹⁴. Moreover, in these frames¹⁵, the 4-dimensional trajectories of free bodies which were straight in orthonormal inertial frames can not be straight lines anymore and similar conclusions can be reached for light rays¹⁶. However, in order for WEP to remain valid, these trajectories must be the same for all the free test massive particles, independently of their mass or composition. This is made possible if all the test particles follow the same *geodesics* of the possibly curved space-time: lines relating two events such that the space-time interval is minimal¹⁷.

In order to encode the geometrical properties of space-time and define the notion of space-time derivation of geometrical objects within it, one further introduces the covariant derivative $\nabla_w v$ which encodes how a vector v can be *parallel transported* in the direction w that is, how v transforms when it is transported as "rigidly" as possible across space-time¹⁸. Let us now pick a frame $e_\mu(x)$ at each space-time point¹⁹ in which to express vectors as $v = v^\mu e_\mu$. Greek indices range from 0 to 4 over the space-time dimensions and we assume Einstein's summation convention over repeated indices. We further use the shorthand

¹⁴Due to LLI, at each point x , it is hence possible to find a transformation towards an inertial frame, that is $g \rightarrow \eta$. But if space-time is curved, it is impossible to find a single frame transformation such that $g = \eta$ everywhere simultaneously.

¹⁵i.e. non orthonormal, accelerated or frames at rest within gravitational fields.

¹⁶Here we mean the following: Let $x^\mu(\tau)$ be the trajectory of a free test particle measured in an orthonormal inertial frame parametrized by its proper time τ . Then, we expect $d^2x^\mu / d\tau^2 = 0$ ("straight" trajectory from an Euclidian perspective). Under a non-linear frame transformation $x^\mu \rightarrow X^\mu$, we must conclude that $d^2X^\mu / d\tau^2 \neq 0$ ($= \Gamma_{\lambda\rho}^\mu \partial_\tau X^\lambda \partial_\tau X^\rho$). This point is interesting as it allows for a reinterpretation of Newton's principle of inertia. Gravity should not be understood anymore as a force, such that when no forces are present, particles follow straight trajectories, but on a curved space-time: in a way, gravitational motion *defines* the notion of straight trajectories through the geodesic equation (see also the discussion in lecture 9 of Schuller (2015)).

¹⁷Interestingly, such an interpretation (geodesic motion in a curved space-time) is already possible in Newtonian mechanics encompassing the WEP. See e.g. Havas (1964), lecture 9 of Schuller (2015) or Nathalie Deruelle (2018). In this case there is no local Poincaré symmetry and there is thus a preferred time direction.

¹⁸More rigorously, establishing ∇_v on a manifold *defines* the notion of parallelism.

¹⁹In practice, it is not possible to find such a single choice of frame (called a "global trivialization") over the whole curved space-time. We will neglect this subtlety here.

3. MODERN COSMOLOGY: THE STANDARD MODELS

notation $\nabla_\mu = \nabla_{e_\mu}$. The covariant derivative can then be explicated as

$$\nabla_\mu v = (\partial_\mu v^\nu + v^\lambda \Gamma_{\mu\lambda}^\nu) e_\nu. \quad (3.1)$$

While the first term corresponds to the standard derivative in the direction given by e_μ , the second term introduces Γ , called the *connection*, which describes how the basis vector e_ν is parallel transported with ∇ in the e_μ direction, and ensures the invariance of the covariant derivative $\nabla_w v$ under any arbitrary frame transformation, called a *gauge transformation*. It thus allows one to "connect" the vectors from a point of space-time to another. As discussed in [Weinberg \(1972\)](#), the EEP is satisfied if Γ is given by the unique *Levi-Civita connection*²⁰, preserving the length of the vectors (metric preserving $\nabla_v g = 0, \forall v$) and satisfying $\Gamma_{\mu\nu} = -\Gamma_{\nu\mu}$ (torsionless²¹). $\Gamma_{\mu\nu}^\lambda$ can be expressed solely from first order derivatives of g , linking it directly with the geometry of space-time. It is common to interpret Γ as the gravitational field²², while g would be the gravitational potential.

A particle is said to follow a geodesic motion if its 4-velocity u obeys the equation

$$\nabla_u u = 0, \quad (3.2)$$

meaning that u follows the "shape"²³ of the possibly curved space-time when the body moves²⁴.

∇ can be curved, translating directly the existence of a curvature of space-time, sourcing gravity. A connection is said to be curved if a vector parallel transported with ∇ around a loop back to the same point acquires a rotation (called *holonomy*). Curvature can be quantified by the Riemann tensor \mathfrak{R} , which is expressed solely from Γ and its first order derivatives. As such, if Γ is identified with the gravitational field, \mathfrak{R} quantifies the tidal forces. Knowing \mathfrak{R} , it is possible to compute the local holonomy acquired by a vector parallel transported around a point, or the gravitational deviation of two nearby geodesics.

The second direction we should follow is to ask for the matter content to also influence the geometry of space-time described above, or as Wheeler famously put it "Spacetime tells matter how to move and matter tells spacetime how to curve" (in [Wheeler & Ford 2000](#) p.

²⁰Allowing for particles to follow geodesics of other connections than the Levi-Civita connection can lead to extensions of GR such as the Einstein-Cartan(-Sciama-Kibble) theory in which particles with intrinsic angular momentum naturally couple through their spin to a connection with non vanishing torsion ([Cartan, 1922](#)). Today, no experiment is able to distinguish between the two theories.

²¹Torsion is the anti-symmetric part of Γ and does not impact the geodesic equation. Asking for a vanishing torsion is hence a "minimal assumption".

²²This interpretation is not always correct as Γ is not vanishing when using curved coordinates on a flat space (without gravity). It can thus also translate the presence of acceleration or a choice of non linear coordinates.

²³Considering the special case of a two dimensional surface embedded in \mathbb{R}^3 (which is convenient for picturing but not faithfully representative of space-time), $\nabla_u u = 0$ would state that $u(\tau + d\tau)$ is the orthogonal projection of $u(\tau) \in \mathbb{R}^3$ to a plane tangent to the surface at $\gamma(\tau + d\tau)$ (that is $u(\tau + d\tau) = P_{\gamma(\tau+d\tau)} u(\tau)$ with the orthogonal projector $P_x : \mathbb{R}^3 \rightarrow T_x M$). Understand here that u is transported "as parallel as possible" over the surface without adding any extra rotations. For an illustration and applications in physics see [Faure \(2021a\)](#).

²⁴In order to preserve the local structure of the theory, it is also required that $g(u, u) > 0$ at every point of the curve γ , preventing massive particles to move faster than c and ensuring that the proper time is real and positive.

3.2. BUILDING OUR STANDARD MODELS FROM GEOMETRY AND SYMMETRIES

593, adapted from Misner et al. 1973 p.130). Doing so will allow massive objects to source the gravitational field and influence the motion of nearby test particles. To every matter present in space-time, one can associate a stress-energy tensor T quantifying its momentum and energy density. The local conservation of energy-impulsion is ensured by the *continuity equation*²⁵, which components in a given frame are given by²⁶

$$\nabla_\mu T^{\mu\nu} = 0. \quad (3.3)$$

Following the principle of general covariance, the simplest expression one can derive relating the geometry of space-time (i.e. \mathfrak{R}) and its content (T) that allows for the continuity equation to be satisfied and giving back Poisson equation in the non-relativistic limit, is given by the Einstein equations

$$\mathcal{G} = 8\pi GT - \Lambda g, \quad (3.4)$$

with the *Einstein tensor* defined as

$$\mathcal{G} = \hat{\mathfrak{R}} - \frac{1}{2}gR. \quad (3.5)$$

where $\hat{\mathfrak{R}}$ is the *Ricci tensor* $\hat{\mathfrak{R}}_{\mu\nu} = \mathfrak{R}_{\mu\delta\nu}^\delta$ and R is the scalar curvature $R = g^{\mu\nu}\hat{\mathfrak{R}}_{\mu\nu}$. Λ is the *cosmological constant*, which can be interpreted as a vacuum energy term allowed in Einstein equations. Here and for the remainder of this work we will use natural units $c = \hbar = 1$ unless otherwise stated. The numerical factor of $8\pi G$ ensures that the theory gives back Newton's law of gravity in the low energy limit. While special relativity asked for a generalization of the principle of relativity to include classical electrodynamics, the fundamental building blocks of GR²⁷ are given by the EEP and the Einstein equations, which allow to interpret the gravitational field as the geometry of a curved space-time and the gravitational motion of particles as geodesic motion²⁸. As all the known fundamental laws of physics, the whole theory can be derived from the extremalization of an action²⁹, which calls for simplicity and makes generalization easier³⁰. The action is a functional written as an integral of a

²⁵Which is the curved space-time generalization of the familiar continuity (mass/energy conservation) equation of fluid dynamics $\frac{\partial \rho}{\partial t} = -\nabla \cdot \mathbf{j}$.

²⁶For test particles $T^{\mu\nu} = mu^\mu u^\nu$ and the continuity equation gives back the geodesic equation.

²⁷One could argue that the so called "Mach principle" must be considered as a fundamental building block of GR. It can also be phrased in multiple ways but states that inertia depends on the matter content of the Universe. GR however, is not fully Machian as space-time and inertia can exist (in some solutions of Einstein equations) independently of any matter content (Sciama, 1953; Brans & Dicke, 1961). Additionally, the requirement for a causal and local description of gravity were arguably another strong requirement in the building of GR.

²⁸Possible equivalent rewriting of the theory in terms of torsion or non-metricity instead of curvature are also possible as teleparallel and symmetric teleparallel gravity (Beltrán Jiménez et al., 2019; Bahamonde et al., 2021).

²⁹There exist also canonical (Hamiltonian) formulations of GR and more powerful formalism using tetrads fields instead of g , allowing to introduce spinors on curved space-time and opening the road for a quantum theory of gravity. Note that multiple different actions than S_{EH} allow to recover Einstein equations and it is straightforward to provide possible extension of GR by adding terms to Eq.(3.6) (or its teleparallel versions) as done in $f(R)$, $f(T)$ and $f(Q)$ theories of gravity, in which T is the torsion and Q the non-metricity (see (Sotiriou & Faraoni, 2010)).

³⁰Our above discussion is somewhat simplified and the only way to properly justify the use of Einstein equations to relate energy distribution and geometry of space-time is to derive it from an action (See also Sec. 4.2.1 for a discussion on alternative formulations of gravity theories).

Lagrangian density \mathcal{L} over space-time. \mathcal{L} must be a scalar, e.g. an invariant quantity under all the symmetries of the theory, i.e. general frame transformations (diffeomorphisms) in the case of GR. Einstein's equation can hence be derived from the Einstein-Hilbert action

$$\mathcal{S}_{\text{EH}} = M_{\text{Pl}}^2 \int \sqrt{-|g|} \left(\frac{R}{2} - \Lambda \right) d^4x + \int \sqrt{-|g|} \mathcal{L}_{\text{mat}} d^4x, \quad (3.6)$$

where $|g|$ is the determinant of the metric³¹, $M_{\text{Pl}} = (\sqrt{8\pi G})^{-1}$ is the reduced Planck mass and \mathcal{L}_{mat} is the matter Lagrangian. On the other hand, the geodesic curve γ of free falling massive bodies as well as the Levi-Civita connection Γ are recovered by extremalization of the space-time interval/distance between two events given by

$$\mathcal{S}_p = \int m ds = \int m \sqrt{g(u_{\gamma(\tau)}, u_{\gamma(\tau)})} d\tau. \quad (3.7)$$

where m is the particle mass, τ is a real parametrization of γ , typically given by the proper time of the particle, and $u_{\gamma(\tau)}$ is the 4-velocity of the particle at the point $\gamma(\tau)$. The mass factor m has no impact on the recovered trajectories, in agreement with the WEP, but is needed to provide inertia when other forces are present.

A large portion of modern cosmology relies on the formalism of GR as introduced above. Firstly, all the known fundamental forces of nature but gravity can form neutral elements which suppresses strongly their effect on large distances, leaving the gravitational force alone to act on galaxies and shape the largest structures of our Universe. Secondly, GR gives a framework in which the Universe can be described entirely as a single geometrical and dynamical space-time. Its observed expansion can thus be interpreted as a "stretching" or "dilution" of this space-time as a whole. Finally, the existence of Λ – naturally present within GR – allows one to explain the late accelerated phase of expansion witnessed in modern cosmological data. For more on GR the technical aspects of GR, we refer to Appendix A and the associated bibliography.

3.2.2 Gauge theories: the geometrization of particle physics

While gravity is thought to be the only fundamental interaction shaping the Universe on large scales, the exact particle content of the Universe and their local interactions still have a strong impact on the cosmic dynamics and history. The standard model of particle physics describes elementary particles as quantized excitation of fields over space-time. These fields associate elements of abstract vector spaces at each point of space-time. These vectors can transform differently than standard vectors under space-time transformations (i.e. with different representations of the Poincaré group), and transform as well through various groups that relates to their internal structure called the *gauge groups*. To all the fields one can associate *charges*, which translate how and if they transform under the action of these gauge groups. One could argue that the gauge group of gravity is thus the group of general frame transformations or the Poincaré group and it is believed that this must be true at some level. However, some fundamental differences must still be considered between GR and gauge theories (for a discussion see Appendix A and the associated references).

³¹The $\sqrt{-|g|}$ factor is here to ensure the invariance of the action integral regardless of the choice of curvilinear coordinates.

The matter fields ψ are described by the value of a complex vector at each point of space-time. Similarly to vectors in GR, the fields can be parallel transported over space-time, using covariant derivatives $D_v\psi$. As GR, these covariant derivatives are associated with connections \mathcal{A} ³², ensuring the parallel transport of frames and the invariance of their equations motion under any change of frames, that is any gauge transformations, whether these frames are space-time (e_μ) or internal abstract frames. The connections \mathcal{A} can be identified with the gauge boson fields interacting with ψ to transmit the fundamental forces. As in GR again, the connections can be curved, with curvature tensor \mathcal{F} , which should not be understood as space-time curvatures (as \mathfrak{R}) but rather as curvatures of the field space in which ψ lives on space-time. The forces/interactions at play between the particles can be expressed by the dynamics of the fields ψ on these curved abstract spaces. We will discuss again these notions in Sec. 9.1.3 and a review of this formalism and its similarities and differences with gravity can be found in Appendix A.

The matter fields ψ are fermions and can be either quarks or leptons (electron/neutrino pairs). Each of them come in three generations. From space-time symmetries, it is possible to associate a mass m and an intrinsic angular momentum, the spin s , to all the fields, which translate how they transform under the Poincaré group from one inertial frame to another (they are Poincaré charges). From the spin s , one can further associate a *chirality* to each particle, which can be either left or right³³.

Besides gravity, two other fundamental forces are known that can act on ψ : the strong and the electroweak force. At low energy, the electroweak force is split in the electromagnetic force and the weak force through the Higgs boson \mathfrak{h} , which gives masses to the matter fields ψ . To each of the fundamental forces, one can associate a connection \mathcal{A} and a corresponding curvature \mathcal{F} . For the strong force, \mathcal{A} are the gluons and the gauge group is SU(3), for weak force it is the W^\pm and the Z^0 bosons while for electromagnetism it is the photon A , associated with gauge groups SU(2) and U(1) respectively. The weak force is only sensitive to the fields with a left chirality. Quarks interact through electroweak and strong forces, electrons with electroweak force and neutrinos only through weak force.

All the equations of motions of the standard model can be recovered from minimization principles. When including gravity, the full standard model action takes the form³⁴

$$\begin{aligned} \mathcal{S}_{\text{SM}} = & \int M_{\text{Pl}}^2 \left(\frac{R}{2} - \Lambda \right) + \sum_{\psi, \mathcal{A}} \bar{\psi} (\not{D} + \frac{\phi}{4}) \psi \\ & - \sum_{\mathcal{F}} \frac{1}{4} \langle \mathcal{F}, \mathcal{F} \rangle + \frac{1}{2} |D\mathfrak{h}|^2 - V(\mathfrak{h}) - \sum_{\psi} \lambda_{\psi} \bar{\psi} \mathfrak{h} \psi \, d\mu. \end{aligned} \quad (3.8)$$

The first term of this action is \mathcal{S}_{EH} (Eq. 9.28), giving back Einstein equations. The second

³²While in GR, ∇_v and Γ translate how the vectors transform when transported over space-time, the more general D_v are associated with different connections \mathcal{A} translating how ψ transforms in different abstract spaces when transported over space-time. Contrarily to Γ , \mathcal{A} can not be expressed from the metric g and is not uniquely defined. Depending on the exact particle field described by ψ , it can be sensitive or not to a specific \mathcal{A} and transform differently with it (with different *representations* associated with different charges of the gauge group). This translates why some particles are charged or not and interact or not through fundamental forces. A more detailed explanation is given in Sec. 9.1.3.

³³Chirality is associated to the exact representation of the Lorentz group under which the field transforms.

³⁴For a similar discussion, see also "Experimental Tests of Gravitational Theory" in Zyla et al. (2020).

term is the *Dirac action* stating how the matter fields ψ move over space-time. $\bar{\psi}$, associated with anti-particle creation, is the dual of ψ , $\bar{\psi} = \psi^\dagger \gamma^0$, where γ^μ are the Dirac matrices³⁵. The contracted covariant derivative $\not{D} = \gamma^\mu D_\mu$ contains all the possible interactions of the fields with the gauge bosons \mathcal{A} . We will come back to it in details in Sec. 9.1.3 (see Eq. 9.3). This derivative further contains a term $\phi = \gamma^\mu \omega_\mu$, translating the interaction with ω , which is the spin-connection, generalizing how the Levi-Civita connection Γ of GR can act on the ψ space. The curvature term $\langle \mathcal{F}, \mathcal{F} \rangle = \text{Tr}(\mathcal{F}_{\mu\nu} \mathcal{F}^{\mu\nu})$ quantifies the dynamics of \mathcal{A} , and can be understood as the kinetic energy of the gauge bosons. This term will for example give back Maxwell equations in vacuum for the photon. Finally \mathfrak{h} is the Higgs boson, with its associated potential $V(\mathfrak{h})$. The interaction term between ψ and \mathfrak{h} can be understood as a mass term for the matter fields through the Yukawa couplings λ_ψ . $d\mu = \sqrt{-|g|} d^4x$ is the invariant infinitesimal space-time volume element one is integrating over. In this thesis, I will use alternatively the actions or the Lagrangian densities \mathcal{L} which should be integrated over space-time $\mathcal{S} = \int \mathcal{L} d\mu$ to recover the action. While not necessary for the present thesis, I give a detailed presentation of these terms and the resulting equations of motions in Appendix A.

Once this action established, the fields can be promoted to particle creation operators on space-time within the framework of quantum field theory (QFT), allowing for the existence of multiple particles in interaction (see the discussion at the end of Appendix A). The metric g , can not easily be treated as a quantum field, and the construction of a quantum theory of gravity requires to go beyond the standard model of particle physics.

Our understanding of the standard model (SM) of particle physics and fundamental interaction is crucial to understand all the phases of the cosmic history (see sec. 3.5). Additionally, the mechanisms at play in numerous of the cosmological probes –presented in Sec. 3.4.1 – involve this physics at some level (light, the messenger of astrophysics, is after all described by electromagnetism, which is a gauge theory). On the other hand, observational cosmology also allows one to test the robustness of our SM on the largest possible scales of space and time as well as in the most extreme conditions witnessed within our Universe. For example, a lot of questions remain about the physics of the very early Universe, in which the mean energy conditions were way beyond the reach of our best particle accelerators. Additionally, the exact nature of dark matter remains unknown while the nature of dark energy given by Λ is vividly questioned. As we will further discuss in Chap. 4, it will however be crucial to understand how and where both can fit within our SM and its extensions.

3.3 The Λ -CDM model

The equations of the standard model presented above are highly non linear and generally non trivial to solve. In order to get a consistent but tractable model to predict the evolution of the Universe, one needs simplifying assumptions, usually based on symmetry considerations. Since the 1990s, the highly successful Λ -cold dark matter (Λ -CDM) model is considered as the canonical model of cosmology. It is built on the three following assumptions:

³⁵Which can be themselves understood as basis vector of the space-time Clifford algebra, providing deep connections between space-time and space of the spinors. On this topic see (Dressel et al., 2015).

- i) **cosmological principle:** on large scale the Universe is isotropic (i.e. invariant under rotations) and homogeneous (i.e. invariant under spatial translations). This principle seems to be largely verified by observation but is still questioned today (see the discussion in Sec. 5.2.1). It strongly constrains the overall shape that the Universe can have, but allows for the existence of a constant spatial curvature.
- ii) **content:** the Universe contains the matter and gauge fields of the standard model of particle physics (Sec. 3.2.2). They can be divided in two broad categories according to their collective behavior on large scales: matter (massive particles) and radiation (relativistic light species). To account for the observations, one has to add an extra source of matter called *cold dark matter* (CDM), which can not be accounted for by the SM fields introduced before.
- iii) **gravity and dynamics:** The theory of gravity, acting on the largest scales is given by GR (Sec. 3.2.1) with a non vanishing cosmological constant Λ , responsible for a late time accelerated expansion phase.

Each of these assumptions can be questioned, and extensively testing their domain of validity represents one of the major challenges of modern cosmology. As we will see, Λ -CDM allows one to make very accurate predictions about the Universe's history while remaining easily interpretable and provides an extremely powerful framework in this regard³⁶.

3.3.1 Cosmological principle and the FLRW metric (i)

Asking for i) strongly constrains the overall possible geometry of the Universe and hence the possible expressions of its metric.

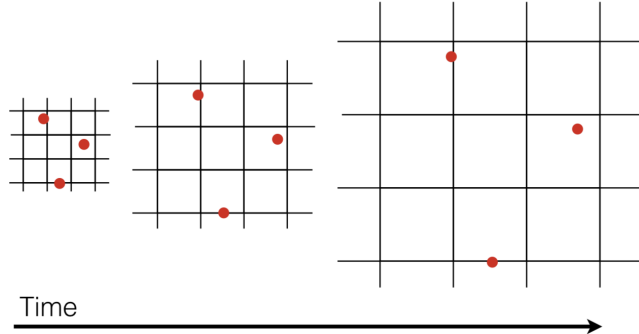


Figure 3.1: Two-dimensional illustration of a comoving frame (black grid) stretching with the comoving time t , as a consequence of the expansion. The scale factor $a(t)$ quantifies the amplitude of this stretch. Picture taken from [Errard \(2012\)](#).

Considering a *comoving frame*, that is a frame carried with the expansion of the Universe (i.e. galaxies always have the same coordinates through cosmic evolution, but the coordinate frame can expand or shrink as illustrated on Fig. 3.1). These frames are preferred by the cosmological principle, in which all observers could hypothetically measure isotropy and

³⁶For complete discussions on the foundations of modern cosmology, see e.g. [Chamcham et al. \(2017\)](#) and [Smeenk & Ellis \(2017\)](#). For complete introduction to modern physical cosmology see e.g. [Peter & Uzan \(2009\)](#) and [Dodelson \(2003\)](#).

homogeneity. The time t is called the *comoving time* and can be interpreted as the physical time measured by an observer dragged by the expansion and free from local gravitational effects. We note t_0 the comoving age of the Universe, i.e. today's value of t .

The *scale factor* $a(t)$ is a dimensionless quantity quantifying the expansion/contraction of the comoving frame. In Cartesian comoving coordinates (x, y, z) and in the case of an Euclidian Universe, the *physical distance* d between two objects is related to the (constant) comoving distance $r = \sqrt{x^2 + y^2 + z^2}$ by $d(t) = a(t)r$. Today, $a(t = t_0) = a_0 := 1$, by definition. In practice, it is impossible to measure the physical distance d and one uses the so-called angular diameter or luminosity distances instead, which reduce to d only for nearby objects.

Introducing the *Hubble parameter*

$$H := \frac{\dot{a}}{a}, \quad (3.9)$$

where dotted quantities represent derivatives with respect to t , we find back the Hubble law by taking the derivative of the physical distance³⁷ $v = \dot{d} = \dot{a}r = H(t)a r = H(t)d$, such that for nearby galaxies $H(t) \simeq H_0$ and hence $v \stackrel{t \sim t_0}{\sim} H_0 d$.

Considering a spherical comoving chart centered at a given point of space-time (t, r, θ, φ) , the most general metric satisfying the cosmological principle is the Friedmann-Lemaître-Robertson-Walker (FLRW) metric, expressed as³⁸

$$g = -dt \otimes dt + a^2(t) \left(\frac{1}{1 - \kappa r^2} dr \otimes dr + r^2 d\theta \otimes d\theta + r^2 \sin^2(\theta) d\varphi \otimes d\varphi \right). \quad (3.10)$$

κ quantifies the spatial Gauss curvature of the Universe³⁹: $\kappa > 0$ corresponds to a spherical geometry, $\kappa < 0$ an hyperbolical one and $\kappa = 0$ an Euclidian one.

To a given value of a , one can associate the *redshift*

$$z = \frac{1}{a} - 1, \quad (3.11)$$

which can be interpreted as the Doppler shift experienced by light from a galaxy carried by the expansion and received by a comoving observer as

$$z = \frac{\nu_e - \nu_r}{\nu_r}, \quad (3.12)$$

where ν_e is the original frequency emitted by the source and ν_r is the received redshifted frequency⁴⁰

³⁷We neglect here the proper motions.

³⁸The tensor product \otimes allows one to define the basis in which to decompose tensors as defined in Appendix A. The component of the metric are more classically given with the differential space-time interval squared $ds^2 = g_{\mu\nu} dx^\mu dx^\nu$, which would correspond to the application of g to general tangent vectors associated to an infinitesimal displacement as in Eq. 3.7.

³⁹ $\kappa = 1/R_0^2$ with R_0 the curvature radius of the Universe at t_0 .

⁴⁰To find back this result, set $g(u_\gamma, u_\gamma) = 0$ in Eq. 3.10 to obtain a massless geodesic, and integrate between the emitter and the receiver.

3.3.2 The components of the Universe (ii)

We will now further discuss the assumption **ii**). For the cosmological principle **i**) to hold, the fluids contained in the Universe should not have any significant flux on large scales since it would select a preferred direction and break isotropy. As such, the fluids can be modeled as *perfect fluids*⁴¹ filling the Universe uniformly. A perfect fluid has an isotropic pressure, no shear, no viscosity, and do not conduct heat. Those consequences of the cosmological principle imply that we neglect the interactions between the constituents (e.g. the galaxies) on the largest scales. The stress energy tensor of a perfect fluid is diagonal and given by⁴²

$$T^\mu_\nu = (\rho + p)u^\mu u_\nu + pg^\mu_\nu = \text{diag}(-\rho, p, p, p), \quad (3.13)$$

where $u = (1, 0, 0, 0)$ is the 4-velocity of the fluid at rest in the comoving frame. ρ and P are respectively the (constant) energy density and pressure of the fluid. Additionally, we assume that the fluid obeys an equation of state of the form

$$p = w\rho. \quad (3.14)$$

A classical example being given by the ideal gas for which interactions between molecules are neglected, leading to $w = RT$ with R the ideal gas constant and T the gas' temperature.

The continuity equation is given by Eq. 3.3 and is expected to hold for every species independently if we neglect their interactions on large scales (which is not expected to be true locally on small scales or in the very early Universe). Evaluating the component $\nabla_\nu T_0^\nu$ coupled with the equation of state given in Eq. 3.14, we obtain

$$\frac{\partial \rho}{\partial t} + 3H(1+w)\rho = 0, \quad (3.15)$$

which can be integrated to obtain

$$\rho(a) = \rho_0 a^{-3(1+w)}. \quad (3.16)$$

To determine the w of a given species, one has to use some considerations of thermodynamics/statistical physics. Usually, one splits the content in the two broad categories of "matter" and "radiation":

- **Matter: baryons and dark-matter.**

By definition, the energy density of matter is dominated by its mass $\rho_m c^2 \gg p_m \propto v_m^2$. Baryonic and dark matter are thus assumed to be pressureless, that is $w_m = 0$. This leads to $\rho_m \propto a^{-3}$, matching the intuition of how the energy of some particle distribution would be diluted within an expanding cube of length a .

⁴¹Let us mention her that the perfect fluid model can be questioned. It is possible to allow for the presence of inhomogeneities by favoring the weaker Copernican principle over the Cosmological principle stating that "we do not lie in a special place (the center) of the Universe" (Peter & Uzan (2009) p.130). Allowing for inhomogeneities can impact the measurement of the cosmological parameters and lead to reinterpretations of the Hubble diagrams Fleury et al. (2013).

⁴²Eq. 3.13 is the only rank-2 tensor one can build out of the metric and the fluid's parameters ($u_\mu(x)$, p and ρ) that gives back the continuity equation and the Navier-Stokes equations for a perfect fluid (Xylyxylxyx, 2020; Misner et al., 1973).

Several astrophysical observations from different probes are indicating that standard baryonic matter of density ρ_b (standard model fermion and boson fields introduced above, which largest mass/energy fraction is made of baryons i.e. triplet of quarks) is expected to represent only $\sim 20\%$ of the matter content of the Universe. The largest amount of the matter mass is hence given by dark matter which true nature remains unknown. Phenomenologically, its behavior is well accounted for by cold dark matter (CDM) models, that is a massive, cold and weakly interactive fluid. The total matter density can hence be split as $\rho_m = \rho_b + \rho_{\text{CDM}}$.

- **Radiation: photons and neutrinos**

Since their pressure is significant compared to their density of energy, massless and light particles as photons and neutrinos have a different equation of state than matter fluids. Statistical physics considerations for a massless relativistic gas give $w_r = 1/3$. This leads to $\rho_r \propto a^{-4}$, indicating the presence an additional source of energy dilution in a^{-1} compared to the matter case of a constant number of particles in an increasing volume. This factor comes from the stretching of the photons' wavelength λ with the expansion as $E \propto hc/\lambda$, where h is Planck's constant. This energy shift is the origin of the observed cosmological redshift (Eq. 3.12)⁴³.

In addition to matter and radiation, one must consider two geometrical terms coming from GR: curvature and the cosmological constant. While in Λ -CDM those terms are not to be understood as additional matter content, they can be identified as such for all practical purposes.

- **Dark energy and Λ**

Since the observation of the accelerated expansion of the Universe by [Riess et al. \(1998\)](#) and [Perlmutter et al. \(1999\)](#), it is clear that some mechanism or entity should be responsible for it. Such a component is called with the general name *dark energy*. The equations of evolution of the Universe that we will soon derive (see Eq. 3.17) will impose that $w_{\text{DE}} < -1/3$ in order to allow for $\ddot{a} > 0$. The cosmological constant appearing in the Einstein equations provides the simplest and perhaps the most natural candidate for dark energy.

Indeed, looking at Einstein equations (Eq. 3.4), one can interpret the Λ term as a contribution to T by defining $T_{\mu\nu}^{\Lambda} = -\Lambda M_{\text{Pl}}^2 g_{\mu\nu}$, with associated density $\rho_{\Lambda} = \Lambda M_{\text{Pl}}^2$.

From Eq. 3.13 and due to the metric signature, we derive $w_{\Lambda} = -1$, leading to $\rho_{\Lambda}(a) = \text{cst}$, which is exactly the behavior that one would expect from a *vacuum energy* which can not be diluted by the expansion.

- **Curvature**

As we saw above, the FLRW metric allows for a uniform spatial curvature κ . Analogously to what was done for Λ , when inserting 3.10 in Einstein equations, it is possible to introduce a curvature density that mimics the behavior of an additional fluid with $\rho_{\kappa} = -3\kappa M_{\text{Pl}}^2$ and $w_{\kappa} = -\frac{1}{3}$, such that $\rho_{\kappa} \propto a^{-2}$.

⁴³The notion of energy conservation for photons and for the Universe as a whole is thorny and is, most generally, not well defined. See e.g. the proposed definitions in [Katz \(2005\)](#); [Lynden-Bell et al. \(2007\)](#) and the discussion in [Weiss & Baez. \(2017\)](#).

3.3.3 Fundamental equations of cosmology (iii)

Friedmann-Lemaître equations

Let us now put all the pieces of the puzzle together. Inserting the expression for the stress-energy tensor (ii)) given in Eq. 3.13 inside the Einstein equations (Eq. 3.4) describing gravity in virtue of iii) and assuming a FLRW metric for g , (Eq. 3.10) to ensure i), one can derive the *Friedmann-Lemaître* equations

$$H^2 = \left(\frac{\dot{a}}{a}\right)^2 = \frac{8\pi G}{3}\rho + \frac{\Lambda}{3} - \frac{\kappa}{a^2}, \quad \frac{\ddot{a}}{a} = H^2 + \dot{H} = -\frac{4\pi G}{3}(\rho + 3p) + \frac{\Lambda}{3}, \quad (3.17)$$

where $\rho = \rho_m + \rho_r$ and $p = p_m + p_r = p_r$ are the standard matter density and pressure. Those are the fundamental equations of standard Cosmology, that can be solved in specific scenarios to obtain the background evolution of the Universe $a(t)$. These equations can be further simplified by introducing densities and pressure for the geometrical components (Λ and κ) as discussed in the previous section.

Introducing the critical density $\rho_c := 3H_0^2 M_{\text{Pl}}^2$, we can associate a so called *density* parameter to each component as

$$\Omega_i := \frac{\rho_0^i}{\rho_c} \quad i \in \{m, r, \Lambda, \kappa\}. \quad (3.18)$$

Combined with Eq 3.16, the fundamental equations of cosmology take the compact form

$$\left(\frac{H}{H_0}\right)^2 = \sum_i \Omega_i a^{-3(1+w_i)}, \quad \frac{\ddot{a}}{aH_0^2} = -\frac{1}{2} \sum_{i \neq \kappa} \Omega_i (1 + 3w_i). \quad (3.19)$$

Evaluating the first equation today ($a_0 = 1, H = H_0$), we obtain $\sum_i \Omega_i = 1$, known as the the *closure equation*, allowing to interpret the Ω_i as fractions of the various components in today's Universe. If there is a single component of density Ω_i and equation of state w with $w \neq -1$, one can integrate Eq. 3.17 to get the time between today and a given scale factor value a

$$\left(\frac{da}{dt}\right)^2 = H_0^2 \Omega_i a^{-3(1+w)+2} \Rightarrow t = \frac{1}{\sqrt{\Omega_i} H_0} \int_0^a a^{\frac{3}{2}(1+w)-1} da = \frac{2a^{\frac{3}{2}(1+w)}}{3(1+w)\sqrt{\Omega_i} H_0}, \quad (3.20)$$

from which we can derive the rate of evolution of the scale factor with time

$$a(t) \propto t^{\frac{2}{3(1+w)}}, \quad (3.21)$$

which is expected to model correctly the evolution of the scale factor whenever the contribution to the Universe's dynamic of a single component is dominant over the others.

3.3.4 Perturbation theory in a nutshell

Friedmann equations only describe the so-called background evolution, assuming only homogeneous fluids and no coupling between the various sectors of the Universe. On small scales however, it is clear that such assumptions must break, as the Universe appears to have local inhomogeneities with the presence of clusters of galaxies and large scale filamentary structures.

3. MODERN COSMOLOGY: THE STANDARD MODELS

These inhomogeneities will be modeled as perturbations of the various cosmological quantities around the homogeneous background. They will evolve first linearly with the expansion and non linearly with gravity to give birth to structure. At the perturbation level, one must also allow for particles of various species to interact, such that they do not satisfy the continuity equation anymore. For a complete introduction see e.g. [Ma & Bertschinger \(1995\)](#) and [Lesgourges \(2001, 2013\)](#).

To do so, we decompose locally any quantity X (e.g. $g_{\mu\nu}$ or $T_{\mu\nu}$) as $X(x^\mu) = \bar{X} + \delta X(x^\mu)$ with the perturbation $\delta X(x^\mu) \ll \bar{X}$ and \bar{X} describes the *background* mean quantity which evolution is given by the Friedmann equations introduced above.

As discussed earlier, there are strong similarities between gauge theories and GR in the way they treat frame transformations. In principle one can always choose a convenient frame i.e. a gauge in which the calculations are easier. From the 10 perturbations present in cosmology, only 6 combinations can not be cancelled using a convenient frame transformation, such that fixing a gauge can drastically reduce the number of degrees of freedoms. The Newtonian gauge or longitudinal gauge is such a choice in which the perturbed metric tensor can be decomposed as⁴⁴

$$g + \delta g = -(1 + 2\Psi) dt \otimes dt + a(t)^2 [(1 - 2\Phi)\delta_{ij} + \hat{h}_{ij}] dx^i \otimes dx^j. \quad (3.22)$$

Φ can be interpreted as local variations of the scale factor and Ψ , called the "lapse function" can be interpreted as local fluctuations in the gravitational potential, satisfying itself the Poisson equation $\nabla^2\Psi/a^2 = 4\pi G\delta\rho$. \hat{h}_{ij} is a tensor term describing perturbations due to gravitational waves.

From this perturbed metric and the perturbations of density, one can create the gauge invariant combination

$$\mathcal{R} = \Phi - \frac{1}{3} \frac{\delta\rho}{\bar{\rho} + \bar{p}}, \quad (3.23)$$

which can be interpreted as a spatial curvature perturbation.

Being mainly interested in the statistical properties of the perturbations one can Fourier-transform any gauge invariant quantity X in the flat 3D space with associated wavevector \mathbf{k} as

$$X(\mathbf{k}) = \int X(\mathbf{x}) e^{i\mathbf{k}\cdot\mathbf{x}} d^3\mathbf{x}. \quad (3.24)$$

If one assumes that the perturbations are Gaussian – which is strongly supported at first order by observations of the CMB as we will detail in [5](#) – the Fourier modes fully describe their statistical properties. The modes evolve independently under their equation of motion extracted from the Einstein equations, that we will not further detail here. From this Fourier expansion one can define the power-spectrum as

$$\langle X(\mathbf{k})X(\mathbf{k}'^*) \rangle = (2\pi)^3 \delta^3(\mathbf{k} + \mathbf{k}') \mathcal{P}^X(k), \quad (3.25)$$

with $k = |\mathbf{k}|$ and δ^3 the three dimensional Dirac distribution. From $\mathcal{P}^X(k)$, one usually introduces the rescaled power spectra

$$\Delta_X^2(k) := \frac{k^3}{2\pi^2} \mathcal{P}^X(k), \quad (3.26)$$

⁴⁴Where we neglected vector perturbations, expected to be small and quickly diluted in standard cosmology.

which quantifies deviations from an homogeneous and scale invariant spectra ($\mathcal{P}^X(k) \propto k^{-3}$). As such, one can introduce the power spectrum of *scalar perturbations*, which is given by the power spectrum of the curvature perturbation

$$\Delta_s^2(k) := \Delta_{\mathcal{R}}^2(k) = \frac{k^3}{2\pi^2} \mathcal{P}^{\mathcal{R}}(k). \quad (3.27)$$

Measuring the shape of $\Delta_s^2(k)$ represents a major challenge of modern cosmology. We define the scalar spectral index n_s and the scalar curvature α_s as

$$n_s - 1 := \frac{d \ln \Delta_s^2}{d \ln k}, \quad \alpha_s := \frac{dn_s}{d \ln k}. \quad (3.28)$$

$n_s = 1$ and $\alpha_s = 0$ would thus correspond to the scale invariance of scalar perturbations. The tensor perturbations quantified by \tilde{h} are also gauge invariant at linear order. As such we introduce the power spectrum of *tensor perturbations* and its corresponding spectral index

$$\Delta_t^2(k) \cong 2\Delta_h^2(k), \quad n_t := \frac{d \ln \Delta_h^2}{d \ln k}. \quad (3.29)$$

Note that n_t is defined differently than n_s , as the first one is expected to be close to zero while the second is expected to be close to unity. If the perturbations are nearly scale invariant, one can assume that the spectra are well modeled by power-laws like

$$\Delta_s^2(k) \simeq A_s \left(\frac{k}{k_0} \right)^{n_s - 1 + 0.5\alpha_s \ln(k/k_0)}, \quad \Delta_t^2(k) \simeq A_t \left(\frac{k}{k_0} \right)^{n_t}. \quad (3.30)$$

The tensor-to-scalar ratio r_{k_0} is defined to be the ratio of the amplitudes

$$r_{k_0} := \frac{A_t}{A_s}. \quad (3.31)$$

It is common to evaluate $r \equiv r_{0.05}$ around $k_0 = 0.05 \text{ Mpc}^{-1}$. Unless some mechanism as inflation is invoked (see Sec. 4.1.2), one expects the tensor perturbations (i.e. the gravitational waves)⁴⁵ to be extremely small such that $A_t \simeq 0$ and $r_{k_0} \simeq 0, \forall k_0$.

3.4 6 parameters to describe the Universe.

3.4.1 Cosmological probes

Modern cosmology is based on a multitude of independent experiments that are agreeing with high accuracy with the Λ -CDM model introduced above, justifying its name of *concordance model*. Combining multiple probes, probing the Universe at very different temporal and spatial scales allows one to break significant degeneracies between parameters of the model.

An inquiry of first cosmological importance is to refine the characterization of the expansion in the local Universe. This goes along the line set by Hubble's measurement and aims to get

⁴⁵Significant gravitational waves can only be generated by matter distribution with a quadrupolar asymmetry.

3. MODERN COSMOLOGY: THE STANDARD MODELS

a fine estimate of H_0 . To do so, one relies heavily on the existence of astrophysical phenomena with invariant intrinsic luminosity, known as *standard candles*. The transformation of degenerated stellar cores, the white dwarves, into neutron stars are expected to provide such standard candles as bright as their host galaxies. This transformation occurs commonly in Supernovae of Type Ia (SNIa) through stellar cannibalism of a nearby companion (typically a red giant) or by the merger of two white dwarves (leaving no compact remnant ([Alsabti & Murdin, 2017](#))). The invariance of their luminosity is due to the quantum threshold of the electron degeneracy pressure set by the Chandrasekhar mass of $\sim 1.4M_\odot$. A recent SNIa catalogue is given by the *Pantheon* dataset, and its recent update *Pantheon+* ([Scolnic et al., 2022](#)). To recover H_0 , SNIa luminosity must be calibrated with other distance estimators. For example, the *SH0ES* experiment provides an estimation of H_0 from SNIa measurements calibrated with Cepheids⁴⁶ measurements using both the *Hubble* space telescope and the *Gaia* data ([Riess et al., 2022](#)). The Rubin Legacy Survey of Space and Time (Rubin *LSST*) survey, will be able to map the light curve of numerous transient objects and widely extend the known SNIa measurements (from ~ 1500 today to $\sim 100\,000$) ([Hambleton et al., 2022](#)). Complementary experiments as ZTF will also significantly constrain observables as the growth rate using SNIa ([Howlett et al., 2017](#); [Carreres et al., 2023](#)).

The cartography of the galaxy distribution on very large scales allows one to access the shape of Δ_s^2 at different epochs. The study of large scale structures of the Universe can be accessed through several observables: galaxy clustering which consists of mapping the galaxy distribution in redshift space, or weak lensing survey which maps the mass in the Universe depending on how strongly deflected is the light of background galaxies. Large photometric and spectroscopic galaxy surveys are able to map these distribution in 3D both in space and time (i.e. redshift). They are able to detect the primordial baryon acoustic oscillations (BAO) patterns in the matter distribution on large scales (and are hence referred to as "BAO" measurements). The five Sloan Digital Sky Surveys (*SDSS*) ([Almeida et al., 2023](#)) of which the *BOSS* survey was part of, and the Dark Energy Spectroscopic Instrument (*DESI*, [Levi et al., 2019](#)) are major major missions designed for this purpose. This year (2023), the *Euclid* satellite was launched to provide a large galaxy survey from space and investigate the nature of dark energy ([Amendola et al., 2018](#)). I have a major interest in the *Euclid* mission – in which IRAP is strongly involved – as I will further discuss in Sec. 9.7. Since 2020, I am an active member of the consortium.

The cosmic microwave background (CMB) radiation is the oldest observable light in the Universe. It was emitted around 380 000 years after the primordial singularity ($t = 0$), when the Universe became neutral due to the formation of the first hydrogen atoms. As a main topic of this thesis, we will review in detail the CMB physics and the CMB missions in Chap. 5. Accurate mapping of the CMB signal and its anisotropies provides a major probe of the cosmological parameters. As a related probe, Big Bang Nucleosynthesis (BBN) infer the primordial abundances created in the early Universe, which constrains cosmology at early times.

Additionally, several emerging independent cosmological probes complete this picture, even though they provide less competitive constraints. For example observation of the 21 cm and Lyman- α lines in the early Universe allow to probe the earliest epochs of the Universe. On

⁴⁶Pulsating stars satisfying a period/intensity relation, making them standard candles.

the other hand, the development of multi-messenger astronomy, which combines light emission with neutrinos and gravitational waves, is gradually entering the field of cosmology, and opens new windows on the cosmological physics at all scales. Additionally, the mapping of cosmic voids, cosmic chronometers, the quest for the redshift drift, etc... are or contributing to our modern understanding of the Universe. For a review see e.g. [Moresco et al. \(2022\)](#).

3.4.2 The picture so far

$\ln(10^{10} A_s)$	n_s	H_0	z_{reio}	Ω_b	Ω_{CDM}
3.047 ± 0.014	0.966 ± 0.004	67.7 ± 0.4	7.64 ± 0.74	0.0331 ± 0.0002	0.2762 ± 0.0013

Table 3.1: Best-fit values of the Λ -CDM parameters with associated 68% confidence level combining data from the *Planck* spectra and lensing combined with BAO measurements ([Planck Collaboration et al., 2020a](#)).

Combining the latest measurements of the CMB by the *Planck* mission with BAO, one obtains the values displayed in Tab. 3.1 ([Planck Collaboration et al., 2020a](#)). Other probes presented in Sec. 3.4.1 are in agreement with these values but do not have enough statistical power to improve these results. We introduce here the redshift at which reionization ended z_{reio} , which quantifies the time at which the ionization of the Universe by the first stars was complete. All other Λ -CDM parameters discussed above but not displayed in the table are either compatible with zero or can be derived from the ones given here. As such, and being conservative, only 6 parameters are required to describe completely the concordance model and obtain the best possible fit of the current available data.

$\Omega_\kappa = 0.0007 \pm 0.0037$ is compatible with zero, in agreement with a flat Universe. Similarly A_t and r are both compatible with zero. From *WMAP* data, $\Omega_r \simeq 1.67219 \times 10^{-5}$, dominated by the CMB radiation ([Bennett et al., 2013](#)). From the closure relation, one can get $\Omega_\Lambda = 0.689 \pm 0.006$ and $\Omega_m = \Omega_b + \Omega_{\text{CDM}} = 0.311 \pm 0.004$, depicting a present Universe mostly dominated by dark matter and dark energy.

3.5 A brief history of the Universe as we know it

The general solutions of the Friedmann equations can be computed numerically, as I did in Fig. 3.2 for the best fit values of the Λ -CDM model. For a detailed discussion see for example my contribution in collaboration with my intern Jehanne Delhomelle on [this website](#)⁴⁷. In agreement with Eq. 3.17, one can witness on Fig. 3.2 that the scale factor has a first brutal increase, due to a first phase of radiation domination $a(t - t_0) \propto \sqrt{t - t_0}$, then matter starts dominating and the expansion is significantly slowed down as $a(t - t_0) \propto (t - t_0)^{2/3}$. Finally, matter gets diluted enough for Λ to dominate. A brutal acceleration phase thus starts as $a(t - t_0) \propto e^{H_0 \sqrt{\Omega_\Lambda}(t - t_0)}$. From the graph, one can evaluate the age of the Universe to be ~ 14 Gyr. As $a(t)$ increases, the density of particles and the effective temperature (assuming thermal equilibrium) decreases. This allows for a hierarchy of new phenomenon as phase transitions to occur gradually as follows⁴⁸:

⁴⁷<https://yolonomy.github.io/codes/cosmo/friedmann/>

⁴⁸Associated comoving times t are given as indicative values, and redshift z are also given when observation start being possible. Educational softwares as <https://github.com/anisotropela/Universe-timeline>

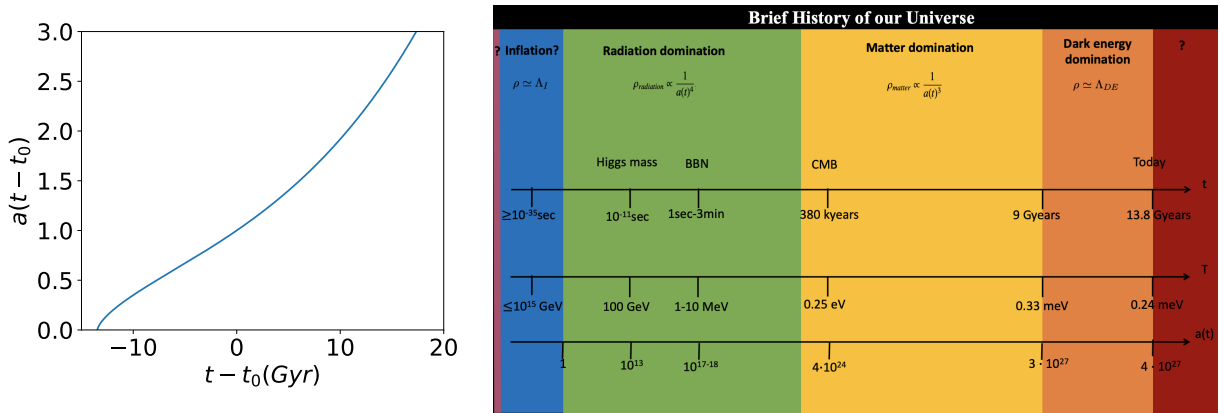


Figure 3.2: Left: evolution of $a(t - t_0)$ in Λ -CDM, with the values given in Tab. 3.1 for the densities Ω_i . Codes can be found on [this page](#). Right: Schematic representation of the cosmic history, green: radiation domination, yellow: matter domination, orange: Λ domination. Taken from [Cicoli et al. \(2023\)](#).

- **Primordial singularity** ($t < 10^{-14}$ s): Extremely early times can not be described by the standard models as presented above. Frameworks beyond SM are required to provide hypothesis on the physical phenomena involved here. We will further discuss them in Chap. 4.
- **Electroweak transition** (10^{-14} s $< t < 10^{-10}$ s): Fundamental physics that can be probed in particle accelerators starts acting. At high energy, electromagnetism and the weak force are unified within a single gauge group $SU(2) \times U(1)_Y$, mediated by three W_i and a B bosons. All particles are massless. For an effective temperature lower than ~ 160 GeV, the Higgs boson's potential acquires a "Mexican hat" shape, allowing the scalar field to vacuum decay and roll down spontaneously to a new vacuum, breaking the gauge group to $U(1)_{\text{em}}$ and $SU(2)_L$, leading to the apparition of two charged massive bosons W^\pm and two neutral bosons: the Z^0 and the photon. The particles of the standard model, can now acquire a mass through their interaction with the Higgs boson h via the Yukawa couplings. As such, an electroweak phase transition occurs in the whole Universe and h transmits its vacuum value to neighboring points at the speed of light. The sphere of space which will be stretched by expansion to become the observable Universe is about 300 light-seconds in radius at that time.
- **Hadron formation** ($t \sim 10^{-5}$ s): After electroweak transition, the primordial fluid is in the state of a quark-gluon plasma. When the Universe cools down, quarks are able to bound and form the first hadrons (baryons and mesons), hence leading to another phase transition in the primordial Universe.
- **Neutrino decoupling** ($t \sim 0.2$ s): The density becomes low enough for neutrinos to stop interacting significantly with the other matter fields. As such, the neutron to proton ratio is fixed at around 1/6, since the weak force stops being able to transform one into the other (this value can be explained by the higher mass of the neutron). The sphere of space which will be stretched by expansion to become the observable Universe is about 10 light-years in radius at that time.

allows one to compute the values of the comoving time, temperature, redshift, densities and size of the observable Universe associated with the different epochs.

- **BBN** ($t \sim 200\text{s} \rightarrow 300\text{s}$): The energy range allows for protons and neutrons to fuse into heavier elements as D (${}^2\text{H}$), ${}^3\text{He}$, ${}^4\text{He}$ and ${}^7\text{Li}$, abundances of which can be predicted with high accuracy, in agreement with standard model predictions (excepted some discrepancy on the lithium which will be discussed in Sec. 9.2). For a review, see [Pitrou et al. \(2018\)](#). The sphere of space which will be stretched by expansion to become the observable Universe is about 300 light-years in radius at the end of BBN.
- **Recombination** ($t \sim 18\text{ kyr} \rightarrow 380\text{ kyr}, z \sim 6000 \rightarrow 1100$): Matter-radiation equality is reached in that period, for $t \sim 50\text{ kyr}$, ending the radiation dominated era and starting the matter dominated one. Gradually, the energy becomes low enough for the first atoms to form without being ionized. Photons thus stop interacting significantly with the other matter fields and decouple. The CMB radiation is emitted.
- **Dark ages** ($t \sim 380\text{ kyr} \rightarrow 150\text{ Myr}, z \sim 1100 \rightarrow 60$): After recombination, all the matter is expected to be in the form of a gas of atoms, interacting solely through gravity. No photon is produced (except from the hydrogen lines in radio bands) and the Universe is hence deprived of visible light.
- **Cosmic Dawn** ($t \sim 150\text{ Myr} \rightarrow 200\text{ Myr}, z \sim 60 - 20$): Over-passing Jeans' mass, clumps of matters start to form and spontaneously collapse around over-densities of dark matter. This lead to the formation of the first stars (so called population III stars) and galaxies.
- **Reionization** ($t \sim 200\text{ Myr} \rightarrow 1\text{ Gyr}, z = 20 - 6$): The birth of the first stars triggers the last phase transition of the Universe. Because of the great amount of energy radiated by population III stars in the UV, the interstellar and intergalactic medium (ISM and IGM) will progressively get ionized again (see e.g. [Wise, 2019](#)). After reionization, the ISM and IGM are almost completely ionized again, in a very hot and highly diffuse state (~ 1 atom per m^3).
- **Large scale structure formation** ($t \sim 1\text{ Gyr} \rightarrow 5\text{ Gyr}, z \sim 6 \rightarrow 1$): The non-linear evolution of gravity shapes the structure on all scales. Stars organize in galaxies, and galaxy clusters start to form around 3 Gyr ($z \sim 2$). These clusters arrange themselves gradually into super-clusters (around 5 Gyr, and $z \sim 1$) forming a cosmic web structure on the largest scales. For a recent review on structure formation see e.g. [Huterer \(2022\)](#).
- **Late Universe** ($t \geq 5\text{ Gyr}, z > 1$): Sun and the Solar system form within the Milky Way at $t \sim 8.8\text{ Gyr}$. The first forms of life are expected to appear very quickly on Earth, for $t \sim 9.3\text{ Gyr}$. They will witness the beginning of the accelerated expansion phase which starts at $t \sim 10.2\text{ Gyr}$ ($z \sim 0.3$).
- **Present times** ($t_0 \sim 13.8\text{ Gyr}, z = 0$): Humans start doing cosmology while the observable Universe reaches a size of ~ 46 billion light-years of radius.
- **Near and far future:** Within standard Λ -CDM model, nothing can stop the present phase of Λ domination. The Universe is hence expected to keep on expanding. When the entropy will be maximal, thermal equilibrium will be reached. In the meanwhile, galaxies will progressively stop forming new stars (quenching), while older stars will gradually die in supernovae and planetary nebulae. Matter is expected to transform into black holes, which will progressively radiate away due to Hawking radiation, when

3. MODERN COSMOLOGY: THE STANDARD MODELS

the CMB signal will no longer be hot enough to prevent their evaporation. The exact evolution on the long term is extremely dependent on the possibilities offered by theories beyond our standard model (as e.g. proton decay in grand unification theories – GUT – or existence of new fields impacting the cosmic dynamics). For an overview see e.g. [Riazuelo \(2011\)](#).

The Λ -CDM model is hence a very powerful framework based on our current understanding of fundamental physics, which allows us to understand most of our cosmic history with only 6 parameters. However, beside its success, this model presents some conceptual limitations and observational puzzles which will be the focus of the next chapter. The challenge to go beyond these limitations and tensions is of first interest as it would refine our understanding of the Universe and allow us to shed some light on new physics.

4

Puzzles and missing pieces of our standard models

Je ne suis pas de ces brutes malavisée qui soulèvent les problèmes et les laissent retomber sauvagement sur la gueule de leur prochain

– Boris Vian. Propos

Contents

4.1	Late and early tensions	35
4.2	Are there new entities awaiting out there to be discovered? . .	40
4.3	A scalar field for each puzzle	44

As we discussed in the previous chapter, the Universe’s dynamics is fully determined by its geometry and content. As such, observational cosmology provides a probe of fundamental physics. For example, it is astonishing that subtle parameters, as the number of lepton generations of the standard model and the total mass of neutrinos can be precisely constrained by the statistics of the matter distribution on cosmological scales (the matter power-spectra). As such, any puzzle and tension between cosmological theory and observation can become a challenge for our standard models and hints for new physics. In such a situation, if we assume the symmetries imposed by the cosmological principle, we are forced to conclude that a modification of either the particle content of our high energy physics or the theory of gravity is needed.

4.1 Late and early tensions

4.1.1 Puzzles in the late universe: the dark sides

Dark energy

In the Λ -CDM model, the accelerated expansion of the Universe can be fully explained by the presence of a non vanishing cosmological constant Λ in the Einstein-Hilbert action (Eq. 3.6),

which can be interpreted as a constant vacuum energy which repulsive pressure balances gravitational attraction. While this description fits elegantly within GR¹, it is not presently reconcilable with quantum field theory (QFT). Indeed, renormalization allows to estimate the vacuum energy contribution of the SM fields and can not be made compatible with the cosmological value of Λ (with a discrepancy of $\sim 10^{120}$! [Weinberg, 1989](#)). This discrepancy is however subject to discussion as we might not fully understand how to compute the zero point energy of quantum fields in a curved space-time ([Moreno-Pulido & Solà Peracaula, 2020](#)). Another potential puzzle is given by the "coincidence problem", stating that it would require some extreme fine tuning to allow for the matter/dark-energy transition to happen in the present cosmological era. For a discussion, see e.g. [Velten et al. \(2014\)](#). However, the coincidence problem reduces to the more general problem of the fine tuning applied to Λ , which arguably applies to all of the fundamental constants (see Chap. 9).

Moreover, some tensions come from the observational side, as estimations from the early Universe (i.e. CMB) seems in significant conflict ($> 4\sigma$) with the local measured value of H_0 estimated using standard candles. If not coming from statistical/methodological errors, this would hence provide a tempting hint that there is more to dark energy than Λ . For a review, see e.g. [Di Valentino et al. \(2021\)](#). Despite the always increasing interest of the cosmological community for the H_0 tension as a probe of new physics, Λ still provides a highly robust explanation for dark energy and systematic errors or methodological flaws – as astrophysical processes rendering the candles non standards e.g. a redshift dependence of the calibration relation of cepheids (see Sec. 7 of [Riess et al. \(2022\)](#)) or the eventual impossibility to apply the FLRW metric at all scales ([Fleury et al., 2013](#)) – might be preferable. The increasing sensitivity of cosmological surveys as well as the use of new standard sirens (as Gravitational waves ([Holz & Hughes, 2005](#))) will undoubtedly shed some light on this tension in the coming decades.

Dark matter

While Λ -CDM requires "CDM" to be in agreement with cosmological observations , it remains agnostic on its nature, and our standard model of particle physics does not seem to provide any candidate that would have the desired properties (see [Bertone et al. \(2005\)](#) and references therein). However, numerous candidates for CDM are provided by theories beyond the standard model, gathered under the name of weakly interactive massive particles (WIMP). Promising WIMP candidates are given by the lightest supersymmetric partners of supersymmetric theories as the neutralinos in the minimal supersymmetric model. CDM could also be explained by baryonic objects as primordial black holes, produced by fluctuations in the plasma of the early Universe ([Frampton et al., 2010](#)). Beyond CDM, some hot dark matter models still remain competitive. For example, the existence of right handed

¹It is however often argued that such a small observed value of Λ is "unnatural" within GR. The question of naturalness in physics (very close to the notion of "fine tuning") is omnipresent in high energy physics and cosmology. It states roughly that the free parameters of our models (and more meaningfully dimensionless ratios) should not have incredibly large or small values, or in other words that they should be of order unity. This relates strongly with the discussions we will have in Chap. 9. This principle can be questioned as the Standard Model already is unnatural since most of its dimensionless parameters are much smaller than unity (see the list given in Tab. 9.1). Whether naturalness is a meaningful physical argument or not is still open to debate. Several refined definitions have emerged, supplementing the debate (see e.g. ['t Hooft, 1980](#)). For a discussion, see also e.g. [Wallace \(2019\)](#).

4.1. LATE AND EARLY TENSIONS

sterile neutrinos could explain dark matter with a very minimal and motivated extension of our SM² (For a review see e.g. [Boyarsky et al., 2019](#)). Dark matter could also be explained by a modification of the behavior of gravity on large scales, as originally suggested by the "MOND theories" (see e.g. [Famaey & McGaugh \(2012\)](#))³. So far, the true nature of dark matter remains frustratingly elusive and the increasing accuracy of laboratory experiments and cosmological surveys do not yet allow to pinpoint a preferable candidate, making it one of the most thorny and exciting problem of contemporary physics.

4.1.2 Puzzles in the early Universe

The Primordial singularity

As one can already see at the level of Friedmann equations (Eq. 3.17), the Big-Bang cosmology becomes mathematically singular when $a \rightarrow 0$ for the measured cosmological parameters. Formally, singularities in GR are hyper-surfaces of space-time where all geodesics converge⁴. Perhaps their most known realization can be found at the center of black holes. They appear to be consequences of Einstein equations themselves (Eq. 3.4) and not only properties of its idealized solutions ([Hawking, 1966](#)). This is a clear indication of the limits of GR as a theory of gravitation in the very strong field limit and the consequences of the existence of singularities has been discussed in great length in the past decades. In conditions of extreme density and energy, gravitation is expected to have a strength comparable to the other forces, requiring a quantum treatment of gravity or at least a classical but quantum-compatible treatment of it. For a review see e.g. [Vasconcellos \(2020\)](#).

The existence of primordial singularity towards $t \rightarrow 0$ actually translates our ignorance on the exact "birth" of our Universe. Several solutions are proposed by quantum gravity models as string theory or loop quantum gravity that we will not further present here.

Initial condition problems and the need for inflation

Regarding the early Universe, puzzles are of various types: either some observables appear to have incredibly specific values (fine tuning), some observables are predicted but not observed (missing observable) and some observables are observed but not explained (unexplained observable).

- **Flatness problem (fine tuning):** Introducing the total density parameter as a function of the scale factor

$$\tilde{\Omega}(a) = \sum_{i \neq \kappa} \frac{8\pi G \rho_i(a)}{3H(a)}, \quad (4.1)$$

one can simply rewrite the Friedmann equation (Eq. 3.17) as

$$1 - \tilde{\Omega}(a) = -\frac{\kappa}{\dot{a}^2}. \quad (4.2)$$

²Remembering here that only left chiral spinors are sensitive to weak interaction, such that an hypothetical right chiral sterile neutrino would only interact through gravity.

³For a review of the dark matter candidates, see the review "Dark Matter" by L. Baudis and S. Profumo in [Zyla et al. \(2020\)](#).

⁴In a broader sense, a singularity is just an indication of the limit of application of a theory, often translating by the apparition of infinities. For example, consider what happens at $r = 0$ for the gravitational force in Newtonian gravity (GM/r^2).

This rewriting renders explicit that, at any time, the difference between $\tilde{\Omega}(a)$ and 1 quantifies deviation to flatness. Derivating Eq. 4.2 with respect to time gives

$$\frac{d}{dt}(1 - \tilde{\Omega}) = -2\frac{\ddot{a}}{\dot{a}}(1 - \tilde{\Omega}). \quad (4.3)$$

As we discussed in Sec. 3.5, until very recent times, the universe only knew phases of decelerated ($\ddot{a} < 0$) expansion ($\dot{a} > 0$)⁵. In this context, the point $1 - \tilde{\Omega} = 0$ is an unstable point and any small deviation from zero would be exponentially amplified. In this regard, observational constrains of $|1 - \tilde{\Omega}(a_0)| < 5 \times 10^{-3}$ (Planck Collaboration, 2016a), suggest that our Universe is spatially flat as already mentionned in Sec. 3.4.2. We can see that having such a flat Universe $\kappa \sim 0$ today requires an incredible fine tuning of the early Universe. More precisely, it would require $|1 - \tilde{\Omega}| \leq 10^{-5}$ at recombination, $|1 - \tilde{\Omega}| \leq 10^{-16}$ during BBN and $|1 - \tilde{\Omega}| \leq 10^{-61}$ at the Planck scale. Indeed, any small deviation from flatness greater than this in the past would have been strongly amplified and would be observable today. One can argue that the Universe is simply flat ($\kappa = 0$ exactly) and hence there should not be any problem of the sort. Note however, that nothing in our building blocks of cosmology (as the cosmological principle), justifies that this value of κ should be preferred over any other.

- **Horizon problem (fine tuning):** As we will discuss in greater details in Chap. 5, the CMB depicts an extremely homogeneous primordial Universe with deviations to the mean temperature of $\Delta T / \bar{T} \sim 1 \times 10^{-5}$ K. However, the CMB signal can be split in $\sim 10^4$ causally independent regions of emission over the celestial sphere. In order to explain how causally disconnected regions can be at the same temperature, they should have been in causal contact in the past to allow for their thermalization. The radius of the region at which points can be in causal contact is typically given by the *Hubble horizon* $(aH)^{-1}$. From Eq. 3.20, we can show that

$$\frac{d}{dt}((aH)^{-1}) = \frac{d}{dt}\left(\frac{1}{\dot{a}}\right) \propto 1 + 3w. \quad (4.4)$$

For all standard fluids dominating the cosmological evolution until now, $1 + 3w \geq 0$ (except dark energy that strikes only at very late times). Thus the $(aH)^{-1}$, can only increase with time, such that it was smaller in the past, before the CMB emission. As such, Λ -CDM can not allow for a previous causal contact and thermalization of the disconnected but homogeneous regions observed in the primordial Universe.

- **Low entropy (fine tuning):** To allow for the present structured and dynamical state, the Universe must have started in a state of extremely low entropy (otherwise it would have already reached its maximum)⁶. This low entropy is not justified by any mean within our standard models.

⁵To obtain $\dot{a} > 0$ and $\ddot{a} < 0$, consider Eq. 3.19 with $w_r = 1/3$ and $w_m = 0$ for radiation domination and matter domination respectively.

⁶This seems to be in contradiction with observations as the CMB radiation displays an early Universe in thermal equilibrium (because of the blackbody radiation see Chap. 5), which corresponds to a state of maximal entropy. However, today's Universe is clearly not in thermal equilibrium as its content appears as structured and dynamical. The (non trivial) solution to this problem is to also consider the entropy associated with the gravitational degree of freedom of the denser early Universe (Penrose, 1979, 2009). This argument can however be misleading and should be taken with care. For clarifications on this point see Wallace (2010) and Rovelli (2019).

4.1. LATE AND EARLY TENSIONS

- **Cosmological topological defects (missing observable):** Statistical physics tells that highly energetic systems tend to be symmetric and loose spontaneously these symmetries in phase transitions by cooling down⁷. Such a behavior is also expected at the Universe's scale with e.g. gauge symmetries and the energy decreasing due to expansion.

A spontaneous gauge symmetry breaking is already required within the standard model of particle physics in the framework of Weinberg-Glashow-Salam electroweak unification and breaking (Weinberg, 1967; Salam, 1969; Glashow, 1961). It must occur in the early Universe as described in Sec. 3.5. There are strong indications that the strong force could also be unified to the other two forces at higher energy within a larger gauge group (de Boer, 1994; Croon et al., 2019). For example, all the coupling constants seem to run with energy towards a similar value (see Chap. 9). A theory unifying the three forces is called a grand unification theory (GUT). SU(5) was favored as a gauge unifying group but was excluded by proton decay experiments⁸. Other groups as SO(10) are still under investigation. Full unification model including gravity seems to require larger gauge groups as e.g. SO(32) or $E_8 \times E_8$ for superstring theory.

When a gauge group is spontaneously broken, the breaking is expected to be different at different points of space-time from which it will propagate at the speed of light. When these regions with different breaking points encounter, the so called "topological defects" form on their point of contact. They can be of different types:

- **Domain walls** are two-dimensional objects which form from a phase transition breaking a discrete symmetry.
- **Cosmic strings** are one-dimensional or line-like objects forming when a phase transition breaks an axial or cylindrical symmetry as U(1). They are thus expected after electroweak symmetry breaking as very dense and thin objects in fast rotation. They must form loops and spontaneously decay. While they have no gravitational pull they must be sources of gravitational waves and lensing.
- **Monopoles** are zero-dimensional point-like objects which form when a phase transition breaks a spherical symmetry (very massive magnetic monopoles are expected in GUT).

These topological defects can then interact together and with the rest of the SM in a rather rich fashion. They are unavoidable and must have strong observational consequences (e.g. in the CMB). It is then a major challenge to justify why they are yet undetectable. For reviews and discussions see (Gangui, 2001; Martins, 2020; Peter & Uzan, 2009).

- **The primordial seed problem (unexplained observable):** while the early Universe looks very homogeneous, some inhomogeneities are still observed, and they are in fact necessary, as they will give rise to all the structure observed today through gravitational interaction. It can be shown that thermal fluctuations (always present

⁷One can think of magnetic moments in ferromagnetic materials lining up with the Earth magnetic field when cooling down.

⁸GUT predict a limited lifetime for the proton. Constraining its stability is thus a powerful probe of unification theories.

in a gas) could not be large enough to explain the deviations to the mean observed in the CMB ([Smoot et al., 1992](#); [Liddle, 1995](#)). As such, what could have sourced these anisotropies and why do they have this amplitude?

Note that it could be (and is) argued that the fine tuning problems should not be considered as relevant. Things could just be "the way they are". The Universe could simply have been born in very specific conditions. However, (almost) all of the above puzzles can be solved elegantly by the introduction of an acceleration phase in the early Universe ($\ddot{a}/a > 0$ and hence $w \leq -1/3$) named "inflation" (for complete reviews see e.g. [Baumann, 2009](#); [Zyla et al., 2020](#)). Such a phase of inflation would indeed:

- solve the flatness problem. In Eq. 4.3 the right hand side would be negative during inflation, making the flat universe $1 - \tilde{\Omega} = 0$ an attractor point, thus pushing any initial condition exponentially towards extreme flatness.
- create a shrinking of the Hubble radius in Eq. 4.4, such that causally disjoint regions could have been in causal contact before inflation, allowing the fluid to thermalize at very early times.
- dilute the topological defects such that they become extremely spread apart and unobservable (yet?).

The duration of inflation is measured in number of "e-folds", that is the logarithm of the ratio of the scale factors between the end (t_e) and the start (t_i) of the inflationary phase: $N_* = \ln(a(t_e)/a(t_i))$. It can be shown that one must have $N_* \sim 50/60$ in order to consistently solve the horizon problem ([Liddle & Lyth, 2000](#)). Such a phase of accelerated expansion can not be introduced by the/a cosmological constant as its value would have to cancel in late times, requiring this constant to be a dynamical entity and hence a field. This additional condition might solve the primordial seed problem by introducing primordial quantum fluctuations if the field is itself a quantum field. These quantum perturbations will then be stretched to macroscopic scales by inflation itself ([Starobinsky, 1982](#))⁹. We will further discuss how to generate inflation from a new field in Sec. 4.3.3. However, inflation is far from an ideal solution as its possible physical origins are highly uncertain and it does not systematically provide an efficient way to homogenize the primordial perturbations ([Pitrou et al., 2008](#)).

4.2 Are there new entities awaiting out there to be discovered?

4.2.1 Going beyond GR and Λ -CDM

Finding solutions to the cosmological puzzles described above calls for an extension of Λ -CDM. Following a minimal approach, and accepting the cosmological principle, we are left with only few options, as to either add new particle/field to the Universe's content, possibly motivated from particle physics or modify GR as a theory of gravity. More specifically, if

⁹The singularity problem remains when including inflation, as discussed in e.g. ([Fernández-Jambrina, 2021](#)). As far as I know, it is also yet unclear how to relate inflation and the entropy problem. For a discussion, see [Albrecht \(2002\)](#).

4.2. ARE THERE NEW ENTITIES AWAITING OUT THERE TO BE DISCOVERED?

one examines how to modify GR, it turns out that the options are rather limited and call for the existence of new fields. Indeed, the Lovelock "no-go" theorem states that all classical actions encompassing the EEP and invoking second order derivatives of g in 4 dimensions, give back a theory equivalent to GR (Lovelock, 1972). As discussed in [Shankaranarayanan & Johnson \(2022\)](#), in order to modify GR non trivially, one has to either:

- (L_1) Add new entities/fields coupled to gravity (through e.g. a term like $R\phi$ in \mathcal{L}_{EH} in Eq. 9.28). Such terms can appear in frameworks beyond the SM (as string theory with the dilaton field which will be discussed in Chap. 9) or when quantifying matter fields over a curved space time. Phenomenologically, these terms are added in the so called *scalar-tensor(-vector) theories*. For reviews see e.g. [Esposito-Farèse \(2004\)](#); [Quiros \(2019\)](#).
- (L_2) Add higher order derivatives of g in the Einstein-Hilbert Lagrangian (as $f(R)$, $f(T)$ or $f(Q)$ theories discussed in [Sotiriou & Faraoni \(2010\)](#); [Beltrán Jiménez et al. \(2019\)](#)). The presence of these higher order terms often appear as unavoidable loop corrections in high-curvature regimes of quantized theories of gravity or QFT in curved space-time.
- (L_3) Increase the number of dimensions of the space-time manifold¹⁰, which is a natural path taken by Kaluza-Klein and string theory. For a review, see e.g. "Extra-dimensions" by Y. Gershtein and A. Pomarol in [Zyla et al. \(2020\)](#).
- (L_4) Violate EEP and/or propose a new coupling of matter with gravity beyond standard minimal coupling. This can be done by the addition of torsion to the connection ([Watanabe & Hayashi, 2004](#); [Delhom, 2020](#)), which could moreover produce a source for dark energy and inflation ([Boehmer, 2005](#); [Benisty et al., 2022](#)) and solve the primordial singularity problem ([Kuchowicz, 1978](#)).
- (L_5) Allow for non local interactions as reviewed in [Capozziello & Bajardi \(2022\)](#).
- (L_6) Build a theory of gravity that is not derived from an action principle. This exciting route lead to the possibility to find back Einstein equations from basic principles of thermodynamics ([Jacobson, 1995](#)). As such space-time and its geometry could simply be emergent from an underlying microscopic dynamics, allowing to understand gravity as an entropic force ([Verlinde, 2012, 2017](#)).

For a review of these points see also [Tino et al. \(2020\)](#). Some of these modifications, as (L_1), (L_3) and (L_6) also imply, or are equivalent to a modification of the standard model of particle physics through the addition of new fields. As such, most of the extensions of Λ -CDM use one or several of the routes given above¹¹. For example we will discuss in Sec. 4.3.3 that models of inflation can be generated by coupling the Higgs field to gravity through (L_1) or by extending GR through (L_2). In this thesis, I will discuss the runaway dilaton model in Sec. 9.6, inspired from string theory, which goes beyond canonical GR through (L_1), (L_3) and (L_4).

¹⁰Note however that the $1/r^2$ decreasing of the gravitational (and EM) force, is a strong constraint on the fact that we are living in 3 extended spatial dimension (gravity dilutes on a expanding 2-sphere from a point source). Adding extra special dimensions have then to be compactified or some other "holographic" mechanism have to be invoked. They will be further introduced in Chap. 9

¹¹Note that most of the proposed alternatives witness a high level of fine tuning in order to match cosmological data and remain effectively close to Λ -CDM.

4.2.2 Scalar fields

Scalar field models propose to add one or several new dynamical entities given by a frame independent value of a real or complex number at every point of space-time. They are very common in the cosmological literature and are so often invoked because:

- They are easy to implement consistently without breaking the general covariance of the theory (Sec. 3.2.1). As such, they allow to build phenomenological "toy models" providing simple solutions to most of the cosmological puzzles introduced above. From the point of view of effective field theory (EFT), they can also reproduce the effective behavior of a more complicated underlying dynamics. They thus provides both simple and consistent modeling in order to seek for effects going beyond the SM, as possible variations of the fundamental constants of nature that we will investigate in Chap. 9.
- Due to Lovelock theorem, we know adding new fields represent one of our only options to go beyond GR (L_1). Moreover, multiple higher order terms modifications of the action of gravity (L_2) can be shown to be equivalent to the addition of one or several scalar fields coupled to gravity (Capozziello & de Laurentis, 2011). Furthermore, the addition of new compact dimensions to space-time gives rise to scalar degrees of freedom in the higher dimensional metric (L_3). Overall, multiple phenomenological routes beyond GR thus lead to scalar fields.
- Furthermore, scalar fields appear as theoretical necessities in plethora of high energy physics models beyond the SM as Kaluza-Klein or string theory. They indeed appear in dimensional compactification as stated before¹² but also as fundamental fields like members of the string spectra (as the string dilaton discussed in Chap. 9). As such, fundamental routes from deeper principles tend also to lead to the existence of scalar fields.
- We know for a fact that they can be part of nature's building blocks as proved by the discovery of the Higgs boson \mathfrak{h} (CMS Collaboration, 2012; Atlas Collaboration, 2012), which is itself a complex scalar field.

However, if the presence of such a field were ever detected on cosmological scales, a change of high energy physics paradigm would have to be considered, in order to understand where this new entity could fit in the realm of gauge theories over curved space-time¹³.

Formally, a *scalar field* ϕ returns a value of \mathbb{R} or \mathbb{C} at every point of space-time. This value remains the same independently of the choice of space-time frame i.e. it is invariant under transformations of the Poincaré group. The evolution of the field is given by the Klein-Gordon equation of motion which is the simplest possible relativistic generalization of the Schrödinger equation¹⁴ $\hat{H} = -i\partial_t$ with the Hamiltonian \hat{H} given by the correspondence principle using the relativistic expression for the energy of a point particle in a given frame $\hat{H}^2 = \hat{p}^2 + m^2\hat{\mathbb{I}}$, in which \hat{p} is the spatial linear momentum and m the mass of the particle ($\hat{\mathbb{I}}$ is the identity operator). This Schrödinger equation yields to the Klein-Gordon equation

¹²Scalar degrees of freedom appearing in dimensional reduction are called the radions and moduli fields in Kaluza-Klein and string theory respectively (Coquereaux & Jadczyk, 1988).

¹³As well as how this new field can remain yet undetected in local/particle physics experiments.

¹⁴The Schrödinger equation simply states that \hat{H} is the generator of the time translation in the sense of Lie Groups presented in Appendix A.

of motion $(\partial_\mu \partial^\mu + m^2)\phi = 0$ (in a flat Minkowski space-time). Note that the Schrödinger equation is generally used to describe the evolution of a particle's wavefunction which is a special type of complex scalar field representing the probability density of presence of the particle at a point x . The field ϕ appearing in the above Klein-Gordon equation can not be interpreted as such, as it would require the existence of a negative probability distribution. This problem was one of the original motivations for the development of quantum field theory. As such, cosmological scalar fields should not be interpreted as wavefunctions but as general classical relativistic fields or as quantum scalar fields if associated to a fundamental particle (i.e. creation/annihilation operators over space-time, see Appendix A). The Klein-Gordon equation can also be derived for a classical scalar field from the Lagrangian density $\mathcal{L}_\phi = \eta^{\mu\nu} \partial_\mu \partial_\nu \phi / 2 - m^2 \phi^2 / 2$ or from the continuous limit of the space-time displacement of a set of coupled harmonic oscillators, which make it a natural relativistic wave equation¹⁵.

Let us now consider the cosmological evolution of such a scalar field in an expanding Universe. To do so, we pursue the above considerations on the FLRW curved space-time, where, in full generality, the scalar field can be self-coupled through some potential $V(\phi)$. The Lagrangian density for ϕ becomes

$$\mathcal{L}_\phi = \frac{1}{2} |D\phi|^2 - V(\phi) = \frac{1}{2} g^{\mu\nu} \partial_\mu \phi \partial_\nu \phi - V(\phi), \quad (4.5)$$

where in the last equality, we supposed that ϕ is real and has thus no direct coupling with the standard model through D ¹⁶. The full cosmological Lagrangian hence becomes $\mathcal{L}_{\text{tot}} = \mathcal{L}_{\text{SM}} + \mathcal{L}_\phi$. From which one can derive¹⁷

$$T_{\mu\nu}^\phi = \frac{\partial \mathcal{L}_\phi}{\partial (\partial_\mu \phi)} \partial_\nu \phi - g_{\mu\nu} \mathcal{L}_\phi = \partial_\mu \phi \partial_\nu \phi - \frac{1}{2} g_{\mu\nu} \partial_\rho \phi \partial^\rho \phi - g_{\mu\nu} V(\phi). \quad (4.6)$$

Neglecting the spatial variations to get an homogeneous scalar field, ϕ acts as a perfect fluid filling the Universe. From the definition of the stress energy tensor (Eq. 3.13)

$$\rho_\phi = \frac{1}{2} \dot{\phi}^2 + V(\phi), \quad P_\phi = \frac{1}{2} \dot{\phi}^2 - V(\phi). \quad (4.7)$$

Inserting these expressions in Eq. 3.15, leads to the Klein-Gordon equation of motion in an homogeneous expanding space-time

$$\ddot{\phi} + 3H\dot{\phi} = -\frac{\partial V}{\partial \phi}. \quad (4.8)$$

Solving this equation hence allow to compute the value of the field ϕ at any point of the cosmic history, from which one can infer its possible impact on cosmological observations. Moreover, the existence of the scalar field will provide an additional term in the density sum of the Friedmann equations (Eq. 3.17), such that it will impact the Universe dynamics on an equal footing with the other matter fields.

¹⁵The Dirac equation describing the space-time evolution of matter fields ψ (see Appendix A) can be thought of four coupled Klein-Gordon equations coupled through the mass. It was found by Dirac as a first order linear generalization of Klein-Gordon equation.

¹⁶The existence of gauge charge requires a multicomponent object which can transform under a frame transformation. Hence a real scalar field can not have charges (it is a singlet of the Lorentz group and all the gauge group, transforming under their trivial representation).

¹⁷ $T_{\mu\nu}$ is expressed from \mathcal{L} as the conserved quantity through invariance under space-time translations.

4.3 A scalar field for each puzzle

4.3.1 Quintessence and dynamical dark energy

If not given by Λ , dark energy must behave as a dynamical fluid (hence called "dynamical dark energy"). A simple candidate for this fluid is given by a scalar field. In its simplest form, such a field is referred to as "quintessence" (Caldwell et al., 1998; Tsujikawa, 2013). Under a suitable choice of potential $V(\phi)$, a late time acceleration of the field is possible, which allows it to contribute significantly to the energy budget, such that it could also provide a solution to the H_0 tension. Some models propose that $w_\phi < 1$, and are dubbed as "phantom fields" (Caldwell, 2002). While such models violate the energy conditions expected for physical fields as we know them¹⁸, they allow to produce very unique predictions (Singh et al., 2003). For example, regarding the fate of the Universe, the presence of a phantom field would lead to the so called "big-rip", where the expansion would end up tearing apart every atoms¹⁹.

Let me stress here that the introduction of such a dynamical dark energy can potentially solve the H_0 tension but does not address directly the problem of the vacuum energy value for Λ (Sec. 4.1.1). As such the hardest problem for Λ remains open with quintessence field with the hope that the vacuum energy can behave more properly than in standard QFT if ϕ appears as a member of a larger quantum gravity theory beyond the standard model (as e.g. string theory).

4.3.2 Parity violating scalar field, axions and the dark side

Scalar field similarly behave in ways that can mimic a dark-matter fluid (or modify gravity accordingly). A particularly interesting special case of this is given by the axion (and axion like particles – ALP), which will further be relevant for our discussions in Sec. 9.7 and Sec. 5.3.2. Weak interaction violates the charge-parity (CP) symmetry by interacting only with left chiral particles and not with right ones. The existence of this CP asymmetric interaction is necessary to partly explain the matter/anti-matter asymmetry of our universe, but the weak one seems not to be enough to fully match the observations (Hambye, 2012). A similar asymmetry could be found for the strong interaction since there is no known group-theoretical reason for quantum chromodynamics (QCD) to be symmetric under CP²⁰. θ_{QCD} is the QCD vacuum phase, quantifying the possible amplitude of such a strong CP violating term. It is experimentally constrained to be extremely small ($\theta_{\text{QCD}} < 10^{-10}$, see also Tab. 9.1). To explain such a small value, it is common to introduce a coupling with a light pseudo-scalar field: the *axion* ϕ^{ax} . Doing so is motivated as a commonly accepted solution to the strong CP problem and provide a compelling light dark matter candidate (Marsh, 2016b). ϕ^{ax} can be possibly coupled similarly to the electromagnetic curvature F through the Lagrangian density

$$\mathcal{L}_{\gamma\phi^{\text{ax}}} = -\frac{1}{2}\partial_\mu\phi^{\text{ax}}\partial^\mu\phi^{\text{ax}} - V(\phi^{\text{ax}}) - \frac{1}{4}\langle F, F \rangle - \frac{1}{4}g_{\gamma\phi^{\text{ax}}}\phi^{\text{ax}}\langle F, \star F \rangle, \quad (4.9)$$

¹⁸Several other problems are raised by phantom fields (as e.g. singularities at $t \rightarrow \infty$), and diverse solutions are proposed.

¹⁹While Λ alone would not be able to split gravitationally bounded objects as Galaxies, leading to thermal death.

²⁰A parity violating term $\propto \theta_{\text{QCD}}\langle G, \star G \rangle$ in the QCD Lagrangian would still be SU(3) gauge invariant (G being the gluon curvature and \star the Hodge dual, defined in Appendix A).

4.3. A SCALAR FIELD FOR EACH PUZZLE

where $(\star F)^{\mu\nu} = \frac{1}{2}\epsilon^{\mu\nu\rho\sigma}F_{\rho\sigma}$ is the Hodge dual of F (see Appendix A). For ALP, one expects a potential of the form

$$V(\phi^{\text{ax}}) = (m_a f_a)^2 \left[1 - \cos \left(\frac{\phi^{\text{ax}}}{f_a} \right) \right]. \quad (4.10)$$

The Chern-Simons coupling $g_{\gamma\phi^{\text{ax}}}$ quantifies the interaction between ϕ^{ax} and the photons, which can have a different impact on the phase velocity of the photons depending on their helicity. This would be a violation of the local Lorentz invariance and thus a violation of the Einstein equivalence principle (Carroll et al., 1990) and could have observational consequences in the CMB as further detailed in Sec. 5.3.2.

Pseudo-scalar²¹ as axions are also predicted in high energy theories as e.g. string theory. Already motivated from the SM, the existence of such a field could provide a candidate for dark matter, and also some form of early dark energy i.e. a form of dynamical dark energy striking at early times to solve the Hubble tension. For an up to date review, see Poulin et al. (2023).

4.3.3 The inflaton

A source for the inflation solving the early Universe puzzles mentioned above is provided by introducing one or several scalar fields ϕ^{inf} called the *inflaton(s)*, dominant at very early times, such that $w_{\phi^{\text{inf}}} < -1/3$, triggering an early phase of accelerated expansion. All the degrees of freedom of the model come from the shape of its potential $V(\phi^{\text{inf}})$. As the field falls down its potential, it releases a lot of kinetic energy. SM particles (ψ) could be generated from this energy through couplings $\tilde{\lambda}_\psi$ with ϕ^{inf} similar to the Yukawa couplings as $\mathcal{L}_{\psi\phi} \propto -\bar{\psi}\phi^{\text{inf}}\tilde{\lambda}_\psi\psi$. As such it could have sourced all the particles of the standard model in a process called *reheating*.

In order for the inflation to happen and last long enough (large enough value of N_* defined in Sec. 4.1.2), the field must be slow-rolling. To do so, its potential energy must dominate ($\dot{\phi}^2 \ll V$) and it must accelerate slowly i.e. $\ddot{\phi} \ll 3H\dot{\phi}$ during inflation. These conditions ensure that the energy density of the Universe is almost constant with $\rho_{\phi^{\text{inf}}} \simeq V$ during inflation, leading to an exponential growth of the scale factor (as the Λ dominated case). The balance between kinetic and potential energy has however to change and whenever $\dot{\phi}^2 \sim V$, inflation stops and reheating starts.

Treating the inflaton as a quantum field, it is possible to predict the perturbations produced by its quantum fluctuations. Hence, the primordial quantum fluctuations are stretched at macroscopic scales by the expansion, and provide the primordial seed for the formation of large scale structures. A perturbative approach allows to predict the evolution of the deviations $\delta\phi$ of the field around homogeneity²². One can show that they evolve as an harmonic oscillator with a time varying mass, allowing for a quantum treatment close to the quantum oscillator. For introductions and complete treatments see e.g. Liddle & Lyth (2000); Baumann & Peiris (2008); Baumann (2009).

²¹Under a parity transformation, ϕ transforms as $-\phi$

²²For simplicity, we focus now only on single field models in slow-roll. A generalization to multiple fields along these lines is similar.

From these considerations, one can link the scalar and tensor perturbations power spectra presented in Sec. 3.3.4 with the field's potential as

$$\Delta_S^2(k) \simeq \frac{1}{12\pi^2 M_{pl}^6} \frac{V^3}{(\partial_\phi V)^2} \Bigg|_{k=aH}, \quad \Delta_T^2(k) \simeq \frac{2V}{3M_{pl}^4 \pi^2} \Bigg|_{k=aH}, \quad (4.11)$$

where the values of the Fourier transforms of V and $\partial_\phi V$ are calculated when a mode of wavevector k exits the causal Horizon, i.e. when $k = aH$ ($\lambda \propto (aH)^{-1}$), after which the perturbation can evolve causally. Scales exit the horizon at different times, associated with different values of V , allowing for the spectra to be scale dependent. From the spectra, one can then express the tensor-to-scalar ratio as

$$r = \frac{\Delta_T^2(k)}{\Delta_S^2(k)} \simeq 8M_{Pl}^2 \left(\frac{\partial_\phi V}{V} \right)^2. \quad (4.12)$$

Similarly, one can derive predictions for the indices

$$n_s - 1 \simeq M_{Pl}^2 \left(2 \frac{\partial_\phi^2 V}{V} - 3 \left(\frac{\partial_\phi V}{V} \right)^2 \right), \quad n_t \simeq -M_{Pl}^2 \left(\frac{\partial_\phi V}{V} \right)^2 = -r/8. \quad (4.13)$$

Thus the choice of potential V for the field drives all the observable predictions (at least for single field models). For a large class of models $n_s \simeq 1 - 2/N_*$ and $r \simeq 12/N_*$. As such, for $N_* \gtrsim 50$, inflation should produce a small but non zero deviation from 1 of n_s as-well as a small value of r . As such, the existence of inflation can be associated with some observational predictions as:

- Nearly scale-invariant primordial power-spectra ($n_s \sim 1$). This is in agreement with the measurement of n_s given in Sec. 3.4.2 and the statistical properties of the CMB radiation discussed in Chap. 5.
- A non-vanishing tensor spectrum due to the presence of a gravitational wave background, observable as primordial B -modes in the CMB. Such tensor modes have not been detected yet and will be one of the main topic of the part II of this thesis.
- Gaussian primordial perturbations are also expected, in agreement with the CMB observation so far. Small deviations from primordial Gaussianity in the perturbation statistics are also predicted in some inflationary models (Bartolo et al., 2004). These are not detected yet and can also be investigated using the CMB.

However, inflation postpones some of the fine tuning problems as numerous questions remain unanswered: where does the inflation belong in the standard model picture, why did the Universe start in such a high energy state? On the other hand, beyond-the-standard-model theories as string theory propose some candidate mechanisms to explain such a phase of early accelerated expansion, which would benefit greatly both theories in case of a detection of r (Baumann & McAllister, 2015).

Some inflationary models

There exists an extremely wide variety of inflation models, all having different motivations and experimental predictions (for a review, see e.g. Martin et al. (2014) referencing more than 70 different models!). Trying to review them all here would be of course impossible.

4.3. A SCALAR FIELD FOR EACH PUZZLE

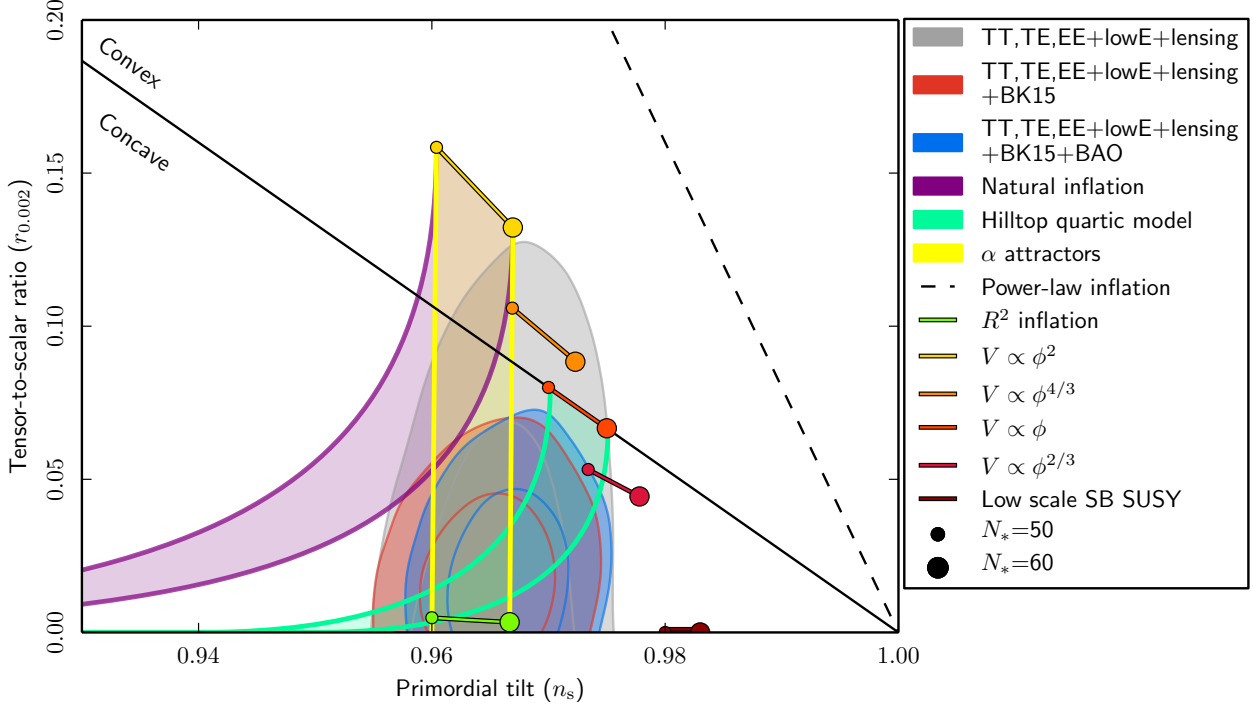


Figure 4.1: Constraints on various inflation models in the $(n_s - r)$ plane using various combination of *Planck*, BAO and BICEP-Keck (BK) data. Taken from [Planck Collaboration et al. \(2020b\)](#)

A model of inflation can be linked to observable predictions in the plane of n_s and r . It depends on several free parameters of the model as well as the duration in number of e-folds N_* . The best-fit constraints in the (n_s-r) plane from the Planck mission can be found in Fig. 4.1 and is compared to some model predictions. Anticipating further discussions (see Sec. 7.1.1 and Fig. 7.2), let us here mention quickly some simple-single field models that are extremely common in the literature:

- **Phenomenological models:** A plethora of $V(\phi^{\text{inf}})$ can be associated with ϕ^{inf} to produce phenomenologically the required phase of inflation (without having to further justify the physical origin of ϕ^{inf}). Let us quickly cite some of them here in order to better understand Fig. 4.1. "Natural inflation" considers a potential form similar to the one of an axion like particle:

$$V_{\text{nat}}(\phi^{\text{inf}}) = \Lambda^4 \left[1 + \cos \left(\frac{\phi}{f} \right) \right]. \quad (4.14)$$

It can be shown to be "natural" in the sense of footnote 1. "Hilltop models" consider instead

$$V_{\text{HT}}(\phi^{\text{inf}}) = \Lambda^4 \left[1 - \cos \left(\frac{\phi}{\mu} \right)^p + \dots \right]. \quad (4.15)$$

Numerous "Power-law" potentials, also called "chaotic" are associated with a potential of the form

$$V_{\text{PL}}(\phi^{\text{inf}}) \propto \mu^{4-\alpha} \phi^\alpha \quad (4.16)$$

which leads to simple predictions as

$$r \simeq \frac{4\alpha}{N_*} \quad n_s - 1 \simeq -\frac{\alpha + 2}{2N_*} \quad (4.17)$$

- **Higgs inflation:** As our standard model already contains a scalar field \mathfrak{h} , it is natural to investigate its possible link with inflation. The Yukawa couplings could also provide a way to generate the SM particles during reheating. To do so, a minimal approach is to couple the Higgs field with gravity by adding a coupling of the form $\mathcal{L}_{R\mathfrak{h}} = \zeta R\mathfrak{h}/2$ to the SM Lagrangian (Eq. 3.8, [Bezrukov & Shaposhnikov, 2008](#)). In the Einstein frame (see e.g. Sec. 9.5.2), the total Lagrangian takes the form of a scalar field ϕ^{inf} in GR with the potential

$$V_{\text{Higgs}}(\phi^{\text{inf}}) = \frac{\lambda}{4\zeta^2} \left[1 + e^{\frac{-2\phi^{\text{inf}}}{\sqrt{6}M_{\text{Pl}}}} \right]^{-2} \quad (4.18)$$

where λ is the quartic term of $V(\mathfrak{h})$.

- **Modified gravity:** As discussed above, a possible generalization of GR is to add higher order terms in the Einstein-Hilbert action. One of the simplest possibility one can think about is to add a quadratic term as $\mathcal{L}_{\text{grav}} = \mathcal{L}_{EH} + R^2/(6M^2)$. Such a term could emerge from quantum effects in a quantum theory of gravity. Under certain conditions, this theory is formally equivalent to GR with a scalar field of mass M able to produce inflation in the early Universe, with a potential of the form

$$V_{R^2}(\phi^{\text{inf}}) = \frac{3}{2}M^2 \left(1 - e^{-\sqrt{2/3}\phi^{\text{inf}}} \right)^2. \quad (4.19)$$

This is the so-called R^2 or Starobinski inflation.

- **Beyond standard models:** Numerous inflationary models can now be built from theories beyond the standard models as supersymmetry, supergravity and string theory. This is especially relevant, as it allows these models to provide observational predictions. Some common supergravity-inspired models are dubbed "Poincaré disks" and " α attractors" ([Ferrara et al., 2013](#); [Kallosh et al., 2017](#)). As supergravity is expected to be the low energy limit of a unifying string theory (called M -theory), these models are deeply linked to quantum strings. For a focused discussion of string inflation see the review in e.g. [Baumann & McAllister \(2015\)](#).

We should balance this presentation by mentioning that, while generally invoked, scalar fields as inflatons are not the only option to produce inflation ([Watson et al., 2007](#)). Additionally, there exist alternatives to inflation in order to solve the puzzles of the early Universe (for a review see e.g. [Brandenberger, 2011](#)). Several of them, known as *Ekpyrotic models*, involve bouncing cosmologies in which our Universe started from the collapse of a previous one. They are able to solve all the puzzles introduced before, and can also rely on high energy (e.g. string and M -theory) models ([Khoury et al., 2001](#); [Steinhardt & Turok, 2002](#)). While appealing, these models also have to face several challenges to present robust alternatives to the inflationary paradigm (see the review in [Battefeld & Peter \(2015\)](#)). Other cyclic cosmologies, as conformal cyclic cosmology (CCC) have been proposed ([Penrose, 2006](#); [Stevens](#)

4.3. A SCALAR FIELD FOR EACH PUZZLE

& Markwell, 2022). CCC builds on the fact that a diluted Universe where all matter decayed to radiation²³ is conformally equivalent to the initial conditions of a new warm Universe. Such theories have unique predictions, as the presence of "Hawking rings" in the CMB, which would be the signature of the Hawking decay of the last supermassive black holes in the previous Universe (An et al., 2018). However, further work remains to be done to propose a dynamical alternative to inflation based on this theory.

A fundamental question also remains to be addressed: what will cosmologists do of the inflationary paradigm if r happens to be too small to ever be detected by CMB experiments (i.e. lower than the cosmic variance (see Chap. 5 and Appendix B))? Indeed, it is possible to build a model in which inflation occurred with an extremely low value for the tensor-to-scalar ratio. If so, it might very well remain out of reach of any experimental verification (or falsification), leaving the cosmologists in a bad place! In such a case, we can only hope that new theoretical or experimental frameworks will emerge allowing to circumvent this pitfall.

²³GUT are thus required to allow for proton decay.

5

Signal from the cosmic origin: the cosmic microwave background

*D'où venons nous ? Où allons nous ?
J'ignore de le savoir*

– Les inconnus. Vice et versa

Contents

5.1	The CMB radiation	51
5.2	The physical origin of the CMB anisotropies	56
5.3	Statistical properties of the CMB anisotropies	64
5.4	Measuring the CMB	70
5.5	CMB and the cosmological parameters	72

5.1 The CMB radiation

As mentioned in the previous chapters, the *cosmic microwave background* (CMB) radiation provides a rich source of information for contemporary cosmology. As an open window on the early Universe, the CMB allows to validate the concordance Λ -CDM model presented in Chap. 3 and look for signature of new physics beyond it, as discussed in Chap. 4. We will also discuss in Chap. 9 that the CMB can be used to measure the values of fundamental constants and their variations at very early times. More significantly, the CMB radiation is extensively probed today in order to investigate the existence of a cosmic inflation phase allowing to solve the early time puzzles of the Big bang model presented in Sec. 4.1.2. A signature of inflation would be brought by a significant measurement of a non-zero tensor-to-scalar ratio r (introduced in Sec. 3.3.4). Such a discovery would represent a major breakthrough in our understanding of the birth of the Universe and the fundamental interactions.

5.1.1 Historical context of discovery

The major problem of cosmology in the ~ 1950 was to understand how to think the evolution and origin of the Universe after the discovery of its expansion by Edwin Hubble ([Hubble, 1926](#)). The framework of general relativity was already understood to allow for a dynamical cosmological space-time ([Lemaître, 1927](#); [Friedmann, 1922](#)). Two major theories were competing at the time: the steady-state and the big-bang models. The steady states model proposed that matter could be constantly created as the Universe expands, such that it remains in an overall invariant state. The big bang model, on the other hand, proposed that matter was indeed diluted with the expansion, such that the Universe was in a state of extreme density, or "primordial atom", at early times ([Lemaitre, 1949](#)). The framework of the Big bang model allowed for the computation of primordial abundances through a phase of primordial nucleosynthesis ([Alpher et al., 1948](#)), and predicted the existence of an astrophysical background radiation, the temperature of which was strongly debated among the supporters of the the big-bang theory ([Gamow, 1948; Kragh, 1996](#)).

In 1941, A. McKellar and W. S. Adams realized the first indirect detection of the CMB radiation, by using the molecular emission lines from the interstellar medium, and concluded that the "effective temperature of space" was ~ 2.3 K ([McKellar, 1941](#)). This CMB radiation was accidentally (re)discovered in 1965 by two radio-astronomers, Arno Penzias and Robert Woodrow Wilson. While using a Dicke radiometer at the Bell Telephone Laboratory (New Jersey) for radio-astronomy and satellite communication purposes, they noticed the presence of an unexplained excess noise of ~ 3.5 K across the whole sky ([Penzias & Wilson, 1965](#)). Robert Dicke, who was himself looking for the presence of such a radiation, was able to interpret this new discovery as the CMB cosmological signal ([Dicke et al., 1965](#)), followed by around one decade of intense debates¹. In 1978, Penzias and Wilson were awarded the Nobel prize as a recognition for this discovery.

5.1.2 Recombination and the last scattering surface

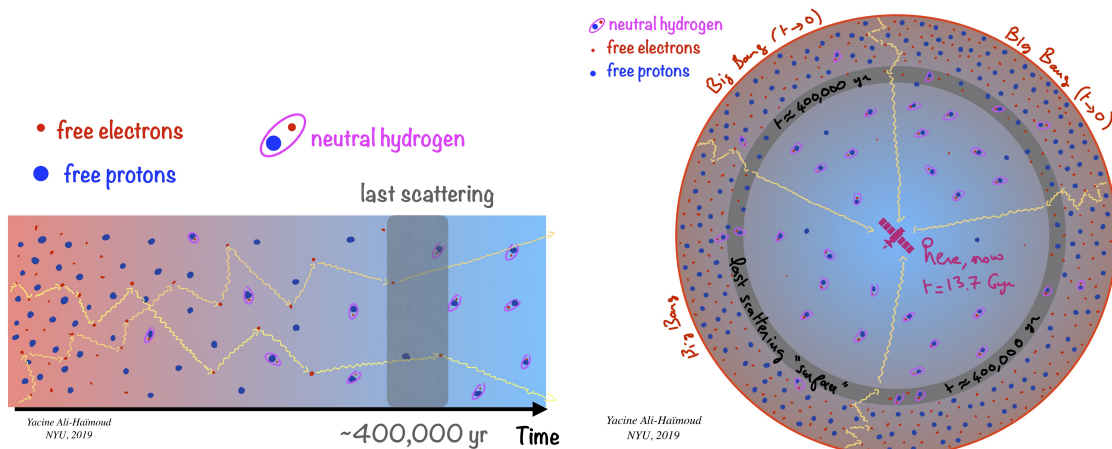


Figure 5.1: Illustration of the formation of the last scattering surface. Taken from [Yacine Ali-Haïmoud](#).

As the expansion goes on, the background energy density gets progressively diluted. As

¹For a detailed presentation of the historical context, see e.g. [Peebles et al. \(2009\)](#); [Jones \(2017\)](#).

already discussed in Chap. 3, this dilution allows for phase transitions to occur across the Universe. Jointly, under very specific thresholds, the probability of interaction between certain particles becomes negligible. If a particle type stops interacting significantly with the rest of the standard model because the background energy density is too low, it is said to be *decoupled*².

As illustrated on the left panel of Fig. 5.1, when the mean energy density of the photon bath becomes so low that atoms can form without being ionized, electrons are able to bind with hadrons in a stable way. Atoms being neutral, the absorption rate of photons falls down, as they stop being continuously scattered with the free electrons of the plasma. This phase transition called recombination witnesses the decoupling of the photons³, which will then be able to propagate freely for billions of years. In other words: the Universe becomes transparent.

As looking further away implies looking in the past due to the finiteness of the speed of light, the signal from this decoupling can be received today from every direction on the celestial sphere (right panel of Fig. 5.1). The origin of this signal is called the *last scattering surface* (LSS), defined as the region of space-time where the photons last scattered on free electrons in the primordial plasma.

Recombination is not instantaneous but is expected to occur progressively around 380 000 years after the primordial singularity ($z \sim 1100$). Hence it is more properly understood as a "shell" than a sphere, with a width of few tenth of thousand of years. The radius of this shell corresponds to the size of the observable Universe, that is ~ 46 Gyr (see Sec. 3.5), as the points where recombination occurred 13 Gyr ago have been carried away by the expansion.

5.1.3 The CMB: Overview of spectral and statistical properties

As displayed in Fig. 5.2, the signal emitted from the LSS which can be observed today peaks in microwave frequencies, hence the name CMB. Today, the value of the radiation density Ω_r is largely dominated by this CMB radiation, bathing the whole observable Universe.

As further detailed? in Appendix. B, the intensity of an electromagnetic signal is characterized by its spectral energy distribution (SED), quantifying how much energy can be associated to each electromagnetic frequency ν . The SED of a signal gives crucial informations about the physical mechanisms at play during the light emission process. The SED of the CMB signal is extremely close to a blackbody radiation, characteristic of thermal emission of a photon gas which was in thermal equilibrium. It can be expressed by the *Planck law* as

$$B_\nu^{\text{Pl}}(T) = \frac{2h\nu^3}{c^2} \left(e^{\frac{h\nu}{k_B T}} - 1 \right)^{-1}. \quad (5.1)$$

This SED allows to associate a temperature to the CMB signal, with a measured average of $\bar{T} = 2.7255 \pm 0.0006$ K (Fixsen, 2009). Deviations away from this blackbody arising from

²Formally, a particle type is said to be decoupled if its mean free path in the cosmological fluid becomes bigger than the Hubble horizon ($c/(aH)$).

³similarly neutrinos and gravitational waves decoupled before. There must hence exist a cosmic neutrino ($C\nu B$) and a (primordial) cosmic gravitational wave background radiation hiding a tremendous amount of cosmological information in them. Unfortunately however, these backgrounds are too faint to be mapped today (Bauer & Shergold, 2023; Christensen, 2019).

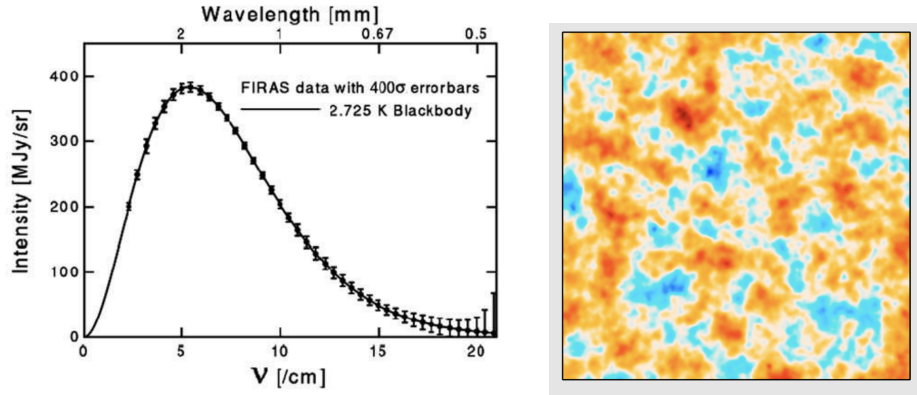


Figure 5.2: Left: spectral energy distribution of the CMB radiation, in perfect agreement with a blackbody spectrum. The error bars are multiplied by 400 to be visible. From [Fixsen & Mather \(2002\)](#). Right: CMB temperature anisotropies over a small patch of the sky distributed as a Gaussian random field. From [\(Planck Collaboration et al., 2020c\)](#).

local deviations to thermal equilibrium are expected to exist, with a very faint amplitude. These deviations are called spectral distortions and remain undetected today. Their mapping would however provide a large amount of information on primordial physics (see e.g. [Chluba et al., 2019](#)).

Moreover, the temperature of the CMB is extremely homogeneous over the whole celestial sphere with deviations of the mean temperature across the sky lower than 1 part in 10 000. This extreme isotropy provides a strong support for the cosmological principle and was at the origin of the horizon puzzle discussed in Sec. 4.1.2. As shown on the right panel of Fig. 5.2, the faint anisotropies over the LSS are spatially distributed very accurately as a Gaussian random field (which would be in agreement with a previous inflationary period, see. Sec. 4.1.2). Mapping the distribution of these anisotropies, both in intensity and polarization over the whole sky is a major challenge for modern cosmology. The maps obtained by the *Planck* mission ([Planck Collaboration et al., 2020c](#)) are displayed in Fig. 5.3. They represent the measured anisotropies over the whole celestial sphere, mapped on an ellipsoid using the Mollweide projection. The mean value of the map (and the dipole due to Earth motion discussed in Sec. 5.2.1) have been subtracted to display only the deviations to the mean signal. The units are μK_{CMB} (often abbreviated μK in our community), which are rescaled by $B_\nu^{\text{Pl}}(\bar{T})$. In this choice of units, the CMB signal is then independent of frequency.

The LSS must be thought as a dynamical entity. The mean value over the sky and the pattern of anisotropies will themselves evolve with time as the LSS is pushed further and further away in the past ([Lange & Page, 2007](#)). As such, the measured temperature of the CMB will evolve with redshift, and measuring its value in previous epochs in cluster of galaxies provides an additional probe of fundamental physics ([Luzzi et al., 2009](#)). This can be done using the SZ effect defined in Sec. 5.2.4.

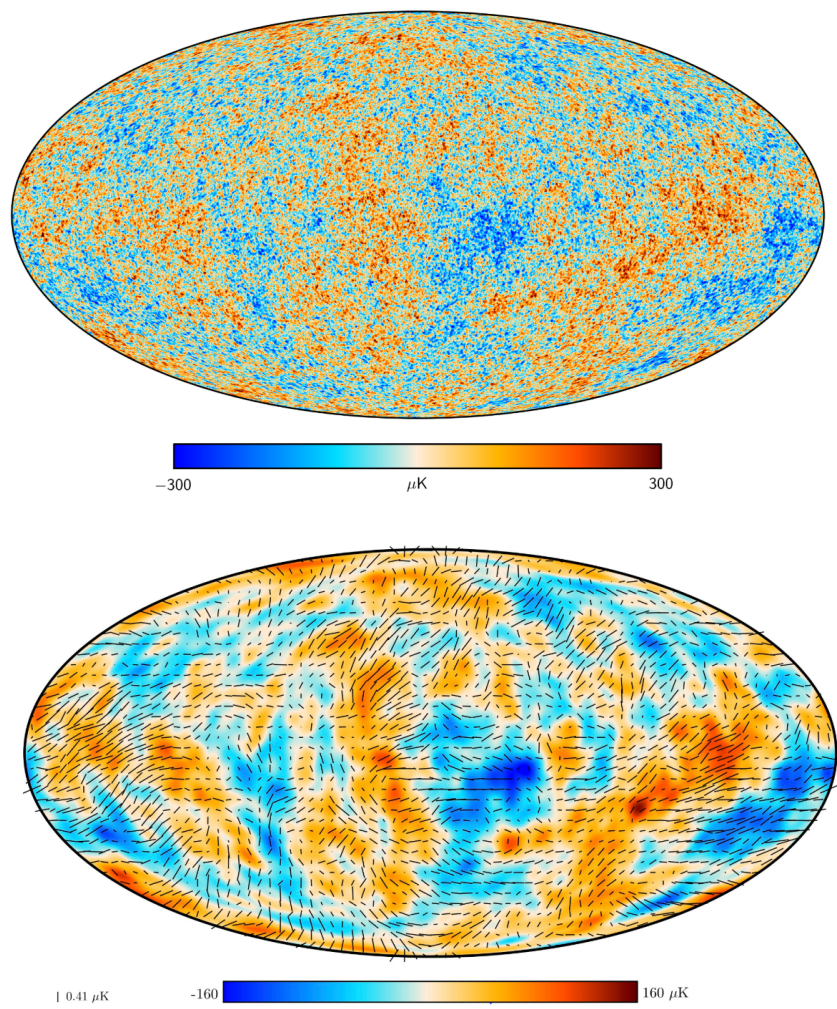


Figure 5.3: Mollweide projection of the CMB anisotropies in intensity (top) and polarization (bottom) as measured by the *Planck* satellite. The values are expressed in μK_{CMB} . The bottom map has been filtered to keep only the largest scales. Taken from [Planck Collaboration et al. \(2020c\)](#)

5.2 The physical origin of the CMB anisotropies

5.2.1 The Dipole: an open window on our location in the local Universe

The largest anisotropy in the CMB signal does not come from the LSS but is imprinted by the motion of the Solar system with respect to the CMB rest frame i.e. the equivalence class of comoving frames. This motion, understood as a boost, will induce the relativistic Doppler shift of the CMB photons, creating a dipole across the sphere with an amplitude of 3.3621 ± 0.0010 mK in our direction of motion (Planck Collaboration et al., 2020c). This dipole allows to better understand the motion of the Solar system and our Galaxy with respect to the structure of clusters and superclusters that surrounds it. It allows to infer a motion of the Solar system barycenter at 369.82 ± 0.11 km.s $^{-1}$ in the $(l, b) = (264.021 \pm 0.011^\circ, 48.253 \pm 0.005^\circ)$ direction (Planck Collaboration et al., 2020c). Removing the motion of the Sun in the local group⁴, one finds a velocity of 620 ± 15 km.s $^{-1}$ towards of towards $(l, b) = (271.9 \pm 2.0^\circ, 29.6 \pm 1.4^\circ)$ (Planck Collaboration et al., 2020c). This organized motion (or *local flow*), shared with all the nearby galaxies is understood as resulting from the complex interplay between various gravitational sources, as the dipole repeller and the Shapley attractor (Hoffman et al., 2017). These two entities being most probably a dense galaxy supercluster and a cosmic void respectively. This dipole is also observed independently on the Doppler shift of the signals of nearby galaxies. A possible tension ($> 4\sigma$) between the recovered amplitudes of the CMB dipole and the one recovered from surveys of quasars and radio galaxies could be a hint for a possible violation of the cosmological principle see e.g. Secrest et al. (2022). When targeting primordial anisotropies however, the dipole signal must be removed (it can also be used for the calibration of instruments).

5.2.2 Primordial temperature anisotropies

We will now review the possible mechanisms in the primordial plasma that could source part of the anisotropies displayed on the top panel of Fig. 5.3 (referred to as *primordial anisotropies*). The fluctuations of the signal observed on the last scattering surface are inherited by the photons which were previously strongly coupled to the fermions. As such, the LSS can be thought as a "snapshot" of the plasma at it was at the moment of decoupling, inheriting the physical anisotropies present in the cosmic fluid. Deviations to the mean temperature $\Delta T = T(\mathbf{n}) - \bar{T}$ are expected to be generated in the plasma in one of the three following ways:

- **Density perturbations (*Adiabatic or intrinsic*):** Over-densities in the primordial plasma are expected to be warmer while under-densities are colder. Over- and under-densities $\delta\rho$ inherited from inflation will evolve through the perturbation equation as

⁴The local group is composed by the several dozens of our nearest Galactic neighbours contained within a sphere of radius of ~ 1.2 Mpc (centered on its barycenter van den Bergh, 1999). The three largest members being Andromeda (M31), the Milky-Way and the triangulum (M33) galaxies (ranked by mass). It is located in a filament connecting the Virgo and the Fornax galaxy clusters, themselves being member of the Laniakea galactic super-cluster (Tully et al., 2014).

discussed in Chap. 3, until decoupling, leaving an imprint of

$$\frac{\Delta T}{T} \simeq \frac{\delta \rho}{3\bar{\rho}} \quad (5.2)$$

in the CMB.

- **Velocity perturbations (Doppler):** Similarly, local flows of velocity \mathbf{v} in the primordial plasma will induce a Doppler shift of the emitted photons, resulting in a different observed temperature, such that

$$\frac{\Delta T}{T} \propto |\mathbf{v}| \quad (5.3)$$

- **Gravitational perturbations (Sachs-Wolfe effect):** Finally, regions associated with a higher density will be also associated with a stronger gravitational field (that we already encountered and noted $\delta\Psi$ in Sec. 3.22). Photons traveling in this perturbed gravitational field will experience a gravitational redshift (Sachs & Wolfe, 1967), resulting in a difference of temperature of

$$\frac{\Delta T}{T} \simeq \frac{\delta\Psi}{3}. \quad (5.4)$$

Contrary to adiabatic perturbations, this effect is expected to produce colder overdensities and warmer underdensities.

5.2.3 Polarization anisotropies

Thomson scattering as a source of linear polarization

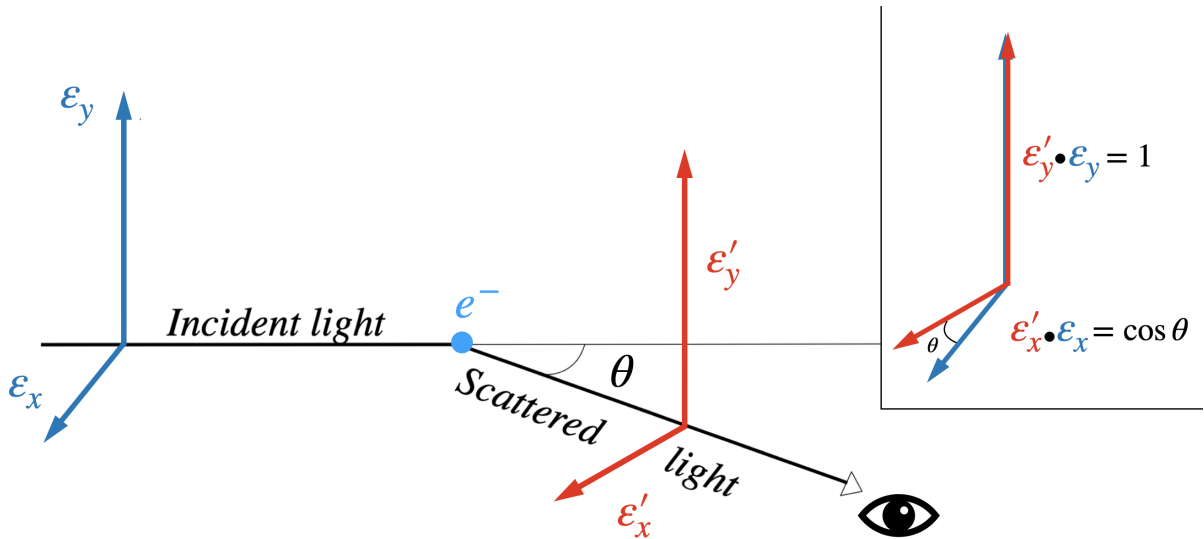


Figure 5.4: Illustration of the Thomson scattering of a photon beam in a direction θ by a motionless electron e^- . Adapted from Melchiorri & Vittorio (1997).

Light is not fully described by an intensity, but also by a direction of oscillation: its polarization. The CMB signal is known to be significantly polarized⁵ and this polarization, only partially mapped today, is expected to hide a lot of physics within and beyond the standard models. A detailed description of the specificities of polarized light can be found in Appendix B.

Before being decoupled, photons interact continuously with the free electrons through electron/photon scattering $e^- + \gamma \rightarrow e^- + \gamma$. At the energy scales of the CMB, one can consider that this scattering is Thomson scattering i.e. "elastic", meaning that the frequency of the photon is unchanged by the interaction (which is the low energy limit of the Compton scattering).

Consider an electron of charge e and mass m , at rest, interacting with an incoming photon of polarization ε^μ ⁶ or, equivalently but more simply for our discussion, an electromagnetic wave with the electric field oscillating along the unit vector ε . After interaction, the outgoing photon will have an associated polarization vector ε' . From considerations of classical electromagnetism and/or QED (see e.g. Jackson, 1998), one can infer the differential cross section of Thomson scattering to be

$$\frac{d\sigma}{d\Omega} = \frac{3\sigma_T}{8\pi} |\varepsilon \cdot \varepsilon'|^2, \quad (5.5)$$

with $\sigma_T = 8\pi(e^2/mc^2)^2/3$. As illustrated on the left pannel of Fig. 5.4, consider the received signal (red) in a direction θ with respect to the incident photon trajectory. Evaluating the dot product $|\varepsilon \cdot \varepsilon'|$ will always give 1 in the y direction and will give $\cos(\theta)$ in the direction x . As such, for an observer located perpendicularly to the incident photon direction, that is $\theta = \pi/2$, the x component of the signal, ε_x , will be completely absorbed.

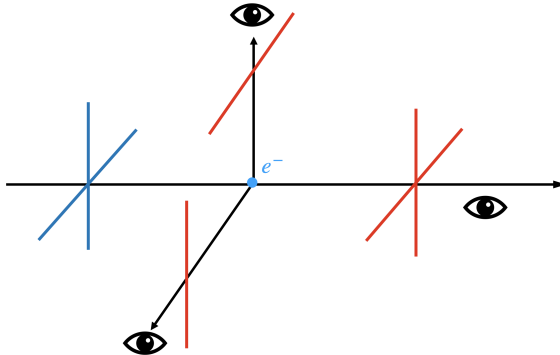


Figure 5.5: Generation of significant linear polarization in the perpendicular directions from Thomson scattering.

As on Fig. 5.5, consider an unpolarized beam of photons i.e. a superposition of plane waves with polarization directions that cancel each others. When this beam of photons interacts with an electron, it scatters in every direction. Overall, for the scattered signal (in red),

⁵i.e. the polarization orientation is not fully random such that it does not cancel on average.

⁶In quantum electrodynamics (QED), one expands the connection A in Fourier modes as $A^\mu = \varepsilon^\mu a_{k,\lambda} e^{-ikx} + (\varepsilon^\mu)^* a_{k,\lambda}^\dagger e^{-ikx}$. The canonical quantification consisting at treating the coefficients $a_{k,\lambda}$ as photon creation/annihilation operators. The polarization vector ε is orthogonal to the wavevector as $\varepsilon^\mu k_\mu = 0$.

the polarization component which is parallel to the direction of propagation of the original signal will always be suppressed, such that a net linear polarization will be observed for the observers located away from the original direction of propagation ($\theta \neq 0$), with a maximum at $\theta = \pi/2$.

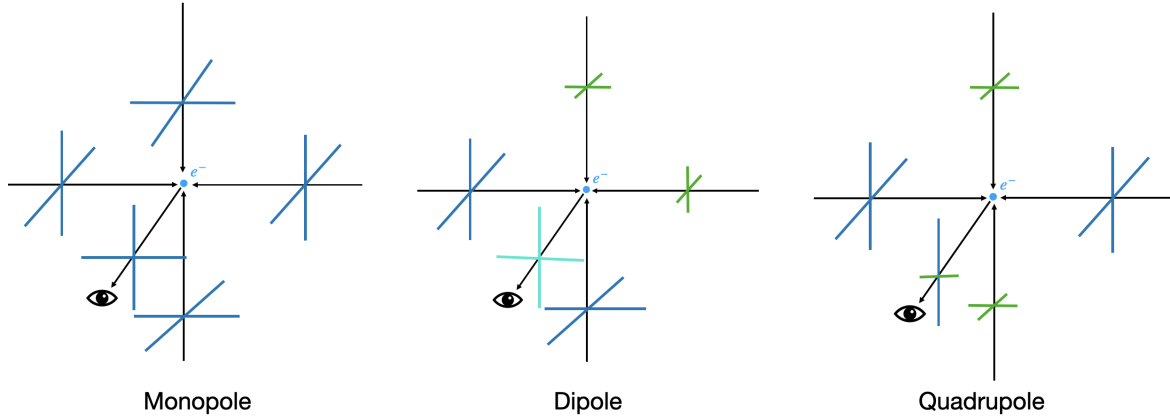


Figure 5.6: Comparaison between monopole, dipole and quadrupole anisotropies in order to generate linear polarization.

In the primordial plasma, unpolarized light is expected to reach electrons from every directions. As illustrated in Fig. 5.6, due to the behavior of the Thomson scattering presented above, if radiation in the primordial plasma is uniform, no significant linear polarization can be produced (monopole case). Similarly, no significant linear polarization can emerge from a dipolar asymmetry. Local quadrupolar anisotropies, however, are able to produce significant linear polarization, as they allow for the combination of two different orthogonal components.

As discussed extensively in Appendix. B, the polarization of an electromagnetic signal can be characterized by the three *Stokes parameters* Q , U and V . While Q and U quantify the linear polarization, V quantifies circular polarization.

Thomson scattering, as described above, can not produce significantly circularly polarized light. As such, we expect $V_{\text{CMB}} \simeq 0$. We note however that, here again, any significant detection of primordial circular polarization would have to be explained and could be a direct hint for new physics as the presence of primordial magnetic fields (Zarei et al., 2010) or new interactions in the electromagnetic sector e.g. photon/photon interactions coming from Euler-Heisenberg-like extensions of the QED Lagrangian (Hoseinpour et al., 2020).

The linear polarization given by Q and U thus allows to fully describe the polarized signal coming from the LSS. As presented in Appendix B, alternative mathematical tools allow to characterize the linear polarization as the spin-2 complex field $\mathcal{P} = Q + iU$ or the polarization tensor Π . Overall, the linear polarized signal can be understood as a "headless" vector associated to each point of the sky⁷. This explains the representation of the CMB polariza-

⁷As for fundamental particles (see Chap. 3 and Appendix. A), the *spin* of a general quantity represents how much this quantity transforms under a spatial rotation of 2π . Under such a rotation, linear polarization (i.e. a headless vectors) rotates such that it comes back to itself two times. This is why it is often referred to as a "spin-2" quantity.

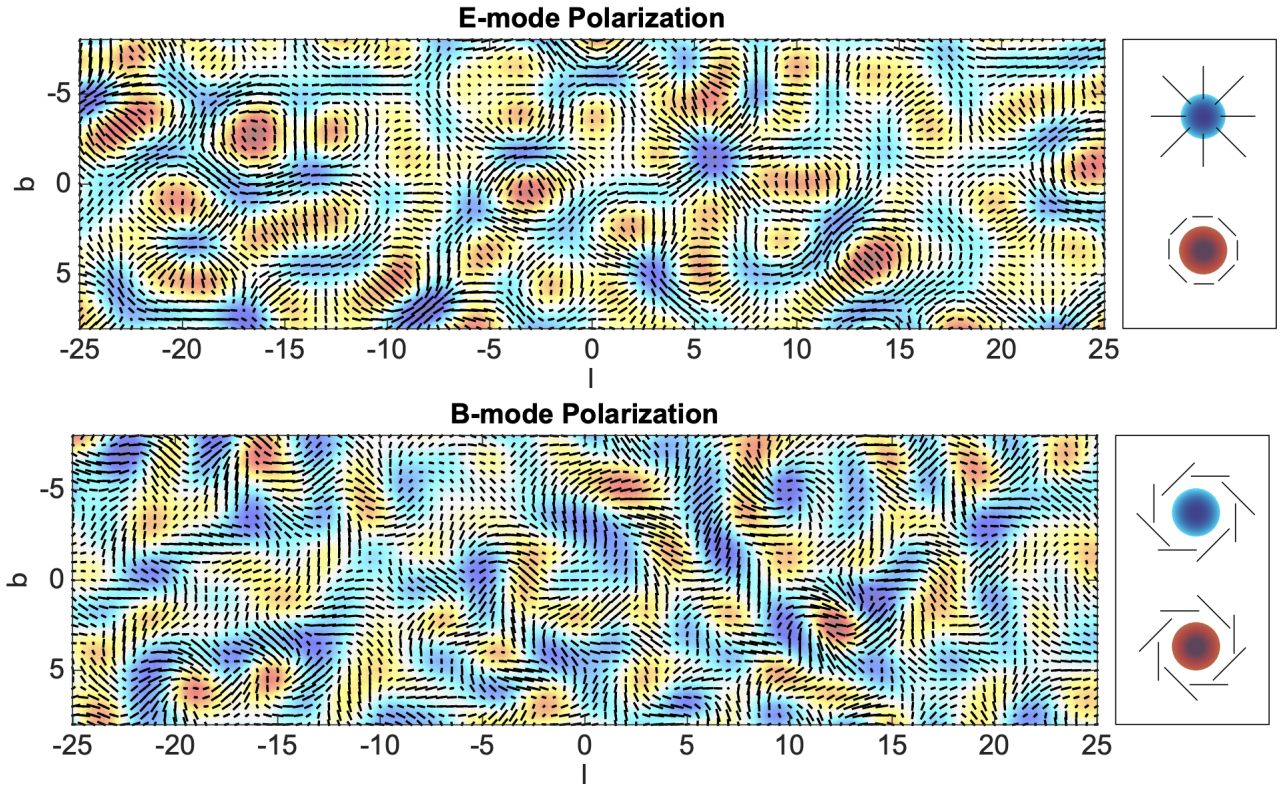


Figure 5.7: Illustration of *E*-modes and *B*-modes fields on a flat sky patch ([Kamionkowski & Kovetz, 2016](#)).

tion on the bottom panel of Fig. 5.3: additionally to the orientation, the length of the lines represent the amplitude of the polarized signal (and the color represent the temperature anisotropies for comparison).

Equivalently, all the information of linear polarization can be characterized using the so-called *E*- and *B*-modes. For a formal introduction see Appendix B and the associated references. These quantities have a powerful geometrical interpretation illustrated in Fig. 5.7. Around each point of the sky, *E*-modes quantifies the contribution of the polarized signal made of headless vectors distributed with a radial symmetry (parity even), while the *B*-modes represent the contribution of the headless vectors distributed with a "vortex shape" (parity odd). Such a geometrical split of the signal allows to separate the different physical mechanisms at play when the light was emitted. This is mostly relevant for the CMB signal as we will see in the next section and in Sec. 5.3.

Quadrupolar asymmetries in the primordial plasma from density fluctuations

As free electrons fall in or out of over- and under-densities of the primordial plasma, they will experience a quadrupolar asymmetric interaction with light, thus generating linear polarization. As illustrated on the left panel of Fig. 5.8, consider an electron falling in a gravitational well generated by an overdensity. Due to the increasing acceleration of gravity ($\propto r^{-2}$) towards the center of the overdensity, in its own reference frame, the electron sees the other electrons in front and behind it moving away (it goes slower than the one in front of it, and

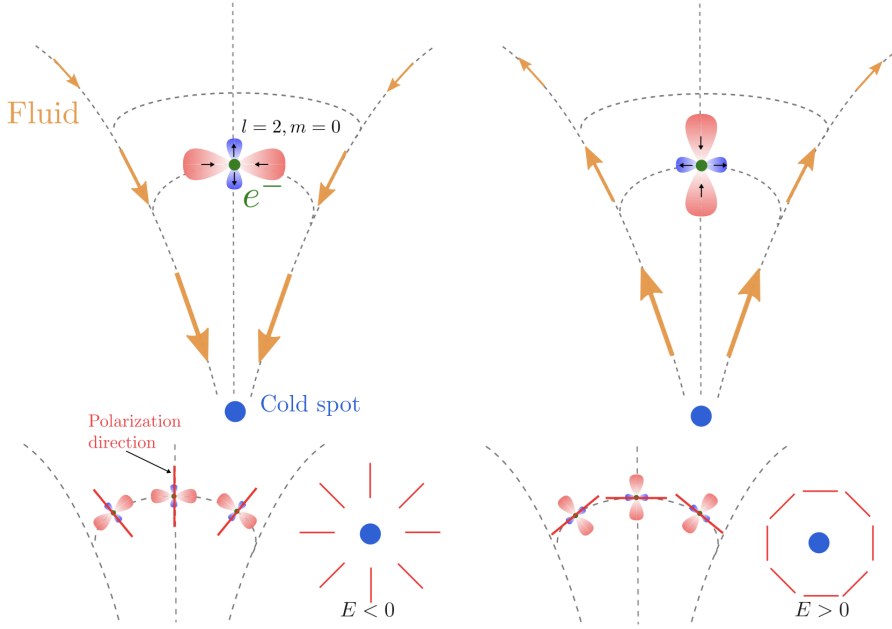


Figure 5.8: Generation of quadrupolar anisotropies from over or under densities in the primordial plasma. From [Mousset \(2021\)](#).

faster than the one behind it). Hence it receives their light as red-shifted. However, due to the radial nature of gravity, the electron sees its right and left neighbors getting closer and closer to it. Hence it receives their light as blue-shifted. This is a quadrupolar asymmetry, thus generating linear polarization through Thomson scattering. Similar reasoning applies for underdensities, from which electrons are moving away in a decelerated way. As described on the bottom panel of Fig. 5.8, the resulting polarization will appear as radial or concentric headless vectors surrounding the over/under-densities. This pattern corresponds to a pure E -mode signal as defined in Appendix. B (see also Fig. 5.7). As such, density fluctuations will significantly polarize the signal emitted by the surrounding moving fluid and only E -modes can be produced this way.

Quadrupolar asymmetries in the primordial plasma from gravitational waves

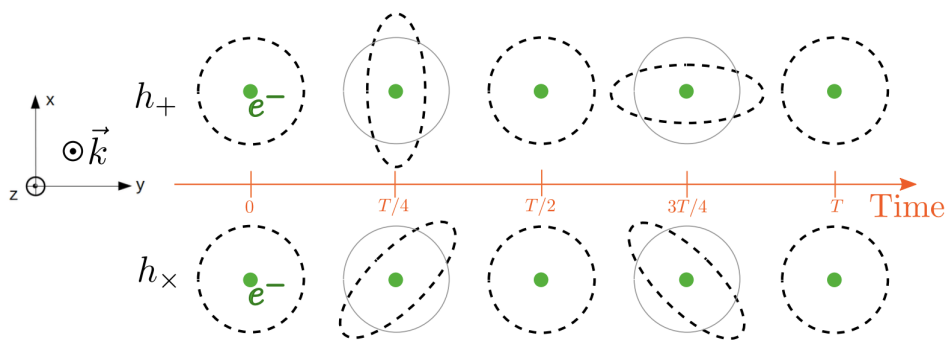


Figure 5.9: Generation of quadrupolar anisotropies (and hence linear polarization) from the propagation of a gravitational wave. From [Mousset \(2021\)](#).

Another physical phenomenon is expected to produce quadrupolar asymmetries in the primordial plasma, responsible for CMB polarization: the propagation of gravitational waves. A gravitational wave is a perturbation h of the metric around Minkowski geometry $g = \eta + h$, which propagates at the speed of light in the primordial plasma. As illustrated on Fig. 5.9, a gravitational wave propagating along the z axis can have two possible helicity in the $(x-y)$ -plane labelled h_+ and h_\times . In the rest frame of an electron, the passage of a gravitational wave will manifest itself as an oscillating deformation of the spatial regions around it, such that a circular ring of particles would transform periodically into ellipses, driving closer and away the surrounding fluid and doing so, generating a time dependent quadrupolar anisotropy by Doppler effect. As no obvious symmetry is present in this context, the propagation of gravitational waves in the plasma is expected to generate both E - and B -modes.

5.2.4 Secondary anisotropies

Even though they are decoupled, photons are still expected to interact (rarely) with the matter in the Universe on their way from the LSS. These interactions will change slightly the primordial pattern of primordial anisotropies, leading to the so-called *secondary anisotropies*. Understanding them accurately is necessary to recover the primordial signal, while they also contain a very large amount of information about fundamental physics, cosmic history and structure that have been probed by the CMB photons in their journey across the Universe. They are mainly produced through the following mechanisms:

- **Integrated Sachs-Wolfe effect (ISW):** we saw in Sec. 5.2.2, that the local presence of gravitational fluctuations could shift the photon's frequency through the Sachs-Wolfe effect. A similar effect will happen on large scales when the photons travel through the large scale structures, leading to a total shift in the photon's frequency resulting from the sum of the mass it encountered.
- **Gravitational lensing:** the trajectories of the photons (null geodesics) will be deflected by the presence of large scale structures, shifting the position of the observed anisotropies on the LSS.
- **Sunyaev-Zel'dovich effect (SZ):** photons might scatter again on electrons at late time in the hot ionized gas of galaxies or galaxy clusters. In this process, they might gain energy/temperature through *inverse Compton scattering*. This is the *Thermal SZ effect*. An additional Doppler shift can also be transmitted to the photons due to the motion of the galaxy clusters relatively to the CMB. We refer to this phenomenon as *Kinetic SZ effect*.
- **Reionization:** As discussed in greater details in Sec. 3.5, the last phase transition in the Universe witnesses the birth of the first stars and leaves the cosmic fluid in a highly ionized state, which is comparable to how it was before recombination, but in a more diffuse and structured form. As such, photons will interact again with free electrons through Compton and Thomson scattering, impacting the distribution of anisotropies at large scales.

5.3. STATISTICAL PROPERTIES OF THE CMB ANISOTROPIES

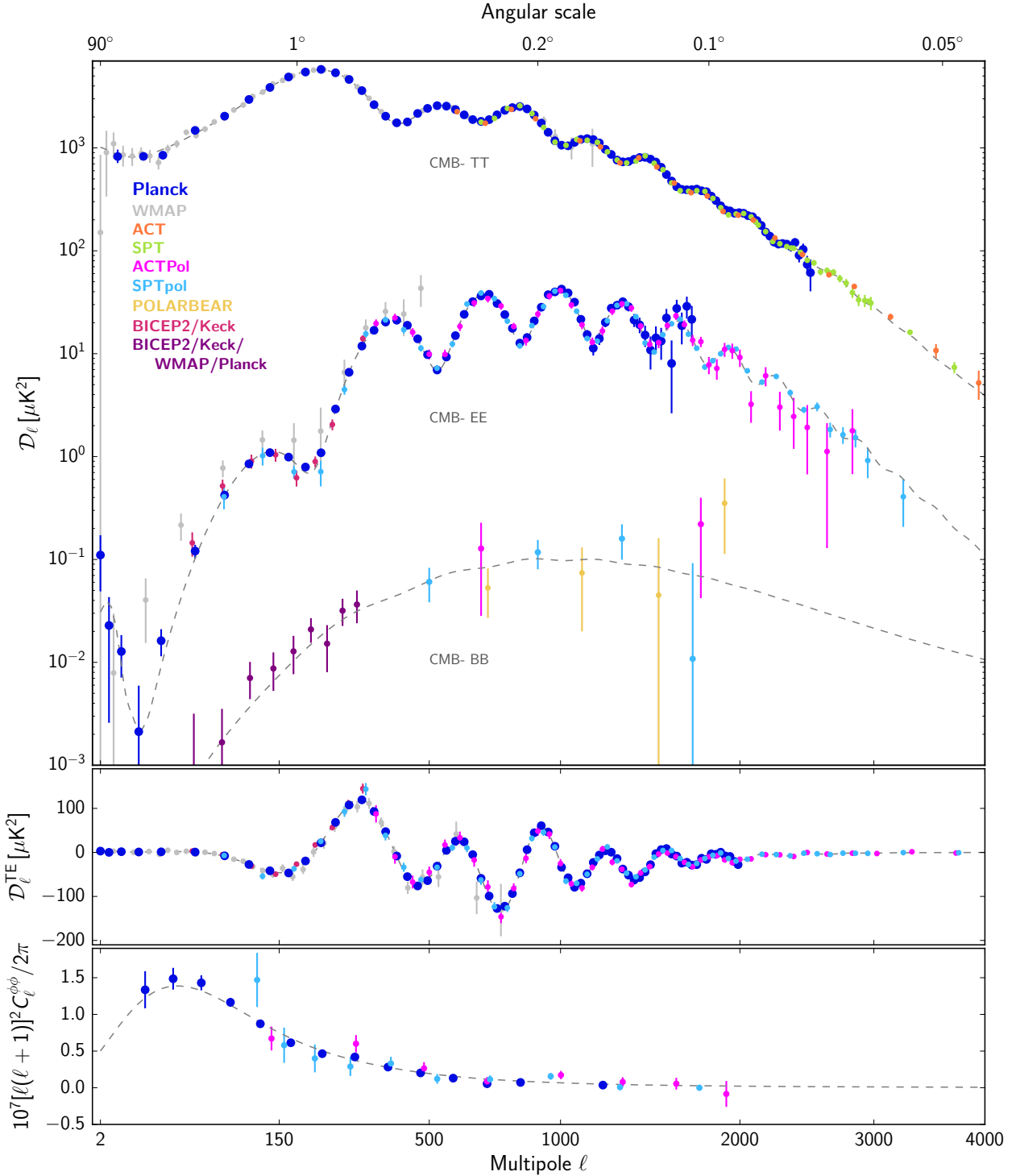


Figure 5.10: Comparaison of the CMB power spectra TT , EE , BB , TE and $\Phi\Phi$ (here noted $C_\ell^{\phi\phi}$) as measured by different experiments (colored points) and the best-fit prediction from the Λ -CDM model (dashed line). From [Planck Collaboration et al. \(2020c\)](#).

5.3 Statistical properties of the CMB anisotropies

While studying anomalous deterministic patterns in the LSS remains a matter of first importance⁸, one needs to confront the predicted and the observed statistical properties of the CMB signal in order to properly test the predictions from the Λ -CDM model.

The statistical properties of a field on a flat patch is commonly characterized by its Fourier transform, associated with an oriented scale \mathbf{k} . For the sphere, an analogous decomposition is given by the "spherical harmonic expansion", decomposing the signal of a field X on the surface of the sphere in its spherical harmonics coefficients $a_{\ell m}^X$ characterized by two integers ℓ and m . The *multipole* ℓ can be associated to the inverse of an angular scale on the sphere, while m can be associated with an orientation. The mathematical properties of such an expansion is presented in great details in Appendix B. From the Fourier transform coefficients, one can average over the possible orientations to build the power-spectrum $\mathcal{P}^X(k)$ and its rescaled version $\Delta_X^2(k)$, as detailed in Sec. 3.3.4. A similar approach can be used on the sphere to build the *angular power spectra* $\mathcal{C}_\ell^{XX'}$ between two fields X and X' on the sphere from their spherical harmonic coefficients. One often uses instead the rescaled spectra $\mathcal{D}_\ell^{XX'} = \ell(\ell+1)\mathcal{C}_\ell^{XX'}/(2\pi)$. For short, they are usually noted XX' . For a linearly polarized signal on the sphere, given by the triplet (I, Q, U) , $X \in \{T, E, B\}$. For a detailed presentation of these quantities, we refer again to Appendix B.

The distribution of the primordial anisotropies is highly homogeneous (and hence does not depend on the orientation m but only on the scale ℓ of the spherical harmonics) and behaves very closely to a Gaussian random field. In such a case, the angular power spectra contain all the statistical information of the field. Note however that faint non-Gaussianities are still expected at some level in the CMB signal in some inflationary models, as briefly discussed in Sec. 4.3.3.

From a signal given over the whole sphere by the triplet of fields (I, Q, U) , one can build the three auto-spectra TT , EE , BB and the cross-spectra TE , TB and EB ⁹. Each of them is probing different physical processes of emission and display unique features. From the evolution of the 3D distribution of the scalar¹⁰ perturbations Δ_s^2 until the emission of the LSS, one can predict the scale dependence of the primordial spectra from our standard models (in order to match observations, one also has to account for secondary anisotropies). This method is so robust that these statistics were already predicted even before being observed (Bond & Efstathiou, 1987). In 5.10, the best-fit spectra agreeing with Λ -CDM are displayed in grey dashed lines and compared with data points of multiple experiments that will be further described in Sec. 5.4. Astonishing agreement can be witnessed between predictions and data points. The intensity signal (TT spectrum) has been very accurately mapped across all the scales up to $\ell \sim 4000$, such that most of the possible cosmological information has already been extracted from it. The polarization signal is several order of magnitudes below, emphasizing the challenge represented by its accurate characterization. While all the polarized spectra have been detected and measured, a lot of room remains for

⁸As the "cold spot", for a review see e.g. Schwarz et al. (2016).

⁹As discussed in Appendix B, the fields ET , BT and BE are given by the complex conjugates of TE , TB and EB and do not contain additional information.

¹⁰Keeping in mind that the tensor modes Δ_t^2 are expected to be negligible in $\Lambda - CDM$ without inflation, while vectorial perturbations are also very faint and get quickly diluted.

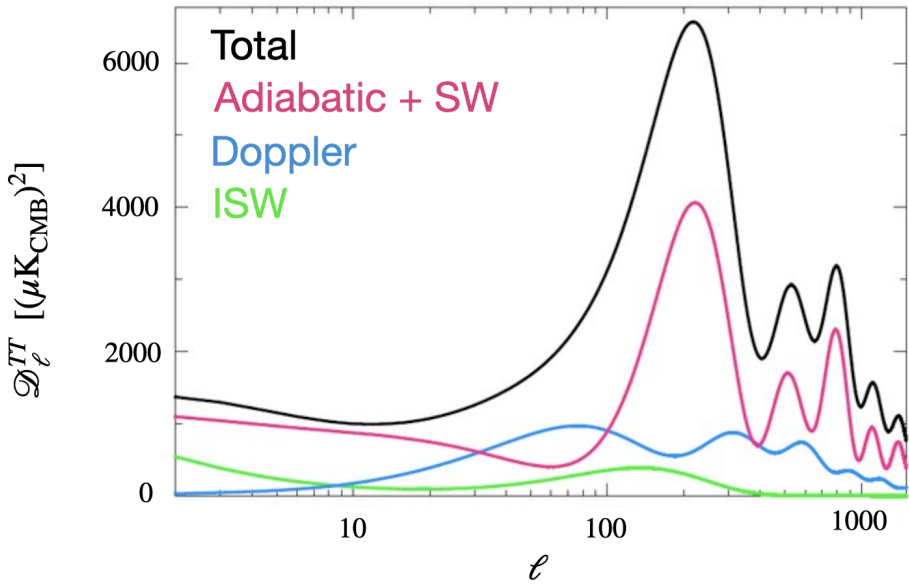


Figure 5.11: Angular power spectra of the dominant contributions from the various temperature anisotropy sources to \mathcal{D}_ℓ^{TT} : total (black), adiabatic and Sachs-Wolf (pink), Doppler (blue) and ISW (green). Adapted from [Ma \(2011\)](#).

sensitivity improvements. This is especially true for B -modes, which represent the largest uncharted territory of modern CMB science. We will now give a focused presentation of the temperature power-spectrum in Sec. 5.3.1 and of the polarization power-spectra in 5.3.2.

5.3.1 TT spectrum

Considered as a field on the celestial sphere, the temperature anisotropies of the CMB can be expanded in spherical harmonics as

$$\frac{\Delta T}{T}(\mathbf{n}) = \sum_{\ell=1}^{\infty} \sum_{m=-\ell}^{\ell} a_{\ell m}^T Y_{\ell m}(\mathbf{n}), \quad (5.6)$$

from which one can compute the angular power spectrum¹¹

$$\mathcal{D}_\ell^{TT} = \frac{\ell(\ell+1)}{2\pi} \mathcal{C}_\ell^{TT} = \frac{\ell(\ell+1)}{2\pi} \left\langle a_{\ell m}^T (a_{\ell m}^T)^* \right\rangle_m, \quad (5.7)$$

often referred to as the " TT " spectrum. The highest amplitudes of the spectrum are given by the $\ell = 0$ component, corresponding to the monopole (mean value of the blackbody signal) and the $\ell = 1$, being the dipole described in Sec. 5.2.1. The predicted and observed higher modes ($\ell \geq 2$), are displayed in the top row of Fig. 5.10, presenting a characteristic

¹¹This expression should involve the measured estimator $\widehat{\mathcal{C}}_\ell^{TT}$ of the theoretical angular power-spectrum $\mathcal{C}_\ell = \left\langle a_{\ell m}^T (a_{\ell m}^T)^* \right\rangle$ on the sky; where $\langle \dots \rangle_m$ is the mean over all the values of m (orientations) while $\langle \dots \rangle$ is the stochastic/statistical average of the theoretical model (for more details on this point see Appendix B). To simplify the discussion in this section, we will not make this distinction and talk only about the measured angular power-spectra.

oscillatory behavior. This spectra is further decomposed in Fig. 5.11, showing the various contribution of the main anisotropies sources introduced in Sec. 5.2.2. The scale dependent behavior of the spectrum can be understood as follows:

- For $\ell < 100$, lays the *Sachs-Wolf plateau*. This range of angular scales are greater than the size of the causal horizon at the LSS. As such, points separated by these scales can not have interacted nor co-evolved significantly (since the end of inflation). This plateau thus quantifies the pristine primordial perturbations, caused solely by the mechanisms detailed in Sec. 5.2.2 and mostly the Sachs-Wolf effect. These perturbations display clearly a scale invariant behavior (which translate in a flat D_ℓ^{TT}), in agreement with the predictions of inflation.
- The $100 \leq \ell \leq 1000$ region, is the regime of the *acoustic peaks*. Scales smaller than the horizon at LSS grasp the causal interactions in the primordial plasma before decoupling. This rich wiggly structure results from the oscillation of the coupled photon/baryon fluid, in the underlying gravitational field. This gravitational field being mostly shaped by the heavy and uncoupled dark matter¹². The pull of gravity competes against the fluid motion, driven by the photon radiation pressure. The acoustic peaks have a maximum at $\ell \simeq 200$, followed by 2 smaller bumps. These visible perturbations in the plasma are analogous to sound waves, hence justifying the name "acoustic".
- The $\ell \geq 1000$ region is the *damping tail*. The spectrum oscillates quickly with a continuously decreasing amplitude. Due to the thickness of the LSS, averaging is done on multiple small scale behaviors that compensate one another, erasing progressively the structures for scales smaller than this thickness.

5.3.2 Polarization spectra

The *EE* and *TE* spectra

Around two orders of magnitude below *TT*, the *EE* power spectrum displays – for the same physical reasons as *TT* – an oscillatory behavior (see Fig. 5.10). These oscillations are however out of phase with the temperature ones, as they are not created by the overdensities themselves (as the adiabatic and Sachs-Wolf mechanisms which are the main contributions to *TT*) but come uniquely from the Doppler shift in the dynamical fluid (see Sec. 5.2.3). The correlation between *T* and *E* (*TE* spectrum) quantifies their inter-relation. It can take both positive and negative values depending on the correlation/anti-correlation of intensity and linear polarization. Being more intense than *EE*, *TE* has been mapped with a greater accuracy. It provides complementary information to *EE* and *TT* alone.

Some excess signal can be clearly identified at very small scales ($\ell < 10$) in both the *EE* and *TE* spectra and behaves exactly as expected from an energy injection to the CMB photons coming from reionization at $z \sim 8$ (hence named the *reionization bump(s)*). For an analysis exploring the history of reionization from the *Planck* CMB spectra, see [Planck Collaboration et al. \(2016a\)](#).

¹²As such, CMB provides a striking hint for the need for dark matter in the early Universe. Indeed, without it, it would be extremely difficult to explain the presence of such acoustic peaks. See for example the analysis in [Komatsu et al. \(2009\)](#).

The BB spectrum and the primordial tensor modes

As discussed in Sec. 5.2.3, density fluctuations can only produce E -mode signal. While B -modes can be produced by the passage of gravitational waves, as described in Sec. 5.2.3, they are expected to be extremely faint without any mechanism in the primordial plasma to significantly source them.

All the B -modes detected on Fig. 5.10 can hence be explained as secondary anisotropies. Indeed, when the trajectory of CMB photons are curved by the presence of foreground mass, the position of the anisotropies get shifted by gravitational lensing, reshuffling the balance between E - and B -modes. This spectrum is hence created by lensing which converts primordial E -modes into secondary B -modes. Its effect gets gradually larger on smaller scales as large scale structures are correlated only at a the characteristic scale on which they can interact. As such, lensing is also impacting similarly the E power spectra by decreasing their amplitude. As primordial EE is however several order of magnitudes more intense than any hypothetical primordial BB , the impact is less noticeable.

No primordial B -mode signal has been detected yet, and its existence is actively searched, as it would be the direct signature of new physics in the early Universe. First and foremost, inflation could produce a gravitational wave background in the primordial plasma that might lead to a significant primordial B -mode signal. Indeed, if inflation occurred, it must have produced tensor modes at some level ($\Delta_h^2 \neq 0$), which amplitude is quantified by the tensor-to-scalar r introduced in Sec. 3.3.4. The presence of some tensor modes should impact all the angular power spectra of the CMB presented above. However, this contribution would be drown in the cosmic variance¹³ of TT and while the EE spectrum can be used to give upper bounds on the value of r , the precision of such measurements is intrinsically limited, as EE is largely dominated by scalar perturbations. Overall, a tensor contribution would thus be only undoubtedly noticeable in the primordial BB spectrum, which must be zero otherwise. In fact, the amplitude of the primordial BB spectrum is directly set by the value of r .

The precise shape of the angular power spectrum expected from inflation can be inferred from perturbation theory (for an example see Fig. 7.1). As the other spectra, it presents oscillations and a major peak around $\ell = 100$, called the *recombination bump*. If such a primordial spectrum exists, it will also be amplified on the lowest multipoles by reionization as EE and TE , leading to a *reionization bump* around $\ell = 10$. Moreover, the impact of lensing becomes negligible on the largest scales. As such, exploring the lowest range of ℓ of the BB spectrum is crucial when looking for the faint primordial B -modes.

At the time of this thesis writing, the lowest bound on r is given by a combination of the *Planck* fourth data release (PR4) and BICEP/Keck Array 2018 measurements (Tristram et al., 2022) (see Sec. 5.4 for a presentation of the missions). It is given by

$$r < 0.032 \quad (95\% \text{CL}). \quad (5.8)$$

Besides CMB, other cosmological probes can be used to constraint the presence of tensor modes. While they are not yet competitive with CMB, they could reveal themselves as complementary in the near future. This is the case of direct and indirect observations of the

¹³For a definition of the cosmic variance, see Appendix B, Eq. B.11.

gravitational wave background in the near Universe, using respectively laser interferometers as LISA and pulsar timing arrays (PTA) (Campeti et al., 2021).

As discussed in Baumann & Peiris (2008), r can be directly related to properties of the inflaton field presented in Sec. 4.3.3, as its potential through

$$V^{1/4} = 1.06 \times 10^{16} \text{ GeV} \left(\frac{r}{0.01} \right)^{1/4}. \quad (5.9)$$

V can be interpreted as the energy scale at which inflation occurred, information which is crucial in order to investigate its possible relationship with GUTs or high energy physics theories. Furthermore, one can derive

$$\frac{\Delta\phi^{\text{inf}}}{M_{\text{Pl}}} \gtrsim \left(\frac{r}{8} \right)^{1/2} N_*, \quad (5.10)$$

where $\Delta\phi^{\text{inf}}$ is the inflaton displacement during inflation and N_* is the number of e-folds, quantifying the duration of inflation (see again (Baumann & Peiris, 2008)). The field displacement is itself directly related to high energy properties of the field (Baumann & Green, 2012). Among other things, measuring or constraining r thus allows to explore the energy scale of inflation and how much the field evolved during this period. For a review on the information on the nature of inflation that can be extracted from a B -mode observation, see Baumann et al. (2015).

$\Phi\Phi$ spectrum

Let us briefly mention here the last spectrum of Fig. 5.10 which was not discussed above. Weak lensing has multiple effect on the CMB power spectra: it tends to smooths the acoustic peaks, introduce non-Gaussianities, add power on small scales and transform E -modes into B -modes. From the CMB power spectra it is hence possible to recover the information about the lensing power spectrum $\mathcal{C}_\ell^{\Phi\Phi}$, which actually corresponds to the effect of the gravitational potential (noted Ψ above) of large scale structures on the CMB photons (Okamoto & Hu, 2003; Planck Collaboration et al., 2014). As such, recovering the lensing spectrum from CMB, and studying its cross-correlation with other probes of mass is an active and fruitful branch of research of contemporary cosmology (for a review see e.g. Kitching et al. (2015)). $\mathcal{C}_\ell^{\Phi\Phi}$ is a sensitive probe of structure formation in the late Universe, neutrino masses and dark energy. As seen on Fig. 5.10, a lot of room is left for improvement coming from new sensitive datasets.

EB , TB and cosmic birefrigence

As detailed in Appendix B.6, the EB spectrum must change sign under a parity transformation, and as such, a signal with no preferred orientation must satisfy $EB = -EB = 0$. Similar considerations also apply for the TB spectrum. The detection of a significant primordial EB or TB signal will hence be a direct evidence for a parity violating signal i.e. polarized pattern with a preferred direction or handedness. No such thing is expected in the CMB as it would violate the isotropy of the cosmological principle and none of the interaction of the standard model are expected to break the parity symmetry in such a way.

As such, the presence of a non zero EB or TB primordial signal would be the direct signature of a violation of the fundamental space-time symmetries on which our standard model is built, as Lorentz invariance or charge-parity-time reversal (CPT) (Carroll et al., 1990; Feng et al., 2006). This could be generated by the presence of primordial magnetic fields (Shiraishi, 2012; Planck Collaboration et al., 2016b), non chiral gravitational waves, signature of parity symmetry breaking in the inflationary or gravitational sector (Lue et al., 1999), or the presence of an axion like particle (ALP), presented in Sec. 4.3.2.

A rotation of the polarization plane, transforming E and B modes into one another, would indicate the presence of such a parity breaking. This phenomenon, known as *cosmic birefringence*, would generate non zero EB and TB spectra. More precisely, one expect to observe

$$\mathcal{D}_\ell^{EB} = \frac{\sin(4\Delta\beta)}{2} (\mathcal{D}_\ell^{EE} - \mathcal{D}_\ell^{BB}), \quad (5.11)$$

where $\Delta\beta$ quantifies the angle of rotation of E -modes into B -modes.

For example, such a rotation would be characteristic of the presence of an axion field coupled to electromagnetism, impacting the phase velocities of the photons with different helicities on their way from the LSS to us, as mentioned in Sec. 4.3.2. More precisely, for an homogeneous axion field filling the Universe and evolving with the Klein-Gordon equation, $\Delta\beta$ is proportional to the field difference (Marsh, 2016b)

$$\Delta\beta = \frac{g_{\gamma\phi^{\text{ax}}}}{2} (\phi_0^{\text{ax}} - \phi_{\text{cmb}}^{\text{ax}}). \quad (5.12)$$

where $g_{\gamma\phi^{\text{ax}}}$ is the Chern-Simons coupling (see Sec. 4.3.2), and ϕ_0^{ax} and $\phi_{\text{cmb}}^{\text{ax}}$ are respectively the values of the field today and at the emission of the CMB.

Recent claim of a $\sim 3\sigma$ detection in Planck data of $\Delta\beta = (0.30 \pm 0.11)^\circ$ has revived the interest for axions and ALP (Minami & Komatsu, 2020; Diego-Palazuelos et al., 2022, 2023) as this detection seems to favor them as source of the parity breaking over primordial magnetic fields¹⁴ (Eskilt, 2022) or chiral gravitational waves (Fujita et al., 2022). Further investigation and new data will shed the light on the significance of this detection.

Investigating the presence of cosmic birefringence is a particularly thorny problem as it is strongly degenerated with the way the polarization angle of the CMB experiment is calibrated, which often requires the vanishing of the EB signal (for a discussion see (Pagano et al., 2009)). Additionally, the signal coming from our Galaxy can generate non trivial TB and EB signal, as we will further discuss in Sec. 6.3.3. As we will see in Sec. 8.5, part of my work during this thesis was to understand how to properly model the frequency dependence of the Galactic parity violating signals, keeping in mind that they could have a big impact on cosmic birefringence study and the detection of $\Delta\beta$.

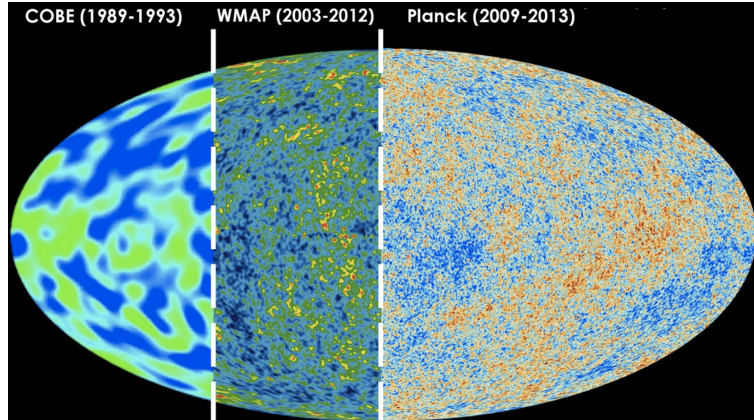


Figure 5.12: Sensitivity improvement between COBE, WMAP and Planck (Gold et al., 2011; Planck Collaboration et al., 2020a).

5.4 Measuring the CMB

5.4.1 CMB science so far: the era of precision cosmology

After the discovery of the CMB discussed in Sec. 5.1.1, it was quickly understood that mapping accurately its signal over the whole celestial sphere would represent a breakthrough for our understanding of the Universe. The *COBE* satellite, launched in 1989, provided the best measurement so far of the CMB blackbody spectra with the *FIRAS* instrument (Fig. 5.2 Fixsen & Mather, 2002) and the first observation of temperature anisotropies with its differential radiometer DMR (Smoot et al., 1992). Later, the *WMAP* satellite, launched in 2001, provided the first fine characterization of the anisotropies allowing to constraint significantly the cosmological parameters and the nature of the Galactic foreground signal (Bennett et al., 2013, and references therein), these later will be discussed in Chap. 6. Finally, the era of high precision cosmology was opened by the *Planck* satellite, launched in 2009, and ground experiments as the Atacama Cosmology Telescope (ACT) observing since 2007 (Thornton et al., 2016), the South Pole Telescope (SPT) (Austermann et al., 2012), observing since 2008, and the BICEP2/Keck array operating since 2010 (BICEP2 Collaboration et al., 2014a). These complementary experiments provided measurements of the anisotropies allowing to provide a characterization of the TT spectra with a cosmic variance limited precision at almost all scales, along with a fine characterization of EE and TE , as displayed on Fig. 5.10. In order to grasp the considerable progress achieved in CMB science within a few decades, a comparison of the characterization of the LSS (in intensity) for the *COBE*, *WMAP* and *Planck* satellites can be found in Fig. 5.12.

5.4.2 Contemporary and future missions

As we discussed in Sec. 5.3, cosmological information still awaits to be extracted from the LSS. Numerous missions and collaborations targeting the CMB are active today. Most of them aim for a better characterization of the polarization signal and the detection of r . CMB

¹⁴The presence of ALP can be distinguished from the one of primordial magnetic fields, as the $E - B$ rotation generated by the latter is expected to be frequency dependent as it is sourced by the Faraday rotation, presented in Sec. 6.3.2.

5.4. MEASURING THE CMB

missions can be of three complementary types, each with their advantages and drawbacks:

- **Ground-based telescopes** are mostly based in Chile and on the south pole, which provide the best observational conditions for CMB science. From the ground, it is possible to build large telescopes, which can easily calibrated, updated and modified during the mission duration. The instrument allow to perform extremely long observations, leading to sensitivity improvement. They are often observing the CMB over a small sky region, relatively clean of Galactic foregrounds. Using large aperture telescopes (LAT) it is hence possible to access the statistics of the highest ℓ of the CMB spectra, but ground experiments are intrinsically blind to the largest scales as they can not cover the whole celestial sphere. Measuring from the ground also presents unique complications as the atmosphere who prevent high frequency observations ($\gtrsim 220$ GHz), contamination from ground signals (ground pick-up), and the day/night alternation. From the Atacama plateau in Chile, the ACT instrument, targeting the largest scales ($\ell \in [225 - 8725]$), received two major sensitivity upgrades, allowing for polarization observations at 97, 148 and 220 GHz: ACTPol (2013-2016) and Advanced ACT (2017-2022) ([Thornton et al., 2016](#); [Henderson et al., 2016](#)). On the same location, the POLARBEAR mission observes since 2012 in polarization at 150 GHz ([Kermish et al., 2012](#)). POLARBEAR has been upgraded to POLARBEAR2 and is part of the Simons Array (SA) project observing additionally at 95 and 220 GHz ([Inoue et al., 2016](#)). The combination of POLARBEAR2 and SA targets $\sigma(r) \sim 0.006$. ACT and SA are now extended and combined within the Simons Observatory (SO), expected to take its first light in 2023. SO will observe at 27, 39, 90, 150, 220 and 270 GHz, covering a range of scales $\ell \in [30 - 8000]$. It targets $\sigma(r) \sim 0.003$ ([Galitzki et al., 2018](#)). On the south pole, SPT was updated to allow for polarization observation of the smallest scales ($\ell \in [50 - 2300]$) at 95, 150, and 220 GHz with SPTPol (2012-2016) and received a major sensitivity upgrade in 2017 (SPT-3G) ([Austermann et al., 2012](#); [Sobrin et al., 2022](#)). The smallest scales ($\ell \in [35 - 300]$) are covered by BICEP3, the extension of BICEP2/Keck observing at 95, 150 and 220 GHz. It will soon be extended to become the BICEP/Keck-Array and target $\sigma(r) \sim 3 \times 10^{-3}$ ([BICEP2 Collaboration et al., 2014a, 2016](#); [Ade et al., 2022](#)). In Argentina, the QUBIC mission was installed in 2022. It is a bolometric interferometer observing at bands centered at 150 and 220 GHz ([Hamilton et al., 2022](#)). QUBIC is proposing a new instrumental design allowing to split its frequency bands in multiple ways, providing a trade-off between interferometry and bolometric measurements. Finally the CMB-S4 project aims for the combination and extension of the SO, SPT-3G and BICEP array instruments, in order to use the combination of 21 ground telescopes based in Chile and Antarctica by 2030 ([Abazajian et al., 2019](#)). Doing so will allow to observe the CMB in 11 frequency bands from 20 to 270 GHz and targets a value of $\sigma(r) \sim 5 \times 10^{-4}$.
- **Balloon-borne telescopes** can observe for a short period of time above the atmosphere. As such, they can access large sky fractions and witness less contamination than ground based instruments. They present the advantage that they can be redeployed for several launches. As they represent a significantly lower budget than satellite mission, they are often used to test instrumental concepts before their spatial launch. As an example, the Archeops balloon was used to test a prototype of the high frequency instrument (HFI) of *Planck*. In the winter of 2022, the SPIDER experiment flight for

the second time over Antarctica, observing large scales ($\ell \sim [10 - 300]$) at 90 and 150 GHz 280 GHz (Crill et al., 2008; Shaw et al., 2020). While numerous balloon born projects have been proposed for the CMB in the recent years, as τ -surveyor (Errard et al., 2022), most of them are being rejected, such that the future of CMB science with balloons remains uncertain today.

- **Satellite telescopes** are able to provide full-sky measurements and map the CMB anisotropies on all scales. The size of the instruments are however tightly constrained by the weight limits of spaceship's cargo and satellite missions represent major investments and risks. Their success is delicate as for example, they can not be updated, modified or calibrated after the launch. After the success of *Planck*, the Japanese space agency (JAXA) proposed the *LiteBIRD* mission planned for ~ 2030 . *LiteBIRD* should observe the largest scales of the sky ($\ell \in [2 - 200]$) in 15 different frequency bands, in order to target the primordial B -modes with $\sigma(r) \sim 1 \times 10^{-3}$ (LiteBIRD Collaboration et al., 2023). The characteristic of the instrument as well as my contribution to the collaboration will be presented in Chap. 7. In the long term, a NASA "probe" class mission named PICO, was proposed to investigate the concept design of a satellite able to detect $r = 5 \times 10^{-4}$ with a 5σ confidence level. To achieve this goal, the instrument would observe the largest scales with 21 frequency bands centered between 21 and 799 GHz (Hanany et al., 2019).

All the above missions are equipped with bolometric detectors, mapping the anisotropies of the LSS in specific frequency bands, and are hence unable to provide an accurate characterization of the spectral properties of the CMB. We should note that no spectroscopic survey has yet been undertaken in order to characterize the SED of the CMB beyond FIRAS measurement, allowing to seek for the spectral distortions. Doing so would nonetheless allow for the investigation of a large class of primordial physical phenomenon allowing for deviation of the blackbody spectrum. Numerous proposals have been recently been rejected as PIXIE (Kogut et al., 2011), PRISTINE and FOSSIL (see Chluba et al. (2021) and reference therein), while the BISOU balloon is in Phase-A (Maffei et al., 2021). High precision spectroscopy of the CMB is however part of the ESA schedule Voyage 2050 (Chluba et al., 2021).

5.5 CMB and the cosmological parameters

5.5.1 Probing Λ -CDM on the last scattering surface

The value of the Λ -CDM parameters have an impact on the CMB spectra, both in intensity and polarization. This impact can be witnessed at different scales and the effects of the parameters can be degenerated. Using the *Planck* 2018 likelihood¹⁵ constructed from the *TT*, *TE* and *EE* spectra¹⁶, I was able to derive the red contours displayed in Fig. 5.13 for the

¹⁵<http://pla.esac.esa.int/>

¹⁶These likelihoods allow to extract the primordial spectra using instrumental simulations for systematic control as well as foreground models for component separation using COMMANDER (see Sec. 6.4). The methodology for their construction is detailed in (Planck Collaboration, 2020).

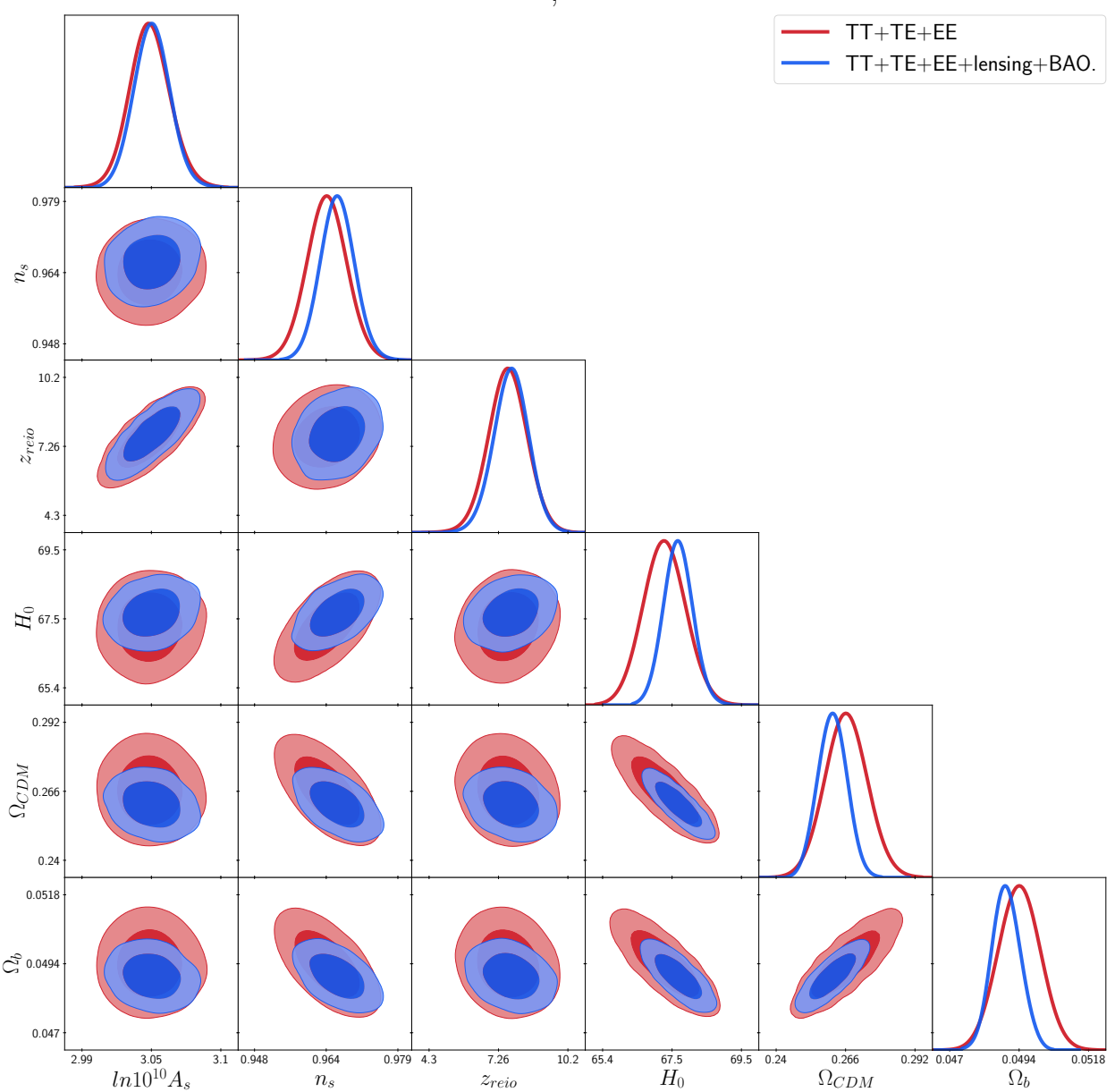


Figure 5.13: Contours on the Λ -CDM model parameter posteriors obtained using the *Planck* 2018 TT-TE-EE likelihood (red) and adding the *Planck* lensing data and BAO data from Beutler et al. (2011); Ross et al. (2015); Alam et al. (2017)).

6 Λ -CDM parameters, using the public version of MONTEPYTHON¹⁷ coupled to the public CLASS version (see Chap. 9 for a detailed presentation of these softwares). As expected, some degeneracies can be witnessed between H_0 and the densities Ω_b and Ω_{CDM} , as they both appear identically in the Friedmann equation (Eq. 3.19). The amplitude of the scalar power-spectra $\ln(10^{10} A_s)$ also shows some degeneracy with the redshift or reionization z_{reio} . Adding *Planck* lensing and BAO data (BOSS DR12, 6dF and SSDS DR7 (Beutler et al., 2011; Ross et al., 2015; Alam et al., 2017)), we get the blue contours, displaying results

¹⁷I considered the chains as converged when the Gellman-Rubin convergence criterion satisfied $|R - 1| < 0.01$ for all the parameters.

5. SIGNAL FROM THE COSMIC ORIGIN: THE COSMIC MICROWAVE BACKGROUND

comparable to the one derived in Tab. 3.1. The improvement brought by the BAO and lensing measurement is rather mild, showing that almost all we know about cosmology so far can be extracted from the CMB spectra presented in the previous section, making CMB an extremely powerful probe. BAO data and other probe can however significantly break specific degeneracies when adding some Λ -CDM parameters to this fit, as further detailed in [Planck Collaboration et al. \(2020a\)](#).

6

Polarized light from the interstellar medium

Sur cette terre, comme l'ombre nous passons. Sortis de la poussière, nous y retourneron.

– Palais idéal du facteur cheval

Contents

6.1	Impact of polarized foregrounds on CMB studies	75
6.2	The interstellar medium	78
6.3	The polarized signals of the ISM in Microwave	80
6.4	Component separation methods	90
6.5	The PySM models	91

6.1 Impact of polarized foregrounds on CMB studies

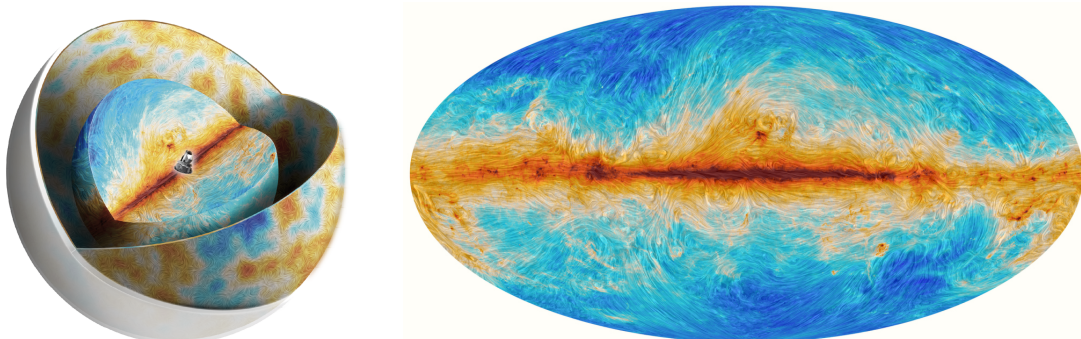


Figure 6.1: Left: Illustration of the component separation problem. Credit: [ESA](#), [Planck](#), [Canopée](#). Right: Magnetic field lines traced by dust polarized emission at 353 GHz by the [Planck](#) mission. Credit: [ESA](#), [Planck](#).

The CMB is not the only signal one can observe in the microwave sky. In turn, any microwave observation will present itself as a mixture of multiple signals having different physical origins. The signals, if not coming from the CMB monopole, primordial and secondary anisotropies (see Chap. 5) or the instrument itself, are called *foregrounds* to the CMB.

The CMB is the furthest possible light source which can be observed in the Universe. As such, it will be observed through all the possible visible astrophysical objects bright in the microwave. As our solar system is located in the spiral arm of our Galaxy, any observation will contain the Galactic signal across the whole celestial sphere. As illustrated on Fig. 6.1, the signal is mostly bright in the center which should be understood as a slice of the Galactic disk. This disk is visible with the naked eye in the right conditions as a band of stars stretching across the sky and emitting a pale, white glow. Besides the various diffuse and localized Galactic sources coming, additional contributions comes from the other galaxies and galaxy-clusters present between us and the CMB. Overall, the possible contributions to the astrophysical foregrounds are:

- **Synchrotron emission** is generated by the electrons accelerated by the Galactic magnetic field (GMF) in the ionized interstellar medium (ISM). We will cover it in detail in Sec. 6.3.2.
- **Thermal dust emission** is due to dust grain present in our Galaxy which are thermally re-emitting starlight. Sec. 6.3.3 will be devoted to its description.
- **Free-free emission**, or Bremsstrahlung, is generated by electrons being deflected by positive ions in the hot ionized ISM. For a review see e.g. [Dickinson et al. \(2003\)](#).
- **Anomalous microwave emission (AME)** is a signal of which the exact nature is still debated ([Dickinson, 2018](#)). A favored explanation is given by the emission of the smallest dust grains in rapid rotation (spinning dust) ([Draine & Lazarian, 1998](#); [Ali-Haïmoud, 2013](#)).
- **Spectral lines** can also be observed, which are the emission lines of atoms and molecules in the microwave domain, as carbon monoxide (CO) present within our Galaxy and other galaxies. For a review, see ([Maniyar et al., 2023](#)).
- **Zodiacal light** is due to the reflection and re-emission of Solar radiation by dust grains in the Solar system. It is mostly visible as a diffuse and poorly polarized signal in the ecliptic plane. For recent reviews, see e.g. ([Lasue et al., 2020](#); [Ganga et al., 2021](#)).
- **Cosmic infrared background (CIB)** presents itself as a diffuse background radiation due to the combined infrared emission of multiple extra-Galactic sources, mostly coming from unresolved dusty galaxies, see e.g. [Lenz et al. \(2019\)](#).
- **Bright point sources** are visible in the radio, microwave and infrared frequencies at which CMB missions are sensitive. They can be extra-Galactic as quasars and radio galaxies (introduced in Sec. 9.2), or Galactic as stellar compact leftovers¹ like pulsars within supernovae remnants as the Crab nebula (discussed in Sec. 6.2).

The contribution of these different sources to the total spectral energy distribution (SED) as seen by *Planck* are displayed on Fig. 6.2. Only synchrotron and thermal dust appear to

¹Galactic stars are not in that list as they do not emit significant amount of radio and microwave radiation.

6.1. IMPACT OF POLARIZED FOREGROUNDS ON CMB STUDIES

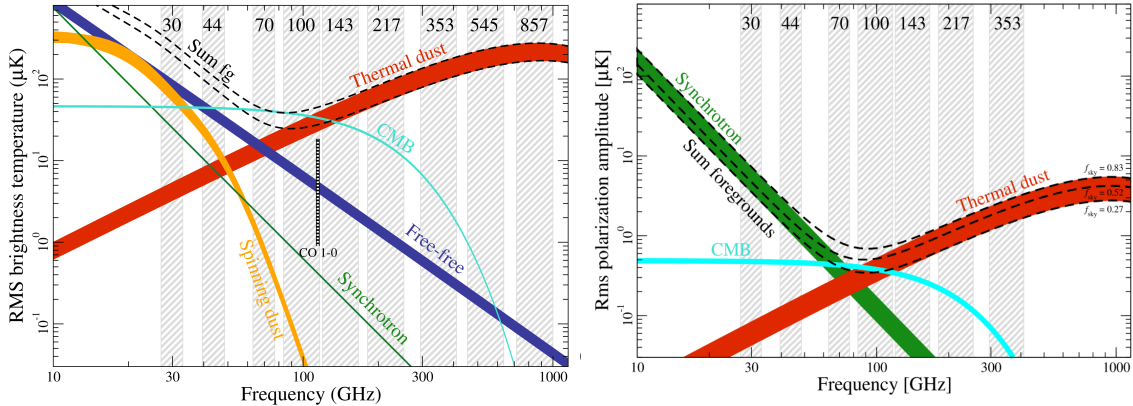


Figure 6.2: Estimated SED for different Galactic foreground components from the *Planck* data (Planck Collaboration et al., 2020c). Left: Intensity I_ν , Right: Estimated $|\mathcal{P}_\nu| = \sqrt{Q^2 + U^2}$. The vertical gray bands represent the *Planck* frequency channels. The thickness of the curves represent the difference of amplitude between two different fractions from $f_{\text{sky}} = 0.81$ and $f_{\text{sky}} = 0.93$ for intensity and $f_{\text{sky}} = 0.73$ to $f_{\text{sky}} = 0.93$ for polarization.

be significantly polarized. Note that, contrarily to CMB, the amplitude of the foreground signal is highly variable on the sky such that it is brighter near the Galactic plane (see also Fig. 6.3). Fig. 6.2 represents this amplitude between two different sky fractions of $f_{\text{sky}} = 0.81$ and $f_{\text{sky}} = 0.93$ for intensity and $f_{\text{sky}} = 0.73$ to $f_{\text{sky}} = 0.93$ for polarization, larger sky fractions including larger portions of the Galactic plane.

In order to extract cosmological information from the early Universe, one should hence characterize and remove these various components. This is the so-called problem of component separation. This exercise is delicate, as the foreground signal can mimic primordial signature of new physics. As an example, the BICEP-2 mission claimed a $\sim 7\sigma$ detection of the primordial B -modes in 2014 (BICEP2 Collaboration et al., 2014b) which revealed itself to be originated by Galactic dust (BICEP2/Keck Collaboration et al., 2015).

Contrary to the CMB signal, Galactic foregrounds have complex and inhomogeneous spatial distributions, as well as a non trivial frequency dependence. The challenge is hence double: both a spectral and a spatial understanding of the foreground properties is required with high accuracy. The stakes are themselves double: while component separation is of first importance to recover an unbiased CMB signal and unveil cosmology, it opens a window on the astrophysics of the sources themselves. From several aspects, diffuse regions are more challenging to model, as they can not simply be masked and their impact can be witnessed at all scales. They are thus unavoidably entangled with the cosmological signal. In the present work, we will focus on the two main sources of Galactic diffuse polarized foregrounds: synchrotron and thermal dust. We will see that they can both be linked to the structure and properties of the interstellar medium.

6.2 The interstellar medium

The interstellar medium (ISM) refers to all the baryonic content of our Galaxy² which is not in the form of stars. It is mostly made of ionized, atomic or molecular gas ($\sim 99\%$ ³), cosmic rays and heavier dust grains ($\sim 1\%$). Regarding its atomic content, the gas itself contains $\sim 70\%$ hydrogen ($\sim 60\%$ of which is in the form of H -atom, $\sim 20\%$ of H^+ ion and $\sim 20\%$ of H_2 molecule), 28% helium and $\sim 2\%$ of heavier elements (the so called "metals", Draine, 2011; Ward-Thompson & Whitworth, 2011). On larger scales, the ISM becomes the inter galactic medium (IGM) separating the galaxies, while on smaller scales surrounding stars it becomes the inter planetary medium (IPM) separating the planets.

While representing only a small fraction ($\sim 10\%$) of the Galactic mass, the ISM has a strong impact on the shape and processes of the Galaxy. The ISM fluid must indeed be understood as a dynamical entity, involving a great range of complex physical processes. Non-linear physics creates turbulent motion, mostly driven by the interplay between gravitational⁴ and magnetic fields acting on and shaping the ISM at different scales. Additionally, electromagnetic starlight radiation fields and fast impact of cosmic rays play major roles in the gas dynamic. Turbulence can lead to the formation of (supersonic) shock fronts and complex instabilities displaying fractal pattern. Additionally, structures as filaments, cores, clumps, proto-stars and stars are able to form within its coldest regions (molecular clouds). In return, stars shape back the ISM with their radiation (pressure and ionization) and with stellar winds. When they die, they return to the ISM in the form of planetary nebulae and supernovae remnants which enrich the ISM back with heavier elements. The shock produced by their explosion can trigger dynamical processes, source turbulence and potentially give birth to new stars. In the meanwhile, the ISM hosts rich chemical processes allowing for the emergence of molecular complexity.

For all these reasons, the gas in the ISM is not in thermal equilibrium and can be found transiting between many different states. In order to simplify the discussions, it is convenient to classify the different phases as follows (inspired from Draine, 2003):

- **Coronal gas or hot ionized medium:** regions of hot, diffuse and ionized gas (conditions similar to the corona of the Sun: $T \geq 10^{5.5}$ K. Ionization is due to collisions). Made from gas shock-heated by supernovae blastwaves, these regions form a network of interconnecting bubbles with a characteristic size of ~ 20 pc, filling \sim half of the volume of the Galactic disk. It cools on time scales of \sim Myr. Additionally, coronal gas might compose much of the volume above and below the disk, and must be representative of the conditions of the gas filling the space between the galaxies: the inter-galactic medium (IGM). See e.g. Ehle (2005).
- **Warm neutral and ionized media:** Most of the volume of the disk which is not made of coronal gas is made of warm neutral gas ($T \simeq 5 \times 10^3$ K), also called H I regions (Wolfire et al., 1995). Some of the warm regions are however completely ionized ($T \simeq 10^4$ K) (Hoyle & Ellis, 1963). This is the case of "H II regions", ionized by UV

²Note that this definition can (and is often) extended to include dark matter and to study other galaxies than the Milky-Way. We will however not need such a broad definition in the present thesis.

³All the percentages given in this paragraph are in term of the total mass of the ISM.

⁴From both baryonic and dark matter.

photons coming from the most massive members of clusters of newborn stars (e.g. type O) which live for ~ 10 Myr. A good example of a H II region is given by the Orion nebula (M42). Warm ionized gas can also be found in planetary nebulae (as e.g. M27) which gets diluted in $\sim 10^4$ years, and within massive stellar outflows built from stellar winds.

- **Cold neutral medium:** A very small fraction of the ISM volume⁵ ($\sim 1\%$) is made of cool clouds of atomic gas ($T \sim 100$ K), presenting themselves as cold H I regions. Some molecular gas can also be found in the cold diffuse regions (Faison & Goss, 2001).
- **Molecular clouds:** Molecular gas can also be found in large self-gravitating clouds mostly located within the Galactic plane. These clouds are dense⁶ and cold ($10 \leq T \leq 50$ K). Moreover, they are opaque and can be seen in absorption in front of brighter backgrounds, as the pillars of creation or the horsehead nebula (hence sometimes sometimes named "dark clouds"). Giants clouds can reach a size of ~ 100 pc, for a mass of $\sim 10^5 M_\odot$. When over-passing Jean's mass, molecular clouds spontaneously collapse under self-gravity. The induced shrinking of their size will be followed by a corresponding increase of angular momentum. Centrifugal force leads to the gradual fragmentation of the cloud in denser and denser subparts, until the formation of newborn star clusters (with associated H II regions). In an ideal case, clouds should collapse spontaneously in a free fall timescale of $\sim 3 \times 10^5$ years. However, observations show that their lifetime is an order of magnitude larger. This is due to complex dynamics of magnetized turbulence which delays the collapse and allows for a wide variety of intermediate structures as filaments to form within the collapsing cloud (Williams et al., 2000).

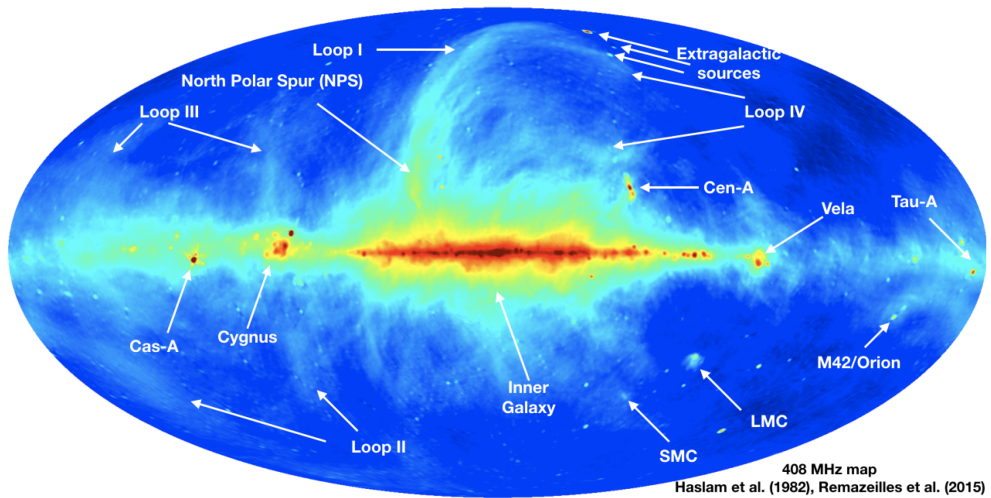


Figure 6.3: Intensity map of the full sky at 408 MHz. Taken from Dickinson (2018) and built from data of Remazeilles et al. (2015); Haslam et al. (1981). The observed signal is mostly due to synchrotron and free-free radiations.

⁵As the cold neutral medium is denser than the other phases, it is subdominant in term of volume but dominant in terms of total mass.

⁶Of order $n_H \sim 10^2 - 10^3 \text{ cm}^{-3}$, which is dense relatively to the other ISM phases: $\sim 0.004 \text{ cm}^{-3}$ for coronal gas, or 0.6 cm^{-3} for the warm H I regions Draine (2011). Of course this is still extremely diffuse compared to human standards ($n_{\text{mol}} \sim 2 \times 10^{19} \text{ cm}^{-3}$).

As the ISM evolves typically on the scale of Myrs, it appears as almost static on human timescales. As displayed in Fig. 6.3, deterministic structures can clearly be identified on the celestial sphere. We focus here on structures visible in microwaves, as they are the primary concern of this thesis. The first striking pattern is the Galactic center and the disk, covering all the equator of the celestial sphere. This is a direct signature that we are living on the edge of the disk of a spiral galaxy, as mentioned already in Sec. 6.1. The brightest regions of the sky are given by the Galactic bulge and the inner Galaxy, constituted of the spiral arms. Other remarkable bright regions can be identified in the equator. On the West, newborn stars in the Orion molecular cloud complex lighted the H II region known as the M42 nebula. Multiple regions of coronal gas built from supernovae remnants (SNR) as Vela, M1 (Crab nebula, or Tau-A), Cassiopeiae A or the Cygnus loop are also clearly visible. Additional features out of the plane can be seen, called the radio loops, the largest one being known as the *North polar spur*. The origin of this large loop structure is still strongly debated today (Lallement, 2022). It can be either understood as an expanding shell of a nearby supernova or as part of the Fermi bubbles of our Galaxy. In the last case, it would be part of a gigantic bubble structure expelled by the Galactic center in a past active phase, with a size comparable to the Milky way itself⁷. We also know that our Solar system is currently crossing an asymmetric hot plasma bubble surrounded by a shell of cold dusty gas, known as the *local bubble*, most certainly expelled by a succession of several supernovae (see e.g.(Zaninetti, 2020; Pelgrims et al., 2020)). As such, all observations of distant astrophysical regions have the signal of this bubble as a foreground (Skalidis & Pelgrims, 2019). Extra-galactic point sources are also visible as our two satellite galaxies, the large and small Magellanic clouds or the radiogalaxy Centaurus A. Looking at Fig. 6.1 and Fig. 6.3, it is now clear that the spatial distribution of the ISM signal is extremely complex, displaying features characteristic of its complex dynamics such as spur, filaments, loops ... From the point of view of spatial distribution, it is hence extremely different from (and richer than) the CMB signal as displayed in Fig. 5.3. We will further investigate how to model this complexity in Sec. 8.6.

6.3 The polarized signals of the ISM in Microwave

6.3.1 Tools to describe the polarized light of the ISM

As we did for the CMB in Sec. 5.2.3 and Sec. 5.3, the polarized Galactic signals can also be described using the Stokes parameters Q , U and V as well as the E - and B -modes decomposition and their corresponding angular power spectra expansion, all introduced in detail in Appendix B.

Additionally, we will here make an extensive use of the *polarization spinor*⁸

$$\mathcal{P}_\nu = Q_\nu + iU_\nu = P_\nu e^{2i\psi}, \quad (6.1)$$

⁷The origin of the Fermi bubbles is also still elusive and debated. It could be originated by a past active phase from our Galaxy's central supermassive black hole, Sgr A* (Yang et al., 2022).

⁸In full rigor, \mathcal{P}_ν represents a spin-2 complex field on the sphere and not a formal spinor as defined in Appendix A (see also the discussion in Appendix B). As no ambiguity is possible here, we will however use this name regardless of this consideration.

where the dependence in frequency is made explicit by the indices ν . The modulus of this complex field, $P_\nu = \sqrt{Q_\nu^2 + U_\nu^2}$ is the *polarized intensity*, quantifying the SED of the polarized signal, while its argument $\psi = 0.5 \arctan(U/Q)$, quantifies the orientation of the polarization headless vector on the sky and is called the *polarization angle*. The factor of 2 in the phase quantifies the spin-2 nature of the polarization field, meaning that, as a headless vector, the polarized signal come backs identical to itself after half a rotation (see Appendix. B). This object provides thus a very natural way to contain both the information about the frequency dependent amplitude (SED) and the orientation of the polarized signal, as well as its transformation properties. We will further see that, for the main astrophysical foreground emission, the orientation given by ψ is induced by the structure of the magnetic field within our Galaxy.

6.3.2 Synchrotron emission

The synchrotron emission and the Galactic magnetic field

Free light charged particles as electrons are omnipresent in the ISM, mostly coming from ionized regions and SNR. Accelerated by shockfronts in supernovae explosions and pulsar winds, they reach relativistic speeds \mathbf{v} and become part of the cosmic rays. In the presence of a strong coherent magnetic field \mathbf{B} , these free charges q will spiral around the magnetic field direction due to Lorentz force⁹ $q(\mathcal{E} + \mathbf{v} \times \mathbf{B})$. In that case, the electron will emit a focalized beam of highly polarized light tangential to its trajectory, as sketched on Fig. 6.4. The polarization direction will be orthogonal to the local direction of the magnetic field. As such, synchrotron polarized emission provides a powerful tracer of the Galactic magnetic field (GMF). Additionally, the polarization direction will rotate when propagating through the magnetized ISM and in the presence of thermal electrons (Faraday rotation, inversely proportional to the square of the frequency), allowing to probe the 3D structure of the GMF through the so called process of "Faraday tomography" (for a pedagogical introduction, see [Takahashi \(2023\)](#)).

For lack of a better model, the GMF is usually described as a superposition of an average component \mathbf{B}_0 and a fluctuating turbulent component \mathbf{B}_τ as $\mathbf{B} = \mathbf{B}_0 + \mathbf{B}_\tau$ ([Chandrasekhar & Fermi, 1953](#)). Both components have comparable amplitude, as the ratio $f_M = |\mathbf{B}_\tau|/|\mathbf{B}_0|$ is measured to be ~ 0.9 , signature of trans-Alfvenic turbulence ([Planck Collaboration et al., 2016c](#)). Several models are proposed for \mathbf{B}_0 , which have to take into account the shape of the spiral arms. For a recent review see e.g. [Pelgrims et al. \(2018\)](#). Over the celestial sphere, the GMF appears as displayed on the right panel of Fig. 6.1, an example of a 3D model explaining this structure, proposed by [Jansson & Farrar \(2012\)](#) and pictured in [Farrar et al. \(2015\)](#), is represented in the right panel of Fig. 6.4.

The synchrotron SED

As depicted in Fig. 6.2, synchrotron emission is the dominant source of polarized emission for $10 < \nu < 100$ GHz. Both in intensity and polarization, the synchrotron SED behaves as a straight line in the loglog plane, which can hence be modeled by a power-law in frequency.

⁹Or in the language of part I, $m \, du_\mu / d\tau = qF_{\mu\nu}u^\nu$, with u the 4-velocity and F the electromagnetic curvature tensor (see Chap. 3).

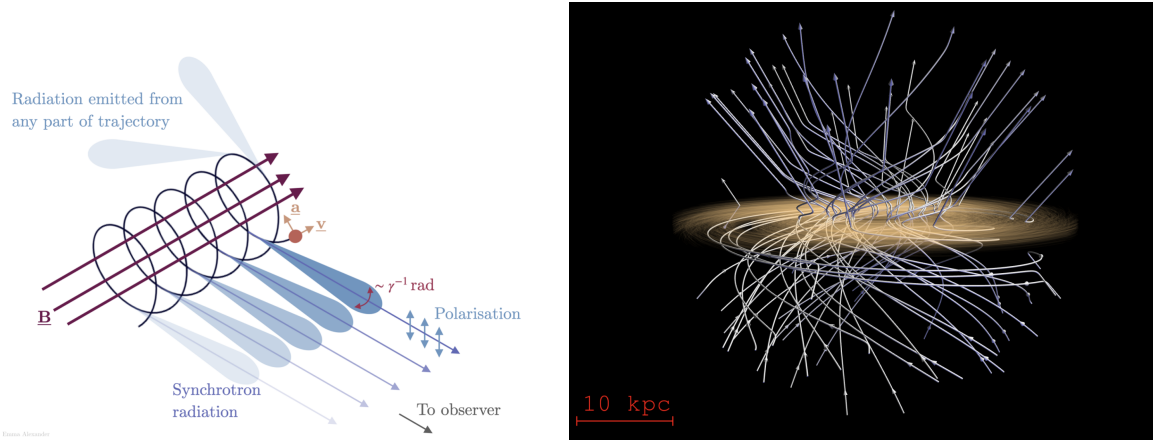


Figure 6.4: Left: Illustration of the synchrotron polarized emission by an accelerated charge. From [Emma Alexander](#). Right: 3D representation of the model of the GMF (\mathbf{B}_0) proposed by [Jansson & Farrar \(2012\)](#) in [Farrar et al. \(2015\)](#).

As such, one expects that, for every line of sight \mathbf{n} , the synchrotron polarization spinor \mathcal{P}_ν^s can be expressed as

$$\mathcal{P}_\nu^s(\mathbf{n}) = A_s(\mathbf{n}) \left(\frac{\nu}{\nu_0^s} \right)^{\beta_s(\mathbf{n})} e^{2i\psi_s(\mathbf{n})}, \quad (6.2)$$

where ν_0^s is a reference frequency used for normalization (typically, in synchrotron models built from the *WMAP* data, one uses $\nu_0^s = 23$ GHz [Bennett et al., 2013](#)). A value of $\beta_s \simeq -3$ allows to reproduce the behavior of the polarized synchrotron signal ([Martire et al., 2022](#)) (see also Fig. 6.5). As already mentioned in the previous section, in the presence of the GMF and thermal electrons along the line of sight, this spinor is expected to experience a frequency dependent rotation such that $\psi_s(\nu) \propto \nu^2$ known as *Faraday rotation*.

The power-law behavior of the SED can be shown to be inherited from the shape of the energy distribution of the cosmic rays ([Padovani et al., 2021](#)). This distribution appears in fact not to be a perfect power law, such that the power law SED of the synchrotron is to be understood as an approximation mostly valid in the CMB frequency interval. In particular it breaks at frequencies close to 100 GHz where higher energy cosmic rays are no longer present in the ISM. At such frequencies the synchrotron SED is expected to turn over.

The synchrotron statistics and power-spectra

Synchrotron radiation requires both sources of free accelerated electrons (cosmic rays) and intense magnetic fields. SNR and star forming regions sourcing will thus appear as brighter in synchrotron, corresponding to the point sources observed in Fig. 6.3. The distribution of this signal is expected to be highly non homogeneous and non Gaussian over the sky. Moreover, the parameters of the synchrotron SED ((6.2)) must be varying across the sky depending on the physical conditions of the region of emission. An extracted map of β_s from the S-PASS data ([Krachmalnicoff et al., 2018](#)) can be found on Fig. 6.5, providing an indicative representation of the variability of the spectral index of synchrotron allowed by data.

On the largest scales, the angular power spectra of the polarized synchrotron signal can be

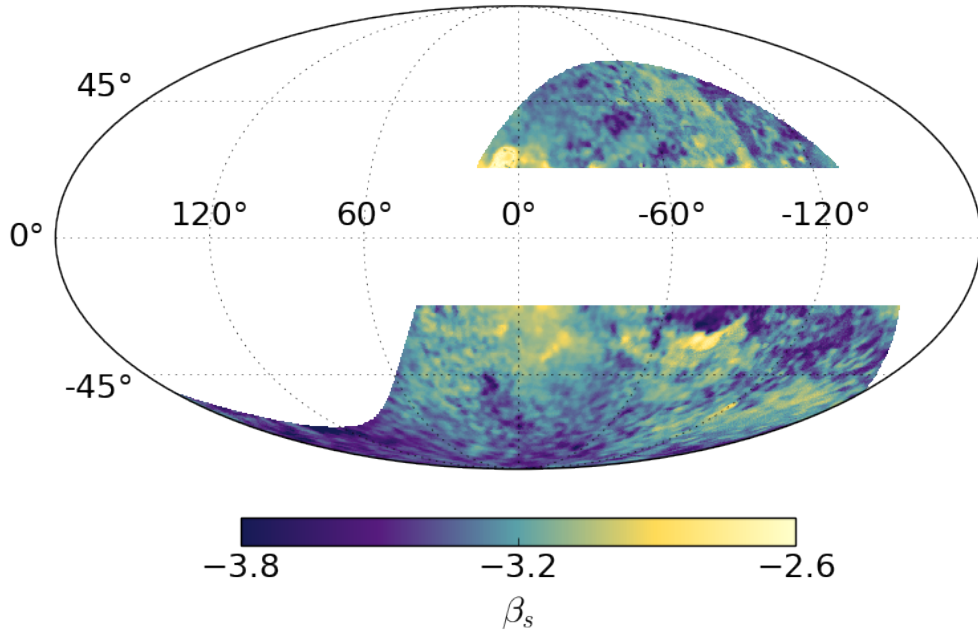


Figure 6.5: β_s estimated on 50% of the sky from the S-PASS mission data (Krachmalnicoff et al., 2018).

well modeled by a power-law of ℓ as

$$\mathcal{D}_\ell^{XX,s}(\nu) = A_\nu^{XX,s}(\nu) \left(\frac{\ell}{\ell_0} \right)^{\alpha_s^{XX}}, \quad (6.3)$$

with $XX \in EE, BB$, when point sources and the Galactic plane are masked ($f_{\text{sky}} = 0.5$). From *Planck* and *WMAP* data $\alpha_s^{EE} = -2.95 \pm 0.04$ and $\alpha_s^{BB} = -2.85 \pm 0.14$ (Martire et al., 2022). This power-law behavior in ℓ traces the GMF structure encountered by cosmic rays and the exact value for the slope represents a complex mixture of Galactic structure (a disk seen edge-on), GMF shape, spatial and energy distributions of cosmic rays, and to some extent, the spatial distribution of thermal electrons responsible for Faraday rotation (expected to be negligible in the CMB frequency range)¹⁰. At $\ell = 80$, $\mathcal{D}_\ell^{BB,s}/\mathcal{D}_\ell^{EE,s} = 0.22 \pm 0.02$. The synchrotron EB correlation $\mathcal{D}_\ell^{EB,s}$ is compatible with zero at 1σ (Martire et al., 2022).

6.3.3 Cosmic dust

A key astrophysical element

The cosmic dust is composed of small solid grains (ranging from the size of a molecule to a fraction of μm). Their chemical composition is varied and can include carbon, silica, silicates, metal oxides, pure metals (iron, magnesium, silicon), metal sulfides, carbides and some other components that remains to be confirmed, see e.g. Molster et al. (2010). The emission properties of the diffuse dust signal can be explained by the existence of two main

¹⁰Thanks to Marc-Antoine Miville-Deschénes for raising this point and stressing the role of thermal electrons in the Faraday rotation process.

6. POLARIZED LIGHT FROM THE INTERSTELLAR MEDIUM

distinct populations of silicate and carbonaceous grains (see e.g. [Guillet et al. \(2018\)](#)) or by a single population of large composite grains, named "astrodust" ([Hensley & Draine, 2023](#)).

As discussed in Sec.[6.2](#), dust represents a relatively small fraction of the mass in the ISM ($\sim 1\%$) but it plays a critical role in the dynamics of all the astrophysical media (IPM, ISM and IGM) as in planetary, stellar and Galactic formation and evolution.

The dust grains formation requires high densities and moderately high temperatures of $\sim 1000 - 2000$ K. As detailed in e.g. [Sarangi et al. \(2018\)](#), it occurs in two steps: the nucleation and the condensation. The conditions allowing this process can be mainly found in the cool and oxygen rich atmospheres of the post main sequence stars of low mass ($< 8M_{\odot}$) evolving in the asymptotic giant branch (AGB) of the Hertzsprung-Russel (HR) diagram ([Höfner, 2009](#); [Höfner & Olofsson, 2018](#)). While the effective temperature of the AGB stars are low by stellar standards (~ 3000 K), they remain too warm to allow the condensation of solids in their external layers. However, these dying stars are affected by strong convective motions and regular pulsations, inducing significant mass loss. Those violent events propagate shock waves in the gas, expelling material out of the star and inducing the periodic formation of a dense, cool layer above the stellar surface where solid dust grains can form. The grains thus formed are carried away from the star by its radiation pressure and tend to drag along a large amount of gas. As such, cosmic dust represents a key component of stellar evolution and drives the mass loss of dying stars. An example of such a dust formation outburst could be responsible for the brutal decrease in the luminosity of the red giant Betelgeuse observed in 2020 ([Montargès et al., 2021](#)). To a lower extent, other pulsating stars of higher mass can also be responsible for dust grain formation in the same way, as the Luminous Blue Variables (LBV) or the Wolf-Rayet stars (WR) ([Harries et al., 2004](#)) ¹¹.

A second phenomenon providing optimal conditions of temperature and density allowing dust production is provided by explosive events like novae, supernovae (SNe) and supernovae remnants (SNR) ([Matsuura, 2017](#); [Sarangi et al., 2018](#); [Sugerman et al., 2006](#)). Core collapse supernovae (CCSNe: Type Ib, Ic and II) represent the fate of all stars massive enough to reach the fusion of iron in their core. After the external layers of the star bounced back on the newly formed neutron core¹², the expelled matter keeps expanding in space for thousands of years. Dust formation requires specific conditions present in the SN ejecta only for a very short time (of around a decade) around a year after the explosion. In the end, dust represents however 3 – 10% of the mass of the SNR and understanding its formation and impact on the fluid dynamics and luminosity is then critical for supernovae physics. While AGB stars are the main dust producer of our galaxy, CCSNe are expected to be the biggest source of dust grains for high z galaxies containing stars of populations II and III and having a high rate of star formation ([Dwek & Cherdneff, 2011](#)).

After their birth, dust grains evolve in and with the ISM. Complex processes can lead to their destruction, rebuilding, reconfiguration and size increase with aggregation. They will remain stable inside the cold molecular clouds, and have a strong impact on their dynamics

¹¹WR stars represent the post main sequence stage of the most massive stars of population I (type O and B). Their radiative pressure is strong enough to expel their outside layers (Eddington limit). Some of the most massive and large stars known as η Carinae-A or R136a1 are WR stars.

¹²This "bouncing back" picture is of course overly simplistic, as SN-II are very complex phenomena, in which neutrino play a major role in matter expulsion. For a review see e.g. [Burrows & Vartanyan \(2021\)](#).

while they collapse and fragment. Even if gas phase chemistry can take place with the help of cosmic radiation, dust grains play a unique key role by allowing some chemical reactions on their surface, playing the role of kinetic energy sinks (Potapov & McCoustra, 2021). This is the case for example of the catalysis of H_2 . Helped by dust, the chemistry taking place in the molecular clouds allows for the formation of complex elements in dust, like organic compounds (see e.g. Jin & Garrod (2020)). All this molecular richness will then be inherited by the newborn stellar systems and must play a central role in the emergence of life.

The grains themselves will remain in the planetary system after its formation, as in the Solar system, becoming part of the planets and satellites themselves, forming the rings of gaseous giants and being contained and expelled by comets and asteroids. The free grains remaining in the IPM will produce the so-called zodiacal light, bright in the ecliptic plane. As such, analyzing dust grains in the Solar system allows us to probe its history.

Besides pure kinematics, it is the thermodynamical properties of the dust grains that cause it to play such an important role in the dynamics of the astrophysical media. By re-radiating heat and coupling to the magnetic field, the grains provide cooling mechanisms in IR regions or heating mechanisms in UV regions (Draine, 1978). They have thus an important impact on the Galactic fluid dynamics itself by transferring radiation pressure from stars or coupling the Galactic magnetic field to the neutral gas (which otherwise would significantly happen only if ionized).

Dust grains are often considered as a nuisance for astrophysical observations, both because of its absorption properties at short wavelengths and also because of its emission properties in the millimeter/radio domains (Draine, 2003). This is typically the case for the CMB foregrounds presented in Sec. 6.1. However, cosmic dust represent a major subject of study by itself both because of the critical role it plays in our understanding of numerous astrophysical phenomena but also as a tracer of the astrophysical conditions (temperature, magnetic field, stellar populations). The microscopic nature of dust grains coupled to their impact on astronomical scales make their study interdisciplinary by nature and is of interest far beyond the scope of astrophysics and cosmology (quantum, statistical or solid state physics and chemistry).

The thermal dust SED

The first historical evidence for the existence of interstellar dust was due to absorption, as dust clouds appear in visible light as dark regions over a brighter background (Barnard, 1919; Trumpler, 1930). Dust grains absorb stellar light which they re-emit in the IR and microwave. With this mechanism, dust grains can be responsible for $\sim 50\%$ of the radiation of some galaxies and in the Universe, at least 30% of the light emitted by stars is re-radiated by dust in the infrared (Stein, 1966; Bernstein et al., 2002). As such, dust shapes both the galaxies and the way they are perceived.

As illustrated on Fig. 6.2, thermal dust represents the major source of polarized signal, for $\nu \geq 100$ GHz. Both from astrophysical observations and lab experiments, it appears that the local SED of a dust grain in the microwave domain is very close to a modified blackbody

(MBB), that is the product of a power-law and a blackbody

$$I_\nu^d = \tau_{\nu_0^d}(\mathbf{n}) \left(\frac{\nu}{\nu_0^d} \right)^{\beta_d} \frac{B_\nu^{\text{Pl}}(T_d)}{B_{\nu_0^d}^{\text{Pl}}(T_d)} = \tau_{\nu_0^d}(\mathbf{n}) \frac{I_\nu(\beta_d, T_d)}{I_{\nu_0^d}(\beta_d, T_d)}. \quad (6.4)$$

For dust models built from the *Planck* data, we choose typically $\nu_0^d = 353$ GHz. The amplitude of this signal is given by the optical depth at the reference frequency $\tau_{\nu_0^d}$ which is given by $\tau_{\nu_0^d} = \mu \kappa_{\nu_0^d} r_d N_H$ where μ is the mean molecular weight, $\kappa_{\nu_0^d}$ is the dust emissivity cross section, r_d is the dust-to-gas ratio and N_H the gas column density. Under the hypothesis of a constant dust-to-gas-ratio and a constant dust emissivity, the thermal dust signal becomes a tracer of the column density of the interstellar gas in the diffuse ISM ([Planck Collaboration, 2014](#)). The blackbody contribution is characteristic of a signal near thermal equilibrium, and allows to associate locally a temperature to the ISM. The modulation by the power-law term with spectral index β_d , is more characteristic of the dust grain properties (e.g. shape and composition). It seems that an anti-correlation exists between β_d and T_d , and it is still debated whether this correlation is physical or a byproduct of the data analysis techniques ([Ysard et al., 2015](#); [Shetty et al., 2009](#); [Liu et al., 2017](#)). We note here that the MBB is an empirical model and it is hence natural to expect deviations from it ([Liu et al., 2017](#)). The observation of such a SED can however be justified from underlying physical principles as follows: the blackbody term is the signature of a photon gas at thermal equilibrium, which is expected to be valid to model the ambient radiation field emitted by a micro-metric dust grain. The power law emissivity factor can be motivated as reproducing asymptotically some simple semi-classical solid state physics models (for the value of $\beta_d = 2$), as the Lorentz oscillator or the Debye model ([Craig F. Bohren, 1983](#); [Henning & Mutschke, 1997](#)). An even deeper motivation comes from the fact that a MBB SED can be recovered from interstellar dust grain analogues in laboratory ([Agladze et al., 1996](#); [Mennella et al., 1998](#)), at least for the frequency range of interest for CMB experiments. Some laboratory measurements tend however to suggest the existence of more complex behaviors, as the frequency dependence of β_d ([Demyk et al., 2017](#)). Note also that the existence of different co-existing dust grain populations with varying compositions and sizes would be associated with different spectral indices and equilibrium temperatures, resulting in a complex SED produced by a sum of MBB, even in a small volume element of the Galaxy. We postpone the discussion of such a complication and its consequences as the main topic of Chap. 8.

Dust grains tend to have asymmetrical and elongated shapes. If they are free, they will naturally rotate such that their angular momentum is aligned with their axis of maximal moment of inertia, i.e. orthogonal to their longer axis (e.g. the semi-minor axis for an ellipsoid). As dust grains are not in thermal equilibrium with the surrounding gas, the grains can have a rotation significantly higher than the random one which would be induced solely by Brownian shocks with the gas particles (they are then in so-called "suprothermal rotation" [Draine, 2011](#)). Suprothermal rotation of grains can be induced by 1) formation and ejection of H₂ molecules on the surface of the grains ([Purcell, 1979](#)) 2) photo-electric effect if dust is exposed to UV starlight ([Purcell, 1979](#)) 3) Gazeous shocks on a irregular grain surface ([Purcell, 1979](#)) 4) radiative torques (RAT) induced by absorption and scattering of anisotropic starlight on irregular grains ([Draine & Weingartner, 1996](#)). This last phenomenon appears to be preferred as the only mechanism able to produce suprothermal rotation stable over long time periods ([Hoang & Lazarian, 2016](#)) and which is compatible with dust emission

6.3. THE POLARIZED SIGNALS OF THE ISM IN MICROWAVE

observed in *Planck* data (Reissl et al., 2020). The resulting rotation period of the grains range from milliseconds to less than a nanosecond (Draine, 2011).

Most dust grains are paramagnetic, i.e. they tend to possess an intrinsic magnetic moment which aligns itself with the presence of an exterior magnetic field. This moment will additionally be increased by the electron spins through the so called "Barnett effect" (Dolginov & Mitrofanov, 1976). The existence of a non-vanishing magnetic moment associated with the grain rotation will induce its precession around the GMF.

Additionally, paramagnetic dust grains in suprathermal rotation will gradually orient themselves such that their angular momentum will be aligned with the GMF direction within a few Myr (Davis & Greenstein, 1951; Andersson et al., 2015)¹³. Indeed, in the frame of the grain, the GMF is rotating and the magnetic moment tries to align with it. This varying magnetization leads to energy dissipation, dissipating the rotational energy. This dissipation will progressively reduce the component of the angular momentum perpendicular to the GMF while leaving the component align with it unchanged. The dust grains in the ISM will thus tend to rotate in a plane perpendicular to the GMF. As a consequence, the grain emits light which will be significantly linearly polarized perpendicularly to the GMF along the preferred direction given by the shape of the asymmetric dust grain.

As for synchrotron, the linear polarization of the dust signal will hence be perpendicular to the GMF, and will provide a very powerful tracer of the GMF structure. On this regard, see e.g. Planck Collaboration (2015a, 2016b).

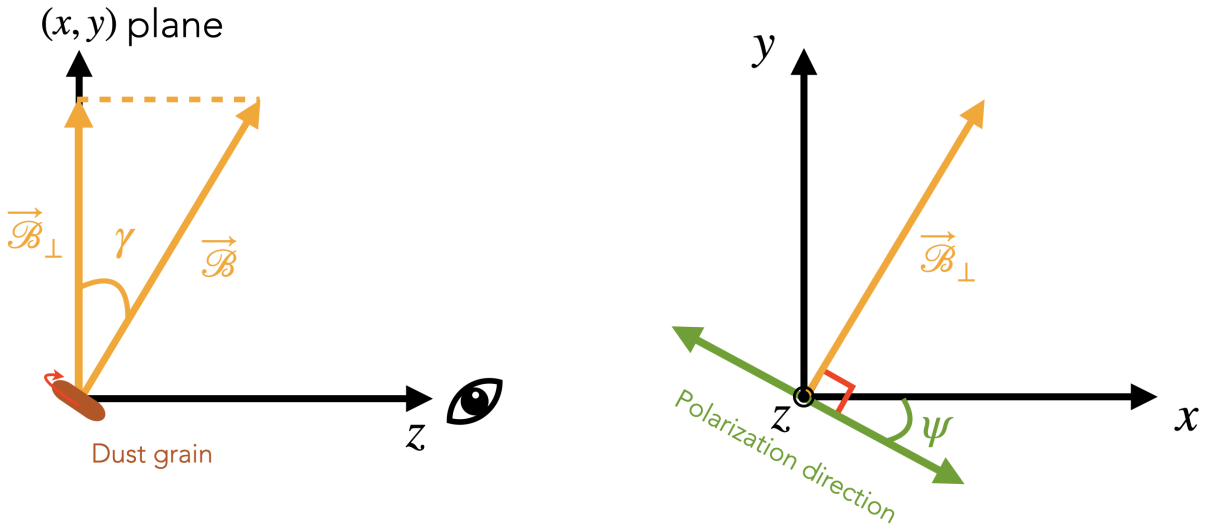


Figure 6.6: 3D representation of a dust grain which momentum is aligned with the GMF \mathcal{B} , and its polarized emission – parallel to the grain big axis – is orthonormal to the GMF projection B_\perp in the (x, y) plane of the sky.

¹³This phenomenon is dependent on the size a of the dust grains. Grains with $a \gtrsim 0.1\mu\text{m}$ are significantly aligned, while the ones with $a < 0.05\mu\text{m}$ can not be significantly impacted by radiative torques to be in suprathermal rotation, and are rapidly misaligned by shocks with the gas. As such, spinning dust (that could be responsible for the AME) might come from grains in Brownian rotation. Composition of the dust grains might also play a significant role in the alignment process.

As in Fig. 6.6, consider an orthonormal frame (\mathcal{O}, x, y, z) centered on a radiating dust grain. It is oriented such that the line of sight (LOS) \mathbf{n} is along the z axis. The plane of the sky (POS) is then given by the (x, y) -plane in which Q and U will be defined. Let \mathbf{B} be the local value of the GMF. If we denote by γ the angle between \mathbf{B} and the (x, y) -plane, we have the projection $B_{\perp} = |\mathbf{B}| \cos(\gamma)$. Locally, the dust polarization spinor \mathcal{P}_{ν}^d is related to the intensity by

$$\mathcal{P}_{\nu}^d = p_0 \cos^2(\gamma) I_{\nu}^d e^{2i\psi^d}. \quad (6.5)$$

p_0 is called the intrinsic polarization fraction, quantifying how much of the intensity signal is transformed into polarization. It is expressed as $p_0 = p_{\max}RF$ where R is the Rayleigh reduction factor quantifying the efficiency of grain alignment, and F is the depolarization factor related to the change of the GMF orientation within the beam. It is common to consider the observed polarization fraction $p = p_0 \cos^2(\gamma)$, which have values comprised between 0% and 20% according to *Planck* data (Planck Collaboration, 2016b). Due to the dependence in $\cos^2(\gamma)$, the dust polarization signal can be null if the GMF is along the line of sight.

Thermal dust statistics and power-spectra

The best fit of the thermal dust SED parameters (Eq. (6.4)) on intensity data from *Planck* (at 353, 545 et 857 GHz) and IRAS (100 μm) can be found in Fig. 6.7. The values are given over the whole sky, illustrating their possible range of variation (Planck Collaboration, 2014). Denser regions near the Galactic plane are colder, while diffuse regions near the poles are hotter. The spectral index follows the opposite pattern, characteristic of the $\beta_d - T_d$ anti-correlation discussed in the previous section. These maps present an unprecedented characterization of the thermal dust signal up to a scale of 5' and a validation of the MBB model. Several alternatives exist in order to derive maps of the spectral properties of the foreground signal across the sky. They can be recovered as byproducts of component separation methods (see Sec. 6.4) or inferred from dedicated studies as Planck Collaboration (2014), Krachmalnicoff et al. (2016). However one should keep in mind that all these methods are unperfect and include possible bias as (depending on the mission and frequency bands under consideration): 1) the maps can contain a significant amount of instrumental noise which could produce some spurious variability of the spectral parameters 2) other signals could be only partially subtracted from dust as CIB and CMB at high frequencies but also free-free and AME at lower frequency 3) bias can occur due to the fitting method from correlations present in the model itself, not the data (as the $\beta_d - T_d$ correlation). As such, surprises are to be expected for more sensitive missions.

The spectral parameter distribution, presented here for intensity only, is expected to be similar for polarisation, such that the difference between the full sky mean spectral indices between polarization and intensity was estimated to be $\beta_d^P - \beta_d^I = 0.05 \pm 0.03$ in (Planck Collaboration et al., 2020d). However, the spectral properties of the polarized foreground signal remains a significantly uncharted territory.

Alike all the distributions of the ISM properties, the dust signal present highly non homogeneous and highly non-Gaussian features due to the existence of several processes depending on the environment under consideration. Such behavior is caused in general by MHD turbulent coupling between scales, but also by gas condensation through thermal instability in

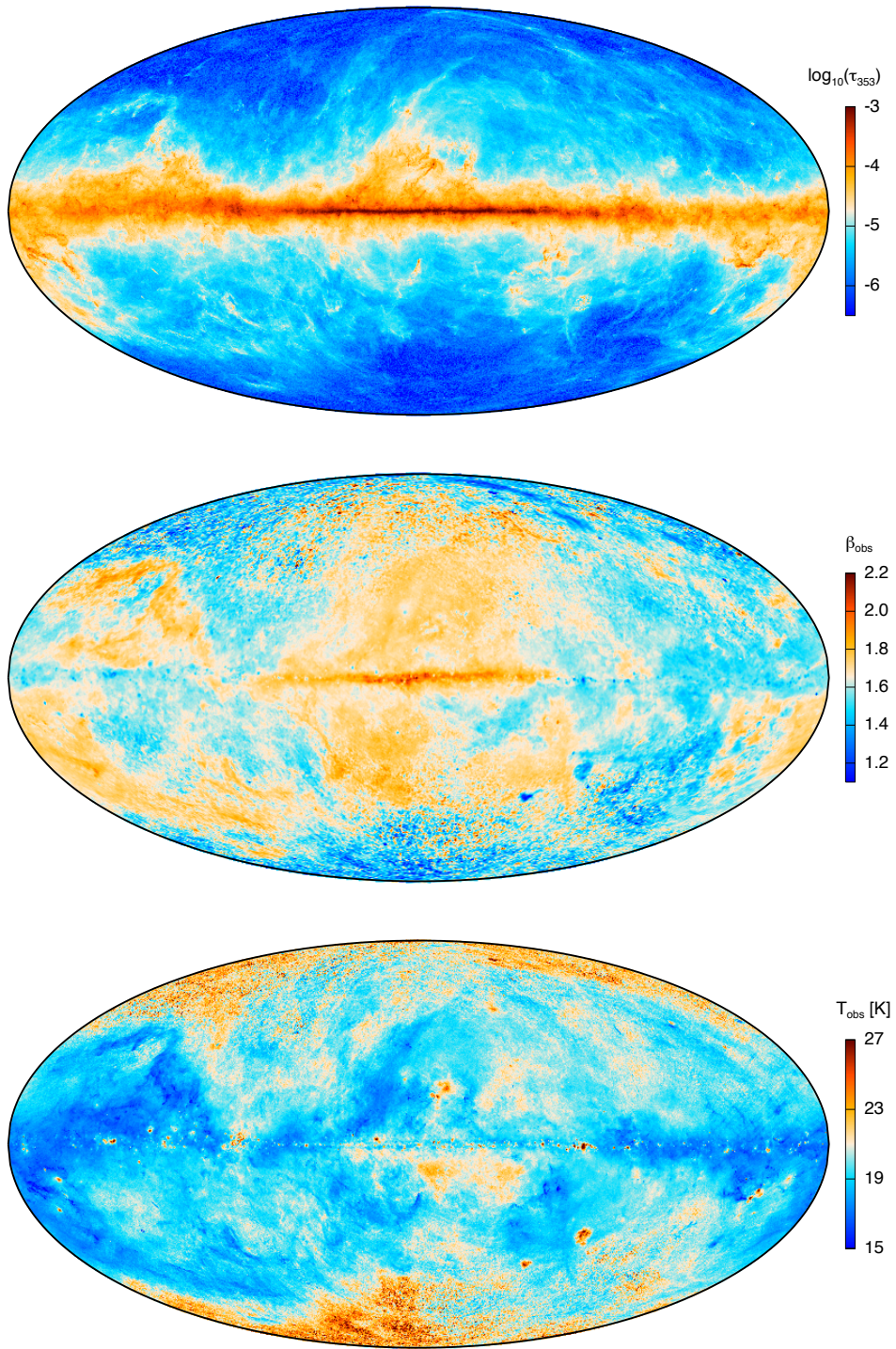


Figure 6.7: All-sky maps of the parameters of a MBB fit on intensity data from *Planck* at 353, 545 et 857 GHz and IRAS 100 μm . Taken from ([Planck Collaboration, 2014](#))

the diffuse ISM, self-gravity in molecular clouds, and stellar feedback in star forming regions ([Draine, 2011](#)). Such non-linear behavior can be clearly seen on the map of the thermal dust opacity (τ_{353}) – tracer of the gas density and structure – which presents volutes and characteristics structures of complex fluid instabilities (as e.g. clouds).

As for synchrotron, the angular power-spectra of polarized dust signal are following a power-law behavior with a gentler slope of $\alpha_d^{XX} = -2.42 \pm 0.02$ ([Planck Collaboration, 2016c](#)). As for synchrotron, the polarized dust signal traces the GMF structure as well as the statistics of the gas column density N_H (while synchrotron was linked to cosmic ray distribution). From *Planck* data, the dust E/B ratio has a surprisingly high value of $\mathcal{D}_\ell^{EE,d}/\mathcal{D}_\ell^{BB,d} \sim 2$ ([Planck Collaboration \(2016c\)](#)). Additionally, a positive $\mathcal{D}_\ell^{TE,d}$ spectrum has been detected, indicating a correlation between the thermal dust intensity and its linear polarization. The dust EB signal remains compatible with zero in *Planck* data ([Planck Collaboration et al., 2020d](#)).

All the above behaviors can be well explained from the geometry of the matter/dust distribution in the ISM, showing linear filamentary structures aligned with the local GMF, also seen in H_I ([Clark & Hensley, 2019](#)). Moreover, numerical models of dust spheroidal filaments reproduce the desired power spectra properties discussed above ([Vansyngel et al., 2017](#); [Huffenberger et al., 2020](#)).

However, these models do not predict accurately the observed $\mathcal{D}_\ell^{TE,d}$ spectrum ([Huffenberger et al., 2020](#)). Moreover, a non zero dust parity violating $\mathcal{D}_\ell^{TB,d}$ spectrum has been observed in Planck data and is equally difficult to retrieve with simple filamentary models.

Supposing some *Magnetic misalignment*, that is a different direction between the GMF and the dust filaments, allows to recover the observed shape of $\mathcal{D}_\ell^{TE,d}$ and predicts the existence of non-zero $\mathcal{D}_\ell^{TB,d}$ and $\mathcal{D}_\ell^{EB,d}$ spectra ([Clark et al., 2021](#); [Cukierman et al., 2023](#)). The latter has never been detected, and understanding it is crucial for component separation in the quest of cosmic birefringence ([Diego-Palazuelos et al., 2023](#)).

6.4 Component separation methods

Now that we are familiar with the physics associated with the various component of the CMB foreground emission, let us review how this emission can be disentangled from the primordial signal. Component separation methods are numerical tools used in order to isolate the CMB signal from the foregrounds using different hypothesis. Different component separation techniques are commonly used, and they are often complementary. They can be roughly divided in the following way:

- **Parametric methods:** Assuming that the spectral dependence of the foreground signals is known, it is possible to model it using parametric models. The parameters can then be fitted in order to capture the foregrounds and remove them from the CMB. To do so, it is common to simply seek for the maximum likelihood of the model. The model building can be done either in the pixels at the map level or in harmonic space on the \mathcal{D}_ℓ , each of them presenting their own advantages and drawbacks. For example, the COMMANDER method uses a Bayesian approach to model the dust signal as a MBB signal and the synchrotron as a power-law at the pixel level using Gibbs sampling ([Eriksen et al., 2008](#)). Similarly FGBUSTER implements a similar modeling in map space, with the possibility to recover the spectral parameters maps of the different components with different resolutions, allowing to minimize the variance of the method ([Stompor et al., 2009](#); [Errard et al., 2011](#)). Along this line, the clustering methods try

to regroup the foreground signal with regions having similar emission properties, in order to ease the component separation (Puglisi et al., 2022). These methods allow to recover astrophysical information about the Galaxy, but the use of too simplistic modeling can have dramatic consequences (while too complex modelings would degrade the accuracy). In this thesis, I will present a new parametric method in harmonic space using the moment expansion for the *LiteBIRD* instrument in Sec. 8.3 and I will further present in Sec. 8.4 a new model of the polarized SED that could be used for parametric methods.

- **Internal linear combinations (ILC)** do not assume a model for the foreground signal. For example the linear combinations focuses only on the knowledge that the CMB signal must be a blackbody in order to subtract all components having a different behavior by minimizing the variance of the recovered CMB. As such, in K_{CMB} units, $s_\nu = c + f_\nu + n_\nu$ where s_ν is the total signal, c the CMB, f_ν the foreground signals and n_ν the instrumental noise. In its simplest form, it consists in finding the weights w_ν in the equation $\hat{c} = c + \sum_\nu w_\nu f_\nu + \sum_\nu w_\nu n_\nu$ and $\sum_\nu w_i = 1$, such that the variance of the recovered CMB estimator $\sigma^2(\hat{c})$ is minimal. This ILC can be done in real space as proposed by the SEVEM method (Fernández-Cobos et al., 2012). Alternatively, one can decompose the signal in the basis of needled space, as proposed by the NILC and GNILC (Remazeilles et al., 2011). Multiple variants of ILC exist, using priors on the dust spectral or spatial complexity in order to optimize the minimization, see e.g. (Rotti & Chluba, 2021).
- **Blind methods** isolate the various component without any model, by assuming that they are statistically independent. This is for example the case of the SMICA method (Cardoso et al., 2008).

As the different approaches are complementary, the *Planck* mission considered four different methods on an equal footing: COMMANDER, NILC, SEVEM, and SMICA (Planck Collaboration et al., 2020e). It is as such very important to encourage the multiplicity of approaches to the component separation problem.

6.5 The PySM models

In order to simulate the foreground emissions on the largest scales, it is common to use the PySM software¹⁴. This software allows to create maps containing the different foreground components over the whole celestial sphere using the HEALPIX software (Górski et al., 2005). These maps represent our best knowledge of the CMB foregrounds over the whole sky after the *Planck* mission. The intensity and polarization models are built at a given resolution and frequency from a reference map, generally built from *Planck* or *WMAP* data, and are extrapolated at any other frequencies using different models of SED. Different models are built from different hypothesis and inject different levels of complexity in order to create optimistic or pessimistic scenarios of the unknown Galactic complexity laying below *Planck*'s sensitivity. Moreover, new models are continuously added to the library, and these models can be used to simulate different CMB missions and confront them to the various component separation methods. We will extensively use this software when we will present new methods

¹⁴<https://github.com/galsci/pysm>

to model the foreground signal in Chap. 8, as a major challenge is to be able to grasp the complexity contained within these models. Let us introduce here some of the foreground templates that were used in the present thesis:

- d_0 is a model of the (I, Q, U) maps of the thermal dust signal over the whole sky. The I map is built from the *Planck* 2015 data at 545 GHz while the (Q, U) maps are built from the same data at 353 GHz ([Planck Collaboration et al., 2016d](#)). Maps at other frequencies are recovered by extrapolating with a single MBB law with constant $\beta_{d0} = 1.54$ and $T_{d0} = 20\text{ K}$ over the whole sky.
- d_1 is built similarly to d_0 , but the extrapolation in frequency is done with a single MBB with a different spectral index and temperature in each pixel (varying spatially). The β_{d1} and T_{d1} maps are the ones recovered on *Planck* data using the COMMANDER code ([Planck Collaboration et al., 2016e](#)).
- d_{10} is a refined version of d_1 , in which the templates of β_{d10} and T_{d10} are based on the GNILC analysis of *Planck* data. Some additional small-scale fluctuations of amplitude, index and temperature have also been introduced.
- d_{12} or "MKD" model, is introducing some 3D complexity of the emission by considering the dust signal as composed of 6 layers of modified black body signal having different amplitude, index and temperature templates ([Martínez-Solaeche et al., 2018](#)).
- s_1 is a synchrotron template at 408 MHz built from the [Remazeilles et al. \(2015\)](#) reprocessed map of [Haslam et al. \(1981\)](#) (presented in Fig. 6.3), as well as the *WMAP* final results at 23 GHz ([Bennett et al., 2013](#)). From it, [Miville-Deschénes et al. \(2008\)](#) extracted a map of spatially varying spectral indices β_{s1} . The template at 23 GHz is thus extrapolated at every frequency with a power-law signal.

Part II

Personal contributions

From the instrument to the fundamental physics through our Galaxy

7

Optimizing the design of the *LiteBIRD* satellite

*De la narine du grand Bouddha
jaillit
une hirondelle*

– Kobayashi Issa, haïku choisi par mon père.

Contents

7.1	The <i>LiteBIRD</i> satellite	95
7.2	The Scanning strategy	100
7.3	From side lobe asymmetry to scanning optimization	101
7.4	Additional personal contribution to the <i>LiteBIRD</i> collaboration	106

In Chap. 5, we discussed the importance of the CMB observation for modern cosmology. I will now present the instrumental characteristics of the *LiteBIRD* mission dedicated to this observation, as well as my contribution to the collaboration. In particular, I will investigate how to optimize the scanning strategy of the instrument such that it suppresses maximally the systematic effects.

7.1 The *LiteBIRD* satellite

The **Lite** (Light) satellite for the study of **B**-mode polarization and **I**nflation from cosmic background **R**adiation **D**etection (*LiteBIRD*) is an international project proposed by the Japanese spatial agency (JAXA), that it selected in May 2019 as a strategic large class mission. The launch is planned for the 2030 decade, for a minimal mission duration of 3 years (LiteBIRD Collaboration et al., 2023).

LiteBIRD is designed to realize a full sky survey of the CMB at large angular scales in order to look for the reionization bump of the primordial *B*-modes and explore the scalar-to-

tensor ratio (r) parameter space with a total uncertainty δr below 10^{-3} , including foreground cleaning and systematic errors. The instrument is composed of three telescopes observing in different frequency intervals: the low-, medium- and high-frequency telescopes (LFT, MFT and HFT). Each of the telescopes illuminates a focal plane composed of hundreds of polarimetric detectors. The whole instrument will be cooled down to 5 K (LiteBIRD Collaboration, 2020) while the focal planes of MFT/HFT will be cooled down to 100 mK (Suzuki et al., 2018). In order to mitigate the instrumental systematic effects, the polarization is modulated by a continuously rotating half-wave plate (HWP). *LiteBIRD* will observe the sky in 15 frequency bands from 40 to 402 GHz. Component separation and systematic control represent the two biggest challenges. While the first point will be discussed in Chap. 8, we will now introduce the second one.

7.1.1 Scientific objectives

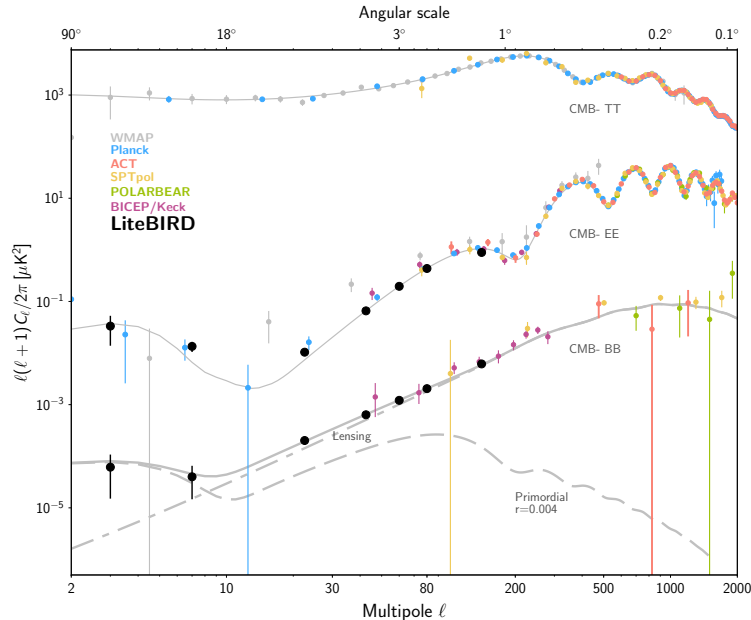


Figure 7.1: Estimation of the measurements of the CMB primordial angular power spectra by *LiteBIRD*, in comparison with other CMB surveys. From LiteBIRD Collaboration et al. (2023).

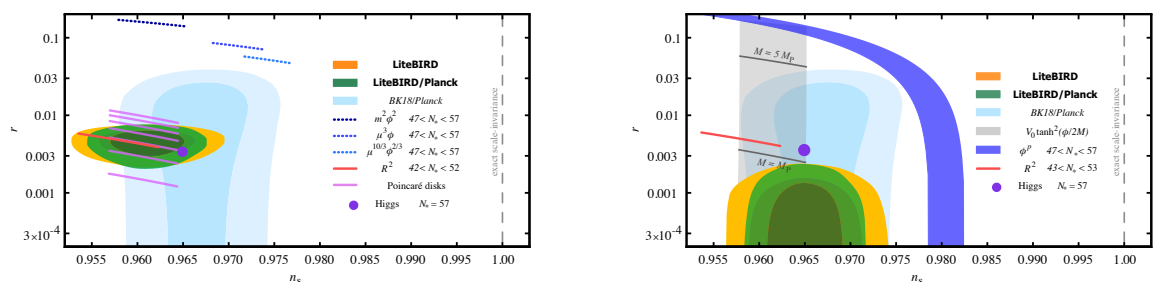


Figure 7.2: Forecasts on the constraining power of *LiteBIRD* on some inflation models in the (r, n_s) space. Left: no detection, Right: Example of a detection of $r = .6 \times 10^{-3}$, taking R^2 -inflation with $N_* = 51$ as a fiducial model. From LiteBIRD Collaboration et al. (2023).

The *LiteBIRD* instrument is designed to measure the CMB polarization on the largest scales

$(\ell < 200)$ with an unprecedented accuracy. The largest scales can indeed only be reached by a satellite experiment which can cover the full sky. Indeed, as depicted on Fig. 7.1, *LiteBIRD* will map the low ℓ primordial angular power spectra in polarization of the CMB, which have only been seen by *WMAP* and *Planck*, but with a sensitivity improved by several orders of magnitudes. From a cosmological point of view, and in regards of our discussion in Chap. 5, two major targets can thus clearly be identified in the low- ℓ polarized spectra: the reionization history and inflation.

LiteBIRD will be able to probe simultaneously the two regions where bumps are expected in the primordial B -modes spectrum: the recombination ($\ell \sim 80$) and reionization ($\ell \leq 10$) bumps, the latter coinciding with the scales for which the lensing signal is minimal. Such a fine characterization of the B -modes, coupled to the E -modes, will then give very strong constraints on the possible amplitude of tensor modes Δ_h^2 , and hence r (see Sec. 5.3.2). As displayed on Fig. 7.2, *LiteBIRD* data, combined with *Planck* data, would drastically reduce the confidence levels in the (r, n_s) parameter space, and thus exclude (or confirm) a large number of inflationary models. The left panel provide the illustration of a detection by *LiteBIRD* for the prediction of R^2 -inflation with $N_* = 51$ (see Sec. 4.3.3). In fact, the *LiteBIRD* collaboration would be able to claim a 5σ detection for $r \simeq 0.01$, while as seen on the right panel, it would set the upper limit of $r < 0.002$ (95% CL) in the absence of primordial B -modes (that is $\sigma(r) = 1 \times 10^{-3}$ including both systematics and component separation).

Moreover, by providing a cosmic-variance-limited measurement of the low ℓ E -mode spectra, *LiteBIRD* would allow to give unprecedented constraints on the reionization history, and hence on z_{reio} (or equivalently, the reionization optical depth τ_{reio}), which is currently the least well constraint parameter of Λ -CDM. Improving our knowledge on reionization would allow to strongly constrain models of the formation of population III stars, and the emergence of the first structures. Combined with ground telescope measurements, the *LiteBIRD* data would provide an almost complete characterization of the polarization information of the CMB, allowing to constrain sharply the 6 Λ -CDM parameters, and fundamental physics parameters as the sum of neutrino masses.

LiteBIRD would also access the EB -correlation signal, and look for the existence of cosmic birefringence in the early Universe, possible signature of the presence of axions (see Sec. 5.3.2). Numerous other cosmological objectives can be thought of, as a refined investigation of the significance of the CMB spatial anomalies, primordial magnetic fields, anisotropic spectral distortions and SZ mapping on large scales. For a complete review, see the discussion in [LiteBIRD Collaboration et al. \(2023\)](#).

Finally, *LiteBIRD* will also map all the other signals in the microwave, and allow a precise characterization of the polarized Galactic emission on large scales. Having 15 frequency bands, *LiteBIRD* will be able to precisely characterize the SED of the foregrounds, which is absolutely critical for component separation, and is also precious for Galactic physics to constrain e.g. dust grain models (see Chap. 6). Furthermore, by accessing polarization, *LiteBIRD* will be able to map the Galactic magnetic field on the largest scales, which represent a first-importance astrophysical information with regard to Galactic dynamics and star formation.

7.1.2 The instrumental design

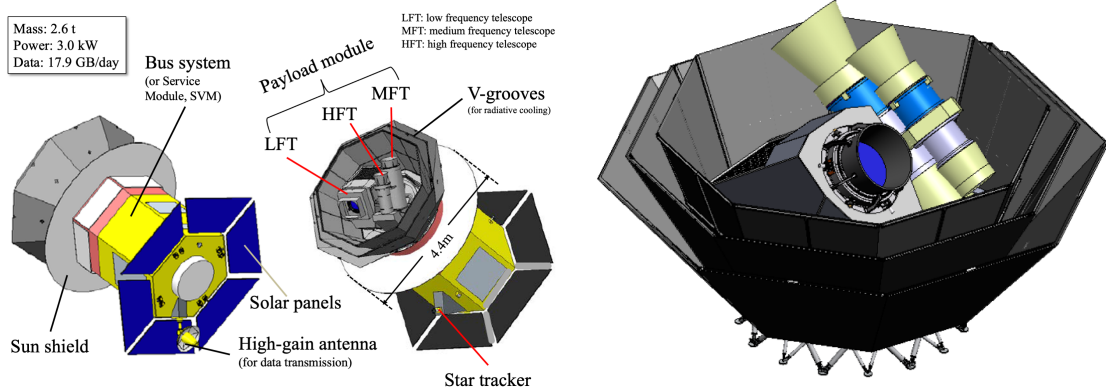


Figure 7.3: Left: Overview of the *LiteBIRD* instrumental design Right: close up view on the PLM. From [LiteBIRD Collaboration et al. \(2023\)](#).

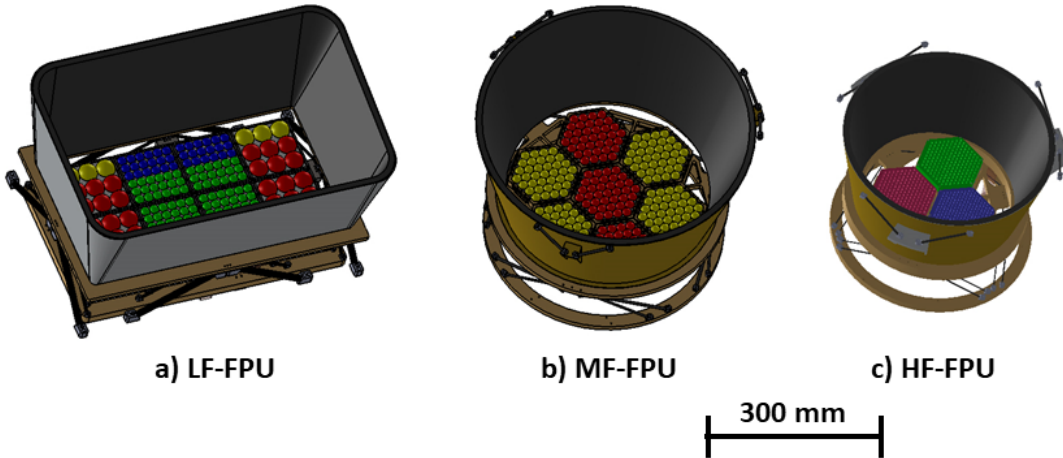


Figure 7.4: Detector positions on the focal planes ([LiteBIRD Collaboration et al., 2023](#)). LFT: red: 40, 60, 78 GHz, orange: 50, 68, 89 GHz, green: 68, 89, 119, blue: 78, 100, 140 GHz. MFT: red: 100, 140, 195 GHz, orange: 119, 166 GHz. HFT: purple: 195, 280 GHz, green: 235, 337 GHz, blue: 402 GHz.

As depicted on the left panel of Fig. 7.3, the *LiteBIRD* satellite is designed with an axisymmetric shape (reducing its moment of inertia). On the top of the spacecraft is located the payload module (PLM) containing the three telescopes: LFT, MFT and HFT. The PLM is itself protected by a Sun-shield blocking Solar radiation coming from the back. On the back of the satellite are some solar panels, powering the spacecraft, and a high gain antenna transmitting data to Earth (for a total of 17.9 Gb per day). The right panel of Fig. 7.3 presents a close-up view of the PLM. The three telescopes are embedded in a structure of V-grooves designed to further cool down and protect the instruments from the Solar radiation. The MFT and the HFT are grouped together (sometimes referred together as the MHFT) while the LFT is pointing towards the opposite direction. The three telescopes are equipped with a rotating HWP modulating the polarization signal and mitigating the systematic effects. A closer view of each focal plane unit (FPU) of the telescopes is given in Fig. 7.4. All of them are populated with hundreds of multichroic polarized transition-edge sensor (TES)

7.1. THE *LiteBIRD* SATELLITE

Telescope	Frequency [GHz]	Sensitivity $\sigma_{Q,U}^{\text{noise}}(\nu)$ [$\mu\text{K}\cdot\text{arcmin}$]	θ_{FWHM} arcmin
LFT	40.0	37.42	70.5
LFT	50.0	33.46	58.5
LFT	60.0	21.31	51.1
LFT	68.0	19.91/31.77	41.6/47.1
LFT	78.0	15.55/19.13	36.9/43.8
LFT	89.0	12.28/28.77	33.0/41.5
LFT/MFT	100.0	10.34/8.48	30.2/37.8
LFT/MFT	119.0	7.69/5.70	26.3/33.6
LFT/MFT	140.0	7.25/6.38	23.7/30.8
MFT	166.0	5.57	28.9
MFT/HFT	195.0	7.05/10.50	28.0/28.6
HFT	235.0	10.79	24.7
HFT	280.0	13.8	22.5
HFT	337.0	21.95	20.9
HFT	402.0	47.45	17.9

Table 7.1: Instrumental characteristics of *LiteBIRD* ([LiteBIRD Collaboration et al., 2023](#)). Some frequency bands are shared by two different telescopes or detector arrays. If so, the two values of polarization sensitivities $\sigma_{Q,U}^{\text{noise}}(\nu)$ and instrumental beam full width at half maximum θ_{FWHM} are displayed on the same line.

detectors, able to observe from one to three bands per pixel ([Hubmayr et al., 2022](#)). All the detectors are expected to collect data with a sampling rate of $f_s = 19\text{ Hz}$. The LFT is a reflective telescope with a large field of view of $18^\circ \times 9^\circ$. All its detectors are observing in three frequency bands and are arranged in a rectangular configuration, itself composed of multiple rectangular wafers (colored on the figure) observing at different frequency trios. On the other hand, the MHFT instruments are refractive telescopes with a circular field of view of 28° diameter. Both FPUs are composed of hexagonal wafers. The MFT is made of 7 wafers, organized in an overall hexagonal shape and sharing two different frequency configurations. It is sharing its lower and higher frequency bands with the LFT and the HFT respectively. The HFT is built of 3 wafers, organized in a triangular shape, each observing in a unique frequency configuration.

The frequency bands of the whole instrument, with associated polarization sensitivities $\sigma_{Q,U}^{\text{noise}}(\nu)$, and full width at half maximum θ_{FWHM} , can be found in Tab. 7.1. If two frequency bands are overlapping, I have computed the effective sensitivity, by taking the average weighted by the FWHM as

$$\sigma_{Q,U}^{\text{noise}}(\nu_{\text{overlapping}}) = \sqrt{\frac{1}{\left(\frac{\theta_{\min}}{\theta_{\max}}\sigma_{Q,U}^{\text{noise}}(\nu_{\theta_{\min}})\right)^{-2} + \left(\sigma_{Q,U}^{\text{noise}}(\nu_{\theta_{\max}})\right)^{-2}}}, \quad (7.1)$$

with θ_{\min} and θ_{\max} respectively the minimal and maximal FWHM observing in the overlapping frequency band.

7.2 The Scanning strategy

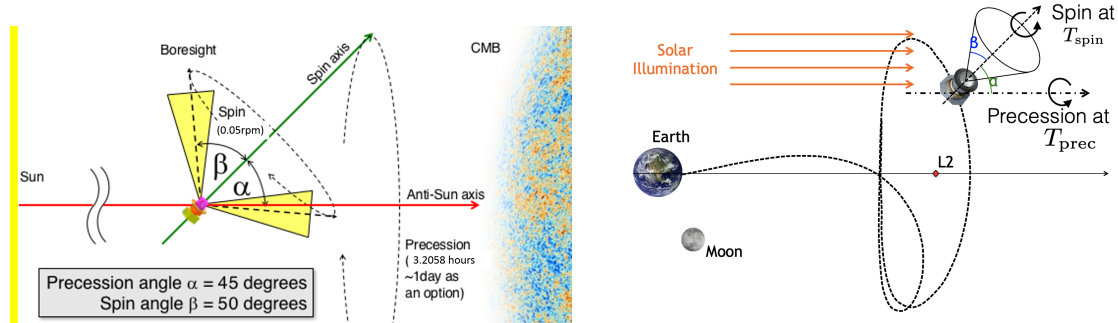


Figure 7.5: Left: Definition of scanning strategy parameters for the *LiteBIRD* mission (LiteBIRD Collaboration et al., 2023). Right: Definition of a general scanning strategy located around L2 (Wallis et al., 2017).

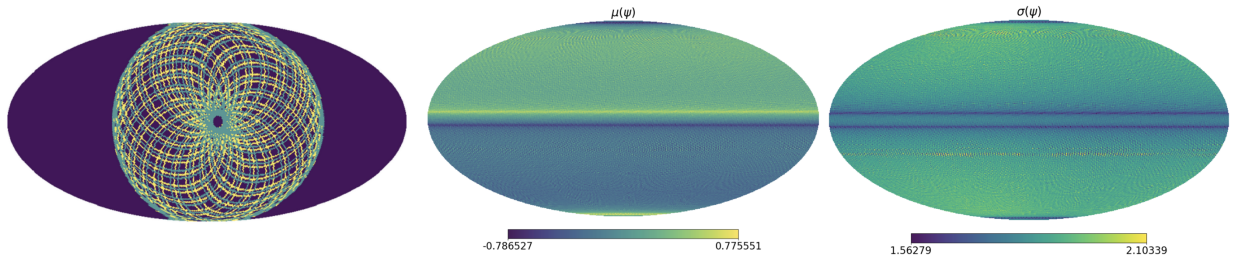


Figure 7.6: Left: scanning of the *LiteBIRD* LFT (blue) and MHFT (yellow) boresights projected on the Mollweide view in ecliptic coordinates, for a duration of 10 hours. Center and Right: mean $\mu(\psi)$ and standard deviation $\sigma(\psi)$ of the crossing-angle ψ , in radian, evaluated in every pixel for a mission duration of 1 year, in ecliptic coordinates.

The *LiteBIRD* satellite will be orbiting around the L2 Lagrange point of the Sun-Earth gravitational system¹, located behind Earth, on the Sun-Earth axis. As illustrated on Fig. 7.5, while orbiting around L2, the satellite will also rotate on himself over two different axis. First, it will spontaneously rotate around its axis of maximal inertia or *spin axis*. The angle between this axis and the center of the boresight(s) is called β . Additionally, the spin axis is precessing around the Earth-Sun axis. The angle between the spin and the precession axis is called α . To avoid Solar radiation and allow for a scanning of the whole sky during the mission duration, the sum of the angles must satisfy $\alpha + \beta > 90^\circ$. In the case of *LiteBIRD*, $\alpha = 45^\circ$ and $\beta = 50^\circ$. The associated period of rotation around the spin-axis and precessions are noted T_β and T_α . For *LiteBIRD*, $T_\alpha = 3.2058$ hours and $T_\beta = 20$ minutes. It is possible to simulate the scanning strategy associated to each detectors using either the TOAST² or LITEBIRD-SIM³ softwares. As an illustration, on the left side of Fig. 7.6, I have computed the scanning strategy of the center of the boresight of the LFT (blue) and MHFT (yellow) for a 10 hours using LITEBIRD-SIM. The Mollweide view is centered on the starting point

¹Equilibrium point where the gravitational fields of the Earth and the Sun are compensating each other.

²<https://github.com/hpc4cmb/toast>

³https://github.com/litebird/litebird_sim

of the scanning in the ecliptic plane (and thus using ecliptic coordinates). The scanning thus describes characteristic "flower-like" patterns. When time passes this pattern is shifted gradually until the whole sphere is covered. Let us now introduce the crossing angle or impacting angle ψ in every pixel, as the angle made between the meridian of the celestial sphere and the scanning direction. Because of the characteristic pattern of the scanning strategy, the sky will not be uniformly scanned and the ecliptic equator and poles will be visited more regularly and with a more homogeneous ψ distribution than the intermediate (ecliptic) latitudes. This is further illustrated on the center and right panels of Fig. 7.6, on which I plotted the mean and standard deviation of ψ in every pixels (respectively $\mu(\psi)$ and $\sigma(\psi)$) for one year of scanning by the *LiteBIRD* instrument. While the scanning is highly symmetric with respect to the ecliptic longitude, It changes widely depending on the ecliptic latitude. A natural question thus arises: does this ψ distribution have a significant impact on the B -mode measurements by *LiteBIRD* and how to quantify it?

7.3 From side lobe asymmetry to scanning optimization

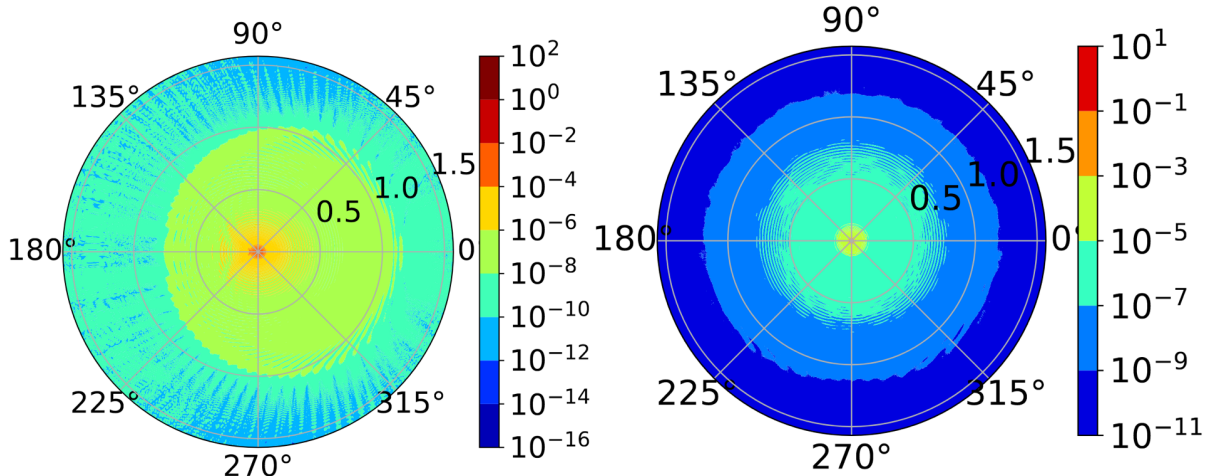


Figure 7.7: Left: Instrumental beam B^{or} on the half sphere for a detector at 100 GHz, located on the edge of the MFT. Right: Effective beam B^{eff} computed from B^{or} with the scanning strategy for one year in a pixel associated to the ecliptic latitude $\theta_{\text{lat}} = 40^\circ$.

A uniform a scanning can be associated with the suppression of numerous systematic effects. For example, as we will discuss, the distribution of the crossing angles can compensate for intrinsic asymmetries of the so-called instrumental beam. On the other hand, if the scanning is not perfectly homogeneous, it will be critical to evaluate the impact of the leftover asymmetries on the measurement of r .

One can associate an instrumental beam to each pixel present on the FPU. This beam quantifies the instrumental response of the detector depending on the direction of the incoming signal on the sky. While detectors are associated with one or several centered frequency bands ν_0 , the beam shape can also depend of the exact frequency ν of the signal around ν_0 , which is called the *bandpass effect*. Additional subtleties exist for polarization, which I will

not discuss here, assuming an identical beam for Q and U . The central and most sensitive part of the beam is called *main beam* (and is often modeled as a Gaussian for simplification). The outer part of the beam are called the near and far side lobes. The beam shape can be asymmetric. This is even more true for detectors located on the edge of the FPU wafers. On the left panel of Fig. 7.7, I have plotted the projection on the half sphere of the beam associated to a detector on the edge of the MFT observing at 100 GHz and used in [LiteBIRD Collaboration et al. \(2023\)](#). Roughly speaking, the main beam is in red, while the side lobes represent the remaining large scale regions in orange, green and blue. One can see, that for this detector, the beam is intrinsically asymmetric and displays complex patterns at all scales. While the instrument is scanning the sky, the beam of each pixel will be dragged along the trajectories depicted in Fig. 7.6. Over the three years of observation planned for the *LiteBIRD* mission, one has to consider the so-called effective beam in every pixel B^{eff} , defined as $B^{\text{eff}} = \sum_i \mathcal{R}(\psi_i) B^{\text{or}}$ where B^{or} is the original beam, \mathcal{R} is a rotation matrix and i ranges over all the *hits*, i.e. the occurrence of the scanning in the pixel. The asymmetry of the original beam will hence be smoothed and symmetrized by the scanning strategy. The more homogeneous is the ψ distribution in each pixel, the better is this symmetrization process. On the right panel of Fig. 7.7, I computed the effective beam resulting from the original beam on the left, for a pixel located at the ecliptic latitude of $\theta^{\text{lat}} = 40^\circ$. While this smoothing is imperfect, one can witness that the beam has been strongly symmetrized.

A major question remaining to be answered regarding the *LiteBIRD* instrument, is whether or not the residual asymmetry of the effective beams will impact the B -modes measurement, and what requirements can be set on the scanning strategy and the instrumental beams in order to minimize this impact. For the past three years, I tried to address this question within the "*LiteBIRD* asymmetry working group" in tight collaboration with Yusuke Takase, Yuya Nagano and Hirokazu Ishino (Okayama University), Guillaume Patanchon (APC), Ludovic Montier and Jonathan Aumont.

From our previous discussion, one expects that this symmetrization will differ depending on the ecliptic latitude considered. To further illustrate this, I have created an artificial Gaussian elliptic beam⁴ with an eccentricity of $a/b = 2$ and an orientation of $\zeta_0 = 45^\circ$ with respect to the scanning direction, displayed on the left side of Fig. 7.8. Considering the effective beam at the ecliptic pole ($\theta = 90^\circ$), one obtains a very symmetric result (up right of Fig. 7.8). Looking at the ψ distribution in this pixel using a "peacock" diagram, it can be seen that this distribution, while having some gaps, is very symmetric, such that every crossing of the pixel with an angle ψ can be compensated by another one with $-\psi$. Doing the same procedure at intermediate latitude ($\theta = 30^\circ$), one finds that the effective beam remains significantly elliptical. Looking at the ψ distribution, one can witness a gap on the bottom that is not compensated, such that the asymmetry of the beam can not be smoothed.

A direct assessment of the impact of r of this asymmetry is very difficult. Firstly, one needs to develop the appropriate conceptual tools to quantify simply the level of asymmetry of the original and the symmetrized far side lobes. After a significant amount of trial and errors, Ludovic Montier and I suggested to use a decomposition in spherical harmonics (See Appendix B), in order to add large scale perturbations to a Gaussian main beam. As such, it

⁴Simply given by a python array representing a 2 dimensional Gaussian curve normalized to 1.

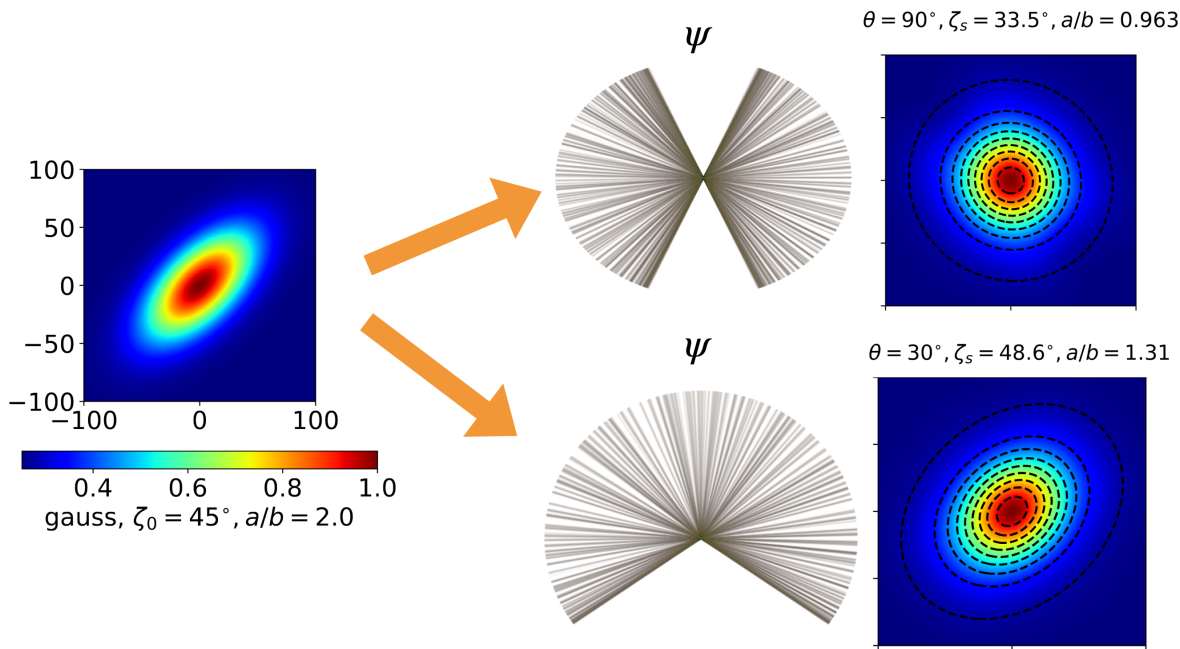


Figure 7.8: Symmetrization of an elliptic Gaussian beam B^{or} (left) by the scanning strategy of *LiteBIRD* at two different ecliptic latitudes: B^{eff} at $\theta = 90^\circ$ (up-right) and B^{eff} at $\theta = 30^\circ$ (bottom-right). The grey lines circular histograms associated to each symmetrized beam ("peacock" diagrams) represent the distribution of the crossing angles ψ in each pixel. ζ , a , b are respectively the orientation, semi-major and semi-minor axis of the beams.

becomes possible to isolate the impact of e.g. dipolar and quadrupolar asymmetries associated with different amplitudes and orientations. As this decomposition and the convolution process are linear, one would simply require to perform the convolution of the whole sky once for perturbations associated with each (ℓ, m) pair and perform linear combinations to study general cases (which still represent a significant amount of parameters to optimize). However, applying these considerations required two tools that were not available at the time of my thesis: polarization beam for the *LiteBIRD* instrument and a software allowing to convolve the sky for polarization signal. Such a tool would moreover have to be able to do so in a minimal time duration, as the tests have to be repeated a significant amount of times in order to explore the consequences on r associated with different amount of asymmetry. So far, doing so even in intensity would be extremely demanding in term of computational hours⁵.

To simplify the analysis, we wondered if the scanning strategy itself could be optimized in order to maximally symmetrize the beams across the whole sky. In collaboration with Ludovic Montier, I implemented several tests in order to quantify this symmetrization power as the Kolmogor-Smirnov test on the ψ -distribution, the harmonic beam smoothing power and the hit-matrix determinant. A brief presentation of these tools is given in Appendix C.

⁵So far, beams for the *LiteBIRD* instrument are created using the ray-tracing GRASP software (<https://www.ticra.com/software/grasp/>). A unique 4π beam can then be associated with every single detector of the instrument. Then convolution is made in each pixel visited by the scanning strategy using the LIBCONVIQT software (Prézeau & Reinecke, 2010).

I also studied extensively how these different indicators could change depending on the mission duration, the scale on the sky considered and the values of α and β . I supervised the internship of Neven Gentil, who helped me running and writing some heavy convolution and scanning codes for these preliminary studies. In the meanwhile, I found that, in the standard configuration of *LiteBIRD*, part of a wafer of the HFT could not reach the ecliptic poles, which could have dramatic consequences as this wafer was associated to a pair of unique frequency band (235 and 337 GHz) for the HFT (See the example of a HFT detector's heatmap on Fig. 7.9 and the discussion in Appendix C.2). A similar problem also exists for the MFT but its impact on data analysis is expected to be smaller as the distribution of the frequency bands of the MFT display more redundancy among its detectors (see an example on Fig. 7.4). I proposed to mitigate this impact by changing the orientation of the focal planes with respect to the direction of scanning. These orientations were never optimized before and chosen arbitrarily. Yusuke provided an analytical estimator of the induced biased δr such that we could properly optimize together the orientation of the focal planes of the MFT and the HFT using several considerations. The optimized choice is presented on the right panel of Fig. 7.9. The black dashed line represents the limit above which the detectors will be penalized by not reaching the ecliptic poles with the canonical choice of scanning parameters ($\alpha = 45^\circ$ and $\beta = 50^\circ$). Besides Δr , this choice can be justified partly from symmetry considerations: all the frequency bands are minimally impacted and the highest frequency band of the HFT (402 GHz) – crucial for component separation and carried by a single wafer – is set to cover the whole sky. The MFT is oriented such that the frequency coverage is as homogeneous as possible in each pixel⁶. This new configuration we proposed was taken into account and implemented in the latest version of the instrument model (IMO). I also runned a study for [LiteBIRD Collaboration et al. \(2023\)](#), in which I checked that the latitude dependence of the effective beam could be neglected under the assumptions made for this analysis.

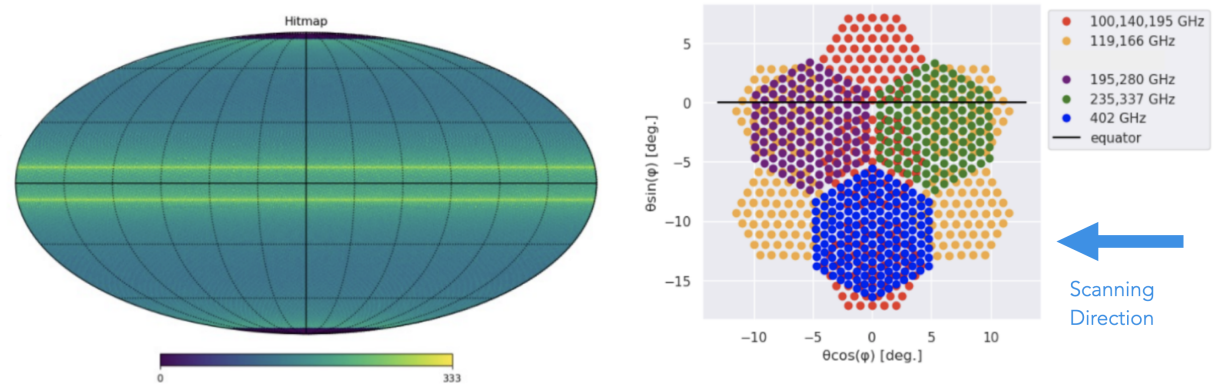


Figure 7.9: Left: Hitmap in ecliptic coordinates of a detector located on the edge of the HFT wafer #1 (235,337 GHz) before optimizing the focal plane orientations. Right: Optimized orientation of the focal planes of the MHFT. Courtesy of Yusuke Takase.

Finally, I was invited by Hirokazu Ishino to visit Okayama University for one month, funded

⁶For example, consider rotating the whole MFT by 90° compared to the choice proposed in Fig. 7.9. In this situation, the red wafers will always scan the center of the pixels, while the yellow ones would only scan the edges of the pixel.

by the H2020-RISE grant. We took this opportunity to further develop and test their independent scanning and convolution codes in Julia, respectively Falcons⁷ and Condor⁸. We decided to use these codes in order to provide an extensive study and justification of the *LiteBIRD* scanning strategy, and a future study of the impact of asymmetric polarized convolution. In our work on the scanning strategy, of which I am the co-leader, we are using different observable to fully explore the scanning parameter space, including the HWP effect (Takase et al., 2023). Considering that the HWP is modulating the polarized signal with an angle ϕ and a period T_ϕ , the full parameter space is given by $\{\alpha, \beta, T_\alpha, T_\beta, T_\phi, f_s\}$, where α, β T_α and T_β are defined in Sec. 7.1.2 and the sampling rate f_s was introduced in Sec. 7.2. The dimensionality of this parameter space can be drastically reduced using constraint equations, such that it depends only on the pair (α, T_α) . Inspired by Wallis et al. (2017), we choose to consider the mean value of the so called *cross-links* as an indicator of the symmetrizing power of the scanning strategy. Including the effect of the HWP, the cross-links $h_{n,m}$ can be defined in each pixel as

$$h_{n,m} = \left| \frac{1}{N_{\text{hits}}} \sum_i^{N_{\text{hits}}} e^{-i(n\psi_i + m\phi_i)} \right|, \quad (7.2)$$

where m and n are spin integer numbers associated respectively to the impact of the HWP and the crossing angles. From Eq. 7.2, one can understand how cross-links provide a good indicator of the smoothing power. Indeed, for $(n, m) = (1, 0)$, two ψ oriented in opposite directions the sum of complex phases $e^{-i\psi}$ will tend to cancel each others, such that $h_{0,1} \rightarrow 0$ for the top right peacock diagram of Fig. 7.8, and not for the bottom one. As such, they allow to condense the information on the homeogeneity of the ψ distribution in the $h_{0,1}$ coefficient. Moreover, it can be shown that multiple systematic effects can be related to specific values of (n, m) . For example, the intensity signal is characterized by $n = 1$, while polarized signal is associated with $n = 2$. On the other hand $m = 0$ evaluates all systematics without the HWP's impact, while the dominant contribution of the HWP modulation is associated with $m = \pm 4$. The intensity of the pointing offset systematic is proportional to the odd spin- (n, m) , with $(\pm 1, 0)$ being the dominant one, followed by $(\pm 1, \pm 4)$, $(\pm 3, \pm 4)$. On the other hand, the effect of temperature to polarization leakage can be modeled solely in term of $(\pm 2, \pm 4)$ and $(\pm 4, \pm 8)$. Finally, a smaller value of $h_{n,m}$ will ease the map-making procedure by making the hit-matrix easily invertible (See Appendix C.2). Finding a configuration minimizing the $h_{n,m}$ for the most relevant (n, m) pairs hence provides an optimization of the scanning strategy. As an example, the mean cross-link maps are displayed on Fig. 7.10 in the (T_α, α) space for specific (n, m) values. The standard *LiteBIRD* configuration (black dot) provides a reasonable trade-off between all the panels, while lower values of T_α and larger values of α (bottom right) seems to be favored. Other criteria also have to be taken into account, especially regarding null-tests, as visit and revisit time of each pixels, allowing to split the datasets in multiple independent sub-datasets, as half-missions, in order to identify and remove systematic effects and observational time for in-flight calibration⁹ on planets, compact sources and the CMB dipole. As an example, the total visible time on planets and the Crab Nebula (all located in the ecliptic plane) is represented on Fig. 7.11 in the (T_α, α) space for the 3 year of the mission duration. This quantity peaks around $\alpha \sim 47.5^\circ$, favoring

⁷<https://github.com/yusuke-takase/Falcons.jl>

⁸<https://github.com/yusuke-takase/Condor.jl>

⁹In-flight calibration is required to estimate the absolute gain, pointing, beam shape, and polarization angle during the mission duration.

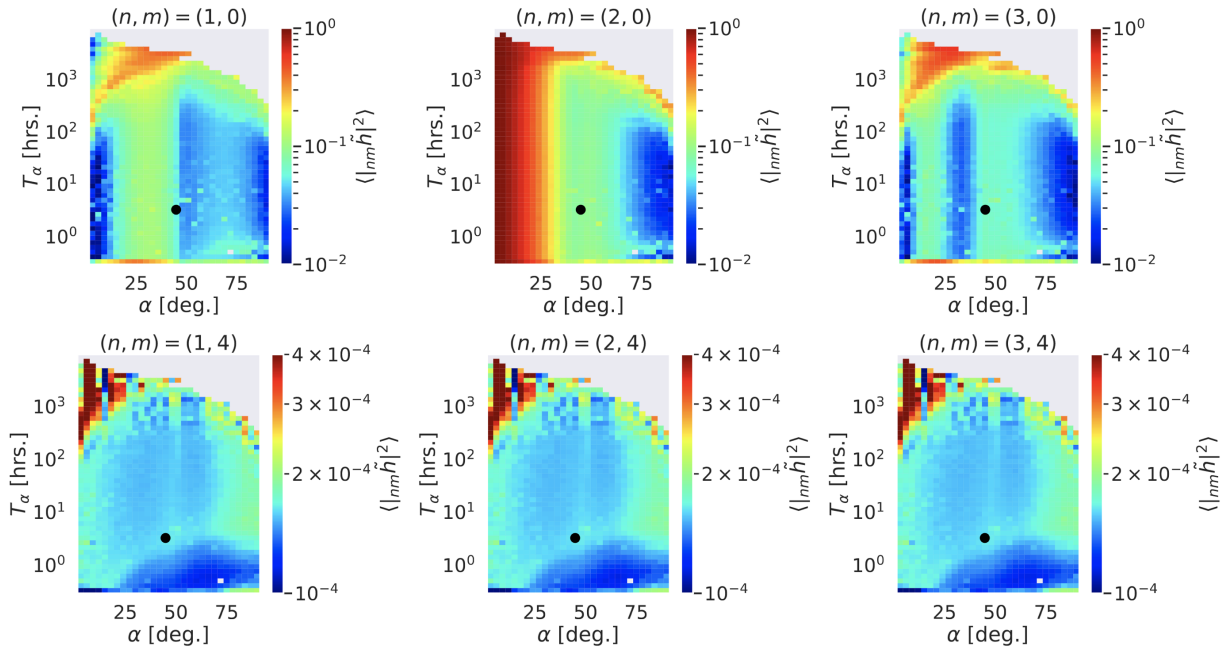


Figure 7.10: Mean value of the cross-link module squared $\langle |h_{n,m}|^2 \rangle$ in the (T_α, α) space for specific values of n and m . The black point represent the standard *LiteBIRD* configuration. Preliminary results from [Takase et al. \(2023\)](#).

a value of $45^\circ \leq \alpha \leq 50^\circ$. While multiple trade-off have to be considered, the standard *LiteBIRD* configuration choice ($\alpha = 45^\circ$) can be justified considering heat input, solar panel efficiency, moon shadow effects and volume allowed for the telescopes. Similar consideration have to be taken into account jointly with the crosslink maps in order to fully optimize the periods T_α and T_β . For example, if the periods are too small (fast rotations), the satellite's angular momentum becomes to high and impact the altitude control and the scanning occurs too quickly in each pixel to let enough time for the HWP to modulate properly the polarized signal. On the other hand, larger periods tend to degrade the cross-links and the calibration time on the CMB dipole. Considering the synergy of multiple observable, as well as technical constraints from instrumental considerations, we thus managed to justify the choice of the current *LiteBIRD* configuration and propose other relevant alternatives in [Takase et al. \(2023\)](#).

7.4 Additional personal contribution to the *LiteBIRD* collaboration

As a member of the systematic joint study group of *LiteBIRD*, I was involved in multiple collaborative discussions and could provide help on studies independent from my main focus. For example, as a daily user of the instrumental configuration files and beam models, I could provide feedback to the modeling and simulation teams. With Yusuke Takase, we found an error in the implementation of the detector position. A factor of two was present in their coordinates, such that the focal planes and the field of views were twice as large as intended. Giuseppe Puglisi (Catania University) corrected this error in the configuration files, such that

7.4. ADDITIONAL PERSONAL CONTRIBUTION TO THE *LITEBIRD* COLLABORATION

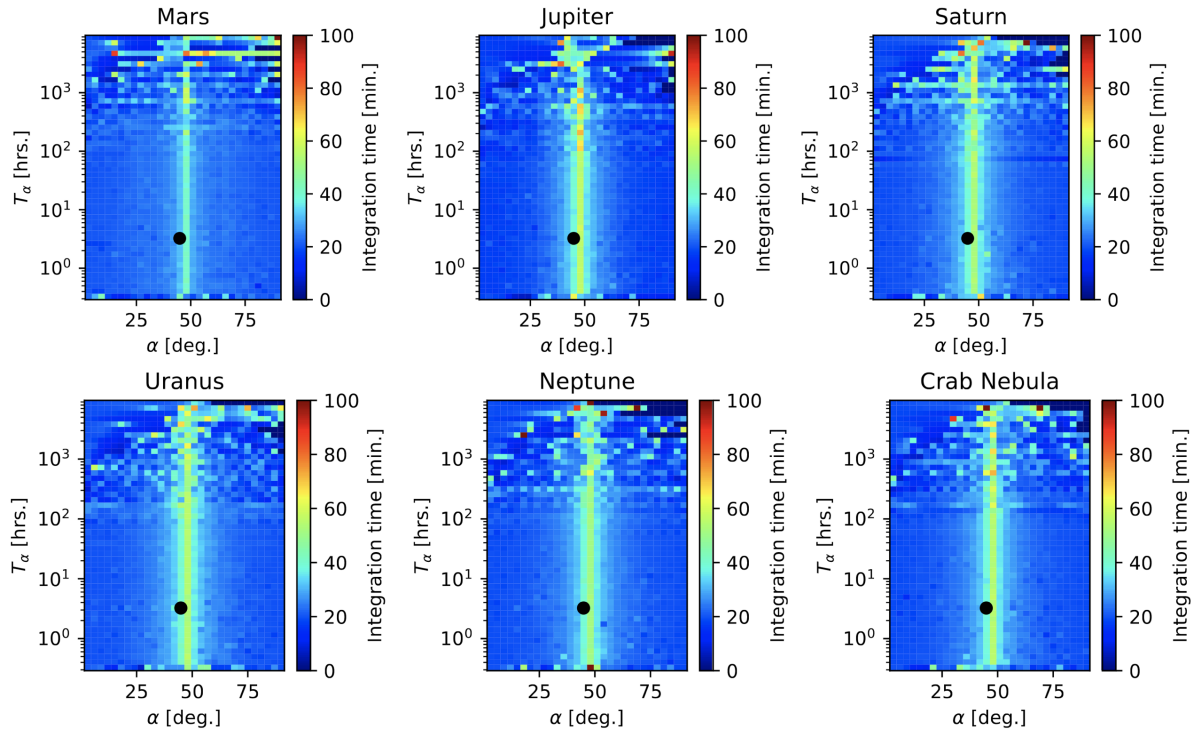


Figure 7.11: Integrated visible time for the 3 year mission on compact sources in the (T_α, α) space. The black point represent the standard *LiteBIRD* configuration. Preliminary results from [Takase et al. \(2023\)](#).

Yusuke Takase, Wang Wang (APC) and myself could re-runned the TOAST convolution codes on the NERSC cluster to produce the final outputs maps that were presented in [LiteBIRD Collaboration et al. \(2023\)](#). These maps were re-used in several studies that I co-authored as [Vielva et al. \(2022\)](#) and [Krachmalnicoff et al. \(2022\)](#).

I also had the chance to participate to some discussions about the influence of Solar and Lunar radiations on the satellite's observation, originally driven by the IRAP team made of Ludovic Montier, Baptiste Mot, Jonathan Aumont and Louise Mousset.

Additionally, I was strongly involved in the foreground joint study group and the Galactic science project study, as I will further discuss in the dedicated Chap. 8.

The *LiteBIRD* mission is an ambitious project supported by a large collaboration. As a junior member of this group, I had the chance to contribute on different aspect of the mission, providing feedback and cross-checks for the key [LiteBIRD Collaboration et al. \(2023\)](#) paper, on which numerous studies rely today. Additionally, I was strongly focused on studying the impact of an inhomogeneous scanning strategy. Thanks to our work, the orientation of the focal planes, which were never considered before, have been fixed and optimized and the current configuration for the scanning strategy used by the collaboration has been properly investigated and justified.

8

Towards an accurate modeling of the spectral and spatial properties of complex foreground polarized light

A moment

*I don't know if this is true to you but for me
sometimes it gets so bad
that anything else
say like
looking at a bird on an overhead
power line
seems as great as a Beethoven
symphony.
then you forget it and you're back
again.*

– Charles Bukowski

Contents

8.1	Spatially varying spectral parameters and the problem of SED distortions	110
8.2	Beyond canonical SEDs: Moment expansion for intensity signal	112
8.3	Applying moment for component separation: application to <i>LiteBIRD</i>	117
8.4	Generalization to polarization: Spin-moments expansion	124
8.5	Applying the spin-moments at the <i>E</i> - and <i>B</i> -modes level	132
8.6	Beyond Gaussianity: The Wavelets	138

In Chap. 6, we discussed the rich physics at the origin of the interstellar medium (ISM) signal and its strong impact on the CMB science. In this chapter, I will detail the origin

of the spectral and spatial complexity of this signal and the progress made during this thesis to better understand and model this complexity. In particular, I will develop a new parametric component separation method using the so-called moment expansion at the cross-frequency angular power spectra level and apply it to *LiteBIRD* in Sec. 8.3. I will then present the first generalization of the moment expansion at the (Q, U) level in Sec. 8.4 and propagate it to the E - and B -modes in Sec. 8.5. These last developments will allow me to derive and quantify new consequences of the spatial variation of the foreground properties in polarization. Finally, we will discuss spatial complexity of the foreground signal and how to model it in Sec. 8.6.

8.1 Spatially varying spectral parameters and the problem of SED distortions

The local physical conditions and the orientation of the galactic magnetic field (GMF) are changing in 3D within the ISM across the Galaxy. This fact is supported both from theoretical considerations and observations. It can be verified locally at the scale of filaments (see e.g. [Ysard et al. \(2013\)](#)) and globally at the scale of the whole Milky-way (see e.g. [Ysard et al. \(2015\)](#); [Planck Collaboration \(2017\)](#); [Jaffe et al. \(2013\)](#); [Ferrière \(2001\)](#); [Schlafly et al. \(2016\)](#); [Planck Collaboration \(2018\)](#)). Such variations can also be witnessed in other galaxies as M82 (see e.g. [Hutton et al. \(2015\)](#)).

The physical conditions witnessed by free charged particles or dust grains will hence depend on their location within our Galaxy. As a consequence, the spectral parameters and polarization angles that can be associated with their polarized signal will accordingly vary from one emission point to another, in 3D. From this fact, one is forced to conclude that every astrophysical observation will have to be understood as resulting of the sum/average of different emission points associated with different emission properties. I will now refer to this averaging process as *mixing* (or *polarized mixing* for the specific case of polarized signal). Mixing can occur:

- **Along the line of sight (LOS)** in the third dimension/depth of the sky. Even in the case of an ideal "pencil beam" associated to the instrument, this averaging is absolutely unavoidable.
- **Inside the instrumental beam** or a **sky-pixel**, both understood as bundles of LOS over the plane of the sky (POS). From an instrumental and data analysis perspective, it is indeed impossible to work with maps having an infinite resolution, this average will hence always be present at some level, being entangled with averages along the LOS.
- **Over large sky regions** of the celestial sphere, when the analysis is done in harmonic space using $a_{\ell m}$ and \mathcal{D}_{ℓ} . The smaller ℓ is, the larger the sky regions one averages over, and the stronger the consequences of mixing are expected to be¹.

¹This would also be true in the map domain if the analysis is done over large pixels. Fitting a modified blackbody in each pixels of the sky at high resolution would significantly reduce the impact of mixing but would not be a viable option for component separation, as it would degrade too strongly the accuracy at which the CMB signal can be recovered due to the tremendous number of free parameters required.

8.1. SPATIALLY VARYING SPECTRAL PARAMETERS AND THE PROBLEM OF SED DISTORTIONS

Let us now refer to the local SED of the ISM signal (e.g. MBB for dust and power law for synchrotron) as the *canonical SED*. The spatial variation of the spectral parameters will have several consequences, that must imperatively be modeled in order to understand properly the foreground signals. We will explore each of them in great depth in the present chapter. They are all interdependent and can be listed as follows:

- **SED distortions:** Because SEDs are nonlinear, the I, Q, U, E and B signals coming from a sky region do not behave as the canonical SED anymore, as resulting unavoidably from the mixing of different (non-linear) SEDs (Chluba et al., 2017; Vacher et al., 2023b). The total SED is thus said to be *distorted*². For example, even if the dust was perfectly described in every point of 3D galaxy by a MBB, the average signal will not be a MBB anymore as e.g. the temperature changes from hotter to colder regions. As mentioned in Chap. 6, SED distortions can also arise from the coexistence of different grain population distributions e.g. with different size or composition. Each grain size would then have a different equilibrium temperature and/or spectral index which will cause distortions locally, even for an infinitesimal element of volume³.
- **Frequency decorrelation:** Because of the spatial variations of the SED, it is not possible anymore to infer the signal of a map \mathcal{M}_{ν_2} at a frequency ν_2 from the signal of a map \mathcal{M}_{ν_1} at frequency ν_1 by using a constant scaling k ($\mathcal{M}_{\nu_1} \neq k\mathcal{M}_{\nu_2}$)⁴. Two frequency bands loose their correlation as the frequency difference increases and the cross-frequency power spectra $\mathcal{D}_\ell(\mathcal{M}_{\nu_1} \times \mathcal{M}_{\nu_2}) := \mathcal{D}_\ell(\nu_1 \times \nu_2)$ will consequently loose its power (Planck Collaboration, 2016c).
- **Polarization angle rotation:** If (and only if) the GMF orientation is varying along with the values of the spectral parameters, U and Q will not only have distorted SEDs but their SEDs will be different. In this case, the polarization angle $\psi \propto U/Q$ (Eq. B.15) becomes a frequency dependent quantity, and \mathcal{P}_ν rotates in the complex plane with frequency (Tassis & Pavlidou, 2015; Planck Collaboration, 2017; Pelgrims et al., 2021; Vacher et al., 2023b).
- **E - B rotation:** Similarly, if (and only if) the GMF orientation is varying along with the values of the spectral parameters, E and B will have different SEDs, such that, at the power spectra level $EE_\nu \neq BB_\nu \neq EB_\nu$. Thus, the E to B ratio EE/BB becomes a frequency dependent quantity (Vacher et al., 2023a).

From an astrophysical perspective, these consequences are welcome, as looking for them could allow to probe variations of the physical properties across the Galaxy. From a CMB foreground perspective, they are a nuisance, and miss-modeling them could have dramatic consequences for cosmological data analysis.

The Planck Collaboration (2017) analysis found some evidence for a suppression of the

²This notion is very similar to the spectral distortions of the CMB mentionned in Sec. 5.1.3. They can be sourced by deviations from thermal equilibrium or as SED distortions induced from mixing of blackbody spectra in the depth of the primordial plasma, if significant energy injection occurs in the early Universe (from standard or non standard physics (Zeldovich & Sunyaev, 1969)). In order to avoid confusion, we distinguish "spectral distortions" (of the CMB) from "SED distortions" (of foregrounds).

³Thanks to Marc-Antoine Miville-Deschénes for pointing this.

⁴While for example, if the signal of the two maps is given in each pixel by a powerlaw with fixed amplitude and spectral index β , then $\mathcal{M}_{\nu_1} = k\mathcal{M}_{\nu_2}$ with $k = (\nu_1/\nu_2)^\beta$

cross-frequency power-spectra due to spatial variations of the SED. Subsequent analyses by (Sheehy & Slosar, 2018; Planck Collaboration, 2018) found no such detection. In order to tackle possible effects of decorrelation on the B -modes analysis level, BICEP2 Collaboration et al. (2018); Ade et al. (2021) used the decorrelation parameter, introduced in Planck Collaboration (2016c) (Appendix E), defined as

$$\Delta_d = \frac{\mathcal{D}_{\ell=80}(217 \times 353)}{\sqrt{\mathcal{D}_{\ell=80}(217 \times 217)\mathcal{D}_{\ell=80}(353 \times 353)}}. \quad (8.1)$$

This parameter was added in the analysis when looking at the cross frequency angular power spectra $\mathcal{D}_{\ell}^{\nu_1 \times \nu_2} = \mathcal{D}_{\ell}(\nu_1 \times \nu_2)$ with an associated spectral dependence of the form

$$\frac{\ln(\nu_1/\nu_2)^2}{\ln(217/353)^2}, \quad (8.2)$$

and a suitable flat ℓ dependence (all being inspired from Planck Collaboration (2017)). Results tend to show that such a term is not favored in the data analysis, traducing that the effect of decorrelation is lower than the noise level. The question of the sensitivity required to get a sensible impact of the spatial variation effects on cosmological analysis is thus still subject to debate, but there is no doubt that all these effect must be present at some level as they can be detected in the *Planck* data using refined analysis methods (Pelgrims et al., 2021; Ritacco et al., 2023). As such, there is no doubt that next generation missions, as Simons observatory will be sensitive to the consequences of SED variation and mixing, even in the more optimistic scenarios (Azzoni et al., 2021; Wolz et al., 2023). This will be even more dramatic for satellite experiments like *LiteBIRD*, scanning large sky fractions with an unprecedented sensitivity (LiteBIRD Collaboration et al., 2023; Vacher et al., 2022a). It is hence critical to find a robust method to be able to tackle these effects.

8.2 Beyond canonical SEDs: Moment expansion for intensity signal

Before treating the consequences of mixing and the solution proposed by moment expansion in full generality, we will focus for now on the intensity signal. We start by the pedagogical example of the sum of two power laws in order to highlight the problematic in the most simple case.

8.2.1 A pedagogical introduction: summing two power laws

Consider two power-law SEDs in intensity given by $I_{\nu}^1 = A_1 \left(\frac{\nu}{\nu_0}\right)^{\beta_1}$ and $I_{\nu}^2 = A_2 \left(\frac{\nu}{\nu_0}\right)^{\beta_2}$. One could for example think about the intensity signal coming from two synchrotron regions with different physical conditions. Let us further assume that these two regions are located one in front of the other along a single LOS as depicted on the right panel of Fig. 8.1. As discussed in Appendix B, Stokes parameters are additive, such that the total observed signal I_{ν} will simply be given by

$$I_{\nu} = I_{\nu}^1 + I_{\nu}^2 = A_1 \left(\frac{\nu}{\nu_0}\right)^{\beta_1} + A_2 \left(\frac{\nu}{\nu_0}\right)^{\beta_2} \neq \tilde{A} \left(\frac{\nu}{\nu_0}\right)^{\tilde{\beta}}. \quad (8.3)$$

Because power-laws are not linear in β_i , it is impossible to find \tilde{A} and $\tilde{\beta}$ such that I_ν can be rewritten as another power-law. This can be clearly seen on Fig. 8.1 as a power-law would be a straight line in the log-log plane, while the total signal is not a straight line anymore. In this example, I have chosen $\nu \in [1, 1000]$ GHz, $\nu_0 = 30$ GHz, $A_1 = 1$, $A_2 = 1.2$ (arbitrary units), $\beta_1 = -3$ and $\beta_2 = -1.3$. At $\nu = \nu_0$ the two SED cross each others and one becomes dominant over the other, thus flipping the behavior of I_ν . This is exactly the phenomenon of SED distortion mentioned in the previous section. As a solution, consider now making a

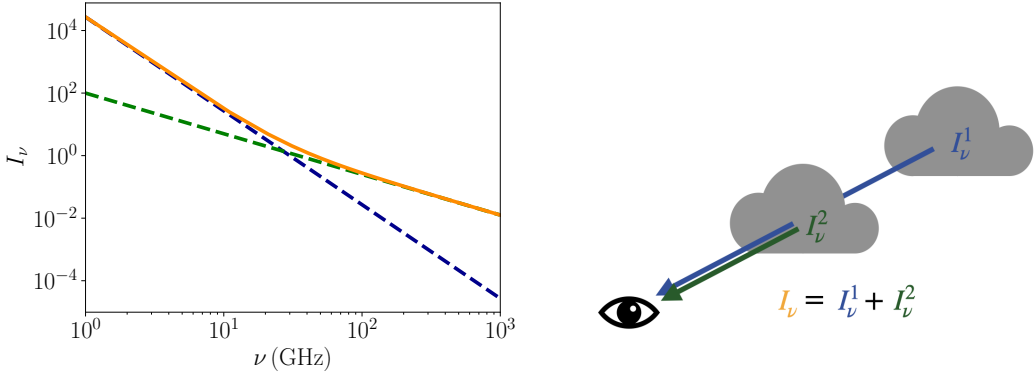


Figure 8.1: Left: sum of two power-law SEDs. Total signal (orange), I_ν^1 (blue dashed) and I_ν^2 (green dashed). Right: sketch of the position of the two regions responsible for I_ν^1 and I_ν^2 along the line of sight.

Taylor expansion of each SED I_ν^i , $i \in \{1, 2\}$ with respect to the spectral parameter β around a common pivot $\bar{\beta}$ (which can be arbitrary for now). This can in principle always be done and is exact as long as the SEDs are continuous and smooth. The Taylor expansion of each SED can be written as

$$\begin{aligned}
 I_\nu^i(\beta) &= I_\nu^i(\bar{\beta}) + (\beta - \bar{\beta}) \frac{\partial I_\nu^i}{\partial \beta} \Big|_{\beta=\bar{\beta}} + \frac{1}{2} (\beta - \bar{\beta})^2 \frac{\partial^2 I_\nu^i}{\partial \beta^2} \Big|_{\beta=\bar{\beta}} + \mathcal{O}(\beta^3) \\
 &= A_i \left(\frac{\nu}{\nu_0} \right)^{\bar{\beta}} \left(1 + (\beta - \bar{\beta}) \ln \left(\frac{\nu}{\nu_0} \right) + \frac{1}{2} (\beta - \bar{\beta})^2 \ln \left(\frac{\nu}{\nu_0} \right)^2 + \mathcal{O}(\beta^3) \right) \\
 &= A_i \left(\frac{\nu}{\nu_0} \right)^{\bar{\beta}} \left(1 + \sum_n \frac{\Delta \beta^n}{n!} \ln \left(\frac{\nu}{\nu_0} \right)^n \right).
 \end{aligned}$$

Introducing the notation $\Delta\beta = \beta - \bar{\beta}$. Performing now the expansion independently for the two intensities with respect to β_1 and β_2 , the total SED now reads

$$\begin{aligned}
 I_\nu &= A_1 \left(\frac{\nu}{\nu_0} \right)^{\beta_1} + A_2 \left(\frac{\nu}{\nu_0} \right)^{\beta_2} \\
 &= A_1 \left(\frac{\nu}{\nu_0} \right)^{\bar{\beta}} \left(1 + \Delta\beta_1 \ln \left(\frac{\nu}{\nu_0} \right) + \frac{1}{2} (\Delta\beta_1)^2 \ln \left(\frac{\nu}{\nu_0} \right)^2 + \mathcal{O}((\Delta\beta_1)^3) \right) \\
 &\quad + A_2 \left(\frac{\nu}{\nu_0} \right)^{\bar{\beta}} \left(1 + \Delta\beta_2 \ln \left(\frac{\nu}{\nu_0} \right) + \frac{1}{2} (\Delta\beta_2)^2 \ln \left(\frac{\nu}{\nu_0} \right)^2 + \mathcal{O}((\Delta\beta_2)^3) \right) \\
 &= \left(\frac{\nu}{\nu_0} \right)^{\bar{\beta}} \left([A_1 + A_2] + [A_1 \Delta\beta_1 + A_2 \Delta\beta_2] \ln \left(\frac{\nu}{\nu_0} \right) \right. \\
 &\quad \left. + \frac{1}{2} [A_1 (\Delta\beta_1)^2 + A_2 (\Delta\beta_2)^2] \ln \left(\frac{\nu}{\nu_0} \right)^2 \right) + \mathcal{O}((\Delta\beta_i)^3) \\
 &= \bar{A} \left(\frac{\nu}{\nu_0} \right)^{\bar{\beta}} \left(1 + \omega_1^\beta \ln \left(\frac{\nu}{\nu_0} \right) + \omega_2^\beta \ln \left(\frac{\nu}{\nu_0} \right)^2 + \mathcal{O}((\Delta\beta_i)^3) \right), \tag{8.4}
 \end{aligned}$$

with $\Delta\beta_i = \beta_i - \bar{\beta}$ and where we defined

$$\bar{A} = A_1 + A_2, \quad \omega_i^n = \frac{A_1(\Delta\beta_1)^n + A_2(\Delta\beta_2)^n}{\bar{A}}. \tag{8.5}$$

The coefficients ω_i^n are called the *moments* as they can be identified with the statistical moments of order n of the $\Delta\beta$ -distribution, if the amplitudes A_i are interpreted as normalization of the probability distribution⁵. The final expansion of the total SED in Eq. 8.4 is hence called a *moment expansion*. Note that the moments can be defined without the \bar{A} normalization depending on the context (and one has to be careful about it!). As statistical moments, it is possible to interpret ω_1^β as a correction to the mean pivot $\bar{\beta}$. The corrected value $\bar{\beta}^{\text{corr}}$ will be the choice of spectral index pivot corresponding to a vanishing of the first order as

$$\omega_1^\beta = 0 \tag{8.6}$$

$$\Rightarrow A_1(\beta_1 - \bar{\beta}^{\text{corr}}) + A_2(\beta_2 - \bar{\beta}^{\text{corr}}) = 0 \tag{8.7}$$

$$\Rightarrow \bar{\beta}^{\text{corr}} = \frac{A_1\beta_1 + A_2\beta_2}{\bar{A}} \tag{8.8}$$

As such, the expansion Eq. 8.4 rewritten around $\bar{\beta}^{\text{corr}}$ instead of $\bar{\beta}$ will have no first order, and will be associated with the smallest values for the higher order moments. In practice, this can be done by evaluating or fitting ω_1^β and replacing

$$\bar{\beta} \rightarrow \bar{\beta} + \omega_1^\beta \tag{8.9}$$

$$= \frac{\bar{\beta}(A_1 + A_2)}{A_1 + A_2} + \frac{A_1\beta_1 - A_1\bar{\beta} + A_2\beta_2 - A_2\bar{\beta}}{A_1 + A_2} \tag{8.10}$$

$$= \frac{A_1\beta_1 + A_2\beta_2}{A_1 + A_2} = \bar{\beta}^{\text{corr}}. \tag{8.11}$$

⁵The statistical moment M^k of order k associated to a variable x with probability $\mathbb{P}(x)$ are given by $M^k = \int x^k \mathbb{P}(x) dx$. Here the variable is $x = \beta - \bar{\beta}$ and $\mathbb{P}(x) = \sum_i A_i \delta(x - x_i)$ (with δ the Dirac distribution). The moments are normalized by the total probability $\int \mathbb{P}(x) dx = \bar{A}$.

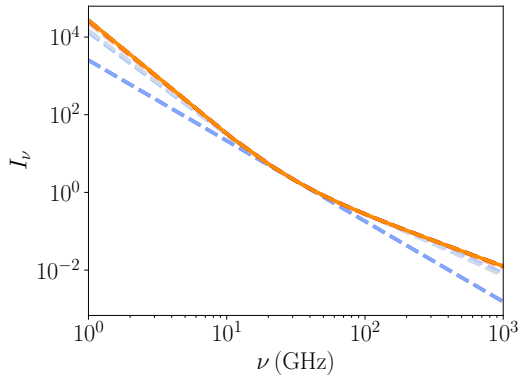


Figure 8.2: Modeling the SED distortions of the total signal (orange) with moment expansion at different orders (colored dashed lines: order 1 with pivot correction (blue), order 2 (light blue), order 3 (grey)). The higher orders are changing color towards the red and merge gradually with the total signal.

The moment expansion is giving a well motivated modeling of the SED distortions. Let us motivate this ascertainment in the extreme case illustrated in Fig. 8.1. In Fig. 8.2, I plotted the canonical SED evaluated at $\bar{\beta} \simeq -2.07$ and $\bar{A} = 2.2$ (in dashed blue). As expected, it is not able to bend in the log-log plane and can not reproduce the total signal (orange). Computing ω_1^β , I find $\sim 1 \times 10^{-16}$, symptomatic of choosing the right pivot values around which we can make the expansion. I further obtain $\omega_2^\beta = 0.716$, the addition of which significantly pushes the signal towards the desired curve (dashed light blue). The addition of the other orders further help (colored dashed lines), until the moment expansion is completely merged with the signal. As such, the moment expansion provides a well motivated and minimal modeling of the SED distortions.

8.2.2 Moments expansion in intensity in their full glory

The original introduction of the moment expansion for CMB foreground modeling was given in Chluba et al. (2017). Following this paper, let us now extend the simple example of the sum of power-laws to a general case. To do so, consider that every point of the 3D Galaxy (every "voxel") is emitting with a canonical SED $I_\nu(\mathbf{p})$ where $\mathbf{p} = (p_1, p_2 \dots p_N)$ is a vector containing N spectral parameters. As a matter of terminology, we define the *weight* (noted A) as the factors in the SED which are not dependent of the frequency (e.g. the amplitudes of power-laws/MBB). On the other hand, the frequency dependent part of the SED, in which the spectral parameters appear, is called the emissivity (noted ε_ν in the following). As such, the local SED in every point can be re-expressed as $I_\nu = A\varepsilon_\nu$.

The total SED $\langle I_\nu(\mathbf{p}) \rangle$, resulting from the mixing inside a beam and/or along the line of sight is then given by

$$\langle I_\nu(\mathbf{p}) \rangle = \int A(s)\varepsilon_\nu(\mathbf{p}(s)) \, ds = \int \mathbb{P}(\mathbf{p})\varepsilon_\nu(\mathbf{p}) \, d^N p \quad (8.12)$$

where s is a continuous dimensionless parametrization labeling the various emission points over which the summation is done (typically a parametrization of the line of sight or the coordinates x of the points in 3D). The second expression makes explicit the link between

the moment expansion and the statistical distributions of the spectral parameters. $\mathbb{P}(\mathbf{p})$ represents the statistical probability distribution of the spectral parameters p over which one is averaging over. As a convenient trick, we absorbed the weights A in the probability density. The probability distribution is then normalized by the weights as $\int \mathbb{P}(\mathbf{p}) d^N p = \int A(s) ds := \bar{A}$. As such, the two last expressions are complementary and give a different intuition on the problem: one is a deterministic sum over all the emission points and the second one is a statistical average over the spectral parameters in the region under consideration.

In both expressions of Eq. 8.12, it is possible to Taylor expand the canonical SED $I_\nu(\mathbf{p})$ with respect to the each spectral parameter p_i around a constant pivot \bar{p}_i . Regrouping the terms as we did in Sec. 8.2.1, the moment expansion takes the general form

$$\begin{aligned} \langle I_\nu(\mathbf{p}) \rangle &= I_\nu(\bar{\mathbf{p}}) + \sum_i \omega_1^{p_i} \partial_{p_i} I_\nu(\mathbf{p})|_{\mathbf{p}=\bar{\mathbf{p}}} \\ &\quad + \frac{1}{2} \sum_{i,j} \omega_2^{p_i p_j} \partial_{p_i} \partial_{p_j} I_\nu(\mathbf{p})|_{\mathbf{p}=\bar{\mathbf{p}}} \\ &\quad + \dots \\ &\quad + \frac{1}{\gamma!} \sum_{i,\dots,k} \omega_\gamma^{p_i \dots p_k} \partial_{p_i} \dots \partial_{p_k} I_\nu(\mathbf{p})|_{\mathbf{p}=\bar{\mathbf{p}}}, \end{aligned} \quad (8.13)$$

where the moments are defined as

$$\omega_\gamma^{p_i \dots p_k} = \frac{\langle (p_i - \bar{p}_i) \dots (p_k - \bar{p}_k) \rangle}{\bar{A}} \quad (8.14)$$

and $\langle X \rangle = \int A(s) X(s) ds = \int \mathbb{P}(\mathbf{p}) X d^N p$ is the integral/sum over all the emission points, weighted by the amplitudes $A(s)$.

For the sake of completeness, let me mention that in order to obtain Eq. 8.13, we made the assumption that the spectral derivatives $\langle \partial_{p_i} \dots \partial_{p_k} I_\nu(\mathbf{p}) \rangle$ where constants $\partial_{p_i} \dots \partial_{p_k} I_\nu(\mathbf{p})$ and could be factorized out of the integrals. Some processes, as bandpass integration makes this simplification impossible, as the integral $\langle X_\nu \rangle = \int X_\nu \mathbb{P}(\mathbf{p}) W(\nu) d^N p d\nu$ must contain a frequency dependent beam window function $W(\nu)$. The moment expression must then take the form given in Chluba et al. (2017) as

$$\begin{aligned} \langle I_\nu(\mathbf{p}) \rangle &= I_\nu(\bar{\mathbf{p}}) + \sum_i \omega_1^{p_i} \langle \partial_{p_i} I_\nu(\mathbf{p}) \rangle_{\mathbf{p}=\bar{\mathbf{p}}} \\ &\quad + \frac{1}{2} \sum_{i,j} \omega_2^{p_i p_j} \langle \partial_{p_i} \partial_{p_j} I_\nu(\mathbf{p}) \rangle_{\mathbf{p}=\bar{\mathbf{p}}} \\ &\quad + \dots \\ &\quad + \frac{1}{\gamma!} \sum_{i,\dots,k} \omega_\gamma^{p_i \dots p_k} \langle \partial_{p_i} \dots \partial_{p_k} I_\nu(\mathbf{p}) \rangle_{\mathbf{p}=\bar{\mathbf{p}}}, \end{aligned} \quad (8.15)$$

with

$$\omega_\gamma^{p_i \dots p_k} = \frac{\langle (p_i - \bar{p}) \dots (p_k - \bar{p}) \partial_{p_i} \dots \partial_{p_k} I_\nu(\mathbf{p}) \rangle}{\langle \partial_{p_i} \dots \partial_{p_k} I_\nu(\mathbf{p}) \rangle}. \quad (8.16)$$

A preliminary version of the moment expansion was introduced to deal with the SZ effect and separate the spectral and spatial information of the signal (Chluba et al., 2013). As

CMB spectral distortions (discussed in Chap. 5) can be produced by some mixing in the depth of the LSS, moments can naturally be invoked to model them and their foregrounds (Abitbol et al., 2017). However, modern applications of the moment expansion can be mostly found in order to model and separate CMB foregrounds. As discussed already in Chap. 6, the dust signal has already been confused with the primordial signature of the inflaton field BICEP2/Keck Collaboration et al. (2015). Moment expansion provides a careful modeling of the dust signal that could help avoiding this confusion through a justified modeling of the expected consequences of mixing introduced in Sec. 8.1.

As such, foreground moments have been included in ILC methods in order to orient the optimization in component separation. This is the proposal of the MILC method (Rotti & Chluba, 2021; Remazeilles et al., 2021). On the other hand, in pixel space, it was suggested to fit the moment coefficients in large pixels to provide a parametric component separation method named the Δ -map method (Ichiki et al., 2019; Minami & Ichiki, 2023).

In this thesis, I will propose in Sec. 8.3 a new parametric component separation method in which this moment expansion is used at the angular power spectra level. This method is applied on simulations for the *LiteBIRD* mission and proves to be able to separate efficiently the foreground signal from the primordial B -modes. Furthermore, in Sec. 8.4, I will derive the first generalization of this formalism to polarization, introducing the "spin-moment" expansion. This framework will allow to understand and model properly the unique consequences of the mixing of polarized signals. Finally, in Sec. 8.5, I will further use the spin-moment expansion to explore the consequences of mixing at the E - and B -modes level. We will then discuss how and why the spin-moments are powerful tools for dust modeling and Galactic science.

8.3 Applying moment for component separation: application to *LiteBIRD*

8.3.1 Context: The challenge of component separation with *LiteBIRD*

As discussed in Sec. 8.1, it is known that the spectral parameters are varying across the 3D Galaxy, and that these variations will have consequences for future CMB missions. In order to recover an unbiased value of the tensor-to-scalar ratio r , it is critical to find a way to model these consequences. However, a trade-off must be found and choosing a very complex modeling of the foregrounds including a large number of parameters is not desirable, as it would degrade the sensitivity at which r can be recovered. As discussed in the previous section, the moment expansion provides a minimal and well motivated modeling of the distorted foreground SED. Depending on the complexity of the component separation problem – set both by the sensitivity of the instrument and the complexity of the Galactic signal – the expansion can be cropped to keep only the minimal number of moments required for a careful modeling of the SED, with a minimal degrading of the sensitivity. Additionally, the amplitude of the recovered moment coefficients allows to properly quantify the foreground complexity under consideration, and infer statistical properties of the ISM.

In the analysis of Mangilli et al. (2021), the moment coefficients were fitted over simulations

and *Planck* data at the cross-frequency power spectra level in intensity $\mathcal{D}_\ell(\nu_i \times \nu_j)$. It was found that moment were needed in order to account for the sky complexity and recover a good fit, as well as an unbiased spectral index in simulations. This work provided a strong indication that moments could be a powerful tool to apply directly at the angular power spectrum level on the B -modes data in order to recover an unbiased value of the tensor to scalar ratio for a mission as *LiteBIRD*.

Component separation can be put forward as one of the biggest challenge that must be overcome for the success of the *LiteBIRD* mission⁶([LiteBIRD Collaboration et al., 2023](#)). This task is especially challenging as the instrument is designed to probe the largest scales of the sky with an unprecedented sensitivity, and will hence be extremely exposed to the consequences of mixing, excluding all the simple methods which were efficient at lower sensitivities. As over-viewed in [Fuskeland et al. \(2023\)](#), several methods have been proposed to deal with this complexity, each with their advantages and drawbacks. As mentioned in Sec. 6.4, this plurality is a strength, and the complementary of the methods will certainly be put forward in front of real sky data. No matter the choice of the method however, recovering an unbiased value of r with a minimal standard deviation at *LiteBIRD*'s sensitivity appears to be a highly non trivial task, even in the simplest foreground scenarios.

In this thesis, I explore the promising direction opened by the moment expansion at the level of the cross-frequency angular power spectra for *LiteBIRD*. We demonstrate its viability and explore its limits.

8.3.2 The paper: Objectives and results

Following the analysis of [Mangilli et al. \(2021\)](#), I was tasked by Jonathan Aumont to explore the possibility to use the moment expansion for B -mode component separation during my master's thesis. Fitting the moment coefficients over the cross-frequency angular power-spectra of *LiteBIRD* simulations, I demonstrated the possibility to recover an unbiased value of r for simple dust models, with a standard deviation compatible with the mission's objectives. Our results were published more than one year later [Vacher et al. \(2022a\)](#) and the complete paper can be found in Appendix D.1.

To perform the analysis, I generated several sets of 500 maps of simulated *LiteBIRD* data on the sphere using the HEALPY software. These simulations were built for the 9 highest frequencies of the instrument, where the dust signal is expected to be dominant (≥ 100 GHz). They include Gaussian white noise realizations with the *LiteBIRD* sensitivity⁷. All of the set contains Gaussian realizations of BB lensing. While the default case has no primordial B -modes ($r_{\text{sim}} = 0$), a set was built containing some primordial signal with $r_{\text{sim}} = 1 \times 10^{-2}$ in order to explore the possible degeneracies between r and the moments⁸. Finally, some foregrounds were added using the PySM models. We explored **d0**, **d1**, **d1T** (a self-made version of **d1** without temperature variation) and in some case we added some synchrotron **s1**. All these foreground models are described in Sec. 6.5. A significant amount of the

⁶The scientific objectives and characteristics of the *LiteBIRD* instrument are detailed in Chap. 7

⁷In order to simulate the use of half-missions, I generated two independent set of noise with an amplitude greater by $\sqrt{2}$ for the computation of auto-frequency angular power-spectra.

⁸I generated the primordial B -modes and lensing spectra with CAMB (<https://github.com/cmbant/CAMB>) using the Λ -CDM best-fit parameters.

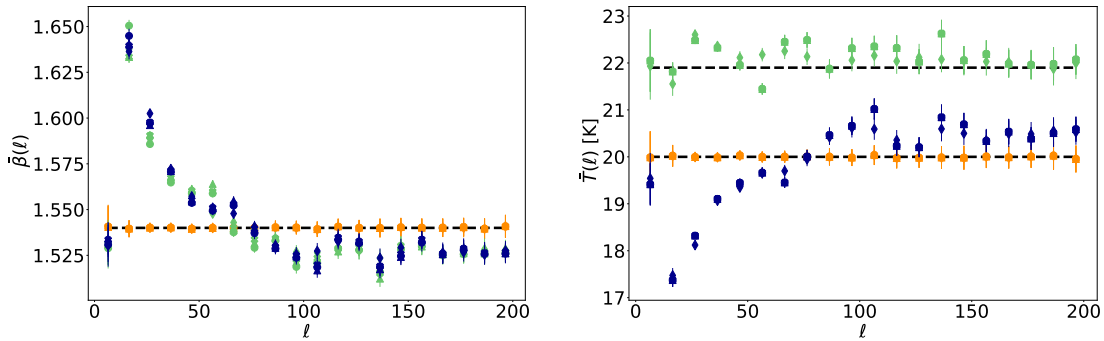


Figure 8.3: (Left): Median and median absolute deviations of the best fit values of $\bar{\beta}(\ell)$ in $d0$ (orange), $d1T$ (green), and $d1$ (blue) for the MBB (circles). For completeness, I also added the correction brought by the other orders: β_1 (crosses), β_2 (triangles), and β_T (diamonds). β_{d0} is marked by the dashed black line. (Right): Same as above but with $\bar{T}(\ell)$, the black dashed-lines being $T_{d0} = 20\text{ K}$ and $T_{d1T} = 21.9\text{ K}$.

work consisted to test these simulations build by hand, in order to make sure that every component was correctly implemented. The maps were then masked using different sky fractions of $f_{\text{sky}} = 70\%$, $f_{\text{sky}} = 60\%$ and $f_{\text{sky}} = 50\%$. From two maps at two-map \mathcal{M}_{ν_i} and \mathcal{M}_{ν_j} at different frequencies ν_i and ν_j , one can compute the cross-frequency angular power spectra $\mathcal{D}_\ell(\nu_i \times \nu_j) = \mathcal{D}_\ell(\mathcal{M}_{\nu_i} \times \mathcal{M}_{\nu_j})$. For a formal definition of the angular power spectra, we refer to Appendix B. In these analysis, we considered only the *BB* cross-frequency angular power spectra. From 9 original frequencies, 45 *BB* cross-spectra can be extracted over which to perform our analysis. In order to extract the cross-frequency angular power-spectra from the maps, I first used the XPOL (Tristram et al., 2005) software, which revealed itself to be too inaccurate for *LiteBIRD*'s sensitivity. I then used the NAMASTER software⁹, with *B*-mode purification of the ambiguous modes, allowing to significantly increase the accuracy of the spectra extraction. The spectra where then binned 10 by 10 in the range $\ell \in \{2, 200\}$.

Once the 45 power-spectra of 20 bins extracted from each of the 500 simulations, it is possible to model their spectral behavior as

$$\mathcal{D}_\ell^{\text{model}}(\nu_i \times \nu_j) = \mathcal{D}_\ell^{\text{dust}}(\nu_i \times \nu_j) + \mathcal{D}_\ell^{\text{lensing}} + \hat{r} \cdot \mathcal{D}_\ell^{\text{tensor}}, \quad (8.17)$$

where $\mathcal{D}_\ell^{\text{lensing}}$ and $\mathcal{D}_\ell^{\text{tensor}}$ are respectively the input lensing and tensor power-spectra (independent of frequency in $(\mu\text{K}_{\text{CMB}})^2$) and \hat{r} is the model's tensor-to-scalar ratio.

Regarding the dust model, Mangilli et al. (2021) showed how to generalize the moment expansion introduced in Sec. 8.2.2 at the cross-frequency angular power spectrum level. Assuming that the dust SED is given by a distorted MBB, $\mathcal{D}_\ell^{\text{dust}}(\nu_i \times \nu_j)$ can be expressed

⁹<https://github.com/LSSTDESC/Namaster>

with a moment expansion with respect to β and T^{10} as¹¹

$$\mathcal{D}_\ell^{\text{dust}}(\nu_i \times \nu_j) = \frac{I_{\nu_i}(\bar{\beta}(\ell), \bar{T}(\ell)) I_{\nu_j}(\bar{\beta}(\ell), \bar{T}(\ell))}{I_{\nu_0}(\bar{\beta}(\ell), \bar{T}(\ell))^2} \cdot \left\{ \begin{array}{l} \text{0}^{\text{th}} \text{ order } \left\{ \begin{array}{l} \mathcal{D}_\ell^{A \times A} \\ + \mathcal{D}_\ell^{A \times \omega_1^\beta} \left[\ln \left(\frac{\nu_i}{\nu_0} \right) + \ln \left(\frac{\nu_j}{\nu_0} \right) \right] \\ + \mathcal{D}_\ell^{\omega_1^\beta \times \omega_1^\beta} \left[\ln \left(\frac{\nu_i}{\nu_0} \right) \ln \left(\frac{\nu_j}{\nu_0} \right) \right] \end{array} \right\} \\ \text{1}^{\text{st}} \text{ order } \beta \left\{ \begin{array}{l} + \mathcal{D}_\ell^{A \times \omega_1^\beta} (\Theta_i + \Theta_j - 2\Theta_0) \\ + \mathcal{D}_\ell^{\omega_1^\beta \times \omega_1^\beta} (\Theta_i - \Theta_0)(\Theta_j - \Theta_0) \end{array} \right\} \\ \text{1}^{\text{st}} \text{ order } T \left\{ \begin{array}{l} + \mathcal{D}_\ell^{A \times \omega_1^T} (\Theta_i - \Theta_0) \\ + \mathcal{D}_\ell^{\omega_1^T \times \omega_1^T} (\Theta_i - \Theta_0)(\Theta_j - \Theta_0) \end{array} \right\} \\ \text{1}^{\text{st}} \text{ order } T\beta \left\{ \begin{array}{l} + \mathcal{D}_\ell^{\omega_1^\beta \times \omega_1^T} \left[\ln \left(\frac{\nu_j}{\nu_0} \right) (\Theta_i - \Theta_0) + \ln \left(\frac{\nu_i}{\nu_0} \right) (\Theta_j - \Theta_0) \right] \\ + \frac{1}{2} \mathcal{D}_\ell^{A \times \omega_2^\beta} \left[\ln^2 \left(\frac{\nu_i}{\nu_0} \right) + \ln^2 \left(\frac{\nu_j}{\nu_0} \right) \right] \\ + \frac{1}{2} \mathcal{D}_\ell^{\omega_1^\beta \times \omega_2^\beta} \left[\ln \left(\frac{\nu_i}{\nu_0} \right) \ln^2 \left(\frac{\nu_j}{\nu_0} \right) + \ln \left(\frac{\nu_j}{\nu_0} \right) \ln^2 \left(\frac{\nu_i}{\nu_0} \right) \right] \\ + \frac{1}{4} \mathcal{D}_\ell^{\omega_2^\beta \times \omega_2^\beta} \left[\ln^2 \left(\frac{\nu_i}{\nu_0} \right) \ln^2 \left(\frac{\nu_j}{\nu_0} \right) \right] \end{array} \right\} \\ \text{2}^{\text{nd}} \text{ order } \beta \left\{ \begin{array}{l} + \dots \end{array} \right\}, \end{array} \right. \quad (8.18)$$

where Θ_i are the first order derivative of the blackbody with respect to the temperature evaluated at a frequency ν_i

$$\Theta_i = \frac{x_i}{T} \frac{e^{x_i}}{e^{x_i} - 1}, \text{ with } x_i = \frac{h\nu_i}{k_B T}. \quad (8.19)$$

We made the hypothesis that this formalism – built for the intensity signal – could be identically applied to the thermal dust *BB* signal when considering the *B*-modes independently from the other polarization angular power spectra (*EE* and *EB*). This hypothesis was proven to be valid a posteriori in Vacher et al. (2023b,a). We also added for the first time the moments in temperature, which were disregarded in Mangilli et al. (2021), as an expansion in β only was enough to recover accurately the dust signal at *Planck*'s sensitivity, which is not possible anymore for *LiteBIRD*.

The moment coefficients and \hat{r} can then be recovered with a fit of Eq. 8.17 on the simulation spectra using a χ^2 minimization with MPFIT¹².

The covariance matrix of all the simulation was used to compute the value of the χ^2 , but appeared to be impossible to invert accurately in general. A way around this issue was found by considering a truncated version of the matrix keeping only the strongest correlation values.

For each simulation, we fit a value for the MBB amplitude, moment coefficients and pivot spectral parameters in every bin of ℓ and a single value of \hat{r} . All the best-fit spectra can be

¹⁰Here and in the remainder of this chapter, we drop the upper labels d for the dust spectral parameters and reference frequency used in Chap. 6, allowing us to make the notations significantly less cluttered.

¹¹A frequency dependent factor must be added to this expression to correctly express this expansion in $(\mu K_{\text{CMB}})^2$.

¹²<https://github.com/segasai/astrolibpy/blob/master/mpfit/mpfit.py>

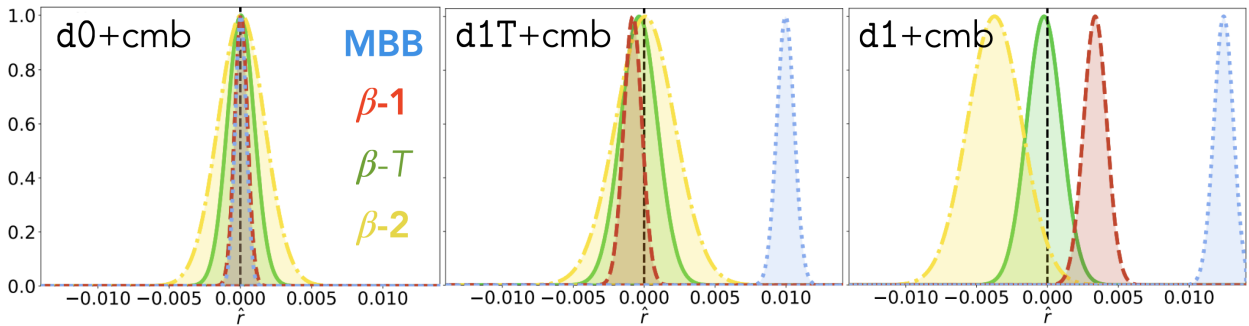


Figure 8.4: Recovered posterior for the tensor to scalar ratio at $f_{\text{sky}} = 70\%$ with the three different kind of dust models; d0 (left), d1T (center) and d1 (right) with different fitting schemes: MBB (blue), first order in β (red), first order in β and T (green) and second order in β (yellow). The black dashed line indicates $r_{\text{sim}} = 0$.

found in the paper (Fig. 4 to 8), as well as their interpretation in term of the dust complexity contained within the simulations. The recovered value of the reduced χ^2 are considered to evaluate the goodness of the fit, and validate our interpretations (see Fig. 3 of the paper).

We used an iterative process to fit the moments: we first fit a MBB (0^{th} order) with ℓ -dependent spectral parameters (see Fig. 8.3), then we fit the moment expansion at order n , keeping fixed the spectral parameters obtain with the MBB, and finally we iterate the fit of all the moment until convergence by correcting the spectral parameter spectra with the first order moments spectra in order to fix the best pivot spectral parameters until convergence is reached when all the first order moment spectral are compatible with zero¹³ (See of Sec.4.2 of the paper in Appendix D.1 for a detailed description). Finally, we decided to fit a Gaussian posterior on the \hat{r} distribution, in order to estimate a final value of $\hat{r} \pm \sigma(\hat{r})$. The recovered Gaussian posteriors for the special case of $r_{\text{sim}} = 0$ and $f_{\text{sky}} = 70\%$ can be found in Fig. 8.4. The results depend strongly on the choice of the fitting scheme as follows:

- **MBB:** Fitting a MBB with ℓ -dependent spectral parameters (blue curves) always lead to a biased value of the \hat{r} posterior except for the d0 dust model, which is exactly a MBB on the sky. As an illustration, the recovered ℓ -dependence of the spectral parameters for the different dust models is given on Fig. 8.3, depicting a consistent story with the different foreground scenarios. After the MBB fit (circles), the values of the spectral parameters are fixed and corrected by iteration when moments are added to the model (other shapes).
- **Expansion in β at first order (β -1):** Fitting only the first order in β drastically reduce the bias but is still not enough to completely suppress it for d1T and d1, indicating that this model is not satisfactory. The reduced χ^2 values are significantly shifted away from unity.
- **Expansion in β at second order (β -2):** As expected, using the moment expansion

¹³A subtle point must be stressed here: contrarily to the expansion in map space (Eq. 8.13), correcting the pivot \bar{p} in harmonic space (Eq. 8.18) suppresses only the term in $A \times \omega_1^p$ but can not cancel the moment term in $\omega_1^p \times \omega_1^p$, such that the first order can not be reduced to a simple correction of the pivot. This translate the fact that it is impossible to find a common pivot correction for Eq. 8.13 suppressing simultaneously the first order in every pixel of the map when spatial variations are present.

up to second order in β only allows to suppress the bias for $\mathbf{d1T}$, which contains only variations of β . However it leads to a significant increase in the width of the posterior as well as a surprising negative bias in \hat{r} for $\mathbf{d1}$. While it took a significant amount of time for us to properly understand the origin of this behavior, our interpretation is the following: significant degeneracies exist between the $\omega_2^\beta \times \omega_2^\beta$ and \hat{r} , leading to an unwanted increase in the standard deviation (compared to the $(\beta-T)$ model which has exactly the same number of free parameters). Moreover, when temperature distortions are present, the second order moment try to account for them with the wrong spectral shape and, due to the correlation mentioned before, $\omega_2^\beta \times \omega_2^\beta$ tends to leak into \hat{r} when it is added to the fit (See Fig. A.2 of the paper and the discussion in Sec. 6.5), leading to the observed bias on the measured tensor-to-scalar ratio.

- **Expansion in β and T at first order ($\beta-T$)**. The expansion of first order in both β and T allows to recover an unbiased value of \hat{r} in all scenario with a minimal standard deviation close to *LiteBIRD* objectives $\sigma_{\hat{r}} \sim 10^{-3}$. We further showed that reducing the number of fitted moments – by setting a threshold in multipole under which they are considered – allowed to significantly reduce this value without introducing bias, such that a careful optimization of the method could drastically improve this result.

The other scenarios I explored, including different f_{sky} , $r_{\text{sim}} \neq 0$ and synchrotron are all detailed in the paper. Overall, the conclusions of our work are the following:

- The moment coefficients are undoubtedly needed to recover a unbiased value of the tensor to scalar ratio for a mission as sensitive as *LiteBIRD*. Without taking them into account, the value of the recovered posterior for \hat{r} is significantly biased ($\sim 61\sigma$ for $\mathbf{d1}$ and $f_{\text{sky}} = 70\%$). When the moments are added to the fit, they are all significantly detected, mostly at the largest scales, were the consequences of mixing are stronger (see Fig.6 to 8 of the paper).
- Larger sky fractions are favored for this method, as they provide more statistics in order to recover a small value of $\sigma(\hat{r})$, while stronger distortions can be easily overcomed with the moments.
- Moments expansion up to order 1 in the cross-power spectra domain allows to reach *LiteBIRD* objectives for the simple $\mathbf{d1}$ model. After optimization, we are able to recover an unbiased value of the tensor-to-scalar ratio with associated $\sigma(\hat{r}) \sim 9 \times 10^{-4}$ for a sky fraction of $f_{\text{sky}} = 70\%$. This result is robust under the addition of a non-zero r_{sim} , change of the sky fraction f_{sky} or addition of synchrotron $\mathbf{s1}$ (with corresponding increases in $\sigma(\hat{r})$).
- Taking into account the temperature moments is crucial when reaching sensitivity level of *LiteBIRD*. A modeling using β moments only, as previously done in harmonic space, or as done for less sensitive missions, now leads to biased results. As the moments are correlated mildly with \hat{r} and between each others, going to higher orders in β without considering the lower terms in T will lead the fit to interpret first order dust complexity as second order index complexity, leading to a miss-modeling of the dust signal.
- Moment expansion allows to recover the spectra of the moment amplitude, and characterizes the dust complexity under consideration as done in (Mangilli et al., 2021). This interpretative power is one of the greatest strength of the method, as it allows to

explain the possible biases and miss-modeling.

8.3.3 Impact, limits and outlooks

This work provides a first proof of concept for the use of moments in harmonic space in the case of the *LiteBIRD* high sensitivity mission. We stressed the power of the method, as it provides a highly interpretable framework, which is mostly justified when considering large sky fractions.

Our analysis could have been done by considering all the frequency bands, but this would be very demanding in term of computational time, and further optimization of the codes would be required in order to properly do so. Lot of room is also left for optimization in order to select the correct moments and reduce the recovered $\sigma(\hat{r})$ value. To do so, one could simply remove the moments coefficients as free parameters when they are not significantly detected in the fit (in the spirit of what we proposed here). Possible combination with other methods as e.g. clustering should also be considered, in order to select the minimal number of free parameters required (Puglisi et al., 2022). Additionally it will be necessary to test our implementation on more complicated dust models than the ones investigated in this analysis. The moments will undoubtedly be able to face the challenge, but the recovered value of $\sigma(\hat{r})$ might be too large for a mission as *LiteBIRD*, which further justifies why an optimization is required. Larger sky fraction could also be considered, under which the method is expected to provide its best performances

We also showed that a careful modeling of the temperature¹⁴ was crucial at high sensitivity and high frequencies. This conclusion about temperature naturally leads us to wonder if the addition of bands at high frequencies could help breaking the degeneracy between the β and T moments in order to ease the component separation. By shifting the frequency bands of the HFT towards high frequencies, I found that one could reduce the value of $\sigma(\hat{r})$ by $\sim 65\%$ using the exact same method. My results were published in the collaborative paper Fuskeland et al. (2023), in which multiple component separation methods reached the same conclusions in the framework of the *LiteBIRD* foreground joint study group.

Within the collaboration, I am also a member of the *LiteBIRD* Galactic project study group in which we investigate how the moments could be used for component separation and foreground modeling. I am now collaborating with Eirik Gjerløw of Oslo University in order to implement the moment coefficients in the COMMANDER framework.

A similar approach than the one I introduced, but using less free parameters, was taken in Azzoni et al. (2021) for the Simons Observatory (SO), published while we were writing the draft of our analysis. This work demonstrates that the moments can also be successfully applied to recover an unbiased value of r for ground experiments with lower sensitivity as SO. Azzoni et al. (2023) further proposed a hybrid method mixing moment expansion and internal linear combination to benefit from both approaches. In this form, moment expansion is now part of the standard procedures used for component separation in the SO collaboration (Wolz et al., 2023). All these works further make the moment expansion approach essential for contemporary and future component separation.

¹⁴Similar conclusions about the effect of temperature were reached in the subsequent analysis of Sponseller & Kogut (2022).

8.4 Generalization to polarization: Spin-moments expansion

Following this first work on component separation, it seemed critical to me that a proper generalization of the moment framework to polarization was required. While using a Taylor expansion approach to the BB signal is justified and had proven functional, I could not help feeling that some links were missing and providing these links would strengthen the method itself.

While it is possible to apply the intensity expansion to Q and U independently, treating them as intensities, we will see that doing so misses the geometrical nature of the polarization field. The preferred treatment of polarization as a complex number allows to generalize the moment expansion to derive and model unique consequences of the averaging polarized signals (polarized mixing). Proposing this generalization and understanding its consequences is one of the major achievements of the present thesis. As such, I would like to give a first pedagogical introduction to this formalism, along the lines of Sec. 8.2.1, attempting a "demystification" of the mathematical formalism that I will propose. This introduction will be followed by a presentation of the original paper introducing the complex moments or *spin-moments*, which treats the formalism in full generality and with greater details.

8.4.1 Context: A second pedagogical introduction: summing two power laws, again

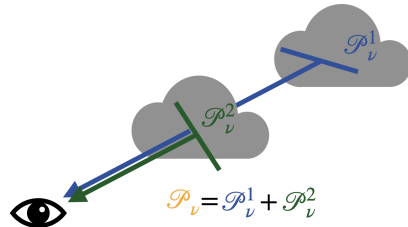


Figure 8.5: Sketch of the position of the two regions responsible for \mathcal{P}_ν^1 and \mathcal{P}_ν^2 along the line of sight.

As I discussed in Sec. 6.3.1 and further explained in Appendix B, the polarized signal is not described by a real number, but by a complex number $\mathcal{P} = Q + iU = P_\nu e^{2i\psi}$, giving a faithful representation of a "headless vector" with frequency dependent length P_ν and orientation ψ on the sky. Consider now two polarized power-law SEDs given by $\mathcal{P}_\nu^1 = A_1 \left(\frac{\nu}{\nu_0}\right)^{\beta_1} e^{2i\psi_1}$ and $\mathcal{P}_\nu^2 = A_1 \left(\frac{\nu}{\nu_0}\right)^{\beta_2} e^{2i\psi_2}$ along a single line of sight. As sketched on Fig. 8.5, one could for example think about the polarized signal coming from two synchrotron regions with different physical conditions and magnetic field orientations, following the emission process discussed in Sec. 6.3.2. As Stokes parameters are additive (Appendix B), so are the spinors

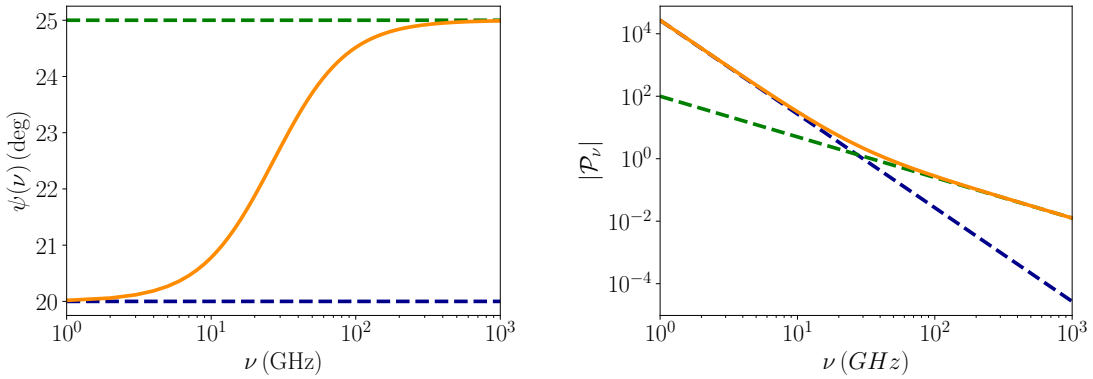


Figure 8.6: Sum of two power-laws in polarization. Total signal (orange), \mathcal{P}_ν^1 (blue dashed) and \mathcal{P}_ν^2 (green dashed). Left: phases $\psi(\nu)$. Right: modulus $|\mathcal{P}_\nu|$.

$\mathcal{P} = Q + iU$, such that the total signal \mathcal{P}_ν is given by

$$\mathcal{P}_\nu = \mathcal{P}_\nu^1 + \mathcal{P}_\nu^2 = A_1 \left(\frac{\nu}{\nu_0} \right)^{\beta_1} e^{2i\psi_1} + A_2 \left(\frac{\nu}{\nu_0} \right)^{\beta_2} e^{2i\psi_2} \neq \tilde{A} \left(\frac{\nu}{\nu_0} \right)^{\tilde{\beta}} e^{2i\tilde{\psi}}. \quad (8.20)$$

Exactly as for intensity in Sec. 8.2.1, the SED is not a power-law anymore, and as a new consequence, the total phase can not simply be the geometrical sum of the individual phases $e^{2i\psi} \neq e^{2i\psi_1} + e^{2i\psi_2}$ as each phase is weighted by a frequency dependent term. In Fig. 8.6, I plotted the same example given in Sec. 8.2.1, with two phases $\psi_1 = 20^\circ$ and $\psi_2 = 25^\circ$. The modulus of the signal $|\mathcal{P}_\nu|$ inherits SED distortions exactly as it was the case for I_ν . The total phase $\psi(\nu)$ becomes a frequency dependent quantity i.e., the total spinor rotates in the complex space with frequency, as we were mentioning in Sec. 8.1. Just like the polarized intensity, the phase makes a transition between the constant values of the dominant power-law at low frequency to the dominant power-law at high frequencies. Note that this would not be the case if $\psi_1 = \psi_2$, as the phases in Eq. 8.20 could then be factorized such that the signal has a single constant phase. Similarly if $\beta_1 = \beta_2$, where the constant phase would be given by $\arg(A_1 e^{i2\psi_1} + A_2 e^{i2\psi_2})$. As such, variation of both the polarization angles *and* the spectral parameters is required to obtain this spectral dependence.

While this was far from obvious when we first thought about the problem, a careful understanding of the intensity moment expansion introduced in Sec. 8.2.1 gives us a clear picture on how to proceed to derive a moment expansion from Eq. 8.20. The solution, here again, is to perform a Taylor expansion of the two polarized intensities with respect to β independently and around a common pivot – as we did in intensity – and leave the angles untouched, treating them as part of the weight coefficients A_i . Indeed, in nature, there is absolutely no reason to expect the polarization angles to be small and a perturbative approach would not

be fruitful. One then gets

$$\begin{aligned}\mathcal{P}_\nu &= A_1 e^{2i\psi_1} \left(\frac{\nu}{\nu_0}\right)^{\beta_1} + A_2 e^{2i\psi_2} \left(\frac{\nu}{\nu_0}\right)^{\beta_2} \\ &= A_1 e^{2i\psi_1} \left(\frac{\nu}{\nu_0}\right)^{\bar{\beta}} \left(1 + \Delta\beta_1 \ln\left(\frac{\nu}{\nu_0}\right) + \frac{1}{2}(\Delta\beta_1)^2 \ln\left(\frac{\nu}{\nu_0}\right)^2 + \mathcal{O}\left((\Delta\beta_1)^3\right)\right) \\ &\quad + A_2 e^{2i\psi_2} \left(\frac{\nu}{\nu_0}\right)^{\bar{\beta}} \left(1 + \Delta\beta_2 \ln\left(\frac{\nu}{\nu_0}\right) + \frac{1}{2}(\Delta\beta_2)^2 \ln\left(\frac{\nu}{\nu_0}\right)^2 + \mathcal{O}\left((\Delta\beta_2)^3\right)\right) \\ &= \left(\frac{\nu}{\nu_0}\right)^{\bar{\beta}} \left([A_1 e^{2i\psi_1} + A_2 e^{2i\psi_2}] + [A_1 e^{2i\psi_1} \Delta\beta_1 + A_2 e^{2i\psi_2} \Delta\beta_2] \ln\left(\frac{\nu}{\nu_0}\right)\right. \\ &\quad \left. + \frac{1}{2}[A_1 e^{2i\psi_1} (\Delta\beta_1)^2 + A_2 e^{2i\psi_2} (\Delta\beta_2)^2] \ln\left(\frac{\nu}{\nu_0}\right)^2\right) + \mathcal{O}\left((\Delta\beta_i)^3\right)\end{aligned}\quad (8.21)$$

$$= \left(\frac{\nu}{\nu_0}\right)^{\bar{\beta}} \left(\mathcal{W}_0 + \mathcal{W}_1^\beta \ln\left(\frac{\nu}{\nu_0}\right) + \frac{1}{2}\mathcal{W}_2^\beta \ln\left(\frac{\nu}{\nu_0}\right)^2 + \mathcal{O}\left((\Delta\beta_i)^3\right)\right). \quad (8.22)$$

Defining

$$\mathcal{W}_0 = \sum_{i=1}^2 A_i e^{2i\psi_i} \quad \mathcal{W}_n^\beta = \sum_{i=1}^2 A_i e^{2i\psi_i} (\Delta\beta_i)^n. \quad (8.23)$$

We should be careful if we want to factorize everything by \mathcal{W}_0 , as we did for intensity, because a new phenomenon exists – unique to polarization – known as *depolarization*. The phases $e^{2\psi_i}$ can cancel each others, such that they can greatly reduce the value of \mathcal{W}_0 . We can even think about the extreme situation where

$$\mathcal{W}_0 = A_1 e^{i\pi} + A_2 e^{-i\pi} \simeq 0, \quad (8.24)$$

if $A_1 \simeq A_2$. The signal would then just be given by its moments, without any leading order. In such case, dividing the whole expression by \mathcal{W}_0 would lead to a divergent expression. We define the *perturbative regime*, as the region in which doing so is possible, that is $\mathcal{W}_0 \gg \mathcal{W}_{n \neq 0}^\beta$. Due to depolarization, the hierarchy between the moment terms is broken and, out of the perturbative regime, it is impossible to assess that the contribution to the signal of a term in \mathcal{W}_i^β will be greater than the one in \mathcal{W}_j^β solely because $m > n$.

Another new unique consequence appears for polarization: the corrected pivot spectral parameter value is a complex number. Indeed, asking for the cancellation of the first order as we did in intensity, one gets¹⁵

$$\mathcal{W}_1^\beta = 0 \quad (8.25)$$

$$\Rightarrow \bar{\beta}^{\text{corr}} = \frac{[A_1 e^{2i\psi_1} \beta_1 + A_2 e^{2i\psi_2} \beta_2]}{[A_1 e^{2i\psi_1} + A_2 e^{2i\psi_2}]} \in \mathbb{C}. \quad (8.26)$$

Which, as for intensity (Sec. 8.2.1), is equivalent to ask for the replacement $\bar{\beta}^{\text{corr}} = \bar{\beta} + (\mathcal{W}_1^\beta / \mathcal{W}_0)$. But how can we make sense of a complex spectral index or a complex temperature? Writing $\bar{\beta}^{\text{corr}} = \text{Re}(\bar{\beta}^{\text{corr}}) + i\text{Im}(\bar{\beta}^{\text{corr}}) = \bar{\beta}_R + i\bar{\beta}_I$, the corrected complex power-law SED becomes

$$\left(\frac{\nu}{\nu_0}\right)^{\bar{\beta}^{\text{corr}}} = \left(\frac{\nu}{\nu_0}\right)^{\bar{\beta}_R + i\bar{\beta}_I} = \left(\frac{\nu}{\nu_0}\right)^{\bar{\beta}_R} e^{i\bar{\beta}_I \ln\left(\frac{\nu}{\nu_0}\right)}. \quad (8.27)$$

¹⁵Note that – again – this computation is valid only in the perturbative regime.

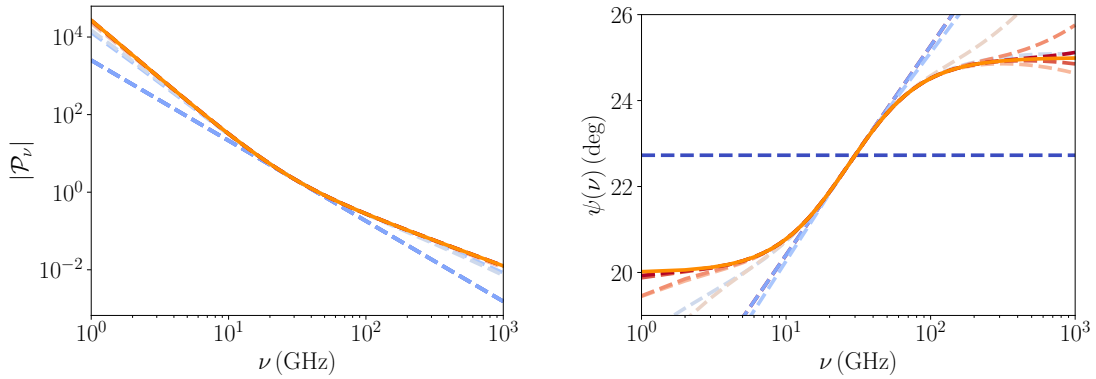


Figure 8.7: Modeling the SED distortions (left) and polarization angle spectral rotation (right) of the total signal of the two power-law model (orange) with the spin-moment expansion at different orders using the complex pivot correction (colored dashed lines from blue at order 1 to red at order 10). The dark blue dashed line represents the phase of \mathcal{W}_0 .

We can thus see that, while the real part of $\bar{\beta}^{\text{corr}}$ can be interpreted as a real correction to the spectral index, the imaginary part of $\bar{\beta}^{\text{corr}}$ can be interpreted as a first order frequency dependent correction to the polarization angle, such that one is now able to predict that

$$\psi(\nu) \simeq \psi(\nu_0) + \frac{\bar{\beta}_I}{2} \ln\left(\frac{\nu}{\nu_0}\right), \quad (8.28)$$

where $\psi(\nu_0)$ is the phase of \mathcal{W}_0 , i.e. the geometrical mean of the polarization angles $\arg(e^{2i\psi_1} + e^{2i\psi_2})$. As such, the complex spectral parameter corrections naturally take place in the framework of polarization. Note that, for more complex SEDs, the impact of a complex parameter can be more complicated than a frequency dependent phase correction, and can also include some correction to the SED itself (e.g. this would be the case for a complex temperature correction in $B_\nu(T)$ as treated below).

As displayed on Fig. 8.7, the spin-moment expansion allows to model both the SED distortions of the modulus $|\mathcal{P}_\nu|$, as for intensity, as well as the spectral rotation of the polarization angle. As I already discussed the SED distortions in Sec. 8.2.1, let us now focus on $\psi(\nu)$. I have plotted here the canonical SED with the intensity spectral index pivot $\bar{\beta}$ and an amplitude given by \mathcal{W}_0 in dashed dark blue. As expected, it simply gives a constant value for ψ , which is the geometrical mean $\tilde{\psi} = 22.5^\circ$. Replacing now the spectral index by $\bar{\beta}^{\text{corr}} = \bar{\beta} + \mathcal{W}_1^\beta \simeq -2.07 + 0.07i$. This allows for a first order correction of $\psi(\nu)$ (in dashed light blue), which is now a straight line tangent to the signal at ν_0 in the lin-log plane. The addition of the higher-order moments allows to bend gradually the expansion until it overlaps with the total signal. Note that, in this extreme case for which $\psi(\nu)$ shifts brutally from one value to another, the expansion requires a relatively large number of terms to accurately model the signal across the whole frequency range.

As a conclusion, let me stress here that these examples are "extreme" for the sake of providing a clear illustration of the problematic. The two power-laws have widely different angles, and considering only two layers makes the distortions conspicuous. Motivated astrophysical examples are expected to have milder distortions that can be treated with the few first terms of the moment expansion.

8.4.2 The paper: Objectives and results (in their full glory)

In the paper available in Appendix D.2, we introduce for the first time the spin-moment expansion in full generality, providing a consistent generalization of the moment expansion to polarization¹⁶. Illustrative examples are given as well as discussions of special cases.

Since I started working on the topic of moment expansion, I was curious on the possible generalization to polarization and its consequences. Such a generalization appeared as a necessity after our first work on component separation. The idea to use complex numbers and complex moments arised from discussions between Jens Chluba, Aditya Rotti and myself at the Moriond conference. After this meeting, I provided quickly some preliminary numerical and analytical applications which supported and guided our ideas, while many details were still missing. The final solution of the problem was found by Jens Chluba, who gave me the extremely highlighting example of the two power law case. He thus understood the consequences of the complex pivot correction as a phase correction. Starting from this more complete picture, I was responsible for the writing of the full draft, under the close supervision of Jens Chluba and Jonathan Aumont. I also provided all the numerical illustrations.

As we discussed in the previous section for two power-laws, the natural way to proceed is to treat linear polarization as a complex number. Taylor expansion should be performed on the modulus of the field, as in intensity, without treating the angles perturbatively. This way of thinking Q and U together as a complex number allows to understand properly how the coupled local variation of spectral parameters and polarization angles induces a spectral rotation of the total spinor in the complex plane, i.e. how the polarization angle can become frequency dependent as anticipated by [Tassis & Pavlidou \(2015\)](#) and observed in *Planck* data by e.g. [Pelgrims et al. \(2021\)](#) and [Ritacco et al. \(2023\)](#). Additionally, the common treatment of Q and U preserves the information about the correlation between the Stokes parameter in data analysis, providing a more complete description of the signal.

Following, the exact same logic as Sec. 8.2.2, the total polarized SED $\langle \mathcal{P}_\nu(\mathbf{p}) \rangle$, resulting from the mixing inside a beam and/or along the line of sight is given by

$$\langle \mathcal{P}_\nu(\mathbf{p}) \rangle = \int A(s) \varepsilon_\nu(\mathbf{p}(s)) e^{2i\psi(s)} ds = \int \mathbb{P}(\mathbf{p}, \psi) \varepsilon_\nu(\mathbf{p}) e^{2i\psi} d^N p d\psi \quad (8.29)$$

where we added the polarization angles ψ in the probability distribution. We kept the normalization $\int \mathbb{P}(\mathbf{p}, \psi) d^N p d\psi = \bar{A}$ for the probability distribution. It is then possible to Taylor expand the emissivity $\varepsilon_\nu(\mathbf{p})$ with respect to the each spectral parameter p_i around a constant pivot \bar{p}_i in Eq. 8.29. Regrouping the terms again, the spin-moment expansion

¹⁶In this work, the polarization angle ψ , is noted γ . The emissivity ε_ν is noted \hat{P}_ν and the frequency dependent angle $\psi(\nu)$ is noted ψ_ν .

takes the general form

$$\begin{aligned} \langle \mathcal{P}_\nu(\mathbf{p}) \rangle &= \mathcal{W}_0 \varepsilon_\nu(\bar{\mathbf{p}}) + \sum_i \mathcal{W}_1^{p_i} \partial_{p_i} \varepsilon_\nu(\mathbf{p})|_{\mathbf{p}=\bar{\mathbf{p}}} \\ &\quad + \frac{1}{2} \sum_{i,j} \mathcal{W}_2^{p_i p_j} \partial_{p_i} \partial_{p_j} \varepsilon_\nu(\mathbf{p})|_{\mathbf{p}=\bar{\mathbf{p}}} \\ &\quad + \dots \\ &\quad + \frac{1}{\gamma!} \sum_{i,\dots,k} \mathcal{W}_\gamma^{p_i \dots p_k} \partial_{p_i} \dots \partial_{p_k} \varepsilon_\nu(\mathbf{p})|_{\mathbf{p}=\bar{\mathbf{p}}}, \end{aligned} \quad (8.30)$$

where the spin-moments are the complex numbers¹⁷

$$\mathcal{W}_\gamma^{p_i \dots p_k} = \langle (p_i - \bar{p}_i) \dots (p_k - \bar{p}_k) e^{2i\psi} \rangle \quad (8.31)$$

and the complex amplitude

$$\mathcal{W}_0 = \langle e^{2i\psi} \rangle \quad (8.32)$$

keeping the same definition for the averages

$$\langle X \rangle = \int A(s) X(s, \psi) \, ds \, d\psi = \int \mathbb{P}(\mathbf{p}, \psi) X \, d^N p \, d\psi, \quad (8.33)$$

with the possible dependence of X in the polarization angles. As such, the formalism is the same as for intensity, with the additional subtlety that the weights are complex numbers, allowing for the rotation of $\langle \mathcal{P}_\nu(\mathbf{p}) \rangle$ in the complex plane. The interpretation of moments as statistical moments is further blurred by the factors of $e^{2i\psi}$, but a comparative analysis of the intensity and the polarization moments must be able to shed some light on the structure of the magnetic field.

The pivot correction of the spin-moment expansion is a complex number, which imaginary part can be understood as a first order correction to the polarization angle and contains additional SED distortions in the case of temperature. As such, the first order can not trivially be cancelled as in the case of intensity, or at the price of spectral parameters that must become complex numbers. Using this fact, we are able to provide simple expressions of $\psi(\nu)$, valid only in the perturbative regime ($\mathcal{W}_0 \gg \mathcal{W}_n^p$). These expressions represent the first general modeling of the spectral dependence of the phase of the astrophysical signal. Extra care should be taken when depolarization is too strong, as expressions can become divergent.

The effect of a complex spectral index in a power-law simply gives a rotation of the spinor in the complex plane proportional to $\ln(\nu)$, as given by Eq. 8.28. The effect of a complex temperature in the Planck law (Eq. 5.1) gives rise to richer and more complex physics. Let me however stress that, while the power-law dependence of the SED is an empirical model, the blackbody law is derived from first principles for a body radiating at thermal

¹⁷As in the paper (Appendix D.2), the spin-moments can be defined alternatively with a normalization by \bar{A} , allowing to express Eq. 8.30 in term of P_ν instead of ε_ν , highlighting the similarities with the intensity moment expansion. To my opinion however, this choice is slightly less intuitive and harder to use in practice. Another relevant normalization is to normalize all the spin-moments by \mathcal{W}_0 . However, as we stressed already in Sec. 8.4.1, doing so is viable only in the perturbative regime.

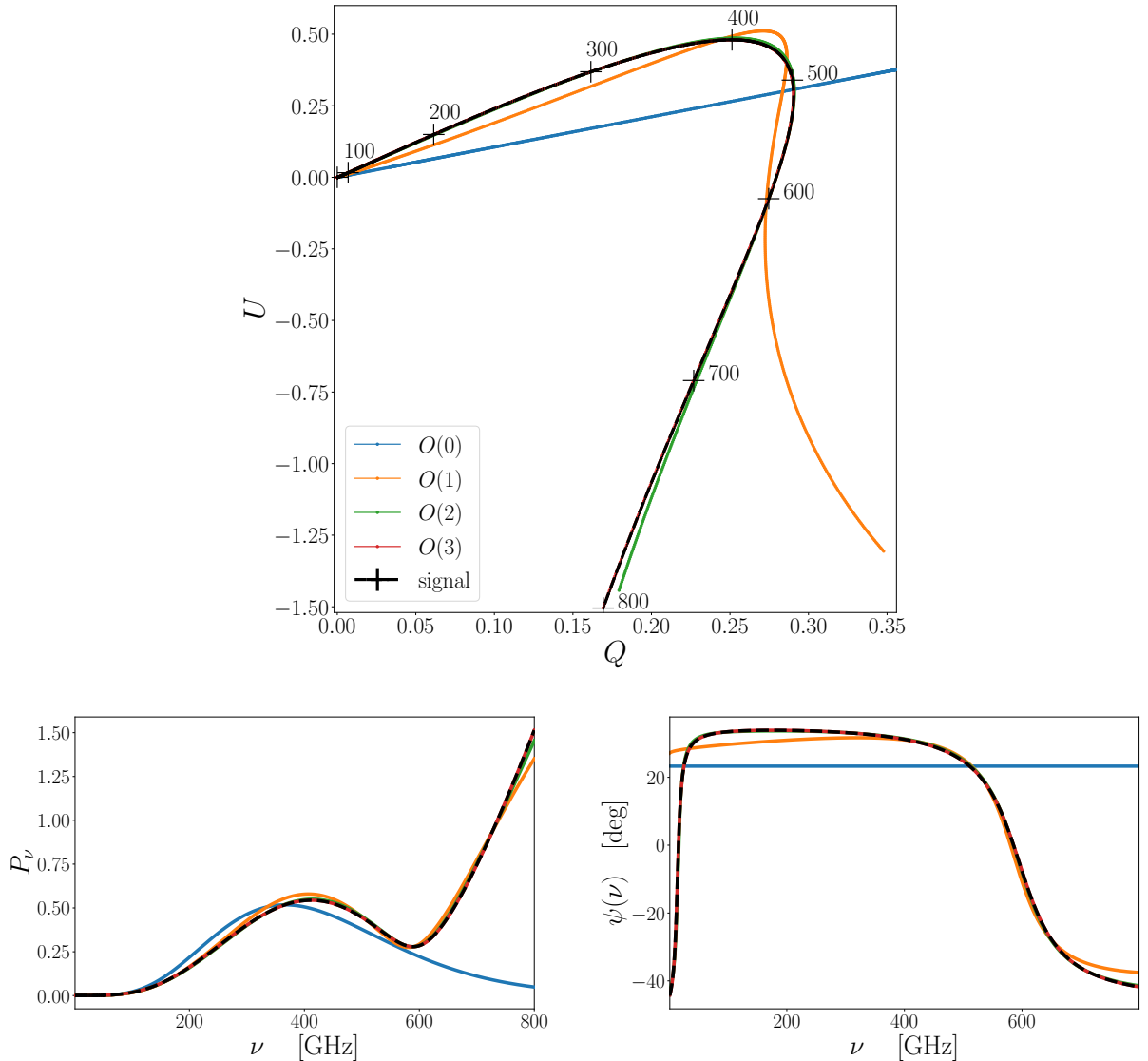


Figure 8.8: Application of the spin-moment expansion for a sum of two modified-blackbodies. The total signal is in black dashed line, while the best fit for the moment expansion is displayed at order zero (a single MBB) in blue, at order one in orange, order two in green and order three in red. The spinor P_ν is showed in the complex plane (Q, U) (*Upper panel*). Black crosses mark the steps of 100 GHz on the signal. The values of frequencies are indicated above the crosses in GHz. The corresponding polarized intensity P_ν (*Bottom left*) and polarization angle ψ_ν (*Bottom right*).

equilibrium. As such, this component is expected to manifest itself at some level in all astrophysical phenomenon with a thermal radiation counterpart, from the SED distortions of dust to the spectral distortions of the CMB. Considering then that some mixing leads to the replacement $\bar{T} \rightarrow \bar{T}^{\text{corr}} = \bar{T}_R + i\bar{T}_I$, the blackbody SED becomes¹⁸

$$B_\nu(\bar{T}^{\text{corr}}) = \frac{2h\nu^3}{c^2} \frac{1}{e^{x_R+i x_I} - 1}, \quad (8.34)$$

¹⁸This replacement is only possible in the perturbative regime as \bar{T}^{corr} is extracted from the moment expansion as $\bar{T}_R + i\bar{T}_I = \bar{T} + \mathcal{W}_1^T / \mathcal{W}_0$.

with¹⁹

$$x_R = \frac{h\nu}{k_B} \frac{\bar{T}_R}{\bar{T}_R^2 + \bar{T}_I^2} \simeq \frac{h\nu}{k_B \bar{T}_R}, \quad x_I = -\frac{h\nu}{k_B} \frac{\bar{T}_I}{\bar{T}_R^2 + \bar{T}_I^2} \simeq -\frac{h\nu \bar{T}_I}{k_B \bar{T}_R^2}, \quad (8.35)$$

from which one can derive²⁰

$$B_\nu(\bar{T}^{\text{corr}}) = \frac{2h\nu^3}{c^2} \frac{e^{2i\Delta\psi_\nu}}{\sqrt{(e^{x_R} - 1)^2 + 2e^{x_R} [1 - \cos(x_I)]}}. \quad (8.36)$$

The spectral dependent correction to the polarization angle is given by $\Delta\psi_\nu = x_I/2 \propto \nu$ at high frequencies (For a discussion see Sec. 4.4 of the paper in Appendix D.2). The modulus of Eq. 8.36 is a classical blackbody with an extra correction at the denominator accounting for SED distortions (which is $\simeq e^{x_R} x_I^2$ if $\bar{T}_I \ll \bar{T}_R$). As such, while in intensity the correction brought by the first order moment could simply be interpreted as a correction to the mean temperature, in polarization the first order temperature distortions are generating a linear rotation of the complex modified blackbody with frequency, as well as some spectral distortions of the black-body.

As illustrations, the three following SEDs are studied in great detail in the paper: power-law, gray-body and modified blackbody. For each case, simple numerical examples are given. In these examples, I fitted the moment coefficients over the signal using the LMFIT²¹ software, and verified that the best fit were matching with the analytical predictions of our formalism. For example, on Fig. 8.8, the spin-moment expansion has been fitted over the sum of two modified blackbodies with parameters $A_1 = A_2 = 1$ (arbitrary units), $\beta_1 = 2$, $\beta_2 = 1$, $T_1 = 5\text{ K}$, $T_2 = 70\text{ K}$, $2\psi_1 = 72^\circ$, $2\psi_2 = -90^\circ$. In the complex (Q, U) plane, the effect of the distortions appears as a rotation and stretching of \mathcal{P}_ν with frequency (black dashed), while the canonical SED of the MBB can only make a straight line (blue). This example is extreme to say the least, and is nonetheless very well modeled by the spin-moment expansion in few terms.

Finally we conclude the paper by presenting natural generalizations of the formalism in the spherical harmonics domain and when beam and bandpass effects are included. As a conclusion, voxel-level SED variations are proven to leave the formalism unchanged, while Faraday rotation presents a trickier challenge that can be dealt with only when doing drastic simplifying assumptions.

8.4.3 Impact, limits and and outlooks

In the above work, we propose a new modeling of the polarized signal that can readily be used for Galactic physics, foreground modeling and component separation. I have worked and I am still working on possible applications within this new framework. While the formalism might seems difficult to apprehend mathematically, it gives a deep understanding of the consequences of mixing.

¹⁹Keeping in mind that $1/(\bar{T}_R + i\bar{T}_I) = (\bar{T}_R - i\bar{T}_I)/(\bar{T}_R^2 + \bar{T}_I^2)$

²⁰To do so, compute the modulus of Eq. 8.34 as $|B_\nu| = \sqrt{B_\nu^* B_\nu}$ and the argument as $2\Delta\psi_\nu = \arctan(\text{Im}(B_\nu)/\text{Re}(B_\nu))$ with $\text{Re}(B_\nu) = (B_\nu + B_\nu^*)/2$ and $\text{Im}(B_\nu) = (B_\nu - B_\nu^*)/(2i)$, leading precisely to $2\Delta\psi_\nu = \arctan(e^{x_R} \sin x_I / (e^{x_R} \cos(x_I) - 1))$.

²¹<https://github.com/lmfit/lmfit-py/>

Additionally, I believe that this work brings further clarification on the proper use of moment expansion for polarized signal, giving a robust theoretical framework ready to be used, in which the spin-moments can be directly related to the statistics of the spectral parameters and polarization angles. Previously, the intensity moment expansion was applied directly on real quantities describing polarization. For example, Ichiki et al. (2019) proposed to use a first order moments for Q and U in temperature. In the meanwhile, other works – including mine – were using the intensity moment expansion directly on the polarized power-spectra (e.g. on BB in Azzoni et al. (2021); Vacher et al. (2022a)), before the polarized formalism was formally settled. Doing so forgets about the geometrical nature of polarization and its relation with the ISM physics at its origin. The goal of this paper (and the next one) was thus to justify this choice and clarify its limits while putting forward all the new features unique to the polarized signal.

One other question remains: how much information can be recovered about the ISM physics from the moment coefficients. Moments undoubtedly "compress" the information of the underlying foreground complexity, but in principle it should be possible to infer statistical properties relevant for Galactic physics from it, as the 3D distribution of spectral parameters and magnetic field orientations, and this point must be further addressed (along that question see e.g. McBride et al. (2023)). I am currently co-leading a study with Vincent Guillet (LUPM) in which the spin-moments are used in map space to recover the dust statistical properties in *Planck* data. We try to address how beneficial is the complex number approach on that regard. The results, to be published soon, are encouraging this approach, showing that using a MBB with complex spectral parameters reproduces the dust behaviour at the residual level (Guillet et al., 2023). Along that line, I am also using the spin-moments to create some foreground template models with extra 3D complexity. In the long term, we intend to propose these models to the PySM team such that they can be used by the CMB community for component separation.

8.5 Applying the spin-moments at the E - and B -modes level

8.5.1 Context: The indispensable E - and B -modes and their distortions

The previous work focused mainly on Q and U and the E - and B -modes are only briefly mentioned in harmonic space (in Sec. 5.1 of the paper). However, the introduction of the spin-moments raised the question of our real understanding of the moment expansion at the E - and B -modes level and my feeling was that we were still missing some pieces in order to clearly see the full picture. Providing a clear understanding of the moment expansion for E - and B -modes in real and harmonic space is however a most important matter, as most of the contemporary cosmological analysis are done at the polarization power-spectra level: the tensor-to-scalar ratio r is measured with BB (and EE), while signatures of cosmic birefringence are investigated in EB (See Chap. 5). In the meanwhile, some apparently unexplainable spectral behavior of the dust E - and B -modes was found in *Planck* data in Ritacco et al. (2023), which required an interpretative framework. Indeed, I had the chance to collaborate on this work, where I could provide some expertise on the moment expansion

and some feedback on the corresponding section of the draft. This analysis witnessed the discovery of different spectral behavior for the dust residual E - and B -modes in *Planck* data. While such a fact did not appear as problematic, we had no way to properly interpret and understand it. Debates at APC and LPENS between François Boulanger, Jonathan Aumont and myself, involving filamentary gedankenexperiment, could not clearly settle the argument.

We should hence try to answer the following questions: Does the mixing simply distort the EE , BB and EB spectra as intensities or is there more to it and how can we relate the distortions occurring in the E - and B -space with the ones of \mathcal{P}_ν ?

8.5.2 The paper: Objectives and results

To clarify the situation, we will have to start from the spin-moment expansion in map space and propagate it to the E - and B -modes and their angular power spectra in the clearest possible way. Let me sketch here our main results, while the whole paper can be found in Appendix D.3. We learnt from the spin-moment expansion that complex numbers provided a very powerful tool in order to understand the polarization signal and its distortions, as well as the inter-relation between the different observable quantities. Can we use the same trick for E - and B -modes? Thankfully the answer is yes. After numerous trial and errors, I figured that the way out is provided by the relation²²

$$E + iB = -\bar{\partial}^2(Q + iU), \quad (8.37)$$

where $\bar{\partial}$, defined formally in Appendix B, is an operator acting like a spatial derivative on the sky, mixing derivatives of Q and U to obtain E and B (Goldberg et al., 1967)²³. This relation is remarkable as it provide a new complex number $\mathcal{S} = E + iB$, which can be directly extracted from $\mathcal{P} = Q + iU$. It is hence now straightforward to propagate our spin-moment expansion, simply by inserting Eq. 8.30 in the right hand side of Eq. 8.37, and let $\bar{\partial}$ act two time on it. $\bar{\partial}$ will leave the frequency dependent functions untouched, such that the moment keep the same structure, but it will mix and transform the spin-moments in a non trivial way, such that the complex moments of \mathcal{S} will be composed of a mixture of the spatial derivatives of the real and imaginary part of the spin-moments. Having an expansion in $E + iB$, similar to the one we had for $Q + iU$, we are lead to reach the same conclusion: while the mixing of both different spectral parameters and spectral parameters (named "polarized mixing") induces a frequency rotation of $\mathcal{P}_\nu = Q + iU$ in the complex plane, predictable by the spin-moments, it must also induce a rotation of $E + iB$ in the complex plane, predictable by the spin-moments: from mixing of polarized signals, E -modes transform into B -modes and vice-versa.

A clearer intuition of this can be found by considering an infinite filament in front of a background as depicted on the left panel of Fig. 8.10. At a given frequency (orange), the polarization angles of the filaments and the background can be perpendicular, which is known to be a pure E case (Zaldarriaga, 2001). However, if the filament and the background have

²² E and B here are the same as the E - and B -modes used in cosmology up to a rescaling factor in harmonic space. To simplify the discussion we will not make the distinction here. For clarifications, see Appendix B.

²³ $\bar{\partial}$ further acts as a spin ladder operator, transforming the spin-2 field $Q + iU$ into a complex scalar field $E + iB$. For more, see again Appendix B.

different spectral parameter, we know that some spectral rotation of the polarization angle must occur in the filament, such that, at another frequency (blue), the pattern will change. At this second frequency, the signal can not be pure E and must also have a B -mode component, and as such, the E/B ratio must change with frequency.

Another way to understand this phenomenon, is that, as for Q and U , polarized mixing should produce different SED (i.e. different values for the moments) for the E - and B -modes expansions, such that, in map space $E_\nu \neq B_\nu$ and E_ν/B_ν must become a frequency dependent quantity. At the power spectra level, this implies that EE , EB and BB have different spectral behaviors, such that EE/BB should be a frequency dependent quantity. Additionally, the polarized mixing can produce and deform the EB signal, thus threatening the claims for the detection of the cosmic birefringence. Indeed, one should be extremely careful when trying to infer the (yet unknown) spectral behavior of dust EB , as it can not be recovered from the properties of the other spectra.

Following the spin-moment direction all the way to the \mathcal{D}_ℓ space, we were able to recover formally expressions similar to the ones introduced in intensity by [Mangilli et al. \(2021\)](#) (See Eq. 8.18) and already used on BB in [Azzoni et al. \(2021\)](#); [Vacher et al. \(2022a\)](#). The pivot spectral parameter, which is a real number, naturally becomes a ℓ -dependent quantity after correction of the first order term, which was an "ad-hock" assumption of [Mangilli et al. \(2021\)](#)²⁴. We thus provide the missing link with the map space, such that E - and B -moment amplitudes can be recovered from the values of the spin moments in every pixel of a map. The spin moment themselves can be derived from the spectral parameters and polarization angles distributions.

We further illustrate the existence of these effects and the possibility to model them with a spin moment expansion in a numerical toy model of filament in front of a background, and in the PySM models.

The toy model filament is illustrated on the left panel of Fig. 8.10. Both the background (bg) and the filament (fl) are emitting with a MBB with $\beta^{\text{fl}} = 1.8$, $\beta^{\text{bg}} = 1.5$, $\bar{T} = T^{\text{fl}} = T^{\text{bg}} = 20$ K, and $A^{\text{fl}} = A^{\text{bg}} = 1$. As a first sanity check, I confirmed in Fig. 8.9 that the analytical predictions given by the spin-moment expansion were able to model the distorted signal at 100 GHz in one pixel of the filament. This example further validate and illustrate the results given in Sec. 8.4.1: on the left panel, the total polarized intensity is distorted from 100 to 400 GHz for different values of the polarization angle of the filament ψ^{fl} , and the distortions are well modeled by the spin-moment expansion up to order 2. The hierarchy between the contribution of the spin-moments is broken due to depolarization (See Sec. 8.4.1 and 8.4), which drastically reduces the value of \mathcal{W}_0 when ψ^{fl} takes large values compared to the one of the background $\psi^{\text{bg}} = 0^\circ$. On the right panel, the polarization angle difference between 100 and 400 GHz also appears to be well modeled for every value of ψ^{fl} by the spin-moment expansion at order 2, while the correction brought by the complex β (Eq. 8.28) is valid only in the perturbative regime.

Turning to the polarized angular power-spectra on the right panel of Fig. 8.10, we can see

²⁴Note however that, as the value of \mathcal{W}_1^p is changing from pixel to pixel, it is not possible to find a pivot value that would cancel the first order everywhere, thus $\mathcal{D}_\ell^{\mathcal{W}_1^p \times \mathcal{W}_1^p}$ does not vanish. We already mentioned this point in Sec. 8.3.

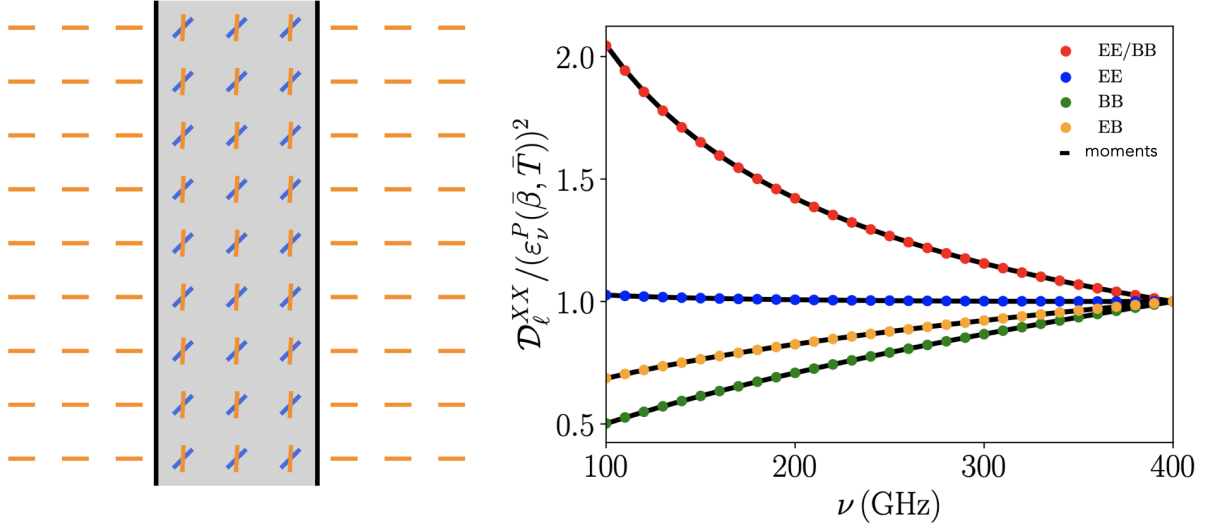


Figure 8.9: Left: Diagram of the toy model composed of an infinite filament (grey) over a background (white). The orientation of the $\psi(\nu)$ field is represented with color bars at two different frequencies: ν_1 (orange) and ν_2 (blue). Right: Spectral dependence of the toy model filament polarized power spectra. Left: Polarized power spectra divided by the pivot-modified blackbody squared for the special case of $\psi^{\text{fil}} = 30^\circ$. All spectra are normalized with respect to their value at ν_0 . The signals are shown in color: EE/BB (red), EE (blue), BB (green), and EB (orange). The black dashed lines were recovered by deriving the moment power spectra from the spin-moment maps.

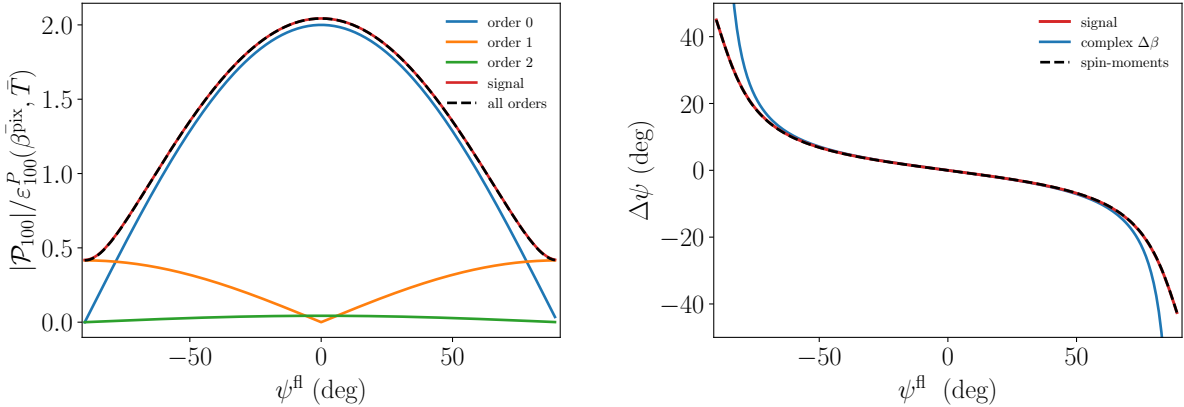


Figure 8.10: Total polarization spinor in a single pixel of the filament of the toy model for $\psi^{\text{bg}} = 0^\circ$ and various values of the filament polarization angle ψ^{fl} . Left: Modulus of the total signal at 100 GHz normalized by the pivot MBB (red) and modulus of the analytical derivation from the spin-moment expansion up to second order (black dashed line). The modulus of each term is displayed: order 0: $|\mathcal{W}_0|$ (blue), order 1: $|\mathcal{W}_1^\beta \ln(100/400)|$ (orange), and order 2: $|0.5\mathcal{W}_2^\beta \ln(100/400)^2|$ (green). Right: Difference of the polarization angles between the two frequencies. Signal (red), prediction from the complex $\Delta\beta$ correction $0.5 \text{Im}(\mathcal{W}_1^\beta / \mathcal{W}_0) \ln(100/400)$ (blue) and from the spin-moment expansion up to second order (black dashed line).

from the colored scatter points that all the measured spectra are distorted away from the pivot MBB (these spectra were extracted using NAMASTER on a flat patch). As we antic-

ipated, the EE/BB ratio has become a frequency dependent quantity. Furthermore, from the value of ψ , β , A and T in every pixel, I computed the spin-moment map (analytically) and derived from it the prediction for the amplitude of moment angular power-spectra. These predictions (in black), matches perfectly the measured spectra, validating our derivation and the predictive power of the moment expansion in harmonic space to account for the consequences of polarized mixing.

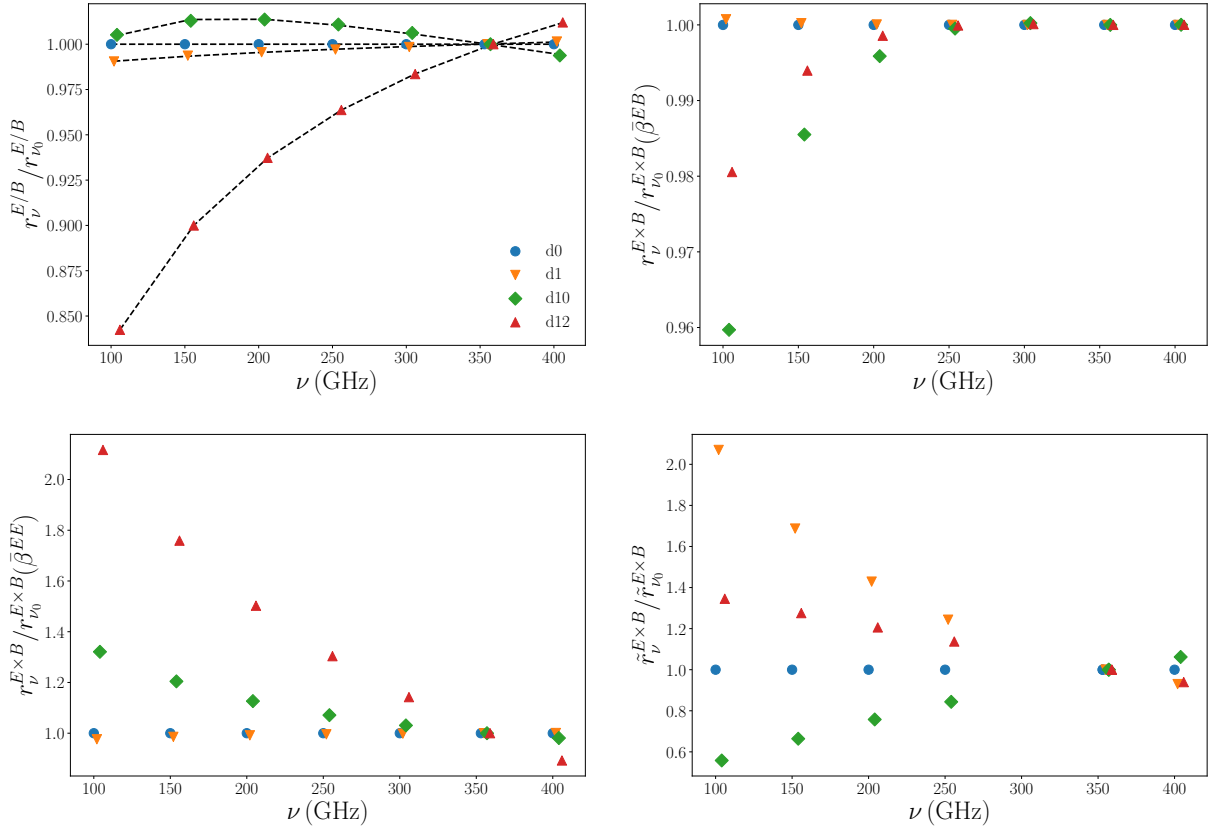


Figure 8.11: Graph of $r_{\ell,\nu}^{E/B}$, $r_{\ell,\nu}^{E \times B}$ and $\tilde{r}_{\ell,\nu}^{E \times B}$ in a single bin of ℓ and normalized at $\nu_0 = 353$ GHz for different PySM dust models. The shapes are defined as follows: d0 (blue circles), d1 (orange reversed triangles), d10 (green diamonds), and d12 (red triangles).

We now want to show that the predicted consequences of polarized mixing are also present in the PySM dust models, ensuring that our considerations go beyond abstract and simple theoretical examples. These models have been introduced in Sec. 6.5. To do so, we define the three ratios:

$$r_{\ell,\nu}^{E/B} = \frac{\mathcal{D}_\ell^{EE}}{\mathcal{D}_\ell^{BB}}, \quad r_{\ell,\nu}^{E \times B} = \frac{\mathcal{D}_\ell^{EB}}{\epsilon^2(\bar{\beta}, \bar{T})}, \quad (8.38)$$

and

$$\tilde{r}_{\ell,\nu}^{E \times B} = \frac{\tilde{\mathcal{D}}_\ell^{EB}}{\mathcal{D}_\ell^{EB}} \quad \text{with} \quad \tilde{\mathcal{D}}_\ell = \frac{\mathcal{D}_\ell^{EE} \mathcal{D}_\ell^{TB}}{\mathcal{D}_\ell^{TE}}. \quad (8.39)$$

The first one, $r_{\ell,\nu}^{E/B}$ simply quantifies the spectral dependence of the E/B ratio. The second one $r_{\ell,\nu}^{E \times B}$ quantifies distortions of the EB signal compared to the emissivity of a modified blackbody squared with spectral parameters $\bar{\beta}$ and \bar{T} . Finally $\tilde{r}_{\ell,\nu}^{E \times B}$ quantifies the deviation

of the EB spectra compared the commonly used approximation of $\tilde{\mathcal{D}}_\ell$ introduced in Clark et al. (2021) and expected to be valid at a given frequency.

In Fig. 8.11, I computed the values of these three quantities for different PySM models. Power spectra were computed again using NAMASTER in a single multipole bin from $\ell_0 = 2$ to $\ell_{\max} = 200$ at a HEALPY resolution of $N_{\text{side}} = 128$. In order to observe a large patch of the sky while still avoiding the central Galactic region, we used the *Planck* GAL080 raw mask with $f_{\text{sky}} = 0.8$ available on the [Planck Legacy Archive](#). We subsequently performed a NAMASTER C2 apodization with a scale of 2° . Both the E - and B -modes were purified during the spectra computations. Overall:

- $r_{\ell,\nu}^{E/B}$ is represented on the top left panel of Fig. 8.11. We see that, despite for d0 which has constant spectral parameters, this ratio is changing with frequency by few percents. Observing this ratio hence provide a model independent (no assumption is made on the SED) probe of the existence of polarized mixing. Seeing its variation with frequency is the direct signature that averages are made over regions with different polarization angles and spectral parameters. From the moment expansions of E and B in β , it is possible to infer the simple three parameters modeling as

$$r_{\ell,\nu}^{E/B} \simeq A_\ell^{E/B} \left(\frac{\nu}{\nu_0} \right)^{\Delta\beta_\ell^{EB}} \left(1 + \delta_\ell \ln \left(\frac{\nu}{\nu_0} \right)^2 \right). \quad (8.40)$$

$A_\ell^{E/B}$ is the amplitude of the variation of E/B , $\Delta\beta_\ell^{EB}$ is the difference of corrected spectral index pivot between E and B and δ_ℓ represents the remaining moment contribution of the E - and B -modes. This model has been fitted on the curves in black dashed lines and reproduces properly the trend of the variations.

- $r_{\ell,\nu}^{E\times B}$ is represented on the top right panel of Fig. 8.11. To compute it, I took the best fit of $\bar{\beta}$ and \bar{T} over the computed EB spectra. Deviations of few % from the MBB are witnessed, which do not appear as dramatic for birefringence analysis. However, in practice, one do not have enough sensitivity to directly fit the spectral parameters on the dust EB spectrum and a proxy must be found to estimate it. On the bottom left panel of Fig. 8.11, I did the same computation but fitting the spectral parameters of the MBB on the EE spectra. $r_{\ell,\nu}^{E\times B}$ now vary strongly, by $\sim 40\%$ for the d10 model and more than a factor of 2 for the d12 model. As such, the spectral properties of the other dust spectra, as EE , can not be used safely as proxies to characterize the spectral dependence of EB .
- $\tilde{r}_{\ell,\nu}^{E\times B}$ is displayed on the bottom right panel of Fig. 8.11. Here again, large variations are witnessed with frequency, signature that the spectral behavior of EB can not be inferred from the ones of EE , TB and TE .

Let me however stress here that these examples are illustrative and the results are expected to change drastically depending on the sky fraction and the multipole range considered.

Even though their impact on cosmological analysis is yet unclear, the consequences of polarized mixing are thus present at the E - and B -mode level in all the realistic dust models used by the CMB community. The spin-moment expansion allows to have a rich understanding on these consequences and provide a minimal approach to model them.

8.5.3 Impact, limits and outlooks

In this work and the previous one, we demonstrated the need for a clear formalization of moment expansion to polarization. Going beyond a dry mathematical tool, the spin-moments allows to explain and model previously known consequences of polarized mixing, and to discover new ones as the E - B spectral rotation. In two papers, we have thus been able to connect all the dots between the spectral parameters and angle distributions in the sky to the amplitude of the moments in \mathcal{D}_ℓ space.

While [Ritacco et al. \(2023\)](#), provided the first experimental hint of the consequences of the polarized mixing that we are highlighting, further work need to be done to quantify how other instruments as *LiteBIRD*, with greater sensitivities would be able to detect such effects. In the end, the EE/BB spectral dependence should not have any impact on component separation when EE and BB are treated independently. However, it should be carefully modeled when both are treated together (e.g. when exploring correlations between the optical depth of reionization τ and r). A deeper investigation is required to see if and how this would be impacting (e.g. for the *LiteBIRD* instrument).

Finally, we showed in this work that the dust EB signal can be distorted away from the local SED by polarized mixing, and perhaps more critically that the resulting EB will not behave as EE or BB (or $TB \times EE/TE$). This could have dramatic consequences when looking for the presence of cosmic birefringence in the CMB. However, our paper simply gives a word of caution on that regard, but do not quantify the potential impact on contemporary cosmic birefringence studies. A detailed study on that matter still need to be performed. On this regard, and in collaboration with Susan Clark and Ari Cukierman (KIPAC), we are investigating if and how the parity violating spectra of the dust signal could be related to the polarized mixing.

8.6 Beyond Gaussianity: The Wavelets

8.6.1 Coupling between scales and the problem of non gaussianities

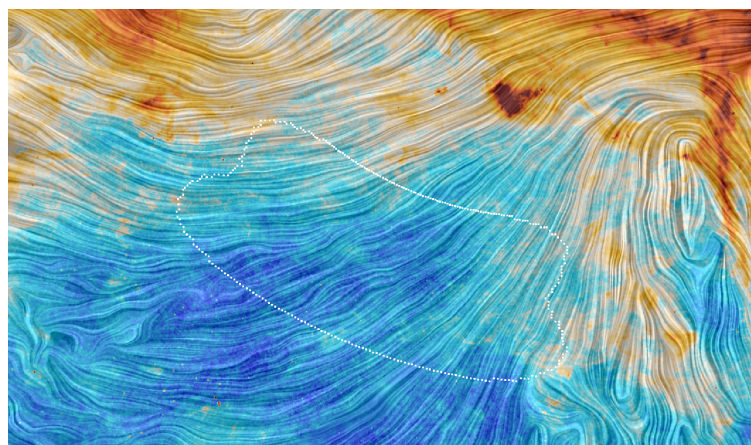


Figure 8.12: BICEP field (in dashed line) viewed by the Planck satellite [ESA/Planck collaboration](#).

In Fig. 8.12, the surrounding region of the *BICEP* field is displayed, as seen by *Planck*. One can witness the very characteristic drapery and filamentary pattern inherited from the GMF structure and the omnipresence of structures as clouds and clumps. As stressed already in Chap. 6, this spatial distribution is very different from a Gaussian random field as the CMB (Fig. 5.2). The turbulent and magnetized ISM fluid introduces coupling between scales and non-linear behaviors. On a flat patch, the Fourier transform is not able to properly account for all the statistical properties of the signal anymore, and new tools must be developed to characterize the complexity witnessed on the plane of the sky. Indeed, the plane waves decomposition of the Fourier transform loose the information about the spatial localization of the structure and possible information on the coupling between the modes \mathbf{k} , which are treated independently. While both are strongly intertwined, the problem of the spatial modeling of dust complexity is by nature very different from the spectral modeling. Indeed, when aiming to model the SED of the foreground signal, one usually have a few number of points, given by the number of bands of the instruments (e.g. 15 for *LiteBIRD*). As such, a minimal approach as the moments expansion is welcome. For the spatial distribution, one needs to model the distribution of dust across a large number of pixels making the map, and a lot more degrees of freedom are required and allowed.

One promising way to model the spatial complexity of foregrounds is given by machine learning models, often based on neural networks (Krachmalnicoff & Puglisi, 2021). The downside of this approach is that the models need to be trained, while there exists only few high resolutions observations of the ISM. Another major problem is that such models are rarely interpretable, and it is impossible to recover physical information from them. Another approach is to use alternative statistical tools to decompose the signal, as chosen by the wavelet scattering transform (WST) (Mallat, 2011). Doing so generalizes and expands the toolbox of the power-spectra introduced in Chap. B. It does not need any training phase and is highly interpretable.

8.6.2 The scattering transform and non-Gaussian signals

The proposal of the WST framework is to build new statistics from a map by convolution with directional wavelets (Mallat, 2011). The signal can be decomposed in scattering coefficients, which give a low-variance and low-dimensional description of non-Gaussian processes.

Consider an image x defined on a grid of pixels of size $M \times N$. x can be real or complex valued, and thus describes the intensity or polarized signal on a patch of the sky. A wavelet ψ is a localized waveform with zero mean, used as a bandpass filter. An original or *mother* wavelet must first be introduced. Depending on the problem under consideration, different type of mother wavelet can be considered. For its generality, the Morlet wavelet, given by a plane wave modulated by a Gaussian envelope is often considered

$$\psi(\mathbf{r}) = \alpha(e^{i\mathbf{k}_0 \cdot \mathbf{r}} - \beta)e^{-|\mathbf{r}|^2/2\sigma^2}, \quad (8.41)$$

where α and β are adjusted such that the spatial integral of $\psi(\mathbf{r})$ vanishes over the map and \mathbf{k}_0 and σ are respectively the wave-vector and the standard deviations associated to the plane wave and the Gaussian envelope. From this mother wavelet, it is possible to build a set of daughter wavelets using dilations and rotations . The set of daughter wavelets $\psi_{j\theta}$ is

thus constructed from $\psi(\mathbf{r})$ as

$$\psi_{j\theta}(\mathbf{r}) = 2^{-2j}\psi(2^{-j}\mathcal{R}(\theta)^{-1}\mathbf{r}), \quad (8.42)$$

where j is the index quantifying the dilation and \mathcal{R} is the rotation matrix by an angle θ .

One can now use this set of wavelets to convolve the original map x under consideration. This way, it is possible to construct the so-called *scattering coefficients*:

$$S_0 = \langle x \rangle \quad \text{if } x \in \mathbb{R}^{M \times N} \quad (8.43)$$

$$S_0 = \langle |x| \rangle \quad \text{if } x \in \mathbb{C}^{M \times N} \quad (8.44)$$

$$S_1(j_1, \theta_1) = \langle |x \star \psi_{j_1, \theta_1}| \rangle, \quad (8.45)$$

$$S_2(j_1, \theta_1, j_2, \theta_2) = \langle ||x \star \psi_{j_1, \theta_1}| \star \psi_{j_2, \theta_2}| \rangle, \quad (8.46)$$

...

Here, \star represents the convolution and $\langle \dots \rangle$ the average over the map. All scattering coefficients are real numbers, capturing statistical properties of the whole map. They can also be computed locally using an extra convolution with a bandpass filter, allowing to select specific regions. From these scattering coefficients, it is possible to define the normalized coefficients, easier to interpret and use in practice:

$$\bar{S}_0 = S_0 \quad (8.47)$$

$$\bar{S}_1(j_1, \theta_1) = \frac{\langle |x \star \psi_{j_1, \theta_1}| \rangle}{S_0}, \quad (8.48)$$

$$\bar{S}_2(j_1, \theta_1, j_2, \theta_2) = \frac{\langle ||x \star \psi_{j_1, \theta_1}| \star \psi_{j_2, \theta_2}| \rangle}{S_1(j_1, \theta_1)}, \quad (8.49)$$

...

\bar{S}_0 is simply the mean value of the map (or the mean of the modulus for complex fields). $\bar{S}_1(j_1, \theta_1)$ quantifies the amplitude of the normalized field $x/\langle x \rangle$ in the oriented scale (j_1, θ_1) . While it is similar to the power spectra it can *not* be identified with it in general. $\bar{S}_2(j_1, \theta_1, j_2, \theta_2)$, measures the coupling between the two oriented scales (j_1, θ_1) and (j_2, θ_2) (for a complete and pedagogical introduction see [Régaldo-Saint Blancard, 2021](#)).

Finally, using symmetries and regularities in the properties of the scattering coefficients, it is possible to introduce the reduced wavelet scattering transform (RWST [Allys et al., 2019](#)). Without further justification, we define them as the coefficients in the following decomposition

$$\log_2(\bar{S}_1(j_1, \theta_1)) = \hat{S}_1^{\text{iso}}(j_1) + \hat{S}_1^{\text{aniso}}(j_1, \theta_1) \cos(2[\theta_1 - \theta^{\text{ref},1}(j_1)]), \quad (8.50)$$

$$\begin{aligned} \log_2(\bar{S}_2(j_1, \theta_1, j_2, \theta_2)) &= \hat{S}_2^{\text{iso},1}(j_1, j_2) + \hat{S}_2^{\text{iso},2}(j_1, j_2) \cos(2[\theta_1 - \theta_2]) \\ &\quad + \hat{S}_2^{\text{aniso},1}(j_1, j_2) \cos(2[\theta_1 - \theta^{\text{ref},2}(j_1, j_2)]) \\ &\quad + \hat{S}_2^{\text{aniso},2}(j_1, j_2) \cos(2[\theta_2 - \theta^{\text{ref},2}(j_1, j_2)]) \end{aligned} \quad (8.51)$$

where the "iso" coefficients are independent of the orientation, while the "aniso" are not. $\theta^{\text{ref},1}$ and $\theta^{\text{ref},2}$ are reference angles used to parametrize the model. As such, the \bar{S}_1 and \bar{S}_2

coefficient can be decomposed in sets of \hat{S}_1 and \hat{S}_2 coefficients which are easier to interpret. Given a map x these coefficients can be immediately computed using the PYWST python package²⁵.

The RWST were introduced in [Allys et al. \(2019\)](#), and demonstrated to provide a very powerful and interpretable framework in order to characterize the non Gaussian emission of the complex ISM signal. As an illustration we displayed in Fig. 8.13 the $\hat{S}_2^{\text{iso}}(j_1, j_2)$

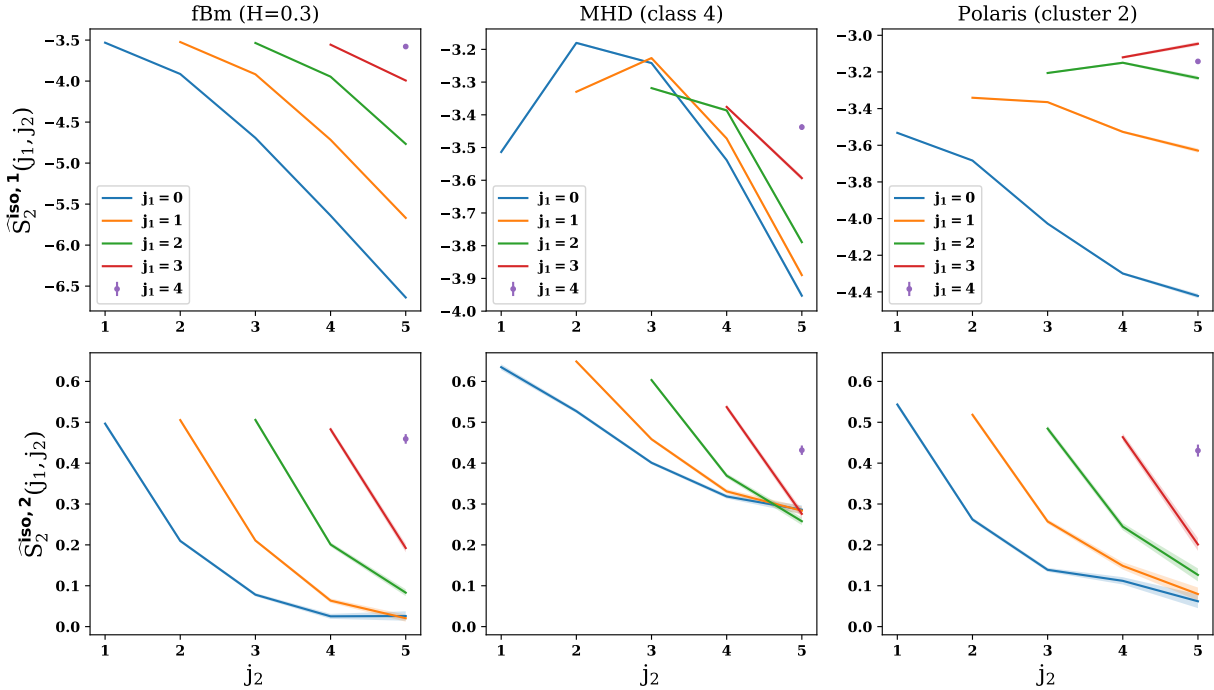


Figure 8.13: $\hat{S}_2^{\text{iso},1}(j_1, j_2)$ and $\hat{S}_2^{\text{iso},2}(j_1, j_2)$ coefficients evaluated on a Brownian random field (fBm), a MHD simulation of the ISM, and observational data of the Polaris region. From [Allys et al. \(2019\)](#).

coefficients from [Allys et al. \(2019\)](#), in three different cases: a Brownian random field (fBm), expected to be Gaussian and scale invariant, a MHD simulation, expected to reproduce the turbulent structure of the ISM, and some astrophysical observations of the Polaris region. The x -axis represents the different values of j_2 while the different colored curves represent the different values of j_1 . Contrarily to the power-spectra, the smaller values of j_i represent the smallest scales, while the greater values represent the largest scales. By exploiting their differences, the WST and the RWST coefficients can characterize and identify the presence of non-Gaussianities in a field. Some hints that can be followed are:

- With identical power-spectra, a non-Gaussian field is expected to display stronger values for the \bar{S}_2 and \hat{S}_2 coefficients than a Gaussian one. As the power-spectra can be expressed as a quadratic sum of the \bar{S}_1 and \hat{S}_2 coefficients, a non-Gaussian field is thus also expected to have lower values for the \bar{S}_1 and \hat{S}_1 coefficients than a Gaussian one.
- Additionally, as seen for the fBm, the \hat{S}_2 coefficients are expected to decrease brutally

²⁵<https://github.com/bregaldo/pywst>

with the scale j_2 , such that no correlation between scales exist on large scales. A very typical feature of Gaussian field is also that $\hat{S}_2^{\text{iso},1}$ and $\hat{S}_2^{\text{iso},2}$ can be recovered one from the other using a dilation. For MHD and Polaris, the damping of the $\hat{S}_2(j_2)$ curves is less strong. Additional $\hat{S}_2^{\text{iso},1}$ for the MHD case is displaying a bump, before decreasing, signature of non Gaussianity and correlation between intermediate scales.

- The $\hat{S}_2^{\text{iso},2}$ coefficient is expected to probe the presence of filamentary structure. It is hence very rapidly decreasing with j_2 in the case of fBm, while it decreases slowly and/or reaches a plateau in the case of MHD and Polaris.
- The fact that the $\hat{S}_2(j_2)$ curves repeat themselves identically for every value of j_1 , as it is the case for fBm, translates a scale invariant behavior. For MHD and Polaris, the curves intersect or deviate from each others, displaying a behavior different from scale invariance.

8.6.3 Synthesis, denoising and wavelet phase harmonics

Besides being able to characterize and interpret the complexity of the signal, this new formalism can be used to build *synthesis* i.e. synthetic ISM maps sharing the same statistical properties as the original signal. It can also be used for component separation, by isolating the components having different statistical properties. The easiest and most promising application of this is given by *denoising*, in which the noise can be removed to recover as accurately as possible the statistics of the signal, assuming that the statistics of the instrumental noise can be well characterized by instrumental simulations. Typically, it consists of generating a map y minimizing the difference of statistics with x . In other words, one must find the minimum of the loss function

$$\mathcal{L}_\varphi = \|\varphi(y) - \varphi(x)\|^2, \quad (8.52)$$

where the statistics φ can be given by the set of the scattering coefficients. For synthesis y needs to be generated from the original map x , while in order to realize a denoising of the map $d = s + n$, one would typically ask to recover the map u which minimizes the loss function

$$\mathcal{L}_\varphi = \sum_i \|\varphi(u + n_i) - \varphi(d)\|^2, \quad (8.53)$$

where i ranges over a set of simulation at hands. Of course, there are several different ways to write the loss, and thus to think the optimization problem, each of them with their upsides and drawbacks. To solve this high-dimensional optimization problem, one can use microcanonical gradient descent models ([Bruna & Mallat, 2018](#)).

A RWST approach using gradient descent models to produce synthesis of the polarized ISM in intensity and polarization have been proposed in [Allys et al. \(2019\)](#) and [Regaldo-Saint Blancard et al. \(2020\)](#). However, it seems that the RWST statistics approach are less appropriate in order to tackle denoising problems. Beside RWST, another type of advanced statistics is given by the Wavelet Phase harmonics (WPH). These statistics have properties inspired from the convolutional neural networks and present numerous advantages, similar to the RWST. They have been applied by [Allys et al. \(2020\)](#) for the analysis and generation of large scale structure models and in [Regaldo-Saint Blancard et al. \(2021\)](#) for the denoising

of MHD simulations and noisy *Planck* data. For this purpose, the authors developed the PYWPH²⁶ python package. For a pedagogical and complete introduction to this formalism, we refer again to [Régaldo-Saint Blancard \(2021\)](#).

In order to define the WPH statistics, one uses a bump-steerable mother wavelet instead of the Morlet wavelet ([Mallat et al., 2018](#)). The daughter wavelet is still generated by dilutions and rotations associated to $\xi_i = (j_i, \theta_i)$. Let X be a random field, of which the map x is a realization. The *WPH moments* of X are defined as the covariance of the phase harmonics of the wavelet transform of X that is

$$C_{\xi_i, p_i, \xi_j, p_j}(\boldsymbol{\tau}) = \text{Cov} \left([X \star \psi_{\xi_i}(\mathbf{r})]^{p_i}, [X \star \psi_{\xi_j}(\mathbf{r} + \boldsymbol{\tau})]^{p_j} \right). \quad (8.54)$$

The phase harmonic operator $z \rightarrow [z]^p$ of a complex field z is defined as $[z]^p = e^{i \cdot p \cdot \arg(z)}$. The WPH moments also provide interpretable sets of coefficients. Optimization can be done considering only a subset of them. Usually one introduces the 5 following sets:

- $S^{(0,0)}$: The set of WPH moments with $p_i = p_j = 0$ and $\xi_i = \xi_j = \xi$. They capture information about the sparsity of the data in the ξ bandpass.
- $S^{(1,1)}$: The set of WPH moments with $p_i = p_j = 1$ and $\xi_i = \xi_j = \xi$. They capture the power spectrum information in the ξ bandpass.
- $S^{(0,1)}$: The set of WPH moments with $p_i = 0, p_j = 1$ and $\xi_i = \xi_j = \xi$, the moments capture information about the coupling between scales in a single ξ bandpass.
- $C^{(0,1)}$: The set of WPH moments with $p_i = 0, p_j = 1$ and $\xi_i \neq \xi_j$. They quantify correlation between local oscillations for the scales associated with ξ_i and ξ_j .
- C^{phase} : The set of WPH moments with $p_1 = 1, \xi_1 \neq \xi_2$ and $p_2 = \xi_1/\xi_2$. They capture informations about the statistical phase alignment of oscillations between the scales associated with ξ_i and ξ_j .

Additionally, one also add to these statistics the *scaling moments* defined as

$$L_{j,0} = \text{Cov} [|X \star \varphi_j|, |X \star \tilde{\varphi}_j|], \quad (8.55)$$

$$L_{j,p} = \text{Cov} [(X \star \varphi_j)^p, (X \star \tilde{\varphi}_j)^p] \quad (p > 0). \quad (8.56)$$

Here, $\tilde{\varphi}_i$ are isotropic Gaussian filters. They allow to probe the largest scales which are poorly captured by the WPH moments.

Overall, WST, RWST and WPH are three different sets of statistics based on wavelets that can be used to characterize a complex signal on a flat patch. They are easily interpretable and can grasp non-Gaussian features. The original WST are probably the simplest form of statistics built from a set of wavelets, while the RWST propose a decomposition which allow to obtain coefficients having a direct interpretation. On the other hand, models built on the more complex WPH statistics share properties with convolutional neural networks and tend to perform better on denoising problems.

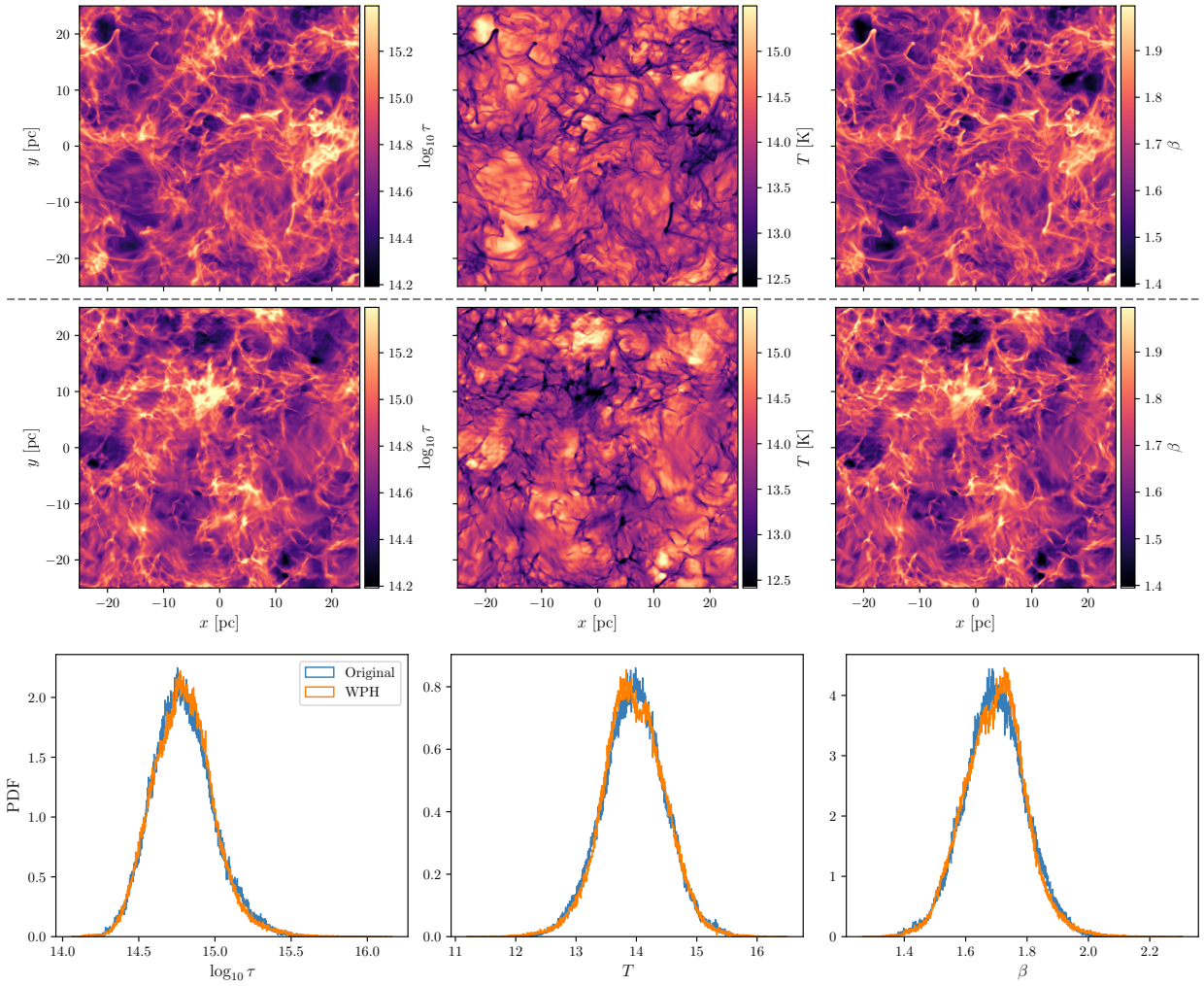


Figure 8.14: Upper pannel, from left to right: original opacity $\log_{10}(\tau)$, temperature T and spectral index β from the MHD simulations. Intermediate, from left to right: similar figures obtained from the synthetic map. Bottom pannel: 1D distributions of the same quantities for the original (blue) and the synthetic (orange) maps. From Régaldo-Saint Blancard et al. (2023).

8.6.4 Personal contribution

During this thesis, I tried to investigate how the spectral dimension could be explored with the framework of the wavelet scattering transform. As such, it might be possible to tackle both the spatial and the spectral complexity of the foreground signal with the same tool. To do so, I collaborated with Bruno Régaldo-Saint Blancard (Flatiron institute), Erwan Ally (LPENS) and Constant Auclair (LPENS) in order to become familiar with the PYWPH software. The first idea was to see if the addition of cross-moments between two maps could help the optimization, i.e. using new statistic defined by

$$C_{\xi_i, p_i, \xi_j, p_j}(\boldsymbol{\tau}) = \text{Cov} \left([X \star \psi_{\xi_i}(\mathbf{r})]^{p_i}, [Y \star \psi_{\xi_j}(\mathbf{r} + \boldsymbol{\tau})]^{p_j} \right). \quad (8.57)$$

where X and Y could be the random field associated with two different frequency maps.

²⁶<https://github.com/bregaldo/pywph>

These cross-spectra were used in the analysis of [Régaldo-Saint Blancard et al. \(2023\)](#), on which I had the chance to collaborate. It was shown that adding these cross-statistics allowed to produce synthesis that capture the spectral dust properties without setting any prior on it. To do so, Bruno Regaldo-Saint Blancard realized MHD simulations on patches that he extrapolated at different frequencies using a modified black body. β and T were randomly generated in the third dimension using two correlated Gaussian distribution for each spectral parameter. The top rows of Fig. 8.14 represent the maps of the opacity $\log_{10}(\tau)$, and the spectral parameters T and β of the original MHD simulation. The intermediate rows show the same maps extracted in every pixel of a synthesis generated using PYWPH. A first visual assessment allows to evaluate the success of the synthesis, as it seems very difficult to distinguish the synthetic map from the original simulation. The non linear patterns and filamentary structures of the original MHD simulation have been inherited in the synthetic map as well as the spatial distribution of the spectral properties: denser regions are colder while diffuse regions are hotter and β and T are anti-correlated as in the simulation. This result is especially impressive as *no* information on the SED were given directly to the optimizer, except the original set of MHD simulations at different frequencies. The code thus inherits these constraints from the spatial distribution of the intensity in each frequency band. The recovered 1D distributions of the spectral parameters, displayed on the bottom panel of Fig. 8.14 seems in agreement between each other. Similar considerations were used in this work to reproduce the statistical properties of the I , E and B fields together. I had the chance to participate to the discussions and to the writing of the draft, helping the author with regarding the understanding of the spectral properties of the dust signal.

The remaining open question is how can the additional information given by the cross-frequencies can be used for denoising. Our main goal was to provide a denoising of the BICEP field using *Planck* data, such that the dust component could be recovered in this region with an unprecedented accuracy. However, this task is far from easy and multiple elementary steps have to be undertaken before. I first tried to see if the addition of a cross-term between two half-mission maps²⁷ in the loss could help the denoising, using *Planck* noises on MHD simulations. As the noise of the half-mission maps is largely decorrelated, it must be possible to use this information at some level. Unfortunately, this did not lead to any significant improvement. This investigation forced us to reconsider the standard normalization of the coefficients used in PYWPH, which were further optimized by Bruno Regaldo-Saint Blancard. The same application using different frequency bands instead of half-mission maps lead to a minimal improvement in the denoising, but a unbiased recovery of the cross-angular power spectra between the two maps, ensuring that the deterministic patterns of dust are better retrieved from one frequency to another. This work is still in progress, and is followed by significant optimization of the PYWPH software itself by Bruno Regaldo-Saint Blancard, considering the feedback given by the users.

Finally, in order to apply it on the largest scales of the sky, it will be necessary to develop the formalism such that it can be used on the celestial sphere. While a lot remains to be done, this direction has been already explored by [Delouis et al. \(2022\)](#) and is currently investigated at IRAP under the lead of Louise Mousset.

²⁷The full data from an experiment as *Planck* can be divided in two set containing the data of half of the mission duration. Doing so allow to have two dataset in which the noise realizations are widely independent.

While the polarized foregrounds to the CMB remains a significant challenge, major breakthroughs have been done in the past years. The new frameworks we discussed in this thesis are not only powerful but they are also interpretable and allows to do both component separation and Galactic science conjointly. A large amount of exploratory work remains to be undertaken in order to develop a robust multi-frequency component separation method based on WPH, but the result promise to be outstanding. On the other hand, the simpler moment expansion framework is now very robust and I am glad to have contributed significantly to this developments, which represented without any doubt the main achievement of this thesis. It has now to be extensively applied in order to assess properly its strength and limits. In there very core, scattering transform methods and moment expansion share deep similarities as they use compressed statistical information to characterize the signal. The first one focusing on spatial information while the second tackle the spectral statistics. On the long term, I would like to investigate if the use of the (spin)-moments could be of any help for multi-frequency synthesis and denoising with the WPH, in order to orient the spectral optimization in the most complex cases, and reduce the number of degrees of freedom. I strongly believe that the conjunction of these two approach would represent a groundbreaking benefit both for CMB and Galactic science.

9

Explaining the values of our standard models' fundamental constants

La constance d'une habitude est d'ordinaire en rapport avec son absurdité.

– Marcel Proust, *La prisonnière*

Contents

9.1	The fundamental constants and their possible variations	148
9.2	The fine structure constant, its astrophysical impacts and the corresponding observables	161
9.3	Building a modified Boltzmann solver to quantify the impact of varying α cosmology	166
9.4	Constraining the Bekenstein model(s)	169
9.5	String theories and varying coupling	174
9.6	Constraining the runaway dilaton model	179
9.7	Varying alpha, late and early dark energy	185

In Chap. 3, we reviewed the theoretical foundations underlying our current cosmological model: Λ -CDM. In this chapter, we will question these very foundations by allowing the fundamental constants of nature to become variable. As in Chap. 4, such a change of paradigm beyond Λ -CDM will see the introduction of new entities, as dynamical scalar fields. Using CMB data from *Planck* introduced in Chap. 5 jointly with a multitude of other experimental probes, I will provide the latest to date constraints on two scalar fields models inducing variations of the fine structure constant: the Bekenstein and the runaway dilaton models.

9.1 The fundamental constants and their possible variations

9.1.1 What is a fundamental constant?

As [Uzan \(2011\)](#) puts it, fundamental constants of a given theory are "*parameters that cannot be explained by this theory*" (p.5). They are omnipresent and maybe unavoidable when building a model aiming at describing physical phenomena. For example, consider modeling the universal force of gravitation between two point masses m_1 and m_2 , separated by a distance d , in the framework of Newton mechanics. To account for observations, it must increase as the product of the masses and decrease as the square of their distance. However one can not simply write $|\mathbf{F}_G| = m_1 m_2 / d^2$, as the units would be inconsistent (and the magnitude of the effect largely over estimated in S.I. units). One is hence forced to introduce a factor G , the value of which can not be predicted within Newtonian mechanics and can only be measured. Similar considerations are reached in all the known theories of physics. In that sense, fundamental constants allow us to draw the limits of the explanatory power of a given theory. The number of fundamental constants also depends on the theory under consideration. From an unifying and reductionist perspective, one would want to find a model able to explain as many phenomenon as possible with less fundamental constants as possible.

At the time being, general relativity and the standard model of particle physics, presented in Chap. 3, provide the most fundamental and empirically validated theories of nature for gravitation and the three other known fundamental interactions, respectively. A list of all the constants required in these models is given in Tab. 9.1. One can find the three dimensional fundamental constants: c , \hbar and G , along with nineteen other coefficients: 9 Yukawa couplings fixing the masses of the quarks and leptons, 2 parameters defining the shape of the Higgs potential $V(\mathbf{h}) = \frac{\mu^2}{2} |\mathbf{h}|^2 - \lambda |\mathbf{h}|^4$, 4 parameters for the Cabibbo-Kobayashi-Maskawa (CKM) matrix (1 phase δ_{CKM} and 3 mixing angles θ_{ij}) quantifying the weak force induced flavor changing of quarks and the amplitude of the weak CP symmetry violation, 2 coupling constants quantifying the strength of the two fundamental forces (strong and electroweak), the Weinberg angle quantifying the symmetry breaking of the electroweak force and a phase for the QCD vacuum. Finally, the cosmological constant Λ can be added to this list, as part of our theory of gravity (see Chap. 3).

The status of the 6 cosmological parameters of Λ -CDM presented in Sec. 3.4.2 is more ambiguous. While we have no way to predict their values within our cosmological theory, they do not appear at the Lagrangian level and are better understood as initial conditions associated to solutions of the theory. Another interesting question would be whether or not the null parameters (i.e. compatible with zero) can be considered as fundamental constants if our standard models can not justify their cancellation from fundamental principles. Overall, we reach a somewhat consensual number of 23 constants in Tab. 9.1, which is arguably a large number of values that can not be explained within our most fundamental models of physics. Moreover, we know for sure that this picture given by the standard models is incomplete. Indeed, some of the theoretical puzzles discussed in Chap. 4 and others observational facts as the masses of neutrinos ([Allanchach, 2019](#)), the anomaly of the $g - 2$ factor for the muon ([Di Luzio et al., 2022](#)) and the matter/antimatter asymmetry ([Hambye, 2012](#)) suggest that new

Constant	Symbol	Value
Speed of light	c	$299792458 \text{ m} \cdot \text{s}^{-1}$
Planck constant (reduced)	$\hbar = h/(2\pi)$	$6.62607015 \times 10^{-34} / (2\pi) \text{ J} \cdot \text{s}$
Newton constant	G	$6.67430(15) \times 10^{-11} \text{ m}^2 \cdot \text{kg}^{-1} \cdot \text{s}^{-2}$
Weak coupling constant (at m_Z)	$g_2(m_Z)$	0.6520 ± 0.0001
Strong coupling constant (at m_Z)	$g_3(m_Z)$	1.221 ± 0.022
Weinberg angle	$\sin^2 \theta_W(91.2\text{GeV})_{\bar{\text{MS}}}$	0.23121 ± 0.00004
Electron Yukawa coupling	λ_e	2.94×10^{-6}
Muon Yukawa coupling	λ_μ	0.000607
Tauon Yukawa coupling	λ_τ	0.0102156
Up Yukawa coupling	λ_u	0.000016 ± 0.000007
Down Yukawa coupling	λ_d	0.00003 ± 0.00002
Charm Yukawa coupling	λ_c	0.0072 ± 0.0006
Strange Yukawa coupling	λ_s	0.0006 ± 0.0002
Top Yukawa coupling	λ_t	1.002 ± 0.029
Bottom Yukawa coupling	λ_b	0.026 ± 0.003
Quark CKM matrix angles	$\sin \theta_{12}$	0.22650 ± 0.00048
	$\sin \theta_{23}$	$0.04053^{+0.00083}_{-0.00061}$
	$\sin \theta_{13}$	$0.00361^{+0.00011}_{-0.00009}$
Quark CKM matrix phase	δ_{CKM}	$1.196^{+0.045}_{-0.043}$
Higgs potential quadratic coefficient	$ \mu $	$\simeq 88.4 \text{ GeV}$
Higgs potential quartic coefficient	λ	$\simeq 0.13$
QCD vacuum phase	θ_{QCD}	$\leq 10^{-10}$
Cosmological constant	Λ	$\simeq 1.1056 \times 10^{-52} \text{ m}^{-2}$

Table 9.1: List of the fundamental constants of the standard models introduced in Chap. 3. Adapted from [Uzan \(2011\)](#) with updated values from [Zyla et al. \(2020\)](#).

parameters and perhaps new fields will have to be introduced, bringing their free parameters with them (masses, coupling constants, coefficients associated with potentials ...).

Theories beyond our standard models can however propose unifying pictures in which the number goes down. For example, string theorists claim to require only two dimensional constants: the string length ℓ_s and the speed of light c ([Veneziano, 1986](#))¹. Indeed, as discussed further in Sec. 9.5, even the number of dimensions of space-time can be predicted in this framework (unfortunately, the answer is 11...). It is yet unclear if a fundamental theory of physics could have no free parameter and whether this even makes sense, as it would represent the ultimate predictive theory².

In any case, wanting some justifications regarding the values of the fundamental constants of our standard models appears as a legitimate inquiry. First, they represent a major fine tuning

¹This picture is however by many ways idealistic, as the number of degrees of freedoms arising from the choice of compactification (the string landscape) is absolutely gigantic (see Sec. 9.5).

²This statement needs to be tempered as such a theory would certainly not be able to predict the initial conditions for the evolution of its field (see the discussion above about the cosmological parameters), initial conditions which are subject to a large amount of fine tuning and are expected to witness a significantly non-linear (chaotic) evolution. As such, a theory for all the interactions of nature without free parameter would doubtly predict specifics events as e.g. the emergence of life. Thanks to Jean-Philippe Uzan for suggesting this correction and asking for a clear distinction between fundamental constants and initial conditions.

problem as their values seem incredibly well adjusted: indeed, as we will further discuss in Sec. 9.1.3, changing the values in Tab. 9.1 by a few percent would drastically transform the structure of the Universe as we know it, making structure formation, chemistry and life impossible. As we know for a fact that life is possible, we would like to explain how come the parameters have such specific values to allow it. This is the so called "anthropic principle", consequences of which were strongly debated in modern literature (see e.g. Carter, 1974; Smolin, 2004). A way to justify such a fine tuning of the constants is to imagine that a multitude of universes/spatial regions exist, in which the constants can take different values. Doing so could solve the problem by suggesting that we happen to be in a statistical realization allowing for our existence (Agrawal et al., 1998). For example, eternal inflation, in which reheating happens only locally in separated independent bubbles, could provide such a scenario (Linde, 1986; Guth, 2007). The value of the fundamental constants in each bubble Universe could then be different with the help of string theory landscape (see e.g. Susskind, 2003). Similarly, cyclic cosmologies can provide an identical solution with a temporal alternation of universes (see e.g. Penrose, 2006). This suggestion is tempting and avoid to invoke some kind of "divine intervention" or "strike of luck". However, such theories are yet extremely far from the reach of empirical verification and a way to derive the exact values of the constants from deeper principles (as e.g. symmetries) appears to me as more satisfying. However, as far as I am aware, no such framework has yet been proposed in a way that could both be consistent and consensual³.

Additionally, any detection of the variation of a fundamental constant would be, by very definition, in direct contradiction with our standard models. As such, testing experimentally their constancy allows to quantify the robustness of our standard models and provides a powerful and model-independent probe for new physics. If a coupling appeared to be dynamical, the challenge would be to predict and interpret its behavior. This can only be done by extending our theories within a larger framework that can explain their dynamics (i.e. which have hence an higher explanatory power).

I will refer to the possible variation of the fundamental constants of our standard models with the oxymoron *varying constants*. Several mechanisms can be invoked to explain such variations within a larger framework while explaining how the constant's values can appear so stable in our measurements. It is sensible to think that the observed constants could be slowly varying compared to the physical scales we are probing, as the Earth gravitational field would appear as a constant $|g| = GM_{\oplus}/(R_{\oplus} + h)^2$ for small altitude $h \ll R_{\oplus}$. Some underlying dynamics could also have been attracted towards the fixed point of a dynamical system, such that they appear stable. Their values could also emerge from a yet unknown underlying behavior as the thermodynamical constants (e.g. heat capacities) emerge from the statistical behavior of microscopic particles. One could also realize that what are considered today as fundamental constants can be computed as derived numbers from a smaller set of fundamental constants.

Constants can play different roles within a theory. While G , our introduction example, quantifies the strength of the gravitational coupling between two masses, the speed of light c sets a fundamental limit for the speed of propagation of information in special relativity.

³For a recent example of an attempt to derive the fine structure constant value from deeper principle, see e.g. Singh (2021). I am unfortunately not qualified enough yet to judge the credibility of such a proposal.

There are numerous ways to classify the zoology of fundamental constants depending on how they appear in a theoretical structure (for a discussion, see e.g. [Lévy-Leblond, 1977](#); [Lévy-Leblond & Sandoval, 2013](#)). It is interesting to see that these roles can change as theories evolve. Following [Duff \(2015\)](#), we will argue that a necessary distinction, going beyond mere zoology, is to wonder whether the constants have dimensions (units) or not.

9.1.2 Dimensional and dimensionless constants

Dimensional: fundamental constants

Dimensional constants are by nature deeply linked to unit choices and metrology. While a detailed presentation of this topic goes far beyond the scope of this thesis⁴, let us here mention a few points necessary for our discussion.

Dimensional constants often (if not always) appear as relating different concepts, providing a connection/identification between seemingly unrelated notions. Consider the example given by energy: energy can be understood as the Noether charge associated to time translations of a system. Depending of the system under consideration, it can be related to a photon's pulsations $E_\omega = \hbar\omega$, the rest energy of a massive body $E_0 = mc^2$ or the temperature of a thermodynamical system $E_T \propto k_B T^5$. In these equations, the constants \hbar , k_B and c could all be interpreted as conversion factors between measurable quantities ω , m , T and the abstract concept of the energy of a system. More radically, equations as $\Delta x = c\Delta t$ for the path of a photon could be interpreted as an identification between space and time as dimensions through c . Choosing the right ("natural") unit choice, it is thus possible to identify the related quantity e.g. the energy of a photon can be identified with its pulsation. From these examples, one can consider the drastic view that all the dimensional constants are conversion factors, e.g. quoting [Duff \(2015\)](#): "[c] merely tells us how to convert one human construct, the meter, into another, the second." (p.2).

It is clear that dimensional constants are intrinsically intertwined with unit systems. As stated in the first paragraph, the introduction of a constant G in the Newtonian force of gravitation ensures the unit consistency of the equation. As such, it requires the definition of units of length, time and mass in which it can be expressed and measured. It is commonly accepted that a minimum of three dimensions are required to build a physical theory: length, time and mass, along with a choice of units to express them. All the other ones, as energy, temperature and charge, can in principle be expressed from them. The S.I. system however, is built on 7 such fundamental units, as this is after all a matter of practical conventions. Setting a unit system requires the choice of a reference quantity that can be considered as a constant unity for the associated dimension. As such, dimensional constants allow us to define unit systems and are widely used to build the S.I. system (note that in the S.I. system, the speed of light c is now defined as a constant number allowing to define the meter ([Conférence générale des poids et mesures, 1983](#))). Another common choice that was ours

⁴For a very complete pedagogical and historical introduction on fundamental constants and their variation, we refer to [Uzan & Leclercq \(2008\)](#).

⁵ k_B also relates the entropy S_T and the number of configurations Ω_T as $S_T = k_B \ln(\Omega_T)$. However, the presence of k_B in this equation is today considered as an historical artifact in the definition of the thermodynamical entropy by Boltzmann, which is absolutely not required if one build statistical physics on Shannon's entropy instead (see Chap I and II of [Landau \(1969\)](#))

9. EXPLAINING THE VALUES OF OUR STANDARD MODELS' FUNDAMENTAL CONSTANTS

in the first section, is the "natural unit system" or "Planck units" in which the numerical values of c , \hbar and G are set to unity, meaning that all speed will be counted in units of c , all actions in units of \hbar ... allowing to set the three minimally required dimensions. In order to do so, this system builds mass length and time units from the three constants G , c and \hbar as⁶

$$m_{\text{Pl}} = \sqrt{\frac{\hbar c}{G}}, \quad \ell_{\text{Pl}} = \sqrt{\frac{\hbar G}{c^3}}, \quad t_{\text{Pl}} = \sqrt{\frac{\hbar G}{c^5}}, \quad T_{\text{Pl}} = \sqrt{\frac{\hbar c^5}{G k_B}}. \quad (9.1)$$

The hope being that these units are more fundamentally meaningful, as they are built only from fundamental constants and they allow for the identification between physical concepts and measurable quantities as discussed above. Historically, Max Planck considered also the need for temperature as a fourth required unit, and k_B as a fundamental dimensional constant. The minimal number of required units and dimensional constants in physics is still debated. While "Planck school" would argue for four, modern metrology has chosen three. A string theoretical standpoint would argue for two while the "conversion factor" point of view would defend that dimensional constants are not needed at all from a "fundamental" perspective. These three points of view are discussed extensively in [Duff et al. \(2002\)](#).

However, without falling into the pit of numerology, it is clear that dimensional constants have played and play a greater role than conversion factors in the history of physical theories. They can be considered to set universal limits as c is the maximal speed of a massive object, \hbar gives minimal quantum of action/phase space volume of a system, and G allows to build the Chandrasekhar mass, setting the maximal amount of mass (and entropy) that can be associated with a space-time region. As such, they are "signatures" of the domain of application of a given theory (\hbar for quantum mechanics, G for gravity and c for special relativity) which allow us to study their asymptotical limits (as the semi-classical limit of quantum mechanics $E\Delta t \gg \hbar$, or non relativistic-limit $v \ll c$). Following this idea, one can build the "Bronshteyn-Zelmanov-Okun" (BZO) cube, with axis c, G, \hbar , to shed some light on the nature of quantum gravity and its domain of validity. For a discussion, see e.g. [Martins & Molaro \(2011\)](#). Similarly, Planck units can be understood as domains of mass, energy, length ... in which the quantum nature of gravity can not be neglected. They are thus associated with regions to investigate, in which our standard models stop being valid, especially in the very early Universe.

Perhaps more strikingly, QFT in curved space-time (and multiple other derivations) allows to compute that the quantum entropy associated to a black hole S_{BH} (Bekenstein entropy, [Bekenstein, 1981](#); [Casini, 2008](#)) must be proportional to its area A as

$$S_{\text{BH}} = \frac{k_B c^3 A}{4G\hbar}. \quad (9.2)$$

The fact that this formula invoke G, c and \hbar (and k_B) is considered as an unambiguous signature of a quantum theory gravity, even though no such theory was needed to derive it. As such, its demonstration has become an unmissable target for string theories, loop quantum gravity and all quantum theories of gravity.

⁶The Planck mass m_{Pl} and the reduced Planck mass M_{Pl} used in the previous chapters are different by a factor of $\sqrt{8\pi}$.

Dimensionless: fundamental parameters

Unitless fundamental constants are often referred to as "fundamental parameters". They can be built from dimensionless ratio of dimensional quantities as e.g. the proton to electron mass ratio $\mu = m_p/m_e \sim 1840$. In the standard models introduced in Chap. 3, dimensionless parameters are either gauge couplings quantifying strength of interactions as g_2 and g_3 , mass ratios μ_i or equivalently values of the Yukawa couplings λ_i , and mixing angles associated to symmetry breaking as θ^W , θ_{ij} and θ_{QCD} .

Dimensionless parameters are arguably more fundamental than dimensional constants, for the following related reasons:

- Their value do not depend on any unit choice. Whether masses are expressed in kg, keV or any other mass unit, μ will always return the same value.
- As such, fundamental parameters can never be reinterpreted as conversion factors and reabsorbed within a choice of natural units. Setting the electron mass $m_e = 1$ would simply mean that we are in a system of unit in which all the masses are expressed in term of m_e . On the other hand, setting the dimensionless ratio $\mu = m_p/m_e$ to 1 would have unrealistic consequences, as it would mean that the proton and the electron physically have the same mass. This would of course be highly incompatible with the physics at work in our Universe. Similar conclusions are reached for e.g. gauge couplings, encoding the relative strength between fundamental forces.
- Finally, even more radically, we can conclude that the values of dimensional parameters have no impact on the physics, as long as all the dimensionless ratios remain unchanged. Indeed, imagine doubling the values of all the masses $m_e \rightarrow 2m_e$ and $m_p \rightarrow 2m_p$, such that μ remains invariant. While this might look like a considerable change, doing so would have absolutely no observational consequences, as would the redefinition of the kg by half its actual value. Similar argument applies to other fundamental couplings as e.g. changing the charge of the electron and the speed of light such that the fine structure constant remains invariant (see Sec. 9.2). In a sense, this is very similar to the case of gauge invariance in the very first sense of the meaning of "Gauge" as choice of scale on a measurement apparatus. In other words: there is no way to distinguish a physical change of quantities with a trivial change of units, as long as all the dimensionless ratios are preserved.

Seeking for variations

Many studies are dedicated to the search for space-time variations of dimensional constants as G or the speed of light (so called "VSL theories", which could provide an alternative for inflation ([Moffat, 2002](#); [Magueijo, 2003](#))). However, as pointed by [Ellis & Uzan \(2005\)](#); [Duff \(2002, 2015\)](#), such inquiries are at best less relevant than looking at dimensionless parameters, and at worse are not even meaningful physically, as they have no real operational meaning. Indeed, as argued in the previous section, dimensionless parameters encode unambiguously physically relevant relationships, while dimensional quantities are always "relative" to some unit choice. As such, any variation of a dimensional constant could also be understood as a change of unit or a variation in the way these units are defined or measured. Dimensionless parameters, however, are invariant quantities, which have the same values independently of

Structure constant	Symbol	Value
Fine structure constant	α_{EM}	$1/137.035999084(21)$
Fine structure constant at m_Z	$\alpha_{\text{EM}}(m_Z)$	$1/(127.952 \pm 0.009)$
Weak structure constant at m_Z	$\alpha_W(m_Z)$	0.03383 ± 0.00001
Strong structure constant at m_Z	$\alpha_S(m_Z)$	0.1185 ± 0.0016
Gravitational structure constant	α_G	$\sim 5.905 \times 10^{-39}$

Table 9.2: List of gauge coupling values, adapted from [Uzan \(2011\)](#) with values of [Zyla et al. \(2020\)](#).

a unit choice.

Furthermore, as the dimensionless ratios are the physically relevant quantities, any theory including variations of a dimensional constant could always be rephrased in a purely equivalent way such that it is another dimensional constant that is variable. As long as the dimensionless ratios are changing in the same way, both theories will have the same observable consequences, such that it is impossible to really identify which of the dimensional constant is varying [Duff \(2002\)](#). To come back to our simple example, if μ changes across space-time, it would be impossible to say whether it is m_e or m_p that is changing, as it is ultimately a choice of unit to decide which mass should be considered as fixed, i.e. in term of which "unit mass" the other are counted. In other words: a change of unit could always allow us to either set $m_e = 1$ or $m_p = 1$ such that the other one is considered as variable. Any choice of unit for mass decides to fix arbitrarily some reference mass. Note however that this last point is very subtle and source a fair amount of discussion and confusion through a large part of the literature in cosmology (see the debates in e.g. [Duff et al. \(2002\)](#); [Duff \(2002\)](#) or the complementary discussion of [Grozier \(2020\)](#)).

For all the above reasons, one should prefer the investigation of the stability of the dimensionless parameters since only dimensionless quantities can unambiguously be measured and promoted as variable.

9.1.3 Gauge couplings and structure constants

In this thesis, I will give constraints on motivated models allowing for a variation of the dimensionless fine structure constant α_{EM} . These models will both be phenomenological in Sec. 9.4 and inspired from string theory in Sec. 9.6. α_{EM} is the so-called gauge structure constant associated to the electromagnetic force, quantifying the strength of this interaction. In this section, I will formally define the notion of structure constant for fundamental forces and its relation with gauge couplings, stressing the importance of this parameters and better understand how and why they appear in our theories. This understanding will further allow us to identify and build models in which the value of α_{EM} can change with space and time in the next section.

An important example of dimensionless fundamental constants within the standard model of particle physics is given by the *gauge couplings* g_A . These numbers quantify the strength of the fundamental interactions of the matter fields with the gauge bosons and are thus setting the intensity of all the fundamental interactions shaping our Universe. From g_A , one can also define the *gauge structure constants* α_{g_A} which are easier to measure. While these parameters are characteristic of gauge theories, they can also be defined for gravity as we

will further see.

As we did in Chap. 3, consider a matter field ψ . Using a choice of basis $e_i(x)$ for the field space over each space-time point, ψ can be expressed as $\psi = \psi^i e_i$. As an illustration, for electromagnetism ψ is a standard wave-function and there exist a single basis vector \hat{r} defining the orientation of the complex plane everywhere over space-time. For weak force, ψ^i is a left chiral lepton doublet on the weak flavor basis e.g. a left electron/neutrino or a left up/down quark pair. For strong force ψ^i would be a color triplet (green, red, blue) while e_i would be the color basis. Forces are nothing less than transformations or rotations of the components of ψ induced by gauge bosons \mathcal{A} . For a detailed discussion, see Appendix A.

The covariant derivative of the field $D_\mu\psi$, in the space-time direction given by the basis 4-vector e_μ ⁷ can be written as⁸

$$D_\mu\psi = (\partial_\mu\psi^i + g_{\mathcal{A}}(\mathcal{A}_\mu)_a(X_j^i)^a\psi^j) e_i, \quad (9.3)$$

here X^a are the generators of the gauge algebra of the gauge group (which can be understood as matrices for all practical purpose), each associated with a gauge boson $(\mathcal{A}_\mu)_a$. $D_\mu\psi$ is quantifying the variation of the field ψ over space-time compared to its parallel transported version in the direction e_μ . It is ensuring the invariance of the theory under a space-time change of the field space frame e_i (a *gauge transformation*) and sources forces through the curvature \mathcal{F} associated to \mathcal{A} . Diagonal generators create neutral currents as they can not rotate ψ , while non diagonal generators are associated to charged currents. We refer again to Appendix A for clarifications on these last points.

The coefficient $g_{\mathcal{A}}$, called the *gauge coupling*, quantifies the strength of the force mediated by \mathcal{A} on ψ ⁹. For the strong force, the coupling is written g_s , while for electroweak force one has two couplings g_w and g_Y associated respectively to the three W^i and the B boson. After symmetry breaking, one can use the so called Weinberg angle to associate the coupling constant to electromagnetism $e = g_w \sin(\theta_W) = g_Y \cos(\theta_W)$, identified with the electron charge. Similarly one can express the couplings of the Z^0 and W^\pm in term of g_w and θ_W .

Under a redefinition of the connections as $\tilde{\mathcal{A}} = g_{\mathcal{A}}\mathcal{A}$, the coupling strength can be absorbed such that they do not appear anymore in the covariant derivatives $D_\mu = \partial_\mu + \tilde{\mathcal{A}}$ (as this is the case for gravity, in the Levi-Civita/spin connections). To be self consistent, one must then consider the curvature associated to this new connection in the Lagrangian which is simply $\tilde{\mathcal{F}} = g_{\mathcal{A}}\mathcal{F}$ ¹⁰. The curvature term becomes

$$\mathcal{L}_F = -\frac{1}{4}\langle\mathcal{F}, \mathcal{F}\rangle = -\frac{1}{4g_{\mathcal{A}}^2}\langle\tilde{\mathcal{F}}, \tilde{\mathcal{F}}\rangle = -\frac{1}{16\pi\alpha_{g_{\mathcal{A}}}}\langle\tilde{\mathcal{F}}, \tilde{\mathcal{F}}\rangle \quad (9.4)$$

⁷As discussed in Appendix A, the basis e_μ is given by the differential operators ∂_μ . We choose to avoid this notation in the thesis to simplify the reading.

⁸This equation is equivalent to the covariant derivative of a vector $\nabla_\mu v$ given in Eq. 3.1, but for the derivation of ψ in the field space over space-time instead of a space-time 4-vector v . To consider how gravity acts on ψ , the Levi-Civita connection Γ acting on vectors has to be replaced by the Levi-Civita spin connection ω acting on spinors as written in Eq. 3.8.

⁹Note that, for a given force, $g_{\mathcal{A}}$ is a single number for all the possible fermion fields ψ , and should not be confused with the *charges* of the fermions. The differences of charge values comes from the fact that different fields live in different representations of the gauge group.

¹⁰From the definition of the curvature given in Appendix A: $\tilde{\mathcal{F}} = d\tilde{\mathcal{A}} + \frac{1}{2}[\tilde{\mathcal{A}}, \tilde{\mathcal{A}}]_g = \mathcal{F}g_{\mathcal{A}}$

where we introduced the *gauge structure constant* $\alpha_{g\mathcal{A}} = (g_{\mathcal{A}})^2/4\pi$. Building a QFT from there, $\alpha_{g\mathcal{A}}$ quantifies the probability of interaction associated to a Feynmann diagram (vertex) involving two fermion lines ψ and a gauge boson line \mathcal{A} (e.g. the probability for an electron to emit a photon).

Even if the Lagrangian and equations of motion of gravity and Yang-Mills fields are different, one can identify G with the gravitational structure constant in $\mathcal{L}_{EH} = R/(16\pi G)$. Theories with dimensional coupling can be showed not to be renormalizable and thus can not easily be quantified (see [Zee \(2003\)](#), Sec. III.2). This is thus a direct signature that GR can not be transformed straightforwardly in a QFT, as the other gauge interactions (this would also be the case for the dimensional Fermi constant G_F in Fermi theory of weak force).

As $[G] = [\text{mass}]^{-2}$ in natural units, one needs to multiply by a mass squared to get a comparable dimensionless number for gravity. Generally, one introduce $\alpha_G = Gm_p^2$, or in S.I. units

$$\alpha_G = \frac{Gm_p^2}{\hbar c}, \quad (9.5)$$

where m_p is the proton mass ([Silk, 1977](#)). It is arguable, for the reasons discussed in the previous sections, that cosmologists should seek for variations of α_G instead of G (contrarily to what is done in almost all of the cosmological literature today). This point has already been advocated in works as e.g. [Narimani et al. \(2012\)](#).

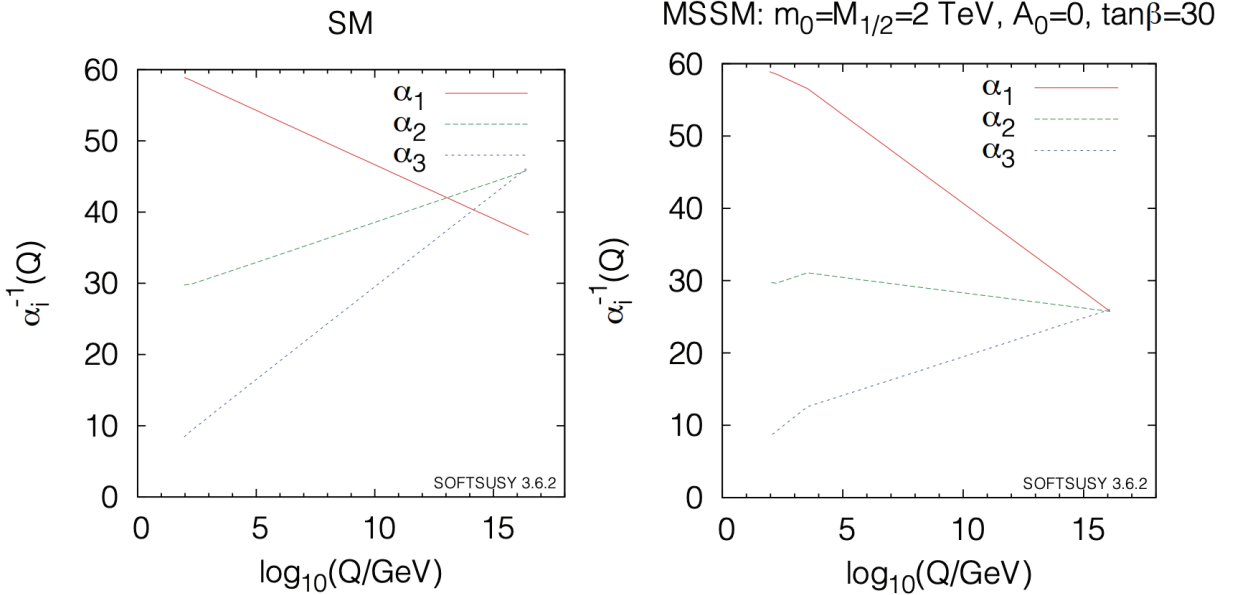


Figure 9.1: Energy running of the gauge structure constants in the SM (left) and minimal supersymmetric model (MSSM) (right). α_1 and α_2 are the electroweak coupling constants while $\alpha_3 \equiv \alpha_S$. Taken from "Grand Unified Theories" in [Zyla et al. \(2020\)](#) (Figure 93.1).

Using the perturbative framework of QFT, the values of the gauge couplings must be running with the energy scale at which they are measured. As displayed in Fig. 9.1, the values of the three structure constants are getting closer at high energies. While they do not converge at a single value within the standard model (left panel of Fig. 9.1), this is lighting the hope to find a theory unifying the three gauge forces at high energy (i.e. a GUT as inspired by supersymmetry (right panel of Fig. 9.1)). As it requires an extremely high energy scale

to make this running significant, it is expected to be extremely small in all the observable Universe. However, in full rigor, when looking for variations of a gauge coupling constant, one should mention that this investigation is done regardless of this running.

By convention, it is usual to compute the values of the α_i at m_Z , the rest mass energy of the W boson. Values of couplings at m_Z can be found in table 9.2. From this list, one can see that α_G is standing out by its incredibly small value compared to the other couplings. This is the so called *hierarchy problem*, directly connected to the questions of fine tuning and anthropic principles we addressed in Sec. 9.1.1.

Let us briefly follow Martins (2020) (chap. 8.2) and highlight how strongly the values of the α_{g_A} shape our Universe. An increase of α_{EM} by a few percents would make chemistry impossible, as atoms would not be able to share electrons anymore. A few percent decrease however, would prevent nuclei to bind with electrons, such that atoms could not form and charged particles would be mostly free, and matter in the form of a plasma. On the other hand, the value of α_W has a strong impact on the structure of the nuclei. An increase in α_W would increase the nuclear decay rate, such that heavy atoms can not be stable anymore. A lower value would lead to the quick conversion of all the hydrogen atoms into Helium. α_S plays a crucial role on stellar nucleosynthesis. Increasing its value would make nuclear fusion easier and allow all stars to reach the fusion of iron in their core, depleting the Universe from light elements as hydrogen. A weaker α_S on the other hand, would make the formation of heavier elements harder to reach in stars, reducing the chemical complexity of the Universe. Finally, among other things, α_G directly impacts the behavior of $a(t)$ in Friedmann equation, such that a greater value could lead the Universe to re-collapse, while a smaller value could accelerate the expansion, preventing the formation of large scale structures. In all the cases discussed here, a few percent change in the coupling's values, or even a fraction of percent of change, would have a most significant impact. As such, the fine tuning problem becomes explicit, and it appears that only very specific values of the α_{g_A} can allow for the Universe as we are experiencing it.

9.1.4 Phenomenology of varying gauge couplings

We stressed that detecting a variation of the fundamental constants, typically the gauge couplings or equivalently the gauge structure constants, would be a major breakthrough in our understanding of fundamental physics. Let us now explore how such a variation could be consistently implemented as an extension of our standard models. If a gauge coupling g becomes a space-time dependent quantity, it is not a constant anymore, but must be promoted as a real (scalar) field $g(x^\mu)$. In order to preserve all the invariances and associated conservation laws of the standard model (gauge and charges, spacetime translations and energy-momentum ...) as well as the general consistency of the theory, the safest (and perhaps the only) way to proceed is to add this variation carefully at the Lagrangian level. The simplest possible option would be to promote g itself as a new fundamental scalar field and add a term $\mathcal{L}_{g_A} = \partial_\mu g_A \partial^\mu g_A / 2 - V(g_A)$ to \mathcal{L}_{SM} , as discussed in Sec. 4.2.2. It is however much more general to assume the existence of another fundamental field ϕ coupled to the SM, such that the gauge coupling g (or equivalently α_{g_A}) are evolving as a function of ϕ ,

$g_A(\phi)$ such that its value today is gives back the measured value in laboratory $g_{A,0}$ ¹¹. If for simplicity one assumes that ϕ is a scalar field, one must then add $\mathcal{L}_\phi = \partial_\mu \phi \partial^\mu \phi / 2 - V(\phi)$ to \mathcal{L}_{SM} . This will not be enough however, as the field would have an impact at the level of the covariant derivative of the theory (Eq. 9.3) which will break the gauge invariance of the newly formed Lagrangian.

In order to preserve this gauge invariance, a function of the field $B_F(\phi)$ must appear in \mathcal{L}_F as

$$\mathcal{L}_F = -\frac{1}{4} B_F(\phi) \langle \mathcal{F}, \mathcal{F} \rangle. \quad (9.6)$$

Turning the problem the other way around, one would legitimately be able to consider that the gauge structure constants of a theory are varying if such a $B_F(\phi)$ appears within its framework¹². In Sec. 9.5.2, we will see that this is for example the case for string theory, in which such a coupling between a scalar field, the dilaton, and the curvature terms appears, without being originally asked for.

The corresponding ϕ -dependent structure constants can be defined as $\alpha_{g_A}(\phi) = g_A(\phi)^2 / 4\pi$. Knowing $B_F(\phi)$, this relative variation of the structure constant can be expressed as

$$\frac{\Delta \alpha_{g_A}}{\alpha_{g_A,0}}(\phi) = B_F(\phi)^{-1} - 1, \quad (9.7)$$

with $\Delta \alpha_{g_A} = \alpha_{g_A}(\phi) - \alpha_{g_A,0}$ and $\alpha_{g_A,0} = g_{A,0}^2 / 4\pi$. This very important equation will be at the starting point of all our models, as it relates a theoretical framework with a given $B_F(\phi)$ to the measurable values of the gauge structure constants.

Let me review briefly here why the curvature Lagrangian must be modified as Eq. 9.6 in order to preserve gauge invariance and why this modification implies Eq. 9.7, as this is rarely discussed in detail in the literature. For simplicity, let us consider the case of the electromagnetic Lagrangian, knowing that a generalization to other forces could be done following the same lines. We recall that gauge invariance can be seen as the invariance of the geometrical objects under the choice of an arbitrary frame in which to express these quantities. It is thus fundamental and must be enforced. Considering only the electromagnetic interaction, the matter fields $\psi = \psi^a e_a$ are given by a set of four complex number values (a spinor) at every point of space-time, where a ranges from 0 to 4¹³. While this is rarely explicated, each of the ψ^a are themselves components of 1-dimensional complex vectors written as $\psi^a \hat{r}$ where \hat{r} is a choice of the orientation of the real axis associated to every point of space-time in which to

¹¹Possibilities that a gauge coupling could be evolving not only as function of the field, but also as function of its speed (kinetically coupled) are explored in Barros & da Fonseca (2023).

¹²In the same spirit, a term as $B_R(\phi)R$ in \mathcal{L}_{EH} would imply a varying G . This is the idea behind the so called *Scalar tensor* (e.g. Brans-Dicke) theories. For a recent review see e.g. Quiros (2019). These theories were originally motivated in order to create a fully Machian version of GR in which inertia can really be defined with respect to the surrounding matter through the scalar field (i.e. the value of α_G) (Brans & Dicke, 1961). This opens the exciting perspective that, in such a theory: the amount of matter in the Universe can be estimated from a knowledge of G or α_G and the WEP/EEP would be a consequence of the theory, not an initial axiom (Sciama, 1953).

¹³which are the components of a Dirac spinor. As such the basis vector e_a and the quadruplet ψ^a are transforming under representations of the Poincaré group as detailed in Appendix A. Note also that expressing the field in a basis as we did is only possible locally in a given trivialization (we will leave aside this subtle point here).

express the complex number ψ^a (on this see Sec. 1.5.3 of the introductory lecture of Faure (2021a)). A gauge transformation consists of changing arbitrarily this choice of complex frames by a rotation $\hat{r} \rightarrow e^{i\lambda}\hat{r}$ where $\lambda(x)$ is an arbitrary function of the space-time point x . Such a frame transformation must leave the physics unchanged. To preserve $\psi^a\hat{r}$ and its physical content under the gauge transformation, the component must then transform correspondingly as $\psi^a \rightarrow e^{-i\lambda}\psi^a$. It can be showed that \mathcal{A} must also transform in this process as $\mathcal{A} \rightarrow \mathcal{A} + \frac{1}{g_{\mathcal{A}}(\phi)} d\lambda$ ¹⁴, which allows to preserve the covariant derivative (Eq. 9.3) appearing in the Dirac Lagrangian $\bar{\psi}(\not{D} - m^2)\psi$. We introduced here the exterior derivative d which should be understood as a derivation of general objects, identical to the differential when applied to a function and satisfying the property of $d^2X = 0$, no matter what object X it acts on. For more on this operator, we refer to Appendix A. For electromagnetism, the curvature \mathcal{F} can be computed immediately from \mathcal{A} with this new operator as $\mathcal{F} = d\mathcal{A}$. Due to the field dependence of $g_{\mathcal{A}}$, \mathcal{F} is not gauge invariant anymore under the gauge transformation of \mathcal{A} as $\mathcal{F} = d\mathcal{A} \rightarrow \mathcal{F} = d\mathcal{A} + d\left(\frac{d\lambda}{g_{\mathcal{A}}(\phi)}\right) \neq d\mathcal{A}$. Gauge invariance can however be preserved if, as in the previous section, one considers instead the rescaled connection $\tilde{\mathcal{A}} = g_{\mathcal{A}}(\phi)\mathcal{A}$. To leave the covariant derivative invariant under gauge transformation, this new connection must transform as $\tilde{\mathcal{A}} \rightarrow \tilde{\mathcal{A}} + d\lambda$, leaving also its curvature invariant as $\tilde{\mathcal{F}} = d\tilde{\mathcal{A}} \rightarrow d\tilde{\mathcal{A}} + d^2\lambda = d\tilde{\mathcal{A}}$. From Eq. 9.4, the gauge invariant Lagrangian for the curvature term can thus be written as

$$\mathcal{L}_{\mathcal{F}} = -\frac{1}{4g_{\mathcal{A}}(\phi)^2} \langle \tilde{\mathcal{F}}, \tilde{\mathcal{F}} \rangle = -\frac{1}{4} B_{\mathcal{F}}(\phi) \langle \mathcal{F}, \mathcal{F} \rangle, \quad (9.8)$$

where we redefined $\mathcal{F} = \tilde{\mathcal{F}}/g_{\mathcal{A},0}$, equal to the standard electromagnetic curvature if $g_{\mathcal{A}}$ is constant and the gauge coupling term $B_{\mathcal{F}}(\phi) = (g_{\mathcal{A},0}/g_{\mathcal{A}}(\phi))^2$, equal to 1 if $g_{\mathcal{A}}$ is a constant. We thus recovered Eq. 9.6. From the definitions of $B_{\mathcal{F}}$ and $\alpha_{g_{\mathcal{A}}}$, one finds that $\alpha_{g_{\mathcal{A}}}(\phi) = \alpha_{g_{\mathcal{A},0}}/B_{\mathcal{F}}(\phi)$ allowing to rederive the expression of Eq. 9.7.

9.1.5 Varying couplings and gravity

If the subatomic constants were to change across space and time, the outcome of a non gravitational experiment would not be invariant through (space or time) translation, in clear violation of the LPI defined in Chap. 3. However one can also see that varying fundamental constants would lead to violations of the WEP and as such lead to violation of the whole EEP by Schiff's conjecture defined in Sec. 3.2.1. The reason is related to the nature of mass itself, which is nothing else but interaction energy bounded in the size of the bodies (between the microscopic constituent themselves and ultimately with the Higgs boson). If the various fundamental constants, as the structure constants $\alpha_{g_{\mathcal{A}}}$ were to change in space and time, the mass of a given body would also be space-time dependent $m \rightarrow m[\alpha_{g_{\mathcal{A}}}(x^\mu)]$ as stated by the Bethe-Weizäcker formula linking the binding energy of a nucleus to its number of nucleons. This dependence of the mass with the couplings must be dependent of the composition of the object that is how and how many of its sub-parts are in interaction. A mass variation

¹⁴For electromagnetism with gauge group U(1), there is only one generator $X = q\mathbf{i}$, with q being the electric charge (associated to the representation of $U(1)$ that can act on ψ), such that in the covariant derivative (Eq. 9.3), $g_{\mathcal{A}}(\mathcal{A}_\mu)_a(X_j^i)^a = iq\epsilon\mathcal{A}_\mu$ with $g_{\mathcal{A}} = e$ being the electron charge. In the above example, we chose the simplest example of $q = 1$.

hence will induce a WEP violation that can be clearly explicated in the framework of GR (see e.g. [Uzan, 2011](#); [Damour, 2012](#)), in which the free particle Lagrangian (Eq. 3.7)

$$\mathcal{S}_p = \int m[\alpha_{g_A}(x^\mu)] \sqrt{g(u_\gamma(\tau), u_\gamma(\tau))} d\tau, \quad (9.9)$$

does not lead to geodesic equation (Eq. 3.2) but instead yields to

$$\nabla_u u = \left(\frac{\partial \ln m}{\partial \alpha_{g_A}} \frac{\partial \alpha_{g_A}}{\partial x^\beta} \right) (g^{\beta\mu} + u^\beta u^\mu) e_\mu \neq 0. \quad (9.10)$$

This phenomenon can also be explicated more simply at the level of Newtonian's gravitation. Indeed, consider the standard Lagrangian of a particle in a gravitational field

$$L = T - V = \frac{m}{2} \dot{x}_k \dot{x}^k - V_g(m, x_i) \quad (9.11)$$

where the latin indices are used for spatial coordinates (x, y, z) . Let $m \rightarrow m[\alpha_{g_A}(x^\mu)]$. Minimizing the action gives back the fundamental principle of Newtonian dynamics

$$\frac{dp_i}{dt} = -\nabla_i V_g, \quad (9.12)$$

with the linear momentum defined as

$$p_i := \frac{\partial L}{\partial \dot{x}_i} = m[\alpha_{g_A}(x^\mu)] \dot{x}_i. \quad (9.13)$$

Assuming for simplicity a vertically oriented gravitational potential along $x_3 = z$, we write locally $V_g \simeq m[\alpha_{g_A}(x^\mu)] g z$. Eq. 9.12 becomes:

$$\frac{\partial m[\alpha_{g_A}(x^\mu)]}{\partial \alpha_{g_A}} \frac{\partial \alpha_{g_A}}{\partial t} \dot{z} + m[\alpha_{g_A}(x^\mu)] \ddot{z} = m[\alpha_{g_A}(x^\mu)] g + \frac{\partial m[\alpha_{g_A}(x^\mu)]}{\partial z} \frac{\partial \alpha_{g_A}}{\partial z} g z. \quad (9.14)$$

One can not simplify anymore the inertial and the gravitational masses to get $\mathbf{a} = \mathbf{g}$ as usual. Generalizing this example or using the Newtonian limit of Eq. 9.10, one can conclude that a new term should be added to the Newtonian acceleration for particles in free-fall due to variation of fundamental couplings:

$$\mathbf{a} = \mathbf{g} + \delta \mathbf{a}, \quad (9.15)$$

with

$$\delta \mathbf{a} = \sum_{g_A} \frac{\partial \ln m}{\partial \alpha_{g_A}} (\nabla \alpha_{g_A} - \dot{\alpha}_{g_A} \mathbf{v}). \quad (9.16)$$

The index g_A ranges over the various varying structure constants α_{g_A} . This $\delta \mathbf{a}$ will unavoidably depend on the composition of the falling material bodies through $\partial \ln m / \partial \alpha_{g_A}$. It is now clear to see why this is a direct violation of the WEP and EEP: two different bodies will not fall identically in the same gravitational field. Deviation to universality of free fall (UFF) is quantified by the value of the Eötvos parameter η , comparing the gravitational acceleration of two bodies A and B with different compositions:

$$\eta = 2 \frac{(m_g/m_i)_A - (m_g/m_i)_B}{(m_g/m_i)_A + (m_g/m_i)_B} = 2 \frac{|\mathbf{a}_A - \mathbf{a}_B|}{|\mathbf{a}_A + \mathbf{a}_B|}. \quad (9.17)$$

If couplings are dynamical, one thus expects to find $\eta \neq 0$ at some level¹⁵. As such, the energy running of the coupling seems to be another signature (with the fact that G has dimensions), that GR is only true at low energy and can not be a high energy quantum theory, as it must be able to induce some small deviations from $\eta = 0$. However, the answer might be subtler and as far as I am aware, this point is not explicitly discussed in the literature. Treating this question might require a proper definition of the EEP at the quantum level as suggested in [Zych & Brukner \(2018\)](#).

The varying coupling field act as a "fifth force" and is sometimes referred to by this name. Indeed, imagine that electromagnetism is an unknown force. Letting a plastic ball and magnet falling freely in a magnetic field, one would conclude that the WEP is violated as they don't fall the same way. While one could conclude that the gravity is non-metric (do not encompass the EEP), this phenomenon is better understood as the fact that the two objects couple differently to the new magnetic force field. Depending on a deeper physical motivation emerging from a model, any violation of EEP induced by varying constants can thus be either interpreted as the need for a non-metric theory of gravity or as the existence of a new fundamental force acting on the fermions. On this topic, see e.g. [Dvali & Zaldarriaga \(2002\)](#); [Bergé et al. \(2022\)](#).

There are multiple ways to tests the EEP in the Solar system and beyond with a very high accuracy (for a review see e.g. [Will, 2014](#)). The most competitive bound to date on η , is by far given by the MICROSCOPE experiment ([Touboul et al., 2022](#)). Using orbiting masses in free fall around the Earth inside a satellite experiment, the final results of the MICROSCOPE mission give a constraint on η for a pair of titanium and platinum of

$$\eta = (-1.5 \pm 2.7) \times 10^{-15}. \quad (9.18)$$

For all the reasons discussed above, this tight limit is not only a direct constraint on the metric nature of gravity, but also an indirect probe of the stability of the fundamental constants. This value was made public during my PHD thesis, improving by one order of magnitude the previous bound of $\eta = (-0.1 \pm 1.3) \times 10^{-14}$ ([Touboul et al., 2017](#)). The anticipation of this update justified a significant amount of the work done during the first two years of my PHD in order to prepare for this data release.

9.2 The fine structure constant, its astrophysical impacts and the corresponding observables

The fine structure constant $\alpha_{\text{EM}} \equiv \alpha$ is the gauge structure constant associated with the electromagnetic force. According to our previous definitions, it is given in natural units by $\alpha = \frac{e^2}{4\pi}$, where e is the electron charge. In S.I. units, $g_e = e/\sqrt{\hbar c \epsilon_0}$, such that

$$\alpha = \frac{e^2}{4\pi \epsilon_0 \hbar c}. \quad (9.19)$$

¹⁵This point is a bit subtler in the case of a varying G or α_{g_A} as the WEP excludes gravitational interaction (as all the points of the EEP, contrarily to the strong equivalence principle (SEP) defined in Sec. 3.2.1). As such, theories with varying G as the one of [Brans & Dicke \(1961\)](#), still embody the WEP (and are hence metric according to Schiff's conjecture) while G is varying through the existence of a scalar field (and hence gravity is not uniquely a geometrical effect). The SEP however, would not be satisfied and can be used to probe theories with varying G .

9. EXPLAINING THE VALUES OF OUR STANDARD MODELS' FUNDAMENTAL CONSTANTS

As stated in Tab. 9.1, $\alpha \simeq 1/137$. In regard with our previous discussion, note that while the vacuum permittivity ϵ_0 plays a central role in electromagnetism, it is never considered as a fundamental constant. This can be confusing as it is introduced in the theory just as G . Indeed, it is required in order to quantify the strength of the electrostatic force between two charges in the framework of Newtonian mechanics: $|\mathbf{F}_q| = k_c q_1 q_2 / d^2$ with $k_c = 1/(4\pi\epsilon_0)$. However, choosing natural units with $c = \hbar = 1$, and counting charges in multiples of the electron charge (i.e. $e = 1$), we obtain $|\mathbf{F}_q| = \alpha q_1 q_2 / d^2$. This last point shows that it is, in turn, α and not ϵ_0 which plays a role similar to G in electromagnetism. Similarly, as we argued already above, one should prefer the use of α_G instead of G , such that $|\mathbf{F}_G| = \alpha_G m_1 m_2 / d^2$ in a system of natural units with $m_p = 1$.

In the quest of varying couplings, the observation of α should be favored over most of the other constants as

- It is dimensionless, and hence favorable over dimensional constants as explained in length in Sec. 9.1.2.
- Its impact on observables is very well understood, controlled and linear, which would not be the case e.g. for QCD constants associated to highly non-linear and non-classical physics. It is hence possible to measure it very precisely using primarily quantum atomic and nuclear transitions.
- As α quantifies the strength of the EM coupling between electrons, photons and hadrons, it is omnipresent in atomic physics and optics. As such, it will play a huge role in the dynamics and observables of astrophysical systems, based on the emission and observation of light. This impact is stronger and more direct than the weaker non-linear effect of gravity through α_G . When seeking for variations on extremely large spatio-temporal scales, astrophysical and cosmological observables are absolutely necessary and α will moreover impact phenomena at every possible scales and times in the cosmic history.

Considering here only the possible time variation of α in an homogeneous universe, we can consider a large panel of measurements spanning the whole redshift range, given in Tab. 9.3. The idea is to find a way to measure how $\alpha(z)$ at a given redshift z , can be compared with the measured value in laboratory today α_0 by considering the quantity

$$\frac{\Delta\alpha}{\alpha_0} := \frac{\alpha(z) - \alpha_0}{\alpha_0} = \frac{\alpha(z)}{\alpha_0} - 1. \quad (9.20)$$

While this value quantify the deviation of α to its value measured on Earth, it is also possible to measure its *drift*, $\dot{\alpha}/\alpha_0$ with a very high accuracy in laboratory. This last quantity put constraints on the possible rate of change of the fine structure constant with time. When investigating the possible variation of the fine structure constant with time, it is not only necessary to have accurate measurements of α , but it is also desirable to have as many measurement points as possible associated to different times of the cosmic history i.e. at many different redshifts z . Combining all these measurements, it becomes possible to use the fine structure constant values to do some " α -cosmography" as in [Martins et al. \(2022a\)](#).

- **Atomic clocks:** The finer way to measure α is through its impact on atomic lines. Indeed, the fine and hyperfine structure of the atomic spectra are directly proportional

Observable	Redshift	Order of magnitude	Indicative references
Atomic clocks	$z = 0$	$\dot{\alpha}/\alpha_0 \sim 10^{-18} \text{ yr}^{-1}$	Lange et al. (2021)
Oklo reactor	$z = 0.14$	$\Delta\alpha/\alpha_0 \sim 10^{-8}$	Gould et al. (2006)
QSO	$0.2 < z \lesssim 5$	$\Delta\alpha/\alpha_0 \sim 10^{-6}$	Martins (2017)
CMB	$z \sim 1100$	$\Delta\alpha/\alpha_0 \sim 10^{-3}$	Hart & Chluba (2018)
BBN	$z \sim 10^8$	$\Delta\alpha/\alpha_0 \sim 10^{-6}$	Fields et al. (2014)

Table 9.3: Major probes of the value of the fine structure constants α at different redshifts.

to α^2 (hence their name). These lines are due to the splitting of degenerated energy states in the atomic Hamiltonian due to relativistic corrections, spin-orbit and spin-spin couplings. The quantum nature of the transitions makes the value of their position exact. Atomic clocks measurements exploit this dependence of the line in α to seek for time variations of the electromagnetic coupling. In this thesis, we considered the constraint obtained by [Lange et al. \(2021\)](#) of $\dot{\alpha}/\alpha_0 = 1.0 \pm 1.1 \times 10^{-18} \text{ yr}^{-1}$. This result, outstanding with regard to human timescales, is obtained by comparison of two atomic clocks based on different atomic transitions of the ion $^{171}\text{Yb}^+$. The stability of the ratio of the transition lines is re-measured and compared over several years. For the sake of completeness, let us mention that improved constraints based on similar measurements where released after the submission of the results I will present in Sec. 9.4 and Sec. 9.6, pushing the constraints one order of magnitude lower: $\dot{\alpha}/\alpha_0 = 1.8 \pm 2.5 \times 10^{-19} \text{ yr}^{-1}$ ([Filzinger et al., 2023](#)). The project of building nuclear clocks based on quantum transition in the nuclei opens the horizon for an improvement on these constraints by several order of magnitudes ([Fadeev et al., 2020](#)).

- **Oklo reactor:** The Oklo mine is located in the Gabon Republic. Rich in Uranium, it behaved spontaneously as a natural nuclear reactor for a few million years around 1.8 billion years ago ([Damour & Dyson, 1996](#)), which correspond to a redshift of $z \simeq 0.14$. Nuclear physics gives the second major impact of the value of α on physics. A different value of the fine structure constant would impact the interaction cross-sections and thus the interaction rates of nuclear reactions. As such, it is possible to recover the value of α with high precision from the observed abundances of the various isotopes in the Oklo mine. The constraint thus obtained is $\Delta\alpha/\alpha_0(z = 0.14) = 0.5 \pm 6.1 \times 10^{-8}$ ([Gould et al., 2006](#); [Onegin et al., 2012](#)).
- **QSO spectroscopy:** Quasars or quasi stellar objects (QSO) are extremely bright active galactic nuclei (AGN) sourced by the accretion of a central supermassive black hole. As such, they are among the most energetic light sources that can be found in the Universe. As proposed by the unified AGN models, QSO are distinct from other AGN types (as blazars or radio-galaxies) because the AGN is seen with an intermediate angle such that the black hole jet is partially oriented towards the line of sight ([Barthel, 1989](#); [Antonucci, 1993](#)). Since they represent early active phases of a galaxy life, they can be mostly found in the early Universe (even though the central black hole can be ignited in late times by galaxy mergers)¹⁶. Hundreds of thousands of QSO are known, spanning a redshift range between 0.056 and 7.64. Low density clouds are present around the AGN

¹⁶The Milky Way most probably knew such an active phase and could know a new one with its merging with M31 [Cox & Loeb \(2008\)](#).

such that the spectra of QSO contain absorption lines. While redshift changes linearly the position of all the absorption lines, the value of the fine structure constant have a non-linear impact on them. It is hence possible to constrain α by looking at the relative positions of different lines within a single QSO spectra. Spectroscopic measurements allow us to obtain very competitive constraints of $\Delta\alpha/\alpha_0 \leq 1 \times 10^{-6}$ this way. The dataset from [Webb et al. \(2011\)](#) contains 293 measurements of $\Delta\alpha/\alpha_0$ obtained by the VLT-UVES and Keck-HIRES instruments for $0.22 \leq z \leq 4.18$. A dipole of the α spatial distribution has been detected within this dataset with a 4.2σ significance. Such a detection would represent a major breakthrough as well as a violation of the cosmological principle. However, further analysis with a larger dataset lowered this significance at 3.7σ , which could favor the presence of a systematic effect ([Wilczynska et al., 2020](#)). Recent measurement points from other spectrometers can be added to this list. Data points from the Subaru telescope and the HARPS spectrograph can be found in [Martins \(2017\)](#), as well as a very recent ESPRESSO data point in [Murphy et al. \(2022\)](#). Further improvement of one order of magnitude are expected with the construction of the ANDES high resolution spectrograph on the ELT, which should also be able to clarify the situation regarding the observed dipole tension ([Marques et al., 2023](#)).

- **CMB:** As discussed in [Galli et al. \(2011\)](#); [Planck Collaboration \(2015b\)](#), a different value of the fine structure constant during recombination (and in a minor fashion during reionization) would impact the statistical distribution of the CMB anisotropies. In the end, it would impact their shape of the resulting angular power spectra as we will further discuss in Sec. 9.3.2. Assuming simply a constant shift of the value of α through the whole cosmic history, one can derive from Planck *Planck* data $\Delta\alpha/\alpha_0(z = 1100) = -0.7 \pm 2.5 \times 10^{-3}$ [Hart & Chluba \(2018\)](#). This constraint could be optimized by one order of magnitude if extracting all the information in the CMB (variance limited), including E -modes polarization data ([Hart & Chluba, 2022](#)). Additionally, it seems that a varying fine structure constant could help relieving the H_0 tension by shifting the redshift at which recombination occurs ([Hart & Chluba, 2022](#); [Lee et al., 2023](#)). Spectral distortions could also provide an independent probe of the value of α in the CMB, with a similar constraining power as anisotropies ([Hart & Chluba, 2023](#)).
- **BBN:** As the value of α impacts the outcome abundances of nuclear reactions, it should also impact the proportions of light elements recovered after BBN. This allows to infer very strong constraints as $\Delta\alpha/\alpha_0 = 2.1^{+2.7}_{-0.9} \times 10^{-6}$ at $z \sim 4 \times 10^8$ ([Deal & Martins, 2021](#)). This result shows a $\sim 2\sigma$ tension which can be related with the so called Lithium problem. Indeed, while BBN allows to predict successfully the observed abundances of light elements in the primordial Universe, a significant discrepancy ($\sim 5\sigma$) is observed for ${}^7\text{Li}$ ([Fields, 2011](#)). A primordial variation of the fine structure constant could thus solve this tension. However a destruction of the lithium atoms in stellar atmospheres (depletion factor) is still statistically preferred ([Deal & Martins, 2021](#)). The derived bound on α is highly model-dependent and requires the variation of all the couplings together to be consistent. A minimal modeling of the BBN impact is to assume that a varying α changes only the Helium-4 abundances (expected to be the most impacted one) as ${}^4\text{Y}_{\text{He}} = \kappa_{\text{BBN}} \Delta\alpha/\alpha_0$, where the value of κ_{BBN} depends on the model under consideration ([Clara & Martins, 2020](#)).

- **Complementary probes:** Other independent but less competitive methods exist to constrain variations of the fine structure constant. For example, using abundance-based dating methods on meteorites, one can derive constraints of order $\Delta\alpha/\alpha_0 \sim 10^{-5}$ using the long α and β radioactive decay rates (with a mean redshift $z \sim 0.43$ [Fujii & Iwamoto, 2005](#)). Stars also gives a probe of varying α . Nucleosynthesis in their core is affected by the value of α ([Uzan, 2011](#)), as well as the position of the absorption lines of their photosphere ([Murphy et al., 2022](#)). However stellar structure involve very complex and turbulent physics, which is hard to control in practice. Finally, the absorption of the CMB radiation by the 21 cm hydrogen line during dark ages can also be used to probe the value of α at early time ([Khatri & Wandelt, 2007](#)). Similarly to the CMB, it is able to provide constraints of order 10^{-3} at very high redshift $3 < z < 30$. Instruments as SKA will be able to derive competitive bounds which will have to be used to complete the canonical dataset given in Tab. 9.3, allowing to cover almost all possible z values ([Lopez-Honorez et al., 2020](#)).

For electromagnetism, we write $\mathcal{F} = F$ and $\mathcal{A} = A$. A variation of the fine structure constant induced by a scalar field would hence translate in the existence of a term $B_F(\phi)$ in the Maxwell Lagrangian as $\mathcal{L}_F = -B_F(\phi)\langle F, F \rangle / 4$, leading to $\Delta\alpha/\alpha_0 = B_F(\phi)^{-1} - 1$ (see Sec. 9.1.4). Such a term would be equivalent to a space-time dependent value of vacuum permeability and would lead to a violation of the EEP as explained in Sec. 9.1.5. Choosing a given space and time frame and writing the electric and magnetic fields respectively \mathbf{E} and \mathbf{B} , this term also induces a field dependent variation of the total electromagnetic energy density $B_F(\phi)(\mathbf{E}^2 - \mathbf{B}^2)$ and a modification of Gauss law as $\nabla \cdot \mathbf{E} = B_F(\phi)^{-1}\rho_e$, where ρ_e is the electric charge density.

All of the above bounds are extremely sharp and thus give very strong constraints on the existence of scalar field model with varying α , as we will further investigate explicitly. Note that the possibility of so called "screening mechanisms" are often invoked (for a review see e.g. [Brax \(2013\)](#)). This is the case of the so-called chameleon mechanism, which would explain why a scalar field could have less impact on observables (as α and η) near compact objects as the Earth ([Khoury & Weltman, 2004](#)), and remain hidden below the current observational bounds.

Let us temperate this picture by insisting on this very important fact: while we will now focus on the time variation of α , spatial variations are still expected at the perturbation level in an homogeneous universe satisfying the cosmological principle. Additionally, we should keep in mind that in every consistent high energy physics theory, coupled variations of all the constants together are expected, unless some specific mechanism prevent it (this will be further explained in Sec. 9.5). However, α is expected to provide the tightest constraints and is by far the best observable in order to investigate the stability of the fundamental constants.

9.3 Building a modified Boltzmann solver to quantify the impact of varying α cosmology

9.3.1 The need and the development of a new tool

I am working on varying fine structure constant models since my first year of master's degree. This work lead to my first publication, [Martins & Vacher \(2019\)](#), under the supervision of Carlos Martins (CAUP, Porto) at the University of Porto, in which we used low redshift data to constrain a model of varying α inspired from string theory: the *runaway dilaton* model. I will come back to this model in Sec. 9.6. In order to extend this study to other models, include high redshift data as the CMB and simulate with a high precision the impact of the fine structure on cosmological observables, I chose to build a robust computational framework which would be able to keep track self-consistently of this impact, along with the rest of the standard cosmology.

It appeared that the proper way to do so was to create a modified version of a so-called Boltzmann solver allowing for a variation of the fundamental constants. Boltzmann solvers are intricate codes computing consistently the evolution of all the cosmological quantities through the Universe history.

We choose to modify the cosmic linear anisotropy solving system (CLASS¹⁷, [Lesgourgues, 2011](#)), which is a software (mostly coded in C) allowing to compute perturbation equation and cosmological outputs from the cosmological parameters. In order to derive constraints on specific models, it can be coupled to a Monte Carlo Markov chain (MCMC) sampler as MONTEPYTHON ([Brinckmann & Lesgourgues, 2018](#); [Audren et al., 2013](#))¹⁸. Finally, contour plots can be made thanks to the GETDIST software¹⁹.

Applying significant modification to the CLASS software is a difficult task without the proper expertise. In order to implement the variations of the fundamental constants, I asked for the help of Nils Schöneberg (ICC, Barcelona University), who is himself a key member of the software development team. Our fortunate encounter was made possible through discussions with Julien Lesgourgues (RWTH Aachen University), Brahim Lamine (IRAP) and Alain Blanchard (IRAP). Answering my request, Nils implemented the impact of a variation of α within the thermodynamics module and in the HYREC and RECFAST recombination codes ([Ali-Haïmoud & Hirata, 2011](#)). After discussion, we decided to account minimally for the impact on BBN, writing the impact on the helium fraction through κ_{BBN} without having to modify the PARTHENOPÉ code in details (yet) ([Consiglio et al., 2018](#)). During the implementation, I helped extensively as a user and tester, making sure the impacts were all accounted for, and were the expected one. This experience was a major opportunity to become familiar with the use and modification of the CLASS code. Our final version was made public and was re-used in several subsequent works with the additional implementation of a varying electron mass ([Schöneberg et al., 2022](#); [Barros & da Fonseca, 2023](#); [da Fonseca et al., 2022](#); [Lee et al., 2023](#)). Starting from this code, and always under the kind supervision of Nils, I implemented my own models in which the variation of α is

¹⁷https://github.com/lesgourg/class_public

¹⁸https://github.com/brinckmann/montepython_public

¹⁹<https://github.com/cmbant/getdist>

driven by a scalar field ϕ , which cosmic evolution are given by modified versions of the Klein-Gordon equations (see Sec. 4.2.2). The modified CLASS software is then able to integrate these equations to compute $\phi(z)$ and $\alpha(z)$, such that I could confront these predictions with data.

9.3.2 An illustration: the impact of varying constants on recombination and the CMB

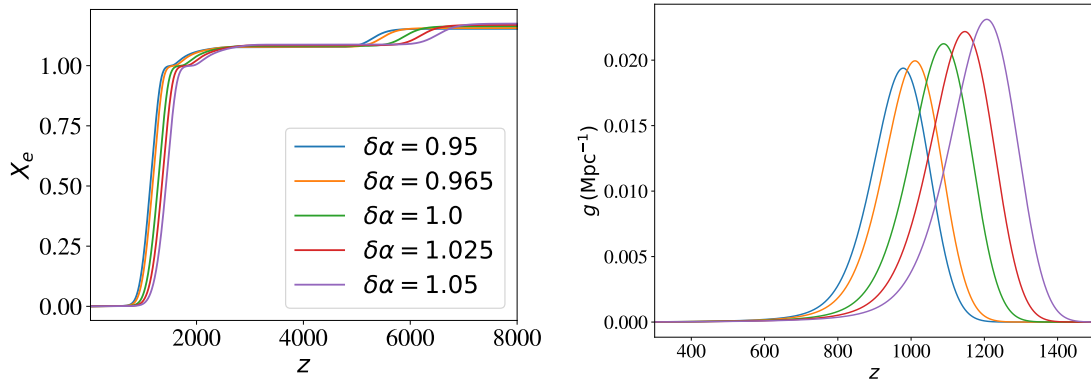


Figure 9.2: Ionization fraction X_e and visibility function g for different values of $\delta_\alpha = \alpha/\alpha_0$ during recombination.

As discussed in Sec. 9.2, the CMB allows to probe the value of the fundamental constants at $z \simeq 1100$. As an illustration, I detail here how the value of α can impact the recombination process and how this can be witnessed in the CMB angular power spectra presented in Chap. 5. By comparing with previous literature, this investigation additionally provides an illustration as well as a test for the validity of our implementation within CLASS.

In Fig. 9.2 and 9.3, I produced plots the recombination history and the CMB angular power spectra respectively, using our modified CLASS version. The derived results are very similar to the ones obtained in previous works as e.g. Galli et al. (2011); Planck Collaboration (2015b). One can witness that a different value of the fine structure constant at the recombination epoch would either intensify or weaken the strength of the interaction between electrons and hadrons, changing the time at which recombination happens (here $\delta_\alpha = \alpha/\alpha_0$, where α is here assumed to be constant for $z \geq 50$ ²⁰). This effect can be observed through the redshift dependence of the ionization/free electron fraction $X_e = n_e/n_H$ and the visibility function g , quantifying the probability distribution that a photon last scatters at a given redshift z . A stronger value of α makes the recombination happen quicker and at earlier time. Indeed, for $\delta_\alpha > 1$, the free electron fraction decreases more brutally and reaches zero earlier i.e. at higher z , while the curve of $g(z)$ is way steeper and also shifted towards higher z . On the other hand, a lower value of α leads to a longer and later recombination time (i.e. at lower z). As such, δ_α is by essence strongly degenerated with the value of H_0

²⁰In this version of the CLASS implementation α is constant for $z \geq 50$ and then suddenly take the values $\alpha = \alpha_0$. Of course, such "threshold" variation of the constant is not physically motivated and used here only for an illustrative purpose. This version is now publicly available on the [class_public](#) repository (commit #aa92943) with the use of the keyword 'varying_fundamental_constants':instantaneous'.

([Hart & Chluba, 2018, 2022](#)). Overall, the value of δ_α impacts the angular power spectra by shifting the position and amplitudes of the acoustic peaks. The effect is dominant at large ℓ . A surprisingly strong and linear impact on the *BB* lensing can be witnessed, which was never discussed in detailed in previous literature as far as I am aware. Incoming CMB experiment targeting polarization on the smallest scales might be able to use this effect to provide competitive constraints on the stability of the fine structure constant. As this topic is at the interface between all my research interests, I am envisioning to further work on it in the future.

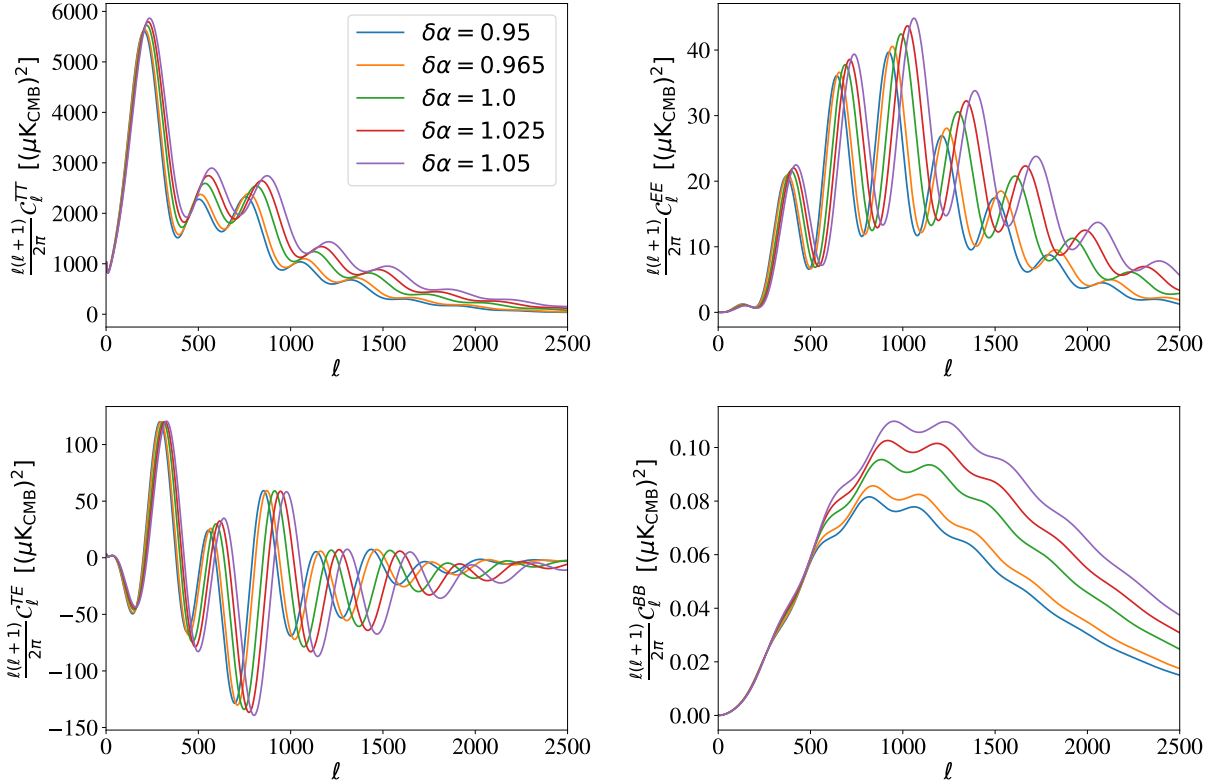


Figure 9.3: CMB power spectra for the best fit values of Λ -CDM with $r = 0.001$ for different values of $\delta_\alpha = \alpha/\alpha_0$.

Due to the high- ℓ impact of a time varying α , the *LiteBIRD* mission presented in Chap. 7 would not be the best suited mission to investigate this physics, or only as a complementary probe breaking degeneracies as it is targeting only the largest scales ($\ell \in [2, 200]$). Spatial variations of α on the LSS could however be probed by such a CMB mission ([Smith et al., 2019](#)). For example, the presence of a large-scale spatial variation of α , as the dipole detection claim by [Webb et al. \(2011\)](#), which could only be verified in the CMB with an experiment as *LiteBIRD*. Unfortunately, I did not further investigate this point in the present thesis, as it would require to set a new complex formalization going beyond the simple use of our modified CLASS version. Still, further exploring the connections between CMB and varying constants remains one of my primary objective for future research.

9.4 Constraining the Bekenstein model(s)

I will now introduce the latest to date observational constraints on three versions of the Bekenstein model, in which a scalar field coupled to electromagnetism induces a time variation of α . The full paper is available in Appendix D.4. The idea of this work emerged from discussions between Carlos Martins, João Dias (CAUP, Porto) and myself at the Azores summer school in 2021. Strong of our new implementation of the varying constants in CLASS – introduced in Sec. 9.3 – it appeared that updating the constraint on Bekenstein models was a timely exercise, with the incoming update of the MICROSCOPE bound (See Sec. 9.1.5). By providing this update, I was also willing to investigate the different ways these models could be implemented and had been constrained in the past. Bekenstein models are both simple and extremely general, such that they represented a natural starting point to explore the stability of α on cosmic time scales.

9.4.1 Context: Zoology of the Bekenstein model(s)

Bekenstein proposes the simplest possible phenomenological model of a general scalar field introducing variations of the fine structure constant, that remains self consistent from the point of view of high energy. In its simplest form, the model assumes a variation of the electromagnetic coupling $g_e = e/\sqrt{\hbar c \epsilon_0}$ which is given by a scalar field ϵ as $g_e = g_{e,0}\epsilon(x^\mu)$ (Bekenstein, 1982, 2002). As such, considering the rescaled connection $\tilde{A} = \epsilon A$, one must add the factor $B_F(\epsilon) = \epsilon^{-2}$ to the curvature Lagrangian in order to preserve gauge invariance as discussed in Sec. 9.1.4. Usually, a redefinition of the field is done as $\phi = \ln(\epsilon)$, such that $B_F(\phi) = e^{-2\phi}$ and thus $\Delta\alpha/\alpha_0 = e^{2(\phi-\phi_0)} - 1$ (see again Sec. 9.1.4). Note that despite the initial conditions for the field (which have a poor impact on cosmology due to the existence of attractor mechanism during radiation domination), this model does not contain any free parameters. Sandvik et al. (2002) further suggested the addition of a degree of freedom, ζ , quantifying violations of the EEP as $\eta \sim 3 \times 10^{-9}\zeta$. Assuming that the field couples also to dark matter, ζ appears in the modified Klein-Gordon equation of motion for the field as

$$\ddot{\phi} + 3H\dot{\phi} = -\frac{2}{M_{\text{Pl}}^2}e^{-2\phi}\zeta\rho_m. \quad (9.21)$$

The value of ζ hence depends strongly on the nature of dark matter. This "vanilla + ζ " model is referred to as the "Bekenstein-Sandvik-Barrow-Magueijo" (BSBM) model.

Going further in generality, Olive & Pospelov (2002) proposed a version of the Bekenstein model in which the field can be coupled to electromagnetism with a general function $B_F(\phi)$. Furthermore, in a high energy theory, if no symmetry principle excludes it, the field is also expected to be similarly coupled to the other sectors of the standard model through functions $B_\psi(\phi), B_\Lambda(\phi), B_\chi(\phi)$ where ψ , Λ and χ are respectively the standard model fermions (hadronic matter), the cosmological constant, and dark matter. This fully coupled model is

called the "Olive & Pospelov" (O&P) model and can be described by the action²¹

$$S = \int d^4x \sqrt{-|g|} \left[M_{\text{Pl}}^2 \left(\frac{R}{2} - B_\Lambda(\phi) \Lambda \right) - \frac{1}{4} B_F(\phi) \langle F, F \rangle \right. \\ \left. + \bar{\psi} (\not{D} - m_\psi B_\psi(\phi)) \psi + \bar{\chi} (\not{D} - m_\chi B_\chi(\phi)) \chi \right. \\ \left. + \frac{1}{2} M_{\text{Pl}}^2 \partial_\mu \phi \partial^\mu \phi - V(\phi) + \dots \right], \quad (9.22)$$

which is a generalization of the SM action (Eq. 3.8) including a coupled scalar field ϕ , and a fermionic dark matter particle χ (which could be the neutralino discussed in Sec. 4.1.1). As such, it is expected to reproduce the low energy limit of multiple varying α models beyond SM with the presence of $B_F(\phi)$. Arguing that observation constrains the field to be weakly varying, this scenario is treated by a first order Taylor expansion of the couplings around today's value as $B_i(\phi) \simeq 1 + \zeta_i(\phi - \phi_0)$. As such $B_F(\phi) = 1 + \zeta_F(\phi - \phi_0)$ and $\Delta\alpha/\alpha_0 \simeq -\zeta_F(\phi - \phi_0)$. Taking the derivative of this expression, one finds that the atomic clocks, presented in Sec. 9.2, will be sensitive to $\dot{\alpha}/\alpha_0 = -\zeta_F \dot{\phi}$. The values of $(\phi - \phi_0)$ and $\dot{\phi}$ are given by the modified Klein-Gordon evolution for the field

$$\ddot{\phi} + 3H\dot{\phi} = -\frac{1}{M_{\text{Pl}}^2} \sum_i \rho_i \zeta_i - \frac{\partial V}{\partial \phi} \quad \{i \in \chi, b, \Lambda\}, \quad (9.23)$$

and are thus directly related to the other values of the coupling ζ_i . Furthermore, using simplifying assumptions, one can approximate that the fully coupled field is related to the Eötvos parameter introduced in Sec. 9.1.5 as

$$\eta \simeq 2.9 \times 10^{-2} \zeta_b \zeta_F. \quad (9.24)$$

This expression, adapted from Olive & Pospelov (2002), assumes an identical coupling of the field with all the baryonic matter (e.g. neutrons and protons) and is actually expected to change slightly depending on the composition of the falling element under consideration. While a more accurate derivation would have been desirable, we expect this expression to give us the correct order of magnitude from the constraining power of the UFF tests between a light and an heavy elements on Bekenstein models, which is our main concern here²².

From the above discussion, we can see that cosmological observables can only be sensitive to the products $\eta_i = \zeta_F \zeta_i$ ²³ which are the real degrees of freedom that can be constrained. The coupling to dark matter η_χ and dark energy η_Λ impact the cosmological evolution of the field and can be constrained by cosmological probes and varying α data, while the coupling to hadrons $\eta_b = \zeta_b \zeta_F$ is driving violations of the EEP in Eq. 9.24.

²¹Note that in the paper, the opposite sign convention $(+, -, -, -)$ was used for the metric, explaining why the expressions of the Lagrangian are different from the one presented in the thesis. We further assume that the mass scale of the theory is given by the Planck mass M_{Pl} .

²²Considering Eq. (3.5) of Olive & Pospelov (2002) and assuming that the mass scale of the theory M_* is the Planck mass M_{Pl} ($\omega = 1/2$) as well as that the field couples identically to protons and neutrons ($\zeta_p = \zeta_n \equiv \zeta_b$), one obtains $\eta = 1.4 \times 10^{-3} \zeta_b \zeta_F (Z_2^2 - Z_1^2) / A_2^{4/3}$ (neglecting the second order term in ζ_F^2). For the two elements used in the MICROSCOPE experiment: platinum ($Z_1 = 78$, $A_1 = 195$) and titanium ($Z_2 = 22$, $A_2 = 48$) one obtains $\eta = 4.49 \times 10^{-2} \zeta_b \zeta_F$. Justifying a posteriori the use of Eq. 9.24. Using the exact expression derived here would have however been preferable but would not have impacted significantly our results and conclusions.

²³The parameters η_i should not be confused with the Eötvos parameter η . This choice of notation has been maintained to stick with previous literature on the topic.

9.4.2 The paper: Objectives and results

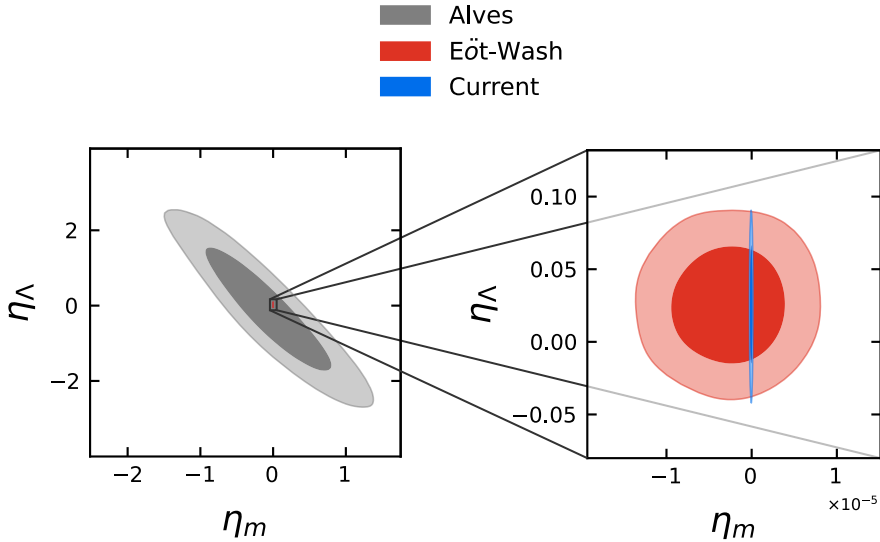


Figure 9.4: Constraints on the O&P model universally coupled to matter with an older version of the atomic-clock constraints (Rosenband et al., 2008) and without the MICROSCOPE bound (grey), with the Eöt-Wash bound (Wagner et al., 2012) on the UFF (red) and with our full dataset (blue). Couplings are expressed in part per millions (10^{-6}).

In the paper (Appendix D.4), we used the latest available data in order to constrain various implementations of the Bekenstein models using the coupling of our CLASS implementation with MONTEPYTHON. Data are made of a combination of cosmological likelihoods, introduced in Chap. 3, constraints on the time variation of α , introduced in Sec. 9.2, and the MICROSCOPE bound given in Sec. 9.1.5. As the first author of the paper, I was responsible for the implementation and test of the Bekenstein scalar field in the three different CLASS versions used for this project under the close supervision and help of Nils Schöneberg. This exercise was far from straightforward, as it requires to keep track of the units and face numerous technical issues unique to the intricate and opaque code of CLASS. A easier way would have been to find an analytical expression for $\phi(z)$ by integrating Eq. 9.21 and Eq. 9.23 under simplifying assumptions and implement this expression directly in the software, as done in all the previous studies of this model. Instead, I decided to integrate numerically the full equation of motion within CLASS in order to account for all the cosmological evolution of the field without any assumptions breaking at high redshift. This requirement certainly had a negligible impact on our results, but I wanted to pave the way towards the implementation of more complicated models. Indeed, developing and presenting a robust framework – easy to use and to modify for model specific considerations – was also one of the primary target of this work.

I further implemented all the relevant likelihoods in MONTEPYTHON, from which I derived all the constraints and contours plots on the three models by running chains. I also had to modify significantly the MONTEPYTHON code for our specific use. João Dias, who came visiting me for one week in Toulouse to focus on this project, provided cross-checks of the results and the last versions of the figures using GETDIST. Finally, I was responsible for the writing of the whole paper, and the corresponding literature survey. I was also in charge of my ex-student and intern Samy Vinzl (undergraduate), who helped testing the implementations

of the CLASS versions by comparing their outputs with our self-made python codes, in collaboration with João Dias.

Our work presents an overview of the different phenomenological implementations of the Bekenstein model as well as a comparative analysis between them. For all the models, we set $V(\phi) = 0$ for simplicity. We provide the latest constraints to date on such models, with the first time introduction of the stringent MICROSCOPE bound. Our conclusions are the following:

- For the **BSBM** model, we find identical constraints as the one derived in the work of [Martins et al. \(2022b\)](#). To match the unit conventions used in this work, we define $\tilde{\zeta} = 8\pi\zeta$. We derive $\tilde{\zeta} = -0.093^{+0.10}_{-0.13}$ ppm (68% C.L.), comparable to the preceding result of $\tilde{\zeta} = -0.10 \pm 0.12$. Doing so, we validate our implementation and conclude that this model is mostly constrained by the atomic-clocks, through the equation of motion (Eq. 9.21). The addition of an updated version of the MICROSCOPE bound had no impact on the result, and a back to the envelope calculation shows that its impact on the confidence levels of $\tilde{\zeta}$ would be one order of magnitude above the current constraint.
- **O&P universally coupled to matter:** As [Alves et al. \(2018\)](#), we explored the constraints on a possible version of the O&P model coupled only to matter and dark energy. Furthermore, we assumed the model to be coupled identically to baryonic and dark matter, that is $\eta_m := \eta_b = \eta_\chi$. On Fig. 9.4, we displayed the constraint on this model in three different scenarios: in grey, without using any bound on η and with an older version of the atomic clocks from [Rosenband et al. \(2008\)](#), getting results comparable to [Alves et al. \(2018\)](#), showing a strong degeneracy between the two parameters. In red, with our dataset but replacing the MICROSCOPE bound by the older "Eöt-Wash" bound on η ([Wagner et al., 2012](#)), depicting how strongly the parameter's degeneracy can be broken using UFF data. In blue, our current constraints using all the datasets and the latest MICROSCOPE bound, putting forward the significant improvement brought by this experiment. The addition of the MICROSCOPE prior with an update of the atomic-clock likelihood hence strongly restricts the previous constraints on this model, improving the bounds on η_Λ by a factor of ~ 100 and on η_m by $\sim 10^7$.
- **Full O&P:** For the first time, we also considered the full O&P model, letting all the coupling being free. As displayed on Fig. 9.5, all the couplings greater than 10^{-6} are excluded at 1σ . η_Λ and η_χ are strongly degenerated as they both have a similar impact on the equation of motion (Eq. 9.23), while η_b is too strongly constrained by the MICROSCOPE bound (Eq. 9.24) to have any cosmological impact.

For all models, constraints appear to be so tight that no significant degeneracy can appear with the cosmological parameters. Overall, all the parameters ζ and η_i greater than part per million ($\times 10^{-6}$) are excluded for all the models. This strong shrinking of the parameter space leaves very few room for simple varying α models and exclude the natural and expected values of many models beyond the standard models presented in [Olive & Pospelov \(2002\)](#). As mentioned above, our work also propose a new powerful framework to implement any varying- α model, which we was used again in Sec. 9.6 for the runaway dilaton model.

Additionally, for low redshift studies, it is usual to ask for the vanishing of the field value at $t = t_0$ and for the cancellation of its speed during radiation domination. In CLASS it is

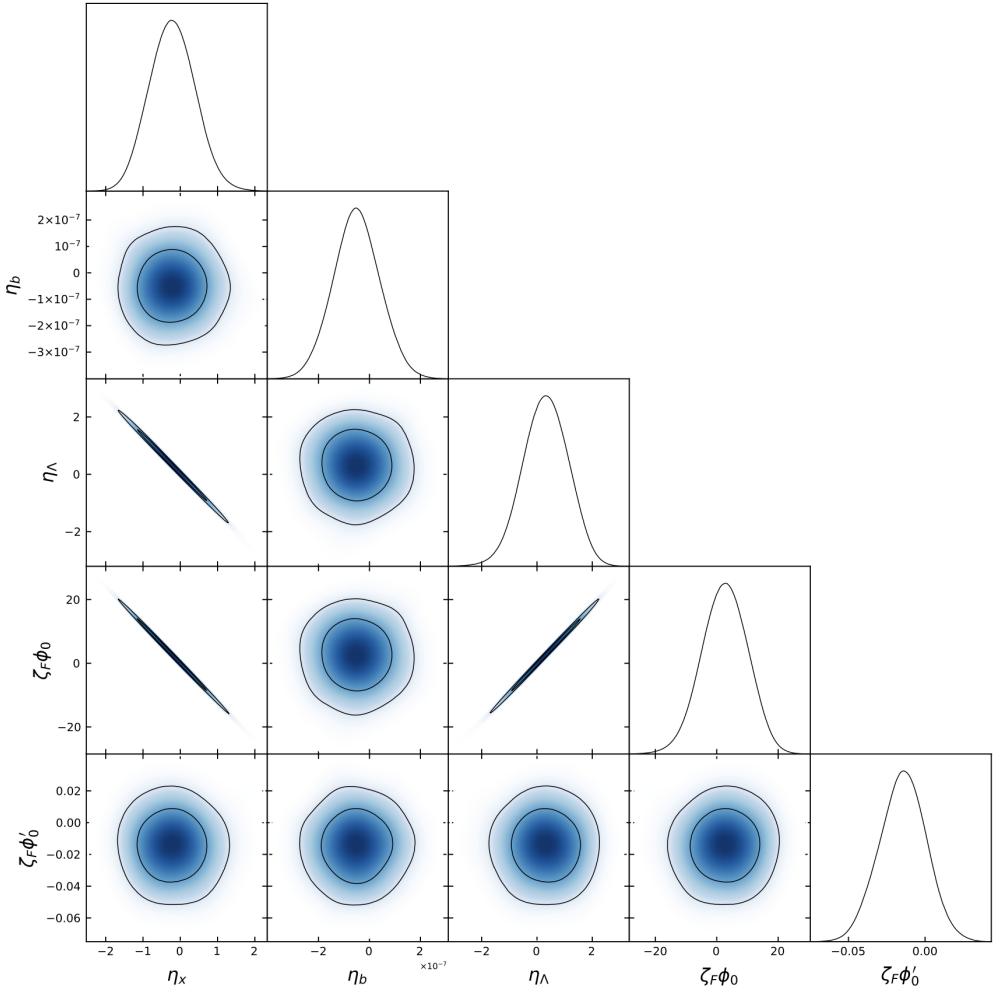


Figure 9.5: Constraints on the full O&P model with all our datasets. All the parameters are expressed in ppm.

only possible to set the initial conditions at $z \sim 10^{14}$ and let the field evolve from here. As such, for all the models we were able to derive constraints on the possible values of ϕ_0 and ϕ'_0 (related to the field's density) after the full cosmological evolution and quantify how the field dynamics can be impacted by the model's parameters.

Impact, limits and outlooks

While setting very strong restrictions on the parameter space of varying α models, this work highlights the power of local data as atomic clocks and MICROSCOPE on them. As such, I am happy that our work was recognized – together with our previous one on the dilaton field (Martins & Vacher, 2019) – in the MICROSCOPE review paper of Bergé (2023). New datasets are expected to further tighten our constraints, as the latest bound given by Filzinger et al. (2023), which was not available at the time of our publication. As detailed in footnote 22, we could also have chosen a more accurate description of the MICROSCOPE likelihood. We plan on updating our results in future related works, but so far these updates would not change our general conclusions regarding these models. This work also gives a "proof of concept" for the implementation of varying α models in our CLASS version, which

allows to keep track consistently of all the cosmological impact of the field up to $z \sim 10^{14}$.

An intrinsic limitation of all the Bekenstein models however, is that they introduce only (time) variation of α , keeping fixed the other fundamental constants. It is of course way harder to propose a self consistent model considering the co-variation of multiple constants on cosmological scales and it would be a real puzzle to implement it in CLASS. However, from a high-energy physics point of view, this choice is preferable (even though the strongest observable impact is expected to come from α). Our preliminary CLASS public implementation allows for variation of m_e and G , such that it should be possible to consider scalar field induced variations of the mass ratio μ and α_G in future works. This is the reason why the BBN bound was not used in this work as it is highly model-dependent and requires variations of all the constants within a single framework in order to be consistent. While it is still unclear if this constraint would add any improvement to the strong constraining power of the MICROSCOPE and atomic clocks combination, we chose to not consider it.

Additionally, for the sake of simplicity, we choose $V(\phi) = 0$ in this work. As Bekenstein models are purely phenomenological, the potential associated to the field could virtually take any form, and it was safer to leave this question behind in this first work. A first exponential potential implementation for a varying α model will be considered in our next work in Sec. 9.6. I am currently exploring gradually other choices of $V(\phi)$ through models with increasing complexity, where the shape of the potential can be assumed from high energy considerations. Note that a "fine tuned" potential can be a real game changer and add strong correlations of the varying- α model with cosmological parameters, as H_0 . For a version of a simple Bekenstein-like model considering decaying exponential potentials, see e.g. [da Fonseca et al. \(2022\)](#).

9.5 String theories and varying coupling

9.5.1 Overview of string theory

String theory is a theoretical framework providing strong hints towards an unification between particle physics and gravity. More precisely, string theories try to interpret all the particles of the standard model, and the gravitational field as vibrational modes of relativistic quantized strings. Those strings can be open or closed and interact between each others by merging or splitting. A major appeal of this formalism is the appearance of an excitation of the closed quantum string behaving as the mediator of gravitational interactions and called *the graviton*. The graviton always come along with another excitation behaving as a scalar field: *the dilaton*. As the Bekenstein field, the dilaton couples to the other particles of the standard model and induces a variation of the gauge couplings. While it is possible to build a string theory with closed strings only, it is impossible to have open strings without closed strings, making the appearance of gravity – and the dilaton – unavoidable in string theory. For a comprehensive and complete introduction to the topic see e.g. [Szabo \(2002\)](#); [Zwiebach \(2009\)](#).

The quantum strings were historically invoked to model the gluon lines linking pairs of quarks in the mesons. With such a model, one was able to reproduce the measured relation $J = \alpha' m^2$ relating the rest mass m of the mesons with their angular momentum J ([Chew & Frautschi](#),

1961; Nambu, 1970; Susskind, 1970). α' is called the *slope parameter*. The quantum nature of the string also allowed to explain why mesons come in discrete numbers with specific values of J and m . It was later found that relativistic quantum string were necessarily producing vibrationnal modes which could be identified as the mediators of gravitational interaction, making this model better suited in the quest of a quantum theory of gravity (Yoneya, 1974; Scherk & Schwarz, 1974). Following the path opened by the mesons, all the seemingly different particles of the SM, having different spin and masses, could be explained as different quantized levels of excitation of a single type of relativistic string in rotation. As such, string theory propose an attempt of unification of all known particles and interactions within the same framework.

The slope parameter α' remains present in modern versions of string theory, and can be directly related to what could be interpreted as a physical tension of the strings by $T_0 = \frac{1}{2\pi\alpha'}$. From α' it is possible to introduce the *string length* as $\ell_S = \hbar c \sqrt{\alpha'}$, such that, overall, only two dimensional constants c and ℓ_s are required in string theory as argued by Veneziano (1986) (see Sec. 9.1.1). Furthermore, within string theory, all the known gauge couplings can vary and are defined from the vibrating modes of the strings, as the dilaton. More specifically, the vacuum expectation value of the dilaton field Φ is setting the intensity of the so called string coupling

$$g_s = e^{\Phi/2}, \quad (9.25)$$

which is the only gauge coupling of string theory, quantifying the strength of the interaction between the strings (Maeda, 1988). As such, it sets the value of all the gauge coupling and structure constants of the SM given in Tab. 9.3, when gauge forces are understood as string interactions.

Even the number of dimensions of space-time D –arguably a fundamental constant in the SM as it can not be recovered from fundamental principles–, can be obtained from string theory when asking for the Lorentz invariance of the theory (defined in 3.2.1). However, one obtain $D = 26$ for the simplest possible string model. It is possible to reduce this number to $D = 10$ when including supersymmetry to the theory. Supersymmetry is one of the only possible extension of space-time transformations, containing the Poincaré group as a subgroup (Coleman & Mandula, 1967) (see Sec. 3.2.1). These new transformations act as raising and lowering operators for the spin s of the particle fields by $\pm 1/2$. As such, it is able to transform fermion fields into boson fields and vice-versa (for more on bosons and fermions see Appendix A). Adding supersymmetry to a theory thus consequently increase its number of existing particle/fields. String theory with supersymmetry, named *superstring* theory allow for the existence of fermions fields (with half integers spins) and is free of tachyon modes. Tachyons are hypothetical particles traveling faster than the speed of light, and are undesirable as they break causality and conservation laws. They are thus considered as a signature of an unstable theory. As we know that the matter fields ψ of nature are fermions and we would like to avoid tachyons, the viability of string theory today strongly rely on supersymmetry.

We are strongly lead by experiment to believe that the dimension of space-time is $D = 4$ and not $D = 10$. The solution commonly invoked in string theory is to *compactify* the 6 extra spatial dimensions i.e. making them compact (closed) and infinitesimal in size, explaining why we could be perpetually going through them without even noticing it. One

can think of "wrapping up" or "curling up" these extra dimensions on themselves such that they become very small. Historically, the idea of compactification is inherited from the so called Kaluza-Klein theories who demonstrated the possibility to recover both classical GR and electromagnetism by the addition a 5th compact dimension to space-time ([Kaluza, 1921](#); [Klein, 1926](#))²⁴. In string theory, the compact dimensions are compactified into very specific shapes, called "Calabi-Yau" manifold. This can be done in multiple different ways, leading to a gigantic ($\gtrsim 10^{755}$ [Halverson et al. \(2017\)](#)) number of different possible solutions for the theory. The choice of the compactification scheme will give rise to new fields, emerging from the compact metric, called the *moduli*, and will impact heavily the behavior of the theory, as the strings can "wind" around the compact dimensions, strongly impacting their effective behavior in 4D. Compactification also gives rise to powerful new symmetries (named dualities). Not all of the compactifications are expected to be physically meaningful and conjectures and consistency criteria can be found in order to distinguish between the viable ones (called the landscape) and the non-physical ones (swampland) (for a review see e.g. [Palti \(2019\)](#)). Such a large set of solutions can provide be used to provide the statistical pool of Universe realizations needed to solve the anthropic principle ([Susskind, 2003](#)) discussed in Sec. 9.1.1. However, the standard model as we know it as not yet been proven to be part of the landscape.

Today, five consistent $D = 10$ superstring theories are established, based on different gauge groups²⁵. A ground breaking discovery was that these theories can be proved to be related to one another through duality transformations ([Duff, 1996](#); [Schwarz, 1997](#)). Finally, exploring the limits of these theories²⁶, it was possible to find a new one, the so-called "M-theory". This theory is not about strings but about 2-branes and 5-branes in $D = 11$ dimensions. p -branes are generalization of p dimensional surfaces on which the endpoint of strings can be attached. They are extremely important in string theories, for multiple reasons, as they can notably behave as particles with associated mass or a charge. The low energy limit of M-theory can be showed to be equivalent to $D = 11$ supergravity, that is a supersymmetric field theory on a curved space-time ([Cremmer et al., 1978](#)). Because they all appear as limits from one another, it is now clear that all these theories are different aspects of a single one and that there must exist a unique theory of nature (not necessarily about strings), of which all these theories are perturbative expansions ([Schwarz, 1997](#)). While the formulation of this unique theory of nature remains to be found, the discovery of the inter-relation between all superstring theories ($D = 10$), supergravity (at $D = 11$) and M-theory ($D = 11$), is a major success of the recent development in string theory.

Another considerable achievement of quantum strings is the ability to recover the correct expressions for the Hawking radiation and the black hole entropy (Eq. 9.2 [Callan & Maldacena, 1996](#); [Strominger & Vafa, 1996](#)), as expected from a viable quantum theory of gravity.

²⁴In Kaluza-Klein theories, the quantization of electric charges comes elegantly from quantization of the momentum in the 5th compact dimension and both the Einstein and Maxwell equations can be recovered from a single 5D action $\propto \int R d^5x$ generalizing \mathcal{L}_{EH} in 5D (Eq. 3.6).

²⁵These five theories are called Type I (with gauge group SO(32)), Type IIA, Type IIB (both with gauge group U(1)), SO(32) heterotic, and $E_8 \times E_8$ heterotic. Heterotic string theories consider both bosonic strings ($D = 26$) and superstrings ($D = 10$). Heterotic string theories consider differently the direction of the modes on the strings: left moving modes are associated with bosonic strings and right moving modes associated with superstrings.

²⁶The strong string coupling limit ($g_s \rightarrow \infty$) of the type IIA and the $E_8 \times E_8$ theories

Furthermore, string theory lead to the recent discovery of the AdS-CFT or gauge/gravity correspondence which can be considered as one of the greatest breakthrough of modern theoretical physics (Maldacena, 1999). In a very few words (and as a special case), the AdS-CFT correspondence demonstrate that a four dimensional supersymmetric gauge theory on a flat space (a super $SU(N)$ Yang–Mills theory) is equivalent to a 5D string theory in an anti-de Sitter space (with gravity)²⁷. This link provides a new strong mathematical connection between gauge QFT and gravity. Additionally, it provides a realization of the so called "holographic principle", stating that an observed theory/behavior in D dimension could be emergent as resulting from the projection of a theory in $D \pm 1$ dimension. This principle gives great promises for modern theoretical physics and was used as arguments to solve the black hole information paradox in the context of string theory, stating that all the information of the 3D black hole is contained within its surface (Susskind, 2006) (explaining why the entropy is proportional to the area in Eq. 9.2). More drastically, the revolution open by the AdS-CFT correspondence lead some string theorists to believe that all the known laws of physics we are experiencing daily could be resulting as a projection of information encoded on the surface of the observable Universe (Susskind, 1995), or to quote Susskind himself "The three-dimensional world of ordinary experience—the universe filled with galaxies, stars, planets, houses, boulders, and people—is a hologram, an image of reality coded on a distant two-dimensional surface" (Susskind (2008), p. 298). All these developments are extremely fruitful as they provide new unexpected directions to explore the quantum nature of gravity, and lead to a recent revival of interest for string theory.

String theory hence provides today the most compelling direction to follow in order to build a theory unifying quantum gravity and gauge field theory within the framework. It seems difficult to believe that all the recent results obtained in string theory in which standard model fields and gravity can emerge from strings are a pure mathematical coincidences. Additionally, recent development in string theory along with its mathematical developments are benefiting fundamental mathematics and all branches of physics from QCD to condensed matter. However, let us stress here again that there is no unified framework for string theory yet, and it is unclear how to recover the standard model from the string landscape. Moreover, while they were strongly expected, no supersymmetric particles have yet been detected at the LHC, and the last development of string theory strongly relies on the existence of a broken supersymmetry (for a review of the current status, see "supersymmetry part I and II" in Zyla et al., 2020).

9.5.2 Dilaton field, coupling to gravity and varying couplings

Let us now mention how the dilaton field arise in string theory, and why it lead to the variation of the gauge couplings. The starting point of string theory, is to generalize the relativistic action of a free massive particle to a string-like object. For a relativistic particle, the action is proportional to the space-time interval on its trajectory (Eq. 3.7). Strings however are one-dimensional spatial objects. For them, the concept of world line is replaced by a 2D surface in space-time called the *world-sheet*. For example, a static closed string would trace a cylinder in space-time. The relativistic action of a string is thus given by the

²⁷5 dimensions of the string theory are in AdS_5 while the 5 others are compactified to form a sphere S^5 . The Minkowski space-time on which the Yang-Mills theory lives can be understood as the boundary of the AdS_5 space.

9. EXPLAINING THE VALUES OF OUR STANDARD MODELS' FUNDAMENTAL CONSTANTS

area of its world-sheet (the so called *Nambu-Goto* action). Supersymmetric fields degrees of freedom can be added directly to the surface of the world sheet. After several rewriting, the action can be quantized by promoting classical variables as operators on which canonical commutation relation are imposed. As for quantum fields, the coefficients of the mode expansion in Fourier space behave like creation and annihilation operators. The states are then the quantized modes of the string, interpreted as particles.

For the open strings, the first excited states behave as a photon while for closed strings, unavoidable in a string theory, the first excited states behaves as a spin-2 tensor: the graviton, which is why string theory is said to predict gravity. This first mode comes along with an anti-symmetric tensor behaving as a generalized electromagnetic field (the Kalb-Ramond field), and a first importance scalar field: the dilaton. The first states are followed by a spectrum of massive modes, which exact content depends on the formulation of string theory and the boundary conditions imposed to the endpoints of the strings. As such, string theory reproduces GR and gauge fields in the low energy limit, and could provide particles behaving as the standard models ones in its higher excited modes, providing a bridge between quantum mechanics and gravity as well as a possible unification road for all particles and interactions.

The role played by the dilaton becomes more obvious when treating all the fields of the string spectrum as quantum field appearing in an action, which is the approach given by string field theory. Starting from the string action and its supersymmetric generalizations, it is indeed possible to derive the effective low energy limit of the action, letting explicitly the various excited modes appear as fields. The exact field content of the resulting $D = 26$ or $D = 10$ action depends on the type of (super)string theory under consideration (Callan et al., 1986). Finally, it is possible to compactify the additional dimensions to obtain an effective 4D action, and the compactifying scheme will also change the exact field content of the theory. However, whatever the scenario, one should find that the dilaton field Φ , is coupled to gravity, and also sets the value of all the gauge couplings, and their possible variations.

Explicitly, the low energy effective action of the massless modes of the string can be written as

$$\begin{aligned} \mathcal{S}_{\hat{\text{SM}}+\Phi} = & \int \sqrt{-|\hat{g}|} \, d^4x \left(\frac{1}{\alpha'} \left[B_{\hat{R}}(\Phi) \hat{R} + B_\Phi(\Phi) \left(2\hat{\square}\Phi - (\hat{\nabla}\Phi)^2 \right) \right] - V(\Phi) \right. \\ & \left. - \frac{1}{4} \sum_{\hat{\mathcal{F}}} B_{\hat{\mathcal{F}}}(\Phi) \langle \hat{\mathcal{F}}, \hat{\mathcal{F}} \rangle - \sum_{\psi, \hat{\mathcal{A}}} B_\psi(\Phi) \hat{\psi} \hat{\mathcal{D}}\psi + \dots \right), \end{aligned} \quad (9.26)$$

assuming a spherical topology for the compactified dimensions (Damour & Polyakov, 1994; Damour & Polyakov, 1994; Damour & Nordtvedt, 1993). For a pedagogical derivation of Eq. 9.26 see e.g. chapter 7 of Tong (2009). \hat{F} and $\hat{\psi}$ are respectively the SM gauge and matter fields as appearing in Eq. 3.8 and expected to arise from the vibration of the string. \hat{g} is the "string metric", with associated curvature scalar \hat{R} taking into account the effect of gravitons as gravitational fields. "... contains all the other fields of the model.

The dilaton Φ is coupled to all the other fields through the functions $B_i(\Phi)$. One can see from Eq. 9.26 that the presence of Φ will lead to a variation of all the gauge couplings,

due to the terms $B_{\mathcal{F}}(\Phi)\langle\hat{\mathcal{F}}, \hat{\mathcal{F}}\rangle$ as explained in details in Sec. 9.1.4 (α_G will also vary due to the presence of $B_{\hat{R}}(\Phi)\hat{R}$). Eq. 9.26 is expressed in the so-called *string frame* or *Jordan frame*. Any such action can be rewritten equivalently in the so-called *Einstein frame*, in which the gravity Lagrangian is \mathcal{L}_{EH} . In this new frame, the impact of the dilaton will be easier to express, and we will not have to consider the variation of α_G . Whether this transformation is physically significant or not is discussed in Faraoni & Nadeau (2007). In general, any theory with a scalar field coupled to \hat{R} can be re-expressed as a theory in which the other gauge couplings are varying. To do so, one have to consider the new variables $g_{\mu\nu} = C_g^{-1}B_{\hat{R}}(\Phi)\hat{g}_{\mu\nu}$, $\psi = (C_g B_{\hat{R}})^{-3/4}B_\psi\psi$ and

$$\phi = \int d\Phi \left[\frac{3}{4} \left(\frac{\partial_\Phi B_{\hat{R}}}{B_{\hat{R}}} \right)^2 + \frac{B'_\Phi}{B_{\hat{R}}} + \frac{1}{2} \frac{B_\Phi}{B_{\hat{R}}} \right]^{1/2}, \quad (9.27)$$

where C_g is a numerical constant. Doing so, the action becomes, in the Einstein frame²⁸

$$\begin{aligned} \mathcal{S}_{SM+\phi} = \int d^4x \sqrt{-|g|} & \left(\frac{M_{Pl}^2}{2} R + \frac{M_{Pl}^2}{2} \partial_\mu \phi \partial^\mu \phi - V(\phi) \right. \\ & \left. - \frac{1}{4} \sum_{\mathcal{F}} B_{\mathcal{F}}(\phi) \langle \mathcal{F}, \mathcal{F} \rangle + \sum_{\psi, \mathcal{A}} \bar{\psi} \not{D} \psi + \dots \right). \end{aligned} \quad (9.28)$$

Surprisingly, the Planck mass itself can be recovered from the slope parameter as $M_{Pl}^2 = 2/(C_g \alpha')$. This action is extremely similar to the Bekenstein one (Eq. 9.22), but is originating from string theory considerations. Here however, instead of Taylor expanding the electromagnetic ($\mathcal{F} = F$) coupling function $B_F(\phi)$, we will try to find some expressions linking the field to the observables that are also rooted in string theory.

Additionally, dark energy can be added to this action. In principle, under a suitable choice of its potential $V(\phi)$, the dilaton field can act as a quintessence field and can be itself the source of dark energy (Gasperini et al., 2001). Otherwise, one can add a cosmological constant Λ or another field behaving like it, to which the dilaton can in principle be coupled with another function as $\mathcal{L} \propto B_\Lambda(\phi)\Lambda$.

9.6 Constraining the runaway dilaton model

In this section, I will present the latest to date constraints on a model in which the string dilaton field can be responsible for violation of the EEP and variation of the fine structure constant: the runaway dilaton model. The full paper can be found in Appendix D.5. As we will see, this model allows to reconcile the existence of a massless dilaton with observables, allowing to derive predictions from a well motivated string theory model, and confront it with experiments. I originally required the implementation of a varying fine structure constant in CLASS in order to explore this model, as a natural follow-up of the previous study that I co-lead, Martins & Vacher (2019). As for the Bekenstein models, I intended to provide here an overview of the model as well as an update of the constraints, considering the full parameter space without previously made assumptions.

²⁸Note that, in agreement with previous literature on the runaway dilaton, field units are defined in units of $M_{Pl}/(\sqrt{4\pi})$ in the paper (Appendix D.5), instead of the choice of M_{Pl} used in this thesis.

9.6.1 Context: The runaway dilaton model(s)

Let us now look for possible expressions for the dilaton coupling $B_i(\Phi)$, allowing us to derive the observational predictions of our model, in order to constrain it. Standard predictions from string theory indicate that the massless dilaton field must be coupled universally to all the fields through $B_i(\Phi) = e^{-\Phi}$. This is a coupling to the inverse of the string structure constant $\propto g_S^{-2}$ (see Eq. 9.25), just as the curvature terms are coupled to the gauge structure constants $\alpha_{g_A} \propto g_A^{-2}$ (see Eq. 9.4), as we discussed in Sec. 9.1.3. However, as detailed in Damour (2003), such coupling would be in violent conflict with experiments, as it predicts violations of the EEP with associated $\eta \sim 10^{-5}$, already excluded by MICROSCOPE (Eq. 9.18). To save string theory, a mechanism must thus be invoked to explain this contradiction. For example, if a large enough mass is acquired for the dilaton, through e.g. supersymmetry breaking, the force mediated by the field will exponentially decrease with distance²⁹, such that no significant cosmological variation of the constants would be expected³⁰. This solution, however, drives string theory further away from experimental predictions. Another option however, allows to reconciles a massless dilaton with data, while preserving some observable consequences as small violations of the EEP and variations of the gauge structure constants. This is the so-called "runaway dilaton" models, in which the dilaton field naturally decouples from the other standard model fields in late-time cosmology (Damour & Nordtvedt, 1993; Damour & Polyakov, 1994; Damour et al., 2002a,b). Due to the existence of an attractor mechanism in the dilaton-matter system, the couplings could be naturally attracted towards smooth finite limit in the $g_s \rightarrow \infty$ regime. One would then expect

$$B_i(\Phi) = C_i + \mathcal{O}(e^{-\Phi}), \quad (9.29)$$

where C_i is a constant (Veneziano, 2002). As such, the couplings are the one of the standard model with small additional corrections $\propto e^{-\Phi}$. As detailed in Damour et al. (2002a), the residual dilaton couplings at the present epoch can be related to the amplitude of density fluctuations generated during inflation. The late-time cosmology impact of the field ϕ in the Einstein frame can be quantified by the coupling functions

$$\alpha_i(\phi) = \frac{\partial \ln(m_i)}{\partial \phi} = \frac{\partial \ln(m_i)}{\partial \alpha_{g_A}} \frac{\partial \alpha_{g_A}}{\partial \phi} \quad (9.30)$$

where i labels different types of matter field coupled to the dilaton. A word of caution is needed here: while previous literature used this notation for the couplings, they are *not* the same quantities as the structure constants α_{g_A} discussed in Sec. 9.1.3. As they make the mass changes with ϕ , the $\alpha_i(\phi)$ will lead to deviation of the UFF Eq. 9.16. Writing α_h the coupling to hadronic matter, one can indeed find that

$$\eta(\phi) \simeq 5.2 \times 10^{-5} \alpha_h(\phi)^2, \quad (9.31)$$

which should be slightly dependent on the compositions of the masses under consideration as Eq. 9.24, but that we will again assume to be valid for the case of MICROSCOPE.

²⁹This is for example why the weak force has such a small range of interaction: the gauge bosons are massive and thus unstable, and they tend to disintegrate quickly.

³⁰One should not confuse the dilaton with moduli fields arising from compactification (sometimes called dilatons!). The behavior of the moduli also sets the values of the fundamental constants and their masslessness is also in strong contradiction with experiment. It is now commonly accepted that it is possible to give them masses through the process called moduli stabilization (DeWolfe et al., 2005).

Furthermore, one can model the impact of the dilaton on matter fields by replacing the Dirac term in the action by the matter geodesic action $S_p = \sum_i m_i(\phi) \sqrt{g(u_\gamma, u_\gamma)} d\tau$. Doing so, the Klein-Gordon equation for the dilaton field is given by

$$\ddot{\phi} + 3H\dot{\phi} = \frac{1}{M_{\text{Pl}}^2} \sum_i \alpha_i (3P_i - \rho_i). \quad (9.32)$$

As such, ϕ does not interact with radiation for which $3P_r - \rho_r = 0$. As explained in (Damour et al., 2002c; Damour, 2003; Martins et al., 2015), the runaway dilaton hypothesis (Eq. 9.29) allows to express all the coupling B_i and α_i of the ϕ with the SM particles. Making minimal assumptions, that we will not detail here, the couplings can all be expressed as

$$B_F^{-1}(\phi) \propto (1 + b_F e^{-\tilde{c}\phi}), \quad (9.33)$$

$$\alpha_h(\phi) \simeq 40b_F \tilde{c}e^{-\tilde{c}\phi}, \quad \alpha_m(\phi) \simeq -b_m c e^{-\tilde{c}\phi}, \quad (9.34)$$

$$\alpha_\Lambda(\phi) \simeq \text{cst}, \quad \alpha_V(\phi) = \frac{M_{\text{Pl}}^2}{4} \frac{\partial \ln(V(\phi))}{\partial \phi}. \quad (9.35)$$

In which \tilde{c} is a constant expected to be of order unity and is usually fixed to 1. b_i are constant numbers while the indices m , h , Λ and V designate respectively hadronic and dark matter, dark energy and a contribution from the dilaton potential $V(\phi)$. The last coupling α_V , is simply a rewriting of the potential term of the Klein-Gordon equation (Eq. 4.8) such that it appears on the same footing as the other components in the equation of motion (Eq. 9.32)³¹.

The couplings can all be normalized by their value today $\alpha_{i,0} = \alpha_i(\phi_0)$ in order to express their variations in term of field displacements $\phi - \phi_0$. Doing so, the variation of the fine structure constant becomes

$$\frac{\Delta \alpha}{\alpha_0} = \frac{\alpha_{h,0}}{40} [1 - e^{-(\phi - \phi_0)}], \quad (9.36)$$

such that atomic-clocks are sensitive to $\dot{\alpha}/\alpha_0 = \alpha_{h,0}\dot{\phi}/40$. The runaway dilaton model thus provides a natural explanation for the small observed values of η and the stability of the fine structure constant through the smallness of $\alpha_{h,0}$. The value of $\alpha_{h,0}$ strongly depends on the relation between the dilaton and the inflaton. Predictions given in Damour et al. (2002a) expect $\alpha_{h,0} \simeq 1.6 \times 10^{-4}$ or $\alpha_{h,0} \simeq 4.2 \times 10^{-3}$. The expected values of $\alpha_{m,0}$, α_V and α_Λ depend on the assumptions made and their possible links with B_F , but could theoretically be of order unity (Martins et al., 2015; Martins & Vacher, 2019). α_Λ is an hypothetical coupling of the dilaton field with another source of dark energy behaving as a cosmological constant Λ . It is often assumed to be independent of ϕ (Martinelli et al., 2015; Martins et al., 2015) and misleading written α_V ³². Degeneracies between parameters in the observable are significantly broken in this parameter space compared to the case of the Bekenstein models, as the coupling to hadron α_h is alone responsible for both the varying fine structure constant and the violation of the UFF.

³¹ $M_{\text{Pl}}^{-2} \alpha_V (3P_V - \rho_V) = -4M_{\text{Pl}}^{-2} \alpha_V V = -\partial V / \partial \phi$

³² Equivalently, one could imagine that there is no cosmological constant at all and that the dilaton instead has a potential of the form $V(\phi) = \alpha_\Lambda M_{\text{Pl}}^2 \Lambda \phi$, impacting the equation of motion for ϕ and its density and pressure (hence behaving like dynamical dark energy). However, this is not how α_Λ is generally introduced and implemented, but instead as a coupling to Λ , as for the Bekenstein model. On the other hand, a constant term $V(\phi) = M_{\text{Pl}}^2 \Lambda$ in the dilaton potential would be purely equivalent to a cosmological constant and will not impact the equation of motion of the field.

9.6.2 The paper: Objectives and results

In this work, available in Appendix D.5, we built from our previously modified version of the CLASS software to create a consistent implementation of the runaway dilaton model. Here again, we intended to present an overview and update of the various ways this model has been studied in the past. We also provide for the first time a constraint of its whole parameter space, freeing ourselves from several simplifying assumptions. This work thus built over precedent phenomenological studies as e.g. [Martins & Vacher \(2019\)](#), with updated datasets (presented above) and larger parameter spaces. For the first time within our CLASS implementation of the varying constants, we study a case with a potential $V(\phi) \neq 0$, assuming an exponential shape $V(\phi) = V_0 + V_1 e^\phi$, motivated from string theory ([Damour et al., 2002c](#)). Adding a potential in CLASS comes with numerous technical complications that we had to face, delaying the publication of our results. Originally, the draft was containing many more cases with different potentials, but they turned out to be cumbersome, and we decided to keep them for further studies focused on this matter. As first author of this paper, I was responsible for the implementation and testing of the dilaton scalar field in CLASS. This time, as I was just starting my PHD, Nils Shöneberg provided the first preliminary implementation in order to help me understand the structure of the code, and I refined it until its final form. Under my co-supervision, Francisco Pimenta (CAUP, Porto), Carlos Martins' intern, provided an easier way to obtain the redshift evolution of the fine structure constant $\alpha(z)$ from CLASS, and helped me with the testing. I runned all the chains and derived all the corresponding contours and constraints. Finally, I was responsible for the figures using GETDIST, paper writing and literature survey (of course, with the help of the other authors).

The most commonly considered scenario for the runaway dilaton, as in [Martinelli et al. \(2015\)](#); [Martins et al. \(2015\)](#); [Martins & Vacher \(2019\)](#), consider $V(\phi) = 0$ and the three couplings α_Λ , $\alpha_{m,0}$ and $\alpha_{h,0}$, with further assumptions to express α_Λ in term of the other parameters, allowing to reduce the dimension of the parameter space. In this work, for the first time, we let bot α_Λ and $\alpha_{m,0}$ free. Additionally, in [Martins & Vacher \(2019\)](#), a prior was used on the field speed ϕ'_0 , derived from back to the envelope considerations from cosmological datasets. As our CLASS implementation allows to use directly the cosmological likelihoods, we could free ourselves from this prior, which turned out to over-estimate their constraining power. Results for this scenario are displayed in Fig. 9.6. We can see that, freeing ourselves from the overoptimistic prior on ϕ'_0 , the field's speed can take larger values and degeneracies between parameters can appear. α_Λ , responsible for the late time acceleration of the field, is strongly degenerated with ϕ'_0 , while $\alpha_{m,0}$, driving the subsequent field evolution during matter evolution, is strongly degenerated with ϕ_0 . Without the prior, the $(\alpha_{h,0}, \phi'_0)$ contour displays a very characteristic shape induced by the atomic-clock likelihood constraining directly the product $\alpha_{h,0} \phi'_0$, forcing both $\alpha_{h,0}$ and ϕ'_0 to have the same sign.

As displayed on the bottom panel of Fig. 9.6 – contrarily to Bekenstein – degeneracies can appear with the cosmological parameters, as H_0 . Freeing ourselves from the prior on ϕ'_0 let the field explore regions with higher speed, and hence with larger energy density today ($\propto (\phi'_0)^2$), driving the late time cosmic acceleration and letting the dilaton play the role of a quintessence dark energy field (see Sec. 4.1.1). These possibilities are however strongly limited and only possible – mildly – in the case where a coupling α_Λ exists with another source of dark energy as a cosmological constant, allowing to significantly accelerate the

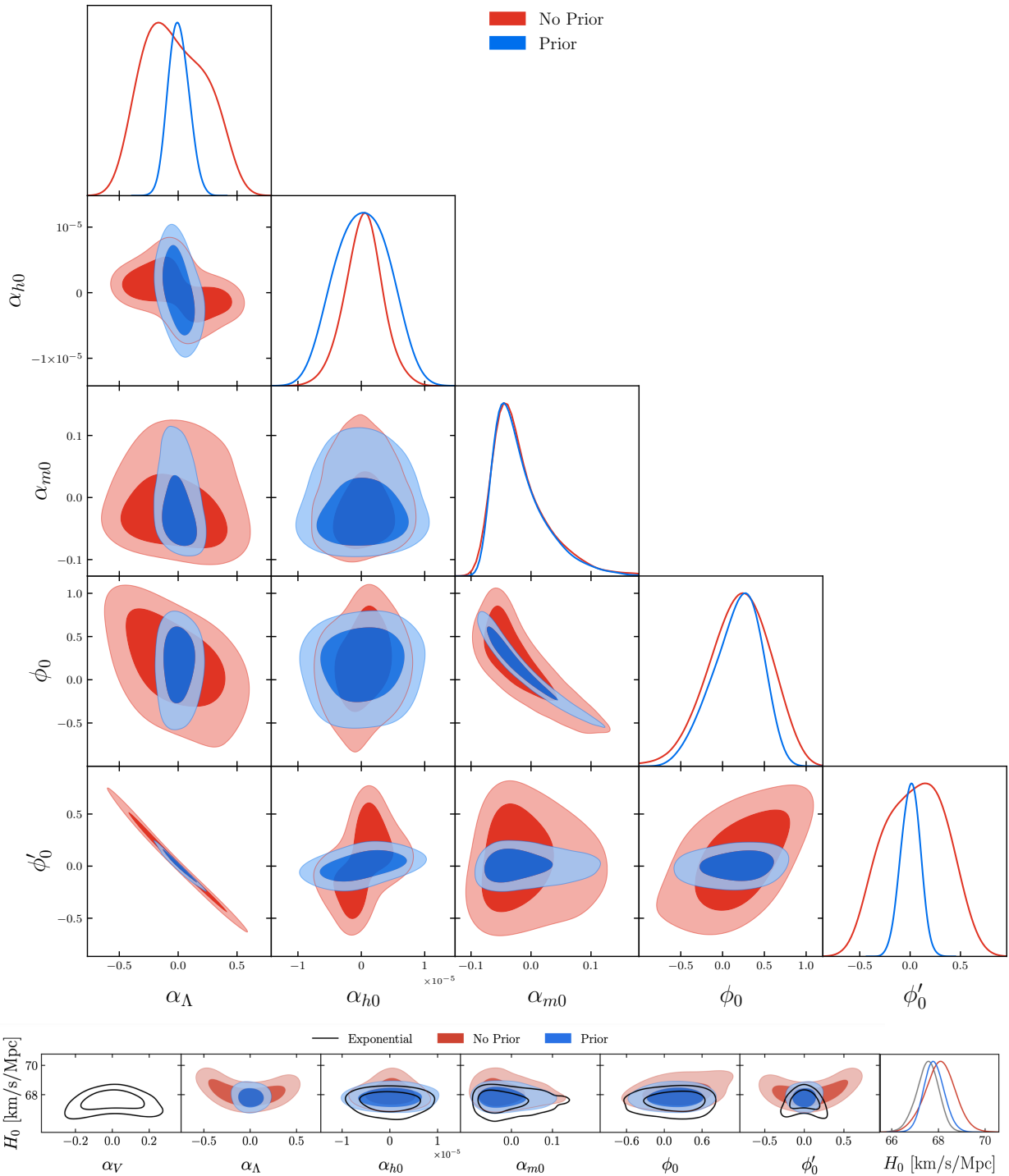


Figure 9.6: Top: Constraints on the full runaway dilaton parameter space with $V(\phi) = 0$. As in [Martins & Vacher \(2019\)](#), a prior can be used on the field speed $\phi'_0 = 0 \pm 0.1$ (blue contours) but appears to be too restrictive (red contours). Bottom: Contour plots showing the degeneracies between the dilaton parameters and H_0 in different scenarios.

field. The bounds provided on the variations of the fine structure constant and violations of the EEP today are however extremely stringent, such that this behavior would be only possible if the coupling $\alpha_{h,0}$ has a very small value ($\sim 10^{-7}$), discouraging the choice of this

model as we implemented it as a source for dark energy. As we will discuss again in Sec. 9.7, an early time impact of such a field would be preferable to ease the tensions, as late time constraints are too restrictive.

We further obtained the constraints on the exponential potential scenario, getting comparable results as the previous case with prior (see black line contours on the bottom panel of Fig. 9.6). This scenario appears to be disfavored as a source of dynamical dark energy, as larger values for the slope α_V tends to lower the value of H_0 .

Overall, the expected natural values³³ for the couplings as well as their predictions detailed in the previous section are all excluded, and the addition of the recent MICROSCOPE bound lowers the constraints on $\alpha_{h,0}$ by one order of magnitude.

9.6.3 Impact, limits and outlooks

In a sense, the runaway dilaton model provides a "concrete" realization of the Bekenstein model, where the shape of the coupling functions can be motivated from string theory. Just as Bekenstein, this model is strongly constrained by data, such that all the natural and expected values for its parameters are excluded. The consequences are however clearer: the runaway dilaton model is disfavored and was proposed to reconcile the uncircumventable existence of a the dilaton field with experiments. As for Bekenstein, new data will sharpen our results, but will doubtfully change our conclusions. Whatever the final form string theory will take, it will have to justify why dimensionless couplings, such as α , are so stable. The simple way out is to invoke a supersymmetry breaking, or some interactions of the dilaton field allowing it to acquire a significant mass ([Seo, 2021](#)). In any way, such an unmovable stability of the constants is not benefiting string theory, as the stability of the couplings provides one of the only open experimental windows on these models (with inflation and black holes). Furthermore, as correctly stated later in ([McGuigan, 2023](#)), our analysis disfavors the runaway dilaton model as a source of quintessence field with an exponential potential, as the combination of atomic clocks and the MICROSCOPE bound strongly constraint the possible value of the field speed ϕ'_0 today, and thus its possible energy density.

Most of the discussion of the Bekenstein paper still applies here. Ideally, one should consider the co-variation of constants and the BBN bound, which are better defined within the dilaton model. Here again, α was the only constant considered and is expected to provide the most sensible probe on cosmological scales. Originally this draft was intended to explore a plethora of shapes for $V(\phi)$, but it turned out to be cumbersome and lacking deep scientific motivation. An extensive study of possible $V(\phi)$ for varying α models is undergoing with the same author team, allowing to identify the phenomenologically relevant cases. As I am developing more and more CLASS versions containing different varying- α models, I would like to explore the similarities between them through a focused comparative study and investigate the possibility to distinguish them experimentally. As a natural follow up of this work, I am now working actively on other string inspired models as the so-called DBI Rolling tachyon ([Tavares & Martins, 2021](#)), project which is lead by João Dias, and requiring the development of a new version of CLASS.

Additionally, I investigated, in collaboration with the same authors as the present paper

³³Which are not all of order unity, contrary to what has been stated in the paper.

and using similar frameworks, how the string inspired Swampland conjectures (see Sec. 9.5) can be applied on scalar field models with a varying fine structure constant. Doing so, we updated the previous constraints on the Swampland parameters to a multitude of single field quintessence models and we stressed the tremendous fine tuning argument imposed by measurements of the fine structure constant on quintessence models coupled to electromagnetism. This work, which I co-lead, has been submitted and the preprint is available at [Schöneberg et al. \(2023\)](#).

9.7 Varying alpha, late and early dark energy

9.7.1 Is dark energy related to varying α ?

While this discussion was opened with the dilaton paper, it is possible to discuss more extensively the possible links between varying couplings and dark energy. In [Martins \(2017\)](#), it was suggested to make the distinction between:

- **Class I fields** for which dark energy and varying constants are commonly sourced by the same field. This would be the case of the quintessence-like runaway dilaton model with a specific potential.
- **Class II fields** for which dark energy and varying constants are two different (and eventually independent) behaviors. This is the case in the Bekenstein model without potential, where Λ was fully responsible for dark energy.

In the case of a general Type I field ϕ , coupled to electromagnetism with a Bekenstein-like coupling (see Sec. 9.4) such that $\Delta\alpha/\alpha_0 \sim \zeta\Delta\phi$, it is possible to show that the variation of the fine structure constant can be expressed as

$$\frac{\Delta\alpha}{\alpha}(z) = \pm\zeta \int_0^z \sqrt{3\Omega_\phi(z')|1+w_\phi(z')|} \frac{dz'}{1+z'} . \quad (9.37)$$

where $\Omega_\phi(z)$ is the field density and $w_\phi(z) = P_\phi/\rho_\phi$ ([Calabrese et al., 2014](#)). The sign \pm is positive for a canonical scalar field and negative for a phantom field ([Vielzeuf & Martins, 2014](#)). This formulation is very powerful, as numerous models of scalar fields provide analytical solutions for Ω_ϕ and w_ϕ and additionally, some phenomenological parameterizations of dark energy exist as the Chevallier Polarski Linder (CPL) parametrization, which is very commonly used as a simple extension beyond a cosmological constant ([Chevallier & Polarski, 2001](#); [Linder, 2003](#)). It assumes

$$w_{\text{CPL}}(z) = w_0 + w_a \frac{z}{1+z} , \quad (9.38)$$

and

$$\Omega_{\text{CPL}}(z) = \frac{1 - \Omega_m}{1 - \Omega_m + \Omega_m(1+z)^{-3(w_0+w_a)} e^{3w_a z/(1+z)}} . \quad (9.39)$$

This analytical parametrization is very common and rather easy to implement, and as such provide a easy way to model the behavior of a scalar field sourcing both dark energy and a variation of the fine structure constant without having to integrate an intricate modified Klein-Gordon equation of motion as we did for the Bekenstein or the dilaton.

9.7.2 Personal contributions on this topic

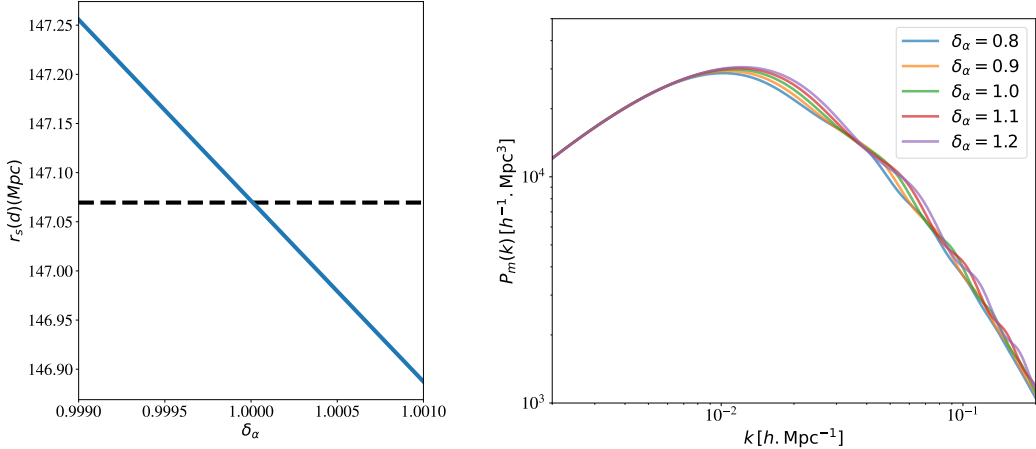


Figure 9.7: Left: Value of the sound horizon at decoupling $r_s(d)$ for different values of $\delta_\alpha = \alpha/\alpha_0$. Right: Matter power spectrum $P_m(k)$ for different values of δ_α .

During this thesis, I was a member of the *Euclid* collaboration, mostly active in the work package WP10 of the theory working group on "new observational probes" lead by Carlos Martins. I was in charge of studying the possibility to quantify the impact of a time dependence of α on cosmology with the *Euclid* satellite (as a natural follow-up of [Martinelli et al., 2021](#)). To do so, I investigated, mostly in collaboration with Savvas Nesseris (IFT, Madrid), how the fine structure constant value can impact large scale structure observables such as the matter distribution power-spectrum $\mathcal{P}_m(\mathbf{k})$ ³⁴ and the sound horizon at decoupling $r_s(d)$ ³⁵. As an example, I computed in Fig. 9.7 the values of these observables for different values of $\delta_\alpha = \alpha/\alpha_0$ at decoupling. While $r_s(d)$ changes linearly with δ_α , it has a very non linear and rich effect on $P_m(k)$. Using these observables alone, I figured that *Euclid* will be able to provide independent constraints on α at high redshift with a sensitivity comparable to *Planck* ($\sim 10^{-3}$) ([Planck Collaboration, 2015b](#); [Hart & Chluba, 2018](#)). Additionally, I implemented and tested a version of CLASS including a varying α with the integral dependence given by Eq. 9.37, in the case of a CPL dependence of Ω_ϕ and w_ϕ , in order to explore the constraining power of *Euclid* on this model and its capability to distinguish between the presence of a Class I or Class II field. Results including the above work are not published yet and the collaboration paper is still being redacted.

Furthermore, I personally implemented alternative versions of the CLASS code in order to further explore the link between varying fine structure constant and dark energy outside of *Euclid*. I am now leading an analysis exploring how Early dark energy, sourced by an axion-like particle presented in Sec. 4.3.2, could be coupled to varying fine structure constant, along the lines of [Calabrese et al. \(2011\)](#). A surprising outcome appears to be that local bounds as atomic clocks are still able to give sharp constraints on models like ALP acting at very early times. The results of this analysis are already available and should be published

³⁴Let $\epsilon = \delta\rho/\bar{\rho}$ be the relative deviation of the mean density observed in the distribution of galaxies on the large scale structures. The matter power spectrum is defined as the other power-spectrum introduced above (Eq. 3.25): $\langle \epsilon(\mathbf{k})(\epsilon(\mathbf{k}')^*) \rangle = (2\pi)^3 P_m(k) \delta^3(\mathbf{k} - \mathbf{k}')$.

³⁵ d here stands for decoupling

soon. Through the presence of both scalar and pseudo-scalar coupling to the EM sector, as mentionned in [Flambaum et al. \(2009\)](#), I am also investigating if such a field could be related to the presence of cosmic birefringence that we will introduce in Sec. 5.3.2. Finally, both axions and dilaton fields are expected in string theory. As discussed in [Alexander & McDonough \(2019\)](#), I would further like to explore the possibility of a standard ALP particle coupled with the runaway dilaton introduced in Sec. 9.6, and its possible cosmological implications.

More generally, as a member of the Φ -in-the-sky grant based in Porto and lead by Carlos Martins, I also had the chance to help, discuss and collaborate with multiple students on the topic of varying constants. Since I started working on this topic, I felt that it significantly regained some interest from the cosmological community, with the study of its link in regards of the cosmological tensions as well as the update of the stringent MICROSCOPE bound. My understanding of the subtleties lying under this rich field grew with it and I am thrilled to have contributed ever so slightly to this research area by providing new bounds on well motivated models and developing new tools to do so.

10

Conclusion and perspectives

In this thesis, I worked on major problems on a great variety of thematics, from experiment to theory in cosmology, through data analysis. In the past three years, significant and exciting developments have been undertaken on all these sides. These developments opened doors for future thrilling research, and I deeply wish to keep playing a major role in it. In particular, I introduced new tools which will now have to be applied on more general problematics, in order to better appreciate their power and draw their limits. I will now summarize point by point the results I have already discussed and the perspective they open.

10.1 Systematic effects for the *LiteBIRD* mission

The *LiteBIRD* satellite will probe the largest scales of the CMB with an unprecedented accuracy. Doing so, it might unveil signatures of high energy physics beyond our standard models in the primeval Universe, as primordial inflation or cosmic birefringence induced by axion like particles. For this challenge to be feasible, it is crucial to find new methods to allow an accurate control of systematic effects and removal of foregrounds. During this thesis, I was strongly involved in these two topics. I provided cross-checks and feedbacks for the major publication ([LiteBIRD Collaboration et al., 2023](#)), on which numerous follow-up studies rely today. In parallel, I investigated the impact of an homogeneous scanning strategy. My study in collaboration with Yusuke Takase allowed to explore and justify rigorously the current configuration of the scanning used by the collaboration. Additionally, we found critical parameters never considered before: the orientations of the focal planes, which we optimized. Given this configuration, requirements still need to be set on the tolerated asymmetry of the beams, especially on the large scale far side lobes, which could induce bias on the measurement of the tensor-to-scalar ratio r . I already started to significantly explore this point but could not yet conclude the analysis. Answering precisely this question is far from trivial and requires the development of new conceptual and numerical tools in order to quantify appropriately and simply the asymmetry and treat efficiently the sky convolution by polarized beams with a minimal computational cost. In order to conclude the assessment of this point and investigate many others, I intent to keep a strong implication within the collaboration in the future.

10.2 Polarized foregrounds

10.2.1 The moment expansion

The race for more and more sensitive CMB missions probing fainter and fainter signals coming from the last scattering surface renders explicit the need for an accurate characterization of the Galactic foregrounds. It is my personal belief that the success of this characterization must go way beyond foreground cleaning by providing methods rooted in the physics of the ISM itself. Doing so would allow us to obtain interpretable component separation models, which would allow to recover the CMB along with some crucial information for Galactic science. As I detailed in Chap. 8, the moment expansion provides a well motivated solution to tackle the complexity of the signal arising from mixing of different signals. In this thesis, I showed that it could successfully be used to allow the component separation for large sky covering and high sensitivity missions as the *LiteBIRD* satellite, providing also a high degree of interpretability. This first work was a proof of concept and further developments remain to be undertaken in order to test and optimize the method, apply it on larger sky fractions, and with more complicated dust models. Doing so would rank the parametric moment expansion among the standard component separation methods, ready to be confronted to real datasets.

I further showed that it was possible to provide a consistent extension of the moment expansion to polarization: the spin-moment expansion. This development fills the gap between intensity and polarized distortions and connects the statistical properties of the foreground to the consequences of mixing. In this new paradigm, the moments become complex numbers and the pivot correction has an imaginary part, from which I could derive analytical expressions giving the frequency rotation of the polarization angle of the total signal. This new framework is robust and needs to be further applied for component separation and dust modeling. After this development, it is also clear that the moments can be used to infer statistical informations about the foreground signal. A lot of work, already ongoing, has to be done in order to evaluate how far one can go in that direction. Additionally, the spin-moments can be used to create and characterize new relatable simulations of the foregrounds that could be used by the CMB community. I am currently exploring this promising direction and I hope to soon release some models readily to be used.

Furthermore, I gave a first application of the spin-moments to the E - and B -modes. In this application, demonstrating the robustness of the spin-moments, I showed how to connect the complexity in pixel space to the observed amplitude of moments in the harmonic space. I also showed that one would expect EE , BB and EB to have different spectral behavior in the presence of polarized mixing, behaviors which can be predicted by the spin-moments. This could have strong consequences for dust modeling, component separation and the quest of cosmic birefringence. The real impact of these effects remain to be properly estimated for ongoing and future CMB missions. Additionally, I showed that the variation of the E/B ratio with frequency provided a model independent probe of polarised mixing. It would be interesting to estimate the sensitivity required to detect such a variation, especially in the case of *LiteBIRD*.

10.2.2 Wavelets Scattering transform

We saw that the scattering transform provides new interpretable statistics in order to tackle the spatial complexity of the Galactic signal. First promising steps have been undertaken in order to understand both the spatial and the spectral complexity of foreground signal using this approach. In this thesis, I used the WPH formalism in order to explore the benefit of using cross-frequency statistics. Promising results were found for synthesis while the applications to denoising are still under investigation. Major steps remain to be taken in order to assess the robustness of this method and being able to use it for proper component separation on the celestial sphere. On the long term, I would like to investigate the possibility to couple the moment expansion and the WPH, in order to tackle both spatial and spectral complexity together using an interpretable, minimal and well motivated approach.

10.3 Varying constants

Investigating the question of the stability of the fundamental constants of our standard model is a first importance matter. First, as I intended to show in Chap. 9, listing the fundamental constants of our models and understanding the role they play within them brings with it a lot of non trivial questions. The answers to these questions – at the interface with philosophy of science – give deep insights on the subtle theoretical constructions of general relativity and quantum field theories which reflect our best understanding of fundamental physics so far, both regarding gravitation and the other fundamental forces. As such, seeking for variations of these constants opens a direct window on new physics and allows to constrain directly some ambitious models trying to unify quantum theory and gravity as string theory. In order to implement consistently the variation of fundamental constants as the fine-structure constant α on cosmological scales, I contributed to the development of a new version of the CLASS software which was made publicly available. This code, which now includes the electron mass and Newton's constant has been and will be further used by myself and others to investigate a broad range of questions and models related to the varying constants. As I originally intended to, I further implemented scalar field models within this code, in order to derive the latest to date constraints on different versions of the Bekenstein phenomenological model, and on the string inspired runaway dilaton model. The parameter spaces of these models are now extremely narrow, excluding couplings to hadronic matter larger than a part per million and rejecting the natural values expected for large classes of models beyond our standard models. Following this line, I am now investigating other well motivated models in the regard of the Swampland conjecture or the cosmological puzzles as the Lithium problem and the H_0 tension. Regarding this last point, it is indeed known that a varying α in the early Universe would impact the BBN and the recombination history, allowing to significantly relieve the observational tensions. It remains however to see if any well motivated model, free of fine tuning, could both allow to relieve these tensions and survive the confrontation with data. Furthermore, I would like to investigate the co-variation of the fundamental constants, expected in the most general case, as gauge couplings and mass ratio together. Tackling consistently this co-variation within our new numerical framework will be a major challenge but might bring with it a fair amount of surprising results.

Next generation of cosmological missions will further and further narrow the possible range of variation for the fundamental constants. As an example, I showed that the *Euclid* satellite

would provide an independent measurement of α at the redshift of decoupling. Additionally, CMB missions succeeding to *Planck* as SO, *LiteBIRD* or CMB-S4 will also have their word to say regarding the space and time variations of the constants during recombination. While I could not derive precise forecasts of such measurements in this thesis, I intend to further explore these questions in the coming years. Finally, I showed extensively that the local bounds as atomic clocks and the upcoming nuclear clocks as well as tests of the universality of free fall give the most striking constraints on varying constant models. Improvement in the next decades are awaited and might significantly change our understanding of physics. However, if deviations to the current paradigm remain undetected, it will become a urgent matter to be able to explain how our fundamental constants can be so stable within the framework of theories beyond the standard model as quantum gravity.

10.4 A final word

Cosmological inquiries can have major impacts on how we picture ourselves in the Universe. We can only be marveled by our current understanding of the cosmic history and the remarkable agreement between our observations of the cosmos and the theories used to model it, built from first principles rooted in particle physics and general relativity. However, while subtle, some observational and theoretical puzzles remain to be put together and it is the role of the researcher to focus on what we don't know. We don't know why the fundamental constants have their current values and why these values seem to allow so precisely for the existence of chemistry and life in an oddly structured Universe. We also ignore the exact conditions in which our Universe was born some 13.8 billions years ago. Here again, we can only be astonished that these questions have now entered the realm of empirical science. As we have discussed, it will however be impossible to answer these questions without a refined modeling of the signals coming from our instruments and from our own Galaxy, to a level of precision never reached before. The understanding of the Galactic signal will also come with a better comprehension of the interplay between turbulent fluids and magnetic fields in the ISM, giving birth to stars and life in our Universe. Major developments are now undertaken to face these challenges through ambitious experimental projects as *LiteBIRD* and *Euclid*, resulting from large international collaborations, as well as numerous theoretical and computational developments at the edge of our current capacities. It is thus fair to bet that time will provide us with some answers, bringing along them new questions in our never ending quest for understanding.

11

Conclusion et perspectives (Français)

Au cours de cette thèse, j'ai pu travailler sur des problèmes majeurs touchant à une grande variété de thématiques, de l'expérience à la théorie en cosmologie, à travers l'analyse de données. Ces trois dernières années, des développements significatifs et stimulants ont été entrepris sur tous les fronts. Ces développements ouvrent la porte à de futures recherches qui promettent d'être exaltantes et j'espère profondément pouvoir continuer à y contribuer significativement. En particulier, j'ai pu introduire de nouveaux outils qui devront être appliqués à des problématiques plus générales, afin d'en apprécier leur puissance et leurs limites. Je vais maintenant résumer point par point les résultats discutés plus haut et les perspectives qu'ils ouvrent.

11.1 Effets systématiques pour la mission *LiteBIRD*

La mission satellite *LiteBIRD* sondera les plus grandes échelles du CMB avec une précision sans précédent. Ce faisant, elle pourra révéler les empreintes laissées dans l'Univers primordial par de la nouvelle physique des hautes énergies au-delà de nos modèles standards, telle que l'inflation primordiale ou la biréfringence cosmique. Pour que ce défi soit réalisable, il est crucial de trouver de nouvelles méthodes permettant le contrôle des effets systématiques et la soustraction des avant-plans. Pendant cette thèse, j'ai été grandement impliqué dans ces deux sujets. J'ai fourni des vérifications et des retours pour la publication majeure ([LiteBIRD Collaboration et al., 2023](#)), sur laquelle de nombreuses études subséquentes reposent aujourd'hui. En parallèle, j'ai étudié l'impact d'une scanning strategy homogène. Mes études en collaboration avec Yusuke Takase ont permis d'explorer et de justifier rigoureusement la configuration de scan actuelle. De plus, nous avons identifié des paramètres critiques qui n'avaient jamais été considérés auparavant, l'orientation des plans focaux, que nous avons optimisé. Dans cette configuration, des critères doivent encore être établis sur les degrés d'asymétries des beams qui peuvent être permis, particulièrement sur les far side lobes, qui pourraient induire un biais dans la mesure du rapport tenseur sur scalaire r . J'ai déjà commencé à explorer significativement ce point, mais n'ai pas pu conclure l'analyse. Répondre précisément à cette question représente une tâche complexe et exige le développement de nouveaux outils conceptuels et numériques afin de pouvoir quantifier le degré d'asymétrie de manière approprié et simple et de pouvoir traiter efficacement la convolution du ciel par les

beams polarisés en un temps de calcul minimal. Afin de pouvoir réaliser cette étude et de nombreuses autres, je souhaite garder une implication future majeure dans la collaboration.

11.2 Avant-plans polarisés

11.2.1 L'expansion en moments

La course pour des missions CMB de plus en plus sensibles, sondant des signaux de plus en plus faibles provenant de la surface de dernière diffusion, rend explicite le besoin d'une caractérisation fine des signaux polarisés d'avant-plans de notre propre Galaxie. Je crois personnellement que le succès d'une telle caractérisation doit aller bien au-delà d'une suppression aveugle des avant-plans en fournissant des méthodes ancrées dans et motivées par la physique du milieu interstellaire. Faire ceci demande d'obtenir des méthodes de séparation de composante interprétables, permettant de retrouver le CMB ainsi que des informations cruciales pour la science Galactique. Comme je l'ai détaillé dans le chapitre 8, l'expansion en moments fournit une solution motivée pour caractériser la complexité émergente des effets de mélange de différents signaux. Dans cette thèse, j'ai montré qu'elle pouvait être utilisée avec succès pour la séparation de composante dans des missions ayant une haute sensibilité et une large couverture du ciel tel que *LiteBIRD*, tout en donnant un grand niveau d'interprétabilité. Ce premier travail est une preuve de concept et des développements subséquents doivent être entrepris afin de pouvoir tester et optimiser cette méthode, en l'appliquant à de plus grandes fractions du ciel et avec des modèles d'avant-plans plus complexes. De telles études pourraient ranger l'expansion en moments paramétriques parmi les méthodes de séparation de composante classiques, prête à être confrontée à de vrai données.

J'ai de plus montré qu'il était possible de fournir une extension cohérente de l'expansion en moments à la polarisation : l'expansion en spin-moments. Ce développement comble le vide entre les distorsions de SED en intensité et en polarisation et connecte les propriétés statistiques des avant-plans aux conséquences du mélange. Dans ce nouveau paradigme, les moments deviennent des nombres complexes et la correction du pivot a une contrepartie imaginaire, à partir de laquelle il est possible de dériver des expressions analytiques donnant la dépendance en fréquence de la rotation de l'angle de polarisation du signal total. Ce nouveau cadre est robuste et demande à être appliqué plus avant pour la séparation de composante et les modèles de poussière. Suite à ce travail, il est aussi clair que les moments peuvent être utilisés pour inférer les informations statistiques des signaux d'avant-plans. Beaucoup de travail, déjà en cours, doit être effectué pour évaluer à quel point cette direction est fructueuse. De plus, les spin-moments peuvent être utilisés pour créer et caractériser de nouvelles simulations d'avant-plans qui soient robustes et utilisable par la communauté CMB. J'explore actuellement cette direction prometteuse et espère pouvoir prochainement publier des modèles prêts à l'emploi.

Enfin, j'ai donné une première application des spin-moments aux modes-*E* et *B*. Dans cette application, démontrant la robustesse des spin-moments, j'ai montré comment connecter la complexité du signal dans un pixel à l'amplitude observée des moments dans l'espace des harmoniques sphériques. J'ai aussi montré qu'il fallait attendre des comportements spectraux différents pour les trois spectres polarisés *EE*, *EB* et *BB* en présence de mélange polarisé. Ces comportements peuvent être modélisés par les spin-moments. Cela pourrait avoir des

conséquences fortes pour la modélisation de la poussière, la séparation de composantes et la quête de biréfringence cosmique. L'impact réel de ces effets doit encore être clairement évalué pour les missions CMB contemporaines et futures. De plus, j'ai montré que la variation du rapport E/B avec la fréquence fournissait une sonde du mélange polarisé, indépendante de tout modèle pour la SED. Il serait alors pertinent d'estimer la sensibilité à laquelle une telle variation pourrait être détectée, en particulier dans le cas de *LiteBIRD*.

11.2.2 Wavelets Scattering transform

Nous avons vu que le scattering transform fournit de nouveaux outils statistiques interprétables pour modéliser la complexité spatiale du signal Galactique. Des premières étapes prometteuses ont été entreprises afin de comprendre comment les complexités spatiales et spectrales pouvaient être conjointement traités avec cette approche. Dans cette thèse, j'ai utilisé le formalisme WPH afin d'explorer le bénéfice d'utiliser des statistiques cross-fréquences. De premiers résultats prometteurs ont été obtenus pour les synthèses alors que les applications au débruitage sont encore en train d'être étudiés. Des développements majeurs doivent encore être effectués afin d'évaluer la robustesse de cette méthode et être capable de l'utiliser pour la séparation de composantes sur la sphère céleste. Sur le long terme, j'aimerais pouvoir étudier la possibilité de coupler l'expansion en spin-moments et les WPH, afin de modéliser ensemble complexité spectrale et spatiale au sein d'une approche interprétable, minimale et motivée.

11.3 Variation des constantes

Enquêter sur la stabilité des constantes fondamentales de notre modèle standard est une tâche de première importance. Premièrement, comme j'ai voulu le montrer dans le chapitre 9, établir une liste des constantes fondamentales de nos modèles et comprendre leur rôle apporte un nombre significatif de questions complexes. Les réponses à ces questions – à l'interface avec la philosophie des sciences – sont éclairantes sur les subtiles constructions théoriques de la relativité générale et de la théorie quantique des champs, qui reflètent à ce jour notre meilleure compréhension de la physique fondamentale au sujet de la gravitation et des autres forces fondamentales. Ainsi, chercher les variations de ces constantes ouvre une fenêtre sur la nouvelle physique et permet de contraindre directement certains modèles ambitieux visant à unifier physique quantique et gravité telle que la théorie des cordes. Afin d'implémenter de manière consistante la variation des constantes fondamentales – telle que la constante de structure fine α – sur des échelles cosmologiques, j'ai contribué au développement d'une nouvelle version du logiciel CLASS qui a été rendue publiquement disponible. Ce code, qui inclut désormais la masse de l'électron et la constante de Newton a été et sera encore utilisé par moi-même et d'autres afin d'étudier un grand nombre de questions et de modèles liés aux constantes fondamentales. Comme je le souhaitais originellement, j'ai implémenté des modèles de champ scalaires dans ce code, afin de dériver les dernières contraintes en date sur différentes versions du modèle phénoménologique de Bekenstein et sur le modèle du runaway dilaton inspiré de la théorie des cordes. Les espaces de paramètres permis pour ces modèles sont désormais extrêmement restreints, excluant les couplages à la matière hadronique plus grands qu'une part par million et rejetant les valeurs naturelles attendues pour de grandes classes de modèles au-delà de notre modèle standard. Suivant cette direction, j'étudie désor-

mais d'autres modèles motivés en lien avec les conjectures du Swampland ou avec les puzzles cosmologiques comme le problème du Lithium ou la tension de H_0 . Sur ce dernier point, il est connu qu'une variation de α dans l'Univers jeune impacterait la BBN et l'histoire de la recombinaison, permettant de soulager significativement les tensions observationnelles. Il reste cependant nécessaire d'étudier si certains modèles bien motivés, sans fine tuning, pourraient permettre de soulager ces tensions tout en survivant à la confrontation aux données. Additionnellement, j'aimerais étudier la co-variation des constantes fondamentales, attendue dans le cas le plus général, comme celui où les couplages de jauge et les ratio de masses ensembles. Prendre en compte cette co-variation de manière cohérente dans nos outils numériques sera un défi majeur qui devrait apporter avec lui son lot de résultats surprenants.

Les missions cosmologiques de prochaine génération vont resserrer de plus en plus le domaine permis pour les variations cosmologique des constantes fondamentales. Par exemple, j'ai montré que le satellite *Euclid* fournirait une mesure indépendante de α au redshift du découplage. De plus, les missions CMB succédant à *Planck*, comme SO, *LiteBIRD* ou CMB-S4 vont aussi avoir leur mot à dire concernant les variations spatio-temporelles des constantes durant la recombinaison. Alors que je n'ai pas pu établir de prédition précise sur ces mesures dans la présente thèse, j'espère pouvoir explorer ces questions plus avant dans les années à venir. Enfin, j'ai montré que les contraintes locales comme les horloges atomiques et les futures horloges nucléaires ainsi que les tests de l'universalité de la chute libre, fournissent les contraintes les plus frappantes sur les modèles de variation des constantes. L'amélioration de ces expériences dans les prochaines décennies est attendue et pourrait significativement transformer notre compréhension de la physique. Cependant, si les déviations aux paradigmes contemporains restent non détectées, il deviendra urgent de chercher à expliquer comment les constantes fondamentales peuvent rester aussi stables au sein des modèles au-delà de nos modèles standards, comme ceux de gravité quantique.

11.4 Le mot de la fin

L'impact des questionnements cosmologiques sur la manière dont nous nous percevons dans l'Univers peut être majeur. Nous ne pouvons qu'être émerveillés par notre compréhension moderne de l'histoire cosmique et l'accord remarquable entre nos observations du cosmos et les théories utilisées pour le modéliser, fondées sur des principes élémentaires ancrés dans la physique des particules et la relativité générale. Cependant, il nous reste encore indubitablement de nombreuses zones d'ombres à éclaircir et c'est le rôle du chercheur que de se concentrer sur ce que nous ignorons. Nous ignorons pourquoi les constantes fondamentales ont les valeurs que nous mesurons et pourquoi ces valeurs semblent si précisément ajustées pour permettre l'existence de la chimie et de la vie dans un Univers étrangement structuré. Nous ignorons aussi les conditions exactes dans lesquelles notre Univers est né, il y a quelque 13.8 milliards d'années. Ici encore, nous ne pouvons qu'être ébahis que de telles questions soient désormais entrées dans le domaine des sciences empiriques. Comme nous l'avons discuté, il sera cependant impossible d'apporter des réponses à ces questions sans une modélisation fine des signaux venant de nos instruments et de notre propre Galaxie et ce, à un niveau de précision jamais encore atteint. La compréhension du signal Galactique viendra aussi avec une meilleure compréhension de la relation entre les fluides turbulents et les champs magnétiques dans le milieu interstellaire, donnant naissance aux étoiles et

11.4. LE MOT DE LA FIN

à la vie dans notre Univers. Des développements majeurs sont désormais entrepris pour faire face à ces défis à travers des projets expérimentaux ambitieux comme *LiteBIRD* ou *Euclid*, résultant de large collaborations internationales ainsi que de nombreux développements théoriques et conceptuels aux limites de nos capacités actuelles. Il est ainsi honnête de parier que le temps apportera quelques réponses à notre curiosité, amenant avec elles de nouvelles questions dans notre quête sans fin de compréhension.

Appendix A

A differential geometric overview of the standard models

A gentleman only chooses a basis if he must, and the stronger widow principle: a lady must never go to the cemetery.

– Prof. F. P. Schuller

Contents

A.1 General relativity	199
A.2 High energies: particle physics and gauge theories	202

As we discussed in Chap. 3, our current understanding of cosmology relies on general relativity describing the gravitational force and particle physics, describing the content of the Universe and their interactions. I mentioned several times that these two theoretical structures were both rooted in geometry, allowing to establish strong connections between them. In this chapter, I will briefly justify this ascertainment within the framework of differential geometry. To my opinion, this understanding allows for a better grasp of the fundamental routes undertaken to go beyond our standard models, at the heart of theoretical cosmology and of some core aspects of this thesis discussed in Chap. 4 and Chap. 9. Moreover, they provide new insights on the tools used to describe the polarized light, use in the other half of this work in Chap. 5, 6, 7 and 8. These aspects will be further detailed in Appendix B. This brief overview is of course extremely superficial, and for introductions assuming no prerequisite, I refer to [Baez & Muniain \(1994\)](#), [Coquereaux \(2002\)](#) and [Faure \(2021a\)](#).

A.1 General relativity

A.1.1 Preliminary definitions and motivation

A (smooth) *manifold* M can be understood as the mathematical construction generalizing the notion of a surface in d dimension. It provides the natural starting point to describe curved space-time which will be used to describe the Universe on cosmological scales. The

sphere S^2 is a typical example of a 2 dimensional manifold (i.e. a surface). A function f on M associates a real number to each point of the manifold $f : M \rightarrow \mathbb{R}$. One could think of a "colormap" on the sphere. It is then possible to map M by defining locally some coordinates charts x^μ , which are functions on open sets¹ $U \subset M$. For example, one could use the spherical coordinates $x^\mu = \{r, \theta, \phi\}$ on the sphere². On every point of this "surface", a tangent (\mathbb{R}^d -vector) space can be defined in which vectors can live. One could think of "arrows" defined in little planes locally on every point of the sphere. The set of all tangent spaces is called the tangent bundle TM . A vector field is a *section* of TM , that is a choice of a vector in every tangent space over M . Vector fields can be represented as differential operators acting on functions such that, in a chart x^μ , $v(f) = v^\mu \partial_\mu f$. v^μ are the components of v in the frame ∂_μ . $v(f)$ quantifies the derivative/variation of the function f along the arrows defined by v . Vectors are geometrical objects in the sense that they are "arrows" which remain the same no matter what the choice of frame and coordinates chosen to express them.

A curve is a map $\mathbb{R} \rightarrow M$, $\tau \rightarrow \gamma(\tau)$ which correspond to the intuitive definition of a curved line over the manifold. At every point of γ one can define a tangent vector γ' to the curve by its action on a function as $\gamma'(f) = \partial_\tau f$. Hence, in a chart $\gamma' = \partial_\tau x^\mu \partial_\mu$.

Less intuitive objects can be defined to generalize the notion of vectors, defining other "exotic" and geometric objects which remain invariant under coordinate changes at every points of the manifold. They are defined on every tangent space by what object they can act on, and what they give in return.

A *1-form* or *co-vector* ω is an operator taking a vector to return a number $\omega(v) \in \mathbb{R}$. The space of all the 1-form is called the cotangent bundle TM^* . A 1-form field is a section of the cotangent bundle, it acts on vector fields to give a function on M . 1-form can be represented as sets of parallel line over each tangent bundles. The exterior derivative $d f$ of a function f is the 1-form field defined as $d f(v) = v(f)$, $\forall v \in TM$. By defining derivative of geometrical objects in each tangent space, d allows to generalizes the notion of gradient, curls and divergence. In a chart, a basis of TM^* is given by the exterior derivative of the coordinates chart dx^μ . A 1-form field acts on a vector field as $\omega(v) = \omega_\mu dx^\mu(v^\nu \partial_\nu) = \omega_\mu v^\mu$. ω_μ are the component of the 1-form. Similarly, vectors can act on 1-form to give a number, such that $v(\omega) = \omega(v)$.

A rank (m, n) *tensor* field T is a map taking m vectors and n 1-form to give a function. Tensors generalize the notion of vectors to higher dimensions. A (m, n) tensor can be built from the *tensor product* of m vectors and n 1-forms $T = \omega_1 \otimes \dots \otimes \omega_n \otimes v_1 \otimes \dots \otimes v_m$. Its action on a set of vectors v_i and forms ω_i is thus defined as $T(v_a, \dots, v_c, \omega_d, \dots, \omega_e) = \omega_1(v_a) \dots \omega_1(v_c) v_1(\omega_d) \dots v_m(\omega_e)$. In a given chart $T = T^{\mu \dots \nu}{}_{\rho \dots \sigma} dx^\rho \otimes dx^\sigma \dots \partial_\mu \dots \otimes \partial_\nu$.

A *metric* g is the definition of an inner product between vectors in each of the tangent spaces $g(u, v) \in \mathbb{R}$. It is as such a rank $(2, 0)$ tensor field $g = g_{\mu\nu} dx^\mu \otimes dx^\nu$. It thus allows to define the notion of orthonormality, length and angles of the vectors on the manifold. A (real and smooth) manifold equipped with a metric in every tangent space is a *Riemannian manifold*. If this scalar product is not positive definite, we talk about semi-Riemannian manifolds. It also allows to associate a 1-form field to every vector field as $\omega = g(v, \cdot)$.

¹In the sense of topology, as explained in [Schuller \(2016\)](#). For all practical purposes, understand here "a portion of M ".

²which is not defined on the poles. As such, a minimal of two charts is required to map S^2 .

A p -form α is a anti-symmetric rank $(p, 0)$ tensor field, meaning that the result of $\alpha(v, w, \dots)$ changes sign under the permutation of two of its entries $\alpha(v, w, \dots) = -\alpha(w, v, \dots)$. A p -form generalizes the notion of vector fields in k -dimensions: 2-forms are oriented surfaces, 3-forms are oriented volumes ... As such, on a d dimensional space, the highest possible form is a d -form. All of these geometrical figures are defined at each point of the manifold and are invariant under coordinate change. A p -form can be built from the *exterior product* of 1-forms, defined for two 1-forms α and β as $\alpha \wedge \beta = \alpha \otimes \beta - \beta \otimes \alpha$. d can be generalized to act on p -forms, such that it gives a $p + 1$ form. By construction, it satisfies $d^2 = 0$.

For an introduction to the framework of differential geometry in physics see e.g. [Coquereaux \(2002\)](#); [Baez & Muniain \(1994\)](#); [Frankel \(1998\)](#).

A.1.2 The geometrization of gravity II

Following the EEP will lead to the deep conclusion that space-time itself is a dynamical entity, and gravitation is the byproduct of its geometrical properties. For a complete review of GR, see e.g. [Wald \(1984\)](#); [Reula \(2010\)](#); [Misner et al. \(1973\)](#); [Marsh \(2014\)](#).

From a theoretical perspective, the EEP and especially the LLI implies that space-time can be modeled by a 4D semi-Riemannian manifold M . In order to capture gravity and deal with accelerated frames, the tangent spaces must be equipped with a general metric tensor field g of signature -1. This manifold is locally Lorentzian, that is, at every point of space-time, it must be possible to find a frame transformation to an inertial (free falling) frame, allowing to rewrite g as the Minkowski metric η and the laws of physics as those of special relativity. The presence of curvature makes it impossible to find a global transformation in which $g = \eta$ everywhere. A local frame transformation e transforming $g \rightarrow \eta$ is called a "tetrad". As it allows to define length and angles, the overall choice of g will define the shape of space-time. Tangent spaces associated to different points of space-time are different vector spaces, and in principle there is no immediate way to compare two vectors coming from such different space. As such, the notion of "differentiation" of vectors is not defined on a semi-Riemannian manifold. To do so, one must introduce a "connection", which defines the notion of "parallel transport" of vectors i.e. defines how vectors from different tangent spaces can be compared.

Following the WEP implies that the velocity of free falling bodies must all be parallel transported by the same connection, ensuring that their velocity vector follow the same trajectories for identical initial conditions, independently of their mass and composition. The simplest connection choice – leading trajectories to be paths of shortest space-time intervals on the curved space-time – is given by the only torsionless ($\forall u, v \in TM : [u, v] = \nabla_v u - \nabla_u v$)³ and metric preserving ($\forall u, v, w \in TM : ug(v, w) = g(\nabla_u v, w) + g(v, \nabla_w u)$)⁴ affine connection ∇_v on the tangent bundle called the *Levi-Civita* connection, with associated vector potential Γ (and $v \in TM$). This vector potential is a $GL(4)$ valued 1-form, where $GL(4)$ is the group of general linear transformation in 4D. As such, it takes a vector field v and returns a 4 dimensional matrix which can act on other vector fields to transform them. Intuitively Γ connects the different tangent spaces to one another and allows to define the notion of differ-

³Adding torsion does not change the geodesic equation for free falling particles. As such, asking for Γ to be torsionless can be considered as a "parsimony" hypothesis.

⁴Roughly speaking, this last condition ensures the invariance of vector length through parallel transport. It can equivalently be written as $\nabla_u g = 0$

entiation (using ∇_v) and parallel transport of vectors and tensors between different points of M in the direction v . Γ additionally ensures the invariance of the derivative ∇_v under the arbitrary choice of frames over the manifold.

In a given frame, one can express the components of Γ only with the first order partial space-time derivatives of the metric g components (as such the metric can be identified with the gravitational potential and Γ the gravitational field). This choice of Γ hence makes GR entirely determined by a single free field being the metric tensor field g , directly defining to the geometry of space-time. Consider now a given chart x^ν and associated natural frame ∂_ν . ∇_v can be explicated as

$$\nabla_v(w^\mu \partial_\mu) = [d(w^\mu)(v) + w^\nu \{\Gamma(v)\}^\mu_\nu] \partial_\mu \quad (\text{A.1})$$

The connexion 1-form Γ hence quantifies the covariant derivative of the basis vectors $\nabla_{\partial_\mu} \partial_\nu = \Gamma(\partial_\mu) \partial_\nu = \Gamma^\lambda_{\mu\nu} \partial_\lambda$, with $\Gamma^\lambda_{\mu\nu} = \frac{1}{2} g^{\lambda\rho} (\partial_\mu g_{\rho\nu} + \partial_\nu g_{\rho\mu} - \partial_\lambda g_{\mu\nu})$, that is how the frames are parallel transported.

The trajectories of any free massive particle on the manifold are curves $\gamma \in M$, parametrized by $\tau \in \mathbb{R}$ (typically the proper time). They are geodesics of ∇ , meaning that their 4-velocity obeys *parallel transport* with respect to ∇_u , written as

$$\nabla_u u = 0, \quad (\text{A.2})$$

where $u := \gamma' = \frac{d}{d\tau} = (\partial x^\mu / \partial \tau) \partial_\mu \in TM$ is the 4-velocity vector of the particle tangent to $\gamma(\tau)$. Eq. A.2 translates that a free particle must move such that its velocity u is transported as rigidly as possible over space-time. Again, the choice of Γ as the Levi-Civita connection implies that γ will correspond to the shortest space-time path between two events, or the one minimizing the proper-time. Additionally, u should always remain in the positive light cone associated to each tangent space, that is $g(u_{\gamma(\tau)}, u_{\gamma(\tau)}) > 0$ (which is equivalent to the choice of a time orientation).

One can compute the curvature $\text{GL}(4)$ -valued 2-form associated to the Levi-Civita connection as

$$\mathfrak{R} = d\Gamma + [\Gamma \wedge \Gamma], \quad (\text{A.3})$$

with $d\Gamma$ the exterior derivative of Γ and $[A \wedge B](v, w) := [A(v), B(w)]$ for $A, B \in \text{GL}(4)$ and $v, w \in TM$. \mathfrak{R} quantifies the holonomy of a small closed path, which is the rotation induced to a vector that is parallel transported back to the same point with Γ along that loop. From its definition, one sees that \mathfrak{R} can be expressed with second and first order derivatives of g .

A.2 High energies: particle physics and gauge theories

A.2.1 Preliminary definitions and motivation

The notion of *bundle* generalizes the notion of the tangent bundle, by setting a new space, called a *fiber*, over each point of the manifold⁵. As such, one can introduce new "spaces"

⁵Formally, a bundle is a pair of smooth manifolds E (the total space) and M the base space, with a map called the projection $\pi : E \rightarrow M$. The fiber over a point $p \in M$ is $\pi^{-1}(p)$.

over each point of space-time. If all the fibers are the same, we talk about a fiber bundle and if they are vector spaces we talk about vector bundles. For example, adding a line fiber to every point of a circle, one obtains a cylinder, which can also be understood as a fiber bundle. TM is thus a vector bundle with \mathbb{R}^d -vector spaces as fibers.

Gauge theories associate complex vector spaces to every point of space-time, in which the fields of the standard models can live, which end up describing the fundamental entities of our standard models. Fields are sections of these bundles i.e. a choice of a vector in every fiber over each point of space-time. For short, to every point of space-time p one associates a pair (v, e) , where v is a complex vector and e is a frame⁶. The group G of frame transformations acting on e is called the structure group, or gauge group. Groups are abstract entities, which can find concrete *representations* as matrix groups acting on vector spaces. Transformations on a d dimensional complex vector space which preserve the hermitian product are given by the so called *fundamental representations* of the special unitary groups $SU(d)$. They are used in quantum physics as they preserve the probability densities and hence the information, which is believed to be one of the most fundamental principles of modern physics. Under a transformation of the frame by eg with $g \in G$, the value of v changes accordingly as $\rho(g^{-1})v$ where ρ is the representation of the group. As such, v and e are related such that they describe the same invariant geometrical object $\psi = v^i e_i$ in a given chart. In physics, both the vector and the field are generally identified such that we note $v^i = \psi^i$. This thus naturally generalizes, in an abstract way, the notion of vectors $v = v^\mu \partial_\mu$ in TM , invariant under any transformation of the local frame $e = \partial_\mu$ under the group preserving the metric product $G=SO(d)$.

General transformations in physics are described by *Lie groups*, which elements are defined by a continuous parameter. For example, the rotations around an axis with an associated angle parameter θ (forming the group $SO(2)$). Lie groups can also be understood as manifolds, entirely generated by their tangent spaces around the unity transformation, which is named the *Lie algebra*, noted \mathfrak{g} . The vectors of the basis of the tangent space of G are called the *generators* of the group, noted X_a . For a matrix Lie group G , any member $g \in G$ can be created from the generators using the exponential map as $g = \sum_a e^{X_a \theta_a}$, with $\theta_a \in \mathbb{R}$. The number of generators is called the *dimension* of the group. $SU(d)$ groups have a dimension of $d^2 - 1$. A vector which commutes with all the generators is called a *Casimir operator*, and is associated with conserved quantities under the group transformations. $SU(d)$ groups are Lie groups.

As for the tangent bundle, covariant derivatives D_v can be defined on the associated bundles, introducing how ψ is parallel transported in the direction given by the vector v . They are associated with connection \mathfrak{g} valued 1-forms $\mathcal{A} = \mathcal{A}_\mu^a X_a \otimes dx^\mu$ expressing how the frame e transforms from point to point and making $D_v \psi$ invariant under any local arbitrary choice of e over M . As such, the generators of \mathfrak{g} are defining the different types of entities that can act on the field. Each generator can be associated to a new particle called a *gauge bosons* \mathcal{A} mediating the interactions. To propagate the conservation of probabilities across space-time, these connexions will be metric preserving for the hermitian metric, as the Levi-

⁶Formally these are sections *associated vector bundles* $E = P \times F / \sim$, where P is a principal G -bundle, F is a manifold or a vector space, and \sim is the equivalence relation $(e, \psi) \sim (eg, \rho(g^{-1})\psi)$, where $\psi \in F$, $e \in P$ and $\rho(g)$ is the representation of $g \in G$ on F . See e.g. [Coquereaux \(2002\)](#) and [Marsh \(2016a\)](#) for more.

Civita connexion Γ is metric preserving for g . However, the notion of torsion is unique to the tangent bundle and does not exists on more general complex bundles. To each connection on can associate a curvature \mathcal{F} . When the connections are curved, translating non trivial geometrical properties of the bundles which translates into fundamental forces.

A.2.2 Gauge theories

In the standard model of particle physics, particles are understood as quantized excitations of fields over space-time. These fields are described as sections of different associated fiber bundles (Marsh, 2016a). As such, over each space-time points, the field values are elements of vector spaces on which the unitary⁷ irreducible representations of various groups can act. Some connection fields will have to be specified to relate these vector spaces from one another across space-time and, just as in GR, these connections can be curved, giving rise to the other fundamental forces of nature.

Regarding their properties under space-time transformations (e.g. rotations or boosts), the fields are constrained by LLI to live in vector spaces on which unitary irreducible representations of the Poincaré group can act (see e.g. Schwichtenberg 2018)⁸. This group has two Casimir operators leading to two conserved quantities labeling the representations: the spin s^9 and the mass m . Roughly speaking, a field of spin s "rotates" by an angle $s\theta$ under a spatial rotation by an angle θ . Fields represented by half-integer spins ($1/2, 3/2, \dots$) are called fermions and integer spins ($0, 1, \dots$) are called bosons. The spin value has strong implications on the behavior of multiple-particle systems through the spin-statistics theorem (Pauli, 1940)¹⁰. Today, only scalar ($s = 0$), spinors ($s = 1/2$) and vector ($s = 1$) fields are known to be part of the building blocks of nature. An hypothetical graviton field, associated to the metric g , would be a boson of spin 2.

The matter fermion fields are sections of spinor bundles associated to the principal frame bundle of space-time. As such, a rotation of the frame of the tangent bundles will correspondingly change the value of their components. They exist in two different chiralities: left ψ_L and right ψ_R transforming respectively with the $(1/2, 0)$ and $(0, 1/2)$ representations of $\text{SO}(1,3)$. They are usually packed in a single Dirac bispinor ψ , such that both chiralities are coupled through the mass m in the Dirac equation (see Eq.(A.7)). The dual of the field $\bar{\psi} = \psi^\dagger \gamma^0$ - where † is the Hermitian conjugaison and γ^0 the 0-th Dirac matrix - can be identified as the "creator" of anti-matter particles, arising as a necessity from space-time symmetries (Feynman et al., 1987; Dressel et al., 2015)¹¹.

⁷Wigner theorem asks for the unitarity (or anti unitarity) of all the transformation operators U acting on wave-vectors $|\psi'\rangle = U|\psi\rangle$ of Hilbert spaces in order to preserve the hermitian product $\langle\psi'|\psi'\rangle = \langle\psi|U^\dagger U|\psi\rangle = \langle\psi|\psi\rangle$ (or equivalently on operators in Heisenberg's picture $\psi' = U^{-1}\psi U$, after second quantization ψ being promoted to an operator on Fock space).

⁸Even deeper insights can come when thinking in terms of Clifford algebra (space-time geometric algebra) and Clifford bundles, see e.g. Benn 1987.

⁹The irreducible representations of the Lorentz group $\text{SO}(1,3)$ are labelled by two numbers s_1 and s_2 . Scalars transform under the $(0,0)$ representation, spinors under $(1/2,0)$ or $(0,1/2)$ and vectors under $(1/2,1/2)$. Higher representations are associated with tensors. The spin associated to the Poincaré group is related by $s = s_1 + s_2$.

¹⁰Boson creation operators commute while fermions' anti-commute. This implies that one can put an infinity of bosons in the same quantum state while this is impossible for fermions (Pauli exclusion principle).

¹¹Explaining why Hermitian metric preserving connection fields, as the photon, are "their own antiparticle".

Two fundamental forces acting on the matter fields ψ are currently known beside gravity: the electroweak and strong forces associated respectively with the Lie groups $SU(2) \times U(1)$ and $SU(3)$. They can both be understood as curvature effects of the vector bundles on which the fermions fields ψ are defined (see e.g. [Derdzinski 1992](#))¹². The invariance of physics under local coordinate transformations with the structure Lie groups G (with respective Lie algebra \mathfrak{g}) are called gauge invariances¹³, The gauge fields \mathcal{A} , associated to the vector bosons transmitting forces¹⁴) are the \mathfrak{g} values 1-form connection fields living in the adjoint bundles of the structure group. As such, the framework of gauge theories is very similar to the one of GR, for which $G=SO(1,3)$ with the tangent bundle as associated bundle. However as the equations of motions are different and due to some specificities of the tangent/spinor bundles for gravity (as the existence of the solder form [Healey 2007](#)), the proper way to think gravity as a gauge theory is still debated¹⁵.

Regarding the gauge groups, all fundamental matter fields known are living either in the trivial or in the fundamental representations of the gauge groups¹⁶, while bosons are living in the adjoint representations. Casimir operators are associated to the various conserved charges as isospins. For electro-weak interaction, ψ are left chiral weak isospin doublets (of $U(1)$ singlets) as e.g. the lepton pair (ν_L, e_L) or the quark pair (u_L, d_L) , \mathcal{A} are the three W bosons and the B boson fields and the gauge group is given by $G = SU(2) \times U(1)$. The rank of group is the number of diagonal generators. Each diagonal generator is associated with a neutral interaction and thus a neutral gauge boson, while non-diagonal generators are associated to charged interactions and charged bosons. As $SU(2)$ is a group of rank 1, there exist two non-diagonal generators associated to charged (flavor changing) currents and a diagonal generator associated to a neutral current. For strong force, ψ is a color triplet (of quarks being themselves $SU(2)$ doublets or singlets of $U(1)$ singlets) and $G = SU(3)$. \mathcal{A} are the 8 colored gluon fields. Interaction of quarks with gluons can then be interpreted as rotations of the triplet ψ in the color space. As for fermions, the standard model contains three generations of quark doublets and three generations of lepton doublets (electrons and

¹²Formally $\psi = \phi \otimes \tilde{\psi}$ is the tensor product of a spinor field $\tilde{\psi}$ on the spinor bundle and a Yang-Mills field ϕ on the gauge vector bundle. To simplify the notation we use ψ both for generic Dirac spinors and their gauged version.

¹³For electromagnetism, the vector bundle is the one of wavefunctions as a bundle of fiber \mathbb{C} . A change of gauge corresponds to a different choice of "real axis" for the complex plane over space-time and \mathcal{A} allows physics to be invariant under such a redefinition. For a pedagogical introduction see [Faure \(2021a,b\)](#).

¹⁴The fact that they are connections \mathfrak{g} valued 1-form implies that all gauge bosons must have $s = 1$ and that there should then be as many gauge bosons as there are generators of the gauge group: 1 for $U(1)$, three for $SU(2)$ and 8 for $SU(3)$.

¹⁵For a discussion of the similarities between GR and gauge theories rooted in differential geometry see e.g. [Weatherall \(2014\)](#). Besides the difference in the equation of motion, the core difference between GR and gauge theories is that GR considers section of the special case of the tangent bundle (see [Healey \(2007\)](#)). Both theories however shares strong geometrical similarities, and the defenders of Einstein-Cartan theory and its generalization as Weyl-Cartan-Yang-Mills theory argue that these theories should be understood as gauge theories of the Poincaré group ([Kibble, 1961](#); [Sciama, 1964](#); [Blagojević & Hehl, 2012](#)), which must however already be true of canonical GR written in the tetrad formalism with a Levi-Civita spin connection (with an additional special constraint relating g and Γ) with the extra requirement that torsion seems to be required for spinor fields ([Weyl, 1950](#)). On the other hand, some authors defend more exotic positions, arguing that in order to identify GR as a gauge theory, the metric field g should be understood as a Higgs field breaking the gauge group $GL(d) \rightarrow SO(d)$ ([Ivanenko & Sardanashvily, 1983](#); [Sardanashvily, 2011](#)).

¹⁶Excepted for the Abelian group $U(1)$ for which the representation is given by the hypercharge or electric charge.

neutrons) of increasing masses. Explaining these three generations and the existence of the three gauge groups from higher unifying symmetries is one of the biggest challenges of modern physics.

In contradiction with observations, the theory can not allow for the gauge bosons of electroweak interaction to be massive and the members of the weak doublets to have different masses without breaking gauge invariance. In order to allow this, one has to introduce a new doublet of complex scalar fields, the Higgs field \mathfrak{h} , spontaneously breaking the $SU(2) \times U(1)$ symmetry with its ground state. The breaking gives rise to the photon A , and the three massive Z (neutral) and W^\pm (flavor changing) bosons from the massless B and the three W bosons respectively. In the presence of \mathfrak{h} , all fermions of the standard model also acquire masses through the Yukawa couplings with \mathfrak{h} .

The field sections are constrained to follow equations of motion, obtained from least action principles. Each corresponding Lagrangian densities can be fully determined from symmetry considerations, asking for the action to be a singlet of all the symmetries of the theory and equation of motion to be at most second order (see e.g. [Allys 2017](#); [Schwichtenberg 2018](#)). The coupled *Yang-Mills* equation of a fermion field ψ interacting with a gauge field \mathcal{A} in flat space-time is given by ¹⁷

$$\mathcal{S}_{\text{YM}} = \int \bar{\psi} (\not{D} - m) \psi \, d\mu - \frac{1}{2} \int \text{Tr}_{\mathfrak{g}}(\mathcal{F} \wedge \star \mathcal{F}), \quad (\text{A.4})$$

where we introduced the volume form $d\mu = \sqrt{|-g|} \, d^4x$. The covariant derivative $\not{D} = \gamma^\mu (\partial_\mu + \sum_{\mathcal{A}} g_{\mathcal{A}} \mathcal{A}_\mu)$ ¹⁸ describes the motion of the fermion field in the curved fiber bundle with the gauge fields $\mathcal{A} = \mathcal{A}_\mu^a X_a \otimes dx^\mu$ appearing as connections \mathfrak{g} valued 1-form (X_a being the generators of \mathfrak{g}) and γ^μ being the Dirac matrices (generators of the space-time Clifford Algebra). $g_{\mathcal{A}}$ are the gauge couplings quantifying the intensity of the interaction between the Dirac fields and the gauge fields \mathcal{A} . m is the mass of ψ , corresponding to a zero point energy. F is the curvature algebra valued 2-form associated to the connection D : $\mathcal{F} = d\mathcal{A} + [\mathcal{A} \wedge \mathcal{A}]_{\mathfrak{g}}$. \star is the Hodge duality, connecting forms of different dimensions and requiring the existence of a metric on space-time¹⁹. The second term in the Lagrangian can be interpreted as a kinetic term for the gauge bosons. It can be equivalently rewritten as

$$\frac{1}{2} \text{Tr}_{\mathfrak{g}}(\mathcal{F} \wedge \star \mathcal{F}) = \frac{1}{4} \text{Tr}_{\mathfrak{g}}(\mathcal{F}_{\mu\nu} \mathcal{F}^{\mu\nu}) \, d\mu := \frac{1}{4} \langle \mathcal{F}, \mathcal{F} \rangle \, d\mu. \quad (\text{A.5})$$

The equation of motion resulting from the above Lagrangian are the following

$$(\not{D} - m) \psi = 0, \quad (\text{A.6})$$

$$\star d \star \mathcal{F} = J. \quad (\text{A.7})$$

The first one is Dirac equation and the second one describes the coupling between the spinor field and the gauge field, with the current-vector $J = q \bar{\psi} \gamma^\mu \psi \partial_\mu$. This second equation is

¹⁷For an introduction to geometrical approaches of the standard model see e.g. [Coquereaux \(2002\)](#); [Schuller \(2016\)](#); [Baez & Muniain \(1994\)](#) and for a more complete review in [Nakahara \(2003\)](#); [Bleeker \(1981\)](#)

¹⁸ $\mathcal{A}_\mu = \mathcal{A}(\partial_\mu)$

¹⁹Defined as $\alpha \wedge \star \beta := (\alpha, \beta) \, d\mu$, where $(\alpha, \beta) \propto \alpha_{i\dots j} \beta^{i\dots j}$ is the scalar product (full contraction) of the forms with the metric g .

equivalent to the charged Maxwell equations if $G = U(1)$. Another important equation is given by the Bianchi identity for curvature $d\mathcal{F} = \mathcal{F} \wedge \mathcal{A} - \mathcal{A} \wedge \mathcal{F}$. For electromagnetism (and Abelian gauge theories), it gives back $d\mathcal{F} = d^2\mathcal{A} = 0$ (from the definition of exterior derivative $d^2 = 0$), encompassing the deep geometrical fact that "the boundary of a boundary is zero". In a given choice of frame it gives the two charge free Maxwell's equations. For non-Abelian gauge groups, this equation encompasses possible interactions between the gauge bosons.

In curved space-time, the full Lagrangian density ($\mathcal{S} = \int \mathcal{L} d\mu$) of the standard model of particle physics and gravity (SM) is given by

$$\begin{aligned}\mathcal{L}_{\text{SM}} = & M_{\text{Pl}}^2 \left(\frac{R}{2} - \Lambda \right) + \sum_{\psi, \mathcal{A}} \bar{\psi} (\not{D} + \frac{\omega}{4}) \psi \\ & - \sum_{\mathcal{F}} \frac{1}{4} \langle \mathcal{F}, \mathcal{F} \rangle + \frac{1}{2} |D\mathbf{h}|^2 - V(\mathbf{h}) - \sum_{\psi} \lambda \bar{\psi} \mathbf{h} \psi.\end{aligned}\quad (\text{A.8})$$

The first term is \mathcal{L}_{EH} and the sum over \mathcal{F} ranges over the curvatures of all the fundamental interactions (electroweak and strong). D contains all the gauge connections fields \mathcal{A}_j that each ψ are interacting with, and ω is the spin-connection²⁰. The mass term is given by the Higgs boson \mathbf{h} through Yukawa couplings λ . The existence of Λ is naturally predicted by GR. From a quantum perspective, it could emerge directly from vacuum energy of the various fields but it is yet unclear how. All matter fields are universally coupled i.e. they are minimally coupled with the same and only metric g appearing in the Lagrangian. This embodies the Einstein equivalence principle and the geometric interpretation of gravitation. A direct consequence is that all massless fields should propagate with the same velocity c . The Yang-Mills equation of motion for fermions and gauge fields extracted from Eq. 3.8 are the same as the ones in Eq. A.7, replacing d by the covariant exterior derivative $d^\nabla \psi(v) = \nabla_v \psi$ (or equivalently replace the metric $\eta \rightarrow g$ and derivatives $\partial \rightarrow \nabla$). This procedure is commonly known as *minimal coupling*.

The fields introduced so far can be understood as classical fields or multi-component relativistic wavefunctions $\psi_i(x^\mu) = \langle x^\mu | \psi_i \rangle$. To allow for multiple particles, one must quantify the fields and build a quantum field theory (QFT) through second quantization such that ψ , \mathcal{A} and \mathbf{h} are promoted to creation/annihilation operators on Fock space over every space-time point. The associated quantum states on which these operators act are the occupation number states of these Fock spaces which are tensor products of single particle Hilbert spaces. The probability amplitudes of interaction between particles are calculated in a perturbative fashion using Feynman graphs. For more on QFT, see e.g. [Ryder \(1996\)](#). So far, this procedure can be done consistently for all the fields but ω , and it is yet unclear how to proceed in order to build a quantum theory of gravity²¹.

²⁰Which is here the generalization of the Levi-Civita connection on the spinor bundle. On this, see e.g. Chap. 19 of [Frankel \(1998\)](#) or Chap. 9 and 10 of [Benn \(1987\)](#) for an approach based on Clifford algebras.

²¹The most advanced quantum treatment of gravity to date is certainly given by covariant loop quantum gravity, which proposes a canonical quantification of GR [Rovelli & Vidotto \(2014\)](#). It should not be confused with e.g. string theory, which attempts an unification of all the particle fields (including gravity) as energy levels of quantum strings.

Appendix B

The mathematical description of polarized light

I think that when you have audacity, you will get polarization.

– Lee Daniels

Contents

B.1	The challenge of polarized light	209
B.2	The local description of polarized light	210
B.3	The polarized signal over the flat sky	214
B.4	The polarized signal over the curved sky	215
B.5	<i>E</i> - and <i>B</i> - modes from ladder operators	217
B.6	The Power spectra	219

B.1 The challenge of polarized light

For astrophysicists, light represents the main source of information on the very distant objects they aim to study. As a vibration of the electromagnetic field, light is not only described by an intensity, but also by a direction of oscillation i.e. a *polarization*. While faint and challenging to measure, the polarization of astrophysical sources contains precious and unique information about the physics and geometry associated to the phenomenon that sourced it. A fine understanding of the polarized light will be necessary in order to extract cosmological information out of the CMB radiation. It will also be needed in order to understand and remove the spurious Galactic signal.

Several equivalent mathematical formulations exist to describe polarized light using complex numbers or tensor fields on the sphere. These approaches are complementary and each of them provide special insights on the geometrical nature of polarization. We will present them in great detail in this chapter.

B.2 The local description of polarized light

B.2.1 The power of the Helmotz decomposition

The Helmotz-Hodge theorem states that any continuous vector field \mathbf{F} on \mathbb{R}^3 with continuous partial derivatives can be uniquely expressed in two orthogonal components as the sum of the gradient¹ of a continuous function λ and the curl² of a vector field \mathbf{A}

$$\mathbf{F} = \mathbf{E} + \mathbf{B} = -\nabla\lambda + \nabla \times \mathbf{A}. \quad (\text{B.1})$$

Due to the properties of ∇ , \mathbf{E} and \mathbf{B} must satisfy

$$\nabla \times \mathbf{E} = \mathbf{0}, \quad (\text{B.2a})$$

$$\nabla \cdot \mathbf{B} = 0. \quad (\text{B.2b})$$

This splitting has a deep geometrical meaning, as it allows to split contributions to a vectors fields which have a "curl-free"³ pattern (\mathbf{E}) and which have a "divergence-free"⁴ pattern (\mathbf{B}). For example, this splitting is hence of first importance for electromagnetism of fluid mechanics. As we will see, this decomposition allows to isolate the components with different physical origins of numerous objects, beyond 3-vector fields. It will reveal especially useful to describe and characterize the phenomenological and statistical properties of light⁵. As illustrated in Fig. B.2, this splitting conserve a geometrical interpretation. Around each point, \mathbf{E} will obey a radial symmetry at every point of space while \mathbf{B} has "vortex" shapes.

B.2.2 The light wave

As discussed in Chap. 3 and Appendix A, light can be understood as the quantum excitation (photon) associated to the $U(1)$ connection A and its corresponding curvature F . In a given inertial frame (t, x, y, z) , a generalization of the Helmotz theorem (stated in Hodge theory see [Sattinger \(2013\)](#)), allows to split the Maxwell 2-form field F in to a space 1-form field \mathcal{E} and a space two-form field \mathcal{B} as⁶

$$F = \mathcal{E} \wedge dt + \mathcal{B}, \quad (\text{B.3})$$

that can both be identified to the electric field vector \mathbf{E} and magnetic field pseudo-vector \mathbf{B} using respectively the metric and the Hodge duality on the Euclidian space embedded in

¹To connect with the notations introduced in the previous chapter: $\nabla f = (\text{d}f)^\sharp$, introducing $\omega^\sharp := g^{-1}(\omega, \cdot)$ with $\omega \in T^*M$ and $\omega^\sharp \in TM$.

² $\nabla \times \mathbf{X} = [\star^{-1} \text{d}(\mathbf{X}^\flat)]^\sharp$ introducing $\mathbf{X}^\flat := g(\mathbf{X}, \cdot)$ with $\mathbf{X} \in TM$ and $\mathbf{X}^\flat \in TM^*$.

³Understand that if the \mathbf{E} was the velocity field of a fluid, it would not be able to rotate a stick floating within it.

⁴Understand that if \mathbf{B} has no point sources or sink: every vector "going in a point" must also go out of this point with the same length.

⁵This decomposition can be generalized to any tensor field. It can also be used on the metric tensor to highlight analogies between electromagnetism and gravity in the framework of Gravitoelectromagnetism. In linearized gravity, Einstein equations have an identical form to Maxwell equations (see e.g. [Clark & Tucker \(2000\); Mashhoon et al. \(2001\)](#)).

⁶The Clifford Algebra structure of spacetime allows to identify the electromagnetic 2-form with the Riemann-Silberstein complex vector $\tilde{F} = \tilde{\mathcal{E}} + i\tilde{\mathcal{B}}$ where the complex unit can be identified with the 4-volume form [Dressel et al. \(2015\)](#). Beside giving deep insights on classical electromagnetism, this quantity is crucial to describe the (first quantization) wavefunction of a single photon as it can be interpreted as a probability amplitude for its energy density see [Bialynicki-Birula & Bialynicka-Birula \(2013\)](#).

Minkowski space-time. The existence and gauge invariance of the electromagnetic potential fields (λ, A) appear as another consequence of the Hodge decomposition of \mathcal{E} and \mathcal{B} .

The Maxwell equations in vacuum ($J = 0$), can be combined to give rise to wave equations for both the electric field $\mathcal{E}(\mathbf{r}, t)$ and the magnetic field $\mathcal{B}(\mathbf{r}, t)$. Focusing only on the electric-field, one gets

$$\square \mathcal{E} - \frac{1}{c^2} \frac{\partial^2 \mathcal{E}}{\partial t^2} = 0. \quad (\text{B.4})$$

Monochromatic plane waves (and their sums) are solutions, and for convenience they can be written in complex form as

$$\mathcal{E} = |\mathcal{E}(t)| e^{i(-\omega t + \mathbf{k} \cdot \mathbf{r})}, \quad (\text{B.5})$$

with ω the pulsation and \mathbf{k} the wavevector of the plane wave⁷, both being related through Eq. B.4 by $\omega = |\mathbf{k}|c$. The free Maxwell-Gauss equation ($\nabla \cdot \mathbf{E} = 0$) immediately gives

$$\mathbf{k} \cdot \mathcal{E} = 0 \quad (\text{B.6})$$

and similarly for the magnetic field. Electromagnetic fields of the plane waves are then transverse to their direction of motion. Using the Maxwell-Faraday equation, \mathcal{E} and \mathcal{B} can be further related by

$$\mathcal{E} \times \mathcal{B} = \mathbf{k}c \quad (\text{B.7a})$$

with \times the standard 3-vector cross-product on \mathbb{R}^3 . As such, \mathcal{E} and \mathcal{B} are not independent and knowing the behavior of one allows to infer the other.

B.2.3 The Stokes parameters, polarization spinor and polarization tensor

Choosing a suitable orthonormal frame $(\mathcal{O}, \mathbf{e}_x, \mathbf{e}_y, \mathbf{e}_z)$ such that the EM wave is propagating in the z direction ($\mathbf{k} = k\mathbf{e}_z$), the notion of polarization is related to the behavior of \mathcal{E} and \mathcal{B} in the $x - y$ plane. Looking at the value of the electric field at the origin \mathcal{O} while the wave is passing, we can write

$$\mathcal{E} = \mathcal{E}_x(t)\mathbf{e}_x + \mathcal{E}_y(t)\mathbf{e}_y. \quad (\text{B.8})$$

The Stokes parameters I, Q, U and V are defined as

$$I = \langle |\mathcal{E}_x|^2 \rangle + \langle |\mathcal{E}_y|^2 \rangle, \quad (\text{B.9a})$$

$$Q = \langle |\mathcal{E}_x|^2 \rangle - \langle |\mathcal{E}_y|^2 \rangle, \quad (\text{B.9b})$$

$$U = 2\text{Re}(\langle \mathcal{E}_x \mathcal{E}_y^* \rangle), \quad (\text{B.9c})$$

$$V = -2\text{Im}(\langle \mathcal{E}_x \mathcal{E}_y^* \rangle). \quad (\text{B.9d})$$

where z^* is the complex conjugate, $|z|^2 = z^*z$ and $\langle . \rangle$ is the time average. I corresponds to the energy density of the electric field and can be understood as the total intensity of the

⁷They can actually naturally be merged in a 4-vector $(\omega/c, \mathbf{k})$, signature of the Lorentz invariance already present in classical electrodynamics.

signal. To give a clearer interpretation of the other parameters, we can introduce two new basis. The first one, $(\mathbf{e}'_x, \mathbf{e}'_y)$ is simply $(\mathbf{e}_x, \mathbf{e}_y)$ rotated by 45°

$$\mathbf{e}'_y = \frac{1}{\sqrt{2}}(\mathbf{e}_x + \mathbf{e}_y), \quad \mathbf{e}'_y = \frac{1}{\sqrt{2}}(\mathbf{e}_y - \mathbf{e}_x). \quad (\text{B.10})$$

The second $(\mathbf{e}_r, \mathbf{e}_\theta)$ is a polar basis in the complex plane

$$\mathbf{e}_r = \frac{1}{\sqrt{2}}(\mathbf{e}_x - i\mathbf{e}_y), \quad \mathbf{e}_\tau = \frac{1}{\sqrt{2}}(\mathbf{e}_x + i\mathbf{e}_y). \quad (\text{B.11})$$

One can now rewrite:

$$U = \langle |\mathcal{E}_{x'}|^2 \rangle - \langle |\mathcal{E}_{y'}|^2 \rangle \quad (\text{B.12a})$$

$$V = \langle |\mathcal{E}_r|^2 \rangle - \langle |\mathcal{E}_\tau|^2 \rangle \quad (\text{B.12b})$$

As illustrated on Fig.B.1, Q and U represent the linear polarization in frames rotated from

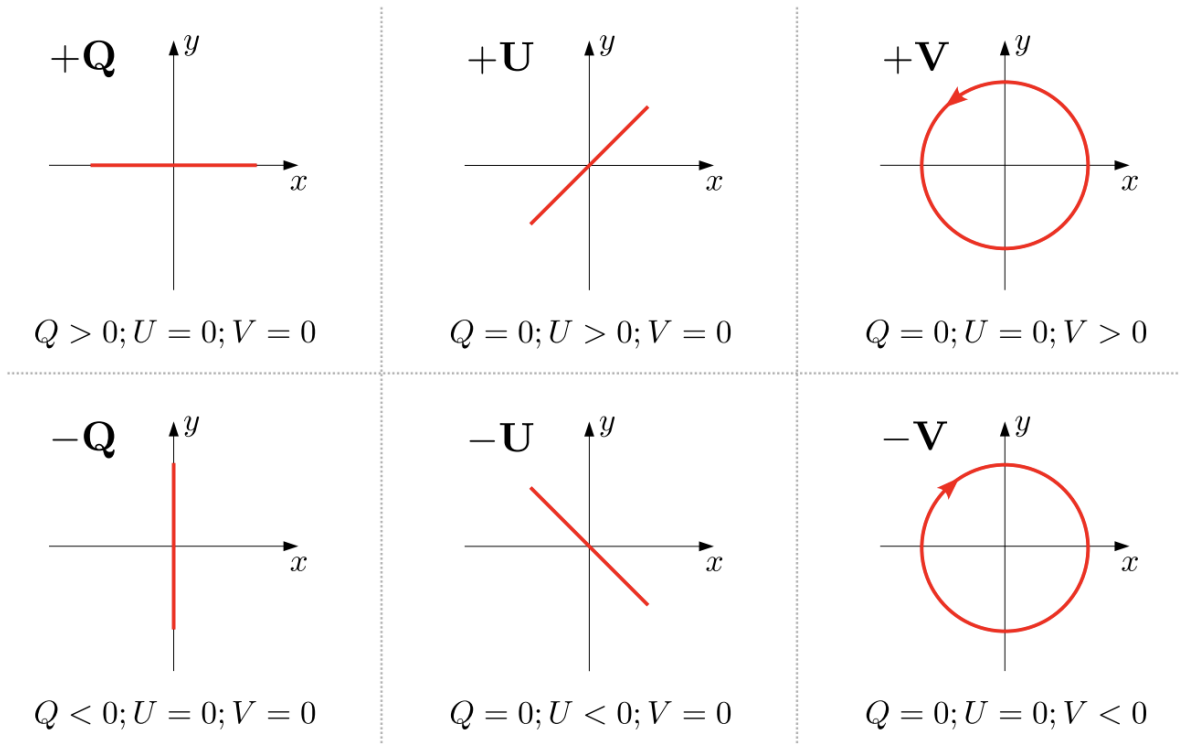


Figure B.1: Geometrical interpretation of the Q , U and V Stokes parameters in a given frame (\mathcal{O}, x, y) . From [Régaldo-Saint Blancard \(2021\)](#).

one another by 45° while V describes circular polarization. The Stokes parameters as defined above are intensive quantities: if two different electric-fields are overlapping $\mathcal{E} = \mathcal{E}_1 + \mathcal{E}_2$, their coordinates can simply be added as $\mathcal{E}_i = \mathcal{E}_{i,1} + \mathcal{E}_{i,2}$ ($i \in \{x, y\}$), such that one gets $I = I_1 + I_2$ and similarly for Q, U and V . By construction

$$P^2 := U^2 + Q^2 + V^2 \geq I^2, \quad (\text{B.13})$$

where we introduced the *polarized intensity* P . The ratio $p = \mathcal{P}/I$ is called the *polarization fraction*. In the case of a monochromatic coherent radiation, $P = I$. Let us introduce now the *linear polarization spinor*

$$\mathcal{P} := Q + iU. \quad (\text{B.14})$$

Then $|\mathcal{P}| = \sqrt{Q^2 + U^2} = \sqrt{P^2 - V^2}$, its complex conjugate is $\mathcal{P}^* = Q - iU$. The phase of the polarization spinor is the *polarization angle*⁸

$$\psi := \frac{1}{2}\arctan2(U, Q), \quad (\text{B.15})$$

where $\arctan2(x, y)$ is a variant of the hyperbolic tangent taking values only in the interval $]-\pi, \pi]$, giving correctly back the argument of the complex number $z = x + iy$. The complex number \mathcal{P} thus becomes in polar form

$$\mathcal{P} = |\mathcal{P}|e^{2i\psi}. \quad (\text{B.16})$$

In the case where no circular polarization is present ($V = 0$), we have $|\mathcal{P}| = P = pI$. The Stokes parameters are then recovered from the spinor by

$$Q = \operatorname{Re}(\mathcal{P}) = pI \cos(2\psi), \quad (\text{B.17a})$$

$$U = \operatorname{Im}(\mathcal{P}) = pI \sin(2\psi). \quad (\text{B.17b})$$

Our above definition of the Stokes parameters is dependent of a choice of frame and coordinate system. It can be shown that under a right handed basis rotation of an angle θ around \mathbf{e}_z , the Stokes parameters transform as

$$I' = I, \quad (\text{B.18a})$$

$$\mathcal{P}' = e^{-2i\theta}\mathcal{P}, \quad (\text{B.18b})$$

$$V' = V. \quad (\text{B.18c})$$

While I and V appears to be scalar quantities, \mathcal{P} behaves as the coordinate of a field of spin-2 as defined in Appendix A. Hence it remains unchanged after a rotation by π and can be represented by a headless vector (i.e. a segment) which is invariant under a half-turn. Note that we use the name *spinor* to describe \mathcal{P} in a rather general way, as \mathcal{P} really is a spin-2 field (section of the spin-2 bundle associated to the frame bundle) defined on S^2 , i.e. a field in the $s = 2$ representation of $U(1)$ (or $SO(2)$) but not a member of the SPIN group associated to the orthogonal Lie group of the metric vector space (or the irreducible representation of the Clifford algebra⁹). Following this nomenclature, an ordinary vector would be a spinor of spin 1.

As the spin-2 graviton can be described by the symmetric metric tensor g , we can describe \mathcal{P} equivalently by the symmetric trace-free 2×2 *polarization tensor* Π , which coordinates are expressed in a given frame by

$$\Pi := \begin{pmatrix} Q & U \\ U & -Q \end{pmatrix} = Q\sigma_z + U\sigma_x, \quad (\text{B.19})$$

⁸Using the so called "Healpy convention" one defines ψ with $-U$ instead of U in Eq. B.15.

⁹That is multivectors members of the minimal left ideals of space-time geometric algebra or members of the even-graded sub-algebra of the space-time geometric algebra (, auth.).

where σ_i are the Pauli matrices (forming a complete basis for the 2×2 complex matrices when including $\sigma_0 = \delta$). Π is build to have the norm $\Pi^{ab}\Pi_{ab} = Q^2 + U^2 = |\mathcal{P}|^2$ (for a pedagogical introduction see e.g. [Kamionkowski & Kovetz \(2016\)](#)).

For a continuous spectra of light (i.e. an infinite superposition of plane waves), the value of the intensities I and P will be dependent on the value of ω/\mathbf{k} . More commonly one introduces the electromagnetic frequency $\nu = \omega/(2\pi) = |\mathbf{k}|c/(2\pi)$. The frequency dependence $I(\nu)$ or $P(\nu)$, (commonly written respectively I_ν and P_ν), is called the *spectral energy distribution* (SED) of the signal.

B.3 The polarized signal over the flat sky

Let's now consider the value of the polarization emission at every point of the sky. For now, we consider the flat sky approximation, in which a portion of the sky can be identified with a region of \mathbb{R}^2 with a metric given by the Kroenecker delta δ . Lines of sights are labeled in a given chart by $\mathbf{n} = (x, y)$. The polarization tensor/spinor are not defined only at a given point \mathcal{O} anymore, but must be treated as fields on the sky manifold.

The Helmotz decomposition can be generalized and used again with the tensor field Π describing linear polarization and taking a value at every point of the sky. Π can thus be expressed as the sum of two components corresponding to a parity symmetric and a parity odd quantity that are called respectively E -modes and B -modes fields. Since Π is symmetric and trace-free (STF), this gives two constraints on its 4 components and 2 real quantities (as Q and U) are enough to fully describe it. Every STF tensor can be decomposed as

$$\Pi_{ab} = E_{ab} + B_{ab} , \quad (\text{B.20})$$

with

$$E_{ab} = \partial_a \partial_b E - \frac{1}{2} \delta_{ab} \partial_c \partial^c E , \quad (\text{B.21a})$$

$$B_{ab} = \epsilon^c_b \partial_a \partial_c B + \epsilon^c_a \partial_b \partial_c B . \quad (\text{B.21b})$$

E and B must satisfy

$$\partial^d \partial_d E = \partial^a \partial^b \Pi_{ab} , \quad (\text{B.22a})$$

$$\partial^d \partial_d B = \epsilon_{ac} \partial^b \partial^c \Pi_{ac} , \quad (\text{B.22b})$$

and ϵ is the anti-symmetric levi-civita tensor of dimension 2. Contrary to Q and U , E and B can be proved to be scalar fields and thus coordinate invariant quantities.

As we will further see, just as one gets deeper insights by merging the quantities Q and U in the complex number \mathcal{P} , E and B can be united to form a complex number $\mathcal{S} = E + iB$. The general solution to Eq. B.22 is given in e.g. [Zaldarriaga \(2001\)](#). The value of the fields at a position \mathbf{n} of the sky, is given by the integral around the point of

$$\mathcal{S}(\mathbf{n}) = \int \omega(\mathbf{n}') (Q_r + iU_r)(\mathbf{n} + \mathbf{n}') d^2\mathbf{n}' , \quad (\text{B.23})$$

with Q_r and U_r being the Stokes parameters evaluated in a polar frame $(\mathbf{e}_r, \mathbf{e}_\zeta)$ having its origin on the point \mathbf{n} . As expected, they are related by $(Q_r + iU_r) = e^{-2i\zeta}(Q + iU) =$

$e^{-2i\zeta}\mathcal{P}$ with ζ the angle of rotation to go from the original (x, y) frame to the polar one. The transformation kernel $\omega(\mathbf{n}')$ is chosen to be the inverse distance between \mathbf{n} and \mathbf{n}' , $\omega(\mathbf{n}') \equiv -1/\mathbf{n}'^2$. Taking the real and imaginary parts of Eq. B.23 leads to intuition illustrated in Fig. B.2: at a given point \mathbf{n} , E -modes are given by sums of all the polarized patterns along \mathbf{e}_r and \mathbf{e}_ζ surrounding \mathbf{n} (showed at every points of a given radius \mathbf{n}' by Q_r in orange) and B -modes are sums of patterns rotated by 45° (showed at every points of a given radius \mathbf{n}' by U_r in blue). The linear part of any polarized signal can then be decomposed into two

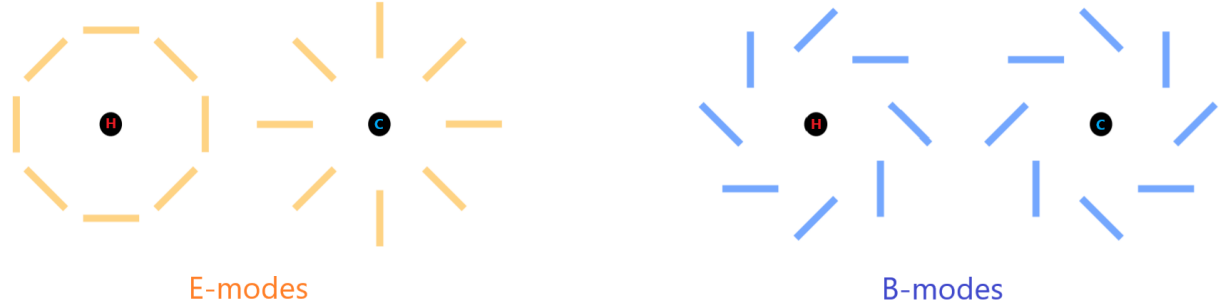


Figure B.2: Illustration of the geometrical nature of E - and B -mode signals associated with a polarization tensor Π around point of the sky.

orthogonal fields with very different geometrical properties as further illustrated in Fig. 5.7. This can allow to split different physical sources for a given polarized signal.

As they result of a spatial integration around all points of the sky, the E - and B -modes fields are by very nature non local: the value of the fields at a point describe the behavior of the polarization field around that point. As such, they are formally equivalent to convolutions and can be defined easily as products in Fourier space

$$\mathcal{S}(\mathbf{k}) = \mathcal{P}(\mathbf{k})e^{-2i\zeta_k}, \quad (\text{B.24})$$

where ζ_k is the angle the mode $\mathbf{k} = k_x \mathbf{e}_x + k_y \mathbf{e}_y$ makes with \mathbf{e}_x in every tangent bundle on the sky. The \mathcal{P} field has been decomposed here on the sky in Fourier space as

$$\mathcal{P}(\mathbf{n}) = \int \mathcal{P}(\mathbf{k})e^{-i\mathbf{k}\cdot\mathbf{n}} d^2\mathbf{k}. \quad (\text{B.25})$$

A parity transformation \hat{P} is a reflexion of the signal around one or several axis of all the local frames in which the Stokes parameters are defined e.g. $\hat{P} : (\mathbf{e}_x, \mathbf{e}_y) \rightarrow (-\mathbf{e}_x, -\mathbf{e}_y)$. Under \hat{P} , the value of E is invariant while B changes sign. By definition E is then a scalar field while B is a *pseudo-scalar* field.

B.4 The polarized signal over the curved sky

B.4.1 The spherical harmonics

While the flat sky approximation can hold on reasonably small patches of the sky, the celestial sphere is better modeled by a unit sphere S^2 . Let $f : S^2 \rightarrow \mathbb{R}$ be a function on the

2-sphere. It can be decomposed on the orthonormal basis of the spherical harmonics $Y_{\ell m}$ as

$$f(\mathbf{n}) = \sum_{\ell=1}^{\infty} \sum_{m=-\ell}^{\ell} a_{\ell m}^f Y_{\ell m}(\mathbf{n}), \quad (\text{B.26})$$

with $a_{\ell m}^f \in \mathbb{C}$ and $Y_{\ell m} : S^2 \rightarrow \mathbb{C}$. Points on S^2 are now labelled locally in a chart by $\mathbf{n} = (\theta, \varphi)$. The spherical harmonics functions are defined as

$$Y_{\ell m}(\theta, \varphi) = \sqrt{\frac{2\ell+1}{4\pi} \frac{(\ell-m)!}{(\ell+m)!}} P_{\ell m}(\cos \theta) e^{-im\varphi}, \quad (\text{B.27})$$

where the $P_{\ell m}$ are the Legendre polynomials. As the plane waves in flat space, the spherical harmonics thus provide a (orthonormal) functional basis to Fourier decompose any function on the sphere. Also as the plane waves are eigenvectors of the derivative function and hence of the linear momentum in quantum mechanics, the $Y_{\ell m}$ are joint eigenvectors of the angular momentum operator J_z (generator of rotations around z), and the Casimir operator J^2 of $\text{SO}(3)$. ℓ is called the multipole, associated to the inverse of an angular scale (as \mathbf{k} for plane waves). $\ell = 0$ is the monopole and covers the whole sphere, $\ell = 1$ are dipoles that cut the sphere in half, $\ell = 2$ are quadrupoles . . . $\ell = 100$ describe features of $\simeq 1^\circ$ squared on the celestial sphere (approximately the size of the full moon). The m label describes the possible orientations on the sphere of a given multipole. For every ℓ , m can take entire values from $-\ell$ to ℓ . Counting $m = 0$, there is then $2\ell + 1$ modes m for a given ℓ . By integrating by parts, one can get the *spherical harmonic coefficients* $a_{\ell m}^f$ associated with f as

$$a_{\ell m}^f = \int f(\mathbf{n}) Y_{\ell m}(\mathbf{n})^* d\mathbf{n}. \quad (\text{B.28})$$

A Gaussian random field will have a Gaussian distribution for its $a_{\ell m}^f$.

B.4.2 *E*- and *B*-modes on curved sky

Generalizing the tools derived to describe the polarized signal on flat sky on a curved sky is straightforward. One must operate the following replacements:

- The flat metric $\delta = \text{diag}(1, 1)$ is replaced by the metric on the unit sphere $g = \text{diag}(1, \sin^2(\theta))$ and the local coordinates in which it is expressed from Cartesian $\mathbf{n} = (x, y)$ to spherical coordinates chart $\mathbf{n} = (\theta, \varphi)$.
- The partial derivatives ∂ are replaced by covariant derivatives $\nabla = \partial + \Gamma$ associated to the Levi-Civita connection $\Gamma^i_{jk} = \frac{1}{2} g^{im} (\partial_k g_{mj} + \partial_j g_{mk} - \partial_m g_{jk})$ on the sphere. The only non vanishing components being $\Gamma^\theta_{\varphi\varphi} = \cos(\theta) \sin(\theta)$, $\Gamma^\varphi_{\theta\varphi} = \Gamma^\varphi_{\varphi\theta} = -\tan(\theta)$.
- The basis in which to decompose every function on the sky must be replaced from the plane waves of wavevector \mathbf{k} to the spherical harmonics coefficients of multipoles ℓ and modes m .

For detailed pedagogical derivations, we refer to [Hu & White \(1997\)](#) and [Kamionkowski et al. \(1997\)](#). Still asking for the tracelessness of Π

$$\Pi^a_a = g^{ab} \Pi_{ab} = 0 \quad (\text{B.29})$$

and symmetry under permutation $\Pi_{ab} = \Pi_{ba}$. These conditions for Π in a chart impose that

$$\Pi(\mathbf{n}) = \frac{1}{\sqrt{2}} \begin{pmatrix} Q(\mathbf{n}) & U(\mathbf{n}) \sin(\theta) \\ U(\mathbf{n}) \sin(\theta) & -Q(\mathbf{n}) \sin^2(\theta) \end{pmatrix}. \quad (\text{B.30})$$

One can then expand Π on the following spherical harmonic basis

$$\Pi_{ab}(\mathbf{n}) = \sum_{\ell=2}^{\infty} \sum_{m=-\ell}^{\ell} \left(a_{(\ell m)}^E Y_{(\ell m)ab}^E(\mathbf{n}) + a_{(\ell m)}^B Y_{(\ell m)ab}^B(\mathbf{n}) \right). \quad (\text{B.31})$$

Where, following from Eq.B.21b, the E and B tensor generalization of spherical harmonics are

$$Y_{(\ell m)ab}^E = \sqrt{2} N_\ell \left(\nabla_a \nabla_b Y_{\ell m} - \frac{1}{2} g_{ab} \nabla_c \nabla^c Y_{\ell m} \right), \quad (\text{B.32a})$$

$$Y_{(\ell m)ab}^B = \frac{N_\ell}{\sqrt{2}} (\epsilon_b^c \nabla_a \nabla_c Y_{\ell m} - \epsilon_a^c \nabla_b \nabla_c Y_{\ell m}). \quad (\text{B.32b})$$

They thus form a complete orthogonal basis on which to decompose any STF tensor field of rank 2. N_ℓ is a normalization coefficient defined as

$$N_\ell = \sqrt{\frac{(\ell-2)!}{(\ell+2)!}}. \quad (\text{B.33})$$

From this expansion, one can calculate the coefficients $a_{\ell m}^{E/B}$ by integrating by parts

$$a_{\ell m}^E = \sqrt{2} N_\ell \int \nabla^a \nabla^b \Pi_{ab} Y_{\ell m}^*(\mathbf{n}) d\mathbf{n}, \quad (\text{B.34a})$$

$$a_{\ell m}^B = \sqrt{2} N_\ell \int \epsilon_c^b \nabla^a \nabla^c \Pi_{ab} Y_{\ell m}^*(\mathbf{n}) d\mathbf{n}. \quad (\text{B.34b})$$

The E - and B -modes are recovered as the scalar fields that can be built from these new set of harmonic coefficients

$$E(\mathbf{n}) = \sum_{\ell=2}^{\infty} \sum_{m=-\ell}^{\ell} a_{\ell m}^E Y_{\ell m}(\mathbf{n}), \quad (\text{B.35a})$$

$$B(\mathbf{n}) = \sum_{\ell=2}^{\infty} \sum_{m=-\ell}^{\ell} a_{\ell m}^B Y_{\ell m}(\mathbf{n}). \quad (\text{B.35b})$$

It can further be shown that, due to the parity properties of the E - and B -modes, under the transformation \hat{P} , $a_{\ell m}^E \rightarrow (-1)^\ell a_{\ell m}^E$ while $a_{\ell m}^B \rightarrow (-1)^{\ell+1} a_{\ell m}^B$.

B.5 E- and B- modes from ladder operators

Another approach to get scalar fields from a spin-2 field is to use spin lowering operators \eth (Goldberg et al., 1967; Newman & Penrose, 1966). Let ψ be a field of spin s that is an object transforming as

$$\psi' = e^{-is\theta} \psi, \quad (\text{B.36})$$

under a tangent bundle frame rotation by an angle θ . As such, for \mathcal{P} , $s = 2$ and for \mathcal{P}^* , $s = -2$. The spin raising operator \eth transforms a field ψ of spin s to a field $\eth\psi$ of spin $s + 1$. Similarly, one can define the complementary spin lowering operator $\bar{\eth} = \eth^*$ transforming a spin s field to a spin $s - 1$ field. That is

$$(\eth\psi)' = e^{-i(s+1)\theta}(\eth\psi), \quad (\text{B.37a})$$

$$(\bar{\eth}\psi)' = e^{-i(s-1)\theta}(\bar{\eth}\psi), \quad (\text{B.37b})$$

where ' denotes the frame rotated field. These operators share numerous similarities with the ladder operators for the angular momentum in quantum mechanics $J_{\pm} := J_x \pm iJ_y$ allowing to go from an eigenstate of the diagonal operator J_z to another i.e. $|\ell, m\rangle$ to $|\ell, m \pm 1\rangle$. Here however, the eigenvalue that is raised is the spin, associated to the representation of the rotation group. As such \eth provides a powerful tool to study the representations of the Lorentz group (Held et al., 1970). In close similarity to the momentum ladder operator, on a flat sky, we can express $\eth = \partial_x - i\partial_y$ and $\bar{\eth} = \partial_x + i\partial_y$. This expression can be generalized to the spherical coordinates on the curved sphere θ, φ as

$$\eth\psi = -(\sin\theta)^s [\partial_\theta + i\sin(\theta)^{-1}\partial_\varphi] \{(\sin(\theta))^{-s}\psi\}, \quad (\text{B.38a})$$

$$\bar{\eth}\psi = -(\sin\theta)^s [\partial_\theta - i\sin(\theta)^{-1}\partial_\varphi] \{(\sin(\theta))^{-s}\psi\}. \quad (\text{B.38b})$$

We can thus immediately define the spin weighted spherical harmonics as

$$Y_{\ell m}^s(\mathbf{n}) := \sqrt{\frac{(\ell-s)!}{(\ell+s)!}} \eth^s Y_{\ell m}(\mathbf{n}) \quad 0 \leq s \leq \ell, \quad (\text{B.39a})$$

$$:= \sqrt{\frac{(\ell+s)!}{(\ell-s)!}} \bar{\eth}^{-s} Y_{\ell m}(\mathbf{n}) \quad -\ell \leq s \leq 0. \quad (\text{B.39b})$$

These new spin weighted spherical harmonics also form an orthonormal basis on which to expand any spin s field on the sphere. Note that they are not defined for $\ell < |s|$. We can now then expand the polarization spin 2 and spin -2 fields \mathcal{P} and \mathcal{P}^* as

$$\mathcal{P}(\mathbf{n}) = \sum_{\ell=2}^{\infty} \sum_{m=-\ell}^{\ell} a_{\ell m}^{\mathcal{P}} Y_{\ell m}^2(\mathbf{n}), \quad (\text{B.40a})$$

$$\mathcal{P}(\mathbf{n})^* = \sum_{\ell=2}^{\infty} \sum_{m=-\ell}^{\ell} a_{\ell m}^{\mathcal{P}^*} Y_{\ell m}^{-2}(\mathbf{n}). \quad (\text{B.40b})$$

The spin ladder operators share identical normalization properties when acting on the spin weighted spherical harmonics than the quantum mechanics latter operators on the eigenvectors of the angular momentum

$$\eth Y_{\ell m}^s(\mathbf{n}) = \sqrt{(\ell-s)(\ell+s+1)} Y_{\ell m}^{s+1}(\mathbf{n}), \quad (\text{B.41a})$$

$$\bar{\eth} Y_{\ell m}^s(\mathbf{n}) = -\sqrt{(\ell+s)(\ell-s+1)} Y_{\ell m}^{s-1}(\mathbf{n}). \quad (\text{B.41b})$$

One can then define the scalar fields \mathfrak{E} and \mathfrak{B} fields from the spin-2 linear polarization field by lowering two time its spin as

$$\mathfrak{E}(\mathbf{n}) + i\mathfrak{B}(\mathbf{n}) := -\bar{\eth}^2 \mathcal{P}(\mathbf{n}), \quad (\text{B.42})$$

that is

$$\mathfrak{E}(\mathbf{n}) = -\text{Re}(\bar{\eth}^2 \mathcal{P}) = -\frac{1}{2} \left[\bar{\eth}^2 \mathcal{P}(\mathbf{n}) + \eth^2 \mathcal{P}(\mathbf{n})^* \right], \quad (\text{B.43a})$$

$$\mathfrak{B}(\mathbf{n}) = -\text{Im}(\bar{\eth}^2 \mathcal{P}) = -\frac{1}{2i} \left[\bar{\eth}^2 \mathcal{P}(\mathbf{n}) - \eth^2 \mathcal{P}(\mathbf{n})^* \right]. \quad (\text{B.43b})$$

For a pedagogical introduction see e.g. (Rotti & Huffenberger, 2019). Knowing the action of $\bar{\eth}$ on the spin weighted harmonics given in Eq.B.41, we can connect the spherical harmonic expansion of \mathfrak{E} and \mathfrak{B} with the one of \mathcal{P} as

$$\mathfrak{E}(\mathbf{n}) = \sum_{\ell=2}^{\infty} \sum_{m=-\ell}^{\ell} \frac{-1}{2N_{\ell}} \left[a_{\ell m}^{\mathcal{P}} + a_{\ell m}^{\mathcal{P}*} \right] Y_{\ell m}(\mathbf{n}), \quad (\text{B.43ca})$$

$$\mathfrak{B}(\mathbf{n}) = \sum_{\ell=2}^{\infty} \sum_{m=-\ell}^{\ell} \frac{-1}{2iN_{\ell}} \left[a_{\ell m}^{\mathcal{P}} - a_{\ell m}^{\mathcal{P}*} \right] Y_{\ell m}(\mathbf{n}). \quad (\text{B.43cb})$$

The direct connection with the previously defined E - and B -modes can be made by the identification

$$a_{\ell m}^E = -\frac{1}{2} \left[a_{\ell m}^{\mathcal{P}} + a_{\ell m}^{\mathcal{P}*} \right] = N_{\ell} a_{\ell m}^{\mathfrak{E}}, \quad (\text{B.43da})$$

$$a_{\ell m}^B = -\frac{1}{2i} \left[a_{\ell m}^{\mathcal{P}} - a_{\ell m}^{\mathcal{P}*} \right] = N_{\ell} a_{\ell m}^{\mathfrak{B}}. \quad (\text{B.43db})$$

\mathfrak{E} and \mathfrak{B} have the same geometrical interpretations as E and B , their harmonic power being simply rescaled by the normalization factor N_{ℓ} .

B.6 The Power spectra

We define the *power-spectra* $\mathcal{C}_{\ell}^{f \times g}$ between two fields f and g on the sphere as

$$\mathcal{C}_{\ell}^{f \times g} = \left\langle a_{\ell m}^f (a_{\ell m}^g)^* \right\rangle. \quad (\text{B.5})$$

$\mathcal{C}_{\ell}^{f \times f}$ is called the auto-spectra of f while for $f \neq g$ we talk about *cross-spectra*. Eq. B.5 defines some kind of Hermitian metric product between the harmonic coefficient, such that $\mathcal{C}_{\ell}^{f \times g} = (\mathcal{C}_{\ell}^{g \times f})^*$. As such, $\mathcal{C}_{\ell}^{f \times g}$ and $\mathcal{C}_{\ell}^{g \times f}$ contains identical informations and only one of the pair is considered when analysing a signal. In cosmology, it is often more useful to consider the rescaled quantity

$$\mathcal{D}_{\ell}^{f \times g} := \frac{\ell(\ell+1)}{2\pi} \mathcal{C}_{\ell}^{f \times g}. \quad (\text{B.6})$$

These two quantities are the equivalent on the sphere to the quantities defined respectively by $\mathcal{P}(\mathbf{k})$ and Δ^2 introduced in Chap. 3 for a 3D flat space. It is actually possible to relate both, in order to compute the statistics of the projection on a sphere of a 3D distribution, which is a very common procedure in cosmology.

From E - and B -modes spherical harmonic coefficients, it is hence possible to compute the three polarization power spectra \mathcal{D}_{ℓ}^{EE} , \mathcal{D}_{ℓ}^{EB} , and \mathcal{D}_{ℓ}^{BB} , respectively called EE , EB , and

BB^{10} . Under a parity transformation \hat{P} , the full EE and BB spectra remain unchanged for every ℓ , as they will get a factor of $(-1)^{2\ell} = 1$ and $(-1)^{2\ell+2} = 1$ respectively. The EB spectrum however, will get a factor of $(-1)^{2\ell+1} = -1$ and will change sign under the transformation \hat{P} . As such, a signal which has no preferred handedness/orientation will have $EB = \hat{P}EB \rightarrow EB = -EB$ and so $EB = 0$.

As for the power spectra on flat space, the $\mathcal{C}_\ell^{f \times f}$ allow to grasp all the statistical properties of a Gaussian random field on the sphere with the additional consideration that the field must be isotropic and hence has no preferred orientation (m). As such, averaging over m does not degrade the information. It can be shown that the $a_{\ell m}$ coefficient of a Gaussian field will themselves follow a Gaussian distribution, such that for centered Gaussian fields (as the CMB perturbations), the angular power spectra correspond to the variance¹¹ of the $a_{\ell m}$ and contain all the statistical informations of the field:

$$\left\langle a_{\ell m}^f \right\rangle = 0 \quad (\text{B.7})$$

$$\left\langle a_{\ell m}^f (a_{\ell m}^f)^* \right\rangle = \mathcal{C}_\ell^{f \times g} \quad (\text{B.8})$$

$$(\text{B.9})$$

As there is only one realisation of the astrophysical sky, the stochastic/statistical mean $\langle \dots \rangle$ of the spherical harmonics coefficients can not be computed in practice as there exists only one observable set of $a_{\ell m}^f$ coefficients. At a given scale (ℓ), all the available statistics is then contained within the $2\ell + 1$ possible orientations (m). From data, one thus can build the unbiased¹² estimator of the angular power-spectra given by

$$\hat{\mathcal{C}}_\ell^{f \times g} := \langle (a_{\ell m}^f)^* \cdot a_{\ell m}^g \rangle_m = \frac{1}{2\ell + 1} \sum_{m=-\ell}^{\ell} (a_{\ell m}^f)^* \cdot a_{\ell m}^g. \quad (\text{B.10})$$

in which the statistics are derived by averaging over all the orientations (m).

Also due to the single realisation of the sky, the power spectra are associated with an intrinsic variance that can not be reduced, called the cosmic variance. In practice one look only at a given sky fraction f_{sky} and average over bins of multipoles of size $\Delta\ell$ (process called *binning*), impacting the uncertainty of the cosmic variance, which now becomes called the *sample variance*. In this context, the sample variance $(\sigma_\ell^{\text{var}})^2$ associated to a power spectrum $\mathcal{C}_\ell^{f \times g}$ can be expressed as

$$(\sigma_\ell^{\text{var}})^2 (\mathcal{C}_\ell^{f \times g}) = \frac{2}{\Delta\ell f_{\text{sky}} (2\ell + 1)} (\mathcal{C}_\ell^{f \times g})^2. \quad (\text{B.11})$$

Logically, one will find that $(\sigma_\ell^{\text{var}})^2$ will be larger at low ℓ , and hence at larger scales, as less statistical sets can be built from larger sky patches. The cosmic variance is obtained by taking $f_{\text{sky}} = \Delta\ell = 1$ in the above expression.

¹⁰and $BE = (EB)^*$.

¹¹Recalling that $\text{Var}(x) = \sigma^2(x) = \langle x^2 \rangle - (\langle x \rangle)^2$.

¹²Instrumental noise, systematic effects and foregrounds will however bias this estimator.

Appendix C

Quantifying the asymmetry of the scanning strategy: first attempts

Strategy without tactics is the slowest route to victory. Tactics without strategy is the noise before defeat.

– Sun Tzu

Contents

C.1	Kolmogorov-Smirnov (KS) test	221
C.2	Hit-matrix	224
C.3	Beam smoothing power	225

In order to optimize the scanning strategy of the *LiteBIRD* mission (Chap. 7), I investigated several quantifiers of the homogeneity of the ψ -distribution before deciding on the cross-links (Eq. 7.2). Some of them will be briefly introduced in what follows, as well as the conclusion they allow to reach on the properties of the standard *LiteBIRD* scanning strategy.

C.1 Kolmogorov-Smirnov (KS) test

In a given pixel (associated to a resolution n_{side} of the map), one can build the histogram of the ψ -distribution for a given duration of the scanning (unless specified, the choice used for the figures in this section is 1 year). From this histogram, the KS test quantifying the homogeneity of the scanning strategy presents itself as illustrated on Fig. C.1. Ordering the values of ψ obtained during the scanning by increasing values (in radian), one obtains the blue curve. If the scanning is perfectly homogeneous, this curve should follow a straight line joining 0 and 2π , translating the fact that each value of ψ has been "encountered" in the pixel during the mission duration. We note Δ_ψ (in radian) the largest deviation between the blue curve and the black dashed one. The larger Δ_ψ , the less homogeneous the scanning strategy is. However, contrarily to the cross-links, Δ_ψ do not account for the fact that some angles can "compensate" one another. However, as I will illustrate through various examples, Δ_ψ is a powerful tool to infer some properties of the scanning strategy.

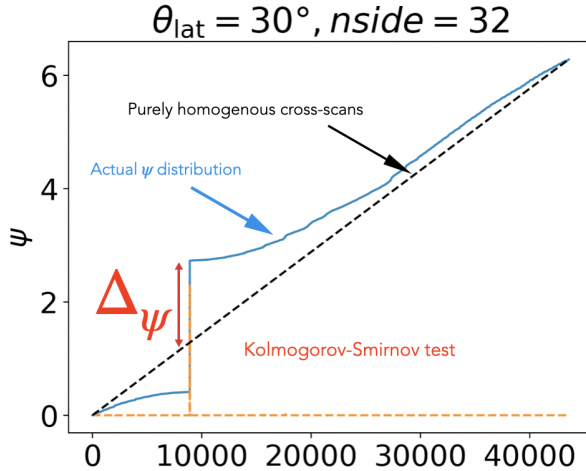


Figure C.1: Illustration of the KS test principle. y -axis: values of ψ in the pixel, x -axis: arbitrary labelling of the value of the hits. The crossing angles ψ are all expressed in radians.

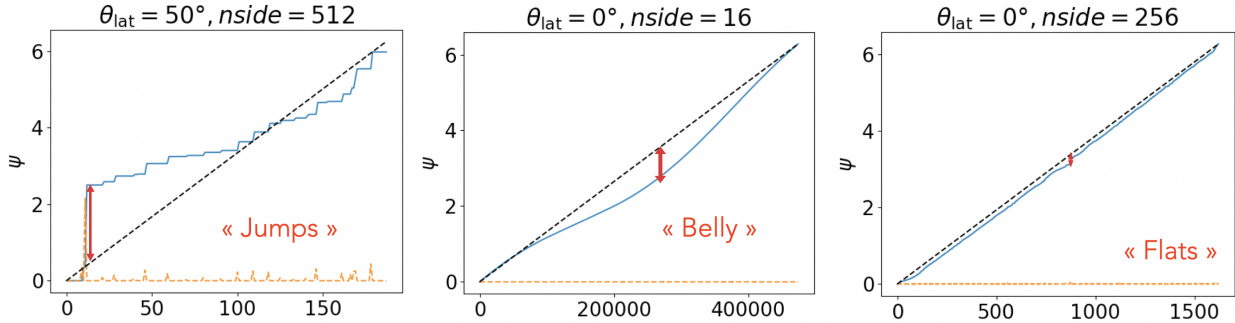
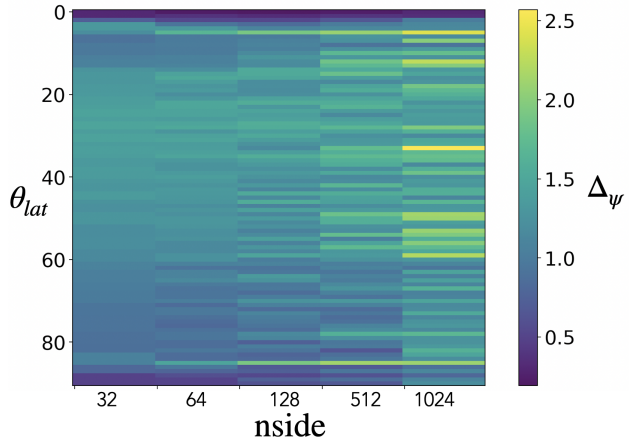
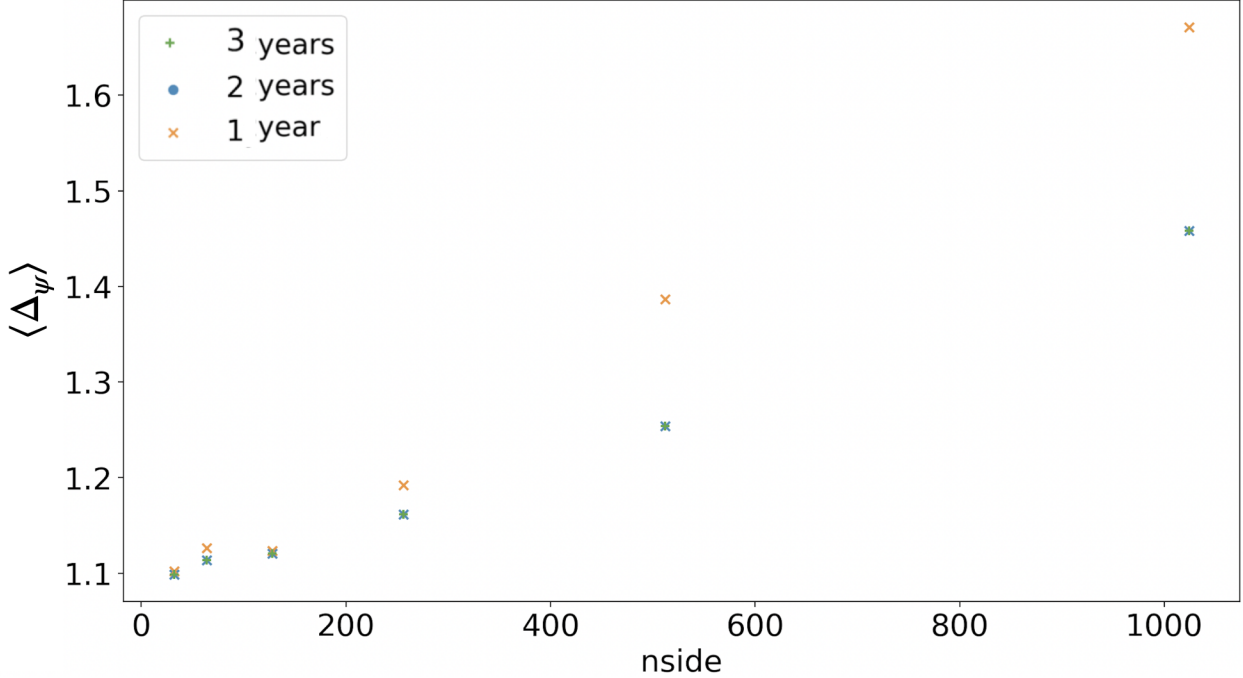


Figure C.2: Examples of ψ -distributions sensitive to the KS tests.

As I illustrated on Fig. C.2, several ψ -distributions can explain a large value of Δ_ψ . A "jump" can be present, translating the fact that a whole range of the ψ values is not explored (e.g. the bottom panel of Fig. 7.8). A "belly" can be seen, illustrating that some range in the values of ψ is less populated than others. A small Δ_ψ will mean that the distribution is "flat", sticking closely to the homogeneous distribution.

As I further illustrated on Fig. C.3, Δ_ψ can be used to quantify simply the impact of some parameters as the ecliptic latitude θ_{lat} , and the map resolution n_{side} . As expected and in agreement with other quantifiers (see Chap. 7), the scanning is more homogeneous near the ecliptic poles ($\theta_{\text{lat}} = 0^\circ$) and equator ($\theta_{\text{lat}} = 90^\circ$), which are more regularly visited through different angles (see Fig. 7.6). The parameter n_{side} can be understood as the inverse size of the pixel (the larger n_{side} , the smaller the pixel). $n_{\text{side}} = 32$ is associated to a pixel size of 109.9 arcminutes, while $n_{\text{side}} = 1024$ has a resolution of 3.43 arcminutes. The smaller the pixel, the less the scanning is homogeneous because the smaller is the probability for the scanning strategy to visit it. This will however not be problematic for *LiteBIRD* which targets the largest scales of the sky (the smallest beam FWHM in Tab. 7.1 being of 17.9 arcminutes, corresponding to $128 < n_{\text{side}} < 254$).

On Fig. C.4 I computed Δ_ψ for different values of the mission duration. The scanning is getting more homogeneous at every scale if the mission last two years instead of one. We


 Figure C.3: Values of Δ_ψ for different values of the ecliptic latitude θ_{lat} , and the map resolution n_{side} .

 Figure C.4: Mean value of Δ_ψ over all the pixels of the maps for different values of n_{side} and different values of the mission duration: 1 year (orange) and 2 years (blue).

can hence conclude that the scanning strategy is not synchronous with solar revolution i.e. it does not repeat itself identically every year. However, for three years, the results overlap with two years, symptomatic that the smoothing power reached its plateau. I computed all the above results for a detector located at the center of the MHFT boresight. However as displayed on Fig. C.5, it can be instructive to investigate how these results change for other detectors located differently on the focal planes. While the trends are similar from one detector to another, the results can change drastically, highlighting than optimizing the scanning strategy for one detector does not necessarily optimize it for the whole instrument.

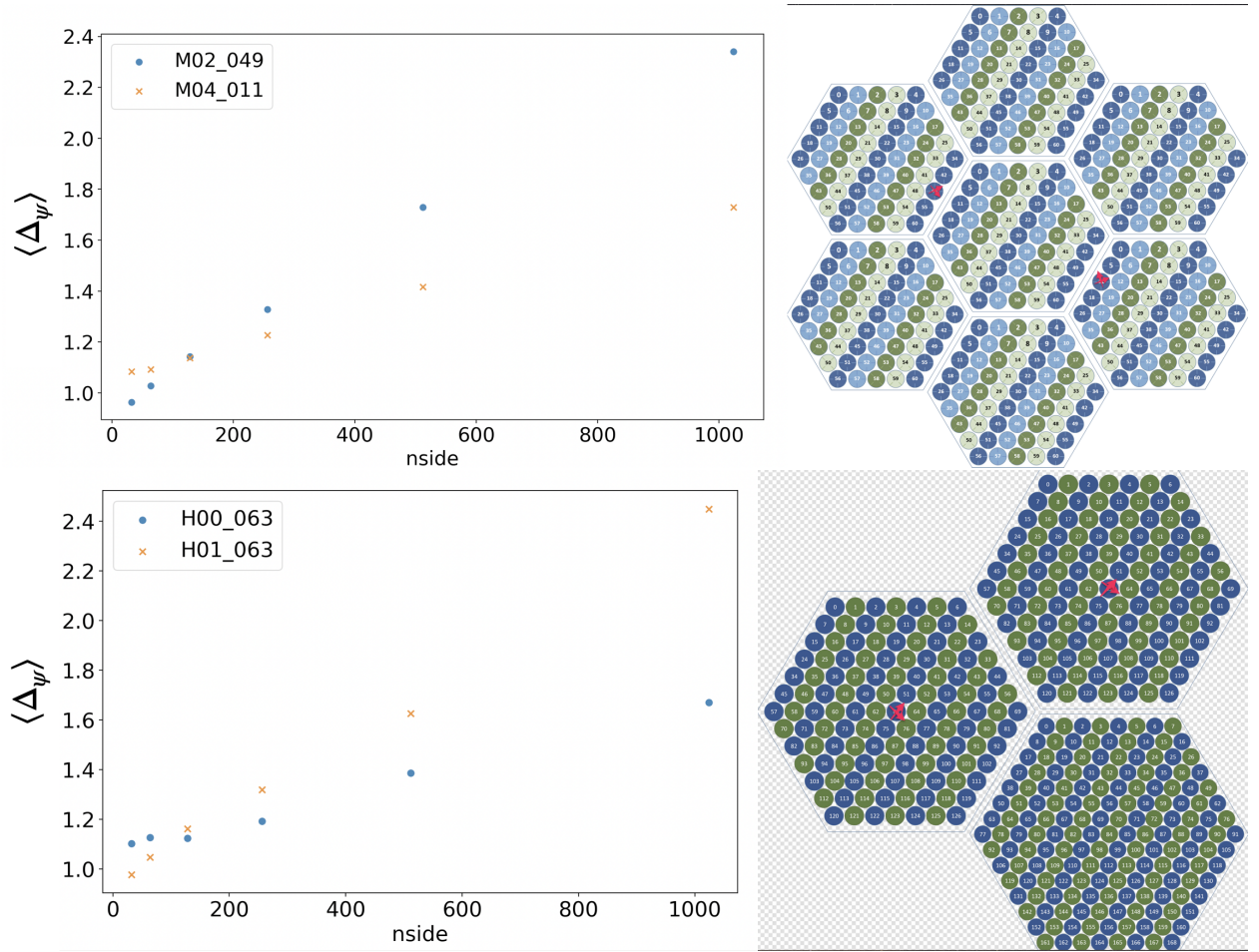


Figure C.5: KS test results for different detectors marked by red crosses for the MFT (top) and HFT (bottom).

C.2 Hit-matrix

An similar (and related) observable to the cross-link is given by the hit-matrix ([McCallum et al., 2022](#))

$$M = \begin{pmatrix} 1 & \langle \cos(2\psi_j) \rangle & \langle \sin(2\psi_j) \rangle \\ \langle \cos(2\psi_j) \rangle & \langle \cos^2(2\psi_j) \rangle & \langle \cos(2\psi_j) \sin(2\psi_j) \rangle \\ \langle \sin(2\psi_j) \rangle & \langle \sin(2\psi_j) \cos(2\psi_j) \rangle & \langle \sin^2(2\psi_j) \rangle \end{pmatrix}, \quad (\text{C.1})$$

where $\langle . \rangle$ is the average over the hits in a pixel. M plays a crucial role for map-making – i.e. building a final map of the sky’s signal (I, Q, U) from the detector’s signal d – as it appears in the equation

$$\begin{pmatrix} I \\ Q \\ U \end{pmatrix} = M^{-1} \begin{pmatrix} \langle d_j \rangle \\ \langle d_j \cos(2\psi_j) \rangle \\ \langle d_j \sin(2\psi_j) \rangle \end{pmatrix}, \quad (\text{C.2})$$

in which it must be inverted. In the case of a perfectly homogeneous scanning strategy:

$$M = \begin{pmatrix} 1 & 0 & 0 \\ 0 & \frac{1}{2} & 0 \\ 0 & 0 & \frac{1}{2} \end{pmatrix}, \quad (\text{C.3})$$

C.3. BEAM SMOOTHING POWER

such that $\det(M) = 0.25$ and $\text{cond}(M) = 2$. One can then look at departures from these values as indicators of the inhomogeneity of the scanning strategy. In Fig. C.6, I computed

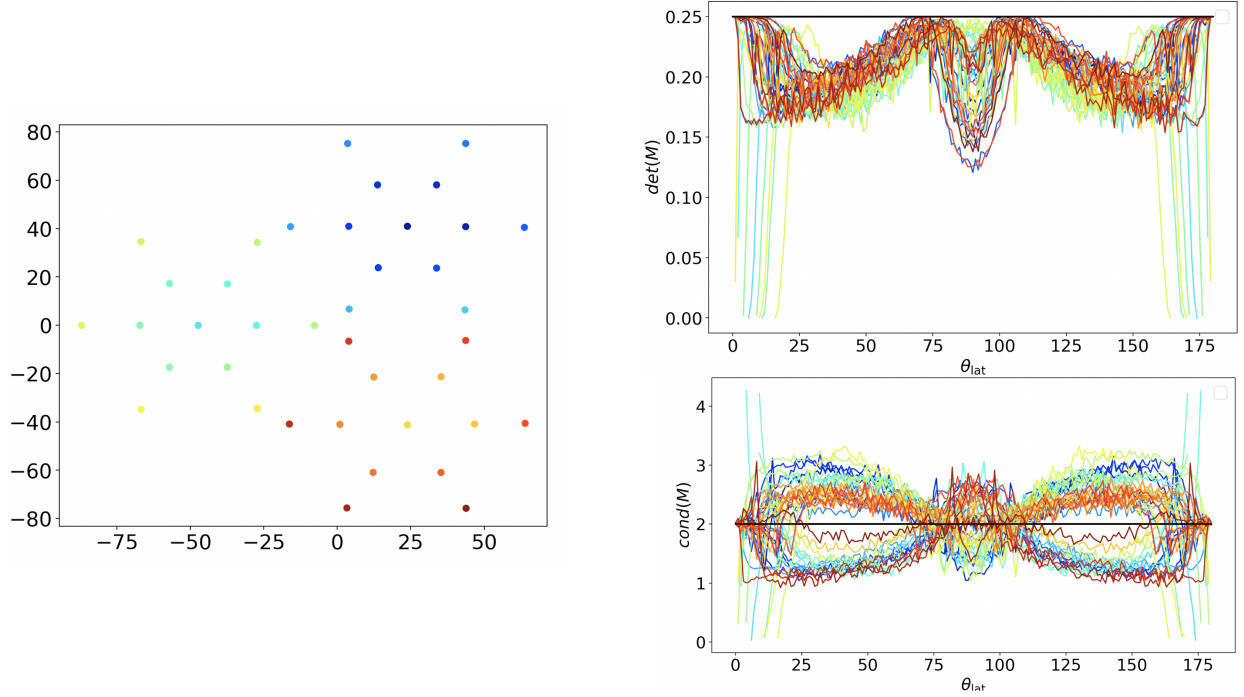


Figure C.6: Values of $\text{cond}(M)$ and $\det(M)$ as a function of θ_{lat} for multiple detectors of the HFT.

the dependence of these values in θ_{lat} for different detectors covering the HFT focal-plane. This result confirm what we already saw with Δ_ψ : the scanning strategy is more homogeneous at the equator and at the poles (and is symmetric over the two hemispheres). This figure was among the first which made me realize that some detectors could not reach the poles (the green/yellow ones), for which the values of $\det(M)$ go toward 0 for $\theta_{\text{lat}} < 150^\circ$ and $\theta_{\text{lat}} > 25^\circ$.

C.3 Beam smoothing power

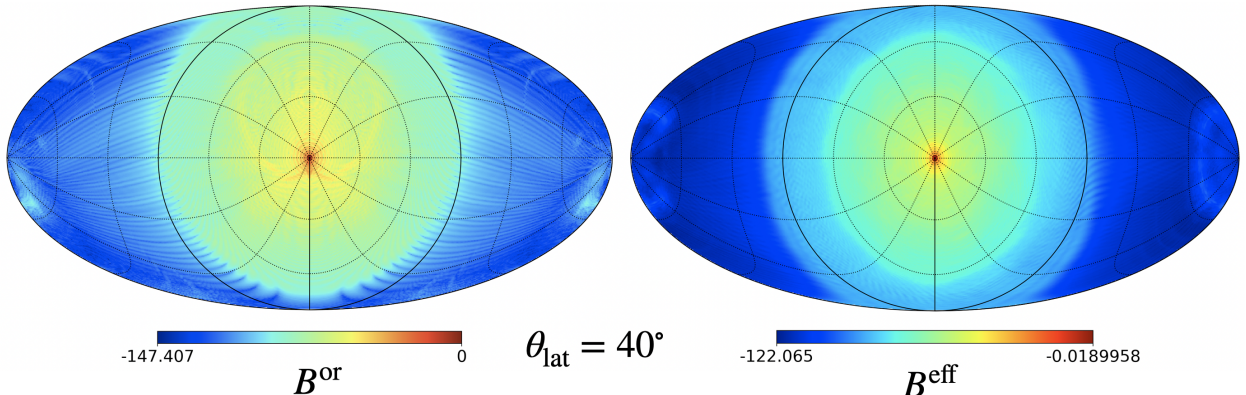


Figure C.7: B^{or} and B^{eff} for *LiteBIRD* GRASP beam over the whole sphere.

As we discussed already in Chap. 7, the homogeneity of the scanning strategy plays a crucial role in order to suppress the asymmetry of the instrumental beams. In Fig. C.7, I computed the original and effective beams associated to a *LiteBIRD* GRASP beam on the whole sphere (4π). While some spurious features from B^{or} remain in B^{eff} , we see that numerous small scales features, presenting themselves as "filamentary" patterns, have been suppressed. From these results, I wanted to further quantify this symmetrizing power of the scanning strategy on the beams, in order to evaluate the potential impact of residual asymmetry. Most of all, I wanted to assess if the large scales asymmetries (of the far side lobes) were sufficiently damped, as they could induce significant bias on the measurement of the tensor-to-scalar ratio r .

My idea was to compute the values of the spherical harmonic coefficients $a_{\ell m}$ for the original and the effective beams such that they can be compared. To do so, I introduced the so called smoothing power Σ_ℓ which quantifies how much the spurious features of a beam at a given scale ℓ are smoothed by the scanning strategy.

$$\Sigma_\ell = \left\langle \frac{|a_{\ell m}^{\text{or}}|}{|a_{\ell m}^{\text{eff}}|} \right\rangle_m , \quad (\text{C.4})$$

where $|.|$ is the complex modulus and $\langle . \rangle_m$ is the average over m . The larger is Σ_ℓ , the more the B^{eff} is smoothed compared to B^{or} at a given angular scale ℓ .

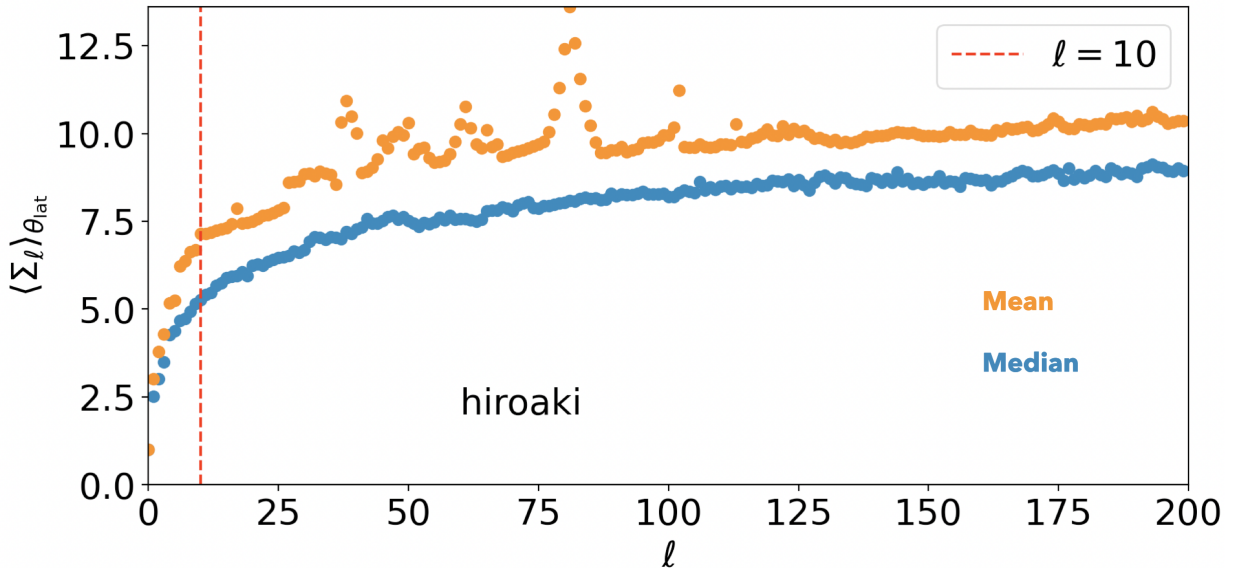


Figure C.8: Mean (orange) and median (blue) values of Σ_ℓ over all the values of θ_{lat} .

On Fig. C.8, I computed this quantity in a pixel associated to each ecliptic latitude from which I derived a median and a mean spectrum. One can see that the largest scales $\ell < 10$ have a smaller value of Σ_ℓ and are hence less symmetrized by the scanning strategy. This point could be critical, as large asymmetries of the far side lobes could remain preserved in the effective beam and induce spurious measurement of tensor-to-scalar ratio. At larger scales $\ell \sim 50$, the spectrum reaches a plateau in which all scales seem to be symmetrized identically. I witnessed similar patterns for the Σ_ℓ function using different types of instrumental and

C.3. BEAM SMOOTHING POWER

artificial beams. Further studies need to be done in order to precisely quantify this impact and find how to mitigate it if necessary.

List of Figures

3.1	Two-dimensional illustration of a comoving frame (black grid) stretching with the comoving time t , as a consequence of the expansion. The scale factor $a(t)$ quantifies the amplitude of this stretch. Picture taken from Errard (2012).	23
3.2	Left: evolution of $a(t - t_0)$ in Λ -CDM, with the values given in Tab. 3.1 for the densities Ω_i . Codes can be found on this page . Right: Schematic representation of the cosmic history, green: radiation domination, yellow: matter domination, orange: Λ domination. Taken from Cicoli et al. (2023).	32
4.1	Constraints on various inflation models in the $(n_s - r)$ plane using various combination of <i>Planck</i> , BAO and BICEP-Keck (BK) data. Taken from Planck Collaboration et al. (2020b)	47
5.1	Illustration of the formation of the last scattering surface. Taken from Yacine Ali-Haïmoud.	52
5.2	Left: spectral energy distribution of the CMB radiation, in perfect agreement with a black-body spectrum. The error bars are multiplied by 400 to be visible. From Fixsen & Mather (2002). Right: CMB temperature anisotropies over a small patch of the sky distributed as a Gaussian random field. From (Planck Collaboration et al., 2020c).	54
5.3	Mollweide projection of the CMB anisotropies in intensity (top) and polarization (bottom) as measured by the <i>Planck</i> satellite. The values are expressed in μK_{CMB} . The bottom map has been filtered to keep only the largest scales. Taken from Planck Collaboration et al. (2020c)	55
5.4	Illustration of the Thomson scattering of a photon beam in a direction θ by a motionless electron e^- . Adapted from Melchiorri & Vittorio (1997).	57
5.5	Generation of significant linear polarization in the perpendicular directions from Thomson scattering.	58
5.6	Comparaison between monopole, dipole and quadrupole anisotropies in order to generate linear polarization.	59
5.7	Illustration of E -modes and B -modes fields on a flat sky patch (Kamionkowski & Kovetz, 2016).	60
5.8	Generation of quadrupolar anisotropies from over or under densities in the primordial plasma. From Mousset (2021).	61
5.9	Generation of quadrupolar anisotropies (and hence linear polarization) from the propagation of a gravitational wave. From Mousset (2021).	61
5.10	Comparaison of the CMB power spectra TT , EE , BB , TE and $\Phi\Phi$ (here noted $C_\ell^{\phi\phi}$) as measured by different experiments (colored points) and the best-fit prediction from the Λ -CDM model (dashed line). From Planck Collaboration et al. (2020c).	63

LIST OF FIGURES

5.11	Angular power spectra of the dominant contributions from the various temperature anisotropy sources to \mathcal{D}_ℓ^{TT} : total (black), adiabatic and Sachs-Wolf (pink), Doppler (blue) and ISW (green) . Adapted from Ma (2011).	65
5.12	Sensitivity improvement between COBE, WMAP and Planck (Gold et al., 2011; Planck Collaboration et al., 2020a).	70
5.13	Contours on the Λ -CDM model parameter posteriors obtained using the Planck 2018 TT-TE-EE likelihood (red) and adding the Planck lensing data and BAO data from Beutler et al. (2011); Ross et al. (2015); Alam et al. (2017)) (blue).	73
6.1	Left: Illustration of the component separation problem. Credit: ESA, Planck, Canopée. Right: Magnetic field lines traced by dust polarized emission at 353 GHz by the Planck mission. Credit: ESA,Planck.	75
6.2	Estimated SED for different Galactic foregrounds components from the Planck data (Planck Collaboration et al., 2020c). Left: Intensity I_ν Right: Estimated $ \mathcal{P}_\nu = \sqrt{Q^2 + U^2}$. The vertical gray bands represent the Planck frequency channels. The thickness of the curves represent the difference of amplitude between two different fractions from $f_{\text{sky}} = 0.81$ and $f_{\text{sky}} = 0.93$ for intensity and $f_{\text{sky}} = 0.73$ to $f_{\text{sky}} = 0.93$ for polarization.	77
6.3	Intensity map of the full sky at 408 MHz. Taken from Dickinson (2018) and built from data of Remazeilles et al. (2015); Haslam et al. (1981). The observed signal is mostly due to synchrotron and free-free radiations.	79
6.4	Left: Illustration of the synchrotron polarized emission by an accelerated charge. From Emma Alexander. Right: 3D representation of the model of the GMF (\mathbf{B}_0) proposed by Jansson & Farrar (2012) in Farrar et al. (2015).	82
6.5	β_s estimated on 50% of the sky from the S-PASS mission data (Krachmalnicoff et al., 2018).	83
6.6	3D representation of a dust grain which momentum is aligned with the GMF \mathbf{B} , and its polarized emission – parallel to the grain big axis – is orthonormal to the GMF projection B_\perp in the (x, y) plane of the sky.	87
6.7	All-sky maps of the parameters of a MBB fit on intensity data from Planck at 353, 545 et 857 GHz and IRAS 100 μm . Taken from (Planck Collaboration, 2014)	89
7.1	Estimation of the measurements of the CMB primordial angular power spectra by LiteBIRD, in comparison with other CMB surveys. From LiteBIRD Collaboration et al. (2023).	96
7.2	Forecasts on the constraining power of LiteBIRD on some inflation models in the (r, n_s) space. Left: no detection, Right: Example of a detection of $r = .6 \times 10^{-3}$, taking R^2 -inflation with $N_* = 51$ as a fiducial model. From LiteBIRD Collaboration et al. (2023).	96
7.3	Left: Overview of the LiteBIRD instrumental design Right: close up view on the PLM. From LiteBIRD Collaboration et al. (2023).	98
7.4	Detector positions on the focal planes (LiteBIRD Collaboration et al., 2023). LFT: red: 40, 60, 78 GHz, orange: 50, 68, 89 GHz, green: 68, 89, 119, blue: 78, 100, 140 GHz. MFT: red: 100, 140, 195 GHz, orange: 119, 166 GHz. HFT: purple: 195, 280 GHz, green: 235, 337 GHz, blue: 402 GHz.	98
7.5	Left: Definition of scanning strategy parameters for the LiteBIRD mission (LiteBIRD Collaboration et al., 2023). Right: Definition of a general scanning strategy located around L2 (Wallis et al., 2017).	100

LIST OF FIGURES

7.6	Left: scanning of the <i>LiteBIRD</i> LFT (blue) and MHFT (yellow) boresights projected on the Mollweide view in ecliptic coordinates, for a duration of 10 hours. Center and Right: mean $\mu(\psi)$ and standard deviation $\sigma(\psi)$ of the crossing-angle ψ , in radian, evaluated in every pixel for a mission duration of 1 year, in ecliptic coordinates.	100
7.7	Left: Instrumental beam B^{or} on the half sphere for a detector at 100 GHz, located on the edge of the MFT. Right: Effective beam B^{eff} computed from B^{or} with the scanning strategy for one year in a pixel associated to the ecliptic latitude $\theta^{\text{lat}} = 40^\circ$	101
7.8	Symmetrization of an elliptic Gaussian beam B^{or} (left) by the scanning strategy of <i>LiteBIRD</i> at two different ecliptic latitudes: B^{eff} at $\theta = 90^\circ$ (up-right) and B^{eff} at $\theta = 30^\circ$ (bottom-right). The grey lines circular histograms associated to each symmetrized beam ("peacock" diagrams) represent the distribution of the crossing angles ψ in each pixel. ζ, a, b are respectively the orientation, semi-major and semi-minor axis of the beams.	103
7.9	Left: Hitmap in ecliptic coordinates of a detector located on the edge of the HFT wafer #1 (235,337 GHz) before optimizing the focal plane orientations. Right: Optimized orientation of the focal planes of the MHFT. Courtesy of Yusuke Takase.	104
7.10	Mean value of the cross-link module squared $\langle h_{n,m} ^2 \rangle$ in the (T_α, α) space for specific values of n and m . The black point represent the standard <i>LiteBIRD</i> configuration. Preliminary results from Takase et al. (2023)	106
7.11	Integrated visible time for the 3 year mission on compact sources in the (T_α, α) space. The black point represent the standard <i>LiteBIRD</i> configuration. Preliminary results from Takase et al. (2023)	107
8.1	Left: sum of two power-law SEDs. Total signal (orange), I_ν^1 (blue dashed) and I_ν^2 (green dashed). Right: sketch of the position of the two regions responsible for I_ν^1 and I_ν^2 along the line of sight.	113
8.2	Modeling the SED distortions of the total signal (orange) with moment expansion at different orders (colored dashed lines: order 1 with pivot correction (blue), order 2 (light blue), order 3 (grey). The higher orders are changing color towards the red and merge gradually with the total signal.	115
8.3	(Left): Median and median absolute deviations of the best fit values of $\bar{\beta}(\ell)$ in d0 (orange), d1T (green), and d1 (blue) for the MBB (circles). For completeness, I also added the correction brought by the other orders: β -1 (crosses), β -2 (triangles), and β -T (diamonds). β_{d0} is marked by the dashed black line. (Right): Same as above but with $\bar{T}(\ell)$, the black dashed-lines being $T_{\text{d0}} = 20\text{ K}$ and $T_{\text{d1T}} = 21.9\text{ K}$	119
8.4	Recovered posterior for the tensor to scalar ratio at $f_{\text{sky}} = 70\%$ with the three different kind of dust models; d0 (left), d1T (center) and d1 (right) with different fitting schemes: MBB (blue), first order in β (red), first order in β and T (green) and second order in β (yellow). The black dashed line indicates $r_{\text{sim}} = 0$	121
8.5	Sketch of the position of the two regions responsible for \mathcal{P}_ν^1 and \mathcal{P}_ν^2 along the line of sight.	124
8.6	Sum of two power-laws in polarization. Total signal (orange), \mathcal{P}_ν^1 (blue dashed) and \mathcal{P}_ν^2 (green dashed). Left: phases $\psi(\nu)$. Right: modulus $ \mathcal{P}_\nu $	125
8.7	Modeling the SED distortions (left) and polarization angle spectral rotation (right) of the total signal of the two power-law model (orange) with the spin-moment expansion at different orders using the complex pivot correction (colored dashed lines from blue at order 1 to red at order 10). The dark blue dashed line represents the phase of \mathcal{W}_0	127

8.8 Application of the spin-moment expansion for a sum of two modified-blackbodies. The total signal is in black dashed line, while the best fit for the moment expansion is displayed at order zero (a single MBB) in blue, at order one in orange, order two in green and order three in red. The spinor \mathcal{P}_ν is showed in the complex plane (Q, U) (<i>Upper panel</i>). Black crosses mark the steps of 100 GHz on the signal. The values of frequencies are indicated above the crosses in GHz. The corresponding polarized intensity P_ν (<i>Bottom left</i>) and polarization angle ψ_ν (<i>Bottom right</i>).	130
8.9 Left: Diagram of the toy model composed of an infinite filament (grey) over a background (white). The orientation of the $\psi(\nu)$ field is represented with color bars at two different frequencies: ν_1 (orange) and ν_2 (blue). Right: Spectral dependence of the toy model filament polarized power spectra. Left: Polarized power spectra divided by the pivot-modified blackbody squared for the special case of $\psi^{\text{fil}} = 30^\circ$. All spectra are normalized with respect to their value at ν_0 . The signals are shown in color: EE/BB (red), EE (blue), BB (green), and EB (orange). The black dashed lines were recovered by deriving the moment power spectra from the spin-moment maps.	135
8.10 Total polarization spinor in a single pixel of the filament of the toy model for $\psi^{\text{bg}} = 0^\circ$ and various values of the filament polarization angle ψ^{f} . Left: Modulus of the total signal at 100 GHz normalized by the pivot MBB (red) and modulus of the analytical derivation from the spin-moment expansion up to second order (black dashed line). The modulus of each term is displayed: order 0: $ \mathcal{W}_0 $ (blue), order 1: $ \mathcal{W}_1^\beta \ln(100/400) $ (orange), and order 2: $ 0.5\mathcal{W}_2^\beta \ln(100/400)^2 $ (green). Right: Difference of the polarization angles between the two frequencies. Signal (red), prediction from the complex $\Delta\beta$ correction $0.5 \text{Im}(\mathcal{W}_1^\beta / \mathcal{W}_0) \ln(100/400)$ (blue) and from the spin-moment expansion up to second order (black dashed line).	135
8.11 Graph of $r_{\ell,\nu}^{E/B}$, $r_{\ell,\nu}^{E\times B}$ and $\tilde{r}_{\ell,\nu}^{E\times B}$ in a single bin of ℓ and normalized at $\nu_0 = 353$ GHz for different PySM dust models. The shapes are defined as follows: $d0$ (blue circles), $d1$ (orange reversed triangles), $d10$ (green diamonds), and $d12$ (red triangles).	136
8.12 BICEP field (in dashed line) viewed by the Planck satellite ESA/Planck collaboration	138
8.13 $\hat{S}_2^{\text{iso},1}(j_1, j_2)$ and $\hat{S}_2^{\text{iso},2}(j_1, j_2)$ coefficients evaluated on a Brownian random field (fBm), a MHD simulation of the ISM, and observational data of the Polaris region. From Allys et al. (2019)	141
8.14 Upper pannel, from left to right: original opacity $\log_{10}(\tau)$, temperature T and spectral index β from the MHD simulations. Intermediate, from left to right: similar figures obtained from the synthetic map. Bottom pannel: 1D distributions of the same quantities for the original (blue) and the synthetic (orange) maps. From Régaldo-Saint Blancard et al. (2023)	144
9.1 Energy running of the gauge structure constants in the SM (left) and minimal supersymmetric model (MSSM) (right). α_1 and α_2 are the electroweak coupling constants while $\alpha_3 \equiv \alpha_S$. Taken from "Grand Unified Theories" in Zyla et al. (2020) (Figure 93.1).	156
9.2 Ionization fraction X_e and visibility function g for different values of $\delta_\alpha = \alpha/\alpha_0$ during recombination.	167
9.3 CMB power spectra for the best fit values of Λ -CDM with $r = 0.001$ for different values of $\delta_\alpha = \alpha/\alpha_0$	168

LIST OF FIGURES

9.4	Constraints on the O&P model universally coupled to matter with an older version of the atomic-clock constraints (Rosenband et al., 2008) and without the MICROSCOPE bound (grey), with the Eöt-Wash bound (Wagner et al., 2012) on the UFF (red) and with our full dataset (blue). Couplings are expressed in part per millions (10^{-6}).	171
9.5	Constraints on the full O&P model with all our datasets. All the parameters are expressed in ppm.	173
9.6	Top: Constraints on the full runaway dilaton parameter space with $V(\phi) = 0$. As in Martins & Vacher (2019), a prior can be used on the field speed $\phi'_0 = 0 \pm 0.1$ (blue contours) but appears to be too restrictive (red contours). Bottom: Contour plots showing the degeneracies between the dilaton parameters and H_0 in different scenarios.	183
9.7	Left: Value of the sound horizon at decoupling $r_s(d)$ for different values of $\delta_\alpha = \alpha/\alpha_0$. Right: Matter power spectrum $P_m(k)$ for different values of δ_α	186
B.1	Geometrical interpretation of the Q , U and V Stokes parameters in a given frame (\mathcal{O}, x, y) . From Régaldo-Saint Blancard (2021).	212
B.2	Illustration of the geometrical nature of E - and B -mode signals associated with a polarization tensor Π around point of the sky.	215
C.1	Illustration of the KS test principle. y -axis: values of ψ in the pixel, x -axis: arbitrary labelling of the value of the hits. The crossing angles ψ are all expressed in radians.	222
C.2	Examples of ψ -distributions sensitive to the KS tests.	222
C.3	Values of Δ_ψ for different values of the ecliptic latitude θ_{lat} , and the map resolution n_{side}	223
C.4	Mean value of Δ_ψ over all the pixels of the maps for different values of n_{side} and different values of the mission duration: 1 year (orange) and 2 years (blue).	223
C.5	KS test results for different detectors marked by red crosses for the MFT (top) and HFT (bottom).	224
C.6	Values of $\text{cond}(M)$ and $\det(M)$ as a function of θ_{lat} for multiple detectors of the HFT.	225
C.7	B^{or} and B^{eff} for <i>LiteBIRD</i> GRASP beam over the whole sphere.	225
C.8	Mean (orange) and median (blue) values of Σ_ℓ over all the values of θ_{lat}	226

List of Tables

3.1	Best-fit values of the Λ -CDM parameters with associated 68% confidence level combining data from the <i>Planck</i> spectra and lensing combined with BAO measurements (Planck Collaboration et al., 2020a).	31
7.1	Instrumental characteristics of <i>LiteBIRD</i> (LiteBIRD Collaboration et al., 2023). Some frequency bands are shared by two different telescopes or detector arrays. If so, the two values of polarization sensitivities $\sigma_{Q,U}^{\text{noise}}(\nu)$ and instrumental beam full width at half maximum θ_{FWHM} are displayed on the same line.	99
9.1	List of the fundamental constants of the standard models introduced in Chap. 3. Adapted from Uzan (2011) with updated values from Zyla et al. (2020)	149
9.2	List of gauge coupling values, adapted from Uzan (2011) with values of Zyla et al. (2020)	154
9.3	Major probes of the value of the fine structure constants α at different redshifts.	163

Main abbreviations and mathematical notations

Abbreviations

BAO	Baryon Acoustic Oscillation
CDM	Cold Dark Matter
CMB	Cosmic Microwave Background
EEP	Einstein Equivalence Principle
GMF	Galactic Magnetic Field
GUT	Grand Unified Theories
ISM	Inter-Stellar Medium
LOS	Line of Sight
LSS	Last Scattering Surface
MBB	Modified Black Body
MHD	Magneto Hydro Dynamics
GR	General Relativity
POS	Plane of the Sky
QFT	Quantum Field Theory
(R)WST	(Reduced) Wavelet Scattering Transform
SED	Spectral Energy Distribution
SM	Standard Model
SN(R)	Super Nova (Remnant)
WPH	Wavelet Phase Harmonics

Notations

- \mathbf{v} : 3-D vector
- $\langle x \rangle$: mean value of the random variable x
- \bar{p} : pivot value for a Taylor expansion in p .
- i : imaginary unit
- z^* : complex conjugate of $z \in \mathbb{C}$
- $|z| = z^*z$: complex number modulus of z
- $|M|$: determinant of the matrix M

Bibliography

- [1] Abazajian, K., Addison, G., Adshead, P., et al. 2019, CMB-S4 Science Case, Reference Design, and Project Plan, arXiv e-prints, arXiv:1907.04473, doi: [10.48550/arXiv.1907.04473](https://doi.org/10.48550/arXiv.1907.04473)
- [2] Abitbol, M. H., Chluba, J., Hill, J. C., & Johnson, B. R. 2017, Prospects for measuring cosmic microwave background spectral distortions in the presence of foregrounds, Monthly Notices of the Royal Astronomical Society, 471, 1126, doi: [10.1093/mnras/stx1653](https://doi.org/10.1093/mnras/stx1653)
- [3] Ade, P. A. R., Ahmed, Z., Amiri, M., et al. 2021, Improved Constraints on Primordial Gravitational Waves using Planck, WMAP, and BICEP/Keck Observations through the 2018 Observing Season, Physical Review Letters, 127, 151301, doi: [10.1103/PhysRevLett.127.151301](https://doi.org/10.1103/PhysRevLett.127.151301)
- [4] —. 2022, BICEP/Keck XV: The BICEP3 Cosmic Microwave Background Polarimeter and the First Three-year Data Set, The Astrophysical Journal, 927, 77, doi: [10.3847/1538-4357/ac4886](https://doi.org/10.3847/1538-4357/ac4886)
- [5] Agladze, N. I., Sievers, A. J., Jones, S. A., Burlitch, J. M., & Beckwith, S. V. W. 1996, Laboratory Results on Millimeter-Wave Absorption in Silicate Grain Materials at Cryogenic Temperatures, The Astrophysical Journal, 462, 1026, doi: [10.1086/177217](https://doi.org/10.1086/177217)
- [6] Agrawal, V., Barr, S. M., Donoghue, J. F., & Seckel, D. 1998, Viable range of the mass scale of the standard model, Phys. Rev. D., 57, 5480, doi: [10.1103/PhysRevD.57.5480](https://doi.org/10.1103/PhysRevD.57.5480)
- [7] Alam, S., Ata, M., Bailey, S., et al. 2017, The clustering of galaxies in the completed SDSS-III Baryon Oscillation Spectroscopic Survey: cosmological analysis of the DR12 galaxy sample, Monthly Notices of the Royal Astronomical Society, 470, 2617, doi: [10.1093/mnras/stx721](https://doi.org/10.1093/mnras/stx721)
- [8] Albrecht, A. 2002, Cosmic Inflation and the Arrow of Time, arXiv e-prints, astro, doi: [10.48550/arXiv.astro-ph/0210527](https://doi.org/10.48550/arXiv.astro-ph/0210527)
- [9] Alexander, S., & McDonough, E. 2019, Axion-dilaton destabilization and the Hubble tension, Physics Letters B, 797, 134830, doi: [10.1016/j.physletb.2019.134830](https://doi.org/10.1016/j.physletb.2019.134830)
- [10] Ali-Haïmoud, Y. 2013, Spinning Dust Radiation: A Review of the Theory, Advances in Astronomy, 2013, 462697, doi: [10.1155/2013/462697](https://doi.org/10.1155/2013/462697)
- [11] Ali-Haïmoud, Y., & Hirata, C. M. 2011, HyRec: A fast and highly accurate primordial

BIBLIOGRAPHY

- hydrogen and helium recombination code, Phys. Rev. D., 83, 043513, doi: [10.1103/PhysRevD.83.043513](https://doi.org/10.1103/PhysRevD.83.043513)
- [12] Allanchach, B. C. 2019, Beyond the Standard Model, CERN Yellow Rep. School Proc., 6, 113, doi: [10.23730/CYRSP-2019-006.113](https://doi.org/10.23730/CYRSP-2019-006.113)
- [13] Ally, E. 2017, Beyond standard models in cosmology (In French), arXiv e-prints, arXiv:1710.02143. <https://arxiv.org/abs/1710.02143>
- [14] Ally, E., Levrier, F., Zhang, S., et al. 2019, The RWST, a comprehensive statistical description of the non-Gaussian structures in the ISM, Astronomy and Astrophysics, 629, A115, doi: [10.1051/0004-6361/201834975](https://doi.org/10.1051/0004-6361/201834975)
- [15] Ally, E., Marchand, T., Cardoso, J.-F., et al. 2020, New interpretable statistics for large-scale structure analysis and generation, Phys. Rev. D, 102, 103506, doi: [10.1103/PhysRevD.102.103506](https://doi.org/10.1103/PhysRevD.102.103506)
- [16] Almeida, A., Anderson, S. F., Argudo-Fernández, M., et al. 2023, The Eighteenth Data Release of the Sloan Digital Sky Surveys: Targeting and First Spectra from SDSS-V, arXiv e-prints, arXiv:2301.07688, doi: [10.48550/arXiv.2301.07688](https://doi.org/10.48550/arXiv.2301.07688)
- [17] Alpher, R. A., Bethe, H., & Gamow, G. 1948, The Origin of Chemical Elements, Physical Review, 73, 803, doi: [10.1103/PhysRev.73.803](https://doi.org/10.1103/PhysRev.73.803)
- [18] Alsabti, A. W., & Murdin, P. 2017, Handbook of Supernovae, doi: [10.1007/978-3-319-21846-5](https://doi.org/10.1007/978-3-319-21846-5)
- [19] Alves, C. S., Leite, A. C. O., Martins, C. J. A. P., et al. 2018, Current and future constraints on extended Bekenstein-type models for a varying fine-structure constant, Phys. Rev. D., 97, 023522, doi: [10.1103/PhysRevD.97.023522](https://doi.org/10.1103/PhysRevD.97.023522)
- [20] Amendola, L., Appleby, S., Avgoustidis, A., et al. 2018, Cosmology and fundamental physics with the Euclid satellite, Living Reviews in Relativity, 21, 2, doi: [10.1007/s41114-017-0010-3](https://doi.org/10.1007/s41114-017-0010-3)
- [21] An, D., Meissner, K. A., Nurowski, P., & Penrose, R. 2018, Apparent evidence for Hawking points in the CMB Sky, arXiv e-prints, arXiv:1808.01740, doi: [10.48550/arXiv.1808.01740](https://doi.org/10.48550/arXiv.1808.01740)
- [22] Andersson, B. G., Lazarian, A., & Vaillancourt, J. E. 2015, Interstellar Dust Grain Alignment, Annual Review of Astronomy and Astrophysics, 53, 501, doi: [10.1146/annurev-astro-082214-122414](https://doi.org/10.1146/annurev-astro-082214-122414)
- [23] Antonucci, R. 1993, Unified models for active galactic nuclei and quasars., Annual Review of Astronomy and Astrophysics, 31, 473, doi: [10.1146/annurev.aa.31.090193.002353](https://doi.org/10.1146/annurev.aa.31.090193.002353)
- [24] Atlas Collaboration. 2012, Observation of a new particle in the search for the Standard Model Higgs boson with the ATLAS detector at the LHC, Physics Letters B, 716, 1, doi: [10.1016/j.physletb.2012.08.020](https://doi.org/10.1016/j.physletb.2012.08.020)
- [25] Audren, B., Lesgourges, J., Benabed, K., & Prunet, S. 2013, Conservative Constraints

BIBLIOGRAPHY

- on Early Cosmology: an illustration of the Monte Python cosmological parameter inference code, *JCAP*, 1302, 001, doi: [10.1088/1475-7516/2013/02/001](https://doi.org/10.1088/1475-7516/2013/02/001)
- [26] Austermann, J. E., Aird, K. A., Beall, J. A., et al. 2012, in Society of Photo-Optical Instrumentation Engineers (SPIE) Conference Series, Vol. 8452, Millimeter, Submillimeter, and Far-Infrared Detectors and Instrumentation for Astronomy VI, ed. W. S. Holland & J. Zmuidzinas, 84521E, doi: [10.1117/12.927286](https://doi.org/10.1117/12.927286)
- [27] (auth.), D. H. 2015, Space-Time Algebra, doi: [10.1007/978-3-319-18413-5](https://doi.org/10.1007/978-3-319-18413-5)
- [28] Azzoni, S., Abitbol, M. H., Alonso, D., et al. 2021, A minimal power-spectrum-based moment expansion for CMB B-mode searches, *J. Cosmology Astropart. Phys.*, 2021, 047, doi: [10.1088/1475-7516/2021/05/047](https://doi.org/10.1088/1475-7516/2021/05/047)
- [29] Azzoni, S., Alonso, D., Abitbol, M. H., Errard, J., & Krachmalnicoff, N. 2023, A hybrid map- C_ℓ component separation method for primordial CMB B-mode searches, *J. Cosmology Astropart. Phys.*, 2023, 035, doi: [10.1088/1475-7516/2023/03/035](https://doi.org/10.1088/1475-7516/2023/03/035)
- [30] Baez, J. C., & Muniain, J. P. 1994, Gauge Fields, Knots and Gravity (Series on Knots and Everything), Series on Knots and Everything (World Scientific Publishing Company)
- [31] Bahamonde, S., Dialektopoulos, K. F., Escamilla-Rivera, C., et al. 2021, Teleparallel Gravity: From Theory to Cosmology, arXiv e-prints, arXiv:2106.13793, doi: [10.48550/arXiv.2106.13793](https://doi.org/10.48550/arXiv.2106.13793)
- [32] Barnard, E. E. 1919, On the dark markings of the sky, with a catalogue of 182 such objects., *The Astrophysical Journal*, 49, 1, doi: [10.1086/142439](https://doi.org/10.1086/142439)
- [33] Barros, B. J., & da Fonseca, V. 2023, Coupling quintessence kinetics to electromagnetism, *Journal of Cosmology and Astroparticle Physics*, 2023, 048, doi: [10.1088/1475-7516/2023/06/048](https://doi.org/10.1088/1475-7516/2023/06/048)
- [34] Barthel, P. D. 1989, Is Every Quasar Beamed?, *The Astrophysical Journal*, 336, 606, doi: [10.1086/167038](https://doi.org/10.1086/167038)
- [35] Bartolo, N., Komatsu, E., Matarrese, S., & Riotto, A. 2004, Non-Gaussianity from inflation: theory and observations, *Phys. Rep.*, 402, 103, doi: [10.1016/j.physrep.2004.08.022](https://doi.org/10.1016/j.physrep.2004.08.022)
- [36] Battfeld, D., & Peter, P. 2015, A critical review of classical bouncing cosmologies, *Phys. Rep.*, 571, 1, doi: [10.1016/j.physrep.2014.12.004](https://doi.org/10.1016/j.physrep.2014.12.004)
- [37] Bauer, M., & Shergold, J. D. 2023, Limits on the cosmic neutrino background, *J. Cosmology Astropart. Phys.*, 2023, 003, doi: [10.1088/1475-7516/2023/01/003](https://doi.org/10.1088/1475-7516/2023/01/003)
- [38] Baumann, D. 2009, TASI Lectures on Inflation, arXiv e-prints, arXiv:0907.5424. <https://arxiv.org/abs/0907.5424>
- [39] Baumann, D., & Green, D. 2012, A field range bound for general single-field inflation, *J. Cosmology Astropart. Phys.*, 2012, 017, doi: [10.1088/1475-7516/2012/05/017](https://doi.org/10.1088/1475-7516/2012/05/017)
- [40] Baumann, D., Green, D., & Porto, R. A. 2015, B-modes and the nature of inflation, *J. Cosmology Astropart. Phys.*, 2015, 016, doi: [10.1088/1475-7516/2015/01/016](https://doi.org/10.1088/1475-7516/2015/01/016)

BIBLIOGRAPHY

- [41] Baumann, D., & McAllister, L. 2015, Inflation and String Theory, doi: [10.48550/arXiv.1404.2601](https://arxiv.org/abs/1404.2601)
- [42] Baumann, D., & Peiris, H. V. 2008, Cosmological Inflation: Theory and Observations, arXiv e-prints, arXiv:0810.3022, doi: [10.48550/arXiv.0810.3022](https://arxiv.org/abs/0810.3022)
- [43] Bekenstein, J. D. 1981, Universal upper bound on the entropy-to-energy ratio for bounded systems, Phys. Rev. D, 23, 287, doi: [10.1103/PhysRevD.23.287](https://doi.org/10.1103/PhysRevD.23.287)
- [44] Bekenstein, J. D. 1982, Fine-structure constant: Is it really a constant?, Phys. Rev. D., 25, 1527, doi: [10.1103/PhysRevD.25.1527](https://doi.org/10.1103/PhysRevD.25.1527)
- [45] —. 2002, Fine-structure constant variability, equivalence principle, and cosmology, Phys. Rev. D., 66, 123514, doi: [10.1103/PhysRevD.66.123514](https://doi.org/10.1103/PhysRevD.66.123514)
- [46] Beltrán Jiménez, J., Heisenberg, L., & Koivisto, T. S. 2019, The Geometrical Trinity of Gravity, Universe, 5, 173, doi: [10.3390/universe5070173](https://doi.org/10.3390/universe5070173)
- [47] Benisty, D., Guendelman, E. I., van de Venn, A., et al. 2022, The dark side of the torsion: dark energy from propagating torsion, European Physical Journal C, 82, 264, doi: [10.1140/epjc/s10052-022-10187-2](https://doi.org/10.1140/epjc/s10052-022-10187-2)
- [48] Benn, I. T. R. 1987, An introduction to spinors and geometry with applications in Physics
- [49] Bennett, C. L., Larson, D., Weiland, J. L., et al. 2013, Nine-year Wilkinson Microwave Anisotropy Probe (WMAP) Observations: Final Maps and Results, ApJ Supplements, 208, 20, doi: [10.1088/0067-0049/208/2/20](https://doi.org/10.1088/0067-0049/208/2/20)
- [50] Bergé, J., Pernot-Borràs, M., Uzan, J.-P., et al. 2022, MICROSCOPE's constraint on a short-range fifth force, Classical and Quantum Gravity, 39, 204010, doi: [10.1088/1361-6382/abe142](https://doi.org/10.1088/1361-6382/abe142)
- [51] Bergé, J. 2023, MICROSCOPE's view at gravitation, Reports on Progress in Physics, 86, doi: [10.1088/1361-6633/acd203](https://doi.org/10.1088/1361-6633/acd203)
- [52] Bernstein, R. A., Freedman, W. L., & Madore, B. F. 2002, The First Detections of the Extragalactic Background Light at 3000, 5500, and 8000 Å. III. Cosmological Implications, 571, 107, doi: [10.1086/339424](https://doi.org/10.1086/339424)
- [53] Bertone, G., Hooper, D., & Silk, J. 2005, Particle dark matter: evidence, candidates and constraints, Physics Reports, 405, 279, doi: [10.1016/j.physrep.2004.08.031](https://doi.org/10.1016/j.physrep.2004.08.031)
- [54] Bertotti, B., & Grishchuk, L. P. 1990, The strong equivalence principle, Classical and Quantum Gravity, 7, 1733, doi: [10.1088/0264-9381/7/10/007](https://doi.org/10.1088/0264-9381/7/10/007)
- [55] Beutler, F., Blake, C., Colless, M., et al. 2011, The 6dF Galaxy Survey: baryon acoustic oscillations and the local Hubble constant, Monthly Notices of the Royal Astronomical Society, 416, 3017, doi: [10.1111/j.1365-2966.2011.19250.x](https://doi.org/10.1111/j.1365-2966.2011.19250.x)
- [56] Bezrukov, F., & Shaposhnikov, M. 2008, The Standard Model Higgs boson as the inflaton, Physics Letters B, 659, 703, doi: [10.1016/j.physletb.2007.11.072](https://doi.org/10.1016/j.physletb.2007.11.072)

BIBLIOGRAPHY

- [57] Bialynicki-Birula, I., & Bialynicka-Birula, Z. 2013, The role of the Riemann-Silberstein vector in classical and quantum theories of electromagnetism, *Journal of Physics A Mathematical General*, 46, 053001, doi: [10.1088/1751-8113/46/5/053001](https://doi.org/10.1088/1751-8113/46/5/053001)
- [58] BICEP2 Collaboration, Ade, P. A. R., Aikin, R. W., et al. 2014a, Detection of B-Mode Polarization at Degree Angular Scales by BICEP2, *Physical Review Letters*, 112, 241101, doi: [10.1103/PhysRevLett.112.241101](https://doi.org/10.1103/PhysRevLett.112.241101)
- [59] —. 2014b, Detection of B-Mode Polarization at Degree Angular Scales by BICEP2, *Physical Review Letters*, 112, 241101, doi: [10.1103/PhysRevLett.112.241101](https://doi.org/10.1103/PhysRevLett.112.241101)
- [60] BICEP2 Collaboration, Keck Array Collaboration, Ade, P. A. R., et al. 2016, Improved Constraints on Cosmology and Foregrounds from BICEP2 and Keck Array Cosmic Microwave Background Data with Inclusion of 95 GHz Band, *Physical Review Letters*, 116, 031302, doi: [10.1103/PhysRevLett.116.031302](https://doi.org/10.1103/PhysRevLett.116.031302)
- [61] —. 2018, Constraints on Primordial Gravitational Waves Using Planck, WMAP, and New BICEP2/Keck Observations through the 2015 Season, *Physical Review Letters*, 121, 221301, doi: [10.1103/PhysRevLett.121.221301](https://doi.org/10.1103/PhysRevLett.121.221301)
- [62] BICEP2/Keck Collaboration, Planck Collaboration, Ade, P. A. R., et al. 2015, Joint Analysis of BICEP2/Keck Array and Planck Data, *Physical Review Letters*, 114, 101301, doi: [10.1103/PhysRevLett.114.101301](https://doi.org/10.1103/PhysRevLett.114.101301)
- [63] Blagojević, M., & Hehl, F. W. 2012, Gauge Theories of Gravitation, arXiv e-prints, arXiv:1210.3775, doi: [10.48550/arXiv.1210.3775](https://arxiv.org/abs/gr-qc/0506033)
- [64] Bleeker, D. 1981, *Gauge Theory And Variational Principles* (Dover)
- [65] Boehmer, C. G. 2005, On inflation and torsion in cosmology, *Acta Phys. Polon. B*, 36, 2841. <https://arxiv.org/abs/gr-qc/0506033>
- [66] Bond, J. R., & Efstathiou, G. 1987, The statistics of cosmic background radiation fluctuations, *Monthly Notices of the Royal Astronomical Society*, 226, 655, doi: [10.1093/mnras/226.3.655](https://doi.org/10.1093/mnras/226.3.655)
- [67] Boyarsky, A., Drewes, M., Lasserre, T., Mertens, S., & Ruchayskiy, O. 2019, Sterile neutrino Dark Matter, *Progress in Particle and Nuclear Physics*, 104, 1, doi: [10.1016/j.ppnp.2018.07.004](https://doi.org/10.1016/j.ppnp.2018.07.004)
- [68] Brandenberger, R. H. 2011, in *International Journal of Modern Physics Conference Series*, Vol. 1, *International Journal of Modern Physics Conference Series*, 67–79, doi: [10.1142/S2010194511000109](https://doi.org/10.1142/S2010194511000109)
- [69] Brans, C., & Dicke, R. H. 1961, Mach's Principle and a Relativistic Theory of Gravitation, *Physical Review*, 124, 925, doi: [10.1103/PhysRev.124.925](https://doi.org/10.1103/PhysRev.124.925)
- [70] Brax, P. 2013, Screening mechanisms in modified gravity, *Classical and Quantum Gravity*, 30, 214005, doi: [10.1088/0264-9381/30/21/214005](https://doi.org/10.1088/0264-9381/30/21/214005)
- [71] Brecher, K. 1977, Is the Speed of Light Independent of the Velocity of the Source?, *Phys. Rev. Lett.*, 39, 1051, doi: [10.1103/PhysRevLett.39.1051](https://doi.org/10.1103/PhysRevLett.39.1051)

BIBLIOGRAPHY

- [72] Brinckmann, T., & Lesgourges, J. 2018, MontePython 3: boosted MCMC sampler and other features. <https://arxiv.org/abs/1804.07261>
- [73] Bruna, J., & Mallat, S. 2018, Multiscale Sparse Microcanonical Models, arXiv e-prints, arXiv:1801.02013, doi: [10.48550/arXiv.1801.02013](https://doi.org/10.48550/arXiv.1801.02013)
- [74] Burrows, A., & Vartanyan, D. 2021, Core-collapse supernova explosion theory, Nature, 589, 29, doi: [10.1038/s41586-020-03059-w](https://doi.org/10.1038/s41586-020-03059-w)
- [75] Calabrese, E., Martinelli, M., Pandolfi, S., et al. 2014, Dark Energy coupling with electromagnetism as seen from future low-medium redshift probes, PRD, 89, 083509, doi: [10.1103/PhysRevD.89.083509](https://doi.org/10.1103/PhysRevD.89.083509)
- [76] Calabrese, E., Menegoni, E., Martins, C. J. A. P., Melchiorri, A., & Rocha, G. 2011, Constraining variations in the fine structure constant in the presence of early dark energy, Phys. Rev. D., 84, 023518, doi: [10.1103/PhysRevD.84.023518](https://doi.org/10.1103/PhysRevD.84.023518)
- [77] Caldwell, R. R. 2002, A phantom menace? Cosmological consequences of a dark energy component with super-negative equation of state, Physics Letters B, 545, 23, doi: [10.1016/S0370-2693\(02\)02589-3](https://doi.org/10.1016/S0370-2693(02)02589-3)
- [78] Caldwell, R. R., Dave, R., & Steinhardt, P. J. 1998, Cosmological Imprint of an Energy Component with General Equation of State, Physical Review Letters, 80, 1582, doi: [10.1103/PhysRevLett.80.1582](https://doi.org/10.1103/PhysRevLett.80.1582)
- [79] Callan, C. G., & Maldacena, J. M. 1996, D-brane approach to black hole quantum mechanics, Nuclear Physics B, 472, 591, doi: [10.1016/0550-3213\(96\)00225-8](https://doi.org/10.1016/0550-3213(96)00225-8)
- [80] Callan, Jr., C. G., Klebanov, I. R., & Perry, M. J. 1986, String Theory Effective Actions, Nucl. Phys. B, 278, 78, doi: [10.1016/0550-3213\(86\)90107-0](https://doi.org/10.1016/0550-3213(86)90107-0)
- [81] Campeti, P., Komatsu, E., Poletti, D., & Baccigalupi, C. 2021, Measuring the spectrum of primordial gravitational waves with CMB, PTA and laser interferometers, J. Cosmology Astropart. Phys., 2021, 012, doi: [10.1088/1475-7516/2021/01/012](https://doi.org/10.1088/1475-7516/2021/01/012)
- [82] Capozziello, S., & Bajardi, F. 2022, Nonlocal gravity cosmology: An overview, International Journal of Modern Physics D, 31, 2230009, doi: [10.1142/S0218271822300099](https://doi.org/10.1142/S0218271822300099)
- [83] Capozziello, S., & de Laurentis, M. 2011, Extended Theories of Gravity, Phys. Rep., 509, 167, doi: [10.1016/j.physrep.2011.09.003](https://doi.org/10.1016/j.physrep.2011.09.003)
- [84] Cardoso, J.-F., Martin, M., Delabrouille, J., Betoule, M., & Patanchon, G. 2008, Component separation with flexible models. Application to the separation of astrophysical emissions, arXiv e-prints, arXiv:0803.1814, doi: [10.48550/arXiv.0803.1814](https://doi.org/10.48550/arXiv.0803.1814)
- [85] Carreres, B., Bautista, J. E., Feinstein, F., et al. 2023, Growth-rate measurement with type-Ia supernovae using ZTF survey simulations, arXiv e-prints, arXiv:2303.01198, doi: [10.48550/arXiv.2303.01198](https://doi.org/10.48550/arXiv.2303.01198)
- [86] Carroll, S. M., Field, G. B., & Jackiw, R. 1990, Limits on a Lorentz- and parity-violating modification of electrodynamics, Phys. Rev. D., 41, 1231, doi: [10.1103/PhysRevD.41.1231](https://doi.org/10.1103/PhysRevD.41.1231)

BIBLIOGRAPHY

- [87] Cartan, E. 1922, Sur une généralisation de la notion de courbure de Riemann et les espaces à torsion, Comptes rendus de l'Académie des Sciences de Paris
- [88] Carter, B. 1974, in Confrontation of Cosmological Theories with Observational Data, ed. M. S. Longair, Vol. 63, 291–298
- [89] Casini, H. 2008, Relative entropy and the Bekenstein bound, Classical and Quantum Gravity, 25, 205021, doi: [10.1088/0264-9381/25/20/205021](https://doi.org/10.1088/0264-9381/25/20/205021)
- [90] Chamcham, K., Barrow, J., Saunders, S., & Silk, J. 2017, The Philosophy of Cosmology (Cambridge University Press)
- [91] Chandrasekhar, S., & Fermi, E. 1953, Magnetic Fields in Spiral Arms., The Astrophysical Journal, 118, 113, doi: [10.1086/145731](https://doi.org/10.1086/145731)
- [92] Chevallier, M., & Polarski, D. 2001, Accelerating universes with scaling dark matter, Int. J. Mod. Phys. D, 10, 213, doi: [10.1142/S0218271801000822](https://doi.org/10.1142/S0218271801000822)
- [93] Chew, G. F., & Frautschi, S. C. 1961, Principle of Equivalence for All Strongly Interacting Particles Within the S Matrix Framework, Phys. Rev. Lett., 7, 394, doi: [10.1103/PhysRevLett.7.394](https://doi.org/10.1103/PhysRevLett.7.394)
- [94] Chluba, J., Hill, J. C., & Abitbol, M. H. 2017, Rethinking CMB foregrounds: systematic extension of foreground parametrizations, Monthly Notices of the Royal Astronomical Society, 472, 1195, doi: [10.1093/mnras/stx1982](https://doi.org/10.1093/mnras/stx1982)
- [95] Chluba, J., Switzer, E., Nelson, K., & Nagai, D. 2013, Sunyaev-Zeldovich signal processing and temperature-velocity moment method for individual clusters, Monthly Notices of the Royal Astronomical Society, 430, 3054, doi: [10.1093/mnras/stt110](https://doi.org/10.1093/mnras/stt110)
- [96] Chluba, J., Kogut, A., Patil, S. P., et al. 2019, Spectral Distortions of the CMB as a Probe of Inflation, Recombination, Structure Formation and Particle Physics, Bulletin of the AAS, 51, 184, doi: [10.48550/arXiv.1903.04218](https://doi.org/10.48550/arXiv.1903.04218)
- [97] Chluba, J., Abitbol, M. H., Aghanim, N., et al. 2021, New horizons in cosmology with spectral distortions of the cosmic microwave background, Experimental Astronomy, 51, 1515, doi: [10.1007/s10686-021-09729-5](https://doi.org/10.1007/s10686-021-09729-5)
- [98] Chris Doran, A. L. 2003, Geometric Algebra for Physicists, 1st edn., N/A (Cambridge University Press)
- [99] Christensen, N. 2019, Stochastic gravitational wave backgrounds, Reports on Progress in Physics, 82, 016903, doi: [10.1088/1361-6633/aae6b5](https://doi.org/10.1088/1361-6633/aae6b5)
- [100] Chupp, T. E., Hoare, R. J., Loveman, R. A., et al. 1989, Results of a new test of local Lorentz invariance: A search for mass anisotropy in ^{21}Ne , Phys. Rev. Lett., 63, 1541, doi: [10.1103/PhysRevLett.63.1541](https://doi.org/10.1103/PhysRevLett.63.1541)
- [101] Cicoli, M., Conlon, J. P., Maharana, A., et al. 2023, String Cosmology: from the Early Universe to Today, arXiv e-prints, arXiv:2303.04819, doi: [10.48550/arXiv.2303.04819](https://doi.org/10.48550/arXiv.2303.04819)

BIBLIOGRAPHY

- [102] Clara, M. T., & Martins, C. J. A. P. 2020, Primordial nucleosynthesis with varying fundamental constants. Improved constraints and a possible solution to the lithium problem, *Astronomy and Astrophysics*, 633, L11, doi: [10.1051/0004-6361/201937211](https://doi.org/10.1051/0004-6361/201937211)
- [103] Clark, S. E., & Hensley, B. S. 2019, Mapping the Magnetic Interstellar Medium in Three Dimensions over the Full Sky with Neutral Hydrogen, *The Astrophysical Journal*, 887, 136, doi: [10.3847/1538-4357/ab5803](https://doi.org/10.3847/1538-4357/ab5803)
- [104] Clark, S. E., Kim, C.-G., Hill, J. C., & Hensley, B. S. 2021, The Origin of Parity Violation in Polarized Dust Emission and Implications for Cosmic Birefringence, *The Astrophysical Journal*, 919, 53, doi: [10.3847/1538-4357/ac0e35](https://doi.org/10.3847/1538-4357/ac0e35)
- [105] Clark, S. J., & Tucker, R. W. 2000, Gauge symmetry and gravito-electromagnetism, *Classical and Quantum Gravity*, 17, 4125, doi: [10.1088/0264-9381/17/19/311](https://doi.org/10.1088/0264-9381/17/19/311)
- [106] CMS Collaboration. 2012, Observation of a new boson at a mass of 125 GeV with the CMS experiment at the LHC, *Physics Letters B*, 716, 30, doi: [10.1016/j.physletb.2012.08.021](https://doi.org/10.1016/j.physletb.2012.08.021)
- [107] Coleman, S., & Mandula, J. 1967, All Possible Symmetries of the *S* Matrix, *Phys. Rev.*, 159, 1251, doi: [10.1103/PhysRev.159.1251](https://doi.org/10.1103/PhysRev.159.1251)
- [108] Conférence générale des poids et mesures. 1983, 17e réunion de la CGPM. <https://www.bipm.org/fr/committees/cg/cgpm/17-1983>
- [109] Consiglio, R., de Salas, P. F., Mangano, G., et al. 2018, PArthENoPE reloaded, *Computer Physics Communications*, 233, 237, doi: [10.1016/j.cpc.2018.06.022](https://doi.org/10.1016/j.cpc.2018.06.022)
- [110] Coquereaux, R. 2002, ESPACES FIBRÉS ET CONNEXIONS
- [111] Coquereaux, R., & Jadczk, A. 1988, Riemannian geometry, fiber bundles, Kaluza-Klein theories, and all that..., Vol. 16, doi: [10.1142/0488](https://doi.org/10.1142/0488)
- [112] Cox, T. J., & Loeb, A. 2008, The collision between the Milky Way and Andromeda, *Monthly Notices of the Royal Astronomical Society*, 386, 461, doi: [10.1111/j.1365-2966.2008.13048.x](https://doi.org/10.1111/j.1365-2966.2008.13048.x)
- [113] Craig F. Bohren, D. R. H. 1983, *Absorption and Scattering of Light by Small Particles* (Wiley-VCH)
- [114] Cremmer, E., Julia, B., & Scherk, J. 1978, Supergravity Theory in Eleven-Dimensions, *Phys. Lett. B*, 76, 409, doi: [10.1016/0370-2693\(78\)90894-8](https://doi.org/10.1016/0370-2693(78)90894-8)
- [115] Crill, B. P., Ade, P. A. R., Battistelli, E. S., et al. 2008, in *Society of Photo-Optical Instrumentation Engineers (SPIE) Conference Series*, Vol. 7010, *Space Telescopes and Instrumentation 2008: Optical, Infrared, and Millimeter*, ed. J. Oschmann, Jacobus M., M. W. M. de Graauw, & H. A. MacEwen, 70102P, doi: [10.1117/12.787446](https://doi.org/10.1117/12.787446)
- [116] Croon, D., Gonzalo, T. E., Graf, L., Košnik, N., & White, G. 2019, GUT Physics in the era of the LHC, *Frontiers in Physics*, 7, 76, doi: [10.3389/fphy.2019.00076](https://doi.org/10.3389/fphy.2019.00076)
- [117] Cukierman, A. J., Clark, S. E., & Halal, G. 2023, Magnetic Misalignment of Interstellar Dust Filaments, *The Astrophysical Journal*, 946, 106, doi: [10.3847/1538-4357/acb0c4](https://doi.org/10.3847/1538-4357/acb0c4)

BIBLIOGRAPHY

- [118] da Fonseca, V., Barreiro, T., Nunes, N. J., et al. 2022, Fundamental physics with ESPRESSO: Constraining a simple parametrisation for varying α , *Astronomy and Astrophysics*, 666, A57, doi: [10.1051/0004-6361/202243795](https://doi.org/10.1051/0004-6361/202243795)
- [119] Damour, T. 2003, String theory, cosmology and varying constants, *Astrophysics and space science*, 283, 445, doi: [10.1023/A:1022596316014](https://doi.org/10.1023/A:1022596316014)
- [120] —. 2012, Theoretical aspects of the equivalence principle, *Classical and Quantum Gravity*, 29, 184001, doi: [10.1088/0264-9381/29/18/184001](https://doi.org/10.1088/0264-9381/29/18/184001)
- [121] Damour, T., & Dyson, F. 1996, The Oklo bound on the time variation of the fine-structure constant revisited, *Nuclear Physics B*, 480, 37, doi: [10.1016/S0550-3213\(96\)00467-1](https://doi.org/10.1016/S0550-3213(96)00467-1)
- [122] Damour, T., & Nordtvedt, K. 1993, General relativity as a cosmological attractor of tensor-scalar theories, *Physical Review Letters*, 70, 2217, doi: [10.1103/PhysRevLett.70.2217](https://doi.org/10.1103/PhysRevLett.70.2217)
- [123] Damour, T., Piazza, F., & Veneziano, G. 2002a, Runaway Dilaton and Equivalence Principle Violations, *Physical Review Letters*, 89, 081601, doi: [10.1103/PhysRevLett.89.081601](https://doi.org/10.1103/PhysRevLett.89.081601)
- [124] —. 2002b, Violations of the equivalence principle in a dilaton-runaway scenario, *Phys. Rev. D.*, 66, 046007, doi: [10.1103/PhysRevD.66.046007](https://doi.org/10.1103/PhysRevD.66.046007)
- [125] —. 2002c, Violations of the equivalence principle in a dilaton-runaway scenario, *Phys. Rev. D.*, 66, 046007, doi: [10.1103/PhysRevD.66.046007](https://doi.org/10.1103/PhysRevD.66.046007)
- [126] Damour, T., & Polyakov, A. 1994, The string dilation and a least coupling principle, *Nuclear Physics B*, 423, 532, doi: [https://doi.org/10.1016/0550-3213\(94\)90143-0](https://doi.org/10.1016/0550-3213(94)90143-0)
- [127] Damour, T., & Polyakov, A. M. 1994, String theory and gravity, *General Relativity and Gravitation*, 26, 1171, doi: [10.1007/BF02106709](https://doi.org/10.1007/BF02106709)
- [128] Davis, Leverett, J., & Greenstein, J. L. 1951, The Polarization of Starlight by Aligned Dust Grains., *The Astrophysical Journal*, 114, 206, doi: [10.1086/145464](https://doi.org/10.1086/145464)
- [129] de Boer, W. 1994, Grand unified theories and supersymmetry in particle physics and cosmology, *Progress in Particle and Nuclear Physics*, 33, 201, doi: [10.1016/0146-6410\(94\)90045-0](https://doi.org/10.1016/0146-6410(94)90045-0)
- [130] Deal, M., & Martins, C. J. A. P. 2021, Primordial nucleosynthesis with varying fundamental constants. Solutions to the lithium problem and the deuterium discrepancy, *Astronomy and Astrophysics*, 653, A48, doi: [10.1051/0004-6361/202140725](https://doi.org/10.1051/0004-6361/202140725)
- [131] Delhom, A. 2020, Minimal coupling in presence of non-metricity and torsion, *European Physical Journal C*, 80, 728, doi: [10.1140/epjc/s10052-020-8330-y](https://doi.org/10.1140/epjc/s10052-020-8330-y)
- [132] Delouis, J. M., Ally, E., Gauvrit, E., & Boulanger, F. 2022, Non-Gaussian modelling and statistical denoising of Planck dust polarisation full-sky maps using scattering transforms, *Astronomy and Astrophysics*, 668, A122, doi: [10.1051/0004-6361/202244566](https://doi.org/10.1051/0004-6361/202244566)

BIBLIOGRAPHY

- [133] Demyk, K., Meny, C., Lu, X. H., et al. 2017, Low temperature MIR to submillimeter mass absorption coefficient of interstellar dust analogues. I. Mg-rich glassy silicates, *Astronomy and Astrophysics*, 600, A123, doi: [10.1051/0004-6361/201629711](https://doi.org/10.1051/0004-6361/201629711)
- [134] Derdzinski, A. 1992, Geometry of the Standard Model of Elementary Particles
- [135] DeWolfe, O., Giryavets, A., Kachru, S., & Taylor, W. 2005, Type IIA moduli stabilization, *Journal of High Energy Physics*, 2005, 066, doi: [10.1088/1126-6708/2005/07/066](https://doi.org/10.1088/1126-6708/2005/07/066)
- [136] Di Casola, E., Liberati, S., & Sonego, S. 2015, Nonequivalence of equivalence principles, *American Journal of Physics*, 83, 39, doi: [10.1119/1.4895342](https://doi.org/10.1119/1.4895342)
- [137] Di Luzio, L., Masiero, A., Paradisi, P., & Passera, M. 2022, New physics behind the new muon g-2 puzzle?, *Physics Letters B*, 829, 137037, doi: [10.1016/j.physletb.2022.137037](https://doi.org/10.1016/j.physletb.2022.137037)
- [138] Di Valentino, E., Mena, O., Pan, S., et al. 2021, In the realm of the Hubble tension—a review of solutions, *Classical and Quantum Gravity*, 38, 153001, doi: [10.1088/1361-6382/ac086d](https://doi.org/10.1088/1361-6382/ac086d)
- [139] Dicke, R. H., Peebles, P. J. E., Roll, P. G., & Wilkinson, D. T. 1965, Cosmic Black-Body Radiation., *The Astrophysical Journal*, 142, 414, doi: [10.1086/148306](https://doi.org/10.1086/148306)
- [140] Dickinson, C. 2018, Large-Scale Features of the Radio Sky and a Model for Loop I, *Galaxies*, 6, 56, doi: [10.3390/galaxies6020056](https://doi.org/10.3390/galaxies6020056)
- [141] Dickinson, C., Davies, R. D., & Davis, R. J. 2003, Towards a free-free template for CMB foregrounds, *Monthly Notices of the Royal Astronomical Society*, 341, 369, doi: [10.1046/j.1365-8711.2003.06439.x](https://doi.org/10.1046/j.1365-8711.2003.06439.x)
- [142] Diego-Palazuelos, P., Eskilt, J. R., Minami, Y., et al. 2022, Cosmic Birefringence from Planck Public Release 4, arXiv e-prints, arXiv:2203.04830, doi: [10.48550/arXiv.2203.04830](https://doi.org/10.48550/arXiv.2203.04830)
- [143] Diego-Palazuelos, P., Martínez-González, E., Vielva, P., et al. 2023, Robustness of cosmic birefringence measurement against Galactic foreground emission and instrumental systematics, *J. Cosmology Astropart. Phys.*, 2023, 044, doi: [10.1088/1475-7516/2023/01/044](https://doi.org/10.1088/1475-7516/2023/01/044)
- [144] Dodelson, S. 2003, Modern cosmology
- [145] Dolginov, A. Z., & Mitrofanov, I. G. 1976, Orientation of Cosmic Dust Grains, *Astrophysics and space science*, 43, 291, doi: [10.1007/BF00640010](https://doi.org/10.1007/BF00640010)
- [146] Draine, B. T. 1978, Photoelectric heating of interstellar gas., *The Astrophysical Journal*, 36, 595, doi: [10.1086/190513](https://doi.org/10.1086/190513)
- [147] —. 2003, Interstellar Dust Grains, 41, 241, doi: [10.1146/annurev.astro.41.011802.094840](https://doi.org/10.1146/annurev.astro.41.011802.094840)
- [148] —. 2011, Physics of the Interstellar and Intergalactic Medium

BIBLIOGRAPHY

- [149] Draine, B. T., & Lazarian, A. 1998, Electric Dipole Radiation from Spinning Dust Grains, *The Astrophysical Journal*, 508, 157, doi: [10.1086/306387](https://doi.org/10.1086/306387)
- [150] Draine, B. T., & Weingartner, J. C. 1996, Radiative Torques on Interstellar Grains. I. Superthermal Spin-up, *The Astrophysical Journal*, 470, 551, doi: [10.1086/177887](https://doi.org/10.1086/177887)
- [151] Dreissen, L. S., Yeh, C.-H., Fürst, H. A., Grensemann, K. C., & Mehlstäubler, T. E. 2022, Improved bounds on Lorentz violation from composite pulse Ramsey spectroscopy in a trapped ion, *Nature Communications*, 13, 7314, doi: [10.1038/s41467-022-34818-0](https://doi.org/10.1038/s41467-022-34818-0)
- [152] Dressel, J., Bliokh, K. Y., & Nori, F. 2015, Spacetime algebra as a powerful tool for electromagnetism, *Phys. Rep.*, 589, 1, doi: [10.1016/j.physrep.2015.06.001](https://doi.org/10.1016/j.physrep.2015.06.001)
- [153] Duff, M. J. 1996, M Theory (the Theory Formerly Known as Strings), *International Journal of Modern Physics A*, 11, 5623, doi: [10.1142/S0217751X96002583](https://doi.org/10.1142/S0217751X96002583)
- [154] —. 2002, Comment on time-variation of fundamental constants, arXiv e-prints, hep, doi: [10.48550/arXiv.hep-th/0208093](https://arxiv.org/abs/hep-th/0208093)
- [155] —. 2015, How fundamental are fundamental constants?, *Contemporary Physics*, 56, 35, doi: [10.1080/00107514.2014.980093](https://doi.org/10.1080/00107514.2014.980093)
- [156] Duff, M. J., Okun, L. B., & Veneziano, G. 2002, Trialogue on the number of fundamental constants, *Journal of High Energy Physics*, 2002, 023, doi: [10.1088/1126-6708/2002/03/023](https://doi.org/10.1088/1126-6708/2002/03/023)
- [157] Dvali, G., & Zaldarriaga, M. 2002, Changing α with Time: Implications for Fifth-Force-Type Experiments and Quintessence, *Physical Review Letters*, 88, 091303, doi: [10.1103/PhysRevLett.88.091303](https://doi.org/10.1103/PhysRevLett.88.091303)
- [158] Dwek, E., & Cherchneff, I. 2011, The Origin of Dust in the Early Universe: Probing the Star Formation History of Galaxies by Their Dust Content, *The Astrophysical Journal*, 727, 63, doi: [10.1088/0004-637X/727/2/63](https://doi.org/10.1088/0004-637X/727/2/63)
- [159] Ehle, M. 2005, in *The Magnetized Plasma in Galaxy Evolution*, ed. K. T. Chyzy, K. Otmianowska-Mazur, M. Soida, & R.-J. Dettmar, 31–38
- [160] Einstein, A. 1905, On the electrodynamics of moving bodies, *Annalen Phys.*, 17, 891, doi: [10.1002/andp.200590006](https://doi.org/10.1002/andp.200590006)
- [161] Ellis, G. F. R., & Uzan, J.-P. 2005, c is the speed of light, isn't it?, *American Journal of Physics*, 73, 240, doi: [10.1119/1.1819929](https://doi.org/10.1119/1.1819929)
- [162] Eriksen, H. K., Jewell, J. B., Dickinson, C., et al. 2008, Joint Bayesian Component Separation and CMB Power Spectrum Estimation, *The Astrophysical Journal*, 676, 10, doi: [10.1086/525277](https://doi.org/10.1086/525277)
- [163] Errard, J. 2012, A hunt for cosmic microwave background B-modes in the systematic contaminants jungle (FRCEA-TH-3920).
- [164] Errard, J., Remazeilles, M., Aumont, J., et al. 2022, Constraints on the Optical Depth to Reionization from Balloon-borne Cosmic Microwave Background Measurements, *The Astrophysical Journal*, 940, 68, doi: [10.3847/1538-4357/ac9978](https://doi.org/10.3847/1538-4357/ac9978)

BIBLIOGRAPHY

- [165] Errard, J., Stivoli, F., & Stompor, R. 2011, Publisher’s Note: Framework for performance forecasting and optimization of CMB B -mode observations in the presence of astrophysical foregrounds [Phys. Rev. D 84, 063005 (2011)], Phys. Rev. D, 84, 069907, doi: [10.1103/PhysRevD.84.069907](https://doi.org/10.1103/PhysRevD.84.069907)
- [166] Eskilt, J. R. 2022, Frequency-dependent constraints on cosmic birefringence from the LFI and HFI Planck Data Release 4, Astronomy and Astrophysics, 662, A10, doi: [10.1051/0004-6361/202243269](https://doi.org/10.1051/0004-6361/202243269)
- [167] Esposito-Farèse, G. 2004, in American Institute of Physics Conference Series, Vol. 736, Phi in the Sky: The Quest for Cosmological Scalar Fields, ed. C. J. A. P. Martins, P. P. Avelino, M. S. Costa, K. Mack, M. F. Mota, & M. Parry, 35–52, doi: [10.1063/1.1835173](https://doi.org/10.1063/1.1835173)
- [168] Fadeev, P., Berengut, J. C., & Flambaum, V. V. 2020, Sensitivity of ^{229}Th nuclear clock transition to variation of the fine-structure constant, Phys. Rev. A., 102, 052833, doi: [10.1103/PhysRevA.102.052833](https://doi.org/10.1103/PhysRevA.102.052833)
- [169] Faison, M. D., & Goss, W. M. 2001, The Structure of the Cold Neutral Interstellar Medium on 10-100 AU Scales, The Astronomical Journal, 121, 2706, doi: [10.1086/320369](https://doi.org/10.1086/320369)
- [170] Famaey, B., & McGaugh, S. S. 2012, Modified Newtonian Dynamics (MOND): Observational Phenomenology and Relativistic Extensions, Living Reviews in Relativity, 15, 10, doi: [10.12942/lrr-2012-10](https://doi.org/10.12942/lrr-2012-10)
- [171] Faraoni, V., & Nadeau, S. 2007, (Pseudo)issue of the conformal frame revisited, Phys. Rev. D., 75, 023501, doi: [10.1103/PhysRevD.75.023501](https://doi.org/10.1103/PhysRevD.75.023501)
- [172] Farrar, G. R., Awal, N., Khurana, D., & Sutherland, M. 2015, The Galactic Magnetic Field and UHECR Optics, arXiv e-prints, arXiv:1508.04530, doi: [10.48550/arXiv.1508.04530](https://doi.org/10.48550/arXiv.1508.04530)
- [173] Faure, F. 2021a, Introduction à la géométrie et la topologie des espaces fibrés en physique. <https://www-fourier.ujf-grenoble.fr/~faure/>
- [174] —. 2021b, Notes de cours en Physique mathématique. <https://www-fourier.ujf-grenoble.fr/~faure/>
- [175] Feng, B., Li, M., Xia, J.-Q., Chen, X., & Zhang, X. 2006, Searching for CPT Violation with Cosmic Microwave Background Data from WMAP and BOOMERANG, Physical Review Letters, 96, 221302, doi: [10.1103/PhysRevLett.96.221302](https://doi.org/10.1103/PhysRevLett.96.221302)
- [176] Fernández-Cobos, R., Vielva, P., Barreiro, R. B., & Martínez-González, E. 2012, Multiresolution internal template cleaning: an application to the Wilkinson Microwave Anisotropy Probe 7-yr polarization data, Monthly Notices of the Royal Astronomical Society, 420, 2162, doi: [10.1111/j.1365-2966.2011.20182.x](https://doi.org/10.1111/j.1365-2966.2011.20182.x)
- [177] Fernández-Jambrina, L. 2021, Singularities in Inflationary Cosmological Models, Universe, 7, 491, doi: [10.3390/universe7120491](https://doi.org/10.3390/universe7120491)
- [178] Ferrara, S., Kallosh, R., Linde, A., & Porrati, M. 2013, Minimal supergravity models of inflation, Phys. Rev. D., 88, 085038, doi: [10.1103/PhysRevD.88.085038](https://doi.org/10.1103/PhysRevD.88.085038)

BIBLIOGRAPHY

- [179] Ferrière, K. M. 2001, The interstellar environment of our galaxy, *Reviews of Modern Physics*, 73, 1031, doi: [10.1103/RevModPhys.73.1031](https://doi.org/10.1103/RevModPhys.73.1031)
- [180] Feynman, R. P., Feynman, R. P., & Weinberg, S. 1987, The reason for antiparticles (Cambridge University Press), 1–60, doi: [10.1017/CBO9781107590076.002](https://doi.org/10.1017/CBO9781107590076.002)
- [181] Fields, B. D. 2011, The Primordial Lithium Problem, *Annual Review of Nuclear and Particle Science*, 61, 47, doi: [10.1146/annurev-nucl-102010-130445](https://doi.org/10.1146/annurev-nucl-102010-130445)
- [182] Fields, B. D., Molaro, P., & Sarkar, S. 2014, Big-Bang Nucleosynthesis, *Chin. Phys. C*, 38, 339. <https://arxiv.org/abs/1412.1408>
- [183] Filzinger, M., Dörscher, S., Lange, R., et al. 2023, Improved limits on the coupling of ultralight bosonic dark matter to photons from optical atomic clock comparisons, arXiv e-prints, arXiv:2301.03433, doi: [10.48550/arXiv.2301.03433](https://doi.org/10.48550/arXiv.2301.03433)
- [184] Fixsen, D. J. 2009, The Temperature of the Cosmic Microwave Background, *The Astrophysical Journal*, 707, 916, doi: [10.1088/0004-637X/707/2/916](https://doi.org/10.1088/0004-637X/707/2/916)
- [185] Fixsen, D. J., & Mather, J. C. 2002, The Spectral Results of the Far-Infrared Absolute Spectrophotometer Instrument on COBE, *The Astrophysical Journal*, 581, 817, doi: [10.1086/344402](https://doi.org/10.1086/344402)
- [186] Flambaum, V., Lambert, S., & Pospelov, M. 2009, Scalar-tensor theories with pseudoscalar couplings, *Phys. Rev. D.*, 80, 105021, doi: [10.1103/PhysRevD.80.105021](https://doi.org/10.1103/PhysRevD.80.105021)
- [187] Fleury, P., Dupuy, H., & Uzan, J.-P. 2013, Interpretation of the Hubble diagram in a nonhomogeneous universe, *Phys. Rev. D.*, 87, 123526, doi: [10.1103/PhysRevD.87.123526](https://doi.org/10.1103/PhysRevD.87.123526)
- [188] Frampton, P. H., Kawasaki, M., Takahashi, F., & Yanagida, T. T. 2010, Primordial black holes as all dark matter, *J. Cosmology Astropart. Phys.*, 2010, 023, doi: [10.1088/1475-7516/2010/04/023](https://doi.org/10.1088/1475-7516/2010/04/023)
- [189] Frankel, Theodore; Mayer, M. E. 1998, The Geometry of Physics: An Introduction, *Physics Today* vol. 51 iss. 12, 51, doi: [10.1063/1.882494](https://doi.org/10.1063/1.882494)
- [190] Friedmann, A. 1922, Über die Krümmung des Raumes, *Zeitschrift für Physik*, 10, 377, doi: [10.1007/BF01332580](https://doi.org/10.1007/BF01332580)
- [191] Fujii, Y., & Iwamoto, A. 2005, How Strongly does Dating Meteorites Constrain the Time-Dependence of the Fine-Structure Constant?, *Modern Physics Letters A*, 20, 2417, doi: [10.1142/S0217732305018499](https://doi.org/10.1142/S0217732305018499)
- [192] Fujita, T., Minami, Y., Shiraishi, M., & Yokoyama, S. 2022, Can primordial parity violation explain the observed cosmic birefringence?, *Phys. Rev. D.*, 106, 103529, doi: [10.1103/PhysRevD.106.103529](https://doi.org/10.1103/PhysRevD.106.103529)
- [193] Fuskeland, U., Aumont, J., Aurlien, R., et al. 2023, Tensor-to-scalar ratio forecasts for extended LiteBIRD frequency configurations, arXiv e-prints, arXiv:2302.05228, doi: [10.48550/arXiv.2302.05228](https://doi.org/10.48550/arXiv.2302.05228)
- [194] Galileo Galilei. 1632, "Dialogue Concerning the Two Chief World Systems "

BIBLIOGRAPHY

- [195] Galitzki, N., Ali, A., Arnold, K. S., et al. 2018, in Society of Photo-Optical Instrumentation Engineers (SPIE) Conference Series, Vol. 10708, Millimeter, Submillimeter, and Far-Infrared Detectors and Instrumentation for Astronomy IX, ed. J. Zmuidzinas & J.-R. Gao, 1070804, doi: [10.1117/12.2312985](https://doi.org/10.1117/12.2312985)
- [196] Galli, S., Martins, C. J. A. P., Melchiorri, A., & Menegoni, E. 2011, in Astrophysics and Space Science Proceedings, Vol. 22, From Varying Couplings to Fundamental Physics, 59, doi: [10.1007/978-3-642-19397-2_7](https://doi.org/10.1007/978-3-642-19397-2_7)
- [197] Gamow, G. 1948, The Evolution of the Universe, Nature, 162, 680, doi: [10.1038/162680a0](https://doi.org/10.1038/162680a0)
- [198] Ganga, K., Maris, M., Remazeilles, M., & LiteBIRD Collaboration. 2021, Interplanetary Dust as a Foreground for the LiteBIRD CMB Satellite Mission, The Open Journal of Astrophysics, 4, 16, doi: [10.21105/astro.2110.13856](https://doi.org/10.21105/astro.2110.13856)
- [199] Gangui, A. 2001, Topological Defects in Cosmology, arXiv e-prints, astro. <https://arxiv.org/abs/astro-ph/0110285>
- [200] Gasperini, M., Piazza, F., & Veneziano, G. 2001, Quintessence as a runaway dilaton, Phys. Rev. D., 65, 023508, doi: [10.1103/PhysRevD.65.023508](https://doi.org/10.1103/PhysRevD.65.023508)
- [201] Glashow, S. L. 1961, Partial Symmetries of Weak Interactions, Nucl. Phys., 22, 579, doi: [10.1016/0029-5582\(61\)90469-2](https://doi.org/10.1016/0029-5582(61)90469-2)
- [202] Gold, B., Odegard, N., Weiland, J. L., et al. 2011, Seven-year Wilkinson Microwave Anisotropy Probe (WMAP) Observations: Galactic Foreground Emission, ApJ Supplements, 192, 15, doi: [10.1088/0067-0049/192/2/15](https://doi.org/10.1088/0067-0049/192/2/15)
- [203] Goldberg, J. N., Macfarlane, A. J., Newman, E. T., Rohrlich, F., & Sudarshan, E. C. G. 1967, Spin-s Spherical Harmonics and $\bar{\partial}$, Journal of Mathematical Physics, 8, 2155, doi: [10.1063/1.1705135](https://doi.org/10.1063/1.1705135)
- [204] Górski, K. M., Hivon, E., Banday, A. J., et al. 2005, HEALPix: A Framework for High-Resolution Discretization and Fast Analysis of Data Distributed on the Sphere, The Astrophysical Journal, 622, 759, doi: [10.1086/427976](https://doi.org/10.1086/427976)
- [205] Gould, C. R., Sharapov, E. I., & Lamoreaux, S. K. 2006, Time variability of α from realistic models of Oklo reactors, Phys. Rev. C, 74, 024607, doi: [10.1103/PhysRevC.74.024607](https://doi.org/10.1103/PhysRevC.74.024607)
- [206] Grozier, J. 2020, Should physical laws be unit-invariant?, Studies in History and Philosophy of Science, 80, 9, doi: [10.1016/j.shpsa.2018.12.009](https://doi.org/10.1016/j.shpsa.2018.12.009)
- [207] Guillet, V., Vacher, L., Ritacco, A., et al. 2023, Analyzing *Planck* polarization data using complex fluctuations of the dust temperature and spectral index, to be submitted
- [208] Guillet, V., Fanciullo, L., Verstraete, L., et al. 2018, Dust models compatible with Planck intensity and polarization data in translucent lines of sight, Astronomy and Astrophysics, 610, A16, doi: [10.1051/0004-6361/201630271](https://doi.org/10.1051/0004-6361/201630271)

BIBLIOGRAPHY

- [209] Guth, A. H. 2007, Eternal inflation and its implications, *Journal of Physics A Mathematical General*, 40, 6811, doi: [10.1088/1751-8113/40/25/S25](https://doi.org/10.1088/1751-8113/40/25/S25)
- [210] Halverson, J., Long, C., & Sung, B. 2017, Algorithmic universality in F-theory compactifications, *Phys. Rev. D.*, 96, 126006, doi: [10.1103/PhysRevD.96.126006](https://doi.org/10.1103/PhysRevD.96.126006)
- [211] Hambleton, K. M., Bianco, F. B., Street, R., et al. 2022, Rubin Observatory LSST Transients and Variable Stars Roadmap, arXiv e-prints, arXiv:2208.04499, doi: [10.48550/arXiv.2208.04499](https://doi.org/10.48550/arXiv.2208.04499)
- [212] Hambye, T. 2012, CP violation and the matter-antimatter asymmetry of the Universe, *Comptes Rendus Physique*, 13, 193, doi: [10.1016/j.crhy.2011.09.007](https://doi.org/10.1016/j.crhy.2011.09.007)
- [213] Hamilton, J. C., Mousset, L., Battistelli, E. S., et al. 2022, QUBIC I: Overview and science program, *J. Cosmology Astropart. Phys.*, 2022, 034, doi: [10.1088/1475-7516/2022/04/034](https://doi.org/10.1088/1475-7516/2022/04/034)
- [214] Hanany, S., Alvarez, M., Artis, E., et al. 2019, PICO: Probe of Inflation and Cosmic Origins, arXiv e-prints, arXiv:1902.10541, doi: [10.48550/arXiv.1902.10541](https://doi.org/10.48550/arXiv.1902.10541)
- [215] Harries, T. J., Monnier, J. D., Symington, N. H., & Kurosawa, R. 2004, Three-dimensional dust radiative-transfer models: the Pinwheel Nebula of WR 104, *Monthly Notices of the Royal Astronomical Society*, 350, 565, doi: [10.1111/j.1365-2966.2004.07668.x](https://doi.org/10.1111/j.1365-2966.2004.07668.x)
- [216] Hart, L., & Chluba, J. 2018, New constraints on time-dependent variations of fundamental constants using Planck data, *Monthly Notices of the Royal Astronomical Society*, 474, 1850, doi: [10.1093/mnras/stx2783](https://doi.org/10.1093/mnras/stx2783)
- [217] —. 2022, Varying fundamental constants principal component analysis: additional hints about the Hubble tension, *Monthly Notices of the Royal Astronomical Society*, 510, 2206, doi: [10.1093/mnras/stab2777](https://doi.org/10.1093/mnras/stab2777)
- [218] —. 2023, Using the cosmological recombination radiation to probe early dark energy and fundamental constant variations, *Monthly Notices of the Royal Astronomical Society*, 519, 3664, doi: [10.1093/mnras/stac3697](https://doi.org/10.1093/mnras/stac3697)
- [219] Hasebe, T., Ade, P. A. R., Adler, A., et al. 2022, Sensitivity Modeling for LiteBIRD, *Journal of Low Temperature Physics*, doi: [10.1007/s10909-022-02921-7](https://doi.org/10.1007/s10909-022-02921-7)
- [220] Haslam, C. G. T., Klein, U., Salter, C. J., et al. 1981, A 408 MHz all-sky continuum survey. I - Observations at southern declinations and for the North Polar region., *Astronomy and Astrophysics*, 100, 209
- [221] Havas, P. 1964, Four-Dimensional Formulations of Newtonian Mechanics and Their Relation to the Special and the General Theory of Relativity, *Rev. Mod. Phys.*, 36, 938, doi: [10.1103/RevModPhys.36.938](https://doi.org/10.1103/RevModPhys.36.938)
- [222] Hawking, S. W. 1966, Singularities in the Universe, *Phys. Rev. Lett.*, 17, 444, doi: [10.1103/PhysRevLett.17.444](https://doi.org/10.1103/PhysRevLett.17.444)
- [223] Healey, R. 2007, Gauging What's Real: The Conceptual Foundations of Contemporary Gauge Theories (Oxford University Press)

BIBLIOGRAPHY

- [224] Held, A., Newman, E. T., & Posadas, R. 1970, The Lorentz Group and the Sphere, *Journal of Mathematical Physics*, 11, 3145, doi: [10.1063/1.1665105](https://doi.org/10.1063/1.1665105)
- [225] Henderson, S. W., Allison, R., Austermann, J., et al. 2016, Advanced ACTPol Cryogenic Detector Arrays and Readout, *Journal of Low Temperature Physics*, 184, 772, doi: [10.1007/s10909-016-1575-z](https://doi.org/10.1007/s10909-016-1575-z)
- [226] Henning, T., & Mutschke, H. 1997, Low-temperature infrared properties of cosmic dust analogues., *Astronomy and Astrophysics*, 327, 743
- [227] Hensley, B. S., & Draine, B. T. 2023, The Astrodust+PAH Model: A Unified Description of the Extinction, Emission, and Polarization from Dust in the Diffuse Interstellar Medium, *The Astrophysical Journal*, 948, 55, doi: [10.3847/1538-4357/acc4c2](https://doi.org/10.3847/1538-4357/acc4c2)
- [228] Hoang, T., & Lazarian, A. 2016, A Unified Model of Grain Alignment: Radiative Alignment of Interstellar Grains with Magnetic Inclusions, *The Astrophysical Journal*, 831, 159, doi: [10.3847/0004-637X/831/2/159](https://doi.org/10.3847/0004-637X/831/2/159)
- [229] Hoffman, Y., Pomarède, D., Tully, R. B., & Courtois, H. M. 2017, The dipole repeller, *Nature Astronomy*, 1, 0036, doi: [10.1038/s41550-016-0036](https://doi.org/10.1038/s41550-016-0036)
- [230] Höfner, S. 2009, in *Astronomical Society of the Pacific Conference Series*, Vol. 414, Cosmic Dust - Near and Far, ed. T. Henning, E. Grün, & J. Steinacker, 3. <https://arxiv.org/abs/0903.5280>
- [231] Höfner, S., & Olofsson, H. 2018, Mass loss of stars on the asymptotic giant branch. Mechanisms, models and measurements, 26, 1, doi: [10.1007/s00159-017-0106-5](https://doi.org/10.1007/s00159-017-0106-5)
- [232] Holz, D. E., & Hughes, S. A. 2005, Using Gravitational-Wave Standard Sirens, *The Astrophysical Journal*, 629, 15, doi: [10.1086/431341](https://doi.org/10.1086/431341)
- [233] Hoseinpour, A., Zarei, M., Orlando, G., Bartolo, N., & Matarrese, S. 2020, CMB V modes from photon-photon forward scattering revisited, *Phys. Rev. D*, 102, 063501, doi: [10.1103/PhysRevD.102.063501](https://doi.org/10.1103/PhysRevD.102.063501)
- [234] Howlett, C., Robotham, A. S. G., Lagos, C. D. P., & Kim, A. G. 2017, Measuring the Growth Rate of Structure with Type IA Supernovae from LSST, *The Astrophysical Journal*, 847, 128, doi: [10.3847/1538-4357/aa88c8](https://doi.org/10.3847/1538-4357/aa88c8)
- [235] Hoyle, F., & Ellis, G. R. A. 1963, On the Existence of an Ionized Layer about the Galactic Plane, *Australian Journal of Physics*, 16, 1, doi: [10.1071/PH630001](https://doi.org/10.1071/PH630001)
- [236] Hu, W., & White, M. 1997, A CMB polarization primer, 2, 323, doi: [10.1016/S1384-1076\(97\)00022-5](https://doi.org/10.1016/S1384-1076(97)00022-5)
- [237] Hubble, E., & Humason, M. L. 1931, The Velocity-Distance Relation among Extra-Galactic Nebulae, *The Astrophysical Journal*, 74, 43, doi: [10.1086/143323](https://doi.org/10.1086/143323)
- [238] Hubble, E., & Tolman, R. C. 1935, Two Methods of Investigating the Nature of the Nebular Redshift, *The Astrophysical Journal*, 82, 302, doi: [10.1086/143682](https://doi.org/10.1086/143682)
- [239] Hubble, E. P. 1926, Extragalactic nebulae., *The Astrophysical Journal*, 64, 321, doi: [10.1086/143018](https://doi.org/10.1086/143018)

BIBLIOGRAPHY

- [240] Hubmayr, J., Ade, P. A. R., Adler, A., et al. 2022, Optical Characterization of OMT-Coupled TES Bolometers for LiteBIRD, *Journal of Low Temperature Physics*, 209, 396, doi: [10.1007/s10909-022-02808-7](https://doi.org/10.1007/s10909-022-02808-7)
- [241] Huffenberger, K. M., Rotti, A., & Collins, D. C. 2020, The Power Spectra of Polarized, Dusty Filaments, *The Astrophysical Journal*, 899, 31, doi: [10.3847/1538-4357/ab9df9](https://doi.org/10.3847/1538-4357/ab9df9)
- [242] Huterer, D. 2022, Growth of Cosmic Structure, arXiv e-prints, arXiv:2212.05003, doi: [10.48550/arXiv.2212.05003](https://doi.org/10.48550/arXiv.2212.05003)
- [243] Hutton, S., Ferreras, I., & Yershov, V. 2015, Variations of the dust properties of M82 with galactocentric distance, *Monthly Notices of the Royal Astronomical Society*, 452, 1412, doi: [10.1093/mnras/stv1335](https://doi.org/10.1093/mnras/stv1335)
- [244] Ichiki, K., Kanai, H., Katayama, N., & Komatsu, E. 2019, Delta-map method of removing CMB foregrounds with spatially varying spectra, *Progress of Theoretical and Experimental Physics*, 2019, 033E01, doi: [10.1093/ptep/ptz009](https://doi.org/10.1093/ptep/ptz009)
- [245] Inoue, Y., Ade, P., Akiba, Y., et al. 2016, in Society of Photo-Optical Instrumentation Engineers (SPIE) Conference Series, Vol. 9914, Millimeter, Submillimeter, and Far-Infrared Detectors and Instrumentation for Astronomy VIII, ed. W. S. Holland & J. Zmuidzinas, 99141I, doi: [10.1117/12.2231961](https://doi.org/10.1117/12.2231961)
- [246] Ivanenko, D., & Sardanashvily, G. 1983, The Gauge Treatment of Gravity, *Phys. Rept.*, 94, 1, doi: [10.1016/0370-1573\(83\)90046-7](https://doi.org/10.1016/0370-1573(83)90046-7)
- [247] Jackson, J. D. 1998, Classical Electrodynamics, 3rd Edition
- [248] Jacobson, T. 1995, Thermodynamics of Spacetime: The Einstein Equation of State, *Physical Review Letters*, 75, 1260, doi: [10.1103/PhysRevLett.75.1260](https://doi.org/10.1103/PhysRevLett.75.1260)
- [249] Jaffe, T. R., Ferrière, K. M., Banday, A. J., et al. 2013, Comparing polarized synchrotron and thermal dust emission in the Galactic plane, *Monthly Notices of the Royal Astronomical Society*, 431, 683, doi: [10.1093/mnras/stt200](https://doi.org/10.1093/mnras/stt200)
- [250] Jansson, R., & Farrar, G. R. 2012, A New Model of the Galactic Magnetic Field, *The Astrophysical Journal*, 757, 14, doi: [10.1088/0004-637X/757/1/14](https://doi.org/10.1088/0004-637X/757/1/14)
- [251] Jin, M., & Garrod, R. T. 2020, Formation of Complex Organic Molecules in Cold Interstellar Environments through Nondiffusive Grain-surface and Ice-mantle Chemistry, *ApJ Supplements*, 249, 26, doi: [10.3847/1538-4365/ab9ec8](https://doi.org/10.3847/1538-4365/ab9ec8)
- [252] Jones, B. J. T. 2017, Precision Cosmology
- [253] Kallosh, R., Linde, A., Wräse, T., & Yamada, Y. 2017, Maximal supersymmetry and B-mode targets, *Journal of High Energy Physics*, 2017, 144, doi: [10.1007/JHEP04\(2017\)144](https://doi.org/10.1007/JHEP04(2017)144)
- [254] Kaluza, T. 1921, Zum Unitätsproblem in der Physik., Preuss. Akad. Wiss. Berlin. (Math. Phys.), 966
- [255] Kamionkowski, M., Kosowsky, A., & Stebbins, A. 1997, Statistics of cosmic microwave background polarization, *Phys. Rev. D.*, 55, 7368, doi: [10.1103/PhysRevD.55.7368](https://doi.org/10.1103/PhysRevD.55.7368)

BIBLIOGRAPHY

- [256] Kamionkowski, M., & Kovetz, E. D. 2016, The Quest for B Modes from Inflationary Gravitational Waves, *Annual Review of Astronomy and Astrophysics*, 54, 227, doi: [10.1146/annurev-astro-081915-023433](https://doi.org/10.1146/annurev-astro-081915-023433)
- [257] Katz, J. 2005, Gravitational energy, *Classical and Quantum Gravity*, 22, 5169, doi: [10.1088/0264-9381/22/23/016](https://doi.org/10.1088/0264-9381/22/23/016)
- [258] Kermish, Z. D., Ade, P., Anthony, A., et al. 2012, in Society of Photo-Optical Instrumentation Engineers (SPIE) Conference Series, Vol. 8452, Millimeter, Submillimeter, and Far-Infrared Detectors and Instrumentation for Astronomy VI, ed. W. S. Holland & J. Zmuidzinas, 84521C, doi: [10.1117/12.926354](https://doi.org/10.1117/12.926354)
- [259] Khatri, R., & Wandelt, B. D. 2007, 21 cm radiation: A new probe of variation in the fine structure constant, *Phys. Rev. Lett.*, 98, 111301, doi: [10.1103/PhysRevLett.98.111301](https://doi.org/10.1103/PhysRevLett.98.111301)
- [260] Khoury, J., Ovrut, B. A., Steinhardt, P. J., & Turok, N. 2001, Ekpyrotic universe: Colliding branes and the origin of the hot big bang, *Phys. Rev. D.*, 64, 123522, doi: [10.1103/PhysRevD.64.123522](https://doi.org/10.1103/PhysRevD.64.123522)
- [261] Khoury, J., & Weltman, A. 2004, Chameleon cosmology, *Phys. Rev. D.*, 69, 044026, doi: [10.1103/PhysRevD.69.044026](https://doi.org/10.1103/PhysRevD.69.044026)
- [262] Kibble, T. W. B. 1961, Lorentz Invariance and the Gravitational Field, *Journal of Mathematical Physics*, 2, 212, doi: [10.1063/1.1703702](https://doi.org/10.1063/1.1703702)
- [263] Kitching, T. D., Heavens, A. F., & Das, S. 2015, 3D weak gravitational lensing of the CMB and galaxies, *Monthly Notices of the Royal Astronomical Society*, 449, 2205, doi: [10.1093/mnras/stv193](https://doi.org/10.1093/mnras/stv193)
- [264] Klein, O. 1926, The Atomicity of Electricity as a Quantum Theory Law, *Nature*, 118, 516, doi: [10.1038/118516a0](https://doi.org/10.1038/118516a0)
- [265] Kogut, A., Fixsen, D. J., Chuss, D. T., et al. 2011, The Primordial Inflation Explorer (PIXIE): a nulling polarimeter for cosmic microwave background observations, *J. Cosmology Astropart. Phys.*, 2011, 025, doi: [10.1088/1475-7516/2011/07/025](https://doi.org/10.1088/1475-7516/2011/07/025)
- [266] Komatsu, E., Dunkley, J., Nolta, M. R., et al. 2009, Five-Year Wilkinson Microwave Anisotropy Probe Observations: Cosmological Interpretation, *ApJ Supplements*, 180, 330, doi: [10.1088/0067-0049/180/2/330](https://doi.org/10.1088/0067-0049/180/2/330)
- [267] Kostelecký, V. A., & Mewes, M. 2016, Testing local Lorentz invariance with gravitational waves, *Physics Letters B*, 757, 510, doi: [10.1016/j.physletb.2016.04.040](https://doi.org/10.1016/j.physletb.2016.04.040)
- [268] Krachmalnicoff, N., Baccigalupi, C., Aumont, J., Bersanelli, M., & Mennella, A. 2016, Characterization of foreground emission on degree angular scales for CMB B-mode observations . Thermal dust and synchrotron signal from Planck and WMAP data, *Astronomy and Astrophysics*, 588, A65, doi: [10.1051/0004-6361/201527678](https://doi.org/10.1051/0004-6361/201527678)
- [269] Krachmalnicoff, N., & Puglisi, G. 2021, ForSE: A GAN-based Algorithm for Extending CMB Foreground Models to Subdegree Angular Scales, *The Astrophysical Journal*, 911, 42, doi: [10.3847/1538-4357/abe71c](https://doi.org/10.3847/1538-4357/abe71c)

BIBLIOGRAPHY

- [270] Krachmalnicoff, N., Carretti, E., Baccigalupi, C., et al. 2018, S-PASS view of polarized Galactic synchrotron at 2.3 GHz as a contaminant to CMB observations, *Astronomy and Astrophysics*, 618, A166, doi: [10.1051/0004-6361/201832768](https://doi.org/10.1051/0004-6361/201832768)
- [271] Krachmalnicoff, N., Matsumura, T., de la Hoz, E., et al. 2022, In-flight polarization angle calibration for LiteBIRD: blind challenge and cosmological implications, *J. Cosmology Astropart. Phys.*, 2022, 039, doi: [10.1088/1475-7516/2022/01/039](https://doi.org/10.1088/1475-7516/2022/01/039)
- [272] Kragh, H. 1996, *Cosmology and Controversy: The Historical Development of Two Theories of the Universe* (Princeton University Press). <http://www.jstor.org/stable/j.ctv1ddd0wx>
- [273] Kuchowicz, B. 1978, Friedmann-like cosmological models without singularity, *General Relativity and Gravitation*, 9, 511, doi: [10.1007/BF00759545](https://doi.org/10.1007/BF00759545)
- [274] Lallement, R. 2022, North Polar Spur/Loop I: gigantic outskirt of the Northern Fermi bubble or nearby hot gas cavity blown by supernovae?, arXiv e-prints, arXiv:2203.01312, doi: [10.48550/arXiv.2203.01312](https://doi.org/10.48550/arXiv.2203.01312)
- [275] Lamoreaux, S. K., Jacobs, J. P., Heckel, B. R., Raab, F. J., & Fortson, E. N. 1986, New limits on spatial anisotropy from optically-pumped sup ^{201}Hg and ^{199}Hg , *Phys. Rev. Lett.*, 57, 3125, doi: [10.1103/PhysRevLett.57.3125](https://doi.org/10.1103/PhysRevLett.57.3125)
- [276] Landau, L. 1969, *Statistical physics Volume 5, Part 1*, 3rd edn. (Pergamon)
- [277] Lange, R., Huntemann, N., Rahm, J. M., et al. 2021, Improved Limits for Violations of Local Position Invariance from Atomic Clock Comparisons, *Physical Review Letters*, 126, 011102, doi: [10.1103/PhysRevLett.126.011102](https://doi.org/10.1103/PhysRevLett.126.011102)
- [278] Lange, S., & Page, L. 2007, Detecting the Expansion of the Universe through Changes in the CMB Photosphere, *The Astrophysical Journal*, 671, 1075, doi: [10.1086/523097](https://doi.org/10.1086/523097)
- [279] Lasue, J., Levasseur-Regourd, A.-C., & Renard, J.-B. 2020, Zodiacal light observations and its link with cosmic dust: A review, *Planetary and Space Science*, 190, 104973, doi: [10.1016/j.pss.2020.104973](https://doi.org/10.1016/j.pss.2020.104973)
- [280] Lee, N., Ali-Haïmoud, Y., Schöneberg, N., & Poulin, V. 2023, What It Takes to Solve the Hubble Tension through Modifications of Cosmological Recombination, *Physical Review Letters*, 130, 161003, doi: [10.1103/PhysRevLett.130.161003](https://doi.org/10.1103/PhysRevLett.130.161003)
- [281] Lemaître, G. 1927, Un Univers homogène de masse constante et de rayon croissant rendant compte de la vitesse radiale des nébuleuses extra-galactiques, *Annales de la Société Scientifique de Bruxelles*, 47, 49
- [282] Lemaitre, G. 1949, L'Hypothèse de l'Atome Primitif, *Publications du Laboratoire d'Astronomie et de Géodésie de l'Université de Louvain*, 12, D1
- [283] Lenz, D., Doré, O., & Lagache, G. 2019, Large-scale Maps of the Cosmic Infrared Background from Planck, *The Astrophysical Journal*, 883, 75, doi: [10.3847/1538-4357/ab3c2b](https://doi.org/10.3847/1538-4357/ab3c2b)
- [284] Lesgourgues, J. 2001, Théorie linéaire des perturbations cosmologiques. https://lesgourg.github.io/courses/Perturbations_LAPTH.pdf

BIBLIOGRAPHY

- [285] Lesgourgues, J. 2011, The Cosmic Linear Anisotropy Solving System (CLASS) I: Overview. <https://arxiv.org/abs/1104.2932>
- [286] Lesgourgues, J. 2013, TASI Lectures on Cosmological Perturbations, arXiv e-prints, arXiv:1302.4640, doi: [10.48550/arXiv.1302.4640](https://doi.org/10.48550/arXiv.1302.4640)
- [287] Levi, M., Allen, L. E., Raichoor, A., et al. 2019, in Bulletin of the American Astronomical Society, Vol. 51, 57, doi: [10.48550/arXiv.1907.10688](https://doi.org/10.48550/arXiv.1907.10688)
- [288] Lévy-Leblond, J., & Sandoval, T. U. 2013, Sur la Nature Conceptuelle des Constantes Physiques, Cahiers Philosophiques, 4, 92, doi: [10.3917/caph.135.0092](https://doi.org/10.3917/caph.135.0092)
- [289] Liddle, A. R. 1995, Inflation as the unique causal mechanism for generating density perturbations on scales well above the Hubble radius, Phys. Rev. D., 51, R5347, doi: [10.1103/PhysRevD.51.R5347](https://doi.org/10.1103/PhysRevD.51.R5347)
- [290] Liddle, A. R., & Lyth, D. H. 2000, itshape Cosmological Inflation and Large-Scale Structure
- [291] Linde, A. D. 1986, Eternal Chaotic Inflation, Modern Physics Letters A, 1, 81, doi: [10.1142/S0217732386000129](https://doi.org/10.1142/S0217732386000129)
- [292] Linder, E. V. 2003, Exploring the expansion history of the universe, PRL, 90, 091301, doi: [10.1103/PhysRevLett.90.091301](https://doi.org/10.1103/PhysRevLett.90.091301)
- [293] LiteBIRD Collaboration. 2020, Updated Design of the CMB Polarization Experiment Satellite LiteBIRD, Journal of Low Temperature Physics, 199, 1107, doi: [10.1007/s10909-019-02329-w](https://doi.org/10.1007/s10909-019-02329-w)
- [294] LiteBIRD Collaboration, Ally, E., Arnold, K., et al. 2023, Probing cosmic inflation with the LiteBIRD cosmic microwave background polarization survey, Progress of Theoretical and Experimental Physics, 2023, 042F01, doi: [10.1093/ptep/ptac150](https://doi.org/10.1093/ptep/ptac150)
- [295] Liu, H., von Hausegger, S., & Naselsky, P. 2017, Towards understanding the Planck thermal dust models, Phys. Rev. D., 95, 103517, doi: [10.1103/PhysRevD.95.103517](https://doi.org/10.1103/PhysRevD.95.103517)
- [296] Lopez-Honorez, L., Mena, O., Palomares-Ruiz, S., Villanueva-Domingo, P., & Witte, S. J. 2020, Variations in fundamental constants at the cosmic dawn, J. Cosmology Astropart. Phys., 2020, 026, doi: [10.1088/1475-7516/2020/06/026](https://doi.org/10.1088/1475-7516/2020/06/026)
- [297] Lopresto, J. C., Schrader, C., & Pierce, A. K. 1991, Solar Gravitational Redshift from the Infrared Oxygen Triplet, The Astrophysical Journal, 376, 757, doi: [10.1086/170323](https://doi.org/10.1086/170323)
- [298] Lorentz, H. A. 1895, "Versuch einer Theorie der electrischen und optischen Erscheinungen in bewegten Körpern."
- [299] Lovelock, D. 1972, The Four-Dimensionality of Space and the Einstein Tensor, Journal of Mathematical Physics, 13, 874, doi: [10.1063/1.1666069](https://doi.org/10.1063/1.1666069)
- [300] Lue, A., Wang, L., & Kamionkowski, M. 1999, Cosmological Signature of New Parity-Violating Interactions, Physical Review Letters, 83, 1506, doi: [10.1103/PhysRevLett.83.1506](https://doi.org/10.1103/PhysRevLett.83.1506)

BIBLIOGRAPHY

- [301] Luzzi, G., Shimon, M., Lamagna, L., et al. 2009, Redshift Dependence of the Cosmic Microwave Background Temperature from Sunyaev-Zeldovich Measurements, *The Astrophysical Journal*, 705, 1122, doi: [10.1088/0004-637X/705/2/1122](https://doi.org/10.1088/0004-637X/705/2/1122)
- [302] Lynden-Bell, D., Katz, J., & Bičák, J. 2007, Energy and angular momentum densities of stationary gravitational fields, *Phys. Rev. D.*, 75, 024040, doi: [10.1103/PhysRevD.75.024040](https://doi.org/10.1103/PhysRevD.75.024040)
- [303] Lévy-Leblond, J. M. 1977
- [304] Ma, C.-P., & Bertschinger, E. 1995, Cosmological Perturbation Theory in the Synchronous and Conformal Newtonian Gauges, *The Astrophysical Journal*, 455, 7, doi: [10.1086/176550](https://doi.org/10.1086/176550)
- [305] Ma, Y.-Z. 2011, Cosmology with CMB and Large Scale Structure, doi: [10.17863/CAM.15994](https://doi.org/10.17863/CAM.15994)
- [306] Maeda, K.-I. 1988, On Time Variation of Fundamental Constants in Superstring Theories, *Modern Physics Letters A*, 3, 243, doi: [10.1142/S0217732388000295](https://doi.org/10.1142/S0217732388000295)
- [307] Maffei, B., Abitbol, M. H., Aghanim, N., et al. 2021, BISOU: a balloon project to measure the CMB spectral distortions, arXiv e-prints, arXiv:2111.00246, doi: [10.48550/arXiv.2111.00246](https://doi.org/10.48550/arXiv.2111.00246)
- [308] Magueijo, J. 2003, New varying speed of light theories, *Reports on Progress in Physics*, 66, 2025, doi: [10.1088/0034-4885/66/11/R04](https://doi.org/10.1088/0034-4885/66/11/R04)
- [309] Maldacena, J. 1999, The Large-N Limit of Superconformal Field Theories and Supergravity, *International Journal of Theoretical Physics*, 38, 1113, doi: [10.1023/A:1026654312961](https://doi.org/10.1023/A:1026654312961)
- [310] Mallat, S. 2011, Group Invariant Scattering, arXiv e-prints, arXiv:1101.2286, doi: [10.48550/arXiv.1101.2286](https://doi.org/10.48550/arXiv.1101.2286)
- [311] Mallat, S., Zhang, S., & Rochette, G. 2018, Phase Harmonic Correlations and Convolutional Neural Networks, arXiv e-prints, arXiv:1810.12136, doi: [10.48550/arXiv.1810.12136](https://doi.org/10.48550/arXiv.1810.12136)
- [312] Mangilli, A., Aumont, J., Rotti, A., et al. 2021, Dust moments: towards a new modeling of the galactic dust emission for CMB B-modes analysis, *Astronomy and Astrophysics*, 647, A52, doi: [10.1051/0004-6361/201937367](https://doi.org/10.1051/0004-6361/201937367)
- [313] Maniyar, A. S., Gkogkou, A., Coulton, W. R., et al. 2023, Extragalactic CO emission lines in the CMB experiments: a forgotten signal and a foreground, arXiv e-prints, arXiv:2301.10764, doi: [10.48550/arXiv.2301.10764](https://doi.org/10.48550/arXiv.2301.10764)
- [314] Marques, C. M. J., Martins, C. J. A. P., & Alves, C. S. 2023, Fundamental cosmology from ANDES precision spectroscopy, arXiv e-prints, arXiv:2305.01446, doi: [10.48550/arXiv.2305.01446](https://doi.org/10.48550/arXiv.2305.01446)
- [315] Marsh, A. 2014, Riemannian Geometry: Definitions, Pictures, and Results, arXiv e-prints, arXiv:1412.2393, doi: [10.48550/arXiv.1412.2393](https://doi.org/10.48550/arXiv.1412.2393)

BIBLIOGRAPHY

- [316] —. 2016a, Gauge Theories and Fiber Bundles: Definitions, Pictures, and Results, arXiv e-prints, arXiv:1607.03089, doi: [10.48550/arXiv.1607.03089](https://doi.org/10.48550/arXiv.1607.03089)
- [317] Marsh, D. J. E. 2016b, Axion cosmology, *Phys. Rep.*, 643, 1, doi: [10.1016/j.physrep.2016.06.005](https://doi.org/10.1016/j.physrep.2016.06.005)
- [318] Martin, J., Ringeval, C., & Vennin, V. 2014, Encyclopædia Inflationaris, Physics of the Dark Universe, 5, 75, doi: [10.1016/j.dark.2014.01.003](https://doi.org/10.1016/j.dark.2014.01.003)
- [319] Martinelli, M., Calabrese, E., & Martins, C. J. A. P. 2015, E-ELT constraints on runaway dilaton scenarios, *J. Cosmology Astropart. Phys.*, 2015, 030, doi: [10.1088/1475-7516/2015/11/030](https://doi.org/10.1088/1475-7516/2015/11/030)
- [320] Martinelli, M., Martins, C. J. A. P., Nesseris, S., et al. 2021, Euclid: Constraining dark energy coupled to electromagnetism using astrophysical and laboratory data, *Astronomy and Astrophysics*, 654, A148, doi: [10.1051/0004-6361/202141353](https://doi.org/10.1051/0004-6361/202141353)
- [321] Martínez-Solaeche, G., Karakci, A., & Delabrouille, J. 2018, A 3D model of polarized dust emission in the Milky Way, *Monthly Notices of the Royal Astronomical Society*, 476, 1310, doi: [10.1093/mnras/sty204](https://doi.org/10.1093/mnras/sty204)
- [322] Martins, C. 2020, The Universe Today; Our Current Understanding and How It Was Achieved, doi: [10.1007/978-3-030-49632-6](https://doi.org/10.1007/978-3-030-49632-6)
- [323] Martins, C., & Molaro, P., eds. 2011, Proceedings, Symposium, from Varying Couplings to Fundamental Physics, JENAM 2010: Lisbon, Portugal, September 6-7, 2010, Astrophysics and Space Science Proceedings, doi: [10.1007/978-3-642-19397-2](https://doi.org/10.1007/978-3-642-19397-2)
- [324] Martins, C., Vielzeuf, P., Martinelli, M., Calabrese, E., & Pandolfi, S. 2015, Evolution of the fine-structure constant in runaway dilaton models, *Physics Letters B*, 743, 377, doi: <https://doi.org/10.1016/j.physletb.2015.03.002>
- [325] Martins, C. J. A. P. 2017, The status of varying constants: a review of the physics, searches and implications, *Reports on Progress in Physics*, 80, 126902, doi: [10.1088/1361-6633/aa860e](https://doi.org/10.1088/1361-6633/aa860e)
- [326] Martins, C. J. A. P., Ferreira, F. P. S. A., & Marto, P. V. 2022a, Varying fine-structure constant cosmography, *Physics Letters B*, 827, 137002, doi: [10.1016/j.physletb.2022.137002](https://doi.org/10.1016/j.physletb.2022.137002)
- [327] Martins, C. J. A. P., & Vacher, L. 2019, Astrophysical and local constraints on string theory: Runaway dilaton models, *Phys. Rev. D.*, 100, 123514, doi: [10.1103/PhysRevD.100.123514](https://doi.org/10.1103/PhysRevD.100.123514)
- [328] Martins, C. J. A. P., Cristiani, S., Cupani, G., et al. 2022b, Fundamental physics with ESPRESSO: Constraints on Bekenstein and dark energy models from astrophysical and local probes, arXiv e-prints, arXiv:2205.13848. <https://arxiv.org/abs/2205.13848>
- [329] Martire, F. A., Barreiro, R. B., & Martínez-González, E. 2022, Characterization of the polarized synchrotron emission from Planck and WMAP data, *JCAP*, 04, 003, doi: [10.1088/1475-7516/2022/04/003](https://doi.org/10.1088/1475-7516/2022/04/003)

BIBLIOGRAPHY

- [330] Mashhoon, B., Gronwald, F., & Lichtenegger, H. I. M. 2001, in Gyros, Clocks, Interferometers: Testing Relativistic Gravity in Space, ed. C. Lämmerzahl, C. W. F. Everitt, & F. W. Hehl, Vol. 562, 83, doi: [10.1007/3-540-40988-2_5](https://doi.org/10.1007/3-540-40988-2_5)
- [331] Matsuura, M. 2017, Dust and Molecular Formation in Supernovae, ed. A. W. Alsabti & P. Murdin, 2125, doi: [10.1007/978-3-319-21846-5_130](https://doi.org/10.1007/978-3-319-21846-5_130)
- [332] Mattingly, D. 2005, Modern Tests of Lorentz Invariance, *Living Reviews in Relativity*, 8, 5, doi: [10.12942/lrr-2005-5](https://doi.org/10.12942/lrr-2005-5)
- [333] McBride, L., Bull, P., & Hensley, B. S. 2023, Characterizing line-of-sight variability of polarized dust emission with future CMB experiments, *Monthly Notices of the Royal Astronomical Society*, 519, 4370, doi: [10.1093/mnras/stac3754](https://doi.org/10.1093/mnras/stac3754)
- [334] McCallum, N., Thomas, D. B., & Brown, M. L. 2022, Fast map-based simulations of systematics in CMB surveys including effects of the scanning strategy, *Monthly Notices of the Royal Astronomical Society*, 513, 3610, doi: [10.1093/mnras/stac561](https://doi.org/10.1093/mnras/stac561)
- [335] McGuigan, M. 2023, Infinity Wars: Three Types of Singularities in Non-supersymmetric Canonical Gravity and String Theory, arXiv e-prints, arXiv:2302.06811, doi: [10.48550/arXiv.2302.06811](https://doi.org/10.48550/arXiv.2302.06811)
- [336] McKellar, A. 1941, Molecular Lines from the Lowest States of Diatomic Molecules Composed of Atoms Probably Present in Interstellar Space, *Publications of the Dominion Astrophysical Observatory Victoria*, 7, 251
- [337] Megidish, E., Broz, J., Greene, N., & Häffner, H. 2019, Improved Test of Local Lorentz Invariance from a Deterministic Preparation of Entangled States, *Physical Review Letters*, 122, 123605, doi: [10.1103/PhysRevLett.122.123605](https://doi.org/10.1103/PhysRevLett.122.123605)
- [338] Melchiorri, A., & Vittorio, N. 1997, in NATO Advanced Study Institute (ASI) Series C, Vol. 502, The Cosmic Microwave Background, ed. C. H. Lineweaver, J. G. Bartlett, A. Blanchard, M. Signore, & J. Silk, 419, doi: [10.48550/arXiv.astro-ph/9610029](https://doi.org/10.48550/arXiv.astro-ph/9610029)
- [339] Mennella, V., Brucato, J. R., Colangeli, L., et al. 1998, Temperature Dependence of the Absorption Coefficient of Cosmic Analog Grains in the Wavelength Range 20 Microns to 2 Millimeters, *The Astrophysical Journal*, 496, 1058, doi: [10.1086/305415](https://doi.org/10.1086/305415)
- [340] Michelson, A. A., & Morley, E. W. 1887, On the relative motion of the Earth and the luminiferous ether, *American Journal of Science*, 34, 333, doi: [10.2475/ajs.s3-34.203.333](https://doi.org/10.2475/ajs.s3-34.203.333)
- [341] Minami, Y., & Ichiki, K. 2023, Extended delta-map: A map-based foreground removal method for CMB polarization observations, *Progress of Theoretical and Experimental Physics*, 2023, 033E01, doi: [10.1093/ptep/ptad016](https://doi.org/10.1093/ptep/ptad016)
- [342] Minami, Y., & Komatsu, E. 2020, New Extraction of the Cosmic Birefringence from the Planck 2018 Polarization Data, *Physical Review Letters*, 125, 221301, doi: [10.1103/PhysRevLett.125.221301](https://doi.org/10.1103/PhysRevLett.125.221301)
- [343] Misner, C. W., Thorne, K. S., & Wheeler, J. A. 1973, *Gravitation*, first edition edn., Physics Series (W. H. Freeman)

BIBLIOGRAPHY

- [344] Miville-Deschénes, M. A., Ysard, N., Lavabre, A., et al. 2008, Separation of anomalous and synchrotron emissions using WMAP polarization data, *Astronomy and Astrophysics*, 490, 1093, doi: [10.1051/0004-6361:200809484](https://doi.org/10.1051/0004-6361:200809484)
- [345] Moffat, J. W. 2002, Variable Speed of Light Cosmology: An Alternative to Inflation, arXiv e-prints, hep, doi: [10.48550/arXiv.hep-th/0208122](https://arxiv.org/abs/hep-th/0208122)
- [346] Molster, F. J., Waters, L. B. F. M., & Kemper, F. 2010, The Mineralogy of Interstellar and Circumstellar Dust in Galaxies, ed. T. Henning, Vol. 815, 143–201, doi: [10.1007/978-3-642-13259-9_3](https://doi.org/10.1007/978-3-642-13259-9_3)
- [347] Montargès, M., Cannon, E., Lagadec, E., et al. 2021, A dusty veil shading Betelgeuse during its Great Dimming, *Nature*, 594, 365, doi: [10.1038/s41586-021-03546-8](https://doi.org/10.1038/s41586-021-03546-8)
- [348] Moreno-Pulido, C., & Solà Peracaula, J. 2020, Running vacuum in quantum field theory in curved spacetime: renormalizing ρ_{vac} without $\sim m^4$ terms, *European Physical Journal C*, 80, 692, doi: [10.1140/epjc/s10052-020-8238-6](https://doi.org/10.1140/epjc/s10052-020-8238-6)
- [349] Moresco, M., Amati, L., Amendola, L., et al. 2022, Unveiling the Universe with emerging cosmological probes, *Living Reviews in Relativity*, 25, 6, doi: [10.1007/s41114-022-00040-z](https://doi.org/10.1007/s41114-022-00040-z)
- [350] Mousset, L. 2021, Exploring the primordial Universe, inflation and primordial gravitational waves with QUBIC, the Q&U Bolometric Interferometer for Cosmology
- [351] Murphy, M. T., Molaro, P., Leite, A. C. O., et al. 2022, Fundamental physics with ESPRESSO: Precise limit on variations in the fine-structure constant towards the bright quasar HE 0515–4414, *Astronomy and Astrophysics*, 658, A123, doi: [10.1051/0004-6361/202142257](https://doi.org/10.1051/0004-6361/202142257)
- [352] Møller, C. 1960, *The Theory of Relativity*, ed. O. Clarendon Press
- [353] Nakahara, M. 2003, *Geometry, Topology and Physics*
- [354] Nambu, Y. 1970, QUARK MODEL AND THE FACTORIZATION OF THE VENEZIANO AMPLITUDE., pp 269-78 of *Symmetries and Quark Models.* /Chand, Ramesh (ed.). New York Gordon and Breach, Science Publishers, Inc. (1970). <https://www.osti.gov/biblio/4118139>
- [355] Narimani, A., Moss, A., & Scott, D. 2012, Dimensionless cosmology, *Astrophysics and space science*, 341, 617, doi: [10.1007/s10509-012-1113-7](https://doi.org/10.1007/s10509-012-1113-7)
- [356] Nathalie Deruelle, J.-P. U. 2018, *Relativity in Modern Physics* (Oxford University Press)
- [357] Newman, E. T., & Penrose, R. 1966, Note on the Bondi-Metzner-Sachs Group, *Journal of Mathematical Physics*, 7, 863, doi: [10.1063/1.1931221](https://doi.org/10.1063/1.1931221)
- [358] Ni, W. T. 1977, Equivalence Principles and Electromagnetism, *Physical Review Letters*, 38, 301, doi: [10.1103/PhysRevLett.38.301](https://doi.org/10.1103/PhysRevLett.38.301)
- [359] Ni, W.-T. 2011, Foundations of Electromagnetism, Equivalence Principles and Cosmic Interactions, arXiv e-prints, arXiv:1109.5501, doi: [10.48550/arXiv.1109.5501](https://arxiv.org/abs/1109.5501)

BIBLIOGRAPHY

- [360] Norton, J. D. 1993, General covariance and the foundations of general relativity: eight decades of dispute, *Reports on Progress in Physics*, 56, 791, doi: [10.1088/0034-4885/56/7/001](https://doi.org/10.1088/0034-4885/56/7/001)
- [361] —. 2022, in *The Stanford Encyclopedia of Philosophy*, Winter 2022 edn., ed. E. N. Zalta & U. Nodelman (Metaphysics Research Lab, Stanford University)
- [362] Okamoto, T., & Hu, W. 2003, Cosmic microwave background lensing reconstruction on the full sky, *Phys. Rev. D.*, 67, 083002, doi: [10.1103/PhysRevD.67.083002](https://doi.org/10.1103/PhysRevD.67.083002)
- [363] Olive, K. A., & Pospelov, M. 2002, Evolution of the fine structure constant driven by dark matter and the cosmological constant, *Phys. Rev. D.*, 65, 085044, doi: [10.1103/PhysRevD.65.085044](https://doi.org/10.1103/PhysRevD.65.085044)
- [364] Onegin, M. S., Yudkevich, M. S., & Gomin, E. A. 2012, Investigation of the Fundamental Constants Stability Based on the Reactor Oklo Burn-Up Analysis, *Modern Physics Letters A*, 27, 1250232, doi: [10.1142/S021773231250232X](https://doi.org/10.1142/S021773231250232X)
- [365] Padovani, M., Bracco, A., Jelić, V., Galli, D., & Bellomi, E. 2021, Spectral index of synchrotron emission: insights from the diffuse and magnetised interstellar medium, *Astronomy and Astrophysics*, 651, A116, doi: [10.1051/0004-6361/202140799](https://doi.org/10.1051/0004-6361/202140799)
- [366] Pagano, L., de Bernardis, P., de Troia, G., et al. 2009, CMB polarization systematics, cosmological birefringence, and the gravitational waves background, *Phys. Rev. D.*, 80, 043522, doi: [10.1103/PhysRevD.80.043522](https://doi.org/10.1103/PhysRevD.80.043522)
- [367] Palti, E. 2019, The Swampland: Introduction and Review, *Fortschritte der Physik*, 67, 1900037, doi: [10.1002/prop.201900037](https://doi.org/10.1002/prop.201900037)
- [368] Pauli, W. 1940, The Connection Between Spin and Statistics, *Phys. Rev.*, 58, 716, doi: [10.1103/PhysRev.58.716](https://doi.org/10.1103/PhysRev.58.716)
- [369] Peebles, P. J. E., Page, Lyman A., J., & Partridge, R. B. 2009, Finding the Big Bang
- [370] Pelgrims, V., Clark, S. E., Hensley, B. S., et al. 2021, Evidence for line-of-sight frequency decorrelation of polarized dust emission in Planck data, *Astronomy and Astrophysics*, 647, A16, doi: [10.1051/0004-6361/202040218](https://doi.org/10.1051/0004-6361/202040218)
- [371] Pelgrims, V., Ferrière, K., Boulanger, F., Lallement, R., & Montier, L. 2020, Modeling the magnetized Local Bubble from dust data, *Astronomy and Astrophysics*, 636, A17, doi: [10.1051/0004-6361/201937157](https://doi.org/10.1051/0004-6361/201937157)
- [372] Pelgrims, V., Macías-Pérez, J. F., & Ruppin, F. 2018, Galactic magnetic field reconstruction using the polarized diffuse Galactic emission: Formalism and application to *Planck* data, arXiv e-prints, arXiv:1807.10515, doi: [10.48550/arXiv.1807.10515](https://doi.org/10.48550/arXiv.1807.10515)
- [373] Penrose, R. 1979, in *General Relativity: An Einstein Centenary Survey* (Cambridge University Press, Cambridge), 581–638
- [374] Penrose, R. 2006, in *Proceedings of EPAC 2006*, 2759–2762
- [375] Penrose, R. 2009, Black holes, quantum theory and cosmology, *Journal of Physics: Conference Series*, 174, 012001, doi: [10.1088/1742-6596/174/1/012001](https://doi.org/10.1088/1742-6596/174/1/012001)

BIBLIOGRAPHY

- [376] Penzias, A. A., & Wilson, R. W. 1965, A Measurement of Excess Antenna Temperature at 4080 Mc/s., *The Astrophysical Journal*, 142, 419, doi: [10.1086/148307](https://doi.org/10.1086/148307)
- [377] Perlmutter, S., Aldering, G., Goldhaber, G., et al. 1999, Measurements of Ω and Λ from 42 High-Redshift Supernovae, *The Astrophysical Journal*, 517, 565, doi: [10.1086/307221](https://doi.org/10.1086/307221)
- [378] Peter, P., & Uzan, J.-P. 2009, *Primordial Cosmology* (Oxford University Press)
- [379] Pitrou, C., Coc, A., Uzan, J.-P., & Vangioni, E. 2018, Precision big bang nucleosynthesis with improved Helium-4 predictions, *Phys. Rep.*, 754, 1, doi: [10.1016/j.physrep.2018.04.005](https://doi.org/10.1016/j.physrep.2018.04.005)
- [380] Pitrou, C., Pereira, T. S., & Uzan, J.-P. 2008, Predictions from an anisotropic inflationary era, *J. Cosmology Astropart. Phys.*, 2008, 004, doi: [10.1088/1475-7516/2008/04/004](https://doi.org/10.1088/1475-7516/2008/04/004)
- [381] Planck Collaboration. 2014, *Planck* 2013 results. XI. All-sky model of thermal dust emission, *Astronomy and Astrophysics*, 571, A11, doi: [10.1051/0004-6361/201323195](https://doi.org/10.1051/0004-6361/201323195)
- [382] —. 2015a, *Planck* intermediate results. XIX. An overview of the polarized thermal emission from Galactic dust, *Astronomy and Astrophysics*, 576, A104, doi: [10.1051/0004-6361/201424082](https://doi.org/10.1051/0004-6361/201424082)
- [383] —. 2015b, *Planck* intermediate results. XXIV. Constraints on variations in fundamental constants, *Astronomy and Astrophysics*, 580, A22, doi: [10.1051/0004-6361/201424496](https://doi.org/10.1051/0004-6361/201424496)
- [384] —. 2016a, *Planck* 2015 results. XIII. Cosmological parameters, *Astronomy and Astrophysics*, 594, A13, doi: [10.1051/0004-6361/201525830](https://doi.org/10.1051/0004-6361/201525830)
- [385] —. 2016b, *Planck* intermediate results. XXXII. The relative orientation between the magnetic field and structures traced by interstellar dust, *Astronomy and Astrophysics*, 586, A135, doi: [10.1051/0004-6361/201425044](https://doi.org/10.1051/0004-6361/201425044)
- [386] —. 2016c, *Planck* intermediate results. XXX. The angular power spectrum of polarized dust emission at intermediate and high Galactic latitudes, *Astronomy and Astrophysics*, 586, A133, doi: [10.1051/0004-6361/201425034](https://doi.org/10.1051/0004-6361/201425034)
- [387] —. 2017, *Planck* intermediate results. L. Evidence of spatial variation of the polarized thermal dust spectral energy distribution and implications for CMB B-mode analysis, *Astronomy and Astrophysics*, 599, A51, doi: [10.1051/0004-6361/201629164](https://doi.org/10.1051/0004-6361/201629164)
- [388] —. 2018, *Planck* 2018 results. XI. Polarized dust foregrounds, arXiv e-prints, arXiv:1801.04945. <https://arxiv.org/abs/1801.04945>
- [389] —. 2020, *Planck* 2018 results. V. CMB power spectra and likelihoods, *Astronomy and Astrophysics*, 641, A5, doi: [10.1051/0004-6361/201936386](https://doi.org/10.1051/0004-6361/201936386)
- [390] Planck Collaboration, Ade, P. A. R., Aghanim, N., et al. 2014, *Planck* 2013 results. XVII. Gravitational lensing by large-scale structure, *Astronomy and Astrophysics*, 571, A17, doi: [10.1051/0004-6361/201321543](https://doi.org/10.1051/0004-6361/201321543)

BIBLIOGRAPHY

- [391] Planck Collaboration, Adam, R., Aghanim, N., et al. 2016a, Planck intermediate results. XLVII. Planck constraints on reionization history, *Astronomy and Astrophysics*, 596, A108, doi: [10.1051/0004-6361/201628897](https://doi.org/10.1051/0004-6361/201628897)
- [392] Planck Collaboration, Ade, P. A. R., Aghanim, N., et al. 2016b, Planck 2015 results. XIX. Constraints on primordial magnetic fields, *Astronomy and Astrophysics*, 594, A19, doi: [10.1051/0004-6361/201525821](https://doi.org/10.1051/0004-6361/201525821)
- [393] Planck Collaboration, Aghanim, N., Alves, M. I. R., et al. 2016c, Planck intermediate results. XLIV. Structure of the Galactic magnetic field from dust polarization maps of the southern Galactic cap, *Astronomy and Astrophysics*, 596, A105, doi: [10.1051/0004-6361/201628636](https://doi.org/10.1051/0004-6361/201628636)
- [394] Planck Collaboration, Adam, R., Ade, P. A. R., et al. 2016d, Planck 2015 results. I. Overview of products and scientific results, *Astronomy and Astrophysics*, 594, A1, doi: [10.1051/0004-6361/201527101](https://doi.org/10.1051/0004-6361/201527101)
- [395] —. 2016e, Planck 2015 results. X. Diffuse component separation: Foreground maps, *Astronomy and Astrophysics*, 594, A10, doi: [10.1051/0004-6361/201525967](https://doi.org/10.1051/0004-6361/201525967)
- [396] Planck Collaboration, Aghanim, N., Akrami, Y., et al. 2020a, Planck 2018 results. VI. Cosmological parameters, *Astronomy and Astrophysics*, 641, A6, doi: [10.1051/0004-6361/201833910](https://doi.org/10.1051/0004-6361/201833910)
- [397] Planck Collaboration, Akrami, Y., Arroja, F., et al. 2020b, Planck 2018 results. X. Constraints on inflation, *Astronomy and Astrophysics*, 641, A10, doi: [10.1051/0004-6361/201833887](https://doi.org/10.1051/0004-6361/201833887)
- [398] Planck Collaboration, Aghanim, N., Akrami, Y., et al. 2020c, Planck 2018 results. I. Overview and the cosmological legacy of Planck, *Astronomy and Astrophysics*, 641, A1, doi: [10.1051/0004-6361/201833880](https://doi.org/10.1051/0004-6361/201833880)
- [399] Planck Collaboration, Akrami, Y., Ashdown, M., et al. 2020d, Planck 2018 results. XI. Polarized dust foregrounds, *Astronomy and Astrophysics*, 641, A11, doi: [10.1051/0004-6361/201832618](https://doi.org/10.1051/0004-6361/201832618)
- [400] —. 2020e, Planck 2018 results. IV. Diffuse component separation, *Astronomy and Astrophysics*, 641, A4, doi: [10.1051/0004-6361/201833881](https://doi.org/10.1051/0004-6361/201833881)
- [401] Poincaré, H. 1901, Électricité Et Optique: La Lumière Et Les Théories Électrodynamiques
- [402] —. 1905, Sur la dynamique de l'électron
- [403] Potapov, A., & McCoustra, M. 2021, Physics and Chemistry on the Surface of Cosmic Dust Grains: A Laboratory View, arXiv e-prints, arXiv:2105.01387, doi: [10.48550/arXiv.2105.01387](https://doi.org/10.48550/arXiv.2105.01387)
- [404] Poulin, V., Smith, T. L., & Karwal, T. 2023, The Ups and Downs of Early Dark Energy solutions to the Hubble tension: a review of models, hints and constraints circa 2023, arXiv e-prints, arXiv:2302.09032, doi: [10.48550/arXiv.2302.09032](https://doi.org/10.48550/arXiv.2302.09032)

BIBLIOGRAPHY

- [405] Prestage, J. D., Bollinger, J. J., Itano, W. M., & Wineland, D. J. 1985, Limits for Spatial Anisotropy by Use of Nuclear-Spin-Polarized ${}^9\text{Be}^+$ Ions, Phys. Rev. Lett., 54, 2387, doi: [10.1103/PhysRevLett.54.2387](https://doi.org/10.1103/PhysRevLett.54.2387)
- [406] Prézeau, G., & Reinecke, M. 2010, Algorithm for the Evaluation of Reduced Wigner Matrices, ApJ Supplements, 190, 267, doi: [10.1088/0067-0049/190/2/267](https://doi.org/10.1088/0067-0049/190/2/267)
- [407] Puglisi, G., Mihaylov, G., Panopoulou, G. V., et al. 2022, Improved galactic foreground removal for B-mode detection with clustering methods, Monthly Notices of the Royal Astronomical Society, 511, 2052, doi: [10.1093/mnras/stac069](https://doi.org/10.1093/mnras/stac069)
- [408] Purcell, E. M. 1979, Suprathermal rotation of interstellar grains., The Astrophysical Journal, 231, 404, doi: [10.1086/157204](https://doi.org/10.1086/157204)
- [409] Quiros, I. 2019, Selected topics in scalar-tensor theories and beyond, International Journal of Modern Physics D, 28, 1930012, doi: [10.1142/S021827181930012X](https://doi.org/10.1142/S021827181930012X)
- [410] Régaldo-Saint Blancard, B., Ally, E., Auclair, C., et al. 2023, Generative Models of Multichannel Data from a Single Example-Application to Dust Emission, The Astrophysical Journal, 943, 9, doi: [10.3847/1538-4357/aca538](https://doi.org/10.3847/1538-4357/aca538)
- [411] Regaldo-Saint Blancard, B., Ally, E., Boulanger, F., Levrier, F., & Jeffrey, N. 2021, A new approach for the statistical denoising of Planck interstellar dust polarization data, Astronomy and Astrophysics, 649, L18, doi: [10.1051/0004-6361/202140503](https://doi.org/10.1051/0004-6361/202140503)
- [412] Regaldo-Saint Blancard, B., Levrier, F., Ally, E., Bellomi, E., & Boulanger, F. 2020, Statistical description of dust polarized emission from the diffuse interstellar medium. A RWST approach, Astronomy and Astrophysics, 642, A217, doi: [10.1051/0004-6361/202038044](https://doi.org/10.1051/0004-6361/202038044)
- [413] Reissl, S., Guillet, V., Brauer, R., et al. 2020, A systematic study of radiative torque grain alignment in the diffuse interstellar medium, Astronomy and Astrophysics, 640, A118, doi: [10.1051/0004-6361/201937177](https://doi.org/10.1051/0004-6361/201937177)
- [414] Remazeilles, M., Delabrouille, J., & Cardoso, J.-F. 2011, Foreground component separation with generalised ILC, Mon. Not. Roy. Astron. Soc., 418, 467, doi: [10.1111/j.1365-2966.2011.19497.x](https://doi.org/10.1111/j.1365-2966.2011.19497.x)
- [415] Remazeilles, M., Dickinson, C., Banday, A. J., Bigot-Sazy, M. A., & Ghosh, T. 2015, An improved source-subtracted and destriped 408-MHz all-sky map, Monthly Notices of the Royal Astronomical Society, 451, 4311, doi: [10.1093/mnras/stv1274](https://doi.org/10.1093/mnras/stv1274)
- [416] Remazeilles, M., Rotti, A., & Chluba, J. 2021, Peeling off foregrounds with the constrained moment ILC method to unveil primordial CMB B modes, Monthly Notices of the Royal Astronomical Society, 503, 2478, doi: [10.1093/mnras/stab648](https://doi.org/10.1093/mnras/stab648)
- [417] Reula, O. 2010, Yvonne Choquet-Bruhat: General relativity and Einstein's equations, General Relativity and Gravitation vol. 42 iss. 5, 42, doi: [10.1007/s10714-010-0933-4](https://doi.org/10.1007/s10714-010-0933-4)
- [418] Riazuelo, A. 2011, L'Univers aux limites de l'éternité, Pour la science #71

BIBLIOGRAPHY

- [419] Riess, A. G., Filippenko, A. V., Challis, P., et al. 1998, Observational Evidence from Supernovae for an Accelerating Universe and a Cosmological Constant, *The Astronomical Journal*, 116, 1009, doi: [10.1086/300499](https://doi.org/10.1086/300499)
- [420] Riess, A. G., Yuan, W., Macri, L. M., et al. 2022, A Comprehensive Measurement of the Local Value of the Hubble Constant with $1 \text{ km s}^{-1} \text{ Mpc}^{-1}$ Uncertainty from the Hubble Space Telescope and the SH0ES Team, *ApJ Letters*, 934, L7, doi: [10.3847/2041-8213/ac5c5b](https://doi.org/10.3847/2041-8213/ac5c5b)
- [421] Ritacco, A., Boulanger, F., Guillet, V., et al. 2023, Dust polarization spectral dependence from Planck HFI data. Turning point for cosmic microwave background polarization-foreground modeling, *Astronomy and Astrophysics*, 670, A163, doi: [10.1051/0004-6361/202244269](https://doi.org/10.1051/0004-6361/202244269)
- [422] Rosenband, T., Hume, D. B., Schmidt, P. O., et al. 2008, Frequency Ratio of Al^+ and Hg^+ Single-Ion Optical Clocks; Metrology at the 17th Decimal Place, *Science*, 319, 1808, doi: [10.1126/science.1154622](https://doi.org/10.1126/science.1154622)
- [423] Ross, A. J., Samushia, L., Howlett, C., et al. 2015, The clustering of the SDSS DR7 main Galaxy sample - I. A 4 per cent distance measure at $z = 0.15$, *Monthly Notices of the Royal Astronomical Society*, 449, 835, doi: [10.1093/mnras/stv154](https://doi.org/10.1093/mnras/stv154)
- [424] Rotti, A., & Chluba, J. 2021, Combining ILC and moment expansion techniques for extracting average-sky signals and CMB anisotropies, *Monthly Notices of the Royal Astronomical Society*, 500, 976, doi: [10.1093/mnras/staa3292](https://doi.org/10.1093/mnras/staa3292)
- [425] Rotti, A., & Huffenberger, K. 2019, Real-space computation of E/B-mode maps. Part I. Formalism, compact kernels, and polarized filaments, *J. Cosmology Astropart. Phys.*, 045, doi: [10.1088/1475-7516/2019/01/045](https://doi.org/10.1088/1475-7516/2019/01/045)
- [426] Rovelli, C. 2019, Where Was Past Low-Entropy?, *Entropy*, 21, 466, doi: [10.3390/e21050466](https://doi.org/10.3390/e21050466)
- [427] Rovelli, C., & Gaul, M. 2000, in *Toward Quantum Gravity*, ed. J. Kowalski-Glikman, Vol. 541, 277
- [428] Rovelli, C., & Vidotto, F. 2014, Covariant Loop Quantum Gravity
- [429] Ryder, L. H. 1996, Quantum Field Theory
- [430] Régaldo-Saint Blancard, B. 2021, Statistical modeling of the polarized emission of interstellar dust
- [431] Sachs, R. K., & Wolfe, A. M. 1967, Perturbations of a Cosmological Model and Angular Variations of the Microwave Background, *The Astrophysical Journal*, 147, 73, doi: [10.1086/148982](https://doi.org/10.1086/148982)
- [432] Salam, A. 1969, Weak and electromagnetic interactions., pp 367-77 of *Elementary Particle Theory*. Svartholm, Nils (ed.). New York, John Wiley and Sons, Inc., 1968. <https://www.osti.gov/biblio/4767615>
- [433] Sandvik, H. B., Barrow, J. D., & Magueijo, J. 2002, A Simple Cosmology with a

BIBLIOGRAPHY

- Varying Fine Structure Constant, Physical Review Letters, 88, 031302, doi: [10.1103/PhysRevLett.88.031302](https://doi.org/10.1103/PhysRevLett.88.031302)
- [434] Sarangi, A., Matsuura, M., & Micelotta, E. R. 2018, Dust in Supernovae and Supernova Remnants I: Formation Scenarios, 214, 63, doi: [10.1007/s11214-018-0492-7](https://doi.org/10.1007/s11214-018-0492-7)
- [435] Sardanashvily, G. 2011, Classical Gauge Gravitation Theory, International Journal of Geometric Methods in Modern Physics, 8, 1869, doi: [10.1142/S0219887811005993](https://doi.org/10.1142/S0219887811005993)
- [436] Sattinger, D. H. 2013, Maxwell's Equations, Hodge Theory, and Gravitation, arXiv e-prints, arXiv:1305.6874. <https://arxiv.org/abs/1305.6874>
- [437] Scherk, J., & Schwarz, J. H. 1974, Dual models for non-hadrons, Nuclear Physics B, 81, 118, doi: [https://doi.org/10.1016/0550-3213\(74\)90010-8](https://doi.org/10.1016/0550-3213(74)90010-8)
- [438] Schlaflfy, E. F., Meisner, A. M., Stutz, A. M., et al. 2016, The Optical-infrared Extinction Curve and Its Variation in the Milky Way, The Astrophysical Journal, 821, 78, doi: [10.3847/0004-637X/821/2/78](https://doi.org/10.3847/0004-637X/821/2/78)
- [439] Schöneberg, N., Abellán, G. F., Sánchez, A. P., et al. 2022, The H_0 Olympics: A fair ranking of proposed models, Phys. Rep., 984, 1, doi: [10.1016/j.physrep.2022.07.001](https://doi.org/10.1016/j.physrep.2022.07.001)
- [440] Schöneberg, N., Vacher, L., Dias, J. D. F., Carvalho, M. M. C. D., & Martins, C. J. A. P. 2023, News from the Swampland - constraining string theory with astrophysics and cosmology, J. Cosmology Astropart. Phys., 2023, 039, doi: [10.1088/1475-7516/2023/10/039](https://doi.org/10.1088/1475-7516/2023/10/039)
- [441] Schuller, F. 2015, International Winter School on Gravity and Light
- [442] —. 2016, Lectures on the Geometric Anatomy of Theoretical Physics
- [443] Schwarz, D. J., Copi, C. J., Huterer, D., & Starkman, G. D. 2016, CMB anomalies after Planck, Classical and Quantum Gravity, 33, 184001, doi: [10.1088/0264-9381/33/18/184001](https://doi.org/10.1088/0264-9381/33/18/184001)
- [444] Schwarz, J. H. 1997, Lectures on Superstring and M Theory Dualities, Nuclear Physics B Proceedings Supplements, 55, 1, doi: [10.1016/S0920-5632\(97\)00070-4](https://doi.org/10.1016/S0920-5632(97)00070-4)
- [445] Schwichtenberg, J. 2018, Physics from Symmetry, ed. Springer
- [446] Sciama, D. W. 1953, On the origin of inertia, Monthly Notices of the Royal Astronomical Society, 113, 34, doi: [10.1093/mnras/113.1.34](https://doi.org/10.1093/mnras/113.1.34)
- [447] —. 1964, The Physical Structure of General Relativity, Reviews of Modern Physics, 36, 463, doi: [10.1103/RevModPhys.36.463](https://doi.org/10.1103/RevModPhys.36.463)
- [448] Scolnic, D., Brout, D., Carr, A., et al. 2022, The Pantheon+ Analysis: The Full Data Set and Light-curve Release, The Astrophysical Journal, 938, 113, doi: [10.3847/1538-4357/ac8b7a](https://doi.org/10.3847/1538-4357/ac8b7a)
- [449] Secrest, N. J., von Hausegger, S., Rameez, M., Mohayaee, R., & Sarkar, S. 2022, A Challenge to the Standard Cosmological Model, ApJ Letters, 937, L31, doi: [10.3847/2041-8213/ac88c0](https://doi.org/10.3847/2041-8213/ac88c0)

BIBLIOGRAPHY

- [450] Seo, M.-S. 2021, Dilaton stabilization in KKLT revisited, Nuclear Physics B, 968, 115452, doi: [10.1016/j.nuclphysb.2021.115452](https://doi.org/10.1016/j.nuclphysb.2021.115452)
- [451] Shankaranarayanan, S., & Johnson, J. P. 2022, Modified theories of gravity: Why, how and what?, General Relativity and Gravitation, 54, 44, doi: [10.1007/s10714-022-02927-2](https://doi.org/10.1007/s10714-022-02927-2)
- [452] Shaw, E. C., Ade, P. A. R., Akers, S., et al. 2020, in Society of Photo-Optical Instrumentation Engineers (SPIE) Conference Series, Vol. 11453, Millimeter, Submillimeter, and Far-Infrared Detectors and Instrumentation for Astronomy X, ed. J. Zmuidzinas & J.-R. Gao, 114532F, doi: [10.1117/12.2562941](https://doi.org/10.1117/12.2562941)
- [453] Sheehy, C., & Slosar, A. 2018, No evidence for dust B-mode decorrelation in Planck data, Phys. Rev. D., 97, 043522, doi: [10.1103/PhysRevD.97.043522](https://doi.org/10.1103/PhysRevD.97.043522)
- [454] Shetty, R., Kauffmann, J., Schnee, S., & Goodman, A. A. 2009, The Effect of Noise on the Dust Temperature-Spectral Index Correlation, The Astrophysical Journal, 696, 676, doi: [10.1088/0004-637X/696/1/676](https://doi.org/10.1088/0004-637X/696/1/676)
- [455] Shiraishi, M. 2012, Parity violation of primordial magnetic fields in the CMB bispectrum, Journal of Cosmology and Astroparticle Physics, 2012, 015, doi: [10.1088/1475-7516/2012/06/015](https://doi.org/10.1088/1475-7516/2012/06/015)
- [456] Silk, J. 1977, Cosmogony and the magnitude of the dimensionless gravitational coupling constant, Nature, 265, 710, doi: [10.1038/265710a0](https://doi.org/10.1038/265710a0)
- [457] Singh, P., Sami, M., & Dadhich, N. 2003, Cosmological dynamics of a phantom field, Phys. Rev. D., 68, 023522, doi: [10.1103/PhysRevD.68.023522](https://doi.org/10.1103/PhysRevD.68.023522)
- [458] Singh, T. P. 2021, Quantum theory without classical time: Octonions, and a theoretical derivation of the fine structure constant 1/137, International Journal of Modern Physics D, 30, 2142010, doi: [10.1142/S0218271821420104](https://doi.org/10.1142/S0218271821420104)
- [459] Skalidis, R., & Pelgrims, V. 2019, Local Bubble contribution to the 353-GHz dust polarized emission, Astronomy and Astrophysics, 631, L11, doi: [10.1051/0004-6361/201936547](https://doi.org/10.1051/0004-6361/201936547)
- [460] Smeenk, C., & Ellis, G. 2017, in The Stanford Encyclopedia of Philosophy, Winter 2017 edn., ed. E. N. Zalta (Metaphysics Research Lab, Stanford University)
- [461] Smith, T. L., Grin, D., Robinson, D., & Qi, D. 2019, Probing spatial variation of the fine-structure constant using the CMB, Phys. Rev. D., 99, 043531, doi: [10.1103/PhysRevD.99.043531](https://doi.org/10.1103/PhysRevD.99.043531)
- [462] Smolin, L. 2004, Scientific alternatives to the anthropic principle, arXiv e-prints, hep, doi: [10.48550/arXiv.hep-th/0407213](https://arxiv.org/abs/hep-th/0407213)
- [463] Smoot, G. F., Bennett, C. L., Kogut, A., et al. 1992, Structure in the COBE Differential Microwave Radiometer First-Year Maps, ApJ Letters, 396, L1, doi: [10.1086/186504](https://doi.org/10.1086/186504)
- [464] Sobrin, J. A., Anderson, A. J., Bender, A. N., et al. 2022, The Design and Integrated Performance of SPT-3G, ApJ Supplements, 258, 42, doi: [10.3847/1538-4365/ac374f](https://doi.org/10.3847/1538-4365/ac374f)

BIBLIOGRAPHY

- [465] Sotiriou, T. P., & Faraoni, V. 2010, f(R) theories of gravity, *Reviews of Modern Physics*, 82, 451, doi: [10.1103/RevModPhys.82.451](https://doi.org/10.1103/RevModPhys.82.451)
- [466] Sponseller, D., & Kogut, A. 2022, Mitigating Bias in CMB B-modes from Foreground Cleaning Using a Moment Expansion, *The Astrophysical Journal*, 936, 8, doi: [10.3847/1538-4357/ac846f](https://doi.org/10.3847/1538-4357/ac846f)
- [467] Stairs, I. H., Faulkner, A. J., Lyne, A. G., et al. 2005, Discovery of Three Wide-Orbit Binary Pulsars: Implications for Binary Evolution and Equivalence Principles, *The Astrophysical Journal*, 632, 1060, doi: [10.1086/432526](https://doi.org/10.1086/432526)
- [468] Stanwix, P. L., Tobar, M. E., Wolf, P., et al. 2005, Test of Lorentz Invariance in Electrodynamics Using Rotating Cryogenic Sapphire Microwave Oscillators, *Physical Review Letters*, 95, 040404, doi: [10.1103/PhysRevLett.95.040404](https://doi.org/10.1103/PhysRevLett.95.040404)
- [469] Starobinsky, A. A. 1982, Dynamics of phase transition in the new inflationary universe scenario and generation of perturbations, *Physics Letters B*, 117, 175, doi: [10.1016/0370-2693\(82\)90541-X](https://doi.org/10.1016/0370-2693(82)90541-X)
- [470] Stein, W. 1966, Infrared Radiation from Interstellar Grains, *The Astrophysical Journal*, 144, 318, doi: [10.1086/148606](https://doi.org/10.1086/148606)
- [471] Steinhardt, P. J., & Turok, N. 2002, A Cyclic Model of the Universe, *Science*, 296, 1436, doi: [10.1126/science.1070462](https://doi.org/10.1126/science.1070462)
- [472] Stevens, C., & Markwell, O. 2022, Toward fixing a framework for conformal cyclic cosmology, arXiv e-prints, arXiv:2212.06914, doi: [10.48550/arXiv.2212.06914](https://doi.org/10.48550/arXiv.2212.06914)
- [473] Stompor, R., Leach, S., Stivoli, F., & Baccigalupi, C. 2009, Maximum likelihood algorithm for parametric component separation in cosmic microwave background experiments, *Monthly Notices of the Royal Astronomical Society*, 392, 216, doi: [10.1111/j.1365-2966.2008.14023.x](https://doi.org/10.1111/j.1365-2966.2008.14023.x)
- [474] Strominger, A., & Vafa, C. 1996, Microscopic origin of the Bekenstein-Hawking entropy, *Physics Letters B*, 379, 99, doi: [10.1016/0370-2693\(96\)00345-0](https://doi.org/10.1016/0370-2693(96)00345-0)
- [475] Sugerman, B. E. K., Ercolano, B., Barlow, M. J., et al. 2006, Massive-Star Supernovae as Major Dust Factories, *Science*, 313, 196, doi: [10.1126/science.1128131](https://doi.org/10.1126/science.1128131)
- [476] Susskind, L. 1970, Structure of Hadrons Implied by Duality, *Phys. Rev. D*, 1, 1182, doi: [10.1103/PhysRevD.1.1182](https://doi.org/10.1103/PhysRevD.1.1182)
- [477] Susskind, L. 1995, The world as a hologram, *Journal of Mathematical Physics*, 36, 6377, doi: [10.1063/1.531249](https://doi.org/10.1063/1.531249)
- [478] Susskind, L. 2003, in *The Davis Meeting On Cosmic Inflation*, 26, doi: [10.48550/arXiv.hep-th/0302219](https://doi.org/10.48550/arXiv.hep-th/0302219)
- [479] —. 2006, The paradox of quantum black holes, *Nature Physics*, 2, 665, doi: [10.1038/nphys429](https://doi.org/10.1038/nphys429)
- [480] Susskind, L. 2008, *The black hole war : my battle with Stephen Hawking to make the world safe for quantum mechanics*, 1st edn. (Little Brown)

BIBLIOGRAPHY

- [481] Suzuki, A., Ade, P. A. R., Akiba, Y., et al. 2018, The LiteBIRD Satellite Mission: Sub-Kelvin Instrument, *Journal of Low Temperature Physics*, 193, 1048, doi: [10.1007/s10909-018-1947-7](https://doi.org/10.1007/s10909-018-1947-7)
- [482] Szabo, R. J. 2002, BUSSTEPP Lectures on String Theory, arXiv e-prints, hep. <https://arxiv.org/abs/hep-th/0207142>
- [483] 't Hooft, G. 1980, Naturalness, chiral symmetry, and spontaneous chiral symmetry breaking, *NATO Sci. Ser. B*, 59, 135, doi: [10.1007/978-1-4684-7571-5_9](https://doi.org/10.1007/978-1-4684-7571-5_9)
- [484] Takahashi, K. 2023, Introduction to Faraday tomography and its future prospects, *Publications of the Astronomical Society of Japan*, 75, S50, doi: [10.1093/pasj/psac111](https://doi.org/10.1093/pasj/psac111)
- [485] Takase, Y., Vacher, L., Ishino, H., et al. 2023, itshape Multi-dimensional optimization of the scanning strategy for CMB satellite polarimetry: suppression of systematic effects and in-flight calibration, to be submitted
- [486] Tassis, K., & Pavlidou, V. 2015, Searching for inflationary B modes: can dust emission properties be extrapolated from 350 GHz to 150 GHz?, *Monthly Notices of the Royal Astronomical Society*, 451, L90, doi: [10.1093/mnrasl/slv077](https://doi.org/10.1093/mnrasl/slv077)
- [487] Tavares, V. C., & Martins, C. J. A. P. 2021, Varying alpha generalized Dirac-Born-Infeld models, *Phys. Rev. D*, 103, 023525, doi: [10.1103/PhysRevD.103.023525](https://doi.org/10.1103/PhysRevD.103.023525)
- [488] The Pierre Auger Collaboration, Abreu, P., Aglietta, M., et al. 2021, Testing effects of Lorentz invariance violation in the propagation of astroparticles with the Pierre Auger Observatory, arXiv e-prints, arXiv:2112.06773, doi: [10.48550/arXiv.2112.06773](https://doi.org/10.48550/arXiv.2112.06773)
- [489] Thornton, R. J., Ade, P. A. R., Aiola, S., et al. 2016, The Atacama Cosmology Telescope: The Polarization-sensitive ACTPol Instrument, *ApJ Supplements*, 227, 21, doi: [10.3847/1538-4365/227/2/21](https://doi.org/10.3847/1538-4365/227/2/21)
- [490] Tino, G. M., Cacciapuoti, L., Capozziello, S., Lambiase, G., & Sorrentino, F. 2020, Precision gravity tests and the Einstein Equivalence Principle, *Progress in Particle and Nuclear Physics*, 112, 103772, doi: [10.1016/j.ppnp.2020.103772](https://doi.org/10.1016/j.ppnp.2020.103772)
- [491] Tong, D. 2009, Lectures on String Theory, arXiv e-prints, arXiv:0908.0333, doi: [10.48550/arXiv.0908.0333](https://doi.org/10.48550/arXiv.0908.0333)
- [492] Touboul, P., Métris, G., Rodrigues, M., et al. 2017, MICROSCOPE Mission: First Results of a Space Test of the Equivalence Principle, *Physical Review Letters*, 119, 231101, doi: [10.1103/PhysRevLett.119.231101](https://doi.org/10.1103/PhysRevLett.119.231101)
- [493] Touboul, P., Métris, G., Rodrigues, M., et al. 2022, *MICROSCOPE* Mission: Final Results of the Test of the Equivalence Principle, *Phys. Rev. Lett.*, 129, 121102, doi: [10.1103/PhysRevLett.129.121102](https://doi.org/10.1103/PhysRevLett.129.121102)
- [494] Tristram, M., Macías-Pérez, J. F., Renault, C., & Santos, D. 2005, XSPECt, estimation of the angular power spectrum by computing cross-power spectra with analytical error bars, *Monthly Notices of the Royal Astronomical Society*, 358, 833, doi: [10.1111/j.1365-2966.2005.08760.x](https://doi.org/10.1111/j.1365-2966.2005.08760.x)

BIBLIOGRAPHY

- [495] Tristram, M., Banday, A. J., Górski, K. M., et al. 2022, Improved limits on the tensor-to-scalar ratio using BICEP and Planck data, *Phys. Rev. D.*, 105, 083524, doi: [10.1103/PhysRevD.105.083524](https://doi.org/10.1103/PhysRevD.105.083524)
- [496] Trumpler, R. J. 1930, Absorption of Light in the Galactic System, *Publications of the Astronomical Society of the Pacific*, 42, 214, doi: [10.1086/124039](https://doi.org/10.1086/124039)
- [497] Tsujikawa, S. 2013, Quintessence: a review, *Classical and Quantum Gravity*, 30, 214003, doi: [10.1088/0264-9381/30/21/214003](https://doi.org/10.1088/0264-9381/30/21/214003)
- [498] Tully, R. B., Courtois, H., Hoffman, Y., & Pomarède, D. 2014, The Laniakea super-cluster of galaxies, *Nature*, 513, 71, doi: [10.1038/nature13674](https://doi.org/10.1038/nature13674)
- [499] Unnikrishnan, C. S., & Gillies, G. T. 2020, Gravitational Wave Test of the Strong Equivalence Principle, arXiv e-prints, arXiv:2007.01828, doi: [10.48550/arXiv.2007.01828](https://doi.org/10.48550/arXiv.2007.01828)
- [500] Uzan, J.-P. 2011, Varying Constants, Gravitation and Cosmology, *Living Reviews in Relativity*, 14, 2, doi: [10.12942/lrr-2011-2](https://doi.org/10.12942/lrr-2011-2)
- [501] Uzan, J.-P., & Leclercq, B. 2008, The Natural Laws of the Universe: Understanding Fundamental Constants, doi: [10.1007/978-0-387-74081-2](https://doi.org/10.1007/978-0-387-74081-2)
- [502] Vacher, L., Aumont, J., Boulanger, F., et al. 2023a, Frequency dependence of the thermal dust E/B ratio and EB correlation: Insights from the spin-moment expansion, *Astronomy and Astrophysics*, 672, A146, doi: [10.1051/0004-6361/202245292](https://doi.org/10.1051/0004-6361/202245292)
- [503] Vacher, L., Aumont, J., Montier, L., et al. 2022a, Moment expansion of polarized dust SED: A new path towards capturing the CMB B-modes with LiteBIRD, *Astronomy and Astrophysics*, 660, A111, doi: [10.1051/0004-6361/202142664](https://doi.org/10.1051/0004-6361/202142664)
- [504] Vacher, L., Chluba, J., Aumont, J., Rotti, A., & Montier, L. 2023b, High precision modeling of polarized signals: Moment expansion method generalized to spin-2 fields, *Astronomy and Astrophysics*, 669, A5, doi: [10.1051/0004-6361/202243913](https://doi.org/10.1051/0004-6361/202243913)
- [505] Vacher, L., Dias, J. D. F., Schöneberg, N., et al. 2022b, Constraints on extended Bekenstein models from cosmological, astrophysical, and local data, *Phys. Rev. D.*, 106, 083522, doi: [10.1103/PhysRevD.106.083522](https://doi.org/10.1103/PhysRevD.106.083522)
- [506] Vacher, L., Schöneberg, N., Dias, J. D. F., Martins, C. J. A. P., & Pimenta, F. 2023c, Runaway dilaton models: Improved constraints from the full cosmological evolution, *Phys. Rev. D.*, 107, 104002, doi: [10.1103/PhysRevD.107.104002](https://doi.org/10.1103/PhysRevD.107.104002)
- [507] van den Bergh, S. 1999, The Nearest Group of Galaxies, *ApJ Letters*, 517, L97, doi: [10.1086/312044](https://doi.org/10.1086/312044)
- [508] Vansyngel, F., Boulanger, F., Ghosh, T., et al. 2017, Statistical simulations of the dust foreground to cosmic microwave background polarization, *Astronomy and Astrophysics*, 603, A62, doi: [10.1051/0004-6361/201629992](https://doi.org/10.1051/0004-6361/201629992)
- [509] Vasconcellos, C. A. Z. 2020, Spacetime Singularities in General Relativity, 1–17, doi: [10.1142/9789813277342_0001](https://doi.org/10.1142/9789813277342_0001)

BIBLIOGRAPHY

- [510] Velten, H. E. S., vom Marttens, R. F., & Zimdahl, W. 2014, Aspects of the cosmological “coincidence problem”, European Physical Journal C, 74, 3160, doi: [10.1140/epjc/s10052-014-3160-4](https://doi.org/10.1140/epjc/s10052-014-3160-4)
- [511] Veneziano, G. 1986, A stringy nature needs just two constants, EPL (Europhysics Letters), 2, 199, doi: [10.1209/0295-5075/2/3/006](https://doi.org/10.1209/0295-5075/2/3/006)
- [512] Veneziano, G. 2002, Large-N bounds on, and compositeness limit of, gauge and gravitational interactions, Journal of High Energy Physics, 2002, 051, doi: [10.1088/1126-6708/2002/06/051](https://doi.org/10.1088/1126-6708/2002/06/051)
- [513] Verlinde, E. 2012, in Black Holes and Information, 20
- [514] Verlinde, E. P. 2017, Emergent Gravity and the Dark Universe, SciPost Physics, 2, 016, doi: [10.21468/SciPostPhys.2.3.016](https://doi.org/10.21468/SciPostPhys.2.3.016)
- [515] Vessot, R. F. C., Levine, M. W., Mattison, E. M., et al. 1980, Test of Relativistic Gravitation with a Space-Borne Hydrogen Maser, Physical Review Letters, 45, 2081, doi: [10.1103/PhysRevLett.45.2081](https://doi.org/10.1103/PhysRevLett.45.2081)
- [516] Vielva, P., Martínez-González, E., Casas, F. J., et al. 2022, Polarization angle requirements for CMB B-mode experiments. Application to the LiteBIRD satellite, J. Cosmology Astropart. Phys., 2022, 029, doi: [10.1088/1475-7516/2022/04/029](https://doi.org/10.1088/1475-7516/2022/04/029)
- [517] Vielzeuf, P. E., & Martins, C. J. A. P. 2014, Varying constants and dark energy with the E-ELT, Mem. Soc. Ast. It., 85, 155. <https://arxiv.org/abs/1309.7771>
- [518] Wagner, T. A., Schlamminger, S., Gundlach, J. H., & Adelberger, E. G. 2012, Torsion-balance tests of the weak equivalence principle, Classical and Quantum Gravity, 29, 184002, doi: [10.1088/0264-9381/29/18/184002](https://doi.org/10.1088/0264-9381/29/18/184002)
- [519] Wald, R. M. 1984, General relativity (University of Chicago Press)
- [520] Wallace, D. 2010, Gravity, Entropy, and Cosmology: in Search of Clarity, British Journal for Philosophy of Science, 61, 513, doi: [10.1093/bjps/axp048](https://doi.org/10.1093/bjps/axp048)
- [521] Wallace, D. 2019, Naturalness and Emergence, The Monist, 102, doi: [10.1093/monist/onz022](https://doi.org/10.1093/monist/onz022)
- [522] Wallis, C. G. R., Brown, M. L., Battye, R. A., & Delabrouille, J. 2017, Optimal scan strategies for future CMB satellite experiments, Monthly Notices of the Royal Astronomical Society, 466, 425, doi: [10.1093/mnras/stw2577](https://doi.org/10.1093/mnras/stw2577)
- [523] Ward-Thompson, D., & Whitworth, A. P. 2011, An Introduction to Star Formation
- [524] Watanabe, T., & Hayashi, M. J. 2004, General Relativity with Torsion, arXiv e-prints, gr, doi: [10.48550/arXiv.gr-qc/0409029](https://arxiv.org/abs/0409029)
- [525] Watson, S., Perry, M. J., Kane, G. L., & Adams, F. C. 2007, Inflation without inflation(s), J. Cosmology Astropart. Phys., 2007, 017, doi: [10.1088/1475-7516/2007/11/017](https://doi.org/10.1088/1475-7516/2007/11/017)
- [526] Weatherall, J. O. 2014, Fiber Bundles, Yang-Mills Theory, and General Relativity, arXiv e-prints, arXiv:1411.3281. <https://arxiv.org/abs/1411.3281>

BIBLIOGRAPHY

- [527] Webb, J. K., King, J. A., Murphy, M. T., et al. 2011, Indications of a Spatial Variation of the Fine Structure Constant, *Physical Review Letters*, 107, 191101, doi: [10.1103/PhysRevLett.107.191101](https://doi.org/10.1103/PhysRevLett.107.191101)
- [528] Weinberg, S. 1967, A Model of Leptons, *Phys. Rev. Lett.*, 19, 1264, doi: [10.1103/PhysRevLett.19.1264](https://doi.org/10.1103/PhysRevLett.19.1264)
- [529] —. 1972, Gravitation and cosmology: principles and applications of the general theory of relativity, first edition edn. (Wiley)
- [530] Weinberg, S. 1989, The cosmological constant problem, *Reviews of Modern Physics*, 61, 1, doi: [10.1103/RevModPhys.61.1](https://doi.org/10.1103/RevModPhys.61.1)
- [531] Weiss, M., & Baez., J. 2017, Is Energy Conserved in General Relativity? https://math.ucr.edu/home/baez/physics/Relativity/GR/energy_gr.html
- [532] Weyl, H. 1950, A Remark on the Coupling of Gravitation and Electron, *Phys. Rev.*, 77, 699, doi: [10.1103/PhysRev.77.699](https://doi.org/10.1103/PhysRev.77.699)
- [533] Wheeler, J., & Ford, K. 2000, Geons, Black Holes and Quantum Foam: A Life in Physics
- [534] Wilczynska, M. R., Webb, J. K., Bainbridge, M., et al. 2020, Four direct measurements of the fine-structure constant 13 billion years ago, *Science Advances*, 6, eaay9672, doi: [10.1126/sciadv.aay9672](https://doi.org/10.1126/sciadv.aay9672)
- [535] Will, C. M. 2014, The Confrontation between General Relativity and Experiment, *Living Reviews in Relativity*, 17, 4, doi: [10.12942/lrr-2014-4](https://doi.org/10.12942/lrr-2014-4)
- [536] —. 2018, Theory and Experiment in Gravitational Physics, 2nd edition
- [537] Williams, J. G., Turyshev, S. G., & Boggs, D. H. 2009, Lunar Laser Ranging Tests of the Equivalence Principle with the Earth and Moon, *International Journal of Modern Physics D*, 18, 1129, doi: [10.1142/S021827180901500X](https://doi.org/10.1142/S021827180901500X)
- [538] Williams, J. P., Blitz, L., & McKee, C. F. 2000, in *Protostars and Planets IV*, ed. V. Mannings, A. P. Boss, & S. S. Russell, 97, doi: [10.48550/arXiv.astro-ph/9902246](https://doi.org/10.48550/arXiv.astro-ph/9902246)
- [539] Wise, J. H. 2019, An Introductory Review on Cosmic Reionization, arXiv e-prints, arXiv:1907.06653. <https://arxiv.org/abs/1907.06653>
- [540] Wolfire, M. G., Hollenbach, D., McKee, C. F., Tielens, A. G. G. M., & Bakes, E. L. O. 1995, The Neutral Atomic Phases of the Interstellar Medium, *The Astrophysical Journal*, 443, 152, doi: [10.1086/175510](https://doi.org/10.1086/175510)
- [541] Wolz, K., Azzoni, S., Hervias-Caimapo, C., et al. 2023, The Simons Observatory: pipeline comparison and validation for large-scale B-modes, arXiv e-prints, arXiv:2302.04276, doi: [10.48550/arXiv.2302.04276](https://doi.org/10.48550/arXiv.2302.04276)
- [542] Xylyxylyx. 2020, Why does it move?
- [543] Yang, H. Y. K., Ruszkowski, M., & Zweibel, E. G. 2022, Fermi and eROSITA bubbles

BIBLIOGRAPHY

- as relics of the past activity of the Galaxy's central black hole, *Nature Astronomy*, 6, 584, doi: [10.1038/s41550-022-01618-x](https://doi.org/10.1038/s41550-022-01618-x)
- [544] Yoneya, T. 1974, Connection of Dual Models to Electrodynamics and Gravidynamics, *Prog. Theor. Phys.*, 51, 1907, doi: [10.1143/PTP.51.1907](https://doi.org/10.1143/PTP.51.1907)
- [545] Ysard, N., Köhler, M., Jones, A., et al. 2015, Dust variations in the diffuse interstellar medium: constraints on Milky Way dust from Planck-HFI observations, *Astronomy and Astrophysics*, 577, A110, doi: [10.1051/0004-6361/201425523](https://doi.org/10.1051/0004-6361/201425523)
- [546] Ysard, N., Abergel, A., Ristorcelli, I., et al. 2013, Variation in dust properties in a dense filament of the Taurus molecular complex (L1506), *Astronomy and Astrophysics*, 559, A133, doi: [10.1051/0004-6361/201322066](https://doi.org/10.1051/0004-6361/201322066)
- [547] Zaldarriaga, M. 2001, Nature of the E-B decomposition of CMB polarization, *Phys. Rev. D.*, 64, 103001, doi: [10.1103/PhysRevD.64.103001](https://doi.org/10.1103/PhysRevD.64.103001)
- [548] Zaninetti, L. 2020, On the Shape of the Local Bubble, *International Journal of Astronomy and Astrophysics*, 10, 11, doi: [10.4236/ijaa.2020.101002](https://doi.org/10.4236/ijaa.2020.101002)
- [549] Zarei, M., Bavarsad, E., Haghishat, M., et al. 2010, Generation of circular polarization of the CMB, *Phys. Rev. D.*, 81, 084035, doi: [10.1103/PhysRevD.81.084035](https://doi.org/10.1103/PhysRevD.81.084035)
- [550] Zee, A. 2003, Quantum field theory in a nutshell
- [551] Zeldovich, Y. B., & Sunyaev, R. A. 1969, The Interaction of Matter and Radiation in a Hot-Model Universe, *Astrophysics and space science*, 4, 301, doi: [10.1007/BF00661821](https://doi.org/10.1007/BF00661821)
- [552] Zwiebach, B. 2009, A First Course in String Theory
- [553] Zych, M., & Brukner, v. 2018, Quantum formulation of the Einstein Equivalence Principle, *Nature Phys.*, 14, 1027, doi: [10.1038/s41567-018-0197-6](https://doi.org/10.1038/s41567-018-0197-6)
- [554] Zyla, P., et al. 2020, Review of Particle Physics, *PTEP*, 2020, 083C01, doi: [10.1093/ptep/ptaa104](https://doi.org/10.1093/ptep/ptaa104)

Appendix D

Papers

This section contains all the papers accepted and published as a first author during this thesis. They are displayed in the following pages in the order in which they are discussed within the main text. Our work on the application of the moment expansion for component separation with *LiteBIRD* is available in Appendix [D.1](#), followed by our work on the definition on the spin-moment expansion in Appendix [D.2](#) and our application of the spin-moments to the *E*- and *B*-modes signal in Appendix [D.3](#). Finally, the paper on the Bekenstein model can be found in Appendix [D.4](#), followed by the paper on the runaway dilaton in Appendix [D.5](#).

D.1 A&A 660, A111

Astronomy & Astrophysics manuscript no. output
August 31, 2023

©ESO 2023

Moment expansion of polarized dust SED: A new path towards capturing the CMB *B*-modes with *LiteBIRD*

L. Vacher¹, J. Aumont¹, L. Montier¹, S. Azzoni^{2,3}, F. Boulanger⁴, and M. Remazeilles^{5,6},
for the *LiteBIRD* Collaboration

¹ IRAP, Université de Toulouse, CNRS, CNES, UPS, Toulouse, France

² Department of Physics, University of Oxford, Denys Wilkinson Building, Keble Road, Oxford OX1 3RH, United Kingdom

³ Kavli Institute for the Physics and Mathematics of the Universe (Kavli IPMU, WPI), UTIAS, The University of Tokyo, Kashiwa, Chiba 277-8583, Japan

⁴ Laboratoire de Physique de l'Ecole normale supérieure, ENS, Université PSL, CNRS, Sorbonne Université, Université Paris-Diderot, Sorbonne Paris Cité, Paris, France

⁵ Instituto de Física de Cantabria (CSIC-Universidad de Cantabria), Avda. de los Castros s/n, E-39005 Santander, Spain

⁶ Jodrell Bank Centre for Astrophysics, Department of Physics and Astronomy, The University of Manchester, Manchester M13 9PL, U.K.

August 31, 2023

ABSTRACT

Accurate characterization of the polarized dust emission from our Galaxy will be decisive in the quest for the cosmic microwave background (CMB) primordial *B*-modes. An incomplete modeling of its potentially complex spectral properties could lead to biases in the CMB polarization analyses and to a spurious measurement of the tensor-to-scalar ratio r . It is particularly crucial for future surveys like the *LiteBIRD* satellite, the goal of which is to constrain the faint primordial signal leftover by inflation with an accuracy on the tensor-to-scalar ratio r of the order of 10^{-3} . Variations of the dust properties along and between lines of sight lead to unavoidable distortions of the spectral energy distribution (SED) that cannot be easily anticipated by standard component-separation methods. This issue can be tackled using a moment expansion of the dust SED, an innovative parametrization method imposing minimal assumptions on the sky complexity. In the present paper, we apply this formalism to the *B*-mode cross-angular power spectra computed from simulated *LiteBIRD* polarization data at frequencies between 100 and 402 GHz that contain CMB, dust, and instrumental noise. The spatial variation of the dust spectral parameters (spectral index β and temperature T) in our simulations lead to significant biases on r ($\sim 21 \sigma_r$) if not properly taken into account. Performing the moment expansion in β , as in previous studies, reduces the bias but does not lead to sufficiently reliable estimates of r . We introduce, for the first time, the expansion of the cross-angular power spectra SED in both β and T , showing that, at the sensitivity of *LiteBIRD*, the SED complexity due to temperature variations needs to be taken into account in order to prevent analysis biases on r . Thanks to this expansion, and despite the existing correlations between some of the dust moments and the CMB signal responsible for a rise in the error on r , we can measure an unbiased value of the tensor-to-scalar ratio with a dispersion as low as $\sigma_r = 8.8 \times 10^{-4}$.

Key words. Cosmology, CMB, Foregrounds

1. Introduction

Our present understanding of the primordial Universe relies on the paradigm of inflation (Brout et al. 1978; Starobinsky 1980; Guth 1981), introducing a phase of accelerated expansion in the first fractions of a second after the primordial singularity. Such a phenomenon is expected to leave a background of gravitational waves propagating in the primordial plasma during recombination, leaving a permanent mark imprinted in the polarization anisotropies of the cosmic microwave background (CMB): the primordial *B*-modes (Polnarev 1985; Kamionkowski et al. 1997; Seljak & Zaldarriaga 1997). The amplitude of the angular power spectrum of those primordial *B*-modes is characterized by the tensor-to-scalar ratio r , which is proportional to the energy scale at which inflation occurred (Lyth 1997). Hence, looking for this smoking gun of inflation allows us to test our best theories of fundamental physics in the primordial Universe at energy scales far beyond the reach of particle accelerators. In this scope, it is

one of the biggest challenges of cosmology set out for the next decades. The best experimental upper limit on the r parameter so far is $r < 0.032$ (95 % C.L., Tristram et al. 2021; Bicep/Keck Collaboration et al. 2021; BICEP2/Keck and Planck Collaborations 2015).

The JAXA Lite (Light) satellite, used for the *B*-mode polarization and Inflation from cosmic background Radiation Detection (*LiteBIRD*) mission, is designed to observe the sky at large angular scales in order to constrain this parameter r down to $\delta r = 10^{-3}$, including all sources of uncertainty (Hazumi 2018; *LiteBIRD* Collaboration 2020). Exploring this region of the parameter space is critical, because this order of magnitude for the tensor-to-scalar ratio is predicted by numerous physically motivated inflation models (for a review see e.g., Martin et al. (2014))

However, the success of this mission relies on our ability to treat polarized foreground signals. Indeed various diffuse astrophysical sources emit polarized *B*-mode signals above the primordial ones, the strongest being due to the diffuse polarized emission of our own Galaxy (Planck Collaboration 2020b).

Send offprint requests to: leo.vacher@irap.omp.eu

Even in a diffuse region like the BICEP/Keck field, the Galactic B -modes are at least ten times stronger at 150 GHz than the $r = 0.01$ tensor B -modes targeted by the current CMB experiments (BICEP2 Collaboration & Keck Array Collaboration 2018).

The true complexity of polarized foreground emission that the next generation of CMB experiments will face is still mostly unknown today. Underestimation of this complexity can lead to the estimation of a spurious nonzero value of r (see e.g., Planck Collaboration 2017; Remazeilles et al. 2016).

At high frequencies (> 100 GHz), the thermal emission of interstellar dust grains is the main source of Galactic foreground contaminating the CMB (Krachmalnicoff et al. 2016; Planck Collaboration 2020c). The canonical model of the spectral energy distribution (SED) of this thermal emission for intensity and polarization is given by the modified black body (MBB) law (Desert et al. 1990). This model provides a good fit to the dust polarization SED at the sensitivity of the *Planck* satellite (Planck Collaboration 2020c) but it may not fully account for it at the sensitivity of future experiments (Hensley & Bull 2018). Furthermore, due to changes of physical conditions across the galaxy, spatial variations of the SEDs are present between and along the lines of sight. The former leads to what is known as *frequency decorrelation* in the CMB community (see e.g. Tasissis & Pavlidou 2015; Planck Collaboration 2017; Pelgrims et al. 2021). Moreover, both effects lead to averaging MBBs when observing the sky (unavoidable line-of-sight or beam-integration effects). Because of the nonlinearity of the MBB law, those averaging effects will distort the SED, leading to deviations from this canonical model (Chluba et al. 2017).

Chluba et al. (2017) proposed a general framework called “moment expansion” of the SED to take into account those distortions, using a Taylor expansion around the MBB with respect to its spectral parameters (Taylor expansion of foreground SEDs was discussed in previous studies; see e.g., Stolyarov et al. 2005). This method is agnostic: it does not require any assumption on the real complexity of the polarized dust emission. The moment expansion approach thus provides a promising tool with which to model the unanticipated complexity of the dust emission in real data.

Mangilli et al. (2021) generalized this formalism for the sake of CMB data analysis in harmonic space and for cross-angular power spectra and applied it successfully to complex simulations and *Planck* High-Frequency Instrument (HFI) intensity data. This latter work shows that the real complexity of Galactic foregrounds could be higher than expected, encouraging us to follow the path opened by the moment expansion formalism.

In the present work, we apply the moment expansion in harmonic space to characterize and treat the dust foreground polarized emission of *LiteBIRD* high-frequency simulations, using dust-emission models of increasing complexity. We discuss the ability of this method to recover an unbiased value for the r parameter, with enough accuracy to achieve the scientific objectives of the *LiteBIRD* mission.

In Sect. 2, we first review the formalism of moment expansion in map and harmonic domains. We then describe in Sect. 3 how we realize several sets of simulations of the sky as seen by the *LiteBIRD* instrument with varying dust complexity and how we estimate the angular power spectra. In Sect. 4, we describe how we estimate the moment parameters and the tensor-to-scalar ratio r in those simulations. The results are then presented in Sect. 5. Finally, we discuss those results and the future work that has to be done in the direction opened by moment expansion in Sect. 6.

2. Formalism

2.1. Characterizing the dust SED in real space

2.1.1. Modified black body model

The canonical way to characterize astrophysical dust-grain emission in every volume element of the Galaxy is given by the modified black body (MBB) function, consisting of multiplying a standard black body SED $B_\nu(T)$ at a given temperature T_0 by a power-law of the frequency ν with a spectral index β_0 . The dust intensity map $I_D(\nu, \mathbf{n})$ observed at a frequency ν in every direction with respect to the unit vector \mathbf{n} , can then be written as:

$$I(\nu, \mathbf{n}) = \left(\frac{\nu}{\nu_0} \right)^{\beta_0} \frac{B_\nu(T_0)}{B_{\nu_0}(T_0)} A(\mathbf{n}) = \frac{I_\nu(\beta_0, T_0)}{I_{\nu_0}(\beta_0, T_0)} A(\mathbf{n}), \quad (1)$$

where $A(\mathbf{n})$ is the dust intensity template at a reference frequency ν_0 ¹. We know that the physical conditions (thermodynamic and dust grain properties) change through the interstellar medium across the Galaxy, depending, in an intricate fashion, on the gas velocity and density, the interstellar radiation field, the distance to the Galactic center (see e.g., Paradis et al. 2009; Ysard et al. 2015; Planck Collaboration 2014a, 2020b; Hutton et al. 2015; Fanciullo et al. 2015). This change of physical conditions leads to variations in β and T depending on the direction of observation \mathbf{n} :

$$I(\nu, \mathbf{n}) = \frac{I_\nu(\beta(\mathbf{n}), T(\mathbf{n}))}{I_{\nu_0}(\beta(\mathbf{n}), T(\mathbf{n}))} A(\mathbf{n}). \quad (2)$$

The SED amplitude and parameters (temperature and spectral index) are then different for every line of sight. It is therefore clear that, in order to provide a realistic model of the dust emission, the frequency and spatial dependencies may not be trivially separated.

2.1.2. Limits of the modified black body

The dust SED model given by the MBB has proven to be highly accurate (Planck Collaboration 2014b, 2015). However, it must be kept in mind that this model is empirical and is therefore not expected to give a perfect description of the dust SED in the general case. Indeed, physically motivated dust grain emission models predict deviations from it (e.g., Draine & Hensley 2013). Surveys tend to show that the dust-emission properties vary across the observed 2D sky and the 3D Galaxy (Planck Collaboration 2020c). Furthermore, in true experimental conditions, one can never directly access the pure SED of a single volume element with specific emission properties and unique spectral parameters. Averages are therefore made over different SEDs emitted from distinct regions with different physical emission properties, in a way that may not be avoided: along the line of sight; between different lines of sight, inside the beam of the instrument or; when doing a spherical harmonic decomposition to calculate the angular power spectra over large regions of the sky.

The MBB function is nonlinear, and therefore summing MBBs with different spectral parameters does not return another MBB function and produces *SED distortions*. For all these reasons, modeling the dust emission with a MBB is intrinsically limited, even when doing so with spatially varying spectral parameters. As a consequence, inaccuracies might appear when modeling the dust contribution to CMB data that will unavoidably impact the final estimation of the cosmological parameters.

¹ Throughout this work, we use $\nu_0 = 353$ GHz.

2.1.3. Moment expansion in pixel space

A way to address the limitation of the MBB model in accurately describing the dust emission is given by the moment expansion formalism proposed by Chluba et al. (2017). This formalism is designed to take into account the SED distortions due to averaging effects by considering a multidimensional Taylor expansion of the distorted SED $I(v, \mathbf{p})$ around the mean values \mathbf{p}_0 of its spectral parameters $\mathbf{p} = \{p_i\}$. This is the so-called moment expansion of the SED, which can be written as

$$\begin{aligned} I(v, \mathbf{p}) &= I(v, \mathbf{p}_0) + \sum_i \omega_1^{p_i} \langle \partial_{p_i} I(v, \mathbf{p}) \rangle_{\mathbf{p}=\mathbf{p}_0} \\ &\quad + \frac{1}{2} \sum_{i,j} \omega_2^{p_i p_j} \langle \partial_{p_i} \partial_{p_j} I(v, \mathbf{p}) \rangle_{\mathbf{p}=\mathbf{p}_0} \\ &\quad + \dots \\ &\quad + \frac{1}{\alpha!} \sum_{i,\dots,k} \omega_\alpha^{p_i \dots p_k} \langle \partial_{p_i} \dots \partial_{p_k} I(v, \mathbf{p}) \rangle_{\mathbf{p}=\mathbf{p}_0}, \end{aligned} \quad (3)$$

where the first term on the right-hand side is the SED without distortion $I(v, \mathbf{p}_0)$ evaluated at $\mathbf{p} = \mathbf{p}_0$, and the other terms are the so-called moments of order α , quantified by the moment parameters $\omega_\alpha^{p_i \dots p_k}$ for the expansion with respect to any parameter of \mathbf{p} . Performing the expansion to increasing order adds increasing complexity to the SED $I(v, \mathbf{p}_0)$.

For the MBB presented in Sect. 2.1.1, there are two parameters so that $\mathbf{p} = \{\beta, T\}$. Thus the dust moment expansion reads

$$\begin{aligned} I(v, \mathbf{n}) &= \frac{I_v(\beta_0, T_0)}{I_{v_0}(\beta_0, T_0)} \left\{ A(\mathbf{n}) + \omega_1^\beta(\mathbf{n}) \ln \left(\frac{v}{v_0} \right) + \frac{1}{2} \omega_2^\beta(\mathbf{n}) \ln^2 \left(\frac{v}{v_0} \right) \right. \\ &\quad \left. + \omega_1^T(\mathbf{n}) (\Theta(v, T_0) - \Theta(v_0, T_0)) + \dots \right\}, \end{aligned} \quad (4)$$

where the expansion has been written up to order two in β (with moment expansion parameters ω_1^β at order one and ω_2^β at order two) and to order one in T (with a moment expansion parameter ω_1^T at order one). The following expression has been introduced to simplify the black body derivative with respect to T :

$$\Theta(v, T) = \frac{x}{T} \frac{e^x}{e^x - 1}, \text{ with } x = \frac{hv}{kT}. \quad (5)$$

The moment expansion in pixel space can be used for component separation and possibly crossed with other methods (see e.g., Remazeilles et al. 2021; Adak 2021). However, in the present work, we are interested in the modeling of the dust at the B -mode angular power spectrum level. Performing the moment expansion at the angular power spectrum level adds some complexity to the SEDs due to the additional averaging occurring when dealing with spherical harmonic coefficients. Indeed, these coefficients are estimated on potentially large fractions of the sky and probe regions with various physical conditions. On the other hand, the expansion at the power spectrum level possibly drastically reduces the parameter space with respect to performing the expansion in every sky pixel.

2.2. Characterizing the dust SED in harmonic space

2.2.1. Dust SED in spherical harmonic space

The expansion presented in Sect. 2.1.3 can be applied in spherical harmonic space using the same logic. The sky emission projection then reads

$$I(v, \mathbf{n}) = \sum_{\ell=0}^{\infty} \sum_{m=-\ell}^{\ell} I_{\ell m}^v Y_{\ell m}(\mathbf{n}). \quad (6)$$

Applying the moment expansion to the spherical harmonics coefficients, with respect to β and T , as in Eq. 4, leads to

$$\begin{aligned} I_{\ell m}^v &= \frac{I_v(\beta_0(\ell), T_0(\ell))}{I_{v_0}(\beta_0(\ell), T_0(\ell))} \left\{ A_{\ell m} + \omega_{1,\ell m}^\beta \ln \left(\frac{v}{v_0} \right) + \frac{1}{2} \omega_{2,\ell m}^\beta \ln^2 \left(\frac{v}{v_0} \right) \right. \\ &\quad \left. + \omega_{1,\ell m}^T (\Theta(v, T_0(\ell)) - \Theta(v_0, T_0(\ell))) + \dots \right\}, \end{aligned} \quad (7)$$

where this time $\beta_0(\ell)$ and $T_0(\ell)$ are the averages of β and T at a given multipole ℓ over the sky fraction we are looking at. We note that the moment parameters $\omega_{\alpha,\ell m}^{p_i}$ involved here are different from the $\omega_i^{p_i}(\mathbf{n})$ appearing in Eq. 4 in the map space because they involve different averaging. In principle, the moment expansion in harmonic space can take into account the three kinds of spatial averages presented in Sect. 2.1.2.

As the dust spectral index and temperature are difficult to separate in the frequency range considered for CMB studies (i.e., Rayleigh-Jeans domain, see e.g. Juvela & Ysard 2012), the moment expansion in harmonic space has only been applied in the past with respect to β , with the temperature being fixed to a reference value $T = T_0$ (Mangilli et al. 2021; Azzoni et al. 2020). In the present paper, for the first time, the moment expansion in harmonic space is instead performed with respect to both β and T , as it was in real space in Remazeilles et al. (2021).

2.2.2. Cross-power spectra

Relying on the derivation made by Mangilli et al. (2021) and Eq. 7, we can explicitly write the cross-spectra between two maps M_{v_i} and M_{v_j} at frequencies v_i and v_j , using the moment expansion in β and T as follows:

$$\begin{aligned} \mathcal{D}_\ell(v_i \times v_j) &= \frac{I_{v_i}(\beta_0(\ell), T_0(\ell)) I_{v_j}(\beta_0(\ell), T_0(\ell))}{I_{v_0}(\beta_0(\ell), T_0(\ell))^2} \cdot \left\{ \right. \\ &\quad \text{0th order } \left\{ \begin{array}{l} \mathcal{D}_\ell^{A \times A} \\ + \mathcal{D}_\ell^{A \times \omega_1^\beta} [\ln \left(\frac{v_i}{v_0} \right) + \ln \left(\frac{v_j}{v_0} \right)] \\ + \mathcal{D}_\ell^{\omega_1^\beta \times \omega_1^\beta} [\ln \left(\frac{v_i}{v_0} \right) \ln \left(\frac{v_j}{v_0} \right)] \end{array} \right\} \\ &\quad \text{1st order } \beta \left\{ \begin{array}{l} + \mathcal{D}_\ell^{A \times \omega_1^\beta} (\Theta_i + \Theta_j - 2\Theta_0) \\ + \mathcal{D}_\ell^{\omega_1^\beta \times \omega_1^\beta} (\Theta_i - \Theta_0)(\Theta_j - \Theta_0) \end{array} \right\} \\ &\quad \text{1st order } T \left\{ \begin{array}{l} + \mathcal{D}_\ell^{A \times \omega_1^T} (\Theta_i + \Theta_j - 2\Theta_0) \\ + \mathcal{D}_\ell^{\omega_1^T \times \omega_1^T} (\Theta_i - \Theta_0)(\Theta_j - \Theta_0) \end{array} \right\} \\ &\quad \text{1st order } T\beta \left\{ \begin{array}{l} + \mathcal{D}_\ell^{\omega_1^\beta \times \omega_1^T} [\ln \left(\frac{v_i}{v_0} \right) (\Theta_i - \Theta_0) + \ln \left(\frac{v_j}{v_0} \right) (\Theta_j - \Theta_0)] \\ + \frac{1}{2} \mathcal{D}_\ell^{A \times \omega_1^\beta} [\ln^2 \left(\frac{v_i}{v_0} \right) + \ln^2 \left(\frac{v_j}{v_0} \right)] \end{array} \right\} \\ &\quad \text{2nd order } \beta \left\{ \begin{array}{l} + \frac{1}{2} \mathcal{D}_\ell^{\omega_1^\beta \times \omega_1^\beta} [\ln \left(\frac{v_i}{v_0} \right) \ln^2 \left(\frac{v_j}{v_0} \right) + \ln \left(\frac{v_j}{v_0} \right) \ln^2 \left(\frac{v_i}{v_0} \right)] \\ + \frac{1}{4} \mathcal{D}_\ell^{\omega_1^\beta \times \omega_1^\beta} [\ln^2 \left(\frac{v_i}{v_0} \right) \ln^2 \left(\frac{v_j}{v_0} \right)] \end{array} \right\} \\ &\quad \left. + \dots \right\}, \end{aligned} \quad (8)$$

where we use the following abbreviation: $\Theta(\nu_k, T_0(\ell)) \equiv \Theta_k$, so that $\Theta_0 = \Theta(\nu_0, T_0(\ell))$, and we defined the moment expansion cross-power spectra between two moments \mathcal{M} and \mathcal{N} as

$$C_\ell^{\mathcal{M} \times \mathcal{N}} = \sum_{m,m'=-\ell}^{\ell} \mathcal{M}_{\ell m} \mathcal{N}_{\ell m'}, \text{ with } (\mathcal{M}, \mathcal{N}) \in \{A, \omega_1^\beta, \omega_1^T, \omega_2^\beta, \dots\}. \quad (9)$$

In the remainder of this article, we use the \mathcal{D}_ℓ quantity, which is a scaling of the angular power spectra, and is defined as

$$\mathcal{D}_\ell \equiv \frac{\ell(\ell+1)}{2\pi} C_\ell. \quad (10)$$

Equation 8 has been written using the expansion with respect to β at order two and T at order one, as in Eq. 7. Nevertheless, the terms involving power spectra between order two in β and order one in T have been neglected so as to match the needs of the implementation of our method in the following.

Hereafter, when we refer to "order k " at the angular power spectrum level, we are referring to moment expansion terms involving the pixel space moment up to order k . For example, $\mathcal{D}_\ell^{A \times \omega_1^T}$ and $\mathcal{D}_\ell^{\omega_1^\beta \times \omega_1^T}$ are order one, while $\mathcal{D}_\ell^{A \times \omega_2^\beta}$, $\mathcal{D}_\ell^{\omega_1^\beta \times \omega_2^\beta}$ and $\mathcal{D}_\ell^{\omega_2^\beta \times \omega_2^\beta}$ are order two. At order zero, one retrieves the MBB description of the cross-angular power spectra SED $\mathcal{D}_\ell(\nu_i \times \nu_j)$ as a function of the frequencies ν_i and ν_j .

This formalism was originally introduced to analyze the complexity of intensity data in [Mangilli et al. \(2021\)](#). In the present work, we focus on B -mode polarization power spectra. This was put forward after analyzing the *Planck* and balloon-borne Large Aperture Submillimeter Telescope for Polarimetry (BLASTPol) data and finding that the polarization fraction appears to be constant in the far-infrared-to-millimetre wavelengths ([Gandilo et al. 2016; Ashton et al. 2018](#)). This allows us to assume that the same grain population is responsible for the total and polarized foreground emission ([Guillet et al. 2018](#)). As a result, intensity and polarization SED complexity may be similar. Nevertheless, Q and U can have a different SED because of the polarization angle frequency dependence (see e.g., [Tassis & Pavlidou 2015; Ichiki et al. 2019](#)) and so can E and B . This could be a limitation when analyzing the dust E and B with a single moment expansion, especially when SED variations occur along the line of sight. Even when trying to model a single polarization component—as we do in the present work, dealing only with B modes—it is not clear whether the distorted SED can be modeled in terms of β and T moments only. Further work needs to be done to assess this question. However, they should not impact the present study in which variations along the line of sight are not simulated.

Modeling the complexity of the foreground signals by means of the moment expansion of the B -mode angular power spectrum has already been successfully applied to Simons Observatory ([The Simons Observatory collaboration 2019](#)) simulated data ([Azzoni et al. 2020](#)). However, the approach taken by these latter authors is different from the one presented above. They apply a *minimal* moment expansion: assumptions are made to keep only the $\mathcal{D}_\ell^{\omega_1^\beta \times \omega_1^\beta}$ and $\mathcal{D}_\ell^{A \times \omega_2^\beta}$ parameters, which are modeled with a power-law scale dependence. These assumptions may not hold for experiments with higher sensitivity and observing wider sky patches. Furthermore, they assume a scale-invariant dust spectral index. In this work, on the other hand, we relax these assumptions in order to characterize the required spectral complexity of the dust emission for *LiteBIRD*.

Telescope	Frequency [GHz]	Sensitivity $\sigma_{Q,U}^{\text{noise}}(\nu)$ [$\mu\text{K}\cdot\text{arcmin}^2$]	θ_{FWHM} arcmin
LFT	40.0	37.42	70.5
LFT	50.0	33.46	58.5
LFT	60.0	21.31	51.1
LFT	68.0	19.91/31.77	41.6/47.1
LFT	78.0	15.55/19.13	36.9/43.8
LFT	89.0	12.28/28.77	33.0/41.5
LFT/MFT	100.0	10.34/8.48	30.2/37.8
LFT/MFT	119.0	7.69/5.70	26.3/33.6
LFT/MFT	140.0	7.25/6.38	23.7/30.8
MFT	166.0	5.57	28.9
MFT/HFT	195.0	7.05/10.50	28.0/28.6
HFT	235.0	10.79	24.7
HFT	280.0	13.8	22.5
HFT	337.0	21.95	20.9
HFT	402.0	47.45	17.9

Table 1: Instrumental characteristics of *LiteBIRD* used in this study (adapted from [Hazumi et al 2020](#), see Sect. 3.2.3). Some frequency bands are shared by two different telescopes or detector arrays. If so, the two values of polarization sensitivities $\sigma_{Q,U}^{\text{noise}}(\nu)$ and instrumental beam full width at half maximum θ_{FWHM} are displayed on the same line.

3. Simulations and cross-spectra estimation

3.1. *LiteBIRD*

LiteBIRD is an international project proposed by the Japanese spatial agency (JAXA), which selected it in May 2019 as a strategic large class mission. The launch is planned for 2029 for a minimal mission duration of 3 years ([Hazumi et al 2020; LiteBIRD Collaboration in prep.](#)).

LiteBIRD is designed to realize a full sky survey of the CMB at large angular scales in order to look for the reionization bump of primordial B -modes and explore the scalar-to-tensor ratio (r) parameter space with a total uncertainty δr below 10^{-3} , including foreground cleaning and systematic errors. *LiteBIRD* is composed of three telescopes observing in different frequency intervals: the Low-, Medium- and High-Frequency Telescopes (LFT, MFT and HFT). Each of the telescopes illuminates a focal plane composed of hundreds of polarimetric detectors. The whole instrument will be cooled down to 5 K ([LiteBIRD Collaboration 2020](#)) while the focal plane will be cooled down to 100 mK ([Suzuki et al. 2018](#)). In order to mitigate the instrumental systematic effects, the polarization is modulated by a continuously rotating half-wave plate. *LiteBIRD* will observe the sky in 15 frequency bands from 40 to 402 GHz. Table 1 gives the details of the frequency bands and their sensitivities in polarization (adapted from [Hazumi et al 2020](#), see Sect. 3.2.3).

3.2. Components of the simulations

We build several sets of *LiteBIRD* sky simulations. These multi-frequency sets of polarized sky maps are a mixture of CMB, dust, and instrumental noise. The simulations are made at the nine highest frequencies accessible by the instrument (≥ 100 GHz), where dust is the predominant source of foreground contamination. For every studied scenario, we built $N_{\text{sim}} = 500$ simulations, each composed of a set of $N_{\text{freq}} = 9$ pairs of sky maps (Q, U) built using the HEALPix package, with $N_{\text{side}} = 256$ ([Górski et al. 2005](#)). All the signals will be expressed in μK_{CMB} units.

3.2.1. Cosmic microwave background signal

To generate the CMB signal, we use the *Code for Anisotropies in the Microwave Background* (CAMB, Lewis et al. 2000) to create a fiducial angular power spectrum from the best-fit values of cosmological parameters estimated by the recent *Planck* data analysis (Planck Collaboration 2020a).

For the B -modes, we consider the two different components of the spectrum: lensing-induced and primordial (tensor), so that $\mathcal{D}_\ell^{BB} = \mathcal{D}_\ell^{\text{lensing}} + r_{\text{sim}} \cdot \mathcal{D}_\ell^{\text{tensor}}$, where $\mathcal{D}_\ell^{\text{tensor}}$ refers to the tensor-to-scalar ratio r contained in the simulation. We use two different values throughout this work: $r_{\text{sim}} = 0$, which is used in the present work as the reference simulations and $r_{\text{sim}} = 10^{-2}$ used for consistency checks when the CMB primordial signal is present.

For all simulations, we then generate the Stokes Q and U CMB polarization Gaussian realization maps $S_{\nu,r_{\text{sim}}}^{\text{CMB}}$ from the angular power spectra using the `synfast` function of HEALPix.

3.2.2. Foregrounds: dust

Our study focuses on high frequencies (≥ 100 GHz) only, where thermal dust emission is the main source of polarized foreground as mentioned in Sect. 1. We make use of two different scenarios of increasing complexity included in the PySM (Thorne et al. 2017) and one of intermediate complexity not included in the PySM:

- d0, included in the PySM: the dust polarization Q and U maps are taken from $S_{\nu=353}^{\text{Planck}}$, the *Planck* 2015 data at 353 GHz (Planck Collaboration 2016a), extrapolated to a frequency ν using the MBB given in Eq. 1 with a temperature $T_0 = T_{d0} = 20$ K and spectral index $\beta_0 = \beta_{d0} = 1.54$ constant over the sky:

$$S_\nu^{\text{dust}} = S_\nu^{\text{d0}} = \frac{I_\nu(\beta_{d0}, T_{d0})}{I_{\nu_0}(\beta_{d0}, T_{d0})} \cdot S_{353}^{\text{Planck}}, \quad (11)$$

- d1T, introduced here: the dust polarization Q and U maps are also taken from Planck Collaboration (2016a) but they are extrapolated to a frequency ν using the MBB given in Eq. 2, with spatially varying spectral index $\beta(\mathbf{n})$, as in d1 and a fixed temperature $T_0 = T_{d1T} = 21.9$ K, obtained as the mean of the *Planck* COMMANDER dust temperature map (Planck Collaboration 2016b) on our $f_{\text{sky}} = 0.7$ sky mask:

$$S_\nu^{\text{dust}} = S_\nu^{\text{d1T}} = \frac{I_\nu(\beta(\mathbf{n}), T_{d1T})}{I_{\nu_0}(\beta(\mathbf{n}), T_{d1T})} \cdot S_{353}^{\text{Planck}}. \quad (12)$$

- d1, included in the PySM: similar to d1T with both a spatially varying temperature $T(\mathbf{n})$ and spectral index $\beta(\mathbf{n})$ obtained from the *Planck* data using the COMMANDER code (Planck Collaboration 2016b):

$$S_\nu^{\text{dust}} = S_\nu^{\text{d1}} = \frac{I_\nu(\beta(\mathbf{n}), T(\mathbf{n}))}{I_{\nu_0}(\beta(\mathbf{n}), T(\mathbf{n}))} \cdot S_{353}^{\text{Planck}}. \quad (13)$$

3.2.3. Instrumental noise

The band polarization sensitivities $\sigma_{Q,U}^{\text{noise}}(\nu)$ are derived from the noise equivalent temperature (NET) values converted into $\mu\text{K}\cdot\text{arcmin}$ for each telescope (LFT, MFT and HFT). As seen

	$S_{\nu,r_{\text{sim}}}^{\text{CMB}}$	S_ν^{d0}	S_ν^{d1T}	S_ν^{d1}	N_ν
c	✓	✗	✗	✗	✓
d0	✗	✓	✗	✗	✓
d1T	✗	✗	✓	✗	✓
d1	✗	✗	✗	✓	✓
d0c	✓	✓	✗	✗	✓
d1Tc	✓	✗	✓	✗	✓
d1c	✓	✗	✗	✓	✓

Table 2: Summary of the different components present in the simulated maps M_ν in Eq. 15, for every *simulation type*. A tick on a green background signifies that the component is present in the simulations, red with a cross symbol shows that it is absent.

in Table 1, some frequency bands are overlapping between two telescopes. In this situation, we take the mean value of the two NETs, weighted by the beam full width at half maximum (FWHM) θ as:

$$\sigma_{Q,U}^{\text{noise}}(\nu_{\text{overlapping}}) = \sqrt{\frac{1}{\left(\frac{\theta_{\text{min}}}{\theta_{\text{max}}}\sigma_{Q,U}^{\text{noise}}(\nu_{\theta_{\text{min}}})\right)^{-2} + \left(\sigma_{Q,U}^{\text{noise}}(\nu_{\theta_{\text{max}}})\right)^{-2}}}, \quad (14)$$

where θ_{min} is the smallest FWHM among the two and θ_{max} the largest. The band polarization sensitivities are displayed in Table 1. For every simulation, the noise component N_ν is generated in every pixel of the maps with a Gaussian distribution centered on zero, with standard deviation $\sigma_{Q,U}^{\text{noise}}(\nu)$ weighted by the pixel size (and $\sqrt{2} \cdot \sigma_{Q,U}^{\text{noise}}(\nu)$ for the maps used to compute the auto-power spectra, see Sect. 3.4.2).

For simplicity, we choose to ignore beam effects in our simulations, assuming they can be taken into account perfectly. Simulations are thus produced at infinite (0 arcmin) resolution and no beam effect is corrected for when estimating the angular power spectrum. This is equivalent to convolving the maps by Gaussian beams of finite resolution and correcting the power spectra for the associated Gaussian beam window functions.

3.3. Combining signals and building the simulated maps

The simulated (Q, U) maps M_ν , for a given simulation, can be expressed as the sum:

$$M_\nu = S_{\nu,r_{\text{sim}}}^{\text{CMB}} + S_\nu^{\text{dust}} + N_\nu. \quad (15)$$

Cosmic microwave background and noise are simulated stochastically: for each simulation, we generate a new realization of the CMB maps $S_{\nu,r_{\text{sim}}}^{\text{CMB}}$ and the noise maps N_ν . The dust map S_ν^{dust} is the same for each simulation, at a given frequency.

Hereafter, we use the notation d0, d1T, and d1 to refer to simulations containing only dust and *LiteBIRD* noise, d0c, d1Tc, and d1c for simulations including CMB, dust, and *LiteBIRD* noise and, finally, and c for the simulation containing only CMB and *LiteBIRD* noise. The different components present in these different simulation types are summarized in Table 2.

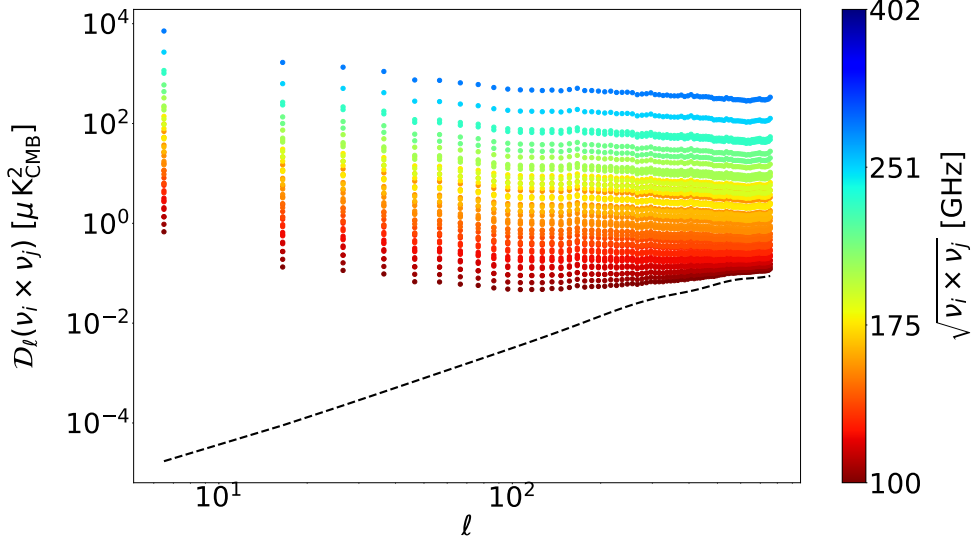


Fig. 1: Mean value over the N_{sim} simulations of the B -mode angular power spectra $\mathcal{D}_\ell(v_i \times v_j)$ for the d1c simulation type, with $r_{\text{sim}} = 0$. The color bar spans all the N_{cross} spectra $\mathcal{D}_\ell(v_i \times v_j)$, associated to their reduced cross-frequency $v_{\text{red.}} = \sqrt{v_i v_j}$, from 100 GHz (dark red) to 402 GHz (dark blue). The input CMB lensing power spectrum is shown as a black dashed line.

3.4. Angular power spectra of the simulations

3.4.1. Mask

A mask is applied on the simulated maps presented in Sect. 3.3 in order to exclude the Galactic plane from the power-spectrum estimation. The mask is created by setting a threshold on the polarized intensity ($P = \sqrt{Q^2 + U^2}$) of the *Planck* 353 GHz map (Planck Collaboration 2020a)², smoothed with a 10° beam. In order to keep $f_{\text{sky}} = 0.7$, $f_{\text{sky}} = 0.6$, and $f_{\text{sky}} = 0.5$, the cut is applied at $121 \mu\text{K}$, $80 \mu\text{K}$, and $53 \mu\text{K}$, respectively. We then realize a C2 apodization of the binary mask with a scale of 5° using NAMASTER (Alonso et al. 2019). The resulting Galactic masks are displayed in Fig. A.1. These masks are similar to those used in Planck Collaboration (2020c).

3.4.2. Estimation of the angular power spectra

We use the NAMASTER³ software (Alonso et al. 2019) to compute the angular power spectra of each simulation. NAMASTER allows us to correct for the E to B leakage bias due to the incomplete sky coverage. Therein we use a *purification* process to suppress the effect of the E to B leakage in the variance. For every simulation, from the set of maps M_{v_i} , we compute all the possible auto-frequency and cross-frequency spectra $\mathcal{D}_\ell(v_i \times v_j) \equiv \mathcal{D}_\ell(M_{v_i} \times M_{v_j})$ with

$$\begin{aligned} v_i \times v_j \in & \{100 \times 100, 100 \times 119, 100 \times 140, \dots, 100 \times 402, \\ & 119 \times 140, \dots, 119 \times 402, \\ & \vdots \\ & 337 \times 337, 337 \times 402, \\ & 402 \times 402\}, \end{aligned} \quad (16)$$

leading to $N_{\text{cross}} = N_{\text{freq}} \cdot (N_{\text{freq}} + 1)/2 = 45$ cross-frequency spectra. These spectra are displayed in Fig. 1 for the case of the d1c simulation type.

In order to avoid noise auto-correlation in the auto-spectra (i.e., $\mathcal{D}_\ell(v_i \times v_j)$ when $i = j$), the latter are estimated in a way that differs slightly from what is presented in Sect. 3.2.3. We simulate two noise-independent data subsets at an observing frequency v_i , with a noise amplitude $\sqrt{2}$ higher than that of the frequency band, and compute the cross-angular power spectrum between those. Thus, $\mathcal{D}_\ell(v_i \times v_i)$ is free from noise auto-correlation bias at the expense of multiplying the noise amplitude in the spectrum by a factor of two. This approach is similar to that commonly used by the *Planck* Collaboration (see e.g., Planck Collaboration 2016c, 2020c; Tristram et al. 2021).

The spectra are evaluated in the multipole interval $\ell \in [1, 200]$ in order to be able to focus on the reionization and recombination bumps of the primordial B -modes spectra. The spectra are binned in $N_\ell = 20$ bins of size $\Delta\ell = 10$ using NAMASTER. The same binning is applied throughout this article such

² <http://pla.esac.esa.int/pla/>

³ <https://github.com/LSSTDESC/NaMaster>

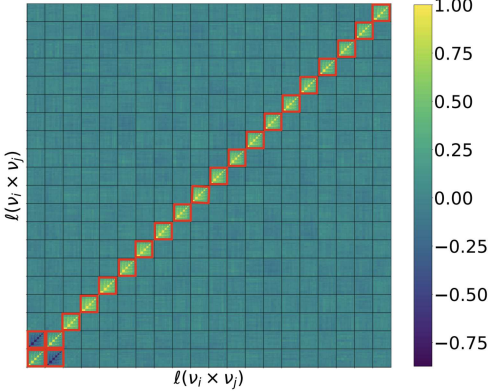


Fig. 2: Correlation matrix ($\text{Corr}_{\ell\ell'} \equiv \mathbb{C}_{\ell\ell'}/\sqrt{\mathbb{C}_{\ell\ell}\mathbb{C}_{\ell'\ell'}}$) for the N_{sim} simulations in d1c. Every block represents a value of ℓ and contains the ordered $N_{\text{cross}} = 45$ cross-spectra. The red squares represent the truncation of the full covariance matrix applied in the analysis (kept entries in red, other entries set to zero).

that, in the following, the multipole ℓ denotes the multipole bin of size $\Delta\ell = 10$ centered on ℓ^4 .

From the sets of (Q, U) maps, NAMASTER computes the \mathcal{D}_{ℓ}^{EE} , \mathcal{D}_{ℓ}^{BB} , and \mathcal{D}_{ℓ}^{EB} angular power spectra; for the sake of the present analysis, we keep only \mathcal{D}_{ℓ}^{BB} . Hence, when we discuss or analyze power spectra, we are referring to the B -mode power spectra \mathcal{D}_{ℓ}^{BB} . All spectra are expressed in $(\mu\text{K}_{\text{CMB}})^2$.

4. Best-fit implementation

In order to characterize the complexity of the dust SED that will be measured by *LiteBIRD*, we modeled the angular power spectra of our simulations described in Sect. 3 over the whole frequency and multipole ranges with the moment expansion formalism introduced in Sect. 2.

4.1. General implementation

For each multipole ℓ , we ordered the angular power spectra $\mathcal{D}_{\ell}^{BB}(v_i \times v_j)$ as in Eq. 16 in order to build a SED that is a function of both v_i and v_j . We fit this SED with models, as in Eq. 8 for example, using a Levenberg-Marquardt χ^2 minimization with `mpfit` (Markwardt 2009)⁵. All the fits performed with `mpfit` were also realized with more computationally heavy Monte Carlo Markov Chains (MCMC) with `emcee` (Foreman-Mackey et al. 2013), giving compatible results, well within the error bars.

The reduced χ^2 minimization is given by

$$\chi^2 = \frac{1}{N_{\text{d.o.f.}}} \mathbf{R}^T \mathbb{C}^{-1} \mathbf{R}, \quad (17)$$

⁴ The N_{ℓ} multipole bins are centered on the following ℓ values: [6.5, 16.5, 26.5, 36.5, 46.5, 56.5, 66.5, 76.5, 86.5, 96.5, 106.5, 116.5, 126.5, 136.5, 146.5, 156.5, 166.5, 176.5, 186.5, 196.5]

⁵ <https://github.com/segasai/astrolibpy/tree/master/mpfit>

where $N_{\text{d.o.f.}}$ is the number of degrees of freedom and \mathbb{C} is the covariance matrix of our N_{sim} simulations, represented in Fig. 2, of dimension $(N_{\ell} \cdot N_{\text{cross}})^2$:

$$\mathbb{C}_{\ell,\ell'}^{ij,k\times l} = \text{cov}(\mathcal{D}_{\ell}^{\text{sim}}(v_i \times v_j), \mathcal{D}_{\ell'}^{\text{sim}}(v_k \times v_l)). \quad (18)$$

The entire covariance matrix \mathbb{C} is, in general, not invertible. To avoid this, we kept only the $\ell = \ell'$ block-diagonal of \mathbb{C} with the strongest correlation values⁶, as well as the $(\ell = 6.5, \ell' = 16.5)$ off-diagonal blocks showing a significant anti-correlation, as illustrated in Fig. 2. It was then possible to invert the thus-defined truncated correlation matrix with the required precision most of the time.

In the case of the d1 simulation type, we experienced a fit convergence issue for $\sim 20\%$ of the simulations, leading to a very large χ^2 . In order to overcome this problem, two options lead to identical results: throwing away the outliers from the analysis or fitting using only the block-diagonal matrix (i.e., the $\ell = 6.5, \ell' = 16.5$ block is set to zero). This last option solves the conversion issue while providing sufficient precision. The results presented in the following are using the block-diagonal matrix when the simulation type is d1.

Finally, in Eq. 17, \mathbf{R} is the residual vector associated with every simulation of size $N_{\ell} \times N_{\text{cross}}$:

$$\mathbf{R} = \begin{pmatrix} \mathcal{R}_{\ell=6.5}(100 \times 100) \\ \mathcal{R}_{\ell=6.5}(100 \times 119) \\ \vdots \\ \mathcal{R}_{\ell=16.5}(100 \times 100) \\ \vdots \\ \mathcal{R}_{\ell=196.5}(402 \times 402) \end{pmatrix}, \quad (19)$$

with $\mathcal{R}_{\ell}(v_i \times v_j) = \mathcal{D}_{\ell}^{\text{sim}}(v_i \times v_j) - \mathcal{D}_{\ell}^{\text{model}}(v_i \times v_j)$.

The expression used for the model to fit is given by:

$$\mathcal{D}_{\ell}^{\text{model}}(v_i \times v_j) = \mathcal{D}_{\ell}^{\text{dust}}(\beta_0(\ell), T_0(\ell), \mathcal{D}_{\ell}^{M\times N}(v_i \times v_j)) + A_{\text{lens}} \cdot \mathcal{D}_{\ell}^{\text{lensing}} + r \cdot \mathcal{D}_{\ell}^{\text{tensor}}, \quad (20)$$

where A_{lens} is not a free parameter and will remain fixed to zero (when there is no CMB, simulation types d0, d1T, and d1) or one (when the CMB is included, simulation types d0c, d1Tc and d1c). We leave the question of the impact of dust modeling with moments on the lensing measurement for future work. In Eq. 20, the free parameters can thus be $\beta_0(\ell)$, $T_0(\ell)$, and $\mathcal{D}_{\ell}^{M\times N}(v_i \times v_j)$ and the tensor-to-scalar ratio r . The estimated value of r is referred to as \hat{r} .

No priors on the parameters are used in order to explore the parameter space with minimal assumptions. Finally, a frequency-dependent conversion factor is included in $\mathcal{D}_{\ell}^{\text{dust}}$ – from $(\text{MJy}\cdot\text{sr}^{-1})^2$ to $(\mu\text{K}_{\text{CMB}})^2$ – to express the dust spectra in $(\mu\text{K}_{\text{CMB}})^2$ units. In those units, $\mathcal{D}_{\ell}^{\text{lensing}}$ and $\mathcal{D}_{\ell}^{\text{tensor}}$ are frequency-independent.

To mitigate the impact of outliers in our simulations, all the final values of the best-fit parameters and χ^2 distributions are represented by their median and median absolute deviations over N_{sim} values. For the tensor-to-scalar ratio \hat{r} , we chose to represent all the best-fit values from the N_{sim} simulations in a histogram and we assume its distribution is normal. Fitting a Gaussian curve on this histogram and getting the mean and standard deviation gives us the final values of \hat{r} and $\sigma_{\hat{r}}$ presented in the paper.

⁶ $\text{Corr}_{\ell\ell'} \equiv \mathbb{C}_{\ell\ell'}/\sqrt{\mathbb{C}_{\ell\ell}\mathbb{C}_{\ell'\ell'}}$

4.2. Implementation for the dust component

For the dust component, we consider four different *fitting schemes*, corresponding to four expressions for the dust model $\mathcal{D}_\ell^{\text{dust}}$ in Eq. 20, which are referred to as "MBB", " β -1", " β - T ", and " β -2". Each of them corresponds to a truncation of Eq. 8, keeping only some selected terms of the moment expansion: MBB stands for those of the modified black body, β -1 for those of the expansion in β at first order, β -2 for the expansion in β at second order, and β - T for the expansion in both β and T at first order. We chose the β -1 and β -2 truncations based on the studies of Mangilli et al. (2021) and Azzoni et al. (2020), where the dust SED moment expansion is performed only with respect to β . The β - T fitting scheme is instead the first-order truncation in both β and T , introduced here for the first time at the power spectrum level. The parameters fitted in each of these fitting schemes are summarized in Table 3. We note that the β -2 and β - T fitting schemes share the same number of free parameters. Finally, when we fit \hat{r} at the same time as the dust parameters, the fitting schemes will be referred to as r MBB, $r\beta$ -1, $r\beta$ - T , and $r\beta$ -2.

Different physical processes are expected to occur at different angular scales, leading to different SED properties. Thus, we estimate the dust-related parameters with one parameter per multipole bin. As an example, we estimate $\beta_0 = \beta_0(\ell)$ and $T_0 = T_0(\ell)$ to be able to take into account their scale dependence, at the cost of increasing the number of free parameters in our model. This is also true for the higher order moments. On the other hand, \hat{r} is not scale dependent and, when it is fitted, we add one single parameter over the whole multipole range.

In Mangilli et al. (2021), the first-order moment expansion parameter $\mathcal{D}_\ell^{A \times \omega^\beta}$ is considered to be the leading order correction to the MBB spectral index. We applied a similar approach in the present work, extending it to the dust temperature when it is fitted. In our pipeline, we proceed iteratively:

1. (i) we fit $\beta_0(\ell)$ and $T_0(\ell)$ at order zero (MBB), for each ℓ ,
2. (ii) we fix $\beta_0(\ell)$ and $T_0(\ell)$ and fit the higher order parameters, as in Eq. 8, (iii) we update the $\beta_0(\ell)$ to $\beta_{\text{corr}}(\ell)$ (and $T_0(\ell)$ to $T_{\text{corr}}(\ell)$ in the case of β - T) as:

$$\beta_{\text{corr}}(\ell) = \beta_0(\ell) + \frac{\mathcal{D}_\ell^{A \times \omega^\beta}}{\mathcal{D}_\ell^{A \times A}}, \quad T_{\text{corr}}(\ell) = T_0(\ell) + \frac{\mathcal{D}_\ell^{A \times \omega_1^T}}{\mathcal{D}_\ell^{A \times A}}, \quad (21)$$

- iv) and we iterate from (ii) fixing $\beta_0(\ell) = \beta_{\text{corr}}(\ell)$, until $\mathcal{D}_\ell^{A \times \omega_1^\beta}$ converges to be compatible with zero (and $T_0(\ell) = T_{\text{corr}}(\ell)$, until $\mathcal{D}_\ell^{A \times \omega_1^T}$ converges to zero in the case of β - T).

We used three such iterations, which we found to be sufficient to guarantee the convergence. As the moment expansion is a nonorthogonal and incomplete basis (Chluba et al. 2017), this iterative process is performed to ensure that the expansions up to different orders share the same $\beta_0(\ell)$ and $T_0(\ell)$ with $\mathcal{D}_\ell^{A \times \omega_1^\beta} = 0$ and $\mathcal{D}_\ell^{A \times \omega_1^T} = 0$.

5. Results

In this section, we present our evaluation of the best-fit parameters for the different fitting schemes presented in Sect. 4.1 on the B -mode cross-angular power spectra computed from the different simulation types presented in Sect. 3.3 and on the Galactic mask keeping $f_{\text{sky}} = 0.7$, which is defined in Sect. 3.4.1. We first

	MBB	β -1	β - T	β -2
	3N $_\ell$	2N $_\ell$	5N $_\ell$	5N $_\ell$
$N_{\text{param.}}$				
$\beta_0(\ell)$	✓	○	○	○
$T_0(\ell)$	✓	✗	○	✗
$\mathcal{D}_\ell^{A \times A}$	✓	✗	✗	✗
$\mathcal{D}_\ell^{A \times \omega_1^\beta}$	✗	✓	✓	✓
$\mathcal{D}_\ell^{\omega_1^\beta \times \omega_1^\beta}$	✗	✓	✓	✓
$\mathcal{D}_\ell^{A \times \omega_1^T}$	✗	✗	✓	✗
$\mathcal{D}_\ell^{\omega_1^T \times \omega_1^T}$	✗	✗	✓	✗
$\mathcal{D}_\ell^{\omega_1^\beta \times \omega_1^T}$	✗	✗	✓	✗
$\mathcal{D}_\ell^{A \times \omega_2^\beta}$	✗	✗	✗	✓
$\mathcal{D}_\ell^{\omega_1^\beta \times \omega_2^\beta}$	✗	✗	✗	✓
$\mathcal{D}_\ell^{\omega_2^\beta \times \omega_2^\beta}$	✗	✗	✗	✓

Table 3: Summary of the fitted parameters in the four dust moment expansion *fitting schemes* we consider (MBB, β -1, β - T , and β -2), in Eq. 8. A tick on a green background signifies that the parameter is fitted, red with a cross symbol shows that the parameter is not fitted, and a circle symbol on yellow means that the parameter is fixed and corrected through an iterative process as presented in Sect. 4.2. $\mathcal{D}_\ell^{A \times A}$ is fixed to the MBB best-fit value in the case of β -1, β - T , and β -2 and all the other moments are set to zero when they are not fitted. When \hat{r} is fitted at the same time, the fitting schemes are denoted r MBB, $r\beta$ -1, $r\beta$ - T , and $r\beta$ -2, and they have one more parameter than the number of parameters reported in the first line.

tested the simulation types containing only dust and noise in order to calibrate the dust complexity of our data sets in Sect. 5.1. We then used CMB only plus noise simulations to assess the minimal error on \hat{r} in Sect. 5.2 and, finally, we explored the dust, CMB, and noise simulation types to assess the impact of the dust complexity on \hat{r} in Sect. 5.3.

5.1. Dust only

To evaluate the amplitude of the dust moment parameters contained in the dust simulations in the absence of CMB, we ran the fitting schemes presented in Sect. 4.1 in the three simulation types d0, d1T, and d1 presented in Sect. 3.3. In these cases, A_{lens} and r in Eq. 20 are both fixed to zero and the fitted parameters are given in Table 3 for every fitting scheme.

5.1.1. d0

The d0 dust maps presented in Sect. 3.2 extrapolate between frequency bands with a MBB SED with constant parameters over the sky: $\beta_{\text{d0}} = 1.54$ and $T_{\text{d0}} = 20$ K. We performed the fit with the four fitting schemes presented in Sect. 4.1.

In Fig. 3 the values of the reduced $\chi^2(\ell)$ for each fitting scheme are displayed. For every fitting scheme (MBB, β -1, β - T and β -2), the reduced χ^2 are close to 1 over the whole multipole range (slightly below 1 for the β -1, β - T and β -2 fitting scheme). This indicates that the MBB is a good fit to the cross-angular power spectra computed from the d0 maps with a spatially invariant MBB SED, as expected. Adding additional (higher order) parameters, such as with β -1, β - T and β -2, has no significant effect on the χ^2 .

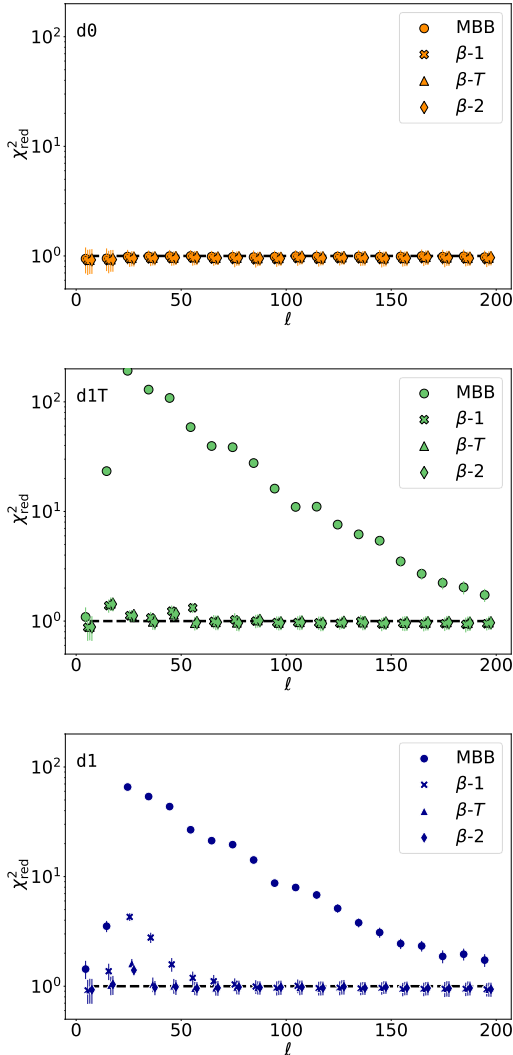


Fig. 3: Median of the reduced χ^2 in every multipole bin ℓ , for all the N_{sim} simulations of d0 (top, orange), d1T (middle, green) and d1 (bottom, blue), on $f_{\text{sky}} = 0.7$. The reduced χ^2 values are reported for the four different fitting schemes: MBB (circles), β -1 (crosses), β -T (diamonds) and β -2 (triangles). The values for the four fitting schemes are shifted from each others by $\ell = 2$, in order to distinguish them. The black dashed line represents $\chi^2_{\text{red}} = 1$.

In Fig. 4 we can see that the best-fit values of $\beta_0(\ell)$ and $T_0(\ell)$ are compatible with constant values $\beta_0(\ell) = \beta_{\text{d}0}$ and $T_0(\ell) = T_{\text{d}0}$, as expected for this simulated data set.

The best-fit values of the dust amplitude and the moment-expansion parameters are presented in Figs. 5, 6, 7, and 8, respectively. The amplitude power spectrum is compatible with that of the dust template map used to build d0 and the moment-expansion parameters are compatible with zero for every fitting

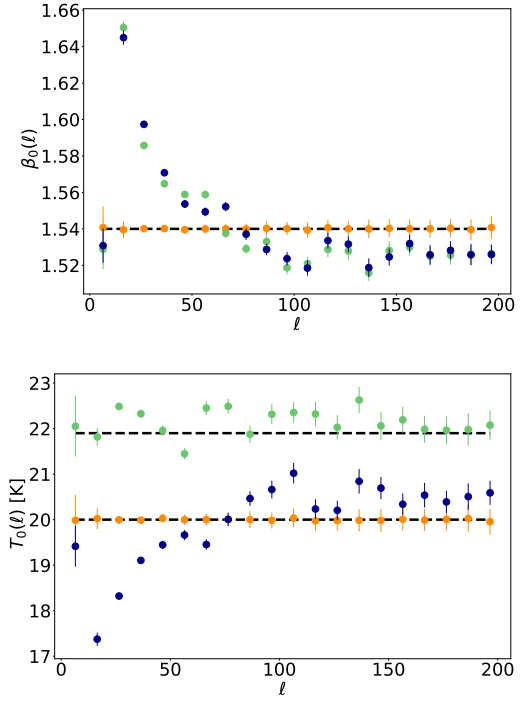


Fig. 4: (Top): Median of the best fit values of $\beta_0(\ell)$ in d0 (orange), d1T (green), and d1 (blue) for the MBB (circles). $\beta_{\text{d}0}$ is marked by the dashed black line. (Bottom): Same as above but with $T_0(\ell)$, the black dashed-lines being $T_{\text{d}0} = 20$ K and $T_{\text{d}1T} = 21.9$ K.

scheme, as expected with no spatial variation of the SED. Therefore, the moment expansion method presented in Sect. 2 passes the *null test* in the absence of SED distortions, with the d0 simulated data set.

5.1.2. d1T

We now introduce, as a first layer of complexity, the spatial variations of the spectral index associated to a fixed temperature over the sky with the d1T simulation type. The dust temperature was fixed to $T_{\text{d}1T} = 21.9$ K while the spectral index $\beta(n)$ was allowed to vary between lines of sight. The four different fitting schemes presented in Sect. 4.1 are fitted over the cross-spectra of our simulations as in Sect. 5.1.1.

The reduced $\chi^2(\ell)$ values for each fitting scheme can be found in Fig. 3. It can be seen that the MBB no longer provides a good fit for the dust SED, especially at low multipoles. Averaging effects of spatially varying SEDs are more important over large angular scales and thus SED distortions and moments are expected to be more significant at low multipoles. Indeed, the moments added to the fit in β -1 are enough to lower the reduced χ^2 such that it becomes compatible with 1 over almost all of the multipole range. The fitting schemes β -T and β -2, including more parameters than β -1, provide a fit of similar goodness, except in the multipole bin $\ell = 66.5$ where they are closer to 1.

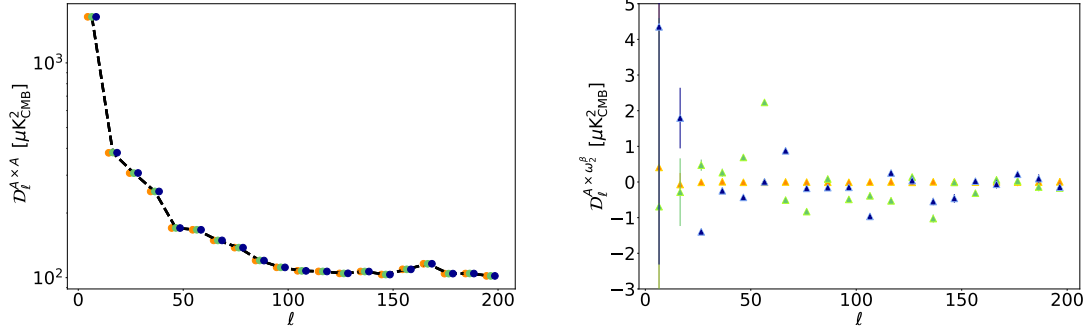


Fig. 5: Median of the best-fit values of $D_\ell^{A \times A}$ for d0 (orange), d1T (green), and d1 (blue) using the MBB fitting scheme. The values for the three simulation types are shifted with respect to one another by $\ell = 2$ in order to distinguish them. The black dashed line is the amplitude power spectrum of the dust template map used to build the three simulation sets d0, d1T, and d1.

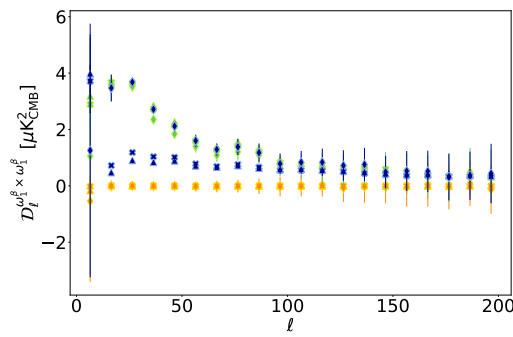


Fig. 6: Best-fit values of the first-order moment $D_\ell^{\omega_1^\beta \times \omega_1^\beta}$ for d0 (orange), d1T (green), and d1 (blue), fitting with β -1 (crosses), β -2 (triangles), and β -T (diamonds).

Figure 4 presents the best-fit values of $\beta_0(\ell)$ in the case of the MBB fit. For the sake of clarity, the values after iteration (see Sect. 4.1) for β -1, β -T, and β -2 are not shown, but they present comparable trends. We can see that the best-fit values of $\beta_0(\ell)$ for this d1T simulation type are no longer compatible with a constant. $\beta_0(\ell)$ fitted values show a significant increase at low (< 100) multipoles, up to $\beta_0(\ell = 16.5) = 1.65$. For $\ell > 100$, $\beta_0(\ell)$ is close to a constant of value ~ 1.53 . This increase towards the low ℓ is correlated to the increase of the MBB χ^2 discussed in the previous paragraph. However, we note that in the lowest ℓ -bin, the $\beta_0(\ell)$ value is close to 1.53 and that the χ^2 of the MBB fit is close to unity.

The best-fit values of $T_0(\ell)$ are also presented in Fig. 4 in the case of the MBB fit. Here again, the values after iteration for the other fitting schemes are not presented, but are similar. The d1T $T_0(\ell)$ best-fit values oscillate around $T_{\text{d1T}} = 21.9$ K, without being strictly compatible with a constant value, as would be expected for this simulation type. This tends to indicate that the SED distortions due to the spectral index spatial variations

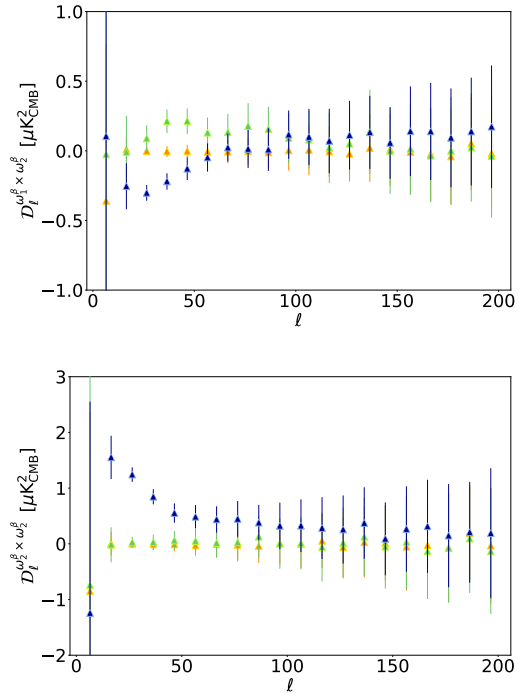


Fig. 7: Best-fit values of the second-order $D_\ell^{A \times A_2^\beta}$, $D_\ell^{\omega_1^\beta \times \omega_2^\beta}$ and $D_\ell^{\omega_2^\beta \times \omega_1^\beta}$ moment parameters in d0 (orange), d1T (green), and d1 (blue) for β -2 (triangles).

are affecting the accuracy at which we can recover the correct angular dependence of the sky temperature.

The amplitude power spectrum is displayed in Fig. 5 for the MBB fitting scheme. The other fitting scheme results are not presented for clarity and would not be distinguishable from those of the MBB. The fitted $D_\ell^{A \times A}$ is compatible with the one of the dust template map used to build the simulations.

All the parameters of the moment expansion with respect to β can be found in Figs. 6 and 7, and are now significantly detected, except for $D_\ell^{\omega_2^\beta \times \omega_2^\beta}$. In Fig. 8, we can observe that the parameters of the moment expansion with respect to the temperature (only

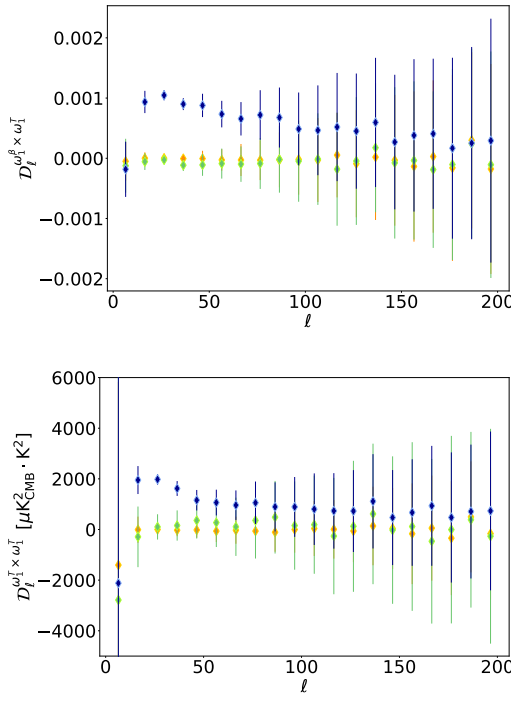


Fig. 8: Best-fit values of the first-order $D_l^{\beta \times \omega_l^T}$ and $D_l^{\omega_l^T \times \omega_l^T}$ moment parameters in d0 (orange), d1T (green), and d1 (blue) for β - T (diamonds).

present in the β - T fit) remain undetected. The SED distortions due to the spatial variations of β are well detected, while no SED distortion linked to the temperature is seen, as expected for the d1T simulation type.

5.1.3. d1

We now discuss the d1 simulations, with the highest complexity in the polarized dust SED. In this more physically relevant simulation type, the dust emission is given by a MBB with variable index $\beta(\mathbf{n})$ and temperature $T(\mathbf{n})$ over the sky. We ran the four different fitting schemes on the d1 simulation type, as we did in Sect. 5.1.1 and 5.1.2.

The values of the reduced $\chi^2(\ell)$ are displayed in Fig. 3. For the MBB and β -1, the reduced χ^2 are not compatible with unity, especially at low multipole. This indicates that none of them are a good fit anymore for the spatially varying SED with $\beta(\mathbf{n})$ and $T(\mathbf{n})$. With β -2 and β - T , the $\chi^2(\ell)$ values become compatible with unity, except for the $\ell = 26.5$ bin. We note that β - T provides a slightly better fit than β -2 in this bin.

Looking at the medians of the best-fit values of $\beta_0(\ell)$ for d1 in Fig. 4, we can see that the spectral index is changing with respect to ℓ , as discussed in Sect. 5.1.2, in a similar manner as for the d1T simulation type. The fitted temperature $T_0(\ell)$ values for d1 show an increasing trend from ~ 17 to ~ 20.5 K and from $\ell = 16.5$ to $\ell \sim 100$. At higher multipoles, $T_0(\ell)$ is close to a constant temperature of 20.5 K. In d1, as for d1T, the angular scales at which we observe strong variations of $\beta_0(\ell)$ and $T_0(\ell)$

are the ones for which we observe a poor χ^2 for some fitting schemes. Also, as for d1T, the largest angular scale ℓ -bin, at $\ell = 6.5$, shows β and T values close to the constant value at high ℓ , which are associated with χ^2 values closer to unity. The best-fit values of the amplitude $D_l^{4 \times 4}$ are shown in Fig. 5. These are similar to those of the other simulation types.

The moment-expansion parameters fitted on d1 are shown in Figs. 6, 7, and 8. For this simulation type, the moment parameters are all significantly detected with respect to both β and T . This was already the case with the *Planck* intensity simulations, produced in a similar way, as discussed in Mangilli et al. (2021). Their detections quantify the complexity of dust emission and SED distortions from the MBB present in the d1 simulation type, due to the spatial variations of $\beta(\mathbf{n})$ and $T(\mathbf{n})$.

5.2. CMB only

In order to calibrate the accuracy at which the r parameter can be constrained with the *LiteBIRD* simulated data sets presented in Sect. 3.3, we tested the simulation type with no dust component, M_v^c , and with no tensor modes ($r_{\text{sim}} = 0$, only CMB lensing and noise). We fit the expression in Eq. 20 with D_l^{dust} fixed to zero and A_{lens} fixed to one (i.e., r is the only parameter we fit in this case). Doing so over the N_{sim} simulations, we obtain $\hat{r} = (0.7 \pm 3.5) \times 10^{-4}$. This sets the minimal value we can expect to retrieve for \hat{r} with our assumptions if the dust component is perfectly taken into account.

5.3. Dust and CMB

We now present our analysis of the simulations including dust, CMB (lensing), and noise (d0c, d1Tc and d1c) with no primordial tensor modes ($r_{\text{sim}} = 0$). As described above, we applied the four fitting schemes for the dust on the three simulation types, fitting \hat{r} and fixing A_{lens} to one (namely rMBB, $r\beta$ -1, $r\beta$ - T and $r\beta$ -2) simultaneously.

The best-fit values of $\beta_0(\ell)$, $T_0(\ell)$ and the moment expansion parameters $D_l^{M \times N}$ derived with the simulation types d0c, d1Tc, and d1c are not discussed further when they are compatible with the ones obtained for the d0, d1T, and d1 simulation types and presented in Sect. 5.1.

5.3.1. d0c

For d0c, as for d0, we recover the input constant spectral index and temperature β_{d0} and T_{d0} at all angular scales for every fitting scheme. Furthermore, we do not detect any moment, when fitting $r\beta$ -1, $r\beta$ - T , and $r\beta$ -2. This simulation type therefore constitutes our null-test when \hat{r} and the dust parameters are fitted at the same time. The addition of the CMB lensing in the simulations and the addition of r to the fits thus does not lead to the detection of the moment parameters nor biases the recovery of the spectral index and the temperature.

The posterior distributions of the estimated tensor-to-scalar ratio \hat{r} are displayed in Fig. 9 and their mean and standard deviations are summarized in Table 4. We note that \hat{r} is compatible with the input value ($r_{\text{sim}} = 0$) for all the fitting schemes. For rMBB and $r\beta$ -1, the dispersion $\sigma_{\hat{r}}$ is comparable with the CMB-only scenario discussed in Sect. 5.2. For $r\beta$ - T and $r\beta$ -2, the width of the distribution increases by a factor of ~ 2 and ~ 4 , respectively.

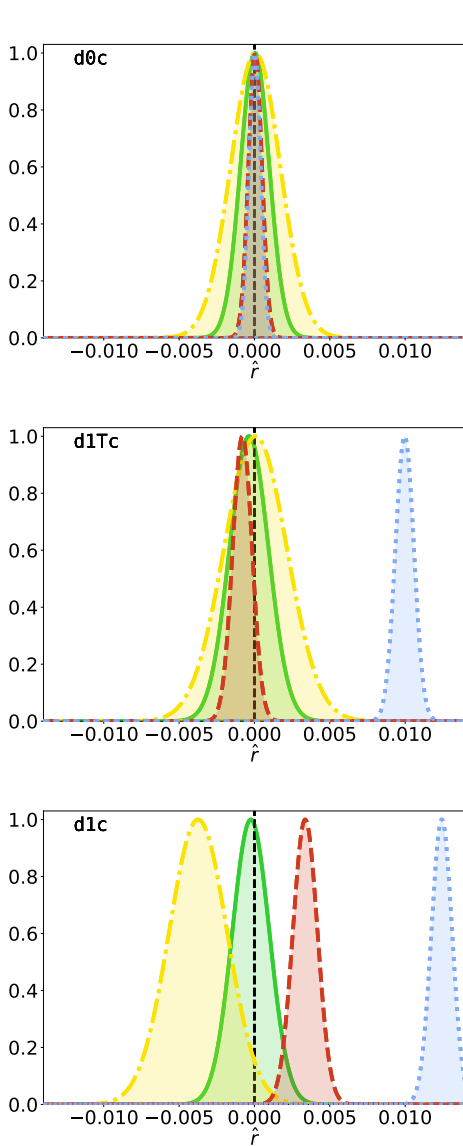


Fig. 9: (Top panel): Posterior on \hat{r} in the d0c simulation type for the different fitting schemes: rMBB (blue, dotted line), $r\beta$ -1 (red, dashed line), $r\beta$ -T (green, solid line), and $r\beta$ -2 (yellow, dash-dotted line). The vertical black dashed line marks the value of $r_{\text{sim}} = 0$. (Central panel): Same, but in the case of the d1Tc simulation type. (Bottom panel): Same, but in the case of the d1c simulation type.

5.3.2. d1Tc

The posterior distribution of \hat{r} in the case of the d1Tc simulation type is displayed in Fig. 9 for the four fitting schemes and the mean value and standard deviation of these distributions are summarized in Table 4. We can see that in the case of rMBB, we fit $\hat{r} \pm \sigma_{\hat{r}} = (99.7 \pm 6.2) \times 10^{-4}$. In that case, the input tensor-

$(\hat{r} \pm \sigma_{\hat{r}}) \times 10^4$	d0c	d1Tc	d1c
rMBB	0.3 ± 3.9	99.7 ± 6.2	125.1 ± 5.9
$r\beta$ -1	0.5 ± 4.5	-8.0 ± 6.4	32.9 ± 6.5
$r\beta$ -T	0.3 ± 9.5	-3.6 ± 13.0	-3.3 ± 11.7
$r\beta$ -2	0.7 ± 16.4	0.7 ± 20.9	-37.4 ± 19.4

Table 4: Best-fit values of \hat{r} in units of 10^{-4} on $f_{\text{sky}} = 0.7$. The green values are compatible with $r_{\text{sim}} = 0$ at $1\sigma_{\hat{r}}$, the yellow values are compatible with $r_{\text{sim}} = 0$ at $2\sigma_{\hat{r}}$ and the red values are incompatible with $r_{\text{sim}} = 0$ at more than $2\sigma_{\hat{r}}$.

to-scalar ratio $r_{\text{sim}} = 0$ is not recovered and we obtain a bias on the central value of \hat{r} of $\sim 16\sigma_{\hat{r}}$. As discussed in Sect. 2.1.2, this is expected because we know that the MBB is not a good dust model for a SED with spatially varying spectral index, as we also verify in Sect. 5.1.2 looking at the χ^2 values.

Using the $r\beta$ -1 fitting scheme allows us to recover $\hat{r} = (-8.0 \pm 6.4) \times 10^{-4}$, where r_{sim} is recovered within $\sim 2\sigma_{\hat{r}}$, while $r\beta$ -2 and $r\beta$ -T recover the input value within $1\sigma_{\hat{r}}$ (with $\hat{r} = (-3.6 \pm 13.0) \times 10^{-4}$ and $\hat{r} = (0.7 \pm 20.9) \times 10^{-4}$, respectively). As in Sect 5.3.1, the deviation remains similar between rMBB and $r\beta$ -1 and increases by a factor of ~ 2 and ~ 4 from $r\beta$ -1 to $r\beta$ -T and $r\beta$ -2, respectively.

5.3.3. d1c

In the case of the d1c simulation type, as in d0c and d1Tc, we fit \hat{r} in addition to the dust-related parameters. In that case, dust moment parameters are recovered as for d1 (see Sect. 5.1.3), except for the $r\beta$ -2 fitting scheme.

Figure A.2 compares the moment parameters between β -2 on the d1c simulations type, fitting only the dust-related parameters and $r\beta$ -2 on d1c when jointly fitting the dust parameters and \hat{r} . We observe that $D_{\ell}^{\omega_2^{\beta} \times \omega_2^{\beta}}$ is not consistently recovered when fitting \hat{r} in addition to the dust parameters.

A similar comparison can be found in Fig. A.3 for the moment parameters between β -T and $r\beta$ -T on the d1c simulation type. Using this fitting scheme, we can see that all the moments are correctly recovered when adding \hat{r} to the fit.

The \hat{r} posterior distributions in the case of d1c are displayed in Fig. 9 and summarized in Table 4. As discussed in Sect. 2.1.2 and observed in Sect. 5.3.3, the rMBB fit is highly biased, with $\hat{r} = (125.1 \pm 5.9) \times 10^{-4}$ (by more than $21\sigma_{\hat{r}}$). When fitting the $r\beta$ -1, this bias is significantly reduced ($\hat{r} = (32.9 \pm 6.5) \times 10^{-4}$, $5\sigma_{\hat{r}}$ away from $r_{\text{sim}} = 0$), illustrating the ability of the first-moment parameters to correctly capture part of the SED complexity. However, performing the expansion in both β and T with $r\beta$ -T allows us to recover r_{sim} without bias ($\hat{r} = (-3.3 \pm 11.7) \times 10^{-4}$), highlighting the need for the description of the SED complexity in terms of dust temperature for this simulated data set where both β and T vary spatially. On the other hand, for $r\beta$ -2, a negative tension ($1.9\sigma_{\hat{r}}$) can be observed: $\hat{r} = (-37.4 \pm 19.4) \times 10^{-4}$. This tension is discussed in Sect. 6.5.

For d1c, the \hat{r} distribution widths roughly meet the foreground cleaning requirements of LiteBIRD presented in Sect. 3.1 for rMBB and $r\beta$ -1 but are higher for $r\beta$ -T and $r\beta$ -2. We also note that, with the same number of free parameters, all the standard deviations $\sigma_{\hat{r}}$ slightly increase compared to the d0c simulation type. This is expected due to the increasing dust complexity.

6. Discussion

6.1. Lessons learnt

In Sect. 5, we apply the fitting pipeline introduced in Sect. 4 on *LiteBIRD* simulated data sets on $f_{\text{sky}} = 0.7$ and for $r_{\text{sim}} = 0$, including the various dust simulation types defined in Sect. 3.2. We fitted the estimated B -mode power-spectra with the four different fitting schemes summarized in Table 3. Our main results can be summarized as follows:

- The MBB fitting scheme provides a good fit for the dust component in the d0 and d0c simulation types. However, when the spectral index changes with the angular scale, such as in the d1T, d1Tc, d1, and d1c simulations, this approach no longer provides a good fit because of the complexity of the dust SED. As a consequence, in the rMBB case, r_{sim} cannot be recovered without a significant bias.
- The β -1 fitting scheme allows us to perform a good fit for the dust complexity using the d0 and d1T simulations but not for d1, while the $r\beta$ -1 fitting scheme yields estimates of \hat{r} close to r_{sim} within $1\sigma_{\hat{r}}$ for d0c, and within $2\sigma_{\hat{r}}$ for d1Tc, but presenting a bias of $\sim 6\sigma_{\hat{r}}$ for d1c.
- The β -T fitting scheme provides a good fit for every dust model, while using the $r\beta$ -T fitting scheme allows us to recover \hat{r} values consistent with r_{sim} within $1\sigma_{\hat{r}}$ for all the simulation types, but is associated with an increase of $\sigma_{\hat{r}}$ by a factor ~ 2 compared to the $r\beta$ -1 case.
- The β -2 fitting scheme also provides a good fit for each dust model, and the $r\beta$ -2 fitting scheme leads to values of \hat{r} compatible with r_{sim} within $1\sigma_{\hat{r}}$ for all the simulation types but d1c. In this last case, there is a negative tension of $\sim 2\sigma_{\hat{r}}$. For all the simulation types, there is an increase of $\sigma_{\hat{r}}$ by a factor of ~ 4 compared to the $r\beta$ -1 case.

The present analysis shows that the temperature could be a critical parameter for the moment expansion in the context of *LiteBIRD*.

Indeed, for simulations including a dust component with a spectral index and a temperature that both vary spatially, as in d1, the only fitting scheme allowing us to recover r_{sim} within $1\sigma_{\hat{r}}$ is $r\beta$ -T, the expansion to first order in both β and T . This shows that expanding in β only, without treating T , is not satisfactory when looking at such large fractions of the sky. Indeed, when applying the β -2 fitting scheme, the $\mathcal{D}_{\ell}^{\omega_2^{\beta} \times \omega_2^{\beta}}$ parameter remains undetected for the d1T simulation type (Sect 5.1.2), while it is significantly detected using the d1 simulation type (Sect 5.1.3). Nevertheless, d1T and d1share the same template of $\beta(\mathbf{n})$ (Sect. 3.2) and they only differ by the sky temperature (constant for d1T and varying for d1). This suggests that the observed $\mathcal{D}_{\ell}^{\omega_2^{\beta} \times \omega_2^{\beta}}$ with the d1 simulations originates from the temperature variations and not those in the spectral index. This observation shows that it is less convenient to use the β -2 fitting scheme than the β -T one in order to correctly recover the moment-expansion parameters and \hat{r} when temperature varies spatially.

Moreover, we saw that $\sigma_{\hat{r}}$ is lower when using the fitting scheme $r\beta$ -T instead of $r\beta$ -2 for every simulation type, even if both have the same number of free parameters. This second observation additionally encourages an approach where the SED is expanded with respect to both β and T . Nevertheless, the uncertainty on \hat{r} we obtain in this case ($\sigma_{\hat{r}} = 1.17 \times 10^{-3}$) is larger than the *LiteBIRD* requirements.

ℓ_{cut}	$(\hat{r} \pm \sigma_{\hat{r}}) \times 10^4$
50	12.0 ± 7.3
60	7.3 ± 7.9
70	4.9 ± 8.1
80	-0.9 ± 8.8
90	-2.1 ± 9.9

Table 5: Best-fit values of $\hat{r} \pm \sigma_{\hat{r}}$ in units of 10^{-4} for different values of ℓ_{cut} for the d1c simulations with $f_{\text{sky}} = 0.7$, when applying the $r\beta$ -T fitting scheme. The green values are compatible with $r_{\text{sim}} = 0$ at $1\sigma_{\hat{r}}$.

$(\hat{r} \pm \sigma_{\hat{r}}) \times 10^4$	$r_{\text{sim}} = 0.01$	$f_{\text{sky}} = 0.5$	$f_{\text{sky}} = 0.6$
rMBB	204.8 ± 7.7	47.3 ± 5.6	59.2 ± 5.4
$r\beta$ -1	129.0 ± 8.3	-8.4 ± 6.7	1.8 ± 6.2
$r\beta$ -T	94.6 ± 15.1	0.02 ± 13.4	-1.1 ± 12.0
$r\beta$ -2	62.5 ± 25.0	4.3 ± 24.2	-3.2 ± 22.4

Table 6: Best-fit values of \hat{r} in units of 10^{-4} for an alternative d1c simulation with $r_{\text{sim}} = 0.01$ on $f_{\text{sky}} = 0.7$, and with $r_{\text{sim}} = 0$ but on $f_{\text{sky}} = 0.5$ and $f_{\text{sky}} = 0.6$. The green values are compatible with r_{sim} at $1\sigma_{\hat{r}}$, the yellow values are compatible with r_{sim} at $2\sigma_{\hat{r}}$, and the red values are incompatible with r_{sim} at more than $2\sigma_{\hat{r}}$.

6.2. Increasing the accuracy on the tensor-to-scalar ratio

In Sect. 5.1.3 and Fig. 3, we see that the MBB and β -1 fitting schemes do not provide good fits for the d1 dust simulations, especially at low multipoles ($\ell \lesssim 100$). Conjointly, in Fig. 8, we can see that the β -T moment parameters are significantly detected for $\ell \lesssim 100$ and compatible with zero above that threshold, suggesting that their corrections to the SED are predominantly required at large angular scales.

This implies that we can improve the pipeline presented in Sect. 4 to keep only the required parameters in order to recover \hat{r} compatible with r_{sim} with a minimal $\sigma_{\hat{r}}$. It can be achieved by applying the $r\beta$ -1 fitting scheme over the whole multipole range, while restricting the $r\beta$ -T-specific ($\mathcal{D}_{\ell}^{\omega_1^{\beta} \times \omega_1^T}$ and $\mathcal{D}_{\ell}^{\omega_1^T \times \omega_1^T}$) moment-expansion parameters fit to the low multipoles range. We note that in order to correct the bias, it is still necessary to keep the $r\beta$ -1 moment parameters even at high multipoles, because the MBB does not provide a good fit even for $\ell \in [100, 200]$, as we can see in Fig. 3. We define ℓ_{cut} as the multipole bin under which we keep all the $r\beta$ -T moment parameters and above which we use the $r\beta$ -1 scheme.

The best-fit values and standard deviations of \hat{r} for different values of ℓ_{cut} are displayed in Table 5. We can see that a trade-off has to be found: the smaller the ℓ_{cut} , the bigger the shift from r_{sim} , and the bigger the ℓ_{cut} , the higher the value of $\sigma_{\hat{r}}$. The trade-off point seems to be found for $\ell_{\text{cut}} \sim 80$, allowing us to recover \hat{r} without tension, with $\sigma_{\hat{r}} = 8.8 \times 10^{-4}$. The error on r is thus reduced by more than $\sim 30\%$ with respect to the nonoptimized fit and meets the *LiteBIRD* requirements.

6.3. Tests with smaller sky fractions

In all the results presented in Sect. 5, we were considering a sky fraction of $f_{\text{sky}} = 0.7$. This sky mask keeps a considerable fraction of the brightest Galactic dust emission. To quantify the impact of the sky fraction on our analysis, we ran the pipeline as in Sect. 5.3.3 with the different masks introduced in Sect. 3.4.1 ($f_{\text{sky}} = 0.5$ and $f_{\text{sky}} = 0.6$). This was done with the d1c simulation type.

The posteriors on \hat{r} for the different fitting schemes are displayed in Fig. 10 and Table 6. We can see that, while the rMBB fitting scheme always leads to biased estimates, the $r\beta$ -1 case allows us to recover \hat{r} at $1.25 \sigma_{\hat{r}}$ for $f_{\text{sky}} = 0.5$ and within $1 \sigma_{\hat{r}}$ for $f_{\text{sky}} = 0.6$. In the two situations, the results using the $r\beta$ - T and β -2 fitting schemes are both unbiased with estimates of \hat{r} compatible with r_{sim} within $1 \sigma_{\hat{r}}$. The $\sigma_{\hat{r}}$ hierarchy between the rMBB, $r\beta$ -1, $r\beta$ - T , and $r\beta$ -2 fitting schemes is the same as for $f_{\text{sky}} = 0.7$ (see Sect. 5.3.3). Nevertheless, we observe that $\sigma_{\hat{r}}$ increases as the sky fraction decreases, as does the statistical error (cosmic variance of the lensing and noise). The bias, on the other hand, decreases for all the fitting schemes with the sky fraction, which is expected because less dust emission contributes to the angular power spectra. The negative tension observed on the \hat{r} posterior in Sect. 5.3.3 for the $r\beta$ -2 case is not present when using smaller sky fractions. In Fig. A.5, the $r\beta$ -2 moment parameters are displayed. We can see that they are not significantly detected for the $f_{\text{sky}} = 0.5$ and 0.6, unlike for $f_{\text{sky}} = 0.7$. As we have seen that some of the moments in the β -2 fitting scheme failed to model SED distortions coming from temperature, we can suppose that, in our simulations, the temperature variations play a less significant role in the dust SED on the $f_{\text{sky}} = 0.5$ and 0.6 masks than they play in the $f_{\text{sky}} = 0.7$ one. As a consequence, they have a smaller impact on r when not properly taken into account.

6.4. Tests with nonzero input tensor modes

We show in Sect. 5.3.3 that the $r\beta$ - T fitting scheme allows us to retrieve \hat{r} compatible with zero when $r_{\text{sim}} = 0$. We now want to assess the potential leakage of \hat{r} in the moment expansion parameters if $r_{\text{sim}} \neq 0$. In this case, primordial tensor signals would be incorrectly interpreted as dust complexity. We run the pipeline as described in Sect. 5.3.3 with $r_{\text{sim}} = 0.01$, in the d1c simulation type. This value of $r_{\text{sim}} = 0.01$ is larger than the value targeted by *LiteBIRD*, but given the order of magnitude of the error on \hat{r} observed in the previous sections, a potential leakage could be left unnoticed using a smaller r_{sim} .

Looking at the final posterior on \hat{r} (Fig. 11 and Table 6), we can see that the results are comparable with the $r_{\text{sim}} = 0$ case, but centered on the new input value $r_{\text{sim}} = 0.01$. The rMBB fitting scheme gives a highly biased posterior of $\hat{r} = (2.048 \pm 0.077) \times 10^{-2}$; the bias is reduced but still significant when using the $r\beta$ -1 scheme ($\hat{r} = 129.0 \pm 8.3 \times 10^{-4}$); in the β - T case we get an estimate of $\hat{r} = 94.6 \pm 15.1 \times 10^{-4}$ compatible with the input value of $r_{\text{sim}} = 100 \times 10^{-4}$; and finally, the β -2 fitting scheme leads to a negative $2 \sigma_{\hat{r}}$ tension ($\hat{r} = 62.5 \pm 25.0 \times 10^{-4}$). This demonstrates the robustness of our method and its potential application to component separation. We note that the negative bias at second order is still present in the $r_{\text{sim}} = 0.01$ case, illustrating that setting a positive prior on \hat{r} would not have been a satisfying solution when $r_{\text{sim}} = 0$.

6.5. Exploring the correlations between the parameters

We now examine the substantial increase in the dispersion on the \hat{r} posteriors between the $r\beta$ -1 fitting scheme on the one hand and the $r\beta$ - T and $r\beta$ -2 ones on the other. Indeed, in Sect. 5.3.3, we show that $\sigma_{\hat{r}}$ is about two times greater when using the $r\beta$ - T scheme than the $r\beta$ -1 one, and about four times larger in the case of $r\beta$ -2, while the $r\beta$ - T and $r\beta$ -2 schemes share the same number of free parameters. Some other points to clarify are the shift on \hat{r} appearing for $r\beta$ -2 in the d1c scenario, discussed in Sect. 5.3.3,

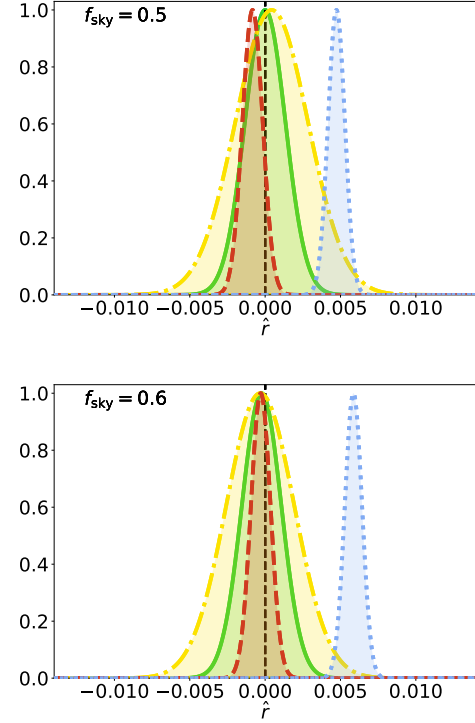


Fig. 10: (Top panel): Posterior on \hat{r} in the d1c simulation type on $f_{\text{sky}} = 0.5$ for the different fitting schemes: rMBB (blue, dotted line), $r\beta$ -1 (red, dashed line), $r\beta$ - T (green, solid line), and $r\beta$ -2 (yellow, dash-dotted line). The vertical black dashed line marks the value of $r_{\text{sim}} = 0$. (Bottom panel): Same, in the case of the d1c simulation type on $f_{\text{sky}} = 0.6$.

and the inability to correctly recover $\mathcal{D}_{\ell}^{\omega_2^{\beta} \times \omega_2^{\beta}}$ when \hat{r} is added to the fit illustrated in Fig. A.2.

The 2D-SED shapes of the parameters $\mathcal{D}_{\ell}^{N \times M}(\nu_i \times \nu_j)$ in the (ν_i, ν_j) space⁷ are displayed in Fig. A.4. We used the nine frequencies of *LiteBIRD* presented in Sect. 3.2.3 and fixed $\beta_0 = 1.54$ and $T_0 = 20$ K. We also introduce the CMB 2D-SED shape with the black body function:

$$B_{\text{CMB}}(\nu_i \times \nu_j) = \frac{B_{\nu_i}(T_{\text{CMB}})B_{\nu_j}(T_{\text{CMB}})}{B_{\nu_0}(T_{\text{CMB}})^2}, \quad (22)$$

where $T_{\text{CMB}} = 2.726$ K.

The 2D correlation coefficients between these 2D-SED shapes are displayed in Fig. 12. We present the correlations between the shapes of the parameters in the case of the $r\beta$ - T and $r\beta$ -2 fitting schemes. We can see that all the moment parameters in ω_2^{β} are strongly correlated with the CMB SED signal, while the ones in ω_1^T are not.

⁷ For example, $S(\nu_i, \nu_j) = \frac{I_{\nu_i}(\beta_0, T_0)I_{\nu_j}(\beta_0, T_0)}{I_{\nu_0}(\beta_0, T_0)^2} \cdot [\ln(\frac{\nu_i}{\nu_0}) \ln(\frac{\nu_j}{\nu_0})]$ is associated to the $\mathcal{D}_{\ell}^{\omega_1^T \times \omega_1^T}$ parameter (see Eq. 8).

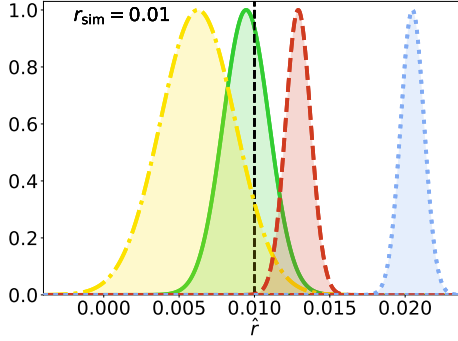


Fig. 11: Posterior on \hat{r} in the d1c simulation type with $r_{\text{sim}} = 0.01$ and $f_{\text{sky}} = 0.7$ for the different fitting schemes: $r\text{-MBB}$ (blue, dotted line), $r\beta\text{-1}$ (red, dashed line), $r\beta\text{-}T$ (green, solid line), and $r\beta\text{-2}$ (yellow, dash-dotted line). The vertical black dashed line marks the value of r_{sim} .

We showed that, when fitting $\beta\text{-2}$ on d1c, the SED distortions due to spatial variations of T are incorrectly detected by the second-order moment parameters with respect to the spectral index β . Due to the correlations highlighted above, those spurious moment parameters could then leak into \hat{r} when adding it to the fit in $r\beta\text{-2}$. This explains both the negative shift on the \hat{r} posterior using $\beta\text{-2}$ in the d1c simulation type with $f_{\text{sky}} = 0.7$ presented in Sect. 5.3.3 and 6.4, and the inability to correctly recover the $\omega_1^\beta \times \omega_2^\beta$ dust moment parameter presented in Fig. A.2. In addition, it gives a natural reason for the surge of $\sigma_{\hat{r}}$ when the second-order moments in β are added to the fit.

On the other hand, the moment parameters in ω_1^T are strongly correlated with the moments in ω_1^β . This behavior is expected due to the strong correlation between β and T (see e.g., Juvela & Ysard 2012). However those moment parameters are less correlated with the CMB signal than the second-order parameters of $\beta\text{-2}$. This points out that the factor of ~ 2 on $\sigma_{\hat{r}}$ between $\beta\text{-}T$ and $\beta\text{-2}$ is due to this correlation of the 2D-SED shapes. As the parameters in ω_1^T are highly correlated with one another, we expect them to be highly redundant in the fit. However, repeating the process described in Sect. 5.3.3 using only $\mathcal{D}_\ell^{A \times \omega_1^T}$ for $\beta\text{-}T$ —which is equivalent to applying the $\beta\text{-1}$ fitting scheme with an iterative correction to the temperature $T_0(\ell)$ — gives a \hat{r} posterior similar to the one obtained for $\beta\text{-1}$ alone. Taking the other ω_1^T terms into account appears to be necessary in order to recover an unbiased distribution of \hat{r} .

6.6. Adding synchrotron to the simulations

Thermal dust is not the only source of polarized foreground that must be considered for CMB studies. Although subdominant at high frequencies (≥ 100 GHz), the synchrotron emission due to accelerated electrons in the interstellar medium is still expected to represent a significant fraction of the total polarized signal.

In order to take one more step towards realistic forecasts for the *LiteBIRD* instrument, we add a synchrotron contribution to the d1c simulations presented in 3.3 using the s1 template included in the PySM. In this scenario, the synchrotron SED for

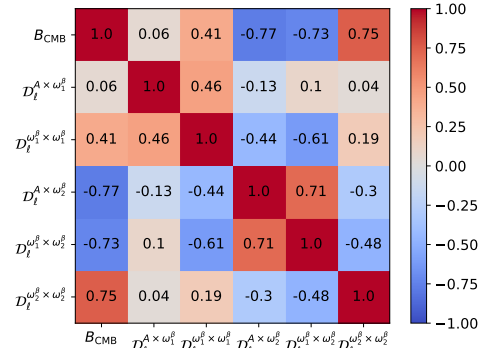


Fig. 12: Correlation matrices of the 2D-SED shapes of the CMB ($B_{\text{CMB}}(v_i \times v_j)$) and dust moments $\mathcal{D}_\ell^{N \times M}(v_i \times v_j)$ in the (v_i, v_j) space. Each element represents the Pearson correlation coefficient between any 2 of these 2D-SED shapes. The correlation matrices are displayed in the case of the $\beta\text{-2}$ fitting scheme (top panel) and the $\beta\text{-}T$ one (bottom panel).

each line of sight is given by a power law of the form (in antenna temperature units)

$$S_v^{\text{s1}} = A_{\text{s1}}(\mathbf{n}) \left(\frac{v}{v_0^{\text{s1}}} \right)^{\beta_{\text{s1}}(\mathbf{n})}, \quad (23)$$

where the amplitude $A_{\text{s1}}(\mathbf{n})$ and the spectral index $\beta_{\text{s1}}(\mathbf{n})$ maps are derived from the combination of the WMAP mission 23 GHz map Bennett et al. (2013) and Haslam 408 GHz map Haslam et al. (1981). v_0^{s1} is defined as 23 GHz. The simulations containing synchrotron are referred to as d1s1c below.

If not treated in the fit, the presence of synchrotron is expected to induce a bias on the \hat{r} posterior distribution. Regarding the dust MBB discussed in Sect. 2.1.2, the synchrotron SED is expected to have distortions. However, as the synchrotron polarized emission is significantly lower than that of dust, in the frequency range considered in the present work, we expect the distortions to be small compared to the ones induced by dust and we leave their modeling to a further study.

In order to minimize the number of free parameters used for fitting the synchrotron emission, we model its power spectrum

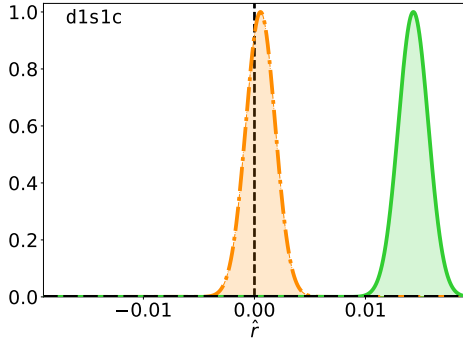


Fig. 13: Posterior on \hat{r} in the d1s1c simulation type with $r_{\text{sim}} = 0$ and $f_{\text{sky}} = 0.7$ for the different fitting schemes: $r\beta\text{-}T$ (green, solid line) and $sr\beta\text{-}T$ (orange, dash-dotted line). The vertical black dashed line marks the value $r_{\text{sim}} = 0$.

as a power law of the multipole ℓ (Krachmalnicoff et al. 2018). Therefore, combining with the synchrotron SED in Eq. 23, the synchrotron component of the cross-angular power spectra reads

$$\mathcal{D}_{\ell}^{\text{sync}}(\nu_i \times \nu_j) = A_s \left(\frac{\nu_i \nu_j}{\nu_0} \right)^{\beta_s} \ell^{\alpha_s}, \quad (24)$$

where the amplitude coefficient A_s is treated as a free parameter while we fix $\beta_s = -3$ (median value of the s1 β_s map on our $f_{\text{sky}} = 0.7$ mask) and $\alpha_s = -1$ (Krachmalnicoff et al. 2018).

When fitting the d1s1c simulations, we either use the $r\beta\text{-}T$ fitting scheme, neglecting the synchrotron component, or we add the synchrotron component in Eq. 24 to the model in Eq. 20. We refer to this latter case as the $sr\beta\text{-}T$ fitting scheme. In Fig. 13, the \hat{r} posteriors derived from the d1s1c simulations are displayed with $r_{\text{sim}} = 0$ and $f_{\text{sky}} = 0.7$.

Using the $r\beta\text{-}T$ fitting scheme, we find $\hat{r} = (143.1 \pm 13.5) \times 10^{-4}$. As expected, even at high frequencies, modeling the synchrotron component is critical and cannot be neglected in order to recover an unbiased value of \hat{r} . On the other hand, using $sr\beta\text{-}T$ fitting scheme, we recover $\hat{r} = (-5.4 \pm 13.2) \times 10^{-4}$. This result is comparable with the one obtained for the d1c simulations in Sect. 5.3.3, with a minor increase in $\sigma_{\hat{r}}$. We can therefore conclude that a model as simple as that of Eq. 24 is sufficient to take into account the s1 component at $\nu > 100$ GHz and the corresponding SED distortions can be neglected in order to recover an unbiased value of \hat{r} . In principle, as we know that the dust-synchrotron spatial correlation is significant at large scales (Planck Collaboration 2020c), Eq. 20 should include a dust-synchrotron term (see e.g., Hensley et al. 2021). In our study, where we consider cross-spectra from 100 to 402 GHz, this dust-synchrotron term is subdominant, but it could be significant when considering cross-spectra between LiteBIRD's extreme frequency bands (e.g., the 40×402 cross-spectrum). The moment expansion might be more complicated as well in this case, as we could expect some correlation between the dust and synchrotron moment-terms.

This result shows that a full polarized foreground content can be treated at high frequencies when using a power law SED for the synchrotron coupled with the moment expansion of the MBB up to first order in both β and T for the dust SED. A full study

remains to be done in that direction using all the frequency bands of the *LiteBIRD* instrument. Eventually, Eq. 24 will also have to be expanded in moments with respect to its parameters. Doing so, one can expect to recover an unbiased value of \hat{r} associated with a decrease in $\sigma_{\hat{r}}$ down to a value compatible with the full success criterion of the mission.

6.7. Limitations of this work and caveats

As discussed in Sect. 2.2.1, we neglected polarization effects through this work by treating the *BB* signal as an intensity signal. This is not problematic in the present work, because no variations along the lines of sight were present in the simulations. However, this point has to be addressed using complex simulations or real sky data.

The choice of reference frequency ν_0 used for the normalization of the MBB in Eq. 1, which is not discussed in this study, can potentially have a significant impact on the moment expansion and, in turn, on the measurement of \hat{r} . Indeed, ν_0 is the pivot frequency of the moment expansion (moments are equal to zero at ν_0) and will determine the shape of the SED distortion around it. A poor choice for this reference frequency can have disastrous consequences for the moment fit: for example, if it is chosen far away from the observed bands, all the moments will become degenerated. In our case, the reference frequency (353 GHz) is within the observed frequency range (100 to 402 GHz), but we have not tried to optimize its position. In addition, the ν_0 pivot of our moment expansion coincides with the one used to extrapolate the dust template map in the PySM and we have not quantified how much this impacts our results.

Finally, as pointed out several times in this work, the quantitative results depend strongly on the sky model of our simulations. Moreover, we lack dedicated sky models where we can control the complexity of the dust SED, either by directly including moments or by averaging the emission from the 3D structure of the Galaxy. However, both methods are beyond the scope of the present work.

7. Conclusion

Being able to precisely characterize the complexity of the Galactic thermal dust polarized SED has become critical for the measurement of the faint primordial *B*-mode signal of the CMB, especially at the sensitivity targeted by future CMB experiments such as the *LiteBIRD* satellite mission.

In this work, we applied the moment expansion formalism to the dust emission SED as a component-separation tool to recover the tensor-to-scalar ratio parameter r in *LiteBIRD*-simulated data. This formalism, proposed by Chluba et al. (2017) and implemented in harmonic space by Mangilli et al. (2021), allows us to deal with the spectral complexity of the Galactic dust signal by modeling its deviations from the canonical MBB model at the cross-angular power spectrum level. In the case of the data-driven realistic dust emission model —we explore (PySM d1) here—, suitably taking into account the dust SED distortions prevents the spurious detection of the primordial *B*-mode signal.

We show that the dust spectral index β and dust temperature T spatial variations significantly distort the dust cross-power spectrum SED. The MBB is not a good model to describe the data in that case and the estimation of r is dramatically affected. In the case where no primordial signal is included in the simulated data sets, not taking into account the dust SED complexity

leads to a highly significant spurious detection of r with *LiteBIRD* (from $\hat{r} \simeq 5 \times 10^{-3}$ to 1.25×10^{-2} , with a 8.4 to 21.2σ significance, from 50 to 70% of the sky, respectively).

To overcome this obstacle, we applied the moment expansion formalism in order to model these SED distortions. We demonstrate that, at *LiteBIRD* sensitivity, the previously studied moment expansion with respect to the dust spectral index β (Mangilli et al. 2021; Azzoni et al. 2020) does not give satisfactory results. Indeed, expanding in β to first order (following the angular power spectrum definition of the order) leads to a significant bias on 70% of the sky ($\hat{r} = (3.29 \pm 0.65) \times 10^{-3}$ when $r_{\text{sim}} = 0$ and $\hat{r} = (1.29 \pm 0.08) \times 10^{-2}$, when $r_{\text{sim}} = 10^{-2}$). At second order in β , we observe a $\sim 2\sigma$ negative tension ($\hat{r} = (-3.7 \pm 1.9) \times 10^{-3}$ when $r_{\text{sim}} = 0$ and $\hat{r} = (6.25 \pm 2.50) \times 10^{-3}$, when $r_{\text{sim}} = 10^{-2}$).

We introduce for the first time in this work the expansion of the dust angular cross-power spectra with respect to both β and T . We show that by using this expansion up to first order, we correctly model the dust SED distortions due to spatial variations of both β and T at the map level. This allows us to recover r parameter without bias, with $\hat{r} = (-3.3 \pm 11.7) \times 10^{-4}$ if $r_{\text{sim}} = 0$ and $\hat{r} = (0.95 \pm 0.15) \times 10^{-2}$ if $r_{\text{sim}} = 10^{-2}$. Thus, despite the known degeneracy between the dust spectral index and its temperature in the Rayleigh-Jeans domain, it is important to correctly model the latter in order to accurately retrieve the tensor-to-scalar ratio r at the unprecedented precision reached by experiments such as *LiteBIRD*.

Adding parameters to tackle the dust SED complexity means an increase in the error budget. Given the *LiteBIRD* bands and sensitivities we consider in this work (frequency bands above 100 GHz), the ideal sensitivity on r without delensing is $\sigma_r = 3.4 \times 10^{-4}$. In the ideal case, where the dust β and T are constant over the sky (PySM d0), separating the CMB from dust leads to $\sigma_r = 3.9 \times 10^{-4}$ on 70% of the sky. Adding the expansion to first order in β does not significantly increase the error ($\sigma_r = 4.5 \times 10^{-4}$), but expanding to first order in both β and T multiplies it by a factor of ~ 2 ($\sigma_r = 9.5 \times 10^{-4}$) and to second order in β by a factor of ~ 4 ($\sigma_r = 16.4 \times 10^{-3}$). We show that the surge of σ_r between the two latter cases, sharing the same number of free parameters, is due to strong correlations between the SED of the second-order moments in β and the CMB. This is an important point, as it could lead to some intrinsic limitation for component-separation algorithms based exclusively on the modeling of the SED. Furthermore, when dealing with real data, if the dust SED is complex enough to have significant second-order distortions with respect to β , CMB experiments might reach a dilemma: either include the second order in the modeling at the cost of losing sensitivity on r , or neglect it at the cost of a potential spurious detection. Coupling the SED-based separation with methods exploiting the diversity of spatial distribution between components (e.g., Regaldo-Saint Blanchard et al. 2021) seems a natural way to overcome this issue.

Nevertheless, moment expansion at the cross-angular power spectrum level provides a powerful and agnostic tool, allowing us to analytically recover the actual dust complexity without making any further assumptions. We additionally show that this method is robust, in the sense that it can effectively distinguish the primordial tensor signal from dust when $r_{\text{sim}} \neq 0$, as in the case of *LiteBIRD* simulations. The dust moments in β and T at first order are needed in order to retrieve a reliable measure of r ; they are significantly detected for $\ell \lesssim 100$. We can therefore define a cut in ℓ above which we do not fit for the whole complexity of the dust (we fit only the expansion up to first order in β and not in β and T). Doing so, we can reduce the error on \hat{r} while

keeping the bias negligible ($\hat{r} = (-0.9 \pm 8.8) \times 10^{-4}$). We could imagine other ways to reduce the number of free parameters in our model (e.g., assuming a power-law of ℓ behavior for the moments, as in Azzoni et al. 2020) and hence reduce the error on r . However, this optimization really depends on the simulated sky complexity and has not been comprehensively explored in the present work.

The PvSM d1 sky simulations, being data-driven, are widely used by the CMB community as they contain some of the real sky complexity. Nevertheless, at high-Galactic latitudes, the dust spectral index and temperature templates from *Planck* are dominated by systematic errors (uncertainty on the assumed zero-level of the *Planck* intensity maps, residual cosmic infrared background (CIB), anisotropies, instrumental noise, etc.). Therefore, some of the complexity we observe far from the Galactic plane in this sky model is not real. On the other hand, the modeled SED of the dust is exactly a MBB in each pixel, and line-of-sight averages or more complex dust models are ignored. As a consequence, our method and CMB B -mode component-separation algorithms in general need to be confronted with more complex models in order to really assess their performances in a quantitative manner.

Finally, although we demonstrate that the synchrotron component can be tackled at frequencies above 100 GHz with a minimal model under our assumptions, a study over the full *LiteBIRD* frequency bands, including synchrotron and the potential moment expansion of its SED, will be considered as a natural next step for a further application.

Acknowledgments

This work is supported in Japan by ISAS/JAXA for Pre-Phase A2 studies, by the acceleration program of JAXA research and development directorate, by the World Premier International Research Center Initiative (WPI) of MEXT, by the JSPS Core-to-Core Program of A. Advanced Research Networks, and by JSPS KAKENHI Grant Numbers JP15H05891, JP17H01115, and JP17H01125. The Italian *LiteBIRD* phase A contribution is supported by the Italian Space Agency (ASI Grants No. 2020-9-HH.0 and 2016-24-H.1-2018), the National Institute for Nuclear Physics (INFN) and the National Institute for Astrophysics (INAF). The French *LiteBIRD* phase A contribution is supported by the Centre National d'Etudes Spatiales (CNES), by the Centre National de la Recherche Scientifique (CNRS), and by the Commissariat à l'Energie Atomique (CEA). The Canadian contribution is supported by the Canadian Space Agency. The US contribution is supported by NASA grant no. 80NSSC18K0132. Norwegian participation in *LiteBIRD* is supported by the Research Council of Norway (Grant No. 263011). The Spanish *LiteBIRD* phase A contribution is supported by the Spanish Agencia Estatal de Investigación (AEI), project refs. PID2019-110610RB-C21 and AYA2017-84185-P. Funds that support the Swedish contributions come from the Swedish National Space Agency (SNSA/Rymdstyrelsen) and the Swedish Research Council (Reg. no. 2019-03959). The German participation in *LiteBIRD* is supported in part by the Excellence Cluster ORIGINS, which is funded by the Deutsche Forschungsgemeinschaft (DFG, German Research Foundation) under Germany's Excellence Strategy (Grant No. EXC-2094 - 390783311). This research used resources of the Central Computing System owned and operated by the Computing Research Center at KEK, as well as resources of the National Energy Research Scientific Computing Center, a DOE Office of Science User Facility supported by the Office of Science of the U.S. Department of Energy.

MR acknowledges funding support from the ERC Consolidator Grant CMBSPEC (No. 725456) under the European Union's Horizon 2020 research and innovation program.

The authors would like to thank David Alonso, Josquin Erard, Nicoletta Krachmalnicoff and Giuseppe Puglisi, for useful discussions as well as Jens Chluba for insightful comments on earlier version of this work.

References

- Adak, D. 2021, MNRAS, 507, 4618
 Alonso, D., Sanchez, J., Slosar, A., & LSST Dark Energy Science Collaboration. 2019, MNRAS, 484, 4127
 Ashton, P. C., Ade, P. A. R., Anglè, F. E., et al. 2018, ApJ, 857, 10
 Azzoni, S., Abitbol, M. H., Alonso, D., et al. 2020, arXiv e-prints, arXiv:2011.11575
 Bennett et al. C. L. 2013, ApJS, 208, 20
 BICEP2 Collaboration & Keck Array Collaboration. 2018, Phys. Rev. Lett., 121, 221301
 BICEP2/Keck and Planck Collaborations. 2015, Phys. Rev. Lett., 114, 101301
 Bicep/Keck Collaboration, Ade, P. A. R., Ahmed, Z., et al. 2021, Phys. Rev. Lett., 127, 151301
 Brout, R., Englert, F., & Gunzig, E. 1978, Annals of Physics, 115, 78
 Chluba, J., Hill, J. C., & Abitbol, M. H. 2017, MNRAS, 472, 1195
 Desert, F. X., Boulanger, F., & Puget, J. L. 1990, A&A, 500, 313
 Draine, B. T. & Hensley, B. 2013, ApJ, 765, 159
 Fanciullo, L., Guillet, V., Aniano, G., et al. 2015, A&A, 580, A136
 Foreman-Mackey, D., Hogg, D. W., Lang, D., & Goodman, J. 2013, PASP, 125, 306
 Gandilo, N. N., Ade, P. A. R., Anglè, F. E., et al. 2016, ApJ, 824, 84
 Gorski, K. M., Hivon, E., Banday, A. J., et al. 2005, ApJ, 622, 759
 Guillet, V., Fanciullo, L., Verstraete, L., et al. 2018, A&A, 610, A16
 Guth, A. H. 1981, Phys. Rev. D, 23, 347
 Haslam, C. G. T., Klein, U., Salter, C. J., et al. 1981, A&A, 100, 209
 Hazumi, M. 2018, in Frontier Research in Astrophysics - III, 79
 Hazumi et al. 2020, in Society of Photo-Optical Instrumentation Engineers (SPIE) Conference Series, Vol. 11443, Society of Photo-Optical Instrumentation Engineers (SPIE) Conference Series, 114432F
 Hensley, B. S. & Bull, P. 2018, ApJ, 853, 127
 Hensley, B. S., Clark, S. E., Fanfani, V., et al. 2021, arXiv e-prints, arXiv:2111.02425
 Hutton, S., Ferreras, I., & Yershov, V. 2015, MNRAS, 452, 1412
 Ichiki, K., Kanai, H., Katayama, N., & Komatsu, E. 2019, Progress of Theoretical and Experimental Physics, 2019, 033E01
 Juvela, M. & Ysard, N. 2012, A&A, 539, A71
 Kamionkowski, M., Kosowsky, A., & Stebbins, A. 1997, Phys. Rev. Lett., 78, 2058
 Krachmalnicoff, N., Baccigalupi, C., Aumont, J., Bersanelli, M., & Mennella, A. 2016, A&A, 588, A65
 Krachmalnicoff, N., Carretti, E., Baccigalupi, C., et al. 2018, A&A, 618, A166
 Lewis, A., Challinor, A., & Lasenby, A. 2000, ApJ, 538, 473
 LiteBIRD Collaboration. 2020, Journal of Low Temperature Physics, 199, 1107
 LiteBIRD Collaboration, in prep., in PTEP, Vol. 11443, PTEP, 114432F
 Lyth, D. H. 1997, Phys. Rev. Lett., 78, 1861
 Mangilli, A., Aumont, J., Rotti, A., et al. 2021, A&A, 647, A52
 Markwardt, C. B. 2009, in Astronomical Society of the Pacific Conference Series, Vol. 411, Astronomical Data Analysis Software and Systems XVIII, ed. D. A. Bohlen, D. Durand, & P. Dowler, 251
 Martin, J., Ringeval, C., & Vennin, V. 2014, Physics of the Dark Universe, 5, 75
 Paradis, D., Bernard, J. P., & Mény, C. 2009, A&A, 506, 745
 Pelgrims, V., Clark, S. E., Hensley, B. S., et al. 2021, A&A, 647, A16
 Planck Collaboration. 2014a, A&A, 571, A11
 Planck Collaboration. 2014b, A&A, 566, A55
 Planck Collaboration. 2015, A&A, 576, A107
 Planck Collaboration. 2016a, A&A, 594, A1
 Planck Collaboration. 2016b, A&A, 594, A10
 Planck Collaboration. 2016c, A&A, 586, A133
 Planck Collaboration. 2017, A&A, 599, A51
 Planck Collaboration. 2020a, A&A, 641, A1
 Planck Collaboration. 2020b, A&A, 641, A4
 Planck Collaboration. 2020c, A&A, 641, A11
 Polnarev, A. G. 1985, Soviet Ast., 29, 607
 Regaldo-Saint Blanchard, B., Ally, E., Boulanger, F., Levrier, F., & Jeffrey, N. 2021, arXiv e-prints, arXiv:2102.03160
 Remazeilles, M., Dickinson, C., Eriksen, H. K. K., & Wehus, I. K. 2016, MNRAS, 458, 2032
 Remazeilles, M., Rotti, A., & Chluba, J. 2021, MNRAS, 503, 2478
 Seljak, U. & Zaldarriaga, M. 1997, Phys. Rev. Lett., 78, 2054
 Starobinsky, A. A. 1980, Physics Letters B, 91, 99
 Stolyarov, V., Hobson, M. P., Lasenby, A. N., & Barreiro, R. B. 2005, MNRAS, 357, 145
 Suzuki, A., Ade, P. A. R., Akiba, Y., et al. 2018, Journal of Low Temperature Physics, 193, 1048
 Tassis, K. & Pavlidou, V. 2015, MNRAS, 451, L90
 The Simons Observatory collaboration. 2019, in BAAS, Vol. 51, 147
 Thorne, B., Dunkley, J., Alonso, D., & Næss, S. 2017, MNRAS, 469, 2821
 Tristram, M., Banday, A. J., Gorski, K. M., et al. 2021, arXiv e-prints, arXiv:2112.07961
 Ysard, N., Köhler, M., Jones, A., et al. 2015, A&A, 577, A110

Appendix A: Complementary figures

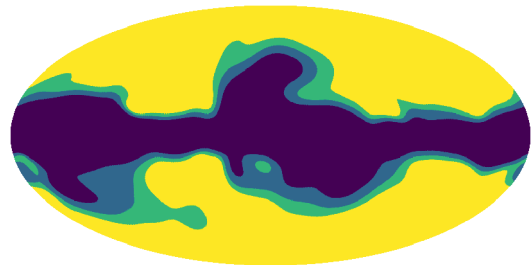


Fig. A.1: Raw masks used in the simulations: $f_{\text{sky}} = 0.7$ (dark blue), $f_{\text{sky}} = 0.6$ (light blue) and $f_{\text{sky}} = 0.5$ (green).

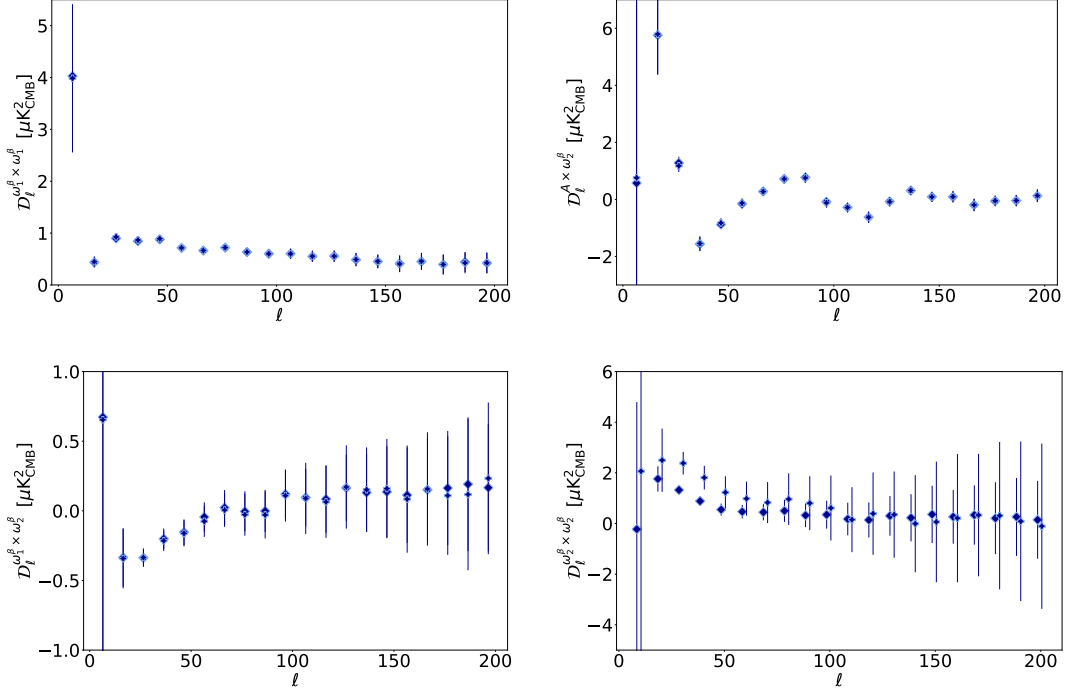


Fig. A.2: Best-fit values of the $D_\ell^{\omega_1^\beta \times \omega_1^\beta}$ (top left), $D_\ell^A \times \omega_2^\beta$ (top right), $D_\ell^{\omega_2^\beta \times \omega_2^\beta}$ (bottom left) and $D_\ell^{\omega_1^\beta \times \omega_2^\beta}$ (bottom right) moment parameters for the β -2 fitting scheme applied on the d1c simulation type (diamonds) and $r\beta$ -2 on d1c (plus sign).

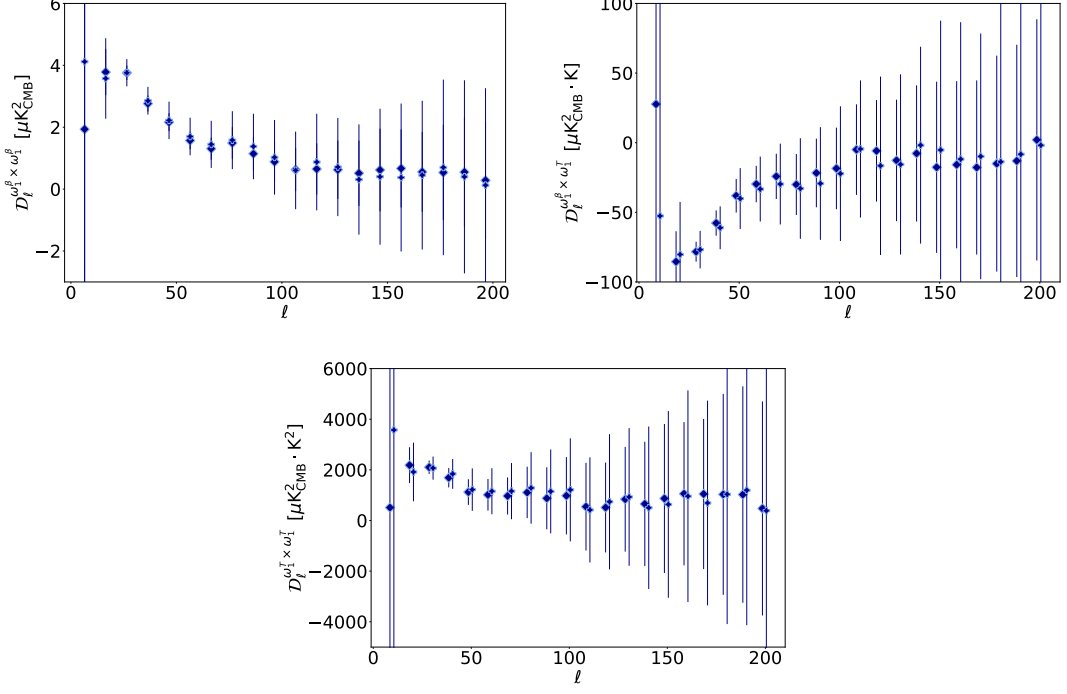


Fig. A.3: Best-fit values of the $D_l^{\omega_1^\beta \times \omega_1^\beta}$ (top left), $D_l^{\omega_1^\beta \times \omega_1^T}$ (top right) and $D_l^{\omega_1^T \times \omega_1^T}$ (bottom) moment parameters for the β - T fitting scheme applied on the d1c simulation type (diamonds) and $r\beta$ - T on d1c (plus sign).

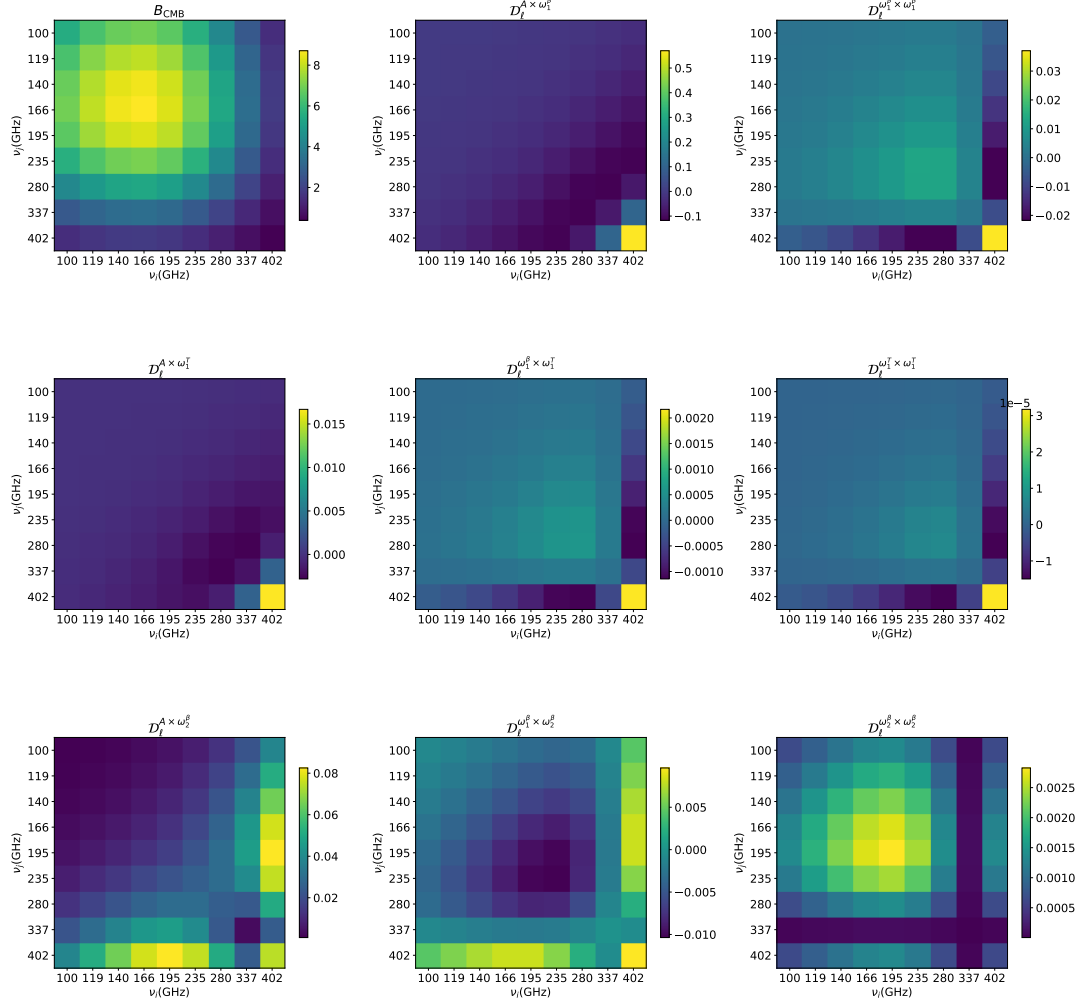


Fig. A.4: Two-dimensional SED shapes of the moment expansion parameters and the CMB in the (ν_i, ν_j) space for the nine LiteBIRD frequencies used throughout this work. The intensities are all expressed in MJy^2 normalized by the squared SED at $\nu_0 = 353$ GHz.

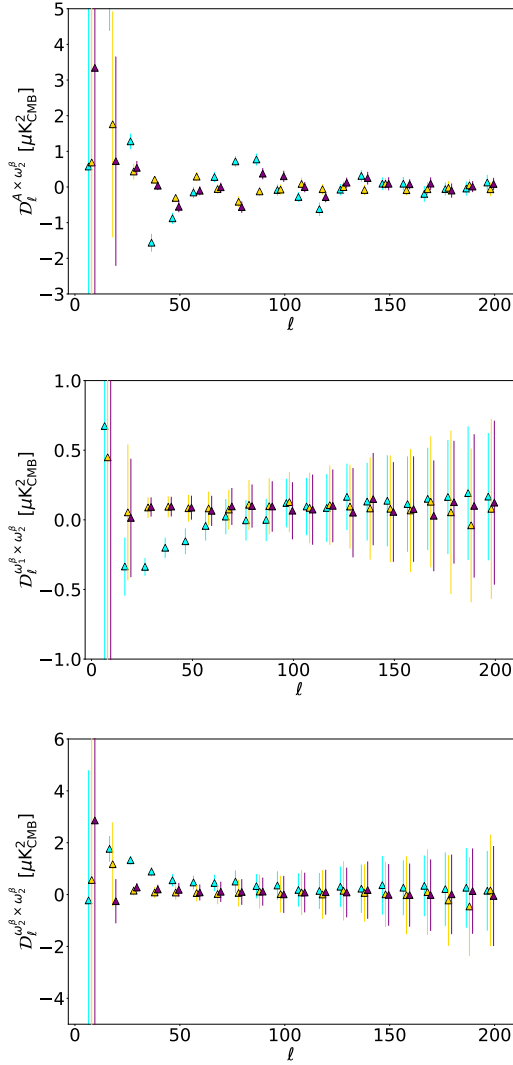


Fig. A.5: $\beta-2$ moment coefficients for different f_{sky} : $f_{\text{sky}} = 0.7$ (cyan), $f_{\text{sky}} = 0.6$ (purple) and $f_{\text{sky}} = 0.5$ (gold).

D.2 A&A 669, A5

Astronomy & Astrophysics manuscript no. output
February 6, 2023

©ESO 2023

High precision modeling of polarized signals: Moment expansion method generalized to spin-2 fields

L. Vacher¹, J. Chluba², J. Aumont¹, A. Rotti², and L. Montier¹

¹ IRAP, Université de Toulouse, CNRS, CNES, UPS, Toulouse, France

² Jodrell Bank Centre for Astrophysics, Alan Turing Building, University of Manchester, Manchester M13 9PL

February 6, 2023

ABSTRACT

The modeling and removal of foregrounds poses a major challenge to searches for signals from inflation using the cosmic microwave background (CMB). In particular, the modeling of CMB foregrounds including various spatial averaging effects introduces multiple complications that will have to be accounted for in upcoming analyses. In this work, we introduce the generalization of the intensity moment expansion to the spin-2 field of linear polarization: the spin-moment expansion. Within this framework, moments become spin-2 objects that are directly related to the underlying spectral parameters and polarization angle distribution functions. In obtaining the required expressions for the polarization modeling, we highlight the similarities and differences with the intensity moment methods. A spinor rotation in the complex plane with frequency naturally arises from the first order moment when the signal contains both spectral parameters and polarization angle variations. Additional dependencies are introduced at higher order, and we demonstrate how these can be accounted with several illustrative examples. Our new modeling of the polarized signals reveals to be a powerful tool to model the frequency dependence of the polarization angle. As such, it can be immediately applied to numerous astrophysical situations.

Key words. Cosmology, CMB, Foregrounds, Interstellar medium

1. Introduction

A significant international effort has been undertaken to deploy large-scale surveys of the cosmic microwave background (CMB) signal in the present, near, and far future. Multiple telescopes, such as ACT (Aiola et al. 2020), SPT (Sayre et al. 2020), The Simons Observatory (The Simons Observatory collaboration 2019), and CMB-S4 (CMB-S4 Collaboration 2019), are or will be observing large portions of the sky from the ground. Similarly, from space we are eagerly awaiting *LiteBIRD* (LiteBIRD Collaboration 2022), and in the future possibly even more ambitious CMB imagers (PICO Collaboration 2019; Delabrouille et al. 2021). In addition, we can hope for a CMB spectrometer such as *PIXIE* (Kogut et al. 2011) to target CMB spectral distortions (Chluba et al. 2021). The scientific targets are manyfold and of prime importance to cosmology, astrophysics, and high-energy physics.

Ever-increasing instrumental sensitivities imply that one also becomes sensitive to faint and complex effects that need to be properly modeled. The fine characterization of polarized astrophysical signals thus becomes an increasingly complicated and important challenge to cosmological analyses. The stakes are twofold: first, we wish to reach a better understanding of the sources themselves and the complex physics at play in the emission. This is of importance for Galactic physics, physics of recombination at the last scattering surface with the primordial anisotropies of the cosmic microwave background (CMB) and their secondary sources from the physics of galaxy clusters with the Sunyaev-Zeldovich (SZ) effect (Carlstrom et al. 2002; Mroczkowski et al. 2019), or lensing (Stompor & Efs-

tathiou 1999). Secondly, high-precision component separation is required to remove the diffuse foregrounds and access the faint perturbations of the CMB polarized signal. Finding how to deal with them is an unavoidable step in addressing questions that concern the cosmic history and high-energy physics through inferring key cosmological parameters as the reionization depth τ (Wise 2019) or the scalar-to-tensor ratio r , which probes inflation (Brout et al. 1978; Starobinsky 1980; Guth 1981). The philosophy of the present work is that one cannot properly deal with the second point without a detailed understanding of the polarized Galactic emission, deeply rooted in the physics.

It is known that the emission properties of the diffuse interstellar medium (ISM) change across the Galaxy on small and large scales. This assertion is well motivated from the Galactic magnetic field physics and the distribution of dust grain shapes and composition (Ferrière 2001; Jaffe et al. 2013), which is supported by numerous observations (Ysard et al. 2013; Hutton et al. 2015; Schlafly et al. 2016; Planck Collaboration 2017, 2020b; Pelgrims et al. 2021). In observational conditions, averages over Galactic voxels with different spectral parameters are then unavoidable. They occur in several situations: along the line of sight inside the Galaxy, which cannot be reduced or avoided with instrumental considerations; between lines of sight inside the instrumental beam; and over patches of the sky when doing a spherical harmonic decomposition of the signal or averaging the data otherwise. Two related consequences follow immediately for the signal in intensity: if the fundamental spectral energy distributions (SEDs) are nonlinear, the average SED of the total signal differs from the canonical SED of the voxel. We refer to this phenomenon as SED distortions. The SED is distorted differently from one point of the sky to another, breaking the correlation between the maps at different frequency bands, lead-

Send offprint requests to: leo.vacher@irap.omp.eu

ing to inaccurate extrapolations from one to another: we refer to this phenomenon as frequency decorrelation (see e.g., [Tassis & Pavlidou 2015](#); [Planck Collaboration 2017](#); [Pelgrims et al. 2021](#)).

To treat these averages in connection with CMB foregrounds, the (Taylor) moment expansion formalism was proposed ([Chluba et al. 2017](#)). A similar idea had been applied to the modeling of Sunyaev-Zeldovich signals, showing how spatial and frequency information can be nicely separated ([Chluba et al. 2013](#)). The moment formalism has proven to be very powerful when applied to component separation at the map level ([Rotti & Chluba 2021](#); [Remazeilles et al. 2016, 2021](#)). A straightforward generalization to harmonic space and cross-frequency power-spectra domain has also proven to be useful ([Mangilli et al. 2021](#); [Azzoni et al. 2021](#); [Vacher et al. 2022](#)).

While the original formulation of the moment method was focused on the intensity, it was stressed that an extension to polarization can be readily obtained ([Chluba et al. 2017](#)), which is what we intend to do in the present work. Indeed, several applications already used the moment expansion method for polarized signals, treating the B -mode signal as an intensity (e.g., [Remazeilles et al. 2021](#); [Azzoni et al. 2021](#); [Vacher et al. 2022](#)). One can also find a similar approach in the Delta-map method ([Ichiki et al. 2019](#)), which used first order terms of the Q/U -intensity moments and already suggested a common treatment for the pair (Q, U) .

In this work, we plan to rigorously derive and extend the moment expansion method to polarized signals. To do so, the Stokes parameters must be treated together, as the components of a single complex object. In the most general cases, extra subtleties come into play, which were not captured or discussed before. There are numerous advantages from thinking of linear polarization as a spin-2 quantity. As such they are not only described by a scalar quantity but also by an angle: the polarization angle. The averaging processes listed above will have one extra consequence for polarized signal: additionally to the spectral parameters, multiple angles will be mixed along and between lines of sight. We refer to this phenomenon as polarized mixing. In the presence of polarized mixing, the total signal will exhibit a frequency-dependent polarization angle. Being able to accurately model this frequency-dependent rotation from physically-motivated considerations represents a thorny challenge. In this work, we attempt to provide this extension to linearly polarized signal in a formal, natural, complete and self-consistent way. We pay particular attention to the formulation in terms of SED parameter distribution functions, which really is the origin of the name "moment expansion". We subsequently see that this rewriting offers a powerful framework to grasp polarized mixing and its consequences.

After a review of the intensity moment formalism in Sec. 2, we discuss the nature of linear polarization and introduce the spin-moment formalism in a single line of sight in Sec. 3. In Sec. 4, we explore different example of sums of canonical SEDs along a line of sight, that are of astrophysical relevance. We study them both analytically and through a fitting procedure, demonstrating the ability of the spin-moment formalism to grasp distortions of the polarized SED. In Sec. 5, we generalize the formalism to deal with other kind of averaging effects: spherical harmonic transforms and instrumental effects. In Sec. 6, we discuss cases with extra complexity as Faraday rotation and more general voxel SEDs. Finally, we conclude in Sec. 7.

Article number, page 2 of 16

2. Intensity moment expansion

Before we discuss the generalization of the moment expansion for polarized light, we briefly recall the logical steps followed in [Chluba et al. \(2017\)](#) to obtain the moment expansion in intensity. For now, we neglect beam averaging effects or expansions into spherical harmonic, but we cover these in Sec. 5.

We start by considering various voxels along a line of sight in the direction $\hat{\mathbf{n}}$, which is described by an affine parameter s . Every voxel emits with an SED¹:

$$I_\nu(A(s), \mathbf{p}(s)) = A(s) \hat{I}_\nu(\mathbf{p}(s)), \quad (1)$$

where \hat{I}_ν is referred to as the fundamental SED with N spectral parameters, $\mathbf{p}(s) = \{p_1(s), p_2(s), \dots, p_N(s)\}$. The amplitude or weight parameter, $A(s)$, determines the relative contribution of each voxel to the total intensity.² The resulting total SED is given by an average along the line of sight, which we shall denote by $\langle \dots \rangle$. This average can be explicitly written in terms of an integral over the affine parameters, s , or, alternatively, as an integral of the intensity over the spectral parameter distribution function in the direction $\hat{\mathbf{n}}$ (e.g., [Chluba et al. 2017](#); [Rotti & Chluba 2021](#)):

$$\langle I_\nu(A, \mathbf{p}) \rangle = \int \frac{dA(s)}{ds} \hat{I}_\nu(\mathbf{p}(s)) ds \equiv \int \mathbb{P}(\mathbf{p}, \hat{\mathbf{n}}) \hat{I}_\nu(\mathbf{p}) d^N p. \quad (2)$$

In the second definition, we introduced the distribution $\mathbb{P}(\mathbf{p}, \hat{\mathbf{n}})$ of the spectral parameters, \mathbf{p} , along the fixed line of sight $\hat{\mathbf{n}}$, with the relative weights absorbed into the distribution itself. We note that the distribution $\mathbb{P}(\mathbf{p}, \hat{\mathbf{n}})$ is not necessarily normalized to unity, as it determines the relative weight of each SED shape to the total. For convenience we shall define the average amplitude parameter as $\bar{A} = \langle A \rangle = \int [dA(s)/ds] ds = \int \mathbb{P}(\mathbf{p}, \hat{\mathbf{n}}) d^N p$.

In order to provide a perturbative model of the average SED, the spectral dependence \hat{I}_ν in Eq. (2) can be expanded into a Taylor series with respect to \mathbf{p} around the pivot $\bar{\mathbf{p}}$ as:

$$\begin{aligned} \hat{I}_\nu(\mathbf{p}) &= \hat{I}_\nu(\bar{\mathbf{p}}) + \sum_j (p_j - \bar{p}_j) \partial_{\bar{p}_j} \hat{I}_\nu(\bar{\mathbf{p}}) \\ &\quad + \frac{1}{2} \sum_{j,k} (p_j - \bar{p}_j)(p_k - \bar{p}_k) \partial_{\bar{p}_j} \partial_{\bar{p}_k} \hat{I}_\nu(\bar{\mathbf{p}}) \\ &\quad + \frac{1}{3!} \sum_{j,k,l} (p_j - \bar{p}_j)(p_k - \bar{p}_k)(p_l - \bar{p}_l) \partial_{\bar{p}_j} \partial_{\bar{p}_k} \partial_{\bar{p}_l} \hat{I}_\nu(\bar{\mathbf{p}}) \\ &\quad + \dots . \end{aligned} \quad (3)$$

Here, we used the shorthand notation $\partial_{\bar{p}_j} X(\bar{\mathbf{p}}) \equiv \partial X(\bar{\mathbf{p}}) / \partial \bar{p}_j$. The pivot value $\bar{\mathbf{p}}$ around which the series is carried out can be fixed by asking for the first term of the expansion to vanish upon averaging: $\langle A \sum_j (p_j - \bar{p}_j) \rangle = 0$. This minimizes the required terms in the Taylor series and leads to:

$$\bar{\mathbf{p}} = \frac{\langle A \mathbf{p} \rangle}{\bar{A}} = \frac{\int \mathbb{P}(\mathbf{p}, \hat{\mathbf{n}}) \mathbf{p} d^N p}{\int \mathbb{P}(\mathbf{p}, \hat{\mathbf{n}}) d^N p}. \quad (4)$$

¹ Hereafter, we use the shorthand notation for frequency dependent quantities $X_\nu \equiv X(\nu)$.

² One simple example is the power law: $I_\nu(A, \beta) = A (\nu/\nu_0)^\beta$ where $\mathbf{p} = \{\beta\}$ has dimension one ($N = 1$) and $\hat{I}_\nu(\beta) = (\nu/\nu_0)^\beta$. In this, ν_0 is arbitrarily defined, but in practical applications the choice is normally data-driven (e.g. motivated by the location of sensitive bands in experiments such as for Planck or WMAP) and A is the overall weight, with dimension that depends on the situation (see Appendix B).

Next we introduce the moment coefficients of order α

$$\omega_a^{p_j \dots p_l} = \frac{\langle A(p_j - \bar{p}_j) \dots (p_l - \bar{p}_l) \rangle}{\bar{A}} \\ = \frac{\int \mathbb{P}(\mathbf{p}, \hat{\mathbf{n}}) (p_j - \bar{p}_j) \dots (p_l - \bar{p}_l) d^N p}{\int \mathbb{P}(\mathbf{p}, \hat{\mathbf{n}}) d^N p}, \quad (5)$$

with α being the number of parameters over which the average is done and the maximal order of the derivative associated with the moment coefficient. One can then write the total intensity as an expansion in terms of these moments:

$$\langle I_\nu(A, \mathbf{p}) \rangle = I_\nu(\bar{A}, \bar{\mathbf{p}}) + \sum_j^N \omega_1^{p_j} \partial_{\bar{p}_j} I_\nu(\bar{A}, \bar{\mathbf{p}}) \\ + \frac{1}{2} \sum_{j,k}^N \omega_2^{p_j p_k} \partial_{\bar{p}_j} \partial_{\bar{p}_k} I_\nu(\bar{A}, \bar{\mathbf{p}}) \\ + \frac{1}{3!} \sum_{j,k,l}^N \omega_3^{p_j p_k p_l} \partial_{\bar{p}_j} \partial_{\bar{p}_k} \partial_{\bar{p}_l} I_\nu(\bar{A}, \bar{\mathbf{p}}) + \dots \quad (6)$$

Here, all the $\omega_1^{p_i}$ are zero when using the value for $\bar{\mathbf{p}}$ as given by Eq. (4), while higher order moments capture the complexities added by line-of-sight averaging effects. In applications, the pivot value can be obtained using an iterative process by starting with a reasonable guess for $\bar{\mathbf{p}}$ and then correcting the solution by the values of $\omega_1^{p_i} \equiv \Delta p_i$ using $\bar{p}_j \rightarrow \bar{p}'_j = \bar{p}_j + \Delta p_j$. This iterative process assumes that the moments are perturbative and convergence can be obtained with a finite number of terms.

3. Moment expansion of polarized signals

In this section, we generalize the intensity moment expansion to polarization. We start by summarizing a few general aspects about how to describe polarized light and then highlight some of the important differences between intensity and polarization.

3.1. General introduction to polarized SED

A polarized signal is fully described by the four real Stokes parameters $I_\nu, Q_\nu, U_\nu, V_\nu$, all of them being frequency dependent quantities. As before, I_ν describes the total (i.e., unpolarized + polarized) intensity, while the pair (Q_ν, U_ν) and V_ν respectively quantify the linearly and the circularly polarized part of the photon field. Both I_ν and V_ν are scalar fields meaning that they are invariant quantities under transformations of the frame in which they are evaluated. As such, they can be described using the intensity moment expansion of Sec. 2. However a general treatment of polarized light including V_ν with the moment expansion could introduce extra subtleties which go beyond the scope of this work. Henceforth, we assume $V_\nu = 0$.³

On the other hand, the Q_ν and U_ν are coordinate-dependent quantities transforming under frame rotations as the components of a spin-2 object. Therefore, they can be more naturally combined into a single spinor field \mathcal{P}_ν :

$$\mathcal{P}_\nu = Q_\nu + iU_\nu = P_\nu e^{2i\gamma_\nu}, \quad \text{with } i = \sqrt{-1}. \quad (7)$$

³ This is justified for CMB signals and component separation since classical physics in the primordial plasma is not expected to be source of any significant circular polarization (Montero-Camacho & Hirata 2018; Inomata & Kamionkowski 2019). Note however that a faint primordial V signal is expected in some models, see e.g. Hoseinpour et al. (2020).

The spinor's modulus, P_ν , is a real positive function called the linear *polarization intensity* and its argument defines the *polarization angle* γ_ν :

$$|\mathcal{P}_\nu| = P_\nu = \sqrt{Q_\nu^2 + U_\nu^2} \quad (8a)$$

$$\arg(\mathcal{P}_\nu) = 2\gamma_\nu = \tan^{-1}(U_\nu/Q_\nu). \quad (8b)$$

As a spin-2 quantity, when the frame in which Q_ν and U_ν are defined (e.g., by modifying the directions of the polarizers) is rotated by a right handed rotation around the $\hat{\mathbf{n}}$ direction by an angle θ , \mathcal{P}_ν transforms as Zaldarriaga & Seljak (1997):

$$(\mathcal{P}_\nu)' = e^{-2i\theta} \mathcal{P}_\nu. \quad (9)$$

Note that, unless stated otherwise, henceforth we use calligraphic variables for complex quantities (e.g., $\mathcal{P}_\nu, \mathcal{W}, \dots$) and italic font for real quantities (e.g., $P_\nu, A, Q_\nu, U_\nu, \omega, \dots$).

3.2. Origin of frequency-dependent polarization angle from polarized mixing

The canonical SEDs usually considered in astrophysics (e.g. power laws, blackbodies, gray-bodies, modified blackbodies) generally assume a constant value for γ , independent of the frequency. This behavior is motivated by the existence of a preferred direction in the physical mechanisms at the origin of polarized emission such as magnetic fields and dust grain shape. A single emitting voxel in the Galaxy is thus expected to emit with a constant polarization angle as a function of frequency.

Adding voxels with the same polarization angle but varying spectral parameters simply leads to spectral complexity, very much like for intensity. Mixing varying polarization states with the same SED simply leads to a change in the direction of the total polarization, but no extra spectral complexity. However, if one mixes various SEDs with different polarization angles *and* various spectral parameters, the resulting polarized signal will inherit a distorted SED $P'_\nu \neq P_\nu$ and a frequency dependent γ_ν .

$$P_\nu(A_1, \mathbf{p}_1) e^{2i\gamma_1} + P_\nu(A_2, \mathbf{p}_2) e^{2i\gamma_2} + \dots = P'_\nu e^{2i\gamma_\nu}. \quad (10)$$

This consequence of polarized mixing is illustrated in Fig. 1 for a sum of two power laws $A_i(v/v_0)^{\beta_i} e^{2i\gamma_i}$ with $v_0 = 300$ GHz, $A_1 = 2$ Jy/sr, $A_2 = 1$ Jy/sr, $\beta_1 = 1.8$, $\beta_2 = 1.2$, $2\gamma_1 = 10^\circ$ and $2\gamma_2 = 80^\circ$. One clearly sees that the resulting spinor \mathcal{P}_ν rotates in the complex plane with frequency. Modeling both the distorted SED P' and the frequency dependence of γ_ν in a physically-motivated fashion is nontrivial, but can be achieved when generalizing the moment expansion to polarization.

3.3. Understanding the link to intensity moment expansion

To generalize the intensity moment expansion to polarization, we have to discuss how Q_ν and U_ν are obtained, and linked to intensity. To characterize the polarization state of the photon field, we measure the intensity with linear polarizers in four directions, $I_{\nu,\parallel}$ and $I_{\nu,\perp}$, which are orthogonal to each other, and $I_{\nu,\times}$ and $I_{\nu,\otimes}$, which are also orthogonal to each other but rotated by 45° relative to the previous system. The total intensity I_ν (polarized + unpolarized), and Stokes Q_ν and U_ν are then given by

$$(I_\nu^{\text{tot}})^2 = (I_\nu^{\text{unpol}})^2 + Q_\nu^2 + U_\nu^2 \quad (11a)$$

$$Q_\nu = \frac{I_{\nu,\parallel} - I_{\nu,\perp}}{2}, \quad U_\nu = \frac{I_{\nu,\times} - I_{\nu,\otimes}}{2}. \quad (11b)$$

This shows that both Q_ν and U_ν describe *differences* between intensities and as such can have positive and negative contributions, depending on which polarizer response dominates. Thinking of each of the intensities $I_{\nu,\parallel}$, $I_{\nu,\perp}$, $I_{\nu,x}$ and $I_{\nu,\otimes}$ as the cumulative signal from various emitters, means that one can create net polarization by i) varying the number of emitters, that is to say the weight parameter A , and ii) changing the spectra of the emitters in the different directions.

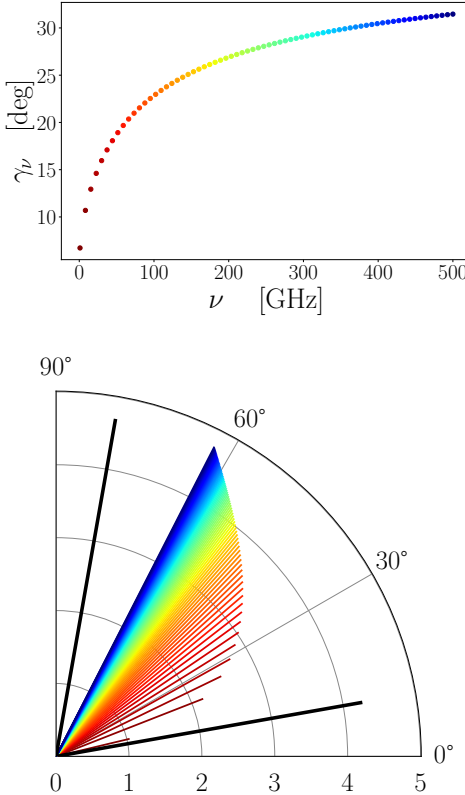


Fig. 1: Illustration of the polarization angle spectral dependence from polarized mixing. *Upper panel:* Polarization angle γ_ν as a function of frequency (in GHz) for the sum of two power laws with parameters $A_1 = 2 \text{ Jy/sr}$, $A_2 = 1 \text{ Jy/sr}$, $\beta_1 = 1.8$, $\beta_2 = 1.2$, $2\gamma_1 = 10^\circ$ and $2\gamma_2 = 80^\circ$. The color labels the frequency between 1 GHz (dark red) and 500 GHz (dark blue). *Lower panel:* Polarization spinor \mathcal{P}_ν (in Jy/sr) in the complex (Q, U) -plane, in the same configuration and with the same color coding. The phase of the spinor is $2\gamma_\nu$. The length of the colored bars and the lines of constant radius represent values of $\log_{10}(P_\nu)$. The two black lines represent the two power laws $A_1(\nu/\nu_0)^{\beta_1} e^{2i\gamma_1}$ and $A_2(\nu/\nu_0)^{\beta_2} e^{2i\gamma_2}$ at 500 GHz.

To give an example, let us assume that in all directions we have a simple gray-body SED, $I_\nu^{\text{GB}} = A B_\nu(T)$, where $B_\nu(T)$ is a blackbody spectrum. The linearly polarized radiation of a single voxel is then given by

$$\mathcal{P}_\nu^{\text{GB}} = \frac{A_\parallel B_\nu(T_\parallel) - A_\perp B_\nu(T_\perp)}{2} + i \frac{A_x B_\nu(T_x) - A_\otimes B_\nu(T_\otimes)}{2}. \quad (12)$$

Starting with this voxel SED renders the problem quite complicated. For example, just considering the SED of Q_ν , we can write

$$\frac{A_\parallel B_\nu(T_\parallel) - A_\perp B_\nu(T_\perp)}{2} = \frac{(A_\parallel - A_\perp)}{2} \frac{B_\nu(T_\parallel) + B_\nu(T_\perp)}{2} + \frac{A_\parallel + A_\perp}{2} \frac{B_\nu(T_\parallel) - B_\nu(T_\perp)}{2}. \quad (13)$$

This means that *two* fundamental SED shapes are required: the sum and difference of two blackbody spectra. These are generally not blackbody spectra again (Chluba & Sunyaev 2004) and the moment expansion requires two series. If the number of spectral parameters is extended (here it was only T), then the number of fundamental voxel spectra increases rapidly, which can quickly make the situation quite complicated.

In astrophysical applications, it is commonly assumed that the only source of polarization is through variations of the number of emitters (i.e., the weight parameter A) at fixed SED parameters. In our example, this means $T_\parallel \approx T_\perp \approx T_x \approx T_\otimes = T$, such that $Q_\nu \approx \frac{(A_\parallel - A_\perp)}{2} B_\nu(T)$. In this case, the fundamental voxel SED is given by $\hat{P}_\nu^{\text{GB}} \approx B_\nu(T)$, such that the single polarization state can be characterized by $\mathcal{P}_\nu^{\text{GB}} \approx A e^{2i\gamma} B_\nu(T)$. For the foreground examples treated below, we similarly assume that inside a given voxel the spectral parameters remain constants. We further discuss how to go beyond this assumption in Sec. 6.1.

3.4. Spin moments: Moment expansion for spin-2 quantities

We now generalize the moment expansion for intensity presented in Sec. 2 to polarized signals. We discuss how this new framework arises naturally from the previous one and provides a powerful tool allowing us to model the frequency dependence of γ_ν in the presence of polarized mixing.

The generalization is indeed quite straightforward. For the intensity moment expansion, we performed a Taylor series in the spectral parameters for each emitting volume element, in Eq. (3). The line-of-sight average in one direction, \hat{n} , is then given by Eq. (2). For polarization, this is equivalent to performing a Taylor expansion of the spinor's modulus⁴ $P_\nu = |\mathcal{P}_\nu|$ with respect to the spectral parameters at each fixed polarization angle γ . However, we cannot use a perturbative approach to average over the polarization angles γ since, in physical situations, one expects them to vary widely in a nontrivial way, such that the situation would quickly become mathematically inconsistent. This means that the line-of-sight average has to be generalized to include the polarization state in the parameter distribution function

$$\langle \mathcal{P}_\nu \rangle = \langle P_\nu(A, \mathbf{p}) e^{2i\gamma} \rangle = \int \mathbb{P}(\mathbf{p}, \gamma, \hat{n}) \hat{P}_\nu(\mathbf{p}) e^{2i\gamma} d^N p d\gamma. \quad (14)$$

Here, we again used $P_\nu(A, \mathbf{p}) = A \hat{P}_\nu(\mathbf{p})$, as for intensity. In analogy to the intensity moment expansion, one then finds

$$\begin{aligned} \langle \mathcal{P}_\nu(A, \mathbf{p}, \gamma) \rangle &= \hat{P}_\nu(\bar{\mathbf{p}}) \langle A e^{2i\gamma} \rangle + \sum_j^N \langle A e^{2i\gamma} (p_j - \bar{p}_j) \rangle \partial_{\bar{p}_j} \hat{P}_\nu(\bar{\mathbf{p}}) \\ &+ \frac{1}{2} \sum_{j,k}^N \langle A e^{2i\gamma} (p_j - \bar{p}_j)(p_k - \bar{p}_k) \rangle \partial_{\bar{p}_j} \partial_{\bar{p}_k} \hat{P}_\nu(\bar{\mathbf{p}}) + \dots, \end{aligned}$$

which depends on the pivot $\bar{\mathbf{p}}$, as we specify in Sect. 3.4.2. Since $\langle A e^{2i\gamma} \rangle$ can vanish, we cannot simply factor it out of the expressions. Instead, like for the intensity moments, we will again use

⁴ Here we make the assumptions discussed in Sec. 3.3.

$\bar{A} = \langle |A e^{2i\gamma}| \rangle \equiv \langle A \rangle$ as a way to normalize the distributions. This allows us to define the spin moments

$$\mathcal{W}_\alpha^{p_j \dots p_l} = \frac{\langle A e^{2i\gamma} (p_j - \bar{p}_j) \dots (p_l - \bar{p}_l) \rangle}{\bar{A}} \equiv \Omega_\alpha^{p_j \dots p_l} e^{2i\gamma_\alpha^{p_j \dots p_l}} \quad (15)$$

very much like for intensity but with an extra spinor weight. The moments are now complex-valued and in the second step we expressed them in terms of the real numbers, $\Omega_\alpha^{p_j \dots p_l}$ and $\gamma_\alpha^{p_j \dots p_l}$. The latter defines average directions of polarization states associated with each of the moments of the SED. While considering the pair $(\Omega_\alpha, \gamma_\alpha)$ or the real and imaginary parts of \mathcal{W}_α give perfectly equivalent descriptions, one could be favored over the other for parameters estimation or physical interpretation. From a numerical perspective, considering the pair (Q, U) as the components of a single object instead of two independent intensities will add correlations between their moments, which is expected to improve the accuracy of the parameter inference. The final polarization moment expansion then takes the form:

$$\begin{aligned} \langle \mathcal{P}_v(A, \mathbf{p}, \gamma) \rangle &= \mathcal{W}_0 P_v(\bar{A}, \bar{\mathbf{p}}) + \sum_j \mathcal{W}_1^{p_j} \partial_{\bar{p}_j} P_v(\bar{A}, \bar{\mathbf{p}}) \\ &+ \frac{1}{2} \sum_{j,k} \mathcal{W}_2^{p_j p_k} \partial_{\bar{p}_j} \partial_{\bar{p}_k} P_v(\bar{A}, \bar{\mathbf{p}}) + \dots \\ &+ \frac{1}{\alpha!} \sum_{j \dots l} \mathcal{W}_\alpha^{p_j \dots p_l} \partial_{\bar{p}_j} \dots \partial_{\bar{p}_l} P_v(\bar{A}, \bar{\mathbf{p}}) + \dots, \end{aligned} \quad (16)$$

which in this form can be interpreted as the sum of multiple SEDs with well-defined polarization states. It is this sum of well-defined single polarization states (i.e., defined by the complex-valued moments) with varying SEDs (i.e., the derivative spectra) that leads to rotation of polarization planes.

We comment that the number of parameters in Eq. (16) depends on the moment order that is used in the modeling. For each moment, two degrees of freedom are added (i.e., the real and imaginary parts). In addition, one has to determine the spectral parameter pivot, $\bar{\mathbf{p}}$. However, the overall normalization \bar{A} does not independently contribute, but was merely chosen to scale the moments. As such, it cannot be independently estimated, and only the values of $\bar{A} \mathcal{W}_\alpha$ actually matter.

3.4.1. Average polarization angle

Since $\mathcal{W}_0 = \Omega_0 e^{2i\gamma_0} = \langle A e^{2i\gamma} \rangle / \bar{A}$ can generally vanish, there is no longer a trivially defined average polarization angle. In particular when $\mathcal{W}_0 \approx 0$, the average polarization angle can be fully determined by the higher order terms in Eq. (16) and also generally becomes frequency-dependent.

To illustrate this aspect, let us consider the simple example of two power law spectra with equal weights A along the $\pm Q$ direction ($\gamma_1 = 0$ and $\gamma_2 = \pi/2$). For these we have $e^{2i\gamma_1} = 1$ and $e^{2i\gamma_2} = -1$ implying $\langle \mathcal{P}_v \rangle = A(v/v_0)^{\beta_1} - A(v/v_0)^{\beta_2}$. For $\beta_1 \neq \beta_2$, we find $\mathcal{P}_v \neq 0$ unless $v \equiv v_0$, which is reflected by the fact that $\mathcal{W}_0 = \langle A e^{2i\gamma} \rangle / \bar{A} \equiv (A - A)/[2A] = 0$, implying that the leading order term in Eq. (16) vanishes. Also, no matter what the frequency, in our example the polarization state will remain Q_v , with a change of sign at $v = v_0$ and hence flip of $0 \leftrightarrow \pi/2$. In this situation, all higher order moments remain real and γ_v is highly non perturbative (i.e., not differentiable) at $v = v_0$.

There must be a way to define a meaningful average polarization angle for each of the moment terms. Indeed, if we simply think of the average of γ along the line of sight in terms of the

distribution, $\mathbb{P}(\mathbf{p}, \gamma, \hat{\mathbf{n}})$. This then results in

$$\bar{\gamma} = \frac{\langle A \gamma \rangle}{\langle A \rangle} = \frac{\int \mathbb{P}(\mathbf{p}, \gamma, \hat{\mathbf{n}}) \gamma d^N p d\gamma}{\int \mathbb{P}(\mathbf{p}, \gamma, \hat{\mathbf{n}}) d^N p d\gamma} \quad (17)$$

as the average polarization angle. This angle can also be used as a pivot when expanding the polarization state:

$$e^{2i\bar{\gamma}} = e^{2i\bar{\gamma}} \left[1 + \sum_{k=1}^{\infty} \frac{(2i)^k}{k!} (\gamma - \bar{\gamma})^k \right]. \quad (18)$$

Using this in Eq. (15), have

$$\mathcal{W}_\alpha^{p_j \dots p_l} = e^{2i\bar{\gamma}} \sum_{k=0}^{\infty} \frac{(2i)^k}{k!} \frac{\langle A(\gamma - \bar{\gamma})^k (p_j - \bar{p}_j) \dots (p_l - \bar{p}_l) \rangle}{\bar{A}}. \quad (19)$$

The first term in the sum (i.e., $k = 0$), is the only non vanishing contribution if the distributions of γ and \mathbf{p} factorize (i.e., the two are uncorrelated variables), as we discuss in Sect. 3.4.3. Adding term by term in the series of Eq. (19) allows us to include information from higher order correlations of γ and \mathbf{p} . However, in terms of *distinguishable* parameters, only the total moments, $\mathcal{W}_\alpha^{p_j \dots p_l}$, can really be constrained.

3.4.2. Definition of the pivot

How do we determine the spectral parameter pivot? In the intensity case, we simply demanded the first moments to vanish to fix the pivot. For polarization, this naively yields the condition

$$\langle A e^{2i\gamma} \rangle \bar{\mathbf{p}} = \langle A e^{2i\gamma} \mathbf{p} \rangle. \quad (20)$$

However, since $\langle A e^{2i\gamma} \rangle$ can vanish, in general this cannot be a meaningful choice.

Above, we already defined $\bar{A} = \langle |A e^{2i\gamma}| \rangle$. In a similar manner, we can introduce the SED pivots as

$$\bar{\mathbf{p}} = \frac{\langle |A e^{2i\gamma}| \mathbf{p} \rangle}{\langle |A e^{2i\gamma}| \rangle} \equiv \frac{\langle A \mathbf{p} \rangle}{\langle A \rangle} = \frac{\int \mathbb{P}(\mathbf{p}, \gamma, \hat{\mathbf{n}}) \mathbf{p} d^N p d\gamma}{\int \mathbb{P}(\mathbf{p}, \gamma, \hat{\mathbf{n}}) d^N p d\gamma}, \quad (21)$$

which is equivalent to the definition for the intensity moments. Physically, this means that we disregard the geometrical properties of \mathcal{P}_v and simply treat its modulus as an intensity. For our power-law example in Sect. 3.4.1, this means $\bar{\mathbf{p}} = (A_1 \beta_1 + A_2 \beta_2)/(A_1 + A_2)$, which is fully analogous to the result of a simple intensity moment expansion. As we shall see below, this choice is well motivated and leads to a well-behaved polarization moment formalism.

In the perturbative regime however, $\Omega_0 = |\langle A e^{2i\gamma} \rangle| \gg 0$, one can safely choose the complex pivot

$$\bar{\mathbf{p}} = \frac{\langle A e^{2i\gamma} \mathbf{p} \rangle}{\langle A e^{2i\gamma} \rangle} \Rightarrow \Delta \bar{p}_j = \frac{\langle A e^{2i\gamma} (p_j - \bar{p}_j) \rangle}{\langle A e^{2i\gamma} \rangle} = \frac{\mathcal{W}_1^{p_j}}{\mathcal{W}_0} \quad (22)$$

While the spectral parameters \mathbf{p} are real quantities, correcting by a complex number might seem incoherent. However, as we will discuss with examples, doing so is deeply relevant. While the real part of $\bar{\mathbf{p}}$ can be interpreted as real correction of \mathbf{p} , its complex part gives rise to the first order frequency dependence of the polarization angle γ_v and can add some spectral modulation to the polarized intensity.

3.4.3. Independent angle distribution and de-polarization

In the definition of the line-of-sight average and spin moments, Eq. (14) and (15), we kept the parameter distribution function general. The discussion is greatly simplified if the probability distributions for the spectral parameters and the polarization angles can be considered as independent. In this case, one has⁵ $\mathbb{P}(\mathbf{p}, \gamma, \hat{\mathbf{n}}) \approx \mathbb{P}(\mathbf{p}, \hat{\mathbf{n}}) \mathbb{P}(\gamma, \hat{\mathbf{n}})$, such that

$$\langle \mathcal{P}_\nu \rangle = \int \mathbb{P}(\mathbf{p}, \hat{\mathbf{n}}) \hat{P}_\nu(\mathbf{p}) d^N p \int \mathbb{P}(\gamma, \hat{\mathbf{n}}) e^{2i\gamma} dy. \quad (23)$$

As this expression shows, spectral mixing and polarization angle averaging become completely independent, such that *no* frequency-dependent polarization angle can be expected. However, when summing over different physical conditions along the line of sight, the probability distribution becomes

$$\begin{aligned} \mathbb{P}(\mathbf{p}, \gamma, \hat{\mathbf{n}}) &= \int A(s) \delta(\gamma - \gamma(s)) \delta^N(\mathbf{p} - \mathbf{p}(s)) ds \\ &\neq \int \delta(\gamma - \gamma(s)) ds \int A(s) \delta^N(\mathbf{p} - \mathbf{p}(s)) ds, \end{aligned} \quad (24)$$

introducing an unavoidable dependence between the angles and the spectral parameters. This dependence disappears if either the polarization angle or the spectral parameters are constant in the line of sight, highlighting that a variation of both γ and \mathbf{p} is required to have a spectral dependence of the polarization angle.

If the angle distribution is Gaussian with average angle $\bar{\gamma}(\hat{\mathbf{n}})$ and width $\sigma_\gamma(\hat{\mathbf{n}})$, then one finds

$$\int \mathbb{P}(\gamma, \hat{\mathbf{n}}) e^{2i\gamma} dy = e^{2i\bar{\gamma}(\hat{\mathbf{n}})} e^{-2\sigma_\gamma^2(\hat{\mathbf{n}})}. \quad (25)$$

This expression highlights that the dispersion of the angles leads to damping of the net polarization amplitude and ultimately complete depolarization if the distribution becomes too wide. In this case, a general perturbative expansion in $\Delta\gamma = \gamma - \bar{\gamma}$, [see e.g. Eq. (18)] is unlikely to converge, but, as stressed already, does not add any new insight anyways.

4. Canonical SEDs

In this section, we illustrate the spin-moment framework on some detailed analytical and numerical examples relevant to astrophysical applications. We consider discrete sums of polarized SEDs along a given line of sight, often focusing on very few contributions. For the moment formalism, this can lead to non-perturbative cases, since in the limit of many emitters, the moments are expected to become more Gaussian due to the central limit theorem. Still, in most cases only a few moments are required to capture the dominant effects.

To highlight the performance of the moment formalism, we treat the sum of SEDs with noise as data and then use the moment representations to finite order as model. We perform a parameter estimation by means of curve fitting with χ^2 minimization in complex-variables using the LMFIT python library (Newville et al. 2016). Hereafter, the model of linear polarization given by the spin-moment expansion is \mathcal{P}_ν^M and the simulated data signal is noted \mathcal{P}_ν^S . We add Gaussian noise N_ν to the simulation, with zero mean and standard deviation $\sigma = \sigma_Q + i\sigma_U$. The values of σ is chosen such that the signal to noise ratios Q_ν^S/Q_ν^M

⁵ In doing so, we can use the normalizations $\int \mathbb{P}(\mathbf{p}, \hat{\mathbf{n}}) d^N p = \bar{A}$ and $\int \mathbb{P}(\gamma, \hat{\mathbf{n}}) d\gamma = 1$.

and U_ν^S/U_ν^M are constants over the whole frequency range (chosen arbitrarily to be 1×10^{-5}).⁶

The χ^2 to minimize is given by $\chi^2 = \frac{1}{2} |\mathcal{P}_\nu^M - \mathcal{P}_\nu^S|^2 / |\sigma|^2$. The signal is considered over a frequency range going from 1 GHz to ν_{\max} in intervals of 1 GHz. The choice of ν_{\max} will depend on the example considered. We introduce the shorthand notation ' $O(\alpha)$ ' to refer to the fit of the spin-moment expansion including all the terms up to order α . ' $O(0)$ ' is the leading order/canonical SED. Two distinct routines are developed, fitting either the pair $(\text{Re}(W_\alpha^p), \text{Im}(W_\alpha^p))$ or the pair (Q_α^p, Q_α^U) . In all the examples considered, both lead to identical results and we leave a further comparison between the two implementations for future work. We are interested in the SED distortions and their behavior in the complex plane, which are only driven by the relative contributions of the different emission points. As such, we use natural units of Jy/sr, for all the SEDs. A more detailed discussion on the relevance of weights, normalization and change of units can be found in Appendices A and B.

4.1. General discrete sums of canonical SEDs

For a discrete sum of M SEDs along a line of sight one can trivially write the distribution function as

$$\mathbb{P}(\mathbf{p}, \gamma, \hat{\mathbf{n}}) = \sum_k^M A_k \delta(\gamma - \gamma_k) \delta^N(\mathbf{p} - \mathbf{p}_k), \quad (26)$$

where $\delta(x - x_0)$ denotes Dirac's distribution and the sum extends over the discrete emission points along the line of sight with SED vectors \mathbf{p}_k and polarization angles γ_k . Inserting this into the definitions of the moments and pivots given in the previous section we trivially find the exact average

$$\begin{aligned} \langle \mathcal{P}_\nu \rangle &= \sum_k^M A_k \int \delta(\gamma - \gamma_k) \delta^N(\mathbf{p} - \mathbf{p}_k) \hat{P}_\nu(\mathbf{p}) e^{2i\gamma} d^N p dy \\ &= \sum_k^M A_k e^{2i\gamma_k} \hat{P}_\nu(\mathbf{p}_k). \end{aligned} \quad (27)$$

Using the polarization moment expansion, we automatically have the normalization, pivot and complex-valued moments as

$$\bar{A} = \sum_k^M A_k \int \delta(\gamma - \gamma_j) \delta^N(\mathbf{p} - \mathbf{p}_j) d^N p dy = \sum_k^M A_k \quad (28a)$$

$$\bar{\mathbf{p}} = \sum_k^M (A_k/\bar{A}) \mathbf{p}_k, \quad \bar{\gamma} = \sum_k^M (A_k/\bar{A}) \gamma_k \quad (28b)$$

$$\mathcal{W}_0 = \sum_k^M (A_k/\bar{A}) e^{2i\gamma_k} \quad (28c)$$

$$\mathcal{W}_\alpha^{p_j \dots p_l} = \sum_k^M (A_k/\bar{A}) e^{2i\gamma_k} (p_{k,j} - \bar{p}_{k,j}) \dots (p_{k,l} - \bar{p}_{k,l}), \quad (28d)$$

where the ratios A_k/\bar{A} determine the probabilities to find \mathbf{p}_k and γ_k . These expressions can then be inserted into Eq. (16) to obtain the polarization moment expansion. The derivatives of the spectra have to be computed individually, but generally the moment expansion is expected to converge with only a few terms.

⁶ The error bars used in all the figures are respectively given by σ_Q^2 , $\sigma_P^2 = (Q^2 \sigma_Q^2 + U^2 \sigma_U^2)/P^2$ and $\sigma_\gamma^2 = 0.5(U^2 \sigma_Q^2 + Q^2 \sigma_U^2)/P^4$.

4.2. Power laws

As a first example of astrophysical relevance, we consider the simple case of power-law SEDs:

$$\hat{P}_v^{\text{PL}}(\beta) = \left(\frac{v}{v_0}\right)^\beta. \quad (29)$$

The polarization state can then be characterized by $\mathcal{P}_v^{\text{PL}} \approx Ae^{2i\gamma} \hat{P}_v^{\text{PL}}$. The only spectral parameter relevant for the moment expansion is the spectral index $p = (\beta)$, normalized at a reference frequency v_0 . This SED plays a crucial role in the foreground modeling of synchrotron on large scales (Planck Collaboration 2020a). In the following numerical applications, we choose $v_{\max} = 150$ GHz below which the synchrotron emission is dominant and $v_0 = 23$ GHz as the WMAP frequency band (Bennett et al 2013). Using $\partial_\beta^k \hat{P}_v^{\text{PL}} = \partial_\beta^k (v/v_0)^\beta = (v/v_0)^\beta \ln(v/v_0)^k$, the spin-moment expansion in Eq. (16) can then be expressed as

$$\langle \mathcal{P}_v^{\text{PL}} \rangle = P_v^{\text{PL}}(\bar{A}, \bar{\beta}) \times \left\{ \mathcal{W}_0 + \mathcal{W}_1^\beta \ln\left(\frac{v}{v_0}\right) + \frac{\mathcal{W}_2^{\beta^2}}{2} \ln\left(\frac{v}{v_0}\right)^2 + \frac{\mathcal{W}_3^{\beta^3}}{6} \ln\left(\frac{v}{v_0}\right)^3 + \dots \right\}. \quad (30)$$

The choice of the reference frequency v_0 , around which to make the expansion, can have an impact on the convergence rate of model, but otherwise leaves the moment expansion unchanged. One choice is to pick a local extremum where the SED changes shape: $\partial_v P_v^S = 0$ or $\partial_v \gamma_v^S = 0$ depending on the distortion type. In front of real data the choice has to be made also from instrumental considerations. As an example, we now consider the superposition of two power laws in more detail.

4.2.1. Hands-on example: two power laws

Consider two power laws ($M = 2$) with different spectral indices (β_1, β_2) and polarization angle (γ_1, γ_2) along the same line of sight. The exact solution then reads

$$\mathcal{P}_v = A_1 \left(\frac{v}{v_0}\right)^{\beta_1} e^{2i\gamma_1} + A_2 \left(\frac{v}{v_0}\right)^{\beta_2} e^{2i\gamma_2}. \quad (31)$$

Carrying out the intensity moment expansion of the two individual power laws with respect to their spectral indices, we obtain

$$\bar{A} = A_1 + A_2 \quad (32a)$$

$$\bar{\beta} = \frac{A_1}{\bar{A}} \beta_1 + \frac{A_2}{\bar{A}} \beta_2, \quad \bar{\gamma} = \frac{A_1}{\bar{A}} \gamma_1 + \frac{A_2}{\bar{A}} \gamma_2 \quad (32b)$$

$$\mathcal{W}_0 = \frac{A_1}{\bar{A}} e^{2i\gamma_1} + \frac{A_2}{\bar{A}} e^{2i\gamma_2} \quad (32c)$$

$$\mathcal{W}_\alpha^{\beta^a} = \frac{A_1}{\bar{A}} e^{2i\gamma_1} (\beta_1 - \bar{\beta})^\alpha + \frac{A_2}{\bar{A}} e^{2i\gamma_2} (\beta_2 - \bar{\beta})^\alpha. \quad (32d)$$

These expressions can be trivially extended to M power laws after extending the sums to M parameters A_k, γ_k and β_k to find the values of the pivot and spin moments (see Sect. 4.1). However, for illustrations the two power-law case is more intuitive.

If $\gamma_1 = \gamma_2 = \bar{\gamma}$ and $\beta_1 \neq \beta_2$, we naturally find that all spin moments are aligned in the same directions of the complex-plane and hence no change in the polarization direction can occur as a function of frequency. In this case, $\langle \mathcal{P}_v^{\text{PL}} \rangle = e^{2i\bar{\gamma}} \langle P_v^{\text{PL}}(A, \beta) \rangle$, trivially describing the effect of spectral mixing only. If on the other hand $\beta_1 = \beta_2 = \bar{\beta}$ and $\gamma_1 \neq \gamma_2$, we naturally have $\mathcal{W}_\alpha^{\beta^a} = 0$

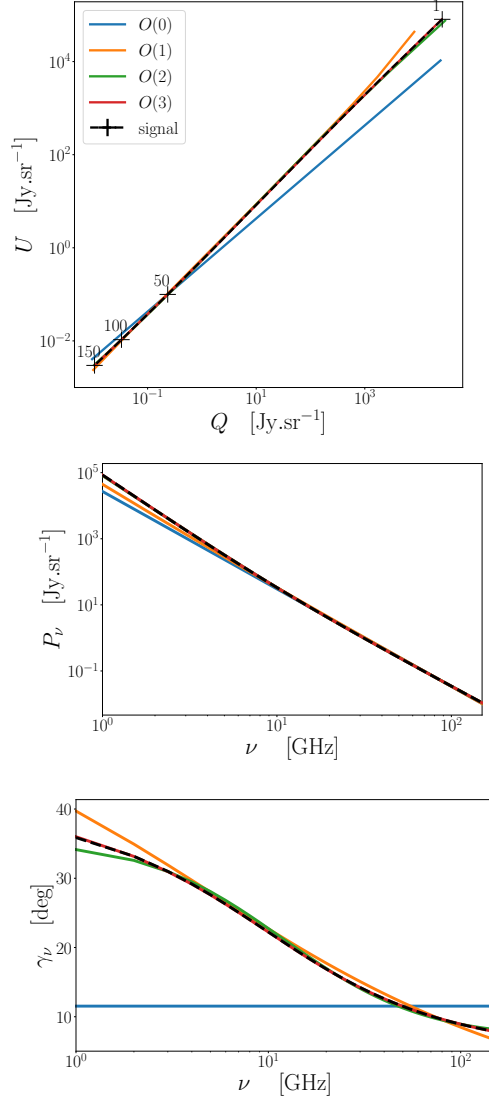


Fig. 2: Illustration of the spinor \mathcal{P}_v in the complex plane (Q, U) for a sum of two power laws (upper panel). Black crosses mark the steps of 50 GHz on the signal. The values of frequencies are indicated above the crosses in GHz. The corresponding polarized intensity P_v (central panel) and polarization angle γ_v (lower panel). The exact result with associated (invisible) error bars (black) is compared to the best-fit moment representation at various orders.

and everything is described by \mathcal{W}_0 with a fixed SED. To obtain nontrivial consequences of polarized mixing, both γ_k and β_k need to vary.

As an illustration, let us consider the highly non-perturbative example, with synchrotron-like behavior: $A_1 = 2$ Jy/sr, $A_2 =$

1 Jy/sr, $\beta_1 = -2.8$, $\beta_2 = -3.6$, $2\gamma_1 = 10^\circ$ and $2\gamma_2 = 80^\circ$, implying $\bar{A} = 3$ Jy/sr, $\bar{\beta} \approx -3.06$ and $\bar{\gamma} \approx 16.6^\circ$. In Fig. 2, the modulus P_ν and the argument γ_ν of the signal together with the recovered spinor representation are displayed for various orders of the expansion going from $O(0)$ to $O(3)$. For such strong deviations of spectral parameters, one cannot expect to find $\bar{\beta} \approx -3.06$ for the expansion at leading order, and it has to be treated as a free parameter of the model. This is particularly important when only a few moment terms are included. The expansion at higher orders then allows us to gradually recover the nontrivial polarization signal over the frequency range. In all cases but $O(0)$, the best fit values for \bar{A} , $\bar{\beta}$ and \mathcal{W}_α^β are all compatible within one standard deviation with those given by Eq. (32). While, by definition, the leading order cannot encompass any rotation of the spinor with frequency, we can see that the moment expansion allows us to correctly model the frequency dependence of γ_ν .

4.2.2. Extreme cases and perturbative regime

To gain further insight, let us just consider the first order terms of the expansion:

$$\langle \mathcal{P}_\nu^{\text{PL}} \rangle \approx \hat{P}_\nu^{\text{PL}}(\bar{A}, \bar{\beta}) \times \left\{ \mathcal{W}_0 + \mathcal{W}_1^\beta \ln\left(\frac{\nu}{\nu_0}\right) \right\}. \quad (33)$$

If $\mathcal{W}_0 \approx 0$, we indeed find the situation where we have a polarization angle fully determined by \mathcal{W}_1^β , with a sign-flip at $\nu = \nu_0$. The polarization SED is then determined by the first β derivative of the power law, and polarization rotation would stem from higher order moments which are not included here. In this situation, we are dealing with two dominant (and near degenerate) contributions to the polarization state that are rotated by 90° to each other (e.g., $+Q_\nu$ and $-Q_\nu$). The moment expansion then describes how much these two power-law terms differ.

This situation is illustrated in Fig. 3 by a sum of two power laws with parameters $A_1 = A_2 = 2$ Jy/sr, $\beta_1 = 1$, $\beta_2 = 2$, $2\gamma_1 = 180^\circ$ and $2\gamma_2 = 0.1^\circ$. One can see that both γ_ν and P_ν do not behave as smooth functions at the breaking point $\nu \approx \nu_0$, where one power law abruptly takes over the other one. Here, γ_ν changes very rapidly from γ_1 to γ_2 . This is, however, not a problem for the spin-moment expansion, which allows us to recover \mathcal{P}_ν correctly. As mentioned above, one recovers a very small best-fit value for \mathcal{W}_0 and $\mathcal{W}_1^\beta \neq 0$ is the dominant term of the expansion, and polarization rotation mainly stems from the second and higher order moments.

If on the other hand we are in the perturbative regime where $|\mathcal{W}_0| \gg |\mathcal{W}_1^\beta| > 0$, we can correct for the first order term of the expansion as in intensity, interpreting it as a correction to the spectral parameters with this correction now being complex-valued. let us split its real and imaginary parts as

$$\Delta\bar{\beta} = \frac{\mathcal{W}_1^\beta}{\mathcal{W}_0} = a_{\Delta\bar{\beta}} + i b_{\Delta\bar{\beta}}. \quad (34)$$

With ⁷ $\mathcal{W}_0 = \Omega_0 e^{2i\gamma_0}$, we can then write the expansion as

$$\begin{aligned} \langle \mathcal{P}_\nu^{\text{PL}} \rangle &\approx \mathcal{W}_0 \hat{P}_\nu^{\text{PL}}(\bar{A}, \bar{\beta}) \times \left\{ 1 + \Delta\bar{\beta} \ln\left(\frac{\nu}{\nu_0}\right) \right\} \\ &\approx \bar{A} \mathcal{W}_0 \left(\frac{\nu}{\nu_0} \right)^{\bar{\beta} + a_{\Delta\bar{\beta}} + i b_{\Delta\bar{\beta}}} \\ &\equiv \bar{A} \Omega_0 \exp\left(2i\left[\gamma_0 + \frac{b_{\Delta\bar{\beta}}}{2} \ln\left(\frac{\nu}{\nu_0}\right)\right]\right) \left(\frac{\nu}{\nu_0} \right)^{\bar{\beta} + a_{\Delta\bar{\beta}}}. \end{aligned} \quad (35)$$

⁷ In general Ω_0 is expected to depart from unity.

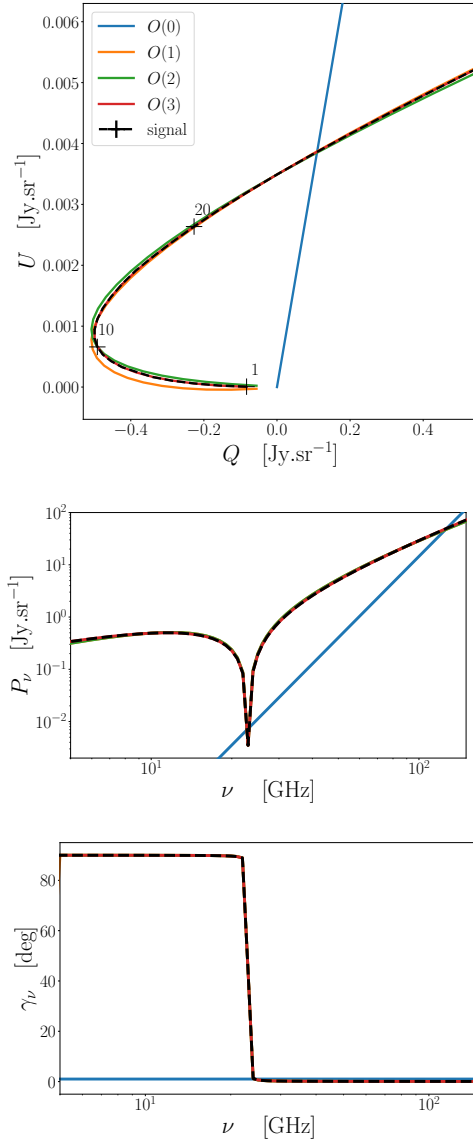


Fig. 3: Illustration of the spinor \mathcal{P}_ν in the complex plane (Q , U) for a sum of two almost anti aligned power laws, with a close-up view around $\nu = \nu_0$ (Upper panel). Black crosses mark the steps of 10 GHz on the signal. The values of frequencies are indicated above the crosses in GHz. The corresponding polarized intensity P_ν (Central panel) and polarization angle γ_ν (Lower panel). We choose logarithmic representations to emphasize the focus on the $\nu \sim \nu_0$ point.

In the perturbative regime, we thus find a polarization SED that is again a power law with a spectral index and frequency-

dependent polarization angle given by

$$\bar{\beta}^{\text{PL}} \approx \bar{\beta} + \text{Re} \left(\frac{\mathcal{W}_1^\beta}{\mathcal{W}_0} \right) \quad (36a)$$

$$\gamma_v^{\text{PL}} \approx \gamma_0 + \frac{1}{2} \text{Im} \left(\frac{\mathcal{W}_1^\beta}{\mathcal{W}_0} \right) \ln \left(\frac{\nu}{\nu_0} \right). \quad (36b)$$

This result clearly shows that even at the lowest order, the superposition of linearly polarized power-law SEDs generally leads to a frequency-dependent rotation of the polarization angle. The rotation is purely driven by the imaginary part of the pivot value in the power-law index. At lowest order, no spectral curvature is added, even if the spectral index departs from that of the simple intensity superposition, $\bar{\beta}$, by $a_{\Delta\bar{\beta}}$. At higher order, the complex-valued moments given in Eq. (32) lead to additional spectral complexity, which in most relevant situations can be captured in a perturbative manner.

Just as for intensity, in the perturbative regime one can cancel \mathcal{W}_1^β and correct the leading order according to Eq. (35). Proceeding iteratively on numerical examples, one can witness the quick convergence of the first order moment toward zero. Doing so allows us to find the right pivot for the expansion while still keeping the pivot $\bar{\beta}$ fixed. As such, one breaks unwanted degeneracies and recovers a physically relevant value for the spectral parameters with a minimal dispersion.

4.3. Blackbodies

As the second example, we briefly consider the superposition of blackbody spectra, a case that is directly relevant to primordial CMB polarization. The only free parameter is the blackbody temperature, and a temperature difference in two orthogonal directions is required to obtain a net polarization. This is an example where the origin of the polarization is due to the spectral parameters *only*. The SED for polarized light, at leading order in the temperature perturbation around the average, is then given by the first temperature derivative of a blackbody:

$$B_\nu(\bar{T}) = \frac{2h}{c^2} \frac{\nu^3}{e^{h\nu/k\bar{T}} - 1}, \quad G_\nu(\bar{T}) = \frac{\partial B_\nu(\bar{T})}{\partial \ln \bar{T}} = \frac{2h\nu^3}{c^2} \frac{x e^x}{(e^x - 1)^2},$$

$$\mathcal{P}_\nu^{\text{BB}} \approx G_\nu(\bar{T}) [\Theta_Q + i\Theta_U] \quad (37)$$

with $x = h\nu/k\bar{T}$ and the usual natural constants. We also introduced the two temperature perturbations $\Theta_Q = \Delta T_Q/\bar{T}$ and $\Theta_U = \Delta T_U/\bar{T}$, which are respectively defined for a coordinate system that is rotated by 45° . At fixed Θ_Q and Θ_U , this means that (at lowest order in the temperature fluctuations) no spectral mixing happens, and hence γ remains frequency-independent.

However, if we include terms at second order in Θ , one finds an additional frequency dependence that is characterized by a y -type distortion (e.g., see Appendix A of Chluba et al. 2015):

$$Y_\nu(\bar{T}) = \frac{2h\nu^3}{c^2} \frac{x e^x}{(e^x - 1)^2} \left[\frac{x e^x + 1}{e^x - 1} - 4 \right],$$

$$\mathcal{P}_\nu^{\text{BB}} = G_\nu(\bar{T}) [\Theta_Q + 2\Theta_I\Theta_Q + i(\Theta_U + 2\Theta_I\Theta_U)] + Y_\nu(\bar{T}) [\Theta_I\Theta_Q + i\Theta_I\Theta_U]. \quad (38)$$

Here, we introduced the total intensity temperature perturbation $\Theta_I = \Delta T_I/\bar{T}$, which generally includes both polarized and unpolarized contributions. Depending on the ratio of Θ_Q to Θ_U , this will cause a small frequency-dependent rotation of the polarization planes. However, since this effect is at second order in the (small) CMB temperature differences, we leave a more detailed discussion to future work.

4.4. Gray-body spectra

In contrast to the blackbody, a gray-body (GB) spectrum also has a free normalization, caused by imperfect reflectivity of the material. As discussed in Sec. 3.3, we only allow variations of A to create polarization. The fundamental SED is thus given by $\hat{P}_v^{\text{GB}} \equiv B_v(T)$, such that the single polarization state can be characterized by $\mathcal{P}_v^{\text{GB}} \approx A e^{2iy} B_v(T)$.

We can then consider general GB superpositions. Following Chluba et al. (2017), we shall use $\beta_{\text{GB}} = 1/T$ as the spectral parameter. The SED derivatives then have a closed form using Eulerian numbers (Chluba et al. 2013), with the first few terms given by (see Eq. (38) of Chluba et al. 2017):

$$\beta_{\text{GB}} \partial_{\beta_{\text{GB}}} \hat{P}_v^{\text{GB}} = -\hat{P}_v^{\text{GB}} \frac{x e^x}{(e^x - 1)} \quad (39a)$$

$$\beta_{\text{GB}}^2 \partial_{\beta_{\text{GB}}}^2 \hat{P}_v^{\text{GB}} = +\hat{P}_v^{\text{GB}} \frac{x e^x}{(e^x - 1)} x \coth(x/2) \quad (39b)$$

$$\beta_{\text{GB}}^3 \partial_{\beta_{\text{GB}}}^3 \hat{P}_v^{\text{GB}} = -\hat{P}_v^{\text{GB}} \frac{x e^x}{(e^x - 1)} \frac{x^2 \cosh(x) + 2}{\cosh(x) - 1} \quad (39c)$$

$$\beta_{\text{GB}}^4 \partial_{\beta_{\text{GB}}}^4 \hat{P}_v^{\text{GB}} = +\hat{P}_v^{\text{GB}} \frac{x e^x}{(e^x - 1)} \frac{x^3 \cosh(x) + 5}{2 \sinh^2(x/2)} \coth(x/2). \quad (39d)$$

with the frequency variable $x = \frac{h\nu}{k} \bar{\beta}_{\text{GB}} \equiv \frac{h\nu}{k\bar{T}}$.

The final GB moment expansion then takes the form:

$$\langle \mathcal{P}_v^{\text{GB}} \rangle = P_v^{\text{GB}}(\bar{A}, \bar{T}) \times \left\{ \mathcal{W}_0 + \mathcal{W}_1^{\beta_{\text{GB}}} Y_1^{\text{GB}}(x) + \frac{1}{2} \mathcal{W}_2^{\beta_{\text{GB}}} Y_2^{\text{GB}}(x) + \frac{1}{6} \mathcal{W}_3^{\beta_{\text{GB}}} Y_3^{\text{GB}}(x) + \dots \right\} \quad (40a)$$

$$\bar{A} = \langle A \rangle, \quad \mathcal{W}_0 = \frac{\langle A e^{2iy} \rangle}{\bar{A}}, \quad \bar{\beta}_{\text{GB}} \equiv \frac{1}{\bar{T}} = \frac{\langle A \beta_{\text{GB}} \rangle}{\bar{A}} \quad (40b)$$

$$\mathcal{W}_\alpha^{\beta_{\text{GB}}} = \frac{\langle A e^{2iy} (\beta_{\text{GB}} - \bar{\beta}_{\text{GB}})^\alpha \rangle}{\bar{A}}, \quad Y_k^{\text{GB}}(x) = \frac{1}{\hat{P}_v^{\text{GB}}} \frac{\partial^k \hat{P}_v^{\text{GB}}}{\partial \beta_{\text{GB}}^k}. \quad (40c)$$

The functions $Y_k^{\text{GB}}(x)$ will also be relevant to the discussion of modified blackbody spectra in Sect. 4.5.

In Fig. 4, we fit the above model on a sum of two gray-bodies with parameters $A_1 = A_2 = 10^6$, $\beta_1 = 1/20 \text{ K}^{-1}$, $\beta_2 = 1/13 \text{ K}^{-1}$, $2\gamma_1 = 72^\circ$, $2\gamma_2 = -90^\circ$. To catch the domain on which β_{GB} has a maximal impact, we choose $\nu_{\text{max}} = 5000 \text{ GHz}$. We note the "loop" trajectory of \mathcal{P}_v in the complex plane (Q, U) inherited from the combination of the shape of the black-body SED and the frequency rotation. By definition again, $O(0)$ can only be a straight line and fail to grasp this complexity. Even if this case again is non-perturbative, we see that the moment expansion up to third order allows us to gradually account for the SED distortions and recover P_v , the polarized mixing inducing a highly nontrivial rotation of the polarization angle.

Like in the power-law example, in the perturbative regime we can obtain a more general expression for the leading order terms. Assuming that $|\mathcal{W}_0| \gg |\mathcal{W}_1^{\beta_{\text{GB}}}|$, we can again use the split $\Delta\bar{\beta}_{\text{GB}} = \mathcal{W}_1^{\beta_{\text{GB}}} / \mathcal{W}_0 = a_{\Delta\bar{\beta}_{\text{GB}}} + i b_{\Delta\bar{\beta}_{\text{GB}}}$ into real and imaginary parts. With this, we can then write

$$\langle \mathcal{P}_v^{\text{GB}} \rangle \approx \bar{A} \mathcal{W}_0 \hat{P}_v^{\text{GB}}(\bar{T}) \times \left\{ 1 + \Delta\bar{\beta}_{\text{GB}} Y_1^{\text{GB}}(x) \right\} \approx \bar{A} \mathcal{W}_0 \hat{P}_v^{\text{GB}}(\bar{T}) \quad (41)$$

with $\bar{T} = 1/(\bar{\beta}_{\text{GB}} + \Delta\bar{\beta}_{\text{GB}})$. The leading order SED term, $\hat{P}_v^{\text{GB}}(\bar{T})$, then depends on the function

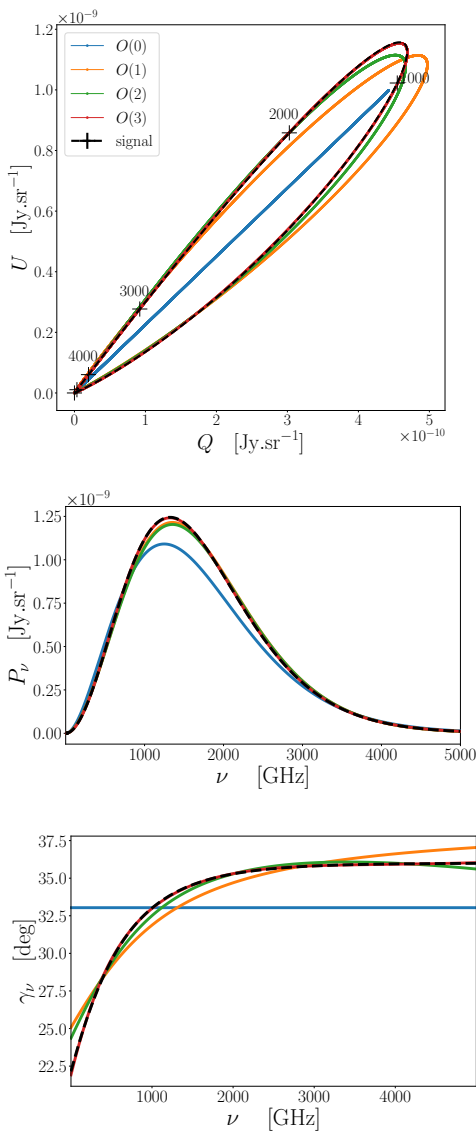


Fig. 4: Illustration of \mathcal{P}_v in the complex plane (Q, U) for a sum of two gray-bodies (Upper panel). Black crosses mark the steps of 1000 GHz on the signal. The values of frequencies are indicated above the crosses in GHz. The corresponding polarized intensity P_v (Central panel) and polarization angle γ_v (Lower panel).

$$\frac{1}{e^{\frac{h\nu}{kT}} - 1} = \frac{1}{e^{x_R + ix_I} - 1} = \frac{e^{2ix\Delta\gamma_v^{\text{GB}}}}{\sqrt{(e^{x_R} - 1)^2 + 2e^{x_R} [1 - \cos(x_I)]}} \quad (42a)$$

$$\Delta\gamma_v^{\text{GB}} = \frac{1}{2} \tan^{-1} \left(\frac{e^{x_R} \sin(x_I)}{e^{x_R} \cos(x_I) - 1} \right) \quad (42b)$$

with $x_R = h\nu(\bar{\beta}_{\text{GB}} + a_{\Delta\bar{\beta}_{\text{GB}}})/k$ and $x_I = h\nu b_{\Delta\bar{\beta}_{\text{GB}}}/k$. One can see that polarized mixing leads to an imaginary photon chemical potential, $\mu = ix_I$. This causes a frequency-dependent rotation of the polarization plane and also modifications to the SED. At high frequencies, one finds $\Delta\gamma_v \approx x_I/2$, while at low frequencies, one has the constant $\Delta\gamma_v \approx \frac{1}{2} \tan^{-1}(b_{\Delta\bar{\beta}_{\text{GB}}}/a_{\Delta\bar{\beta}_{\text{GB}}})$.

4.5. Modified blackbodies

Another highly relevant SED is given by the modified blackbody spectrum. It is expected to provide a good model for the thermal dust intensity and polarized signal (Planck Collaboration 2014b, 2015). In principle, one should allow for amplitude, temperature and spectral index variations inside each voxel. This provides multiple ways of creating polarization (see Sec. 3.3 for discussion). However, we assume that the voxel polarization is again only given by amplitude variations in the four emission directions. The fundamental voxel SED then reads $\hat{P}_v^{\text{mBB}} \equiv (\nu/\nu_0)^{\beta_d} B_v(T)$, such that the single polarization state can be characterized by $\mathcal{P}_v^{\text{mBB}} \approx A e^{2iy} (\nu/\nu_0)^{\beta_d} B_v(T)$ ⁸. Using the results for the power law and gray-body spectra of the previous sections, we then have

$$\begin{aligned} \langle \mathcal{P}_v^{\text{mBB}} \rangle &= P_v^{\text{mBB}}(\bar{A}, \bar{T}, \bar{\beta}_d) \times \left\{ W_0 + W_1^{\beta_d} \ln(\nu/\nu_0) + W_1^{\beta_{\text{GB}}} Y_1^{\text{GB}}(x) \right. \\ &+ \frac{1}{2} W_2^{\beta_d^2} \ln^2(\nu/\nu_0) + W_2^{\beta_{\text{GB}}\beta_d} \ln(\nu/\nu_0) Y_1^{\text{GB}}(x) + \frac{1}{2} W_2^{\beta_{\text{GB}}^2} Y_2^{\text{GB}}(x) \\ &+ \frac{1}{6} W_3^{\beta_d^3} \ln^3(\nu/\nu_0) + \frac{1}{2} W_3^{\beta_{\text{GB}}\beta_d^2} \ln^2(\nu/\nu_0) Y_1^{\text{GB}}(x) \\ &\left. + \frac{1}{2} W_3^{\beta_{\text{GB}}^2\beta_d} \ln(\nu/\nu_0) Y_2^{\text{GB}}(x) + \frac{1}{6} W_3^{\beta_{\text{GB}}^3} Y_3^{\text{GB}}(x) + \dots \right\} \end{aligned} \quad (43a)$$

$$\bar{A} = \langle A \rangle, \quad W_0 = \frac{\langle A e^{2iy} \rangle}{\bar{A}}, \quad (43b)$$

$$\bar{\beta}_{\text{GB}} \equiv \frac{1}{\bar{T}} = \frac{\langle A \beta_{\text{GB}} \rangle}{\bar{A}}, \quad \bar{\beta}_d = \frac{\langle A \beta_d \rangle}{\bar{A}} \quad (43c)$$

$$W_{\alpha+\delta}^{\beta_{\text{GB}}^{\alpha}\beta_d^{\delta}} = \frac{\langle A e^{2iy} (\beta_{\text{GB}} - \bar{\beta}_{\text{GB}})^{\alpha} (\beta_d - \bar{\beta}_d)^{\delta} \rangle}{\bar{A}} \quad (43d)$$

up to third order. Due to the dimensionality of the problem, the moment representation quickly becomes cumbersome, but can be easily handled using modern computers.

In Fig. 5, we applied this expansion on the sum of two normalized⁹ modified blackbodies of parameters $A_1 = A_2 = 1$, $\beta_1 = 2$, $\beta_2 = 1$, $T_1 = 5 \text{ K}$, $T_2 = 70 \text{ K}$, $2\gamma_1 = 72^\circ$, $2\gamma_2 = -90^\circ$. To simulate the thermal dust signal over the CMB missions frequency ranges and in order to witness the transition between the effect of the power-law factor at low frequencies and the gray-body factor at high frequencies, we choose $\nu_{\text{max}} = 800 \text{ GHz}$. Accordingly to the *Planck* high frequency bands, we choose $\nu_0 = 353 \text{ GHz}$ (Planck Collaboration 2016). One can see that the different power laws induce strong distortions at low frequencies $\leq 100 \text{ GHz}$ while the temperature induces an additional bending at high frequencies. In this very extreme case, all the moments up to order 3 are required to correctly model the signal. However, even in this nontrivial situation the moment expansion performs

⁸ This is the standard way to model polarized dust emission locally, with $A = \pi_{\text{dust}} \tau_{\text{dust}} \cos^2(\Gamma_{\text{dust}})$, π_{dust} being the polarization fraction, τ_{dust} the opacity and Γ_{dust} the angle between the Galactic magnetic field and the plane of the sky (Draine & Faisse 2009). In practice one would have to consider a correlation between Γ_{dust} and γ .

⁹ The two modified blackbodies are here normalized by a reference blackbody at $\nu = \nu_0$, as further discussed in Appendix A. As such, Q , U and P_v are unitless.

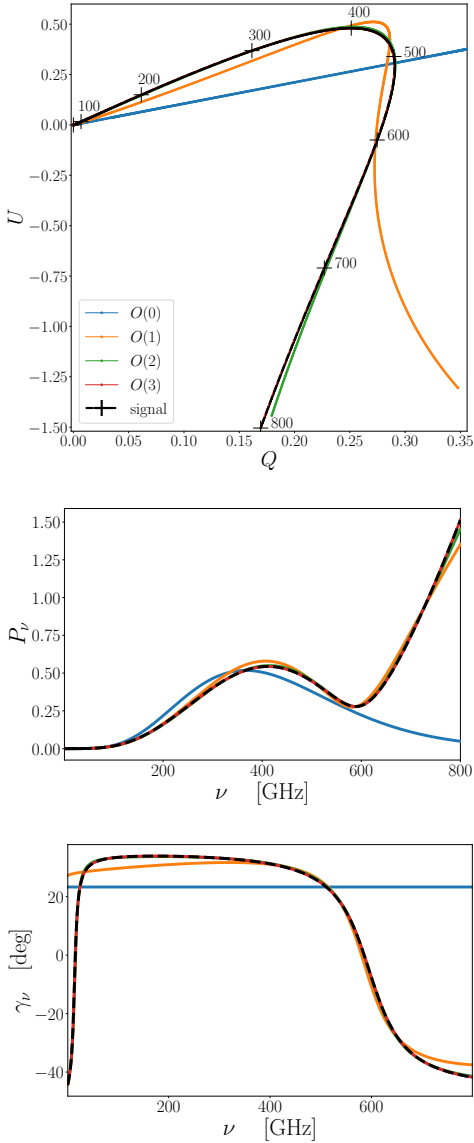


Fig. 5: Illustration of the spinor \mathcal{P}_v in the complex plane (Q, U) for a sum of two modified-blackbodies (Upper panel). Black crosses mark the steps of 100 GHz on the signal. The values of frequencies are indicated above the crosses in GHz. The corresponding polarized intensity P_v (Central panel) and polarization angle γ_v (Lower panel).

extremely well. The leading order fit $O(0)$ interprets a local maximum of the polarized intensity and as the peak of the gray-body spectra, leading to a wrongly small value for the recovered temperature. In astrophysical situations one expects the central limit theorem to render the examples more moderate, with fewer moments required at a given precision.

In the perturbative regime, using the results from the previous sections, the leading order moment description then is

$$\langle \mathcal{P}_v^{\text{mBB}} \rangle \approx \frac{2h\nu^3}{c^2} \frac{\bar{A}\Omega_0(\nu/\nu_0)^{\tilde{\beta}_d+a_{\Delta\tilde{\beta}_d}} e^{2i\gamma_v}}{\sqrt{(e^{x_R}-1)^2+2e^{x_R}[1-\cos(x_L)]}} \quad (44a)$$

$$\gamma_v = \gamma_0 + \frac{1}{2} b_{\Delta\tilde{\beta}_d} \ln(\nu/\nu_0) + \Delta\gamma_v^{\text{GB}}, \quad (44b)$$

with definitions as in the previous section. This expression demonstrates that the rotation of the polarization plane now has two contributions, one from the power-law modulation, one from the temperature terms. The rotation caused by temperature terms is particularly important at high frequencies and can become rapid due to a near linear scaling with ν .

5. Generalizations of the formalism

In this section, we discuss additional averaging processes, covering the spherical harmonic decomposition and beam averaging effects. These cases all naturally lead to a redefinition of the meaning and values of the moments and spectral pivot, but they *do not* actually change the structure of the moment representation. For each case, we briefly recap how the problem is treated in intensity before generalizing to spin moments.

5.1. Generalization to spherical harmonics

As it was done for intensity in Chluba et al. (2017), one can immediately generalize the spin-moment expansion in harmonic space. For that we have to leave the above restriction of considering a single line of sight \hat{n} and consider the intensities as fields over the celestial sphere. Using the moment expansion formalism at the power spectra level is especially useful for component separation on large sky fractions as it has been already shown for *Planck* data (Mangilli et al. 2021), The Simons Observatory telescope (Azzoni et al. 2021) and *LiteBIRD* (Remazeilles et al. 2021; Vacher et al. 2022).

5.1.1. In intensity

While in the above, we described the signal along a given line of sight \hat{n} , we now turn ourselves to averages between different lines-of-sights across sky patches. The average intensity, $\langle I_v \rangle$, which generally depends on the line-of-sight moments and pivots of the SED expansion in the direction \hat{n} , is a scalar field on the S^2 -manifold. As such, it can be expanded on the orthogonal basis of the spherical harmonic functions $Y_{\ell m}(\hat{n})$. We shall denote the spherical harmonic coefficients of a quantity X as

$$(X)_{\ell m} = \int Y_{\ell m}^*(\hat{n}) X(\hat{n}) d^2\hat{n}. \quad (45)$$

The spherical harmonic coefficients of the average intensity SED can then be expressed as:

$$\begin{aligned} \langle I_v \rangle_{\ell m} &\equiv \langle (I_v)_{\ell m} \rangle = \int Y_{\ell m}^*(\hat{n}) \mathbb{P}(\mathbf{p}, \hat{n}) \hat{I}_v(\mathbf{p}) d^N p d^2\hat{n} \\ &= \int \mathbb{P}_{\ell m}(\mathbf{p}) \hat{I}_v(\mathbf{p}) d^N p, \end{aligned} \quad (46)$$

where $\mathbb{P}_{\ell m}(\mathbf{p})$ is the harmonic coefficient of the parameter distribution, $\mathbb{P}(\mathbf{p}, \hat{n})$. Just as the single line-of-sight average, this superposition will introduce some additional mixing between intensities with different spectral parameters $\mathbf{p}(\hat{n})$ and introduces

extra distortions. The spherical harmonic functions introduce a reweighting of the parameter distribution, which essentially implies that all moments can be directly computed using the harmonic coefficients of the parameter distribution, $(P)_{\ell m}(\mathbf{p})$.

Expanding $\hat{I}_v(\mathbf{p})$ in Eq. (46) and following the same steps introduced in Sec. 2, one can derive the moment expansion in harmonic space having the exact same structure as Eq. (6):

$$\begin{aligned} \langle I_v \rangle_{\ell m} &= \delta_{\ell 0} I_v(\bar{A}, \bar{\mathbf{p}}) + \sum_j (\omega_1)_{\ell m}^{p_j} \partial_{\bar{p}_j} I_v(\bar{A}, \bar{\mathbf{p}}) \\ &\quad + \frac{1}{2} \sum_{j,k} (\omega_2)_{\ell m}^{p_j p_k} \partial_{\bar{p}_j} \partial_{\bar{p}_k} I_v(\bar{A}, \bar{\mathbf{p}}) \\ &\quad + \frac{1}{3!} \sum_{j,k,l} (\omega_3)_{\ell m}^{p_j p_k p_l} \partial_{\bar{p}_j} \partial_{\bar{p}_k} \partial_{\bar{p}_l} I_v(\bar{A}, \bar{\mathbf{p}}) + \dots, \end{aligned} \quad (47)$$

where δ_{ij} is the Kronecker- δ and we introduced the (complex-valued) moment multipoles

$$(\omega_\alpha)_{\ell m}^{p_j \dots p_l} = \frac{\langle A(p_j - \bar{p}_j) \dots (p_l - \bar{p}_l) \rangle_{\ell m}}{\bar{A}}. \quad (48)$$

In Eq. (47), we used the average of all the parameters across the sky to define the average SED amplitude and pivot¹⁰

$$\bar{A} = \int \mathbb{P}(\mathbf{p}, \hat{\mathbf{n}}) d^N p \frac{d^2 \hat{\mathbf{n}}}{4\pi} \quad \text{and} \quad \bar{\mathbf{p}} = \frac{\int \mathbb{P}(\mathbf{p}, \hat{\mathbf{n}}) \mathbf{p} d^N p \frac{d^2 \hat{\mathbf{n}}}{4\pi}}{\int \mathbb{P}(\mathbf{p}, \hat{\mathbf{n}}) d^N p \frac{d^2 \hat{\mathbf{n}}}{4\pi}}. \quad (49)$$

This choice might be best suited for convergence (canceling the first order moment of the intensity expansion over the whole sky) when done in real space. This expansion is straightforward to generalize to angular power-spectra and cross-frequency power spectra (Mangilli et al. 2021) and is what has so far been used to describe B -modes signal.

5.1.2. In Polarization

The averaged polarized signal $\langle \mathcal{P}_v(\mathbf{p}(\hat{\mathbf{n}})) \rangle = \langle \mathcal{P}_v(\hat{\mathbf{n}}) \rangle$ is now a section of the spin-2 bundle on the S^2 -manifold. It can be expanded on the orthogonal basis of the spin-2 weighted spherical harmonics ${}_{\pm 2}Y_{\ell m}$ (Newman & Penrose 1966; Goldberg et al. 1967). One can evaluate the spherical-harmonic coefficients of a general frequency dependent spinor field ${}_{\pm 2}\mathcal{X}_v$ for $\ell \geq 2$ as¹¹

$${}_{\pm 2}(\mathcal{X}_v)_{\ell m} = \int {}_{\pm 2}Y_{\ell m}^*(\hat{\mathbf{n}}) \mathcal{X}_v(\hat{\mathbf{n}}) d^2 \hat{\mathbf{n}} \quad (50)$$

For convenience, we then also define the harmonic expansion of the line-of-sight average of the polarization field as

$$\begin{aligned} {}_{\pm 2}\langle \mathcal{P}_v \rangle_{\ell m} &= \int {}_{\pm 2}Y_{\ell m}^*(\hat{\mathbf{n}}) \mathbb{P}(\mathbf{p}, \gamma, \hat{\mathbf{n}}) \mathcal{P}_v(\mathbf{p}, \gamma) d^N p d\gamma d^2 \hat{\mathbf{n}} \\ &= \int {}_{\pm 2}\mathbb{P}_{\ell m}(\mathbf{p}, \gamma) \mathcal{P}_v(\mathbf{p}, \gamma) d^N p d\gamma, \end{aligned} \quad (51)$$

where we define the harmonic coefficient of the parameter distribution function, $\mathbb{P}(\mathbf{p}, \gamma, \hat{\mathbf{n}})$, as ${}_{\pm 2}\mathbb{P}_{\ell m}(\mathbf{p}, \gamma)$. When applied to the

¹⁰ Note that in Mangilli et al. (2021) and its follow-up papers (e.g. Vacher et al. (2022)), the existence of a scale dependent pivot $\bar{\mathbf{p}}(\ell)$ in the harmonic space level has been assumed. Proving or discussing formally this assumption is left for future work.

¹¹ The spin-weighted harmonics function ${}_s Y_{\ell m}$ are defined for $\ell \geq |s|$.

spin-moment expansion of the polarization field, we then obtain

$$\begin{aligned} {}_{\pm 2}\langle \mathcal{P}_v \rangle_{\ell m} &= \sum_j {}_{\pm 2}(\mathcal{W}_1^{p_j})_{\ell m} \partial_{\bar{p}_j} P_v(\bar{A}, \bar{\mathbf{p}}) \\ &\quad + \frac{1}{2} \sum_{j,k} {}_{\pm 2}(\mathcal{W}_2^{p_j p_k})_{\ell m} \partial_{\bar{p}_j} \partial_{\bar{p}_k} P_v(\bar{A}, \bar{\mathbf{p}}) \\ &\quad + \frac{1}{3!} \sum_{j,k,l} {}_{\pm 2}(\mathcal{W}_3^{p_j p_k p_l})_{\ell m} \partial_{\bar{p}_j} \partial_{\bar{p}_k} \partial_{\bar{p}_l} P_v(\bar{A}, \bar{\mathbf{p}}) + \dots, \end{aligned} \quad (52)$$

with the spin-moment multipoles

$${}_{\pm 2}(\mathcal{W}_\alpha^{p_j \dots p_l})_{\ell m} = \frac{{}_{\pm 2}\langle A e^{2i\gamma} (p_j - \bar{p}_j) \dots (p_l - \bar{p}_l) \rangle_{\ell m}}{\bar{A}}. \quad (53)$$

Since this expansion is not defined for $\ell \leq 2$, one does not have any leading order (monopole) term. Nevertheless, the spectral pivot is again defined by the average over the full sky,

$$\bar{A} = \int \mathbb{P}(\mathbf{p}, \gamma, \hat{\mathbf{n}}) d^N p d\gamma \frac{d^2 \hat{\mathbf{n}}}{4\pi} \quad (54a)$$

$$\bar{\mathbf{p}} = \frac{\int \mathbb{P}(\mathbf{p}, \gamma, \hat{\mathbf{n}}) \mathbf{p} d^N p d\gamma \frac{d^2 \hat{\mathbf{n}}}{4\pi}}{\int \mathbb{P}(\mathbf{p}, \gamma, \hat{\mathbf{n}}) d^N p \frac{d^2 \hat{\mathbf{n}}}{4\pi}} \quad (54b)$$

which is the only physically motivated choice. It now has to include the average over γ .

5.1.3. E - and B -modes

From the harmonic coefficients of the polarized spinor, one can then obtain the E - and B -mode coefficients of the polarized SED as (Zaldarriaga & Seljak 1997; Kamionkowski et al. 1997):

$$\langle \mathcal{P}_v \rangle_{\ell m}^E = -\frac{1}{2} [{}_{+2}\langle \mathcal{P}_v \rangle_{\ell m} + {}_{-2}\langle \mathcal{P}_v^* \rangle_{\ell m}] \quad (55a)$$

$$\langle \mathcal{P}_v \rangle_{\ell m}^B = -\frac{1}{2i} [{}_{+2}\langle \mathcal{P}_v \rangle_{\ell m} - {}_{-2}\langle \mathcal{P}_v^* \rangle_{\ell m}]. \quad (55b)$$

One can then expand both \mathcal{P}_v and its complex conjugate using Eq. (52) and insert them into Eq. (55). Going from the expansion of the previous section to the E - and B -modes adds *no extra averaging* effect. For each mode, we get a moment expansion with the same structure as Eq. (52) with spin moments:

$$({\mathcal{W}}_\alpha^{p_j \dots p_l})_{\ell m}^E = -\frac{1}{2} [{}_{+2}({\mathcal{W}}_\alpha^{p_j \dots p_l})_{\ell m} + {}_{-2}({\mathcal{W}}_\alpha^{p_j \dots p_l*})_{\ell m}], \quad (56a)$$

$$({\mathcal{W}}_\alpha^{p_j \dots p_l})_{\ell m}^B = -\frac{1}{2i} [{}_{+2}({\mathcal{W}}_\alpha^{p_j \dots p_l})_{\ell m} - {}_{-2}({\mathcal{W}}_\alpha^{p_j \dots p_l*})_{\ell m}]. \quad (56b)$$

Since this new expansion is simply derived from the one of \mathcal{P}_v , it inherits its amplitude and pivot defined with the γ -weighted full sky averages. This justifies the approximation used in previous studies where the B -mode signal was treated as an intensity at the map (e.g., Remazeilles et al. 2021) or power-spectra level (e.g., Azzoni et al. 2021; Vacher et al. 2022). We leave a detailed discussion on the subtleties of E - and B - modes and power-spectra generalizations for future work.

5.2. Averages inside the beam and bandpass effects

Introducing the general instrumental transfer function $W(v, \gamma, \hat{\mathbf{n}})$ will add additional mixing between the lines of sight but also new nontrivial spectral dependencies from the mixing in frequency. In practice, this very general W function could also account for some effects due to intensity to polarization leakage.

The total polarized signal in a frequency band of width $\Delta\nu$ at average frequency ν_c and within the spatial support of the beam, Ω , centered in an average line of sight $\hat{\mathbf{n}}_c$ then becomes:

$$\langle \mathcal{P}_\nu \rangle_W = \int_{\Omega} \mathbb{P}(\mathbf{p}, \gamma, \hat{\mathbf{n}}) W(\nu, \gamma, \hat{\mathbf{n}}) \hat{P}_\nu(\mathbf{p}) e^{2i\gamma} d^N p d\gamma d^2 \hat{\mathbf{n}} d\nu. \quad (57)$$

Here, $\langle \mathcal{P}_\nu \rangle_W$ is now a function of ν_c and the corresponding moments and pivots in the average direction $\hat{\mathbf{n}}_c$.

Due to the ν integration in the above expression, it is not possible to simply factor the spectral shapes in the Taylor expansion of \hat{P}_ν out of the integral as we did before (Chluba et al. 2017). The band-pass function of the instrument therefore couples different spatial regions with different spectral forms. One can still generalize the spin-moment expansion to account for this extra averaging. The new expansion becomes:

$$\begin{aligned} \langle \mathcal{P}_\nu \rangle_W &= \mathcal{W}_0 \langle \hat{P}_\nu(\bar{A}, \bar{\mathbf{p}}) \rangle_W + \sum_j \mathcal{W}_1^{p_j} \langle \partial_{\bar{p}_j} \hat{P}_\nu(\bar{A}, \bar{\mathbf{p}}) \rangle_W \\ &\quad + \frac{1}{2} \sum_{j,k} \mathcal{W}_2^{p_j p_k} \langle \partial_{\bar{p}_j} \partial_{\bar{p}_k} \hat{P}_\nu(\bar{A}, \bar{\mathbf{p}}) \rangle_W \\ &\quad + \frac{1}{\alpha!} \sum_{j,\dots,l} \mathcal{W}_\alpha^{p_j \dots p_l} \langle \partial_{\bar{p}_j} \dots \partial_{\bar{p}_l} \hat{P}_\nu(\bar{A}, \bar{\mathbf{p}}) \rangle_W + \dots, \end{aligned} \quad (58)$$

with the new averages defined as

$$\langle X \rangle_W = \int \mathbb{P}(\mathbf{p}, \gamma, \hat{\mathbf{n}}) W(\nu, \gamma, \hat{\mathbf{n}}) X d^N p d\gamma d^2 \hat{\mathbf{n}} d\nu. \quad (59)$$

The pivot is chosen to be the same as in intensity:

$$\bar{p}_j = \frac{\langle A p_j \partial_{\bar{p}_j} P_\nu(\bar{\mathbf{p}}) \rangle_W}{\langle A \partial_{\bar{p}_j} P_\nu(\bar{\mathbf{p}}) \rangle_W} \quad (60)$$

and the spin moments become:

$$\mathcal{W}_\alpha^{p_j \dots p_l} = \frac{\langle A e^{2i\gamma} (p_j - \bar{p}_j) \dots (p_l - \bar{p}_l) \partial_{\bar{p}_j \dots \bar{p}_l} \hat{P}_\nu(\mathbf{p}) \rangle_W}{\langle A \partial_{\bar{p}_j \dots \bar{p}_l} \hat{P}_\nu(\mathbf{p}) \rangle_W}. \quad (61)$$

These expressions assume that the various SED derivative averages do not vanish, however, the conclusions are not affected.

Generally, one cannot disentangle the mixing due to the physics of the source and the one due to the instrumental response, and in practice this moment expansion can become awfully complicated. A frequent assumption is to introduce a factorization of W as a band-pass term F times a spatial polarized beam shape \mathfrak{B} as $W(\nu, \hat{\mathbf{n}}) = \mathfrak{B}(\nu, \hat{\mathbf{n}}) F(\nu)$ see e.g. Planck Collaboration (2014a). In this case, it is possible to split the integral of Eq. (57) to factorize the frequency dependent terms, allowing the vanishing of the spectral averages such that the expressions for the pivot and the spin moments are similar to the ones derived for the single line-of-sight case, extending only the averages to the multiple lines of sight included in \mathfrak{B} . The result remains nontrivial since the spectral dependence of the moments need to be computed through the potentially complicated integral of $F(\nu) \partial_{p_j \dots p_k} \hat{P}_\nu$ over $\Delta\nu$. The expansion can also be different in each band of the instrument, since they can have a different instrumental response W . Treating these cases in more detail is beyond the scope of this work.

6. Additional aspects

6.1. Effect of voxel-level SED variations

As stressed in Sect. 3.3, in most of this work we considered that inside each voxel, the net linear polarization have a single SED of which Q and U are the projections. The average signal then inherits a frequency-dependent polarization angle solely from polarized mixing across voxels. Among our examples in Sect. 4, the only exception was the mixing of blackbody spectra, where the polarization degree was caused by variations of the main spectral parameter, the blackbody temperature.

Can we extend the moment formalism to include voxel-level SED mixing caused by variations of the spectral parameters? Let us use the power-law SED as the example. In addition to the weight parameter variations in the different directions, we now also have variations of the spectral index, β . Considering only Q_ν , from the discussion in Sect. 3.3 we then have

$$Q_\nu = \frac{A_{||} \hat{P}_\nu^{\text{PL}}(\beta_{||}) - A_{\perp} \hat{P}_\nu^{\text{PL}}(\beta_{\perp})}{2} = \frac{(A_{||} - A_{\perp})}{2} \frac{\hat{P}_\nu^{\text{PL}}(\beta_{||}) + \hat{P}_\nu^{\text{PL}}(\beta_{\perp})}{2} + \frac{A_{||} + A_{\perp}}{2} \frac{\hat{P}_\nu^{\text{PL}}(\beta_{||}) - \hat{P}_\nu^{\text{PL}}(\beta_{\perp})}{2}. \quad (62)$$

A similar expression follows for U_ν , with the relevant parameters $A_x, \beta_x, A_\otimes, \beta_\otimes$. Let us again expand the fundamental SEDs around some average index $\bar{\beta}$ inside each voxel.¹² This then yields

$$\begin{aligned} Q_\nu &= \frac{(A_{||} - A_{\perp})}{2} \hat{P}_\nu^{\text{PL}}(\bar{\beta}) \left[1 + \sum_{k=1}^{\infty} \frac{\Delta\beta_{||}^k + \Delta\beta_{\perp}^k}{2k!} \ln^k(\nu/\nu_0) \right] \\ &\quad + \frac{A_{||} + A_{\perp}}{2} \hat{P}_\nu^{\text{PL}}(\bar{\beta}) \left[\sum_{k=1}^{\infty} \frac{\Delta\beta_{||}^k - \Delta\beta_{\perp}^k}{2k!} \ln^k(\nu/\nu_0) \right] \\ &= \hat{P}_\nu^{\text{PL}}(\bar{\beta}) \left(\frac{(A_{||} - A_{\perp})}{2} + \sum_{k=1}^{\infty} \frac{A_{||}\Delta\beta_{||}^k - A_{\perp}\Delta\beta_{\perp}^k}{2k!} \ln^k\left(\frac{\nu}{\nu_0}\right) \right) \end{aligned} \quad (63)$$

with $\Delta\beta_k = \beta_k - \bar{\beta}$. We already considered the first term for which spectral index variations between voxels lead to the moment expansion. In addition to these voxel-to-voxel variations one now obtains additional terms that are related to variations within the voxel. All these will cause a redefinition of the SED parameter distribution, however, no new spectral shapes are introduced and hence the moment method equally describes both averaging processes, after the moments are reinterpreted. However, to explicitly make the link to the underlying spectral parameter distributions along the line of sight and within each voxel involves a more complicated description, which we do not provide here.

We close by remarking that, if even the fundamental SEDs in each of the directions differ, then one should simply perform two independent moment expansions accounting for the independent types of SEDs individually. This will quickly increase the number of moments that are required to describe the complexity of the polarized field, but it should nevertheless work even if the physical properties are not independent. The main hope then is that line-of-sight averaging effects reduce the dimensionality of the problem to a manageable level. A more detailed discussion is, however, beyond the scope of this work.

¹² This in fact is $\bar{\beta}_\nu = (A_{||}\beta_{||} + A_{\perp}\beta_{\perp} + A_x\beta_x + A_\otimes\beta_\otimes)/(A_{||} + A_{\perp} + A_x + A_\otimes)$.

6.2. Frequency dependence of the polarization angle without mixing: the case of Faraday rotation

In the presence of magnetic fields, photons experience Faraday rotation while they propagate through the interstellar medium (e.g., Heald 2015). The polarization angle for one voxel at affine parameter s then changes as

$$\gamma_v \approx \gamma + \Gamma f_v, \quad (64)$$

where $f_v = v^{-2}$ and $\Gamma(s) \propto \int_0^s n_e(s') B(s') ds'$ is an integral along the line of sight, with the electron density $n_e(s)$ and the component of the magnetic field in the direction of propagation, $B(s)$. Averaging over various emission points experiencing Faraday rotation adds some extra complications to the moment expansion in a way that is truly unique to polarization. For simplification let us consider the average over a single line of sight. The averaged spinor now becomes:

$$\langle \mathcal{P}_v \rangle_{\text{FR}} = \int \mathbb{P}(\mathbf{p}, \gamma, \Gamma, \hat{\mathbf{n}}) \hat{P}_v(\mathbf{p}) e^{2i\gamma} e^{2i\Gamma f_v} d^N p d\gamma d\Gamma, \quad (65)$$

where we added the level of Faraday rotation as another parameter to the distribution. Taylor expanding the polarized intensity, one can define the spin-moment using the moments

$$W_{\alpha, \text{FR}}^{p_j \dots p_l} = \frac{\langle A e^{2i\gamma} e^{2i\Gamma f_v} (p_j - \bar{p}_j) \dots (p_l - \bar{p}_l) \rangle_{\text{FR}}}{\bar{A}_{\text{FR}}}. \quad (66)$$

with $\bar{A}_{\text{FR}} = \langle A \rangle_{\text{FR}}$. The spin moments now become highly non-trivial and generally frequency dependent.

As discussed in Sec. 3.4.3, under simplifying assumptions one can assume that the emission processes themselves (quantified by the spectral parameters \mathbf{p}) are de-correlated from the Faraday rotation experienced by light on its way along the line of sight. This would allow us to write $\mathbb{P}(\mathbf{p}, \gamma, \Gamma, \hat{\mathbf{n}}) \approx \mathbb{P}(\mathbf{p}, \gamma, \hat{\mathbf{n}}) \mathbb{P}(\Gamma, \hat{\mathbf{n}})$. Physically, this is indeed well-motivated unless the emission process in one voxel knows about the structure of the magnetic field in another (more distant) voxel. The Faraday rotation and the SED averaging in the moments then becomes separable:

$$\begin{aligned} W_{\alpha, \text{FR}}^{p_j \dots p_l} &\approx \frac{\int \mathbb{P}(\mathbf{p}, \gamma, \hat{\mathbf{n}}) \hat{P}_v(\mathbf{p}) e^{2i\gamma} d^N p d\gamma}{\int \mathbb{P}(\mathbf{p}, \gamma, \hat{\mathbf{n}}) d^N p d\gamma} \frac{\int \mathbb{P}(\Gamma, \hat{\mathbf{n}}) e^{2i\Gamma f_v} d\Gamma}{\int \mathbb{P}(\Gamma, \hat{\mathbf{n}}) d\Gamma} \\ &= W_\alpha^{p_j \dots p_l} \frac{\int \mathbb{P}(\Gamma, \hat{\mathbf{n}}) e^{2i\Gamma f_v} d\Gamma}{\int \mathbb{P}(\Gamma, \hat{\mathbf{n}}) d\Gamma}. \end{aligned} \quad (67)$$

This expression shows that no new spectral mixing occurs in this case, as all moments are multiplied by the same frequency-dependent factor. The average Faraday rotation coefficient is simply given by

$$\bar{\Gamma}(\hat{\mathbf{n}}) = \frac{\langle A \Gamma \rangle_{\text{FR}}}{\langle A \rangle_{\text{FR}}} \approx \frac{\int \mathbb{P}(\Gamma, \hat{\mathbf{n}}) \Gamma d\Gamma}{\int \mathbb{P}(\Gamma, \hat{\mathbf{n}}) d\Gamma}. \quad (68)$$

Using this as a pivot, we can then write series

$$\frac{\langle A e^{2i\Gamma f_v} \rangle_{\text{FR}}}{\bar{A}_{\text{FR}}} = e^{2i\bar{\Gamma} f_v} \left[1 + \sum_{k=1}^{\infty} \frac{(2i f_v)^k}{k!} \frac{\langle A(\Gamma - \bar{\Gamma})^k \rangle_{\text{FR}}}{\bar{A}_{\text{FR}}} \right], \quad (69)$$

illustrating how a complicated frequency structure can be created from higher order moments of $\Gamma - \bar{\Gamma}$. Given that these depend on

powers of f_v , one can in principle determine these moments observationally. Finally, if the simple factorization of the parameter distribution function is not possible, one can write

$$\begin{aligned} W_{\alpha, \text{FR}}^{p_j \dots p_l} &= e^{2i\bar{\Gamma} f_v} \left[W_\alpha^{p_j \dots p_l} \right. \\ &\quad \left. + \sum_{k=1}^{\infty} \frac{(2i f_v)^k}{k!} \frac{\langle A e^{2i\gamma} (p_j - \bar{p}_j) \dots (p_l - \bar{p}_l) (\Gamma - \bar{\Gamma})^k \rangle_{\text{FR}}}{\bar{A}_{\text{FR}}} \right]. \end{aligned} \quad (70)$$

This generally introduces a complicated voxel SED reweighting by factors of $(f_v)^k$ and hence new SED shapes that in principle can all be separately accounted for. As is understood, the number of variables quickly becomes unmanageable unless highly perturbative situations are encountered. A more detailed discussion is, however, beyond the scope of this work.

7. Conclusion

In the present work, we introduced the spin moments, the natural generalization of the intensity moment expansion introduced in Chluba et al. (2017) to polarized signals. We developed the formalism from basic principles, showing that the moments are promoted to spin-2 complex coefficients that can be expressed in term of the SEDs parameter distribution [see e.g. Eq. (15)].

Thinking about the spin moments in the form of spinors allows us to treat several subtleties due to the geometrical nature of polarization. A clear interpretation of the polarized mixing distortions arises, as we show that a rotation of the spinor with frequency is naturally induced from the distribution of spectral parameters and polarization angles. We demonstrate that, no general pivot can be defined ensuring the vanishing of the first order in the non-perturbative regime. In the perturbative regime, however, such a pivot can be found and hides interesting physics. Correcting for this pivot naturally gives rise, in addition to a shift of the spectral parameters, to a frequency-dependent rotation of the polarization angle of predictable spectral dependence. It can also bring extra modulations to the polarized intensity, for example in the case of gray-bodies.

We explored scenarios of increasing complexity, considering several canonical SEDs examples of first importance for astrophysics. Even when dealing with highly complex signals along the line of sight, we showed that the use of spin moments allows us to model the distorted polarized intensity and the frequency dependent rotation of the polarization angle, including only a few terms in the expansion.

We also discussed the effect of more complex averaging processes such as spherical harmonics mixing and instrumental mixing as well as non trivial polarization specific situations like SED variations at the voxel-level and Faraday rotation effect. The spin-moment formalism still applies in all these scenarios. In these increasingly complex cases, however, the interpretation of the moment coefficients becomes blurry and the various mixing processes cannot be expected to be properly disentangled. Doing so, we also rederived formally the expressions used in previous works, treating B -mode signal as an intensity at the map (Remazeilles et al. 2016) and power-spectra levels (Azzoni et al. 2021; Vacher et al. 2022).

This work opens the door to several follow-up applications. On the theoretical side, several discussions remain open on the details of the generalization of the formalism at the power-spectrum level, especially for E - and B -mode applications. One could also think of links with cosmic birefringence, which recently received increased attention (see e.g. Diego-Palazuelos

et al. 2022). More broadly, a lot of room is left for application of the spin moments as we defined them. One can think first to component separation where the spin moments could be competitive to model foreground distortions at the map level on large scales where a lot of averaging is done, calling for a comparative study with other pixel-based methods of component separation. Interesting questions related to Galactic physics have also to be addressed with the spin moments, such as the possibility to disentangle dust composition and Galactic magnetic field effects or tackle the Faraday rotation. One can also think of applications to SZ effect or spectral distortions, all topics that are left for future explorations.

Acknowledgments: LV would like to thanks François Boulanger for numerous and fruitful discussions.

JC was supported by the Royal Society as a Royal Society University Research Fellow at the University of Manchester, UK (No. URF/R/191023). This work was also supported by the ERC Consolidator Grant *CMBSPEC* (No. 725456) as part of the European Union's Horizon 2020 research and innovation program.

References

- Aiola, S., Calabrese, E., Maurin, L., et al. 2020, J. Cosmology Astropart. Phys., 2020, 047
- Azzoni, S., Abitbol, M., Alonso, D., et al. 2021, Journal of Cosmology and Astroparticle Physics, 2021, 047
- Bennett et al. C. L. 2013, ApJS, 208, 20
- Brout, R., Englert, F., & Gunzig, E. 1978, Annals of Physics, 115, 78
- Carlstrom, J. E., Holder, G. P., & Reese, E. D. 2002, ARA&A, 40, 643
- Chluba, J., Abitbol, M. H., Aghanim, N., et al. 2021, Experimental Astronomy, 51, 1515
- Chluba, J., Dai, L., Grin, D., Amin, M. A., & Kamionkowski, M. 2015, MNRAS, 446, 2871
- Chluba, J., Hill, J. C., & Abitbol, M. H. 2017, MNRAS, 472, 1195
- Chluba, J. & Sunyaev, R. A. 2004, A&A, 424, 389
- Chluba, J., Switzer, E., Nelson, K., & Nagai, D. 2013, MNRAS, 430, 3054
- CMB-S4 Collaboration. 2019, arXiv e-prints, arXiv:1907.04473
- Delabrouille, J., Abitbol, M., Aghanim, N., et al. 2021, Experimental Astronomy, 51
- Diego-Palazuelos, P., Eskilt, J. R., Minami, Y., et al. 2022, Phys. Rev. Lett., 128, 091302
- Draine, B. T. & Fraisse, A. A. 2009, The Astrophysical Journal, 696, 1
- Ferrière, K. M. 2001, Reviews of Modern Physics, 73, 1031
- Goldberg, J. N., Macfarlane, A. J., Newman, E. T., Rohrlich, F., & Sudarshan, E. C. G. 1967, Journal of Mathematical Physics, 8, 2155
- Guth, A. H. 1981, Phys. Rev. D, 23, 347
- Heald, G. 2015, in Astrophysics and Space Science Library, Vol. 407, Magnetic Fields in Diffuse Media, ed. A. Lazarian, E. M. de Gouveia Dal Pino, & C. Melioli, 41
- Hoseinpour, A., Zarei, M., Orlando, G., Bartolo, N., & Matarrese, S. 2020, Phys. Rev. D, 102, 063501
- Hutton, S., Ferreras, I., & Yershov, V. 2015, MNRAS, 452, 1412
- Ichiki, K., Kanai, H., Katayama, N., & Komatsu, E. 2019, Progress of Theoretical and Experimental Physics, 2019, 033E01
- Inomata, K. & Kamionkowski, M. 2019, Phys. Rev. D, 99, 043501
- Jaffe, T. R., Ferrière, K. M., Banday, A. J., et al. 2013, MNRAS, 431, 683
- Kamionkowski, M., Kosowsky, A., & Stebbins, A. 1997, Phys. Rev. D, 55, 7368
- Kogut, A., Fixsen, D. J., Chuss, D. T., et al. 2011, J. Cosmology Astropart. Phys., 2011, 025
- LiteBIRD Collaboration. 2022, in PTEP, Vol. 11443, PTEP, 114432F
- Mangilli, A., Aumont, J., Rotti, A., et al. 2021, A&A, 647, A52
- Montero-Camacho, P. & Hirata, C. M. 2018, J. Cosmology Astropart. Phys., 2018, 040
- Mroczkowski, T., Nagai, D., Basu, K., et al. 2019, Space Sci. Rev., 215, 17
- Newman, E. T. & Penrose, R. 1966, Journal of Mathematical Physics, 7, 863
- Newville, M., Stensitzki, T., Allen, D. B., et al. 2016, Lmfit: Non-Linear Least-Square Minimization and Curve-Fitting for Python
- Pelgrims, V., Clark, S. E., Hensley, B. S., et al. 2021, A&A, 647, A16
- PICO Collaboration. 2019, in BAAS, Vol. 51, 194
- Planck Collaboration. 2014a, A&A, 571, A9
- Planck Collaboration. 2014b, A&A, 566, A55
- Planck Collaboration. 2015, A&A, 576, A107
- Planck Collaboration. 2016, A&A, 594, A1
- Planck Collaboration. 2017, A&A, 599, A51
- Planck Collaboration. 2020a, A&A, 641, A4
- Planck Collaboration. 2020b, A&A, 641, A11
- Remazeilles, M., Dickinson, C., Eriksen, H. K. K., & Wehus, I. K. 2016, MNRAS, 458, 2032
- Remazeilles, M., Rotti, A., & Chluba, J. 2021, MNRAS, 503, 2478
- Rotti, A. & Chluba, J. 2021, MNRAS, 500, 976
- Sayre, J. T., Reichardt, C. L., Henning, J. W., et al. 2020, Phys. Rev. D, 101, 122003
- Schlafly, E. F., Meisner, A. M., Stutz, A. M., et al. 2016, ApJ, 821, 78
- Starobinsky, A. A. 1980, Physics Letters B, 91, 99
- Stompor, R. & Efstathiou, G. 1999, Monthly Notices of the Royal Astronomical Society, 302, 735
- Tassis, K. & Pavlidou, V. 2015, MNRAS, 451, L90
- The Simons Observatory collaboration. 2019, in BAAS, Vol. 51, 147
- Thorne, B., Dunkley, J., Alonso, D., & Næss, S. 2017, MNRAS, 469, 2821
- Vacher, L., Aumont, J., Monfier, L., et al. 2022, A&A, 660, A111
- Wise, J. H. 2019, Contemporary Physics, 60, 145
- Ysard, N., Abergel, A., Ristorcelli, I., et al. 2013, A&A, 559, A133
- Zaldarriaga, M. & Seljak, U. 1997, Phys. Rev. D, 55, 1830

Appendix A: Alternative approaches

For astrophysical applications, it is common to normalize the modified blackbody SED in every pixel as in Thorne et al. (2017)

$$\hat{P}_v^{\text{mBB}}(\hat{n}) = \frac{\hat{P}_v^{\text{mBB}}(T(\hat{n}), \beta(\hat{n}))}{\hat{P}_{v_0}^{\text{mBB}}(T(\hat{n}), \beta(\hat{n}))}. \quad (\text{A.1})$$

Since here both β and T are treated as spatially varying parameters, this is no longer a constant SED renormalization once line-of-sight effects are included. This choice therefore complicated the expansion, leading to rescaling of the moments (e.g., see Eq.(4) of Vacher et al. 2022), without any physical meaning or insight being added. At the pixel level, this complication can be avoided by setting

$$\hat{P}_v^{\text{mBB}*}(\hat{n}) = \frac{\hat{P}_v^{\text{mBB}}(T(\hat{n}), \beta(\hat{n}))}{\hat{P}_{v_0}^{\text{mBB}}(\bar{T}(\hat{n}), \bar{\beta}(\hat{n}))}, \quad (\text{A.2})$$

which simply takes out the leading order term in the expansion in Eq. (43). However, when extending to applications on the full sky (or when averaging pixels), pixel to pixel variations of $\bar{\beta}$ and \bar{T} will come into play. In this case, one should better normalize using one constant $\bar{\beta}$ and \bar{T} across the sky to avoid additional complications from the variation of the normalization.

Appendix B: Choice of weights

As discussed already in Chluba et al. (2017), when deriving the moment expansion, one can always reexpress the SEDs with another choice of units¹³ or with respect to an alternative choice of spectral variables. Such a choice should be motivated by the physics and the numerical behavior of the problem considered. Ultimately, doing so will simply be equivalent to a re-scaling of the weight coefficients appearing in the moment expansion. Such a change can have a significant impact on the convergence rate of the expansion and the interpretations of the moments coefficients but is mathematically equivalent.

For example, in the case of the gray-body, one could equivalently define the new weights $A'(T) = AT^3$ and expand around T instead of β_{GB} . The fundamental SED then reads

$$\hat{P}_v^{\text{GB}} = A' \left(\frac{\bar{T}}{T} \right)^3 \frac{x^3}{e^{\frac{x}{T}} - 1}. \quad (\text{B.1})$$

The moment expansion will change accordingly as displayed in Eq. (43) of Chluba et al. (2017). This allows us to interpret the spin moments and pivot directly in term of temperatures:

$$\bar{A}' = \langle A' \rangle = \langle AT^3 \rangle \quad (\text{B.2a})$$

$$\bar{T} = \frac{\langle A'T \rangle}{\bar{A}'} = \frac{\langle AT^4 \rangle}{\langle AT^3 \rangle} \quad (\text{B.2b})$$

$$\mathcal{W}_\alpha^T = \frac{\langle A'(T - \bar{T})^\alpha e^{2i\gamma} \rangle}{\bar{A}'} = \frac{\langle AT^3(T - \bar{T})^\alpha e^{2i\gamma} \rangle}{\langle AT^3 \rangle}. \quad (\text{B.2c})$$

The exact same reasoning applies to a change of the power law's reference frequency $v_0 \rightarrow v'_0$ with the simple reweighting $A' = A(v'_0/v_0)^\beta$. However, in this case, no new SED derivatives are created, so the two expansions are identical.

¹³ Some changes of units as e.g. Jy.sr⁻¹ → μK_{CMB} are slightly subtler and introduce new frequency-dependent terms.

D.3 A&A 672, A146

Astronomy & Astrophysics manuscript no. main
May 2, 2023

©ESO 2023

Frequency dependence of the thermal dust E/B ratio and EB correlation: Insights from the spin-moment expansion

L. Vacher¹, J. Aumont¹, F. Boulanger², L. Montier¹, V. Guillet^{3,4}, A. Ritacco^{5,2}, and J. Chluba⁶

¹ IRAP, Université de Toulouse, CNRS, CNES, UPS, 9 Av. du Colonel Roche, 31400 Toulouse, France

² Laboratoire de Physique de l'Ecole normale supérieure, ENS, Université PSL, CNRS, Sorbonne Université Paris-Diderot, Sorbonne Paris Cité, 24 rue Lhomond 75005 Paris, France

³ Institut d'Astrophysique Spatiale, CNRS, Université Paris-Saclay, CNRS, Rue Jean-Dominique Cassini Bât. 121, 91405 Orsay, France

⁴ Laboratoire Univers et Particules de Montpellier, Université de Montpellier, CNRS/IN2P3, CC 72, Place Eugène Bataillon, 34095 Montpellier Cedex 5, France

⁵ INAF-Osservatorio Astronomico di Cagliari, Via della Scienza 5, 09047 Selargius, Italy

⁶ Jodrell Bank Centre for Astrophysics, Alan Turing Building, University of Manchester, Oxford Rd M13 9PL, Manchester, United Kingdom

May 2, 2023

ABSTRACT

The change of physical conditions across the turbulent and magnetized interstellar medium induces a 3D spatial variation of the properties of Galactic polarized emission. The observed signal results from the averaging of different spectral energy distributions (SEDs) and polarization angles along and between lines of sight. As a consequence, the total Stokes parameters Q and U will have different frequency dependencies, both departing from the canonical emission law, so that the polarization angle becomes frequency dependent. In the present work, we show how this phenomenon similarly induces a different, distorted SED for the three polarized angular power spectra \mathcal{D}_ℓ^{EE} , \mathcal{D}_ℓ^{BB} , and \mathcal{D}_ℓ^{EB} , implying a variation of the $\mathcal{D}_\ell^{EE}/\mathcal{D}_\ell^{BB}$ ratio with frequency. We demonstrate how the previously introduced "spin-moment" formalism provides a natural framework to grasp these effects and enables us to derive analytical predictions for the spectral behaviors of the polarized spectra, focusing here on the example of thermal dust polarized emission. After a quantitative discussion based on a model combining emission from a filament with its background, we further reveal that the spectral complexity implemented in the dust models commonly used by the cosmic microwave background (CMB) community includes different distortions for the three polarized power-spectra. This new understanding is crucial for CMB component separation, in which extreme accuracy is required for the modeling of the dust signal to allow for the search of the primordial imprints of inflation or cosmic birefringence. For the latter, as long as the dust EB signal is not measured accurately, great caution is required regarding the assumptions made to model its spectral behavior, as it may not be inferred from the other dust angular power spectra.

Key words. Cosmology, CMB, Foregrounds, Interstellar medium

1. Introduction

Understanding Galactic foregrounds is a critical challenge for the success of cosmic microwave background (CMB) experiments searching for primordial B -modes leftover by inflationary gravitational waves (see e.g., Kamionkowski & Kovetz 2016) and signatures of cosmic birefringence (see e.g., Planck Collaboration 2016b; Diego-Palazuelos et al. 2022). In these quests, both the structure on the sky and the frequency-dependence of the foreground signal need to be modeled.

The two-point statistical properties of a polarized signal are described by angular auto- and cross-power spectra, hereafter simply written as XY , where X and Y refer to E - and B -mode polarization or the total intensity T . Thermal dust polarization is the main polarized foreground at frequencies above approximately 70 GHz (Krachmalnicoff et al. 2016). Based on observations of the *Planck* satellite at 353 GHz, dust power spectra in polarization have been found to be well fitted by power laws in ℓ of similar indices with an EE/BB power ratio of about two. A positive TE and a weaker parity violating TB signal have been sig-

nificantly detected using the same dataset (Weiland et al. 2020; Planck Collaboration 2016c, 2020a). The dust EB signal, however, remains compatible with zero at *Planck* sensitivity (Planck Collaboration 2020a).

The EE/BB asymmetry and TE correlation relate to the anisotropic structure of the magnetized interstellar medium with filamentary structures in total intensity preferentially aligned with the Galactic magnetic field (Clark et al. 2015; Planck Collaboration 2016e). Statistical properties of dust polarization have been discussed on theoretical grounds as signatures of magnetized interstellar turbulence (Caldwell et al. 2017; Kandé et al. 2018; Bracco et al. 2019). Various empirical and phenomenological models have been proposed (Ghosh et al. 2017; Clark & Hensley 2019; Huffenberger et al. 2020; Hervías-Caimapo & Huffenberger 2022; Konstantinou et al. 2022). Within a phenomenological framework, a coherent misalignment between filamentary dust structures and the magnetic field can account for the dust TB signal and should also imply a positive EB (Clark et al. 2021; Cukierman et al. 2022). The possibility of a nonzero dust EB signal is at the heart of recent analyses of *Planck* data that seek to detect cosmic birefringence because it complicates attempts to measure a CMB- EB correlation (Minami et al. 2019;

Send offprint requests to: leo.vacher@irap.omp.eu

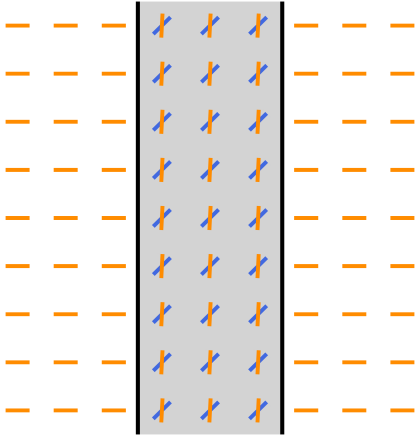


Fig. 1. Diagram of the toy model composed of an infinite filament (grey) over a background (white). The orientation of the $\psi(v)$ field is represented with color bars at two different frequencies: v_1 (orange) and v_2 (blue).

(Diego-Palazuelos et al. 2022; Eskilt & Komatsu 2022; Diego-Palazuelos et al. 2023).

While evaluating the amplitudes of the foreground EE/BB ratio and EB correlation are central subjects in the literature, their frequency dependence is rarely discussed. In the present work, we intend to open this discussion. Given the level of accuracy targeted by future experiments (e.g., LiteBIRD Collaboration 2022; CMB-S4 Collaboration 2019), the frequency dependence of dust polarization is a critical issue for CMB component separation, which relates CMB experiments to the modeling of dust emission (Guillet et al. 2018; Hensley & Draine 2022). The *Planck* data have also been crucial in building our current understanding of this topic (Planck Collaboration 2015b, 2016c). The mean spectral energy distribution (SED), derived from EE and BB power spectra, is found to be well fitted by a single modified blackbody (MBB) law (Planck Collaboration 2020a), but this empirical law does not fully characterize the frequency dependence of dust polarization. Indeed, integration along the line of sight and within the beam of multiple polarized signals with different spectral parameters and polarization angles must induce departures from the MBB coupled to variations of the total polarization angle with frequency (Tassis & Pavlidou 2015; Planck Collaboration 2017; Vacher et al. 2023).¹ This effect has been detected in *Planck* data by Pelgrims et al. (2021) for a discrete set of lines of sight selected based on H I data. From a power spectra analysis of *Planck* polarization maps, Ritacco et al. (2022) revealed an unanticipated impact of the polarization angles' frequency dependence on the decomposition of the dust polarized emission into E - and B -modes. Their result emphasizes the need to account for variations of polarization angles in order to model the dust foreground to the CMB.

The moments expansion formalism, introduced in intensity by Chluba et al. (2017), proposes to treat the distortions from averaging over different emission points by Taylor expanding the canonical SED – the MBB for dust polarization – with re-

¹ These behaviors are sometimes referred to as "frequency decorrelation" (see e.g., Pelgrims et al. 2021).

spect to its spectral parameters. This framework has proven to be a powerful tool for component separation and Galactic physics (Remazeilles et al. 2016, 2021; Rotti & Chluba 2021; Sponseller & Kogut 2022). When carried out at the power-spectrum level, as in Mangilli et al. (2021), the expansion can be applied directly to the B -mode signal as an intensity (Azzoni et al. 2021; Vacher et al. 2022; Ritacco et al. 2022). A recent generalization of this formalism to polarization in Vacher et al. (2023), that is, the "spin-moment" expansion, provides a natural framework to treat for the spectral dependence of the polarization angle. In the present paper, we provide the missing links between the spin-moments maps and the treatment of E - and B -modes. We hence connect the statistical studies of the sky maps with the modeling of the frequency dependence of dust polarization angular power spectra, enabling the prediction of new consequences unique to polarization. In particular, we discuss how and when the assumption of a common SED for EE and BB (and EB) stops being valid.

This article is organized as follows. In Sec. 2, we introduce the specificity of the polarized signal and explain qualitatively why we expect the frequency dependence of EE , BB , and EB to differ. In Sec. 3, we establish how the formalism of the spin-moments can naturally describe these effects and give an analytical expression for their frequency dependence. In Sec. 4, we illustrate the derived formalism on a filament model. Then, in Sec. 5, we show that the frequency dependence of the EE/BB ratio and the nontrivial dependence of EB are already present in dust models extensively used by the CMB community, which brings us to stress the need for caution when inferring the spectral properties of the dust EB signal from other angular power spectra. Finally, we present our conclusions in Sec. 6.

2. Combination of polarized signals

2.1. Mixing of polarized signals in the $Q-U$ plane

The frequency-dependent linear polarization² of a signal is described by a "polarization spinor" \mathcal{P}_v .³ It is a complex-valued object that can be expressed both in Cartesian and exponential form as

$$\mathcal{P}_v \equiv Q_v + iU_v = P_v e^{2i\psi(v)}, \quad (1)$$

where $i^2 = -1$ is the imaginary unit. The spinor components (Q_v, U_v) are two of the Stokes parameters, and they are proportional to the difference of intensities in two orthogonal directions rotated from one another by an angle of 45° . Reportedly, \mathcal{P}_v is a spin-2 object due to its transformation properties under rotations. It rotates in the complex plane by an angle -2θ under a right-handed rotation around the line of sight by an angle θ of the coordinates in which the Stokes parameters are defined.

The modulus of the spinor in Eq. (1) is the linear "polarized intensity"

$$P_v = \sqrt{Q_v^2 + U_v^2}, \quad (2)$$

encoding the SED of the total polarized signal. Depending on the physics of the emission, P_v can be a function of various parameters, p , called the "spectral parameters."

² We do not discuss the circular polarization quantified by V_v in this work.

³ Note that here, as in Vacher et al. (2023), we use the word "spinor" in a general sense which must be understood as "spin- s field on the sphere".

Both the total intensity and the polarized intensity of the thermal dust grains at a given point of the Galaxy are expected to follow an MBB law (see e.g., [Planck Collaboration 2015a](#))

$$P_v^{\text{MBB}} = A \left(\frac{v}{v_0} \right)^\beta B_v^{\text{Pl}}(T) = A \epsilon_v^P(\beta, T), \quad (3)$$

with the corresponding spectral parameters being $\mathbf{p} = \{\beta, T\}$, where β is the spectral index, related to dust grain properties, and T is the temperature associated to the blackbody law B_v^{Pl} . The arbitrary reference frequency v_0 is used for normalization, and the dust polarization amplitude $A = p_0 \tau \cos^2(\gamma)$ can be expressed in terms of the intrinsic degree of polarization p_0 , the dust optical depth τ evaluated at v_0 , and the angle between the Galactic magnetic field and the plane of the sky γ (see e.g., [Planck Collaboration \(2015a\)](#)). The polarized emissivity function $\epsilon_v^P(\beta, T)$ encodes all the spectral dependence of the MBB law.⁴

The spinor phase in Eq. (1) is the so-called polarization angle⁵

$$\psi = \frac{1}{2} \arctan \left(\frac{U_v}{Q_v} \right). \quad (4)$$

This definition explicitly shows that if Q_v and U_v have the same SED, ψ is a constant number defining a single orientation at all frequencies. This assumption is usually made when locally modeling the dust signal, as ψ is orthogonal to the local orientation of the Galactic magnetic field,⁶ which is well motivated by the behavior of the elongated dust grains. If however Q_v and U_v behave differently, the polarization orientation defined by ψ will change with frequency so that $\psi \rightarrow \psi(v)$.

In observational conditions, the mixing of multiple signals coming from emission points with different physical conditions are unavoidable along the line of sight \mathbf{n} , between the lines of sight, inside the instrumental beam, or over patches of the sky when using spherical harmonic transformations. As discussed in [Chluba et al. \(2017\)](#), this mixing will induce departures from the canonical SED of the total intensity, known as "SED distortions," that can be properly modeled using a Taylor expansion of the signal with respect to the spectral parameters themselves. This expansion is known as "moment expansion". The mixing also has unique consequences in polarization. In the rest of this work, we refer to the combination of individual polarized signals with different spectral parameters and polarization angles as the "polarized mixing." The resulting spinor obtained through polarized mixing will inherit both the SED distortions and a spectral dependence of the polarization angle, which can be modeled using a complex moment expansion of \mathcal{P}_v ([Vacher et al. 2023](#)). In principle, it is even possible to predict the value of $\psi(v)$ from the distribution of polarization angles and spectral parameters. For example, considering a sum of MBBs with different polarization

⁴ For comparison, in [Vacher et al. \(2023\)](#), ϵ_v^P was as written \hat{P}_v^{mbb} and $\psi(v)$ was as written γ_v .

⁵ The polarization angle is defined here in the IAU convention (counted positively from Galactic north toward Galactic east), provided that both Q and U also respect this convention. If, however, the healpix convention is used (as is the case for *Planck* data, for example), U must be replaced by $-U$ to recover the IAU defined convention for ψ . (See e.g., [Planck Collaboration \(2020b\)](#)).

⁶ The two angles ψ and γ together quantify the 3D orientation of the Galactic magnetic field and as such are not independent quantities. In the remainder of this work, however, we consider the case of a constant γ , and we do not further discuss the statistical dependence of the two angles.

angles and spectral indices, one expects at first order that

$$\psi(v) \simeq \psi(v_0) + \frac{\text{Im}(\Delta\beta)}{2} \ln \left(\frac{v}{v_0} \right), \quad (5)$$

with $\Delta\beta \in \mathbb{C}$ as the complex spectral index correction,

$$\Delta\beta = \frac{\langle A e^{2i\psi} (\beta - \bar{\beta}) \rangle}{\langle A e^{2i\psi} \rangle}, \quad (6)$$

and $\langle \dots \rangle$ indicating sums or integrals along the line of sight or in the beam of the A , β , and ψ distributions. The value represented by $\bar{\beta}$ is the pivot spectral index around which the expansion is performed.

2.2. Mixing of polarized signals in the E - B plane

In analogy with electromagnetism, the E - and B -modes are scalar and pseudo-scalar fields respectively quantifying the existence of curl-free and divergence-free patterns of the ψ field over the sky. As such, the E and B fields are nonlocal quantities equivalent to convolutions of the Q and U fields around each point of the sky. From a generalization of the Helmholtz decomposition theorem, a linearly polarized signal can be fully split into E and B components. The E - and B -modes of the polarized dust emission are frequency dependent quantities. When all the emission points share the same spectral parameters, E_v and B_v will have the same SED. In this case, the EE/BB ratio is constant with frequency, and the EB correlation has the same SED as EE and BB . As we show, polarized mixing imposes a different SED for E_v and B_v (as Q_v and U_v), and in such cases, the three angular power spectra should inherit a different distorted SED, while the EE/BB ratio becomes frequency dependent.

To illustrate this effect, we start with a very simple example inspired from [Zaldarriaga \(2001\)](#) and [Planck Collaboration \(2016e,d\)](#). As in Fig. 1, we consider an infinite filament⁷ in front of a polarized background. If the background and the filament have different polarization angles and spectral parameters, polarized mixing will unavoidably occur from their superposition, and the resulting ψ field over the filament will rotate with frequency. As sketched out with Fig. 1, one would imagine that at a given frequency, v_1 , the configuration is such that $\psi(v_1)$ in the filament is perpendicular to $\psi(v_1)$ in the background. Similar to the case of [Zaldarriaga \(2001\)](#), such a pattern is curl-free, and one expects to find $B_{v_1} = 0$ and that the signal can be purely described by E -modes. Due to the spectral rotation, at any other frequency (v_2) , $\psi(v_2)$ will be rotated uniformly over the filament, necessarily leading to a different configuration in which $B_{v_2} \neq 0$. It is then clear that the signal's EE/BB ratio must be a frequency dependent quantity. For this to be possible, one would hence conclude that E_v and B_v do not share the same SED anymore and neither do EE , BB , and EB .

3. Insights from the spin-moments

In this section, we explore how to quantify and model the frequency dependence of the EE/BB ratio and the distortions of the EB correlation predicted in Sec. 2.2. As we reveal, the spin-moment expansion formalism provides a natural framework to do so. To keep our discussion as simple as possible, we consider only the case of averaging MBB with different values of A , β , and

⁷ The situation would be different for a finite filament. On this point, see the discussions in [Rotti & Huffenberger \(2019\)](#).

ψ and we display expansions only up to first order. All the following derivations can however be straightforwardly generalized at any order and used to consider variations of temperatures. All our conclusions about the behavior of the spectra would remain true for any choice of SED (e.g., for the synchrotron signal).

3.1. Q/U spin-moment expansion

As presented in Sec. 2.1, we consider that the dust grain polarized signal is given locally by the spinor \mathcal{P}_v in every point of the Galaxy, with $P_v = |\mathcal{P}_v|$ as an MBB and ψ as a frequency independent quantity. The average spinor over different emission points centered on a given line of sight \mathbf{n} is given by the spin-moment expansion around an arbitrary pivot value $\bar{\beta}$ ⁸ for the spectral index as

$$\langle \mathcal{P}_v(\mathbf{n}) \rangle = \varepsilon_v^P(\bar{\beta}, \bar{T}) \left(\mathcal{W}_0 + \mathcal{W}_1^\beta \ln\left(\frac{v}{v_0}\right) + \dots \right). \quad (7)$$

The spin-moments \mathcal{W}_k^β of order k associated to the spectral index can be estimated directly from the distribution of ψ , A , and β as⁹

$$\mathcal{W}_k^\beta = \langle A e^{2i\psi} (\beta - \bar{\beta})^k \rangle, \quad (8)$$

where $\mathcal{W}_0 = \langle A e^{2i\psi} \rangle$ plays the role of a total complex amplitude that satisfies $|\mathcal{W}_0| \leq \langle A \rangle$. Purely geometrical phenomenon can greatly decrease the value of \mathcal{W}_0 . For example, the cancellation of the phases known as "depolarization" ($\langle e^{2i\psi} \rangle \approx 0$), or a significant inclination of the Galactic magnetic field toward the plane of the sky ($\cos(\gamma) \approx 0$), would both lead to $\mathcal{W}_0 \approx 0$. The condition $|\mathcal{W}_0| \gg |\mathcal{W}_k^\beta|$ defines the "perturbative regime" such that one can consider the total signal as a perturbed MBB. However, as discussed in Vacher et al. (2023), one would expect the existence of configurations where the canceling effects are strong enough such that the total signal is mostly or fully given by its moments and thus loses its MBB behavior. In general, the phase weighting¹⁰ in Eq. (8), which is unique to polarization, breaks the expected hierarchy between the moments, and one would not be able to ascertain that $\mathcal{W}_k^\beta > \mathcal{W}_m^\beta$ solely because $k > m$.

The expansion can equivalently be split into Q and U coordinates as¹¹

$$\mathcal{W}_{k,Q}^\beta = \text{Re}(\mathcal{W}_k^\beta), \quad (9)$$

$$\mathcal{W}_{k,U}^\beta = \text{Im}(\mathcal{W}_k^\beta). \quad (10)$$

Different moments in Q and U , expected in the general case, will necessarily imply a frequency dependence of the polarization angle $\psi \rightarrow \psi(v)$ from the definition given in Eq. (4). In the

⁸ The choice of the weighted average $\bar{\beta} = \langle A\beta \rangle / \langle A \rangle$, which cancels the first order moment in intensity, is expected to be best suited for convergence.

⁹ For simplicity, we chose a different choice of normalization for the spin-moments than Vacher et al. (2023), simplifying the \bar{A} of the derivatives with the ones in the original definition of the spin-moments.

¹⁰ While the two angles ψ and γ have a common geometrical origin in the Galactic magnetic field, they play a very different role here. The angle ψ is a complex phase allowing for "interference"-type cancellation of the moment terms, while $\cos^2(\gamma)$ (as p_0) plays the role of a real and positive weight.

¹¹ By treating the expansions of Q and U independently (instead of considering them together in \mathcal{P}_v), one would lose the information on their correlation.

perturbative regime, the first order $\mathcal{W}_1^\beta / \mathcal{W}_0$ can be interpreted as a complex correction to the pivot spectral index, leading to

$$\psi(v) \simeq \psi(v_0) + \frac{1}{2} \text{Im} \left(\frac{\mathcal{W}_1^\beta}{\mathcal{W}_0} \right) \ln \left(\frac{v}{v_0} \right), \quad (11)$$

and giving back the result mentioned in Eq. (5). We note again that both variations of the polarization angles and the spectral indices are required for the second term to be nonzero.

3.2. E_v and B_v in map space

As for Q and U in Eq. (1), the E and B fields can be grouped in a single complex scalar field (Zaldarriaga & Seljak 1997):

$$S_v \equiv E_v + iB_v = S_v e^{i\vartheta(v)}, \quad (12)$$

of modulus and phase (which we refer to as the E - B angle)

$$S_v = \sqrt{E_v^2 + B_v^2}, \quad (13)$$

$$\vartheta = \arctan \left(\frac{B_v}{E_v} \right). \quad (14)$$

The frequency dependence of the EE/BB ratio discussed in Sec. 2.2 would then translate itself into the rotation of S_v in the complex plane, and the E - B angle would become frequency dependent, that is, $\vartheta \rightarrow \vartheta(v)$.

A straightforward way to obtain the S_v field from the previously introduced polarization spinor field \mathcal{P}_v is to use the spin-raising operator $\bar{\delta}$ – the conjugate of the spin-lowering operator δ – as

$$S_v(\mathbf{n}) = -\bar{\delta}^2 \mathcal{P}_v(\mathbf{n}), \quad (15)$$

where $\bar{\delta}$ is acting both as an angular momentum ladder operator and as a covariant derivative on the sphere (see, e.g., Goldberg et al. (1967); Rotti & Huffenberger (2019)). As such, it contains derivatives with respect to the spherical coordinates θ and φ . More technically, for a spin-s field η on the sphere,

$$\bar{\delta}\eta = -(\sin\theta)^s [\partial_\theta - i \sin(\theta)^{-1} \partial_\varphi] [\sin(\theta)^{-s} \eta]. \quad (16)$$

This operator mixes the real and imaginary parts of η in a non-trivial way. It is however linear and does not act on the spectral dependence, and as a result, the moment expansion will keep the same structure

$$\langle S_v(\mathbf{n}) \rangle = \varepsilon_v^P(\bar{\beta}, \bar{T}) \left(\mathbb{W}_0 + \mathbb{W}_1^\beta \ln\left(\frac{v}{v_0}\right) + \dots \right), \quad (17)$$

where the scalar moment maps are extracted from the spin-moments as

$$\mathbb{W}_k^\beta = -\bar{\delta}^2(\mathcal{W}_k^\beta). \quad (18)$$

As in Remazeilles et al. (2016, 2021), one can split the E and B expansions in order to treat them as two scalar spin-0 fields¹² (and thus they loose their correlation)

$$\mathbb{W}_{k,E}^\beta = \text{Re}(\mathcal{W}_k^\beta) = -\text{Re}(\bar{\delta}^2(\mathcal{W}_k^\beta)), \quad (19)$$

$$\mathbb{W}_{k,B}^\beta = \text{Im}(\mathcal{W}_k^\beta) = -\text{Im}(\bar{\delta}^2(\mathcal{W}_k^\beta)), \quad (20)$$

¹² The (Q, U) and (E, B) expansions still differ from two independent intensity expansions, as they can take negative values.

where δ induces a mixing of the Q and U moments into E and B such that different moments for Q and U necessarily imply different moments for E and B .

A clear way to make the action of δ explicit is to consider the flat sky approximation, for which $\delta = \partial_x + i\partial_y$, allowing the expression of the E and B moments map in terms of the two Q and U spin-moment maps as

$$\begin{pmatrix} \mathbb{W}_{k,E}^\beta \\ \mathbb{W}_{k,B}^\beta \end{pmatrix}_{\text{flat}} = \begin{pmatrix} \partial_y^2 - \partial_x^2 & 2\partial_x\partial_y \\ -2\partial_x\partial_y & \partial_y^2 - \partial_x^2 \end{pmatrix} \begin{pmatrix} \mathcal{W}_{k,Q}^\beta \\ \mathcal{W}_{k,U}^\beta \end{pmatrix}_{\text{flat}}. \quad (21)$$

E and B moments are thus expressed as different linear combinations of second order spatial derivatives of the Q and U spin-moments.

Whenever a spectral rotation, $\psi \rightarrow \psi(\nu)$, is induced by polarized mixing, an equivalent rotation, $\vartheta \rightarrow \vartheta(\nu)$, must occur in the E/B plane, introducing the EE/BB frequency dependence discussed in Sec. 2.2. This rotation can be similarly modeled at first order as

$$\vartheta(\nu) \simeq \vartheta(\nu_0) + \text{Im}\left(\frac{\mathbb{W}_1^\beta}{\mathbb{W}_0}\right) \ln\left(\frac{\nu}{\nu_0}\right). \quad (22)$$

3.3. E_ν and B_ν in harmonic space

The spherical harmonic transformation of a spin s field X ,¹³ that is,

$$(X)_{\ell m} \equiv \int X(\mathbf{n})_s Y_{\ell m}^*(\mathbf{n}) d^2\mathbf{n}, \quad (23)$$

creates additional mixing over angular scales ℓ . As such, it is expected to increase the moment amplitudes. Consequently, averaging over patches of the sky with a different β in each pixel but with no variation along the line of sight is still expected to create SED distortions (see e.g., Vacher et al. (2022)), and it is expected to make the EE/BB ratio frequency dependent and distort the EB correlation. Since the transformation is linear, one can simply derive for $\ell \geq 2$ ¹⁴

$$(\mathcal{S}_\nu)_{\ell m} = (E_\nu)_{\ell m} + i(B_\nu)_{\ell m}. \quad (24)$$

With Eq. (17), the expansion becomes

$$(\mathcal{S}_\nu)_{\ell m} = \varepsilon_\nu^P(\bar{\beta}, \bar{T}) \left((\mathbb{W}_0)_{\ell m} + (\mathbb{W}_1^\beta)_{\ell m} \ln\left(\frac{\nu}{\nu_0}\right) + \dots \right). \quad (25)$$

We note, however, that the pivot $\bar{\beta}$ maximizing the convergence of the expansion in harmonic space might be different than in real space. Hence, one can split the expansion of E and B separately as

$$(\mathbb{W}_k^\beta)_{\ell m}^E = \text{Re}((\mathbb{W}_k^\beta)_{\ell m}) = \frac{(\mathbb{W}_k^\beta)_{\ell m} + (\mathbb{W}_k^\beta)_{\ell m}^*}{2}, \quad (26)$$

$$(\mathbb{W}_k^\beta)_{\ell m}^B = \text{Im}((\mathbb{W}_k^\beta)_{\ell m}) = \frac{(\mathbb{W}_k^\beta)_{\ell m} - (\mathbb{W}_k^\beta)_{\ell m}^*}{2i}. \quad (27)$$

¹³ $s Y_{\ell m} \propto (\delta)^s Y_{\ell m}$ ($s > 0$) and $\propto (\tilde{\delta})^s Y_{\ell m}$ ($s < 0$) are the spin-weighted spherical harmonics, defined only for $\ell \geq |s|$.

¹⁴ In order to recover the standard $(E)_{\ell,m}$ and $(B)_{\ell,m}$ as usually defined in cosmology, an extra normalization factor of $[(\ell-2)!/(\ell+2)!]^{1/2}$ must be added when applying the transformation given by Eq. 23, leaving our discussion unchanged.

3.4. Power spectra

3.4.1. The EE and BB power spectra

When carrying the moment expansion at the power-spectrum level, we found expressions comparable to the ones introduced in intensity by Mangilli et al. (2021) and applied to B -modes in Azzoni et al. (2021); Vacher et al. (2022). The cross angular power spectra $\mathcal{D}_\ell^{XX'}$ of two fields X and X' are defined as

$$\mathcal{D}_\ell^{XX'} = \frac{\ell(\ell+1)}{2\pi} \sum_{m=-\ell}^{\ell} X_{\ell m} (X'_{\ell m})^*, \quad (28)$$

with $X, X' \in \{E, B, \mathbb{W}_{0,E}, \mathbb{W}_{0,B}, \mathbb{W}_{k,E}^\beta, \mathbb{W}_{k,B}^\beta\}$. For the EE and BB power spectra, when replacing E and B by the moment expansion of the real or imaginary parts of \mathcal{S}_ν , one obtains

$$\begin{aligned} \mathcal{D}_\ell^{XX}(\nu) = & \left(\varepsilon_\nu^P(\bar{\beta}, \bar{T}) \right)^2 \left[\mathcal{D}_\ell^{\mathbb{W}_{0,X}\mathbb{W}_{0,X}} + 2\mathcal{D}_\ell^{\mathbb{W}_{0,X}\mathbb{W}_{1,X}^\beta} \ln\left(\frac{\nu}{\nu_0}\right) \right. \\ & \left. + \mathcal{D}_\ell^{\mathbb{W}_{1,X}^\beta\mathbb{W}_{1,X}^\beta} \ln\left(\frac{\nu}{\nu_0}\right)^2 \dots \right], \end{aligned} \quad (29)$$

with $XX \in \{EE, BB\}$. Hence, by knowing the spin-moment maps \mathcal{W}_k^β , one can in principle derive their E and B spectra to obtain

the $\mathcal{D}_\ell^{\mathbb{W}_{k,X}^\beta\mathbb{W}_{m,X}^\beta}$ appearing in Eq. 29. Just as with Q and U , the E and B expansions are not expected to be independent, as they are the expressions of the real and imaginary parts of the same complex number \mathcal{S}_ν .¹⁵ While the analysis of Planck Collaboration (2016c) found no significant difference between the $EE(\nu)$ and $BB(\nu)$ SEDs, a recent analysis by Ritacco et al. (2022) did detect a significant difference between these SEDs in the *Planck* data. As discussed, this detection would be a direct indication of the existence of polarized mixing, which would lead to a spectral phase rotation $\vartheta(\nu)$, that is, $(\mathbb{W}_k^\beta)^E \neq (\mathbb{W}_k^\beta)^B$, and one would then expect to find a frequency dependence of the EE/BB ratio in sky observations. The EE/BB ratio can be expressed at first order as

$$\begin{aligned} (r_\nu^{E/B})_\ell \equiv & \frac{\mathcal{D}_\ell^{EE}(\nu)}{\mathcal{D}_\ell^{BB}(\nu)} \\ = & \frac{\mathcal{D}_\ell^{\mathbb{W}_{0,E}\mathbb{W}_{0,E}} + 2\mathcal{D}_\ell^{\mathbb{W}_{0,E}\mathbb{W}_{1,E}^\beta} \ln\left(\frac{\nu}{\nu_0}\right) + \mathcal{D}_\ell^{\mathbb{W}_{1,E}^\beta\mathbb{W}_{1,E}^\beta} \ln\left(\frac{\nu}{\nu_0}\right)^2}{\mathcal{D}_\ell^{\mathbb{W}_{0,B}\mathbb{W}_{0,B}} + 2\mathcal{D}_\ell^{\mathbb{W}_{0,B}\mathbb{W}_{1,B}^\beta} \ln\left(\frac{\nu}{\nu_0}\right) + \mathcal{D}_\ell^{\mathbb{W}_{1,B}^\beta\mathbb{W}_{1,B}^\beta} \ln\left(\frac{\nu}{\nu_0}\right)^2}. \end{aligned} \quad (30)$$

We note that this expression does not depend on the modified blackbody and gives a pure ratio of moments. Therefore, looking for the EE/BB ratio will probe the existence of differences between the SEDs of E and B due to polarized mixing independent of any choice of canonical SED for modeling dust at the voxel level. Variations of spectral parameters alone would identically distort E and B , leading to the same moments and leaving the EE/BB ratio constant. Therefore, $(r_\nu^{E/B})_\ell$ provides, at the power-spectra level, an observable equivalent to $\tan(\psi(\nu))$ or $\tan(\vartheta(\nu))$ at the map level.

As in Mangilli et al. (2021) and Vacher et al. (2022), one can consider Eq. (29) as two independent moment expansions for EE and BB and interpret the order one term as a leading-order correction to the spectral index. A scale-dependent pivot can be obtained by canceling the first order term and inserting the replacement

$$\bar{\beta} \rightarrow \bar{\beta}_\ell^{XX'} = \bar{\beta} + 2\mathcal{D}_\ell^{\mathbb{W}_{0,X}\mathbb{W}_{1,X}^\beta} / \mathcal{D}_\ell^{\mathbb{W}_{0,X}\mathbb{W}_{0,X}}. \quad (31)$$

¹⁵ To keep this link explicit, one could consider $\mathcal{D}_\ell^{SS} = \mathcal{D}_\ell^{EE} + \mathcal{D}_\ell^{BB}$.

Hence, in the presence of polarized mixing, the moments are different in EE and BB , and it is impossible to find a common pivot simultaneously canceling the first order for EE and BB (i.e., $\bar{\beta}_\ell^{EE} \neq \bar{\beta}_\ell^{BB}$). In the perturbative regime, $\mathcal{D}_\ell^{\mathbb{W}_{0,X}\mathbb{W}_{0,X}} \gg \mathcal{D}_\ell^{\mathbb{W}_{1,X}^\beta\mathbb{W}_{1,X}^\beta}$, one can approximate Eq. (30) as

$$(r_\nu^{E/B})_\ell \simeq A_\ell^{E/B} \left(\frac{\nu}{\nu_0} \right)^{2\Delta\bar{\beta}_\ell^{E/B}} \left(1 + \delta_\ell^{11} \ln \left(\frac{\nu}{\nu_0} \right)^2 \right). \quad (32)$$

As such, while the amplitude of the power-law term $A_\ell^{E/B} = \mathcal{D}_\ell^{\mathbb{W}_{0,E}\mathbb{W}_{0,E}} / \mathcal{D}_\ell^{\mathbb{W}_{0,B}\mathbb{W}_{0,B}}$ indicates the value of the EE/BB ratio at $\nu = \nu_0$, its exponent $2\Delta\bar{\beta}_\ell^{E/B} = 2\bar{\beta}_\ell^{EE} - 2\bar{\beta}_\ell^{BB}$ provides an indication of how the pivot spectral indices of EE and BB are expected to differ. The moment term, that is,

$$\delta_\ell^{11} = \frac{\mathcal{D}_\ell^{\mathbb{W}_{1,E}^\beta\mathbb{W}_{1,E}^\beta}}{\mathcal{D}_\ell^{\mathbb{W}_{0,E}\mathbb{W}_{0,E}}} - \frac{\mathcal{D}_\ell^{\mathbb{W}_{1,B}^\beta\mathbb{W}_{1,B}^\beta}}{\mathcal{D}_\ell^{\mathbb{W}_{0,B}\mathbb{W}_{0,B}}}, \quad (33)$$

quantifies the difference between the auto-correlation of the order one spin-moments in EE and BB and cannot be strictly equal to zero if the EE/BB ratio is spectral dependent.

3.4.2. The EB power spectrum

A similar calculation can be done for the cross EB spectra, leading to

$$\begin{aligned} \mathcal{D}_\ell^{EB}(\nu) = & \left(\epsilon_\nu^P(\bar{\beta}, \bar{T}) \right)^2 \left[\mathcal{D}_\ell^{\mathbb{W}_{0,E}\mathbb{W}_{0,B}} \right. \\ & + \left(\mathcal{D}_\ell^{\mathbb{W}_{0,E}\mathbb{W}_{1,B}^\beta} + \mathcal{D}_\ell^{\mathbb{W}_{0,B}\mathbb{W}_{1,E}^\beta} \right) \ln \left(\frac{\nu}{\nu_0} \right) \\ & \left. + \mathcal{D}_\ell^{\mathbb{W}_{1,E}^\beta\mathbb{W}_{1,B}^\beta} \ln \left(\frac{\nu}{\nu_0} \right)^2 \dots \right]. \end{aligned} \quad (34)$$

The zeroth order term solely quantifies the structure of the magnetized interstellar medium, as it depends only on the maps of \mathcal{W}_0 and hence on the distribution of the matter density and magnetic field orientations. From parity considerations, this term is expected to be very small (Planck Collaboration 2020a; Clark et al. 2021). Even if the leading term in Eq (34) is null, a nonzero frequency dependent \mathcal{D}_ℓ^{EB} can be generated by the two other terms, which follow from variations of dust emission properties.

Isolating the EB moments is not a trivial task, as, for example, the EB/EE quantity could be dominated by the EE distortions. The favorable option would be to analytically correct for the scale dependent pivot as

$$\bar{\beta} \rightarrow \bar{\beta}_\ell^{EB} = \bar{\beta} + \left(\mathcal{D}_\ell^{\mathbb{W}_{0,E}\mathbb{W}_{1,B}^\beta} + \mathcal{D}_\ell^{\mathbb{W}_{0,B}\mathbb{W}_{1,E}^\beta} \right) / \mathcal{D}_\ell^{\mathbb{W}_{0,X}\mathbb{W}_{0,X}}, \quad (35)$$

assuming that the first term is the dominant order, which should always be true if the mean signal is in the perturbative regime. Here again, in the presence of polarized mixing, we observe that $\bar{\beta}^{EB} \neq \bar{\beta}^{EE} \neq \bar{\beta}^{BB}$ such that the three polarized spectra will have a different effective SED. This highlights that observing a spectral dependence of the EE/BB ratio guarantees the existence of EB distortions at some level.

However, in observational conditions, we cannot analytically compute the pivot defined in Eq. (35), as we do not have access

to the 3D distribution of spectral parameters and polarization angles. Therefore, in order to highlight the EB SED distortions, one can choose any $\bar{\beta}^{EB}$ and consider the ratio

$$(r_\nu^{E\times B})_\ell \equiv \frac{\mathcal{D}_\ell^{EB}}{\left(\epsilon_\nu^P(\bar{\beta}_\ell^{EB}, \bar{T}) \right)^2}. \quad (36)$$

The amplitude of the variations of $(r_\nu^{E\times B})_\ell$ will depend strongly on the choice of $\bar{\beta}_\ell^{EB}$. Thus, one could imagine fitting $\bar{\beta}_\ell^{EB}$ directly onto the EB data and minimizing the amplitude of the distortions. But as the EB Galactic signal is very low, this fit might dramatically increase the Galactic modeling uncertainty. One could also use a proxy for $\bar{\beta}_\ell^{EB}$ (for example, from the high signal-to-noise $\bar{\beta}_\ell^{EE}$), but this will result in enhancing the EB distortions if $|\bar{\beta}_\ell^{EB} - \bar{\beta}_\ell^{EE}| \gg 0$. Still, since EE , BB , and EB have a common physical origin, they should be treated together with a shared $\bar{\beta}$ in the spin-moment formalism.

4. The toy model filament

In order to refine the toy model of the infinite filament presented in Sec. 2.2, we consider again an infinite filament in front of a polarized background having both an MBB emission law with different spectral indices and polarization angles. The frequency dependence of the polarization angle ψ field in the filament would arise naturally from the polarized mixing described in Sec. 2.1 (see Fig. 1). We chose $\psi^{\text{bg}} = 0^\circ$ and considered various cases for ψ^{fl} (where the superscripts bg and fl stand for background and filament, respectively). From astrophysical considerations, one might expect filaments to be colder than the diffuse background, that is, $T^{\text{fl}} < T^{\text{bg}}$. Here again, for the sake of simplicity, we do not consider temperature variations, fixing $\beta^{\text{fl}} = 1.8$, $\beta^{\text{bg}} = 1.5$, and $\bar{T} = T^{\text{fl}} = T^{\text{bg}} = 20$ K. We also used $A^{\text{fl}} = A^{\text{bg}} = 1$, assuming that the background and the filament share the same optical depth and the same inclination with respect to the Galactic magnetic field. In order to keep the analysis easy to interpret, we also ignored the impact of the size and orientation of the filament. Changing these parameters is expected to change the relative amplitudes of the spectra (Huffenberger et al. 2020), but our conclusions should not be impacted regarding the moment expansion formalism and the impact of polarized mixing on the angular power spectra.

The toy model map is a 32×32 flat pixel grid on which the filament represents a 11×32 vertical rectangle (see Fig. 1). The filament is still assumed to be infinite, as the power spectra computation assumes periodic boundary conditions. We treated this example numerically using the NAMESTER library (Alonso et al. 2019) in order to evaluate the polarized power spectra $\mathcal{D}_\ell^{XX'}$ of the flat sky maps in a single multipole bin containing the 15 first values of ℓ . The frequency range was chosen to be an array from 100 to 400 GHz with intervals of 10 GHz and spanning a frequency interval relevant for CMB missions, under which the effect of the spectral index variations is expected to be dominant over possible temperature variations (LiteBIRD Collaboration 2022). The reference frequency was chosen to be $\nu_0 = 400$ GHz.

4.1. Single pixel analysis

In this section, we attempt to evaluate how the geometrical and spectral aspects of the signal are intertwined to produce the resulting angular power spectra. As a first step, we focus on the benefits of the spin-moment approach in a single filament pixel.

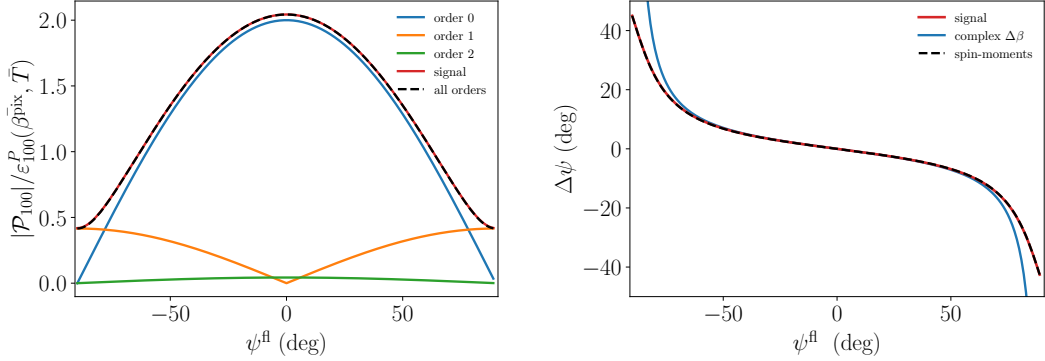


Fig. 2. Total polarization spinor in a single pixel of the filament of the toy model for $\psi^{\text{bg}} = 0^\circ$ and various values of the filament polarization angle ψ^{fl} . Left: Modulus of the total signal at 100 GHz normalized by the pivot MBB (red) and modulus of the analytical derivation from the spin-moment expansion up to second order (black dashed line). The modulus of each term is displayed: order 0: $|\mathcal{W}_0|$ (blue), order 1: $|\mathcal{W}_1^\beta \ln(100/400)|$ (orange), and order 2: $|0.5\mathcal{W}_2^\beta \ln(100/400)^2|$ (green). Right: Difference of the polarization angles between the two frequencies. Signal (red), prediction from the complex $\Delta\beta$ correction $0.5 \text{Im}(\mathcal{W}_1^\beta/\mathcal{W}_0) \ln(100/400)$ (blue) and from the spin-moment expansion up to second order (black dashed line).

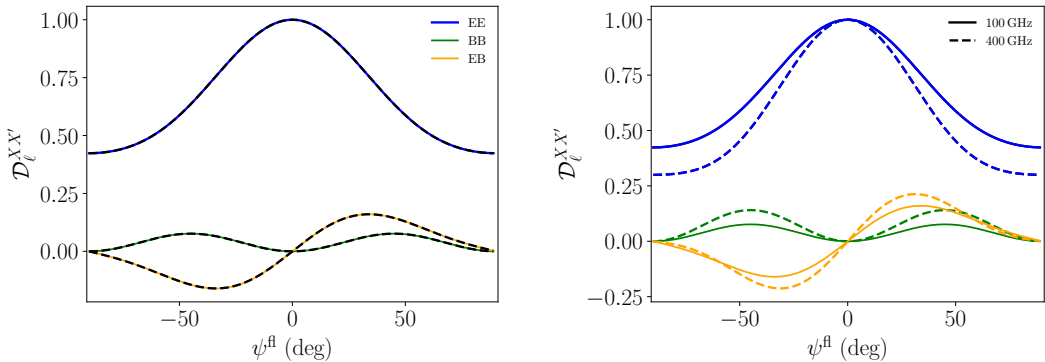


Fig. 3. Mean polarized power spectra for the toy model filament with $\psi^{\text{bg}} = 0^\circ$ and various values of the filament polarization angle ψ^{fl} . The EE (blue), BB (green), and EB (orange) angular power spectra are given at two different frequencies: 100 (continuous line) and 400 GHz (dashed line). Each spectra was normalized by the maximum value of $\left(\langle \mathcal{D}_\ell^{EE} \rangle^2(\nu) + \langle \mathcal{D}_\ell^{BB} \rangle^2(\nu)\right)^{1/2}$. Left: No SED distortions: $\beta^{\text{fl}} = \beta^{\text{bg}} = 1.5$. Right: with SED distortions: $\beta^{\text{fl}} = 1.8$ and $\beta^{\text{bg}} = 1.5$.

We first considered only the two frequencies $\nu_1 = 100$ GHz and $\nu_2 = 400$ GHz and tested how the results changed under a variation of ψ^{fl} in the range $[-90^\circ, 90^\circ]$. The modulus $|\mathcal{P}_\nu|$ and phase $\psi(\nu)$ of the total polarization spinor in the filament are displayed in Fig. 2. In the left panel, we display the departures from the pivot modified blackbody of the total signal modulus in the filament at 100 GHz, $|\mathcal{P}_{100}|/|\varepsilon_{100}^P(\bar{\beta}^{\text{pix}}, \bar{T})|$ with $\bar{\beta}^{\text{pix}} = (\beta^{\text{fl}} + \beta^{\text{bg}})/2 = 1.65$. These departures were well modeled by the spin-moment expansion up to order two, which one can derive analytically using Equations (7) and (8), for every value of ψ^{fl} . The modulus of the signal appears to become smaller when ψ^{fl} goes away from 0° . This is due to a corresponding vanishing of the amplitude of $\mathcal{W}_0 = A_{\text{fl}} e^{2i\psi^{\text{fl}}} + A_{\text{bg}} e^{2i\psi^{\text{bg}}}$, which is due to progressive depolarization. Indeed at $\psi^{\text{fl}} = 0^\circ$, the phases are aligned, and the complex amplitude reaches its maximal value:

$\mathcal{W}_0 = A_{\text{bg}} + A_{\text{fl}} = 2$. Moving away from $\psi^{\text{fl}} = 0^\circ$, the phases cancel each other down to $\mathcal{W}_0 = A_{\text{bg}} e^{2i\theta} + A_{\text{fl}} e^{-2i\theta} = 0$. We note that this is a pure geometrical "spin-2" effect independent of the values of the spectral parameters. In contrast, the first order moment increases when going away from $\psi^{\text{fl}} = 0^\circ$, producing an increase of the distortion amplitudes and a change of polarization angle with frequency $\Delta\psi = \psi(400) - \psi(100)$, as shown in the right panel of Fig. 2. The behavior of $\Delta\psi$ with ψ^{fl} is well modeled by the complex pivot correction (Eq. (5) and (11)), except in the nonperturbative regime when \mathcal{W}_1^β becomes large compared to \mathcal{W}_0 , as discussed in Vacher et al. (2023). In this regime, a pivot correction is impossible, and all the terms of the expansion must be kept. We note that the second moment \mathcal{W}_2^β is still required to obtain a good model for $|\mathcal{P}_\nu|$ around $\psi^{\text{fl}} = 0^\circ$ when it is greater than the first order ($\mathcal{W}_2^\beta > \mathcal{W}_1^\beta \simeq 0$). Indeed, as already

discussed in Sec. 2.1, it is impossible to always guarantee the hierarchy between the moments due to the complex nature of the expansion and its nonperturbative treatment of polarization angles. Overall, both the modulus and the phase of the complex signal in the pixel are fully predicted by the spin-moment expansion.

4.2. Power spectra analysis

As a second step, we studied the behavior of the power spectra, displayed in Fig. 3, for the same filament model. In order to compare the frequencies, which have orders of magnitudes of differences, we normalized all the spectra by the maximal value of $\left(\left(\mathcal{D}_\ell^{EE}\right)^2(v) + \left(\mathcal{D}_\ell^{BB}\right)^2(v)\right)^{1/2}$ at each frequency. In the case without distortions, when $\beta^{\text{fl}} = \beta^{\text{bg}} = 1.5$, all the polarized angular power spectra displayed an identical behavior between the two frequencies, as the E - and B -modes shared the same SED. Hence, no moments were expected in either \mathcal{P}_v or in \mathcal{S}_v . The overall behavior of the angular power spectra with respect to the filament's angle displayed in Fig. 3 is very similar to the magnetic misalignment phenomenon (see Fig. 2 of Clark et al. (2021)), considering the extra depolarization effect. At $\psi^{\text{fl}} = 0^\circ$, the sum of the MBBs in the filament is aligned with the MBB in the background. The E -modes are hence maximal, and there is no B -mode or EB correlation. For $\psi^{\text{fl}} = \pm 45^\circ$, B -modes are maximal but lower than the maximum of the E -modes due to the progressive depolarization and corresponding amplitude loss discussed above. At $\psi^{\text{fl}} = \pm 90^\circ$, the E -modes are expected to peak again, but they did not due to depolarization that makes the signal minimal, and B -modes returned to zero. The absolute value of EB is maximal when $\sqrt{EE^2 + BB^2}$ is maximal.

When considering our example with $\beta^{\text{fl}} \neq \beta^{\text{bg}}$, distortions appeared, as indicated by the rotation of ψ between 100 and 400 GHz in Fig. 2. No matter what the value of ψ^{fl} was, ψ drifted away from alignment between the two frequencies (according to Fig. 2, with a positive angle for $\psi^{\text{fl}} > 0$ and negative for $\psi^{\text{fl}} < 0$), leading to an increase of the E -modes and a corresponding decrease of the B -modes from 100 to 400 GHz such that one would expect $r_v^{E/B}$ to decrease with frequency. The distortion was greater as ψ^{fl} went away from 0° , which is in agreement with the values of \mathcal{W}^β in Fig. 2. Distortions were also witnessed for the EB spectra, illustrating how the mixing of polarized signals can increase the amplitude of this parity, thus violating spectra from one frequency to another. Changing the value of ψ^{bg} would not change the above conclusions but would change the relative amplitudes of the EE , BB , and EB angular power spectra. In order to remain concise, other cases with $\psi^{\text{bg}} = 45^\circ$ (B -modes maximum) and $\psi^{\text{bg}} = 22.5^\circ$ (equipartition of E - and B -modes) are displayed in Appendix A.

4.3. Predicting the spectral dependence of the power spectra.

The spectral behavior of the angular power spectra discussed above can be predicted by the spin-moment expansion. From Eq. (8), one can build maps of the spin-moments by knowing the ψ and β distributions in each pixel and using, as a common pivot, the mean spectral parameter over the whole map $\bar{\beta} = \langle A\beta \rangle / \langle A \rangle \sim 1.55$. It is then straightforward to compute the corresponding $\mathcal{D}_\ell^{\mathbb{W}_{k,X}\mathbb{W}_{k,X'}}$ for each pair of moments. To do this, we again used NAMASTER on the flat sky moment maps. We then obtained the frequency dependent power spectra by insert-

ing the $\mathcal{D}_\ell^{\mathbb{W}_{k,X}\mathbb{W}_{k,X'}}$ in Eqs. (29) and (34). Figure 4 shows a comparison between the spin-moment prediction up to order three and the signal over the whole frequency range for the special case $\psi^{\text{bg}} = 30^\circ$. These examples demonstrate that the expansion we derived is correct, and that it is possible to infer the polarized power spectra from the spin-moment maps, which themselves are derived from the spectral parameter and polarization angle distributions. In experimental conditions, however, one cannot directly access the distributions of spectral parameters and polarization angles, making this derivation impossible. We show, however, that the spin-moments and their expansion at the power-spectra level provide robust models for an accurate characterization of the polarized signal regardless of the distributions of β and ψ . A detailed study of how far one can go by inferring the dust properties from the power spectra and/or spin-moment maps is left for future work. First steps toward that direction can be found in recent works such as Sponseller & Kogut (2022) and McBride et al. (2022), which are aimed at quantifying the resulting biases obtained on the recovered CMB and dust parameters, depending on the underlying probability distributions of the spectral parameters integrated into the signal.

In order to assess the validity of the EE/BB ratio approximation in Eq. (32), we fit the EE/BB ratio with a weighting proportional to the signal itself using the LMFit software (Newville et al. 2016). In Fig. 4, good agreement between the fit and the data points can be observed. The best-fit values of $A_\ell^{E/B}$, $2\Delta\beta_\ell^{E/B}$ and δ_ℓ^{11} can be found in Tab. 1. We compared the values to the ones predicted using the moment maps and from computing the pivots β_ℓ^{EE} . The values are close but not equal because Eq. (32) stops at order one and the fit compensates for the higher-order moments. Still, the expression provides a simple and interpretable model to characterize the spectral dependence of the EE/BB ratio.

Finally, as discussed in Sec. 3.4.2, we used a pivot β_ℓ^{EB} in order to evaluate r_v^{EXB} . Both fitting and analytical derivations allowed us to find $\beta_\ell^{EB} \sim 1.69 \neq \beta$. The ratio r_v^{EXB} is displayed in Fig. 5, quantifying the amplitude of the residual distortions of higher orders. The variations are at the percent level. Once again, the prediction from moment expansion overlaps with the signal, validating our methodology.

5. PySM 3 models

In this section, we illustrate the previously discussed phenomenon on the PySM 3 models¹⁶ (Thorne et al. 2017; Zonca et al. 2021). Computations are made on the sphere using the HEALPY package (Górski et al. 2005). We considered the four following models:

- d0: This model was built with polarization Q and U map templates from the Planck 2015 data at 353 GHz (Planck Collaboration 2016a) and extrapolated at all frequencies using a single MBB with a fixed $\beta = 1.54$ and $T = 20$ K over the sky.
- d1: This model uses the same Q and U map templates as d0 and was extrapolated to other frequencies using an MBB with a varying β and T between pixels across the sky.
- d10: This model is a refined version of d1. The extrapolation was performed using an MBB with spectral parameters in each pixel coming from templates of the Generalized Needlet Internal Linear Combination (GNILC) needlet-based analysis of Planck data (Remazeilles et al. 2011) and includes a color correction and random fluctuations of β and T on small scales.

¹⁶ The version 3.4.0b4 of the PySM 3 was used in this work.

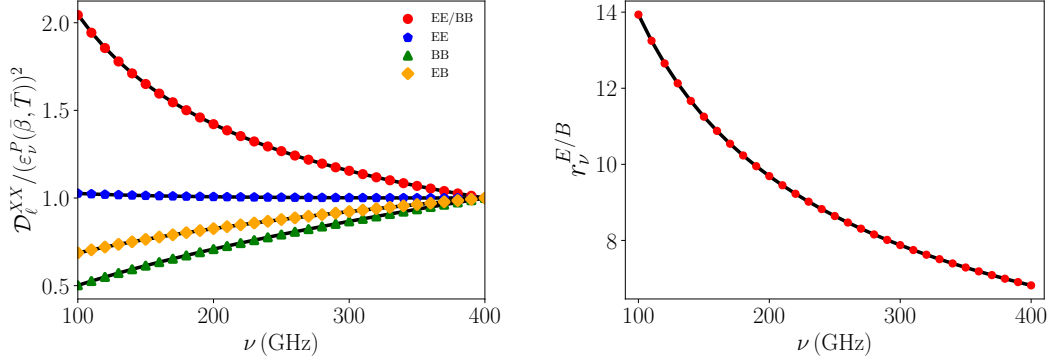


Fig. 4. Spectral dependence of the toy model filament polarized power spectra. Left: Polarized power spectra divided by the pivot-modified blackbody squared for the special case of $\psi^{\text{bg}} = 30^\circ$. All spectra are normalized with respect to their value at ν_0 . The signals are shown in color: EE/BB (red), EE (blue), BB (green), and EB (orange). The black dashed lines were recovered by deriving the moment power spectra from the spin-moment maps. Right: Close up view on $r_v^{E/B}$. The black curve represents the best-fit of Eq.(30).

Table 1. Best-fit and predicted values for the parameters entering in the perturbative expression of $(r_v^{E/B})_\ell$. (See Eq. (32) for the case of the toy model filament.)

	$A_\ell^{E/B}$	$2\Delta\bar{\beta}_\ell^{E/B}$	δ_ℓ^{11}
Prediction	6.818	-0.4977	0.00178
Best fit	6.818 ± 0.0001	-0.4986 ± 0.0001	0.01251 ± 0.00006

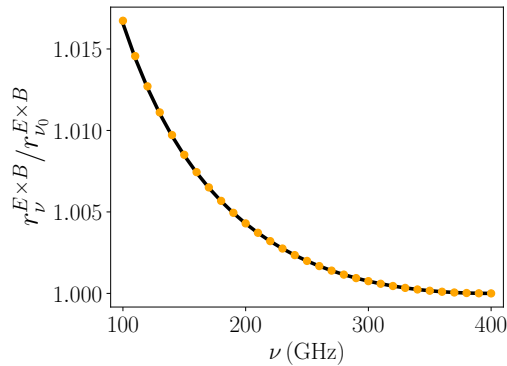


Fig. 5. Graph of $r_v^{E\times B}$ normalized at ν_0 for the toy model filament. The black curve represents the analytical prediction from the spin-moment maps.

- d12: This model was built out of six overlapping MBBs, as detailed in Martínez-Solaeche et al. (2018). This is the only model that has variations of the spectral parameters and polarization angles along the line of sight, which is the same as in the toy model filament presented in Sec. 4.

We again chose the frequency interval $\nu \in \{100, 400\}$ GHz, with steps of 50 GHz replacing the value at 350 GHz by the reference frequency of the models $\nu_0 = 353$ GHz. Power spectra were computed again using NAMASTER in a single multipole bin

from $\ell_0 = 2$ to $\ell_{\text{max}} = 200$ at a HEALPY resolution of $N_{\text{side}} = 128$. In order to observe a large patch of the sky while still avoiding the central Galactic region, we used the *Planck* GAL080 raw mask with $f_{\text{sky}} = 0.8$ available on the [Planck Legacy Archive](#). We subsequently performed a NAMASTER C2 apodization with a scale of 2° . Both the E - and B -modes were purified during the spectra computations.

In principle, by knowing the A , ψ , β , and T templates of the PySM maps, it is possible to analytically compute the spectra expansion as we did in Sec. 4.3. This would however require consideration of the temperature effects and the $\beta - T$ correlations, which are expected to have a significant impact on the modeling, as discussed in Vacher et al. (2022) and Sponseller & Kogut (2022).

5.1. The EE/BB ratio

In this section, we first focus on the EE/BB ratio. The ratio $r_v^{E/B}$ is displayed in the left panel of Fig. 6. As expected, no departure from constancy is observed for the EE/BB ratio in the case of d0. We note that this result would remain valid even if the canonical SED was not given by an MBB, as long as the associated spectral parameters remained constant over the sky.¹⁷ A frequency dependent EE/BB ratio is expected only in the presence of polarized mixing, that is, between or along the lines of sight. As previously stressed, this makes the EE/BB ratio a powerful probe of these variations independent of the SED effectively used to locally describe the signal.

¹⁷ An example would be given by the d8 model where SED is given by an adjusted version of the model proposed in Hensley & Draine (2017) with constant spectral parameters across the sky.

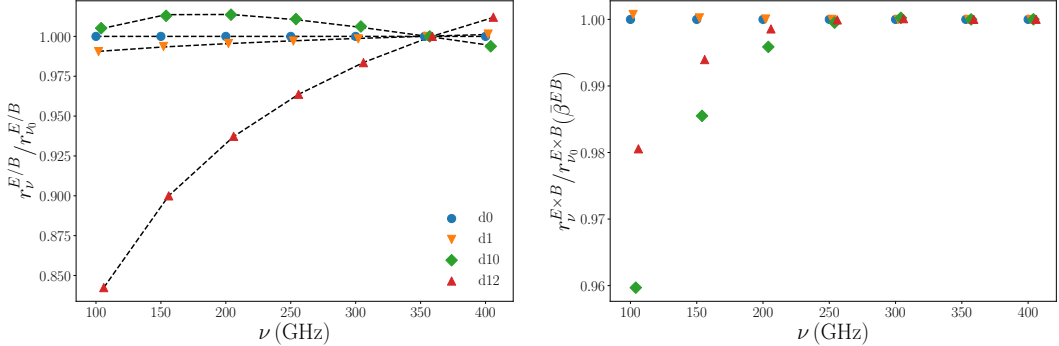


Fig. 6. Graph of $r_v^{E/B}$ and $r_v^{E\times B}$ for different PySM dust models. The shapes are defined as follows: d0 (blue circles), d1 (orange reversed triangles), d10 (green diamonds), and d12 (red triangles).

For d1 and d10, we found variations on the order of a few percentage points. Even if the SEDs in each pixel are nondistorted MBBs, variations between lines of sight are enough to produce a frequency dependence of the EE/BB power spectra. The d12 model, which contains both variations of the spectral properties along and between the lines of sight, displayed stronger variations of up to 15%.

A fit of Eq. (32) for each model is also displayed in Fig. 6. The resulting curve from the fit appeared to be in good agreement with the signal in all cases, ensuring that the perturbative expression proposed in Sec. 3.4 remains a good way to quantify the departures from constancy of EE/BB on realistic dust templates.

In all cases, the observed amplitudes of variations were expected to change widely depending on the sky fraction and the range of multipoles considered, as averages were made over different Galactic regions. As spectral parameters and magnetic field orientations are expected to have distinct scale dependences, averaging over different multipoles when binning spectra represents an additional source of distortions. The impact of such variations of the EE/BB ratio on cosmological analysis is left for future work, but we expect it to be substantial for CMB B -mode analyses, as mismodeling of the dust component by a few percentage points will have a significant impact when trying to reach a measurement, for example, of $r = 0.001$ (Planck Collaboration 2020a).

5.2. The EB spectra and cosmic birefringence

As discussed in Sec. 3.4.2, highlighting the EB distortions is not trivial. In order to do so, we first performed a fit of $\bar{\beta}^{EB}$ and \bar{T}^{EB} directly on the signal and considered $r_v^{E\times B}$. The results are displayed in the right panel of Fig. 6. The changes with frequency at the percent level for all but the d0 model are clear, indicating the presence of distortions at a level that could be neglected for these sky models in contemporary birefringence analysis.

As discussed in Sec. 3.4.2, however, because the dust EB signal is currently very small compared to the measurement errors in real observational conditions (and will probably remain modest in the future), it is impossible to access these quantities as directly as we did here, and one would instead be tempted to use the high signal-to-noise $\bar{\beta}^{EE}$ and \bar{T}^{EE} as proxies for the EB spectra. In the left panel of Fig. 7, we show $r_v^{E\times B}$ using the best

fits of the EE spectral parameters as a pivot. The figure shows the existence of spectral variations from a few percentage points for the d1 model to approximately 40% for the d10 model and up to a factor of two for the d12 model. As such, the choice of spectral parameters used to highlight the EB SED is extremely important and requires particular attention.

It is also relevant to consider the quantity

$$\tilde{\mathcal{D}}_\ell^{EB} \simeq A_\ell^{E\times B} \frac{\mathcal{D}_\ell^{EE} \mathcal{D}_\ell^{TB}}{\mathcal{D}_\ell^{TE}}, \quad (37)$$

which can provide a higher signal-to-noise estimator of the foreground EB signal (Clark et al. 2021; Diego-Palazuelos et al. 2022). As a scale dependent amplitude, $A_\ell^{E\times B}$ is frequency independent by construction. In order to quantify the deviations to this approximation, we considered the ratio

$$(\tilde{r}_v^{E\times B})_\ell = \frac{\mathcal{D}_\ell^{EB}}{\tilde{\mathcal{D}}_\ell^{EB}}. \quad (38)$$

Results are presented in Fig. 7. Large departures from Eq. 37 can be observed away from v_0 for all the models but the d0 model. According to the moment formalism presented above, the SEDs of EE , TB , and TE present distinct distortions in the presence of polarized mixing and are in turn different from that of EB , thus explaining why this approximation becomes invalid when at different frequencies. For an accurate modeling of the parity violating foreground signal and in order to probe the existence of cosmic birefringence, great care must therefore be taken with spectral distortions that may be induced by polarized mixing.

6. Conclusion

In the present work, we discuss how the combination of multiple polarized signals with different spectral parameters and polarization angles (referred to as polarized mixing) unavoidably leads to a different spectral behavior for the polarized angular spectra EE , BB , and EB , thus implying spectral dependence of the EE/BB ratio and nontrivial distortions of the EB correlation. We show how this phenomenon can be understood and tackled using the spin-moment expansion, formally deriving all the analytical expressions at order one in the case of Galactic dust modified black bodies with varying spectral indices while keeping in mind

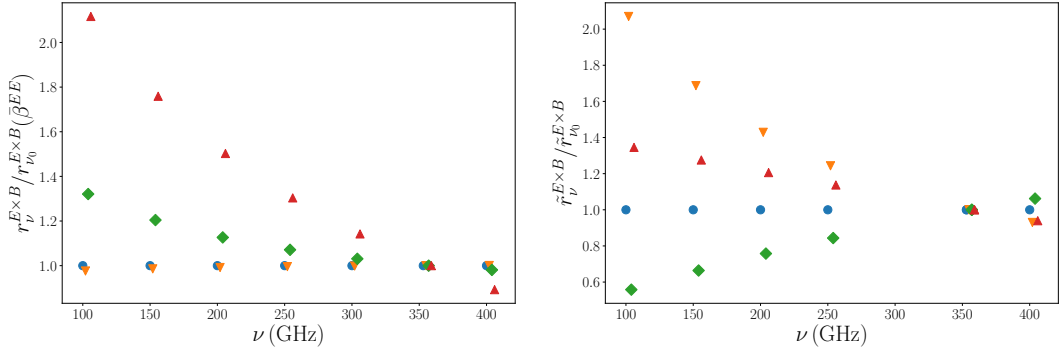


Fig. 7. Graph of r_v^{EB} and \tilde{r}_v^{EB} for different PySM dust models. The symbols are defined as follows: d0 (blue circles), d1 (orange reversed triangles), d10 (green diamonds), and d12 (red triangles).

that this would be straightforward when generalizing for any polarized SED (e.g., synchrotron) and at any order.

We thoroughly discuss the toy model example of a dust-emitting filament in front of a background. A careful understanding of the geometrical and spectral properties of the signal in the filament itself in pixel space allowed us to explain the shape of the total polarization angular power spectra when changing the value of the polarization angle of the filament, ψ^f , as well as the amplitude of the observed distortions between 100 and 400 GHz. Moreover, we show how one could accurately recover the spectral dependence of the polarization angular power spectra from the spin-moment maps, validating our previous theoretical considerations. Finally, we considered some of the PySM models on the sphere. We show that these models intrinsically contain variations of the EE/BB ratio through the frequency and distortions of the EB correlation, whose amplitudes are expected to strongly depend on the sky fraction and multipole range considered. This allowed us to stress that seeking a spectral dependence of EE/BB provides a way to explore the existence of polarized mixing and thus independently of the canonical SED used to model the signal. In these PySM models, simple assumptions about the frequency dependence of the dust EB signal used in CMB cosmic birefringence analysis become invalid due to the polarized mixing.

Further studies need to be done in order to precisely assess the expected amplitude of both these effects on real sky data. Meanwhile, it will be necessary to quantify the impact of the assumptions made on the dust EE/BB ratio and EB SEDs on cosmology. Map-based component separation is sensitive to the variation of the foreground's polarization angle with frequency, source of the power-spectrum effects discussed in the present work. However, current B -mode only analyses at the power spectrum level are, in principle, immune to the potential variation of the dust EE/BB , as they model the BB SED independently of the EE SED. Still, next-generation experiments probing the CMB reionization bump (as e.g., the *LiteBIRD* mission [LiteBIRD Collaboration \(2022\)](#)) might consider simultaneously EE and BB in order to tackle the correlations between the tensor-to-scalar ratio r and the re-ionization optical depth τ . These experiments would therefore be sensitive to the assumptions made about the dust EE/BB ratio frequency dependence. Regarding the dust EB correlation, as already stressed in [Diego-Palazuelos et al. \(2023\)](#), distortions of the MBB SED could impact cosmic birefringence

studies to some degree, but as long as this signal remains undetected, using higher signal-to-noise spectra as proxies to EB has to be done with even more caution. In any case, the 3D variation of the dust composition, physical conditions, and the orientation of the Galactic magnetic field produce complex polarization effects in map space and at the angular power-spectrum level, and their impact have to either be ruled out or taken into account for precise B -mode and birefringence measurements.

Acknowledgements. L.V. would like to thanks Aditya Rotti and Louise Mousset for precious feedback and discussions. A.R. acknowledges financial support from the Italian Ministry of University and Research - Project Proposal CIR01_00010. JC was supported by an ERC Consolidator Grant *CMBSPEC* (No. 725456) and the Royal Society as a Royal Society University Research Fellow at the University of Manchester, UK (No. URF/R/191023).

References

- Alonso, D., Sanchez, J., Slosar, A., & LSST Dark Energy Science Collaboration. 2019, MNRAS, 484, 4127
- Azzoni, S., Abitbol, M. H., Alonso, D., et al. 2021, J. Cosmology Astropart. Phys., 2021, 047
- Bracco, A., Candelaresi, S., Del Sordo, F., & Brandenburg, A. 2019, A&A, 621, A97
- Caldwell, R. R., Hirata, C., & Kamionkowski, M. 2017, ApJ, 839, 91
- Chluba, J., Hill, J. C., & Abitbol, M. H. 2017, MNRAS, 472, 1195
- Clark, S. E. & Hensley, B. S. 2019, ApJ, 887, 136
- Clark, S. E., Hill, J. C., Peek, J. E. G., Putman, M. E., & Babler, B. L. 2015, Phys. Rev. Lett., 115, 241302
- Clark, S. E., Kim, C.-G., Hill, J. C., & Hensley, B. S. 2021, ApJ, 919, 53
- CMB-S4 Collaboration. 2019, arXiv e-prints, arXiv:1907.04473
- Cukierman, A. J., Clark, S. E., & Halal, G. 2022, arXiv e-prints, arXiv:2208.07382
- Diego-Palazuelos, P., Eskilt, J. R., Minami, Y., et al. 2022, Phys. Rev. Lett., 128, 091302
- Diego-Palazuelos, P., Martínez-González, E., Vielva, P., et al. 2023, J. Cosmology Astropart. Phys., 2023, 044
- Eskilt, J. R. & Komatsu, E. 2022, Phys. Rev. D, 106, 063503
- Ghosh, T., Boulanger, F., Martin, P. G., et al. 2017, A&A, 601, A71
- Goldberg, J. N., Macfarlane, A. J., Newman, E. T., Rohrlich, F., & Sudarshan, E. C. G. 1967, Journal of Mathematical Physics, 8, 2155
- Górski, K. M., Hivon, E., Banday, A. J., et al. 2005, ApJ, 622, 759
- Guillet, V., Fanciullo, L., Verstraete, L., et al. 2018, A&A, 610, A16
- Hensley, B. S. & Draine, B. T. 2017, ApJ, 836, 179
- Hensley, B. S. & Draine, B. T. 2022, arXiv e-prints, arXiv:2208.12365
- Hervías-Caimapo, C. & Huffenberger, K. M. 2022, ApJ, 928, 65
- Huffenberger, K. M., Rotti, A., & Collins, D. C. 2020, ApJ, 899, 31
- Kamionkowski, M. & Kovetz, E. D. 2016, ARA&A, 54, 227
- Kandé, D., Lazarian, A., & Pogosyan, D. 2018, MNRAS, 478, 530
- Konstantinou, A., Pelgrims, V., Fuchs, F., & Tassis, K. 2022, A&A, 663, A175

- Krachmalnicoff, N., Baccigalupi, C., Aumont, J., Bersanelli, M., & Mennella, A. 2016, A&A, 588, A65
- LiteBIRD Collaboration. 2022, in PTEP, Vol. 11443, PTEP, 114432F
- Mangilli, A., Aumont, J., Rotti, A., et al. 2021, A&A, 647, A52
- Martinez-Solaeche, G., Karakci, A., & Delabrouille, J. 2018, MNRAS, 476, 1310
- McBride, L., Bull, P., & Hensley, B. S. 2022, arXiv e-prints, arXiv:2207.14213
- Minami, Y., Ochi, H., Ichiki, K., et al. 2019, Progress of Theoretical and Experimental Physics, 2019, 083E02
- Newville, M., Stensitzki, T., Allen, D. B., et al. 2016, Lmfit: Non-Linear Least-Square Minimization and Curve-Fitting for Python
- Pelgrims, V., Clark, S. E., Hensley, B. S., et al. 2021, A&A, 647, A16
- Planck Collaboration. 2015a, A&A, 576, A105
- Planck Collaboration. 2015b, A&A, 576, A107
- Planck Collaboration. 2016a, A&A, 594, A1
- Planck Collaboration. 2016b, A&A, 596, A110
- Planck Collaboration. 2016c, A&A, 586, A133
- Planck Collaboration. 2016d, A&A, 586, A136
- Planck Collaboration. 2016e, A&A, 586, A141
- Planck Collaboration. 2017, A&A, 599, A51
- Planck Collaboration. 2020a, A&A, 641, A11
- Planck Collaboration. 2020b, A&A, 641, A12
- Remazeilles, M., Delabrouille, J., & Cardoso, J.-F. 2011, MNRAS, 418, 467
- Remazeilles, M., Dickinson, C., Eriksen, H. K. K., & Wehus, I. K. 2016, MNRAS, 458, 2032
- Remazeilles, M., Rotti, A., & Chluba, J. 2021, MNRAS, 503, 2478
- Ritacco, A., Boulanger, F., Guillet, V., et al. 2022, arXiv e-prints, arXiv:2206.07671
- Rotti, A. & Chluba, J. 2021, MNRAS, 500, 976
- Rotti, A. & Huffenberger, K. 2019, J. Cosmology Astropart. Phys., 045
- Sponseller, D. & Kogut, A. 2022, ApJ, 936, 8
- Tassis, K. & Pavlidou, V. 2015, MNRAS, 451, L90
- Thorne, B., Dunkley, J., Alonso, D., & Næss, S. 2017, MNRAS, 469, 2821
- Vacher, L., Aumont, J., Montier, L., et al. 2022, A&A, 660, A111
- Vacher, L., Chluba, J., Aumont, J., Rotti, A., & Montier, L. 2023, A&A, 669, A5
- Weiland, J. L., Addison, G. E., Bennett, C. L., Halpern, M., & Hinshaw, G. 2020, ApJ, 893, 119
- Zaldarriaga, M. 2001, Phys. Rev. D, 64, 103001
- Zaldarriaga, M. & Seljak, U. 1997, Phys. Rev. D, 55, 1830
- Zonca, A., Thorne, B., Krachmalnicoff, N., & Borrill, J. 2021, Journal of Open Source Software, 6, 3783

Appendix A: Impact of the background polarization angle

We present the dependence in ψ^{fl} of the polarization power spectra of the toy model filament. We consider two different values for the background angle, $\psi^{\text{bg}} = 22.5^\circ$ and $\psi^{\text{bg}} = 45^\circ$.

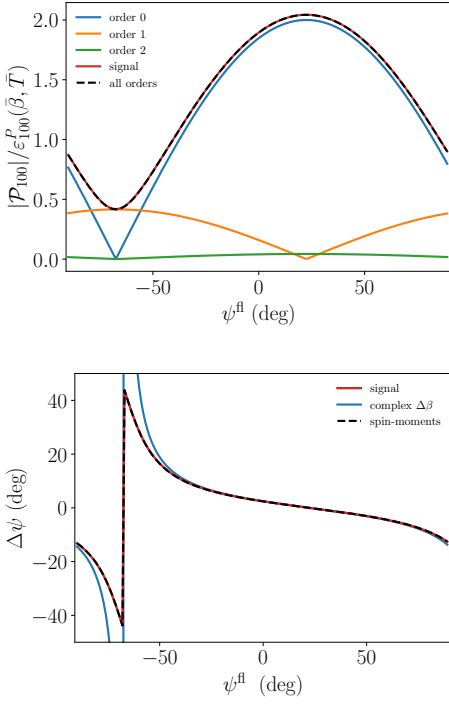


Fig. A.1. Total polarization spinor in the filament of the toy model for $\psi^{\text{bg}} = 22.5^\circ$ and various values of the filament polarization angle ψ^{fl} . Left: Modulus of the total signal at 100 GHz normalized by the pivot MBB (red) and modulus of the analytical derivation from the spin-moment expansion up to second order (black dashed line). The modulus of each term is displayed: order 0: $|W_0|$ (blue), order 1: $|W_1^\beta \ln(100/400)|$ (orange), and order 2: $|0.5 W_2^\beta \ln(100/400)^2|$ (green). Right: Difference of the polarization angles between the two frequencies (red), prediction from the complex $\Delta\beta$ correction $0.5 \text{Im}(W_1^\beta/W_0) \ln(100/400)$ (blue) and from the spin-moment expansion up to second order (black dashed line).

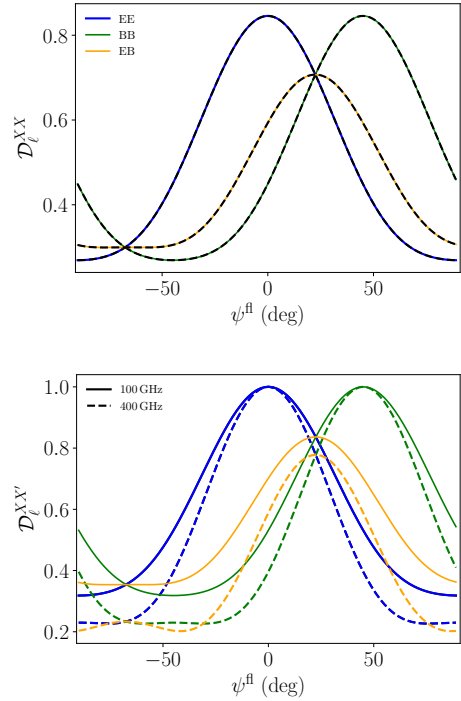


Fig. A.2. Mean polarized power spectra for the toy model filament with $\psi^{\text{bg}} = 22.5^\circ$ and various values of the filament polarization angle ψ^{fl} . The EE (blue), BB (green), and EB (orange) angular power spectra are given at two different frequencies: 100 (continuous) and 400 GHz (dashed). Each spectra is normalized by the maximum value of $\left(\left(\mathcal{D}_\ell^{EE}\right)^2(\nu) + \left(\mathcal{D}_\ell^{BB}\right)^2(\nu)\right)^{1/2}$. Left: No SED distortions: $\beta^{\text{fl}} = \beta^{\text{bg}} = 1.5$. Right: with SED distortions: $\beta^{\text{fl}} = 1.8$ and $\beta^{\text{bg}} = 1.5$.

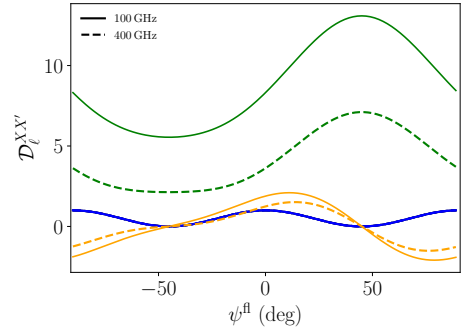
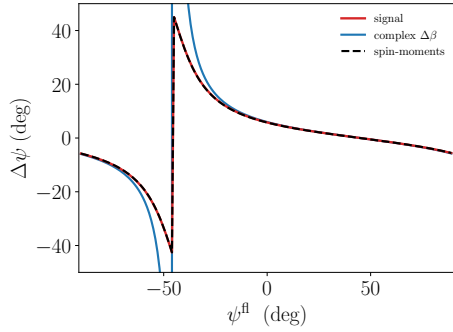
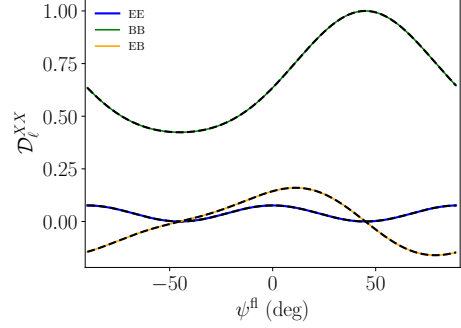
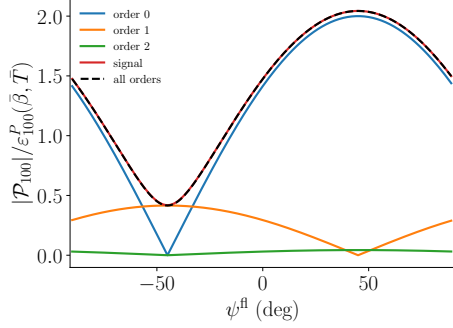


Fig. A.3. Same as Fig. A.1 but for $\psi^{bg} = 45^\circ$.

Fig. A.4. Same as Fig. A.2 but for $\psi^{bg} = 45^\circ$.

D.4 PhysRevD.106.083522

Constraints on extended Bekenstein models from cosmological, astrophysical, and local data

Léo Vacher,^{1,2,*} J. D. F. Dias,^{3,4} Nils Schöneberg,^{5,†} C. J. A. P. Martins,^{3,6,‡} Samy Vinzl,² Savvas Nesseris,⁷ Guadalupe Cañas-Herrera,^{8,9,10} and Matteo Martinelli¹¹

¹*Institut de Recherche en Astrophysique et Planétologie, CNRS, CNES, Toulouse, France*

²*Université de Toulouse UPS, Toulouse, France*

³*Centro de Astrofísica da Universidade do Porto, Rua das Estrelas, 4150-762 Porto, Portugal*

⁴*Faculdade de Ciências, Universidade do Porto, Rua Campo Alegre, 4169-007, Porto, Portugal*

⁵*Dept. Física Quântica i Astrofísica, Institut de Ciències del Cosmos (ICCUB), Facultat de Física, Universitat de Barcelona (IEEC-UB), Martí i Franqués, 1, E08028 Barcelona, Spain*

⁶*Instituto de Astrofísica e Ciências do Espaço, CAUP, Universidade do Porto, Rua das Estrelas, 4150-762, Porto, Portugal*

⁷*Instituto de Física Teórica UAM-CSIC, Universidad Autónoma de Madrid, Cantoblanco, 28049 Madrid, Spain*

⁸*Leiden Observatory, Leiden University, PO Box 9506, Leiden 2300 RA, The Netherlands*

⁹*Lorentz Institute for Theoretical Physics, Leiden University, PO Box 9506, Leiden 2300 RA, The Netherlands*

¹⁰*European Space Agency (ESA), European Space Research and Technology Centre (ESTEC), Keplerlaan 1, 2201 AZ Noordwijk, The Netherlands*

¹¹*INAF - Osservatorio Astronomico di Roma, via Frascati 33, 00040 Monteporzio Catone (Roma), Italy*

(Dated: October 24, 2023)

Searching for variations of nature's fundamental constants is a crucial step in our quest to go beyond our current standard model of fundamental physics. If they exist, such variations will be very likely driven by the existence of a new fundamental field. The Bekenstein model and its extensions introduce such a scalar field in a purely phenomenological way, inducing a variation of the fine-structure constant on cosmological scales. This theoretical framework is as simple and general as possible while still preserving all the symmetries of standard quantum electrodynamics. When allowing for couplings to the other sectors of the Universe, such as baryons, dark matter, and the cosmological constant, the Bekenstein model is expected to reproduce the low energy limits of several grand unification, quantum gravity, and higher dimensional theories. In this work, we constrain different versions of the Bekenstein model by confronting the full cosmological evolution of the field with an extensive set of astrophysical, cosmological, and local measurements. We show that couplings of the order of parts per million (ppm) are excluded for all the cases considered, imposing strong restrictions on theoretical frameworks aiming to deal with variations of the fine-structure constant.

I. INTRODUCTION

The fundamental constants of a given theory are quantities that can be measured but not derived within it. As such, they set the intrinsic boundaries of what a given model can explain. The contemporary standard model of particle physics contains at least 19 such parameters (a complete list can be found in [1]). The detection of a space-time variation of one of them would be a groundbreaking discovery as it would indicate that an underlying dynamical mechanism must exist to explain their values, proving that new physics is yet to be discovered. Moreover, such a variation would be in direct violation with the universality of free fall¹ (in other words, the

weak equivalence principle) and the local position invariance.

According to Schiff's conjecture, this would mean a violation of the broader Einstein equivalence principle, one of the cornerstones of the general theory of relativity and, more broadly, of all metric theories of gravity (see e.g. [2–4]).

If so, gravity could no longer be described as a geometrical phenomenon of space-time alone and/or the existence of a fifth force would be required (see e.g. [5]). As such, testing the stability of fundamental constants on local and cosmological scales provides a powerful test of fundamental physics beyond the reach of particle accelerators (see e.g. [1, 6, 7]).

Since fundamental constants appear as theoretical foundations of a theory, the variations of the free parameters of our standard model are expected in most of the theoretical frameworks aiming to extend it, such as quantum gravity, grand unification and/or theories involving extra dimensions. One such example is the dilaton field in string theories [8].

The fine-structure constant $\alpha_{\text{EM}} \equiv \alpha = e^2/(4\pi\epsilon_0\hbar c)$ is the dimensionless gauge coupling quantifying the

* leo.vacher@irap.omp.eu

† nils.science@gmail.com

‡ Carlos.Martins@astro.up.pt

¹ A variation of any of the fundamental constants would make binding energies, and thus masses of elements, space-time dependent quantities. As discussed in [1] this implies a non-geodesic motion (regarding the Levi-Civita connexion) depending on the composition of the element.

strength of the electromagnetic interaction between charged particles. As such it can be measured very accurately using various local and astrophysical phenomena involving light.

Using a great variety of independent datasets, one can then accurately map the value of α across space and time (see e.g. [9]).

While the values of fundamental constants with dimensions (e.g. c , \hbar or G) are dependent of the choice of a unit system, dimensionless ratios (as gauge couplings, mass ratios, and symmetry breaking angles) will always have the same values in any units. One can indeed safely choose the natural units $\hbar = c = G = 1$ while instead setting $\alpha = 1$ would deeply change all the physics of the Universe. Therefore, looking for variations of dimensionless constants is the only fully consistent approach, since their values are universal. Moreover, the dimensionless constants deeply quantify the behavior of physical phenomena.

However, from a theoretical point of view, the fine-structure constant cannot vary arbitrarily through cosmic history. Indeed, one would like to preserve fundamental symmetries of physics and their associated conservation laws such as local stress-energy conservation or gauge invariance. A safe way to do so is to implement the variation of α from an action principle. As originally proposed in [10, 11], one can promote the electric charge of the electron itself to a scalar field. This model, called the Bekenstein model, has been further generalized accounting for interactions with matter into the Bekenstein-Sandvik-Barrow-Magueijo (BSBM) model [12–15] and finally by allowing for different couplings of the field with baryons, dark matter and dark energy by Olive and Pospelov (O&P) in [16, 17]. In the later form, the model provides a very general framework to constrain variations of α induced by a scalar field that could be motivated by a high energy physics theory.

In the present work, we provide updated constraints on the BSBM and O&P models, treating for the first time their full cosmological evolution by doing a full Bayesian Statistical analysis that combines a modified version of the CLASS Boltzmann-solver [18] and Monte-Carlo Markov Chains (MCMC) using MONTEPYTHON [19, 20].

We start by introducing the notation and theory underlying the BSBM and O&P models in Sec. II, we then introduce the data in Sec. III, which is later used in Sec. IV to constrain these models. Finally, we conclude by summarizing our most important results in Sec. V.

II. THEORETICAL BACKGROUND

A. Bekenstein's model and the Bekenstein-Sandvik-Barrow-Magueijo extension

The original Bekenstein model introduced in [10] and discussed more extensively in [11] seeks a purely phenomenological minimalist implementation of a varying

fine-structure constant α , that remains theoretically self-consistent with standard quantum electrodynamics (for a discussion on self-consistency of varying α models see e.g. [1] and [11]).

To do so, one assumes that a variation of the electron charge² e is induced by a free scalar field ϵ as $e(x^\mu) \propto \epsilon(x^\mu)$. The fine-structure constant will then change according to $\alpha \propto \epsilon^2$. At the action level, ϵ must have a kinetic term. Its presence will also change the couplings (charges) appearing in the electromagnetic covariant derivatives, leading to a necessary redefinition of the connection coefficients $A \rightarrow \epsilon A$ and its associated 2-form curvature/field strength $F(A) \rightarrow F(\epsilon A)$. In order to preserve the gauge invariance of the theory under the unitary group $U(1)$, an extra factor of $\epsilon^{-2} \propto \alpha^{-1}$ is required in the kinetic Lagrangian density of the photon field. Such a term is formally equivalent to a space- and time-dependent change in the vacuum's permeability.

With the additional change of variable $\phi \equiv \ln(\epsilon)$, the variation of the fine-structure constant with redshift is then given by

$$\frac{\Delta\alpha}{\alpha_0}(z) = \frac{\alpha - \alpha_0}{\alpha_0} = \left(\frac{\epsilon}{\epsilon_0} \right)^2 - 1 = e^{2(\phi - \phi_0)} - 1, \quad (1)$$

with the index 0 labelling values of objects at $z = 0$ and $\alpha_0 \sim 1/137$ being the value of the fine-structure constant as measured locally in the laboratory [21]. From Eq. 1, one can derive the expected rate of variation of the fine-structure constant today as

$$\frac{1}{H_0} \left(\frac{\dot{\alpha}}{\alpha_0} \right)_{z=0} = 2\phi'_0. \quad (2)$$

Hereafter primes denote derivatives with respect to $\ln(a)$ and dotted quantities refer to derivatives with respect to the cosmic time t . In this basis of the field ϕ , the full $U(1)$ invariant action for the cosmological model is given by

$$\mathcal{S} = \int d^4x \sqrt{-g} \left[\frac{M_*^2}{2} \partial_\mu \phi \partial^\mu \phi - \frac{1}{4} F_{\mu\nu} F^{\mu\nu} e^{-2\phi} - \frac{1}{2} M_{\text{Pl}}^2 R + \mathcal{L}_m + \dots \right], \quad (3)$$

where R is the Ricci scalar, $M_{\text{Pl}} = (8\pi G)^{-1/2}$ the reduced Planck mass and we set $c = \hbar = 1$. M_* is a mass scale associated to the ϕ sector, and $F^{\mu\nu}$ is the electromagnetic field tensor associated to the connection ϵA_μ . In the present work, we will assume that $M_* = M_{\text{Pl}}$, meaning that the energy scale of the varying constant theory is close to the one of quantum gravity as one would expect from a great unification theory. Varying fundamental constants would also imply direct violations of

² We are already here implicitly in natural units, and considering the QED unitless gauge coupling $e/\sqrt{\hbar c \epsilon_0}$ (here in S.I. units).

the Einstein equivalence principle and/or the existence of a fifth force mediated by ϕ (see e.g. [1, 3, 4]). As in [12, 14, 15] we introduce an additional free parameter quantifying this effect, $\zeta \equiv \mathcal{L}_{EM}/\rho$, where ρ is the energy density, assessing the change of electromagnetic binding energies of matter (and thus masses) in the presence of ϕ . This ζ can be connected to the Eötvos parameter η , quantifying the violation of universality of free fall as

$$\eta \sim 3 \cdot 10^{-9} \zeta . \quad (4)$$

As discussed in [12], the value and sign of ζ strongly depend on the nature of dark matter and its ability to interact with ϕ . Extremizing the action given by Eq. (3) with respect to ϕ and including this extra coupling to matter, one obtains the equation of motion for the field

$$\ddot{\phi} + 3H\dot{\phi} = -\frac{2}{M_*^2}e^{-2\phi}\zeta\rho_m . \quad (5)$$

When extremizing the action with respect to the metric $g_{\mu\nu}$, one can derive a modified version of the Friedmann equation as

$$H^2 = \frac{8\pi G}{3} [\rho_m(1 + \zeta e^{-2\phi}) + \rho_r e^{-2\phi} + \rho_\phi + \rho_\Lambda] , \quad (6)$$

where the field density and pressure can be deduced from the action Eq. (3) as

$$\rho_\phi = \frac{M_*^2 \dot{\phi}^2}{2} , \quad P_\phi = \frac{M_*^2 \dot{\phi}^2}{2} . \quad (7)$$

From previous constraints on its coupling (e.g. [15]), we expect the contribution of the energy density of the ϕ -field to be subdominant. As such, also its linear theory perturbations do not contribute meaningfully to the gravitational potential and can be neglected. Hence, we only show the unperturbed Friedmann equation. The same reasoning is applied to all the models considered in the present work.

B. The Olive & Pospelov extension

The Bekenstein model can be generalized in a straightforward way, by letting ϕ be a scalar field inducing any possible variations of the fine-structure constant through a general function $\alpha \propto B_F(\phi)^{-1}$. Here again, in order to preserve gauge invariance, the field has to couple to the electromagnetic Lagrangian as

$$\mathcal{L}_{EM} = -\frac{1}{4}B_F(\phi)F_{\mu\nu}F^{\mu\nu} . \quad (8)$$

A simple extension to this model is to assume that ϕ can have analogous couplings with all the fermion fields of the standard model ψ , the dark energy assumed to be a cosmological constant Λ , and a dark matter particle³ χ .

We will refer to this version of the model, proposed in [16], as O&P. The cosmological action becomes

$$S = \int d^4x \sqrt{-g} \left[-\frac{1}{2}M_{Pl}^2 R + \frac{1}{2}M_*^2 \partial_\mu \phi \partial^\mu \phi - M_{Pl}^2 \Lambda_0 B_\Lambda(\phi) \right. \\ \left. - \frac{1}{4}B_F(\phi) F_{\mu\nu} F^{\mu\nu} + \bar{\psi}(i\gamma^\mu D_\mu - m_\psi B_\psi(\phi))\psi \right. \\ \left. + \bar{\chi}(i\gamma^\mu D_\mu - M_\chi B_\chi(\phi))\chi - V(\phi) \right] . \quad (9)$$

We will consider for this work that $V(\phi) = 0$ and leave the discussion of cases with nonzero potentials for future work. As justified above, the field will be considered as homogeneous and we will not solve its perturbations equations. The $B_i(\phi)$, $i \in [\psi, F, \chi, \Lambda]$ are the coupling functions of the field with the different sectors. Their deviation from 1 encodes the strength of the scalar field coupling. Assuming that the field value remains small on cosmological time scales, one can expand the couplings up to first order as

$$B_i(\phi) = 1 + \zeta_i(\phi - \phi_0) , \quad (10)$$

around today's value $\Delta\phi = \phi - \phi_0 \ll 1$. This expansion is expected to be a very good approximation as the B_i are already constrained to be very close to unity by observations [16, 17]. Given the already relatively wide allowed parameter space of the model, including the second order or higher order terms in this expansion is not necessary as their contribution to the field evolution is subdominant. Using this expansion for $B_F(\phi)$, one immediately obtains the first order evolution of the fine-structure constant with the field

$$\frac{\Delta\alpha}{\alpha_0} = \frac{\alpha(\phi)}{\alpha_0} - 1 = B_F^{-1}(\phi) - 1 = -\zeta_F \Delta\phi , \quad (11)$$

where we again Taylor expanded in $\Delta\phi$ and stopped at first order. From this expression, one can derive today's time derivative of α as

$$\frac{1}{H_0} \left(\frac{\dot{\alpha}}{\alpha_0} \right)_{z=0} = -\zeta_F \phi'_0 . \quad (12)$$

As in [16, 17], we will also further assume that the background cosmology evolution in the O&P model remains given by the canonical Friedmann-Lemaître equation

$$\left(\frac{H}{H_0} \right)^2 = \frac{8\pi G}{3} \sum_i \rho_i , \quad (13)$$

where the sum extends to the field's density that remains given by Eq. (7). This assumption is reasonable since, as we will show, those corrections are expected to be extremely small. Minimizing the action with respect to ϕ gives the coupled Klein-Gordon equation of motion

$$\ddot{\phi} + 3H\dot{\phi} = -\frac{1}{M_*^2} \sum_i \rho_i \zeta_i , \quad (14)$$

³ The model was originally conceived with the light supersymmetric neutralino forming the WIMP.

where $\zeta_i = (\zeta_\chi, \zeta_\Lambda, \zeta_b)$. Note that ζ_F does not appear in equation of motion due to a null averaging of the photon fields $\langle F^2 \rangle$.

For a system of two masses of Aluminium and Platinum, the Eötvos parameter η , quantifying deviations from the weak equivalence principle can be expressed as [16]

$$\eta \simeq \zeta_p (\zeta_n - \zeta_p + 2.9 \cdot 10^{-2} \zeta_F), \quad (15)$$

where ζ_p and ζ_n are respectively the coupling constants of the field to protons and neutrons. To simplify the parameter space, in the following we will assume that there exists a single coupling to baryons ζ_b such that $\zeta_p \simeq \zeta_n \simeq \zeta_b$, allowing us to write the simple expression for the Eötvos parameter η in term of the couplings constants as

$$\eta \simeq 2.9 \cdot 10^{-2} \zeta_b \zeta_F. \quad (16)$$

Due to the degeneracies of the parameter space appearing in the observables, one can only constrain their product. As such, we introduce the new product parameters η_i defined as

$$\eta_\chi = \zeta_F \zeta_\chi, \quad (17)$$

$$\eta_b = \zeta_F \zeta_b, \quad (18)$$

$$\eta_\Lambda = \zeta_F \zeta_\Lambda. \quad (19)$$

Since we are constraining these new product parameters instead of the ζ , we will only be able to recover properly the product quantities $\zeta_F \phi_0$ and $\zeta_F \phi'_0$ instead of the raw field parameters themselves.

III. DATASETS AND LIKELIHOODS

We exploit the synergy of multiple datasets and their corresponding likelihoods in order to constrain the models. All these measurements are independent and probe fundamental physics at a great variety of space-time scales. The Cosmology data sets are already implemented in the MONTEPYTHON code, while the fine-structure constant and Einstein equivalence principle likelihoods are implemented as gaussian priors.

A. Cosmological datasets

In order to constrain the background cosmology, we use the likelihood based on the Pantheon Type Ia Supernovae sample [22]. We also include large scale structures and baryon acoustic oscillation data from the BOSS DR-12 galaxy survey [23] as well as cosmic clocks measurements from [24]. All of these give sharp constraints on the possible evolution of the Hubble parameter $H(z)$.

We also include the cosmic microwave background (CMB) intensity, polarization and lensing power spectra likelihoods from the latest *Planck* 2018 data release

[25, 26]⁴. This likelihood is giving a unique lever arm at $z \sim 1100$, further constraining the cosmology and the scalar field evolution at very high redshift.

B. Fine-structure constant and Einstein equivalence principle

Using high-resolution spectroscopy, one can obtain very accurate measurements of α from astrophysical sources. Doing so is possible from the position of absorption lines of the gas along the line of sight of quasi-stellar objects (QSO or quasars) at high redshifts. The positions of the lines are expected to change with α in a transition-specific fashion (quantified by a so-called sensitivity coefficient) that can be disentangled from the linear effect of redshift. We use a collection of measurements of the fine-structure constant from [27] and [28] as well as a recent precise and accurate measurement from the ESPRESSO spectrograph [29].

The value of α at $z = 0.14$ can also be inferred from abundances in the Oklo natural reactor on Earth [30].

$$\frac{\Delta \alpha}{\alpha_0}(z = 0.14) = (0.005 \pm 0.061) \text{ ppm}. \quad (20)$$

Laboratory atomic clock experiments can use optics to constrain the current rate of change of α [31], which can be expressed in a dimensionless form as

$$\frac{1}{H_0} \left(\frac{\dot{\alpha}}{\alpha_0} \right)_{z=0} = (0.014 \pm 0.015) \text{ ppm}. \quad (21)$$

Finally, sharp constraints can be added to the models considering limits on the violation of the weak equivalence principle by the MICROSCOPE satellite testing the universality of free fall with two test bodies orbiting earth [32]

$$\eta = (-1.5 \pm 2.7) \cdot 10^{-9} \text{ ppm}. \quad (22)$$

IV. RESULTS

We constrain the models by sampling over their parameters using MCMC chains with MONTEPYTHON [19, 20] combined with a modified CLASS version [18]. A discussion of the impact of a varying α on cosmology can be found in [33, 34]. The contour plots are made using the GETDIST python package [35]. Computations are made on the cluster of the Marseille dark energy center (mardec).

The cosmological parameters we are sampling over are the reduced baryon and cold dark matter densities $\omega_b = \Omega_b h^2$ and $\omega_{cdm} = \Omega_{cdm} h^2$, the reionization redshift z_{reio} ,

⁴ Likelihoods can be found on the *Planck* legacy archive.

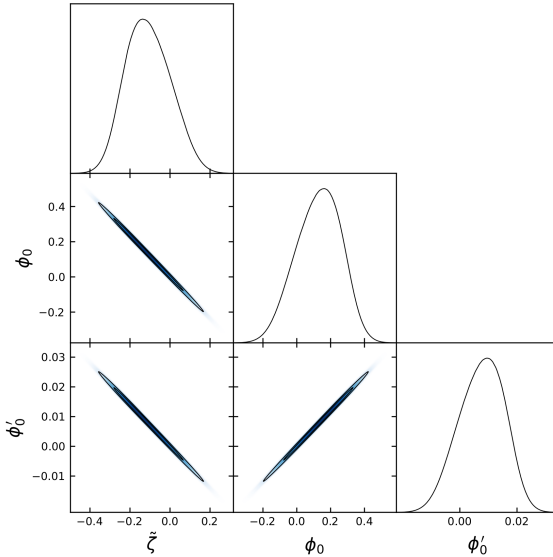


FIG. 1. Contour plots for the single rescaled BSBM parameter $\tilde{\zeta}$ and the two derived parameters ϕ_0 and ϕ'_0 , expressed in ppm. The contours lines are representing the 68 and 95 % confidence levels.

the Hubble constant H_0 , the amplitude and tilt of the primordial power spectrum n_s and $\ln(10^{10} A_s)$, and the couplings ζ or η_i of the Bekenstein models. We adopt flat and unbounded priors for all of these parameters. We are additionally sampling over the 21 nuisance parameters of the *Planck* likelihood and the absolute magnitude M of the reduced Pantheon likelihood. The $|R-1|$ convergence values, further chain information, and full corner plots can be found in appendix A.

We fix the values of the initial field value and speed to zero when $z \rightarrow \infty$, since one can show that these parameter choices in the radiation era do not impact the late time evolution of the field, due to the existence of attractor behaviors. The actual value of the field ϕ_0 (or $\zeta_F \phi_0$) and its speed ϕ'_0 (or $\zeta_F \phi'_0$) are derived but not sampled over.

A. BSBM model

Originally, the BSBM model has been introduced using a length scale ω to define the field units in the action (Eq. 3) instead of the mass scale M_* [12]. The parameter ω is then assumed to be close to the Planck length $\omega \sim G$ [14, 15]. In our notation this would correspond to $M_* = 1$, but we choose to instead absorb this different choice in a redefinition of the coupling constant, with $\tilde{\zeta} = 8\pi\zeta$ in order to allow for a direct comparison with previous literature. In Fig. 1, the derived contours of $\tilde{\zeta}$, ϕ_0 and ϕ'_0 are displayed using all the likelihoods introduced in

TABLE I. Best-fit values of the BSBM parameters with associated 68% confidence levels (C.L.) in ppm.

Parameter	68% C.L.
$\tilde{\zeta}$	$-0.09_{-0.13}^{+0.11}$
ϕ_0	$0.11_{-0.12}^{+0.16}$
ϕ'_0	$0.0066_{-0.0073}^{+0.0093}$

Sec. III. The corresponding best-fit values and their σ values can be found in Tab. I. We derive

$$\tilde{\zeta} = -0.09_{-0.13}^{+0.11} \text{ ppm}. \quad (23)$$

This result coincides with the one obtained in [15], providing a validation of our methodology. Note that adding the recent update of the MICROSCOPE bound in the present work does not change this result. Indeed, a back to the envelope calculation combining (22) and (4) allows us to evaluate the width of the Gaussian prior expected from the MICROSCOPE likelihood on $\tilde{\zeta}$ to be ~ 22 ppm, which is one order of magnitude larger than the one we obtained. We can hence conclude that atomic clocks measurements provide most of the constraining power on the BSBM model. For the first time however, the full model has been constrained together with the cosmological parameters and full evolution of the field right after inflation (the full plot can be found in appendix A 2, in Fig. 4).

The only parameter $\tilde{\zeta}$ appears however to be largely uncorrelated with cosmological parameters, explaining why the two analyses lead to identical results. The field speed is constrained at one sigma as $\phi'_0 = (6.6_{-7.3}^{+9.3}) \cdot 10^{-3}$ ppm while the field itself is constrained as $\phi_0 = 0.11_{-0.12}^{+0.16}$ ppm. As expected, $\tilde{\zeta}$ and the field parameters are highly correlated since they are directly related through the equation of motion (Eq. 5).

B. O&P model: Universal coupling to gravity

Before constraining the full parameter space of the O&P model, we first assume that the field couples identically to baryons and dark matter through a single parameter $\zeta_m \equiv \zeta_b = \zeta_\chi$. As in Sec. II B, one can then introduce the corresponding product parameter $\eta_m \equiv \zeta_F \zeta_m$. This reduction of the parameter space allows a direct comparison with previous works, such as [17]. We ran a first set of chains with all the likelihoods introduced in Sec. III (hereafter noted ‘Current’) and a second one removing the MICROSCOPE prior and replacing our atomic-clock likelihood by the one used in [17] and originally obtained in [36] (hereafter noted ‘Alves’). We also consider a third situation replacing the MICROSCOPE likelihood by the earlier measurement of η from torsion balance by the Eöt-Wash group [37] (hereafter noted ‘Eöt-Wash’). This last test allows us to assess the impact of WEP tests on the

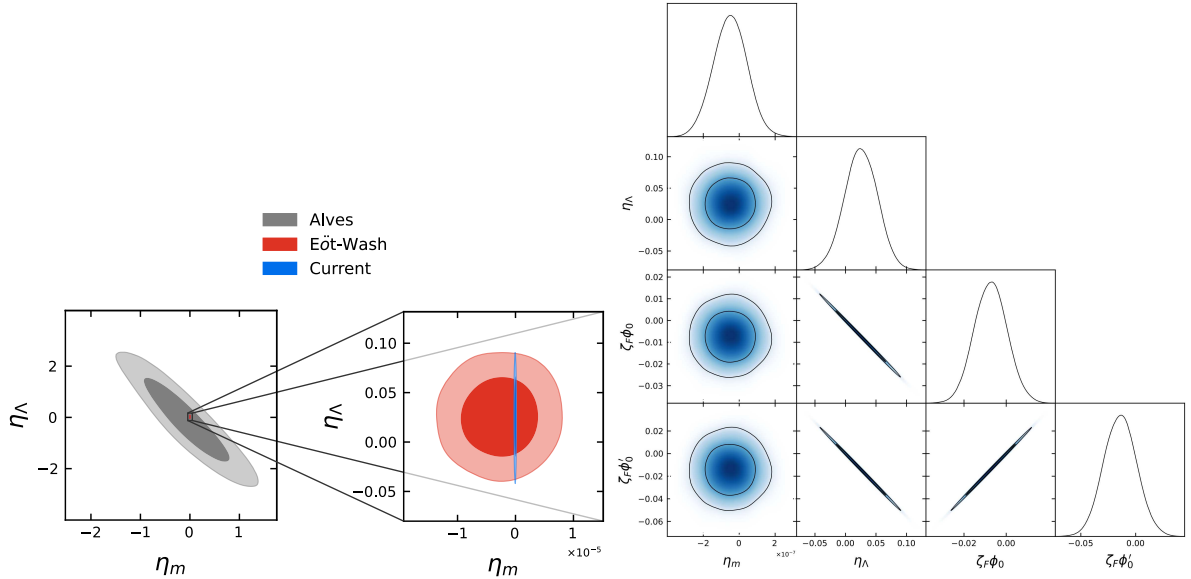


FIG. 2. Left: Contour plots for the O&P model under the universal matter coupling assumption with three different likelihood sets: 'Alves' (Gray), 'Eöt-Wash' (Red) and 'Current' (Blue). Right: Close-up view on the O&P parameter space using the 'Current' likelihood set. For both plots all parameters are expressed in ppm.

parameter space and quantify the improvement brought by the recent MICROSCOPE results.

A contour plot comparison of the O&P parameters in the three scenarios can be found in Fig. 2 and the corresponding best-fits and confidence interval values are displayed in Tab. II. As expected, the 'Alves' case gives results comparable with the ones of [17], constraining the two parameters η_m and η_Λ at the ppm level, displaying a strong degeneracy between the two parameters, as they both appear on the same footing in the equation of motion (Eq. 14). Adding a prior coming from experiments searching for violations of the WEP allows us to strongly break degeneracies as it directly constrains the coupling to matter η_m . Indeed, as shown in Fig. 2, adding either the MICROSCOPE or Eöt-Wash likelihood severely restricts the otherwise very degenerate combination of η_m and η_Λ . MICROSCOPE provides however sharper constraints on the matter coupling by two orders of magnitudes. By setting the constraint

$$\eta_m = (-0.54^{+0.86}_{-0.90}) \cdot 10^{-7} \text{ ppm}, \quad (24)$$

this parameter relaxes its correlation with $\zeta_F\phi_0$ and $\zeta_F\phi_0'$ and cannot significantly impact the field equation of motion anymore.

Comparing the 'Current' and 'Eöt-Wash' cases clearly shows that an improvement of the accuracy of WEP measurements does not further sharpen the posterior distribution of the coupling to dark energy, which is mainly set by the atomic-clock likelihood, constraining η_Λ at one

sigma to

$$\eta_\Lambda = (0.025 \pm 0.027) \text{ ppm}. \quad (25)$$

Here again, as shown in Fig. 5 of the appendix, the constraints on the parameters of the Bekenstein field are strong enough to largely break all possible degeneracies with cosmological parameters, leaving both mostly independently constrained. Overall, this leads to an improvement of the previous constraints of a factor of $\sim 10^8$ for η_m and ~ 100 for η_Λ , considering this time the full cosmological evolution of the field with minimal assumptions. Couplings of order ppm are now excluded for this model.

C. Full O&P model

We now turn to the full O&P model. We propose here for the first time a constraint of its full parameter space as no previous such studies can be found in the literature. The contour plots for the field parameters can be found in Fig. 3 and the associated best-fits with confidence levels are displayed in Tab. III. The MICROSCOPE prior is acting here directly on η_b , analogously to what occurred for η_m in the previous subsection, leaving the strong degeneracy between η_χ and η_Λ . The atomic-clock likelihood indeed, is sharp enough to break the degeneracies between $\zeta_F\phi'$ and $(\eta_\chi, \eta_\Lambda)$, by constraining the field speed to be so small that the impact of both couplings on the speed is indistinguishable. Nevertheless, here again we

TABLE II. Best-fit values of the parameters for the O&P model universally coupled to matter with associated 68% confidence levels (C.L.) in ppm, from the combination of currently available data. For comparison, the analogous constraints for two earlier sets 'Alves' and 'Eöt-Wash' (see the main text) are also shown.

Parameter	68% C.L. Current	68% C.L. Eöt-Wash	68% C.L. Alves
η_m	$ (-0.54^{+0.86}_{-0.90}) \cdot 10^{-7} $	$ (-0.25^{+0.45}_{-0.44}) \cdot 10^{-5} $	$0.05^{+0.60}_{-0.67}$
η_Λ	0.025 ± 0.027	$0.024^{+0.03}_{-0.027}$	-0.4 ± 1.1
$\zeta_F\phi_0$	$-0.0073^{+0.0081}_{-0.0076}$	$-0.007^{+0.0077}_{-0.0086}$	$-0.7^{+9.6}_{-8.5}$
$\zeta_F\phi'_0$	$-0.0014^{+0.0016}_{-0.0015}$	$-0.015^{+0.015}_{-0.017}$	0.17 ± 0.27

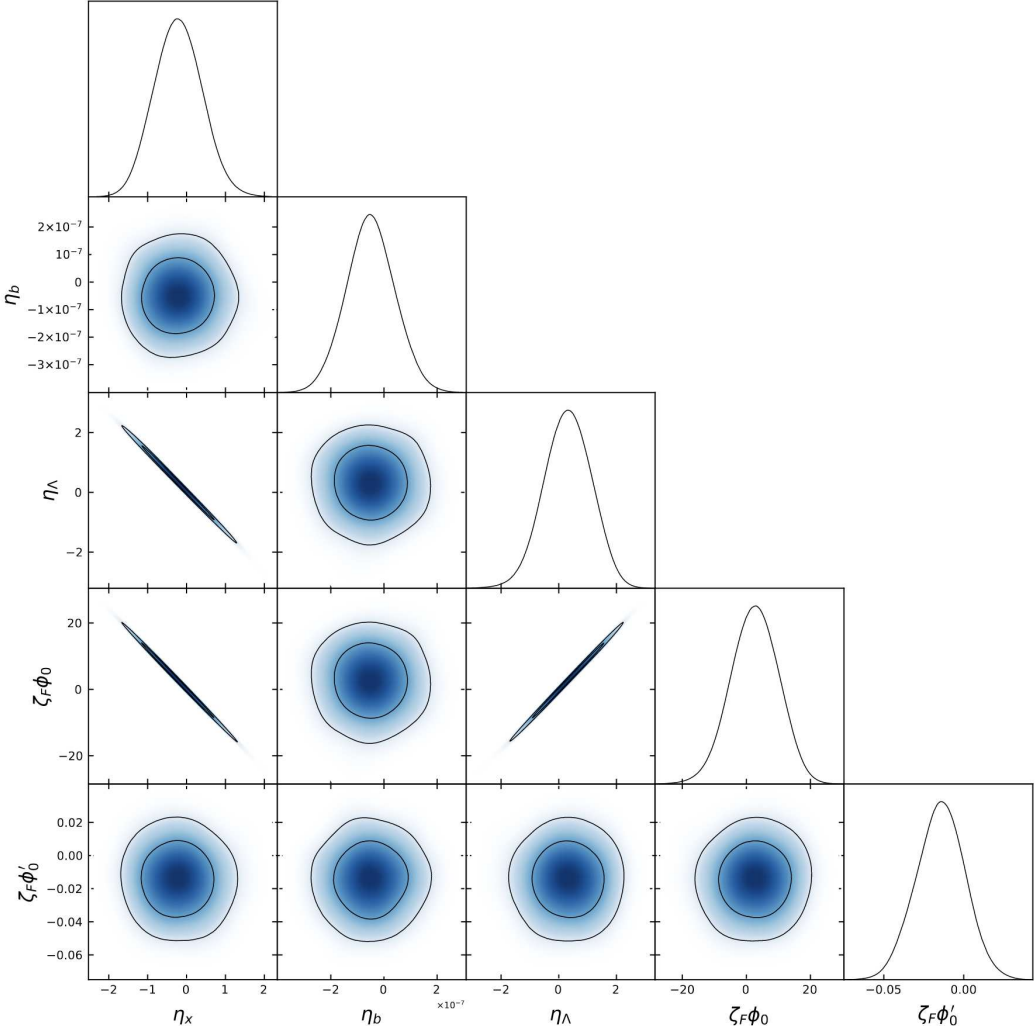


FIG. 3. Contour plots of the Bekenstein parameters in the full O&P model in ppm.

see that order ppm parameters are excluded by our combination of datasets.

As shown in Fig. 6, even this full model with a wide parameter space shows few degeneracies with the cosmo-

logical parameters, and as such it is constrained to have a minimal impact on the standard expansion history of the universe.

As shown in Tab. 1 of [16], several models beyond the

TABLE III. Best-fit values of the parameters for the full O&P model with associated 68% confidence levels (C.L.) in ppm.

Param	68% C.L.
η_x	$-0.24^{+0.63}_{-0.66}$
η_b	$ (-0.54^{+0.93}_{-0.94}) \cdot 10^{-7} $
η_Λ	$0.34^{+0.88}_{-0.85}$
$\zeta_F \phi_0$	$2.87^{+8.0}_{-7.7}$
$\zeta_F \phi'_0$	$-0.015^{+0.016}_{-0.015}$

standard model of cosmology and particle physics such as Brans-Dicke, Supersymmetry, or String Theory inspired models are supposed to be contained within the framework of this extended parameter space. By excluding couplings greater than fractions of ppm, our constraints exclude their naturally expected values for most of these models.

V. DISCUSSION AND CONCLUSION

Bekenstein models offer a very general and consistent framework for tests for variations of the fine-structure constant on cosmic scales. Even though it is expected to describe the low energy limit of several models beyond the standard models of cosmology and particle physics, it is tightly constrained by contemporary data, and expected to behave very close to the standard model. Specifically, we found that in all the generalizations considered, couplings of order of parts per million are excluded. The synergy of local, astrophysical and cosmological measurements of high precision applies an increasingly strong pressure on the credible models encompassing variations of the fundamental constants.

In this work, we constrained three implementations of the Bekenstein model. First, for the BSBM model, we have recovered, with a wider parameter space and a different methodology, the constraints derived in [15]. This also provides a validation of our numerical analysis pipeline. Then, we constrained a variation of O&P having a common coupling for baryonic and dark matter as in [17]. We improve previous constraints on this model by a factor of ~ 100 for η_Λ and $\sim 10^8$ for η_m . This large improvement is mainly due to the addition of very accurate local data as the MICROSCOPE prior on the universality of free fall and an improvement of the atomic-clock constrain on the time variation of the fine structure constant by an order of magnitude.

Finally, we provided a constraint of the full O&P model for the first time, allowing us to exclude natural values for the couplings for almost all the high energy physics theories encompassing a varying α proposed in the original paper of [16], excluding a large part of the parameter space of the models.

In all these analyses, we saw that parameters are too

sharply constrained by fine structure constant and Einstein Equivalence Principle measurements to have a significant impact on cosmological evolution, as the parameters of the Bekenstein field become mostly decorrelated from cosmological ones. As it quantifies the interaction between photons and matter, it is however known that a varying α could have a strong impact on the physics of recombination, changing its overall duration and the width of the last scattering surface. As such, some models inspired by the Bekenstein one could significantly impact the recovered value of H_0 and provide ways to relax the Hubble tension (see [34, 38], or [39] for a similar idea with the electron mass). One way to do so could be to introduce a more complex parameter space, with a different ϕ dependence of the couplings, the possibility of a decay of ϕ at intermediate times, or a non-zero potential $V(\phi)$. We note that the latter option might be subject to fine-tuning issues. As such, this kind of investigation is left for future works.

In this quest for high precision tests of fundamental physics, further progress is to be foreseen. In the long term, new experiments, under construction or being planned, will enable direct tests of the stability of fundamental constants with an accuracy never reached before. In particular the high-resolution spectrograph for the Extremely Large Telescope, formerly called ELT-HIRES and now known as ANDES [40] (whose Phase B of construction is starting, and expected to be operational in about 8 years) should improve the sensitivity of astrophysical measurements of α by at least one order of magnitude, while also extending the range of redshifts that ESPRESSO can probe. Moreover, recent theoretical and experimental developments open the possibility of improving the sensitivity of local atomic clock tests on the current drift rate of α by several orders of magnitude, by relying on Thorium-229 based nuclear clocks [41].

Constrains on the stability of fundamental constants on very large scales are also expected from wide cosmological surveys. Synergies between ground and space observations are expected from galaxy surveys performed from space with *Euclid* and from the ground with *DESI* [42, 43]. Similarly, recent or incoming observations of the CMB from the ground with telescopes such as *ACT* [44], *SPT* [45] and the *Simons Observatory* [46] could surpass the last bounds set by *Planck* in [33] on the value of the fine structure constant at $z \sim 1100$. Further high precisions improvements from the CMB polarization are also to be expected in the next decades from ground with the *CMB Stage-4* telescope and from space with the *Lite-BIRD* satellite [47, 48].

The pipeline developed in the present work can easily be generalized to constrain all possible variations of the fine-structure constant driven by a scalar field and could be extended to other fundamental constants. Instead of constraining the field parameters alone, it allows to evaluate its impact in relation with all the cosmological parameters.

VI. ACKNOWLEDGMENTS

L.V. would like to thank J. Aumont and L. Monnier for their support through all this project and A. Blanchard, B. Lamine as well as J. Lesgourgues for crucial discussions at the origin of this work. Computations were made on the Mardec cluster supported by the OCEVU Labex (ANR-11-LABX-0060) and the Excellence Initiative of Aix-Marseille University - A*MIDEX, part of the French “Investissements d’Avenir” program. LV would also like to thanks B. Carreres for several helps with the use of Mardec. J.D.F.D. is supported by an FCT fellowship, grant number SFRH/BD/150990/2021. CJM acknowledges FCT

and POCH/FSE (EC) support through Investigador FCT Contract 2021.01214.CEECIND/CP1658/CT0001. NS acknowledges the support of the following Maria de Maeztu fellowship grant: Esta publicación es parte de la ayuda CEX2019-000918-M, financiada por MCIN/AEI/10.13039/501100011033. SN acknowledges support from the research project PGC2018-094773-B-C32, and the Spanish Research Agency (Agencia Estatal de Investigación) through the Grant IFT Centro de Excelencia Severo Ochoa No CEX2020-001007-S, funded by MCIN/AEI/10.13039/501100011033. GCH acknowledges support from the Delta Institute for Theoretical Physics (D-ITP consortium), a program by the NWO. MM acknowledges funding by the Agenzia Spaziale Italiana (ASI) under agreement n. 2018-23-HH.0.

-
- [1] J.-P. Uzan, Varying Constants, Gravitation and Cosmology, *Living Reviews in Relativity* **14**, 2 (2011), arXiv:1009.5514 [astro-ph.CO].
 - [2] E. Di Casola, S. Liberati, and S. Sonego, Nonequivalence of equivalence principles, *American Journal of Physics* **83**, 39 (2015), arXiv:1310.7426 [gr-qc].
 - [3] C. M. Will, The Confrontation between General Relativity and Experiment, *Living Reviews in Relativity* **17**, 4 (2014), arXiv:1403.7377 [gr-qc].
 - [4] C. M. Will, *Theory and Experiment in Gravitational Physics (2nd edition)* (2017).
 - [5] G. Dvali and M. Zaldarriaga, Changing α with Time: Implications for Fifth-Force-Type Experiments and Quintessence, *Phys. Rev. Lett.* **88**, 091303 (2002), arXiv:hep-ph/0108217 [hep-ph].
 - [6] C. J. A. P. Martins, The status of varying constants: a review of the physics, searches and implications, *Reports on Progress in Physics* **80**, 126902 (2017), arXiv:1709.02923 [astro-ph.CO].
 - [7] C. J. A. P. Martins, Cosmology with varying constants, *Philosophical Transactions of the Royal Society of London Series A* **360**, 2681 (2002), arXiv:astro-ph/0205504 [astro-ph].
 - [8] T. Damour and J. F. Donoghue, FAST TRACK COMMUNICATION: Phenomenology of the equivalence principle with light scalars, *Classical and Quantum Gravity* **27**, 202001 (2010), arXiv:1007.2790 [gr-qc].
 - [9] C. J. A. P. Martins, F. P. S. A. Ferreira, and P. V. Marto, Varying fine-structure constant cosmography, *Physics Letters B* **827**, 137002 (2022), arXiv:2203.02781 [astro-ph.CO].
 - [10] J. D. Bekenstein, Fine-structure constant: Is it really a constant?, *Phys. Rev. D* **25**, 1527 (1982).
 - [11] J. D. Bekenstein, Fine-structure constant variability, equivalence principle, and cosmology, *Phys. Rev. D* **66**, 123514 (2002), arXiv:gr-qc/0208081 [gr-qc].
 - [12] H. B. Sandvik, J. D. Barrow, and J. Magueijo, A Simple Cosmology with a Varying Fine Structure Constant, *Phys. Rev. Lett.* **88**, 031302 (2002), arXiv:astro-ph/0107512 [astro-ph].
 - [13] P. M. M. Leal, C. J. A. P. Martins, and L. B. Ventura, Fine-structure constant constraints on Bekenstein-type models, *Phys. Rev. D* **90**, 027305 (2014), arXiv:1407.4099 [astro-ph.CO].
 - [14] A. C. O. Leite and C. J. A. P. Martins, Current and future constraints on Bekenstein-type models for varying couplings, *Phys. Rev. D* **94**, 023503 (2016), arXiv:1607.01677 [astro-ph.CO].
 - [15] C. J. A. P. Martins, S. Cristiani, G. Cupani, V. D’Odorico, R. Génova Santos, A. C. O. Leite, C. M. J. Marques, D. Milaković, P. Molaro, M. T. Murphy, N. J. Nunes, T. M. Schmidt, V. Adibekyan, Y. Alibert, P. Di Marcantonio, J. I. González Hernández, D. Mégevand, E. Palle, F. A. Pepe, N. C. Santos, S. G. Sousa, A. Sozzetti, A. Suárez Mascareño, and M. R. Zapatero Osorio, Fundamental physics with ESPRESSO: Constraints on Bekenstein and dark energy models from astrophysical and local probes, arXiv e-prints , arXiv:2205.13848 (2022), arXiv:2205.13848 [astro-ph.CO].
 - [16] K. A. Olive and M. Pospelov, Evolution of the fine structure constant driven by dark matter and the cosmological constant, *Phys. Rev. D* **65**, 085044 (2002), arXiv:hep-ph/0110377 [hep-ph].
 - [17] C. S. Alves, A. C. O. Leite, C. J. A. P. Martins, T. A. Silva, S. A. Berge, and B. S. A. Silva, Current and future constraints on extended Bekenstein-type models for a varying fine-structure constant, *Phys. Rev. D* **97**, 023522 (2018), arXiv:1801.08089 [astro-ph.CO].
 - [18] J. Lesgourgues, The cosmic linear anisotropy solving system (class) i: Overview (2011), arXiv:1104.2932 [astro-ph.IM].
 - [19] B. Audren, J. Lesgourgues, K. Benabed, and S. Prunet, Conservative Constraints on Early Cosmology: an illustration of the Monte Python cosmological parameter inference code, *JCAP* **1302**, 001, arXiv:1210.7183 [astro-ph.CO].
 - [20] T. Brinckmann and J. Lesgourgues, MontePython 3: Boosted MCMC sampler and other features, *Physics of the Dark Universe* **24**, 100260 (2019), arXiv:1804.07261 [astro-ph.CO].
 - [21] P. A. Zyla *et al.* (Particle Data Group), Review of Particle Physics, *PTEP* **2020**, 083C01 (2020).
 - [22] A. G. Riess, S. A. Rodney, D. M. Scolnic, D. L. Shafer, L.-G. Strolger, H. C. Ferguson, M. Postman, O. Graur, D. Maoz, S. W. Jha, B. Mobasher, S. Casertano, B. Haynes, and J. J. Newman, Discovery of a High-Z Type Ia Supernova at $z = 1.73$ and its Use to Break the Degeneracy Between the Cosmological Constant and Dark Energy, *Science* **346**, 938 (2014), arXiv:1401.4544 [astro-ph.CO].

- den, A. Molino, J. Hjorth, P. M. Garnavich, D. O. Jones, R. P. Kirshner, A. M. Koekemoer, N. A. Grogan, G. Brammer, S. Hemmati, M. Dickinson, P. M. Challis, S. Wolff, K. I. Clubb, A. V. Filippenko, H. Nayyeri, V. U. D. C. Koo, S. M. Faber, D. Kocevski, L. Bradley, and D. Coe, Type Ia Supernova Distances at Redshift >1.5 from the Hubble Space Telescope Multi-cycle Treasury Programs: The Early Expansion Rate, *Astrophys. J.* **853**, 126 (2018), arXiv:1710.00844 [astro-ph.CO].
- [23] T. B. collaboration, The clustering of galaxies in the completed SDSS-III Baryon Oscillation Spectroscopic Survey: cosmological analysis of the DR12 galaxy sample, *MNRAS* **470**, 2617 (2017), arXiv:1607.03155 [astro-ph.CO].
- [24] M. Moresco, L. Pozzetti, A. Cimatti, R. Jimenez, C. Maraston, L. Verde, D. Thomas, A. Citro, R. Tojeiro, and D. Wilkinson, A 6% measurement of the Hubble parameter at $z \sim 0.45$: direct evidence of the epoch of cosmic re-acceleration, *J. Cosmology Astropart. Phys.* **2016**, 014 (2016), arXiv:1601.01701 [astro-ph.CO].
- [25] N. Aghanim, Y. Akrami, F. Arroja, M. Ashdown, J. Aumont, C. Baccigalupi, M. Ballardini, A. J. Banday, R. B. Barreiro, and et al., Planck2018 results, *Astronomy & Astrophysics* **641**, A1 (2020).
- [26] Planck Collaboration, Planck 2018 results. V. CMB power spectra and likelihoods, *A&A* **641**, A5 (2020), arXiv:1907.12875 [astro-ph.CO].
- [27] M. T. Murphy and K. L. Cooksey, Subaru Telescope limits on cosmological variations in the fine-structure constant, *Monthly Notices of the Royal Astronomical Society* **471**, 4930 (2017), <https://academic.oup.com/mnras/article-pdf/471/4/4930/19650209/stx1949.pdf>.
- [28] J. K. Webb, J. A. King, M. T. Murphy, V. V. Flambaum, R. F. Carswell, and M. B. Bainbridge, Indications of a Spatial Variation of the Fine Structure Constant, *Phys. Rev. Lett.* **107**, 191101 (2011), arXiv:1008.3907 [astro-ph.CO].
- [29] M. T. Murphy, P. Molaro, A. C. O. Leite, G. Cupani, S. Cristiani, V. D’Odorico, R. Génova Santos, C. J. A. P. Martins, D. Milaković, N. J. Nunes, T. M. Schmidt, F. A. Pepe, R. Rebolo, N. C. Santos, S. G. Sousa, M.-R. Zapatero Osorio, M. Amate, V. Adibekyan, Y. Alibert, C. A. Prieto, V. Baldini, W. Benz, F. Bouchy, A. Cabral, H. Dekker, P. Di Marcantonio, D. Ehrenreich, P. Figueira, J. I. González Hernández, M. Landdoni, C. Lovis, G. Lo Curto, A. Manescu, D. Mégevand, A. Mehner, G. Micela, L. Pasquini, E. Poretti, M. Riva, A. Sozzetti, A. S. Mascareño, S. Udry, and F. Zerbini, Fundamental physics with ESPRESSO: Precise limit on variations in the fine-structure constant towards the bright quasar HE 0515–4414, *A&A* **658**, A123 (2022), arXiv:2112.05819 [astro-ph.CO].
- [30] Y. V. Petrov, A. I. Nazarov, M. S. Onegin, V. Y. Petrov, and E. G. Sakhnovsky, Natural nuclear reactor at Oklo and variation of fundamental constants: Computation of neutronics of a fresh core, *Phys. Rev. C* **74**, 064610 (2006), arXiv:hep-ph/0506186 [hep-ph].
- [31] R. Lange, N. Huntemann, J. M. Rahm, C. Sanner, H. Shao, B. Lipphardt, C. Tamm, S. Weyers, and E. Peik, Improved Limits for Violations of Local Position Invariance from Atomic Clock Comparisons, *Phys. Rev. Lett.* **126**, 011102 (2021), arXiv:2010.06620 [physics.atom-ph].
- [32] P. Touboul, G. Métris, M. Rodrigues, J. Bergé, A. Robert, Q. Baghi, Y. André, J. Bedouet, D. Boulanger, S. Bremer, P. Carle, R. Chhun, B. Christophe, V. Cipolla, T. Damour, P. Danto, L. Demange, H. Dittus, O. Dhuicque, P. Fayet, B. Foulon, P.-Y. Guidotti, D. Hagedorn, E. Hardy, P.-A. Huynh, P. Kayser, S. Lala, C. Lämmerzahl, V. Lebat, F. m. c. Liorzou, M. List, F. Löffler, I. Panet, M. Pernot-Borràs, L. Perraud, S. Pires, B. Pouilloux, P. Prieur, A. Rebray, S. Reynaud, B. Rievers, H. Selig, L. Serron, T. Sumner, N. Tanguy, P. Torresi, and P. Visser, *microscope* mission: Final results of the test of the equivalence principle, *Phys. Rev. Lett.* **129**, 121102 (2022).
- [33] Planck Collaboration, Planck intermediate results. XXIV. Constraints on variations in fundamental constants, *A&A* **580**, A22 (2015), arXiv:1406.7482 [astro-ph.CO].
- [34] L. Hart and J. Chluba, New constraints on time-dependent variations of fundamental constants using Planck data, *MNRAS* **474**, 1850 (2018), arXiv:1705.03925 [astro-ph.CO].
- [35] A. Lewis, GetDist: a Python package for analysing Monte Carlo samples, *arXiv e-prints*, arXiv:1910.13970 (2019), arXiv:1910.13970 [astro-ph.IM].
- [36] T. Rosenband, D. B. Hume, P. O. Schmidt, C. W. Chou, A. Brusch, L. Lorini, W. H. Oskay, R. E. Drullinger, T. M. Fortier, J. E. Stahlaker, S. A. Didams, W. C. Swann, N. R. Newbury, W. M. Itano, D. J. Wineland, and J. C. Bergquist, Frequency ratio of al^+ and hg^+ single-ion optical clocks: metrology at the 17th decimal place, *Science* **319**, 1808 (2008), <https://www.science.org/doi/pdf/10.1126/science.1154622>.
- [37] T. A. Wagner, S. Schlamming, J. H. Gundlach, and E. G. Adelberger, Torsion-balance tests of the weak equivalence principle, *Classical and Quantum Gravity* **29**, 184002 (2012), arXiv:1207.2442 [gr-qc].
- [38] L. Hart and J. Chluba, Varying fundamental constants principal component analysis: additional hints about the Hubble tension, *Mon. Not. Roy. Astron. Soc.* **510**, 2206 (2022), arXiv:2107.12465 [astro-ph.CO].
- [39] N. Schöneberg, G. F. Abellán, A. Pérez Sánchez, S. J. Witte, V. Poulin, and J. Lesgourgues, The H_0 Olympics: A fair ranking of proposed models, *arXiv e-prints*, arXiv:2107.10291 (2021), arXiv:2107.10291 [astro-ph.CO].
- [40] J. Liske, G. Bono, J. Cepa, et al., *Top Level Requirements For ELT-HIRES*, Tech. Rep. (Document ESO 204697 Version 1, 2014).
- [41] P. Fadeev, J. C. Berengut, and V. V. Flambaum, Sensitivity of ^{229}Th nuclear clock transition to variation of the fine-structure constant, *Phys. Rev. A* **102**, 052833 (2020), arXiv:2007.00408 [physics.atom-ph].
- [42] M. Martinelli, C. J. A. P. Martins, S. Nesseris, I. Tuttusaus, A. Blanchard, S. Camera, C. Carbone, S. Casas, V. Pettorino, Z. Sakr, V. Yankelevich, D. Sapone, A. Amara, N. Auricchio, C. Bodendorf, D. Bonino, E. Branchini, V. Capobianco, J. Carretero, M. Castellano, S. Cavauti, A. Cimatti, R. Cledassou, L. Corcione, A. Costille, H. Degaudenzi, M. Douspis, F. Dubath, S. Dusini, A. Ealet, S. Ferriol, M. Frailis, E. Franceschi, B. Garilli, C. Giocoli, A. Grazian, F. Grupp, S. V. H. Haugan, W. Holmes, F. Hormuth, K. Jahnke, A. Kiessling, M. Kümmel, M. Kunz, H. Kurki-Suonio, S. Ligori, P. B. Lilje, I. Lloro, O. Mansutti,

- O. Marggraf, K. Markovic, R. Massey, M. Meneghetti, G. Meylan, L. Moscardini, S. M. Niemi, C. Padilla, S. Paltani, F. Pasian, K. Pedersen, S. Pires, M. Poncet, L. Popa, F. Raison, R. Rebolo, J. Rhodes, M. Roncarelli, E. Rossetti, R. Saglia, A. Secroun, G. Seidel, S. Serrano, C. Sirignano, G. Sirri, J. L. Starck, D. Tavagnacco, A. N. Taylor, I. Tereno, R. Toledo-Moreo, L. Valenziano, Y. Wang, G. Zamorani, J. Zoubian, M. Baldi, M. Brescia, G. Congedo, L. Conversi, Y. Copin, G. Fabbian, R. Farinelli, E. Medinaceli, S. Mei, G. Polenta, E. Romelli, and T. Vassallo, Euclid: Constraining dark energy coupled to electromagnetism using astrophysical and laboratory data, *A&A* **654**, A148 (2021), arXiv:2105.09746 [astro-ph.CO].
- [43] DESI Collaboration, The DESI Experiment Part I: Science, Targeting, and Survey Design, arXiv e-prints , arXiv:1611.00036 (2016), arXiv:1611.00036 [astro-ph.IM].
- [44] S. Aiola, E. Calabrese, L. Maurin, S. Naess, B. L. Schmitt, M. H. Abitbol, G. E. Addison, P. A. R. Ade, D. Alonso, M. Amiri, S. Amodeo, E. Angile, J. E. Austermann, T. Baildon, N. Battaglia, J. A. Beall, R. Bean, D. T. Becker, J. R. Bond, S. M. Bruno, V. Calafut, L. E. Campusano, F. Carrero, G. E. Chesmore, H.-m. Cho, S. K. Choi, S. E. Clark, N. F. Cothard, D. Crichton, K. T. Crowley, O. Darwishi, R. Datta, E. V. Denison, M. J. Devlin, C. J. Duell, S. M. Duff, A. J. Duivenvoorden, J. Dunkley, R. Dünner, T. Essinger-Hileman, M. Fankhael, S. Ferraro, A. E. Fox, B. Fuzia, P. A. Gallardo, V. Gluscevic, J. E. Golec, E. Grace, M. Gralla, Y. Guan, K. Hall, M. Halpern, D. Han, P. Hargrave, M. Hasselfield, J. M. Helton, S. Henderson, B. Hensley, J. C. Hill, G. C. Hilton, M. Hilton, A. D. Hincks, R. Hložek, S.-P. P. Ho, J. Hubmayr, K. M. Huffenberger, J. P. Hughes, L. Infante, K. Irwin, R. Jackson, J. Klein, K. Knowles, B. Koopman, A. Kosowsky, V. Lakey, D. Li, Y. Li, Z. Li, M. Lokken, T. Louis, M. Lungu, A. MacInnis, M. Madhavaricheril, F. Maldonado, M. Mallaby-Kay, D. Marsden, J. McMahon, F. Menanteau, K. Moodley, T. Morton, T. Namikawa, F. Nati, L. Newburgh, J. P. Nibarger, A. Nicola, M. D. Niemack, M. R. Nolta, J. Orlowski-Sherer, L. A. Page, C. G. Pappas, B. Partridge, P. Phakathi, G. Pisano, H. Prince, R. Puddu, F. J. Qu, J. Rivera, N. Robertson, F. Rojas, M. Salatino, E. Schaan, A. Schillaci, N. Sehgal, B. D. Sherwin, C. Sierra, J. Sievers, C. Sifon, P. Sikhosana, S. Simon, D. N. Spergel, S. T. Staggs, J. Stevens, E. Storer, D. D. Sunder, E. R. Switzer, B. Thorne, R. Thornton, H. Trac, J. Treu, C. Tucker, L. R. Vale, A. Van Engelen, J. Van Lanen, E. M. Vavagiakis, K. Wagoner, Y. Wang, J. T. Ward, E. J. Wollack, Z. Xu, F. Zago, and N. Zhu, The Atacama Cosmology Telescope: DR4 maps and cosmological parameters, *J. Cosmology Astropart. Phys.* **2020**, 047 (2020), arXiv:2007.07288 [astro-ph.CO].
- [45] J. T. Sayre, C. L. Reichardt, J. W. Henning, P. A. R. Ade, A. J. Anderson, J. E. Austermann, J. S. Avva, J. A. Beall, A. N. Bender, B. A. Benson, F. Bianchini, L. E. Bleem, J. E. Carlstrom, C. L. Chang, P. Chaubal, H. C. Chiang, R. Citron, C. Corbett Moran, T. M. Crawford, A. T. Crites, T. de Haan, M. A. Dobbs, W. Everett, J. Gallicchio, E. M. George, A. Gilbert, N. Gupta, N. W. Halverson, N. Harrington, G. C. Hilton, G. P. Holder, W. L. Holzapfel, J. D. Hrubes, N. Huang, J. Hubmayr, K. D. Irwin, L. Knox, A. T. Lee, D. Li, A. Lowitz, J. J. McMahon, S. S. Meyer, L. M. Mocanu, J. Montgomery, A. Nadolski, T. Natoli, J. P. Nibarger, G. Noble, V. Novosad, S. Padin, S. Patil, C. Pryke, J. E. Ruhl, B. R. Saliwanchik, K. K. Schaffer, C. Sievers, G. Smecher, A. A. Stark, C. Tucker, K. Vanderlinde, T. Veach, J. D. Vieira, G. Wang, N. Whitehorn, W. L. K. Wu, V. Yefremenko, and SPTpol Collaboration, Measurements of B-mode polarization of the cosmic microwave background from 500 square degrees of SPTpol data, *Phys. Rev. D* **101**, 122003 (2020), arXiv:1910.05748 [astro-ph.CO].
- [46] The Simons Observatory collaboration, The Simons Observatory, in *BAAS*, Vol. 51 (2019) p. 147, arXiv:1907.08284 [astro-ph.IM].
- [47] CMB-S4 Collaboration, CMB-S4 Science Case, Reference Design, and Project Plan, arXiv e-prints , arXiv:1907.04473 (2019), arXiv:1907.04473 [astro-ph.IM].
- [48] LiteBIRD Collaboration, Probing Cosmic Inflation with the LiteBIRD Cosmic Microwave Background Polarization Survey, in *PTEP*, PTEP, Vol. 11443 (2022) p. 114432F, arXiv:2101.12449 [astro-ph.IM].

Appendix A: MCMC chain plots and tables

We display here information about the chains and their convergence derived using MONTEPYTHON in subsection A 1. Full plots using GETDIST and including the cosmological parameters are also displayed in subsection A 2.

1. Convergence information

Tables IV, V, and VI list the convergence of the chain specified through the Gelman-Rubin criterion $|R - 1|$. Values much smaller than 0.1 typically indicate well converged chains, which is the case for all parameters across all chains. We further show for reproducibility the initial guesses for mean and standard deviation (μ_0 and σ_0 , respectively) to reduce the burn in of the MCMC chains. We stress that these are not Gaussian priors imposed on our parameters.

TABLE IV. Complementary information for the free parameters of the BSBM model (not including nuisance parameters). In the first column we show the parameter name, in the second column the $|R - 1|$ Gelman-Rubin convergence criterion, and in the third and fourth column the mean and standard deviation to initialize the chains with (these are not priors). Total number of accepted steps: 3736795 for 16 chains.

Parameter	R-1	μ_0	σ_0
$100\omega_b$	0.005936	2.2377	0.015
ω_{cdm}	0.003368	0.12010	0.0013
H_0	0.002793	67.8	0.5
$\ln 10^{10} A_s$	0.005616	3.0447	0.015
n_s	0.005490	0.9659	0.0042
z_{reio}	0.006086	8	0.5
ζ (ppm)	0.002793	0	0.1
$-\ln \mathcal{L}_{\min} = 2047.22,$			

TABLE V. Same as table IV, but for the O&P model universally coupled to matter. Total number of accepted steps: 1174065 for 14 chains.

Parameter	R-1	μ_0	σ_0
$100\omega_b$	0.013401	2.2377	0.015
ω_{cdm}	0.018249	0.12010	0.0013
H_0	0.020532	67.8	0.5
$\ln 10^{10} A_s$	0.013956	3.0447	0.015
n_s	0.033703	0.9659	0.0042
z_{reio}	0.010774	8	0.5
η_m (ppm)	0.020532	0	10^{-6}
η_Λ (ppm)	0.017963	0	0.01
$-\ln \mathcal{L}_{\min} = 2048.09$			

TABLE VI. Same as table IV, but for the full O&P model. Total number of accepted steps: 1143660 for 28 chains.

Parameter	R-1	μ_0	σ_0
$100\omega_b$	0.007294	2.2377	0.015
ω_{cdm}	0.005807	0.12010	0.0013
H_0	0.005984	67.8	0.5
$\ln 10^{10} A_s$	0.006341	3.0447	0.015
n_s	0.005657	0.9659	0.0042
z_{reio}	0.005787	8	0.5
η_x (ppm)	0.005984	0	0.01
η_b (ppm)	0.005984	0	10^{-6}
η_Λ (ppm)	0.037416	0	0.01
$-\ln \mathcal{L}_{\min} = 2047.41$			

2. Full corner plots

In this section we display the full corner plots for the three models analyzed in section IV. The very good convergence is immediately apparent in the figures, as well as the lack of any significant degeneracy with the parameters of the given model. A very attentive reader might notice that the correlations of the Bekenstein and cosmological parameters are not always perfect ellipses, hence indicating the non-triviality of such a study.

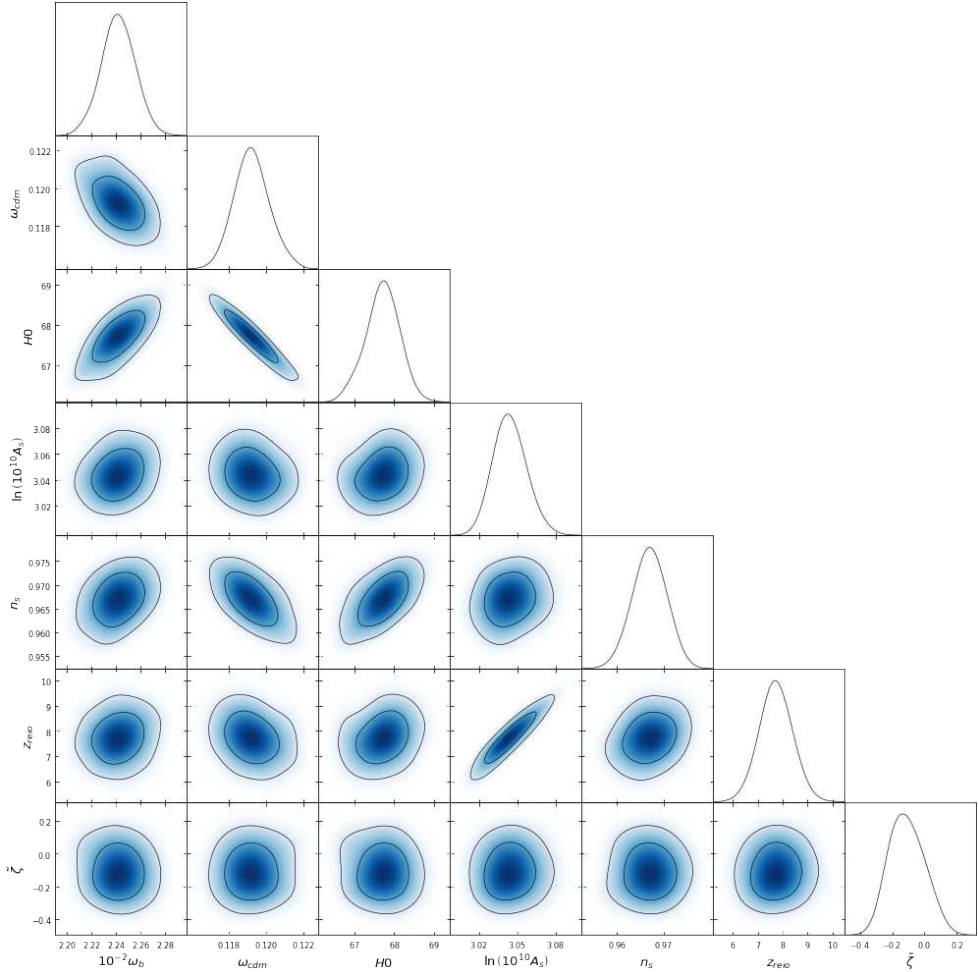


FIG. 4. Contour plots for the full parameter space (Bekenstein + cosmology) in the case of the BSBM model. Note that $\tilde{\zeta}$ is presented in ppm.

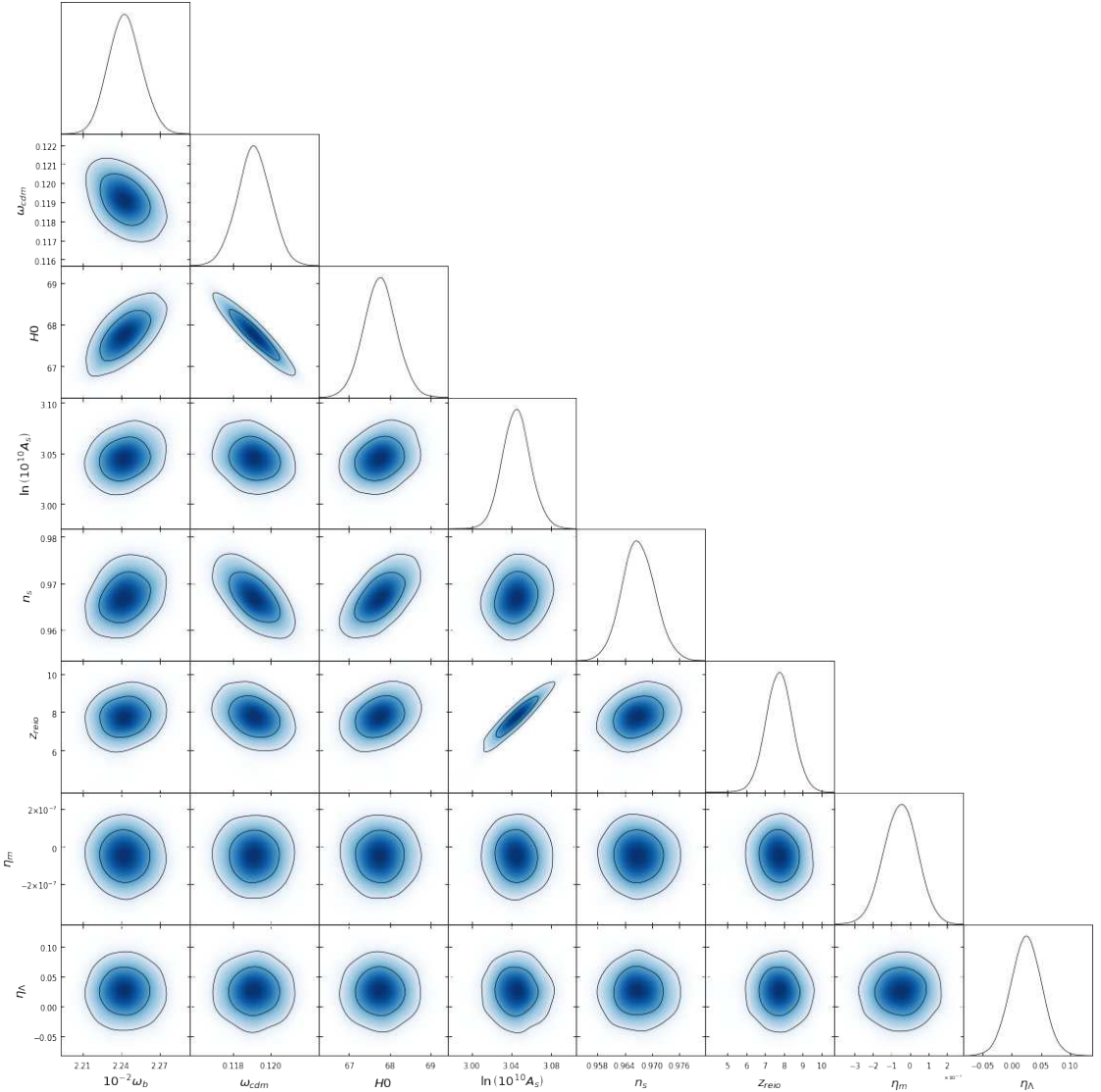


FIG. 5. Contour plots for the full parameter space (Bekenstein + cosmology) in the case of the O&P model universally coupled to gravity. Note that η_m and η_Λ are presented in ppm (and for η_m there is an additional scaling of 10^{-6}).

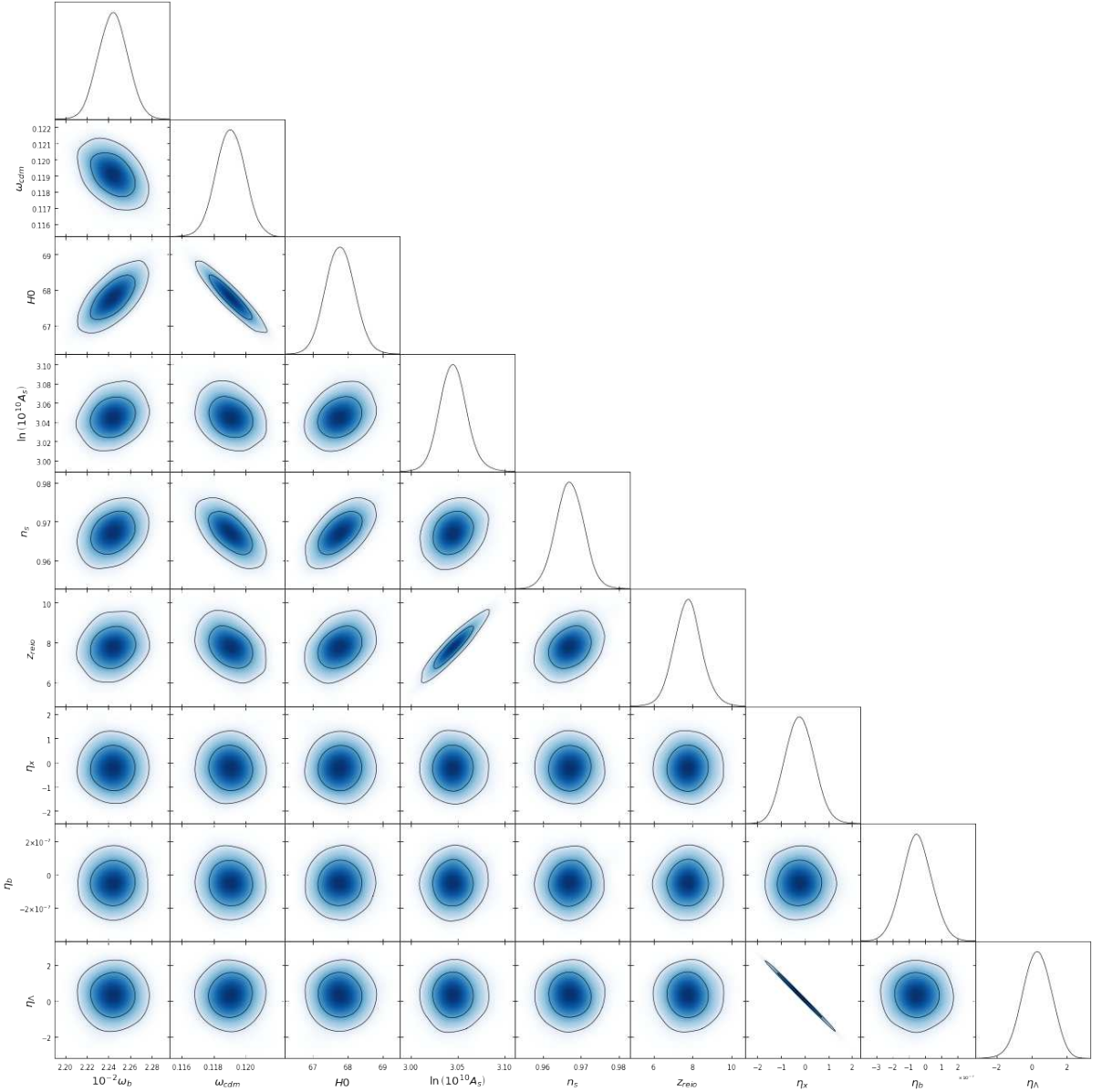


FIG. 6. Contour plots for the full parameter space (Bekenstein + cosmology) in the case of the full O&P model. Note that η_χ , η_b and η_Λ are presented in ppm (and for η_b there is an additional scaling of 10^{-6}).

D.5 PhysRevD.107.104002

Runaway dilaton models: Improved constraints from the full cosmological evolution

Léo Vacher,^{1, 2,*} Nils Schöneberg,^{3, †} J. D. F. Dias,^{4, 5, 6} C. J. A. P. Martins,^{4, 5, ‡} and Francisco Pimenta^{4, 6}

¹*Institut de Recherche en Astrophysique et Planétologie, CNRS, CNES, 31028 Toulouse, France*

²*Université de Toulouse UPS, 31028 Toulouse, France*

³*Dept. Física Quântica i Astrofísica, Institut de Ciències del Cosmos (ICCUB), Facultat de Física, Universitat de Barcelona (IEEC-UB), Martí i Franqués, 1, E08028 Barcelona, Spain*

⁴*Centro de Astrofísica da Universidade do Porto, Rua das Estrelas, 4150-762 Porto, Portugal*

⁵*Instituto de Astrofísica e Ciências do Espaço, CAUP,*

Universidade do Porto, Rua das Estrelas, 4150-762, Porto, Portugal

⁶*Faculdade de Ciências, Universidade do Porto, Rua Campo Alegre, 4169-007, Porto, Portugal*

(Dated: May 13, 2023)

One of the few firm predictions of string theory is the existence of a massless scalar field coupled to gravity, the dilaton. In its presence, the value of the fundamental constants of the universe, such as the fine-structure constant, will vary with the time-dependent vacuum expectation value of this field, in direct violation of the Einstein equivalence principle. The *runaway dilaton* proposed by Damour, Piazza, and Veneziano provides a physically motivated cosmological scenario which reconciles the existence of a massless dilaton with observations, while still providing nonstandard and testable predictions. Furthermore, the field can provide a natural candidate for dynamical dark energy. While this model has been previously constrained from local laboratory experiments and low-redshift observations, we provide here the first full self-consistent constraints, also including high redshift data, in particular from the cosmic microwave background. We consider various possible scenarios in which the field could act as quintessence. Despite the wider parameter space, we make use of recent observational progress to significantly improve constraints on the model, showing that order unity couplings (which would be natural in string theory) are ruled out.

Keywords: Cosmology, varying constants, dark energy, string theory, scalar fields, modified gravity

I. INTRODUCTION

The discovery of the Higgs boson at the LHC [1, 2], confirmed that spin-0 scalar fields are part of the building blocks of nature. As they are easy to couple to gravity without breaking covariance, they are now commonly invoked as a powerful tool to model cosmological paradigms, including quintessence, early dark energy, inflation, symmetry breaking phase transitions (with their associated topological defects), and—last but not least—dynamical varying couplings [3].

Moreover, they appear as a theoretical necessity in most of grand unification scenarios and attempts of building a quantum theory of gravity. This is the case of string theory, one of the most promising paths connecting quantum field theories and gravity (for a review see e.g. [4]). Indeed, many bridges have already been built between gravity and quantum fields thanks to quantum strings, such as the recent AdS–CFT correspondence and similar applications of the holographic principle (see e.g. [5]). Even though it is still impossible to tell what the final form of the theory should be, one of its uncircumventable predictions seems to be the existence of a scalar partner to the graviton field, called the *dilaton*. Its dynamics sets the intensity of the various interactions between strings through the *string coupling*, and therefore that of the

fundamental forces of the standard model. Among other things, the evolution of the dilaton field implies a variation of all the fundamental dimensionless couplings, such as the fine-structure constant. In turn, this implies a violation of the Einstein equivalence principle [6, 7]).

Theory suggests that the dilaton should be massless, which would be in violent contradiction with observations. To overcome such an issue in a physically motivated manner, it has been proposed that the dilaton coupling to other matter fields is attracted toward finite smooth limits [8–10]. This model is called the *runaway dilaton* and has the advantage of providing clear predictions, that can be confronted with observations. As such, it can be used as a very compelling testbed model to implement and study variations of fundamental constants on cosmological scales. Moreover, with a suitable choice of potential $V(\phi)$ or extra couplings, the dilaton field can provide a physically motivated source of dynamical dark energy [11].

The present work builds upon several previous phenomenological studies [11–14] while aiming to be more accurate and more general. This is achieved by confronting the full cosmological field evolution with the latest datasets, as done in [15] for Bekenstein models, while freeing ourselves from assumptions made in previous studies. In section II we introduce the evolution equations of the coupled dilaton field, as well as their impact on various observables. In section III we present the datasets we use in order to obtain the constraints discussed in section IV. Finally, we present our conclusions in section V.

* leo.vacher@irap.omp.eu

† nils.science@gmail.com

‡ Carlos.Martins@astro.up.pt

II. PHENOMENOLOGY OF THE COUPLED RUNAWAY DILATON

The dilaton field Φ appears in every string and superstring theory as a massless scalar excitation of the bosonic string. It comes as a massless scalar mode on the first excited state of the closed string along with two rank-2 tensor fields: the symmetric metric tensor $\tilde{g}_{\mu\nu}$ and the antisymmetric Neveu-Schwarz B -field $B_{\mu\nu}$, which plays a role comparable to an electromagnetic gauge field for extended objects. As such, Φ is a partner of the graviton and contributes to the behavior of gravity itself (for an elementary introduction see e.g. [16]). At tree level, it is expected to be coupled to the various sectors in the string-frame Lagrangian through coupling functions $B_i(\Phi)$ with $i = \tilde{g}, F, \psi, \Phi \dots$. While string theory cannot predict the exact form of these coupling functions, the assumption underlying the *runaway dilaton* model is that they can naturally be attracted toward a finite smooth limit [9] as

$$B_i(\Phi) = C_i + \mathcal{O}(e^{-\Phi}), \quad (1)$$

this can reconcile a massless dilaton with experimental observations while still providing many nonstandard but observable predictions.

The direct coupling of Φ to gravity is reabsorbed in a conformal transformation of the metric $\tilde{g} \rightarrow g$ and a redefinition of the field $\Phi \rightarrow \phi$ [8], leading to an effective low energy Lagrangian density in the Einstein frame

$$\mathcal{L} = \frac{R}{16\pi G} + \frac{1}{8\pi G} (g^{\mu\nu} \partial_\mu \phi \partial_\nu \phi - V(\phi)) - \frac{1}{4} B_F(\phi) F_{\mu\nu}^a F^{a\mu\nu} - B_\psi(\phi) \bar{\psi} D\psi + \dots, \quad (2)$$

where R is the Ricci scalar and F and ψ are respectively the various gauge field strengths and fermion fields. D are the covariant derivatives including the coupling between fermions and gauge fields. In principle the sum extends infinitely over all the massive modes of the string, and they can potentially be coupled. Note that we adopt the notation of previous literature, in which ϕ is measured in units of $\sqrt{\hbar \cdot c / (4\pi G)} = m_{\text{pl}} / \sqrt{4\pi}$ with the Planck mass $m_{\text{pl}} \approx 2.176 \cdot 10^{-8} \text{ kg}$. In particular, the normalization is not the usual $m_{\text{pl}} / \sqrt{8\pi}$ used in many other contexts in cosmology, leading to slightly unconventional kinetic energy terms in the Lagrangian of equation (2) as well as in equations (3) and (4) below. We set $\hbar = c = 1$.

The field's density and pressure are

$$\rho_\phi = \rho_T + \rho_V = \frac{1}{8\pi G} [\dot{\phi}^2 + V(\phi)], \quad (3)$$

$$P_\phi = P_T + P_V = \frac{1}{8\pi G} [\dot{\phi}^2 - V(\phi)], \quad (4)$$

where T and V denote the kinetic and potential contributions respectively. To these densities, one can associate their corresponding energy density parameters, and their

sum $\Omega_\phi = \Omega_T + \Omega_V$. The dotted quantities are derivatives with respect to the cosmic time t , while $\phi' = \frac{d\phi}{d\ln a}$ denotes derivatives with respect to the logarithm of the scale factor, and $\partial_\tau \phi = (aH)\phi'$ for derivatives with respect to conformal time τ .

The model's Friedmann and Klein-Gordon equations are

$$H^2 = \frac{8\pi G}{3} \rho, \quad (5a)$$

$$\ddot{\phi} + 3H\dot{\phi} = 4\pi G\sigma, \quad (5b)$$

where the ρ is the total density of all components of the universe (including the dilaton) and $H = \dot{a}/a$ is the usual Hubble parameter. Furthermore, the interaction of the field is described by

$$\sigma = \sigma_V + \sigma_m = -\frac{1}{8\pi G} \frac{\partial V(\phi)}{\partial \phi} + \sum_i \alpha_i(\phi) (3P_i - \rho_i), \quad (6)$$

whose first term describes the self-interactions of the dilaton from the potential, while the second term describes the dilaton couplings to the other components of the universe.¹ The index i spans all components (hadrons, dark matter, radiation ...) with corresponding densities ρ_i and pressures P_i . The coupling strengths are quantified by coefficients² α_i given by the logarithmic gradients of their masses

$$\alpha_i(\phi) = \frac{\partial \ln m_i(\phi)}{\partial \phi}. \quad (7)$$

This field induced mass variation is a direct signature of the theory of gravity being non-metric.

As discussed in [10], one can model the ϕ dependence of the hadron coupling α_h and dark matter coupling α_m using

$$\alpha_h(\phi) = \alpha_{h,0} e^{-(\phi - \phi_0)}, \quad (8a)$$

$$\alpha_m(\phi) = \alpha_{m,0} e^{-(\phi - \phi_0)}, \quad (8b)$$

where we introduced the notations $\alpha_{i,0} = \alpha_i(\phi_0)$ and $\phi_0 = \phi(z=0)$. Doing so, the Klein-Gordon equation can be entirely described in terms of the difference $\phi - \phi_0$. The couplings to hadrons leptons/dark matter are driving most of the late time cosmological evolution of the field. Another important interaction, albeit more speculative, is that to a model of dark energy (if not generated through the dilaton itself), through a coupling term α_{DE} . If this component behaves as a cosmological constant, we

¹ Note the perhaps surprising extra factor of 1/2 in front of the potential derivative in the source term of the Klein-Gordon equation (5b). This is due to the definition we choose for the action of the field's potential in equation (2) with an unconventional $(8\pi G)^{-1}$ factor.

² Not to be confused with the fine-structure constant α and its value at redshift zero $\alpha(z=0) = \alpha_0$.

have $\sigma_{\text{DE}} = \alpha_{\text{DE}}(3P_{\text{DE}} - \rho_{\text{DE}}) \sim -4\alpha_{\Lambda}\rho_{\Lambda}$. We will only consider the case where α_{Λ} is a constant, which was assumed in most of the previous phenomenological studies [12–14] where α_{Λ} was denoted α_V . Note however that this notation was misleading, as this behavior cannot be simply created by some fine tuned potential of ϕ , but requires some interaction between the dilaton and dark energy.

The coupling to radiation is always irrelevant, since in that case $\rho_r = 3P_r$ and the term of equation (6) always vanishes. The only other interaction of cosmological interest might be that with massive neutrinos, which is left for future work.

It is convenient to treat the contribution from the dilaton potential simply as another species in the σ sum, with coupling³ $\alpha_V = \frac{1}{4} \frac{\partial \ln V}{\partial \phi}$. Note that any constant in the potential $V(\phi) = \Lambda$ adds a term to the Lagrangian equation (2) that is effectively equivalent to a cosmological constant. As such, while being conceptually different, the situation in which the runaway dilaton provides the source for dark energy with a constant potential is phenomenologically equivalent to a runaway dilaton field completely decoupled from dark energy ($V = 0, \alpha_{\Lambda} = 0$) plus a cosmological constant. However, for α_{Λ} to be non-zero requires that $V = 0$ and Λ to be a different source of dark energy. In addition to these two simple scenarios, we will consider the exponential potential $V(\phi) = A_x e^{c_x(\phi - \phi_0)}$, leading to $\alpha_V = c_x/4$ which represents a well motivated potential from string theory [10, 11].

The field equations with the couplings as presented thus far display an attractor behavior, shown in fig. 1. First, the initial value of the field is irrelevant in the overall evolution. This is naturally expected from the equations (5b) and (8b) (which only depend on field differences, not the overall value). Second, there could be, in principle, a dependence on the initial velocity. We observe in fig. 1 that due to Hubble friction the field velocity quickly decays from whatever velocity is chosen at the beginning of the evolution to the value that is forced by its interaction with massive species (the “attractor”). This causes the field ϕ to eventually reach a plateau. The overall displacement of the field from its initial value ($\phi - \phi_0$) can take on different values at the plateau, depending on the precise initial condition. However, for a large range of initial velocities the late time field velocity (and thus also the overall displacement) is most significant around matter domination, where the acceleration from the coupling is strongest compared to the Hubble friction. In this range the initial velocity is irrelevant. The starting redshift (here 10^{14}) is of course set arbitrarily, but this choice does not significantly impact our results.

³ The normalization is set to ensure consistency with the definitions in the literature [10]

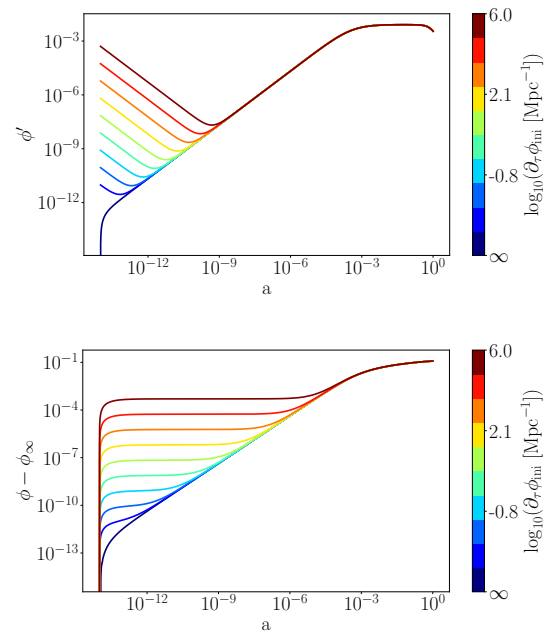


FIG. 1: Evolution of the dilaton field and its speed with respect to the scale factor for different values of its initial speed. Here $V(\phi) = 0, \alpha_{m,0} = -1 \times 10^{-2}$, and $\alpha_{h,0} = -1 \times 10^{-5}$.

A. Impact on observations

All the dimensionless coupling coefficients quantifying fundamental interactions of the standard model are expected to be dynamical quantities evolving with the dilaton field itself. The fine-structure constant α , quantifying the strength of the electromagnetic interaction, is for this reason expected to exhibit a dynamical behavior and will be directly proportional to the field's coupling to the kinetic term of the Maxwell field strength F , $B_F(\phi)$ in the Lagrangian (equation (2)). This is particularly relevant due to the extensive astrophysical and laboratory measurements of α .

One can show that the time evolution of α can be linked to the dilaton coupling and field speed as [10, 12]:

$$\frac{1}{H} \frac{\dot{\alpha}}{\alpha_0} \approx \frac{\alpha_h(\phi)}{40} \phi' , \quad (9)$$

where α_0 is today's value of the fine-structure constant. This leads to the following redshift dependence

$$\frac{\Delta \alpha}{\alpha_0}(z) := \frac{\alpha(z) - \alpha_0}{\alpha_0} = \frac{\alpha_{h,0}}{40} \left[1 - e^{-(\phi(z) - \phi_0)} \right] . \quad (10)$$

An example of this evolution for various dilaton coupling values to hadrons is given in fig. 2.

A different value of α during big bang nucleosynthesis (BBN) also impacts the values of primordial abundances.

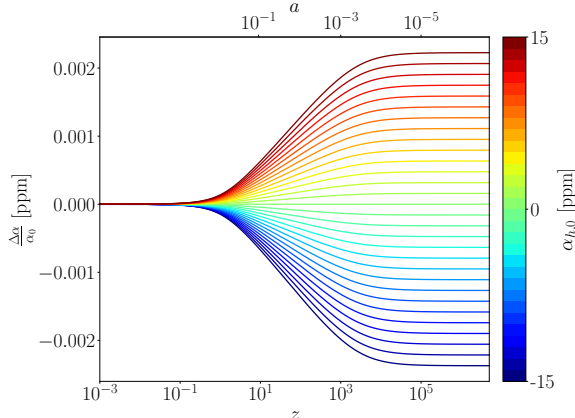


FIG. 2: $\frac{\Delta\alpha}{\alpha_0}$ as a function of z and a for different values of $\alpha_{h,0}$. The dark matter coupling is fixed to $\alpha_{m,0} = 10^{-3}$ and $\phi_{\text{ini}} = \phi'_{\text{ini}} = V = 0$.

The most significant of these is the Helium-4 fraction. One can simply model that the induced variation of Y_{He} as

$$\frac{\Delta Y_{\text{He}}}{Y_{\text{He}}} = \kappa_{\text{BBN}} \frac{\Delta\alpha}{\alpha_0}. \quad (11)$$

For the runaway dilaton, the sensitivity coefficient κ_{BBN} is expected to be of order unity [17]. We will hence set $\kappa_{\text{BBN}} = 1$ for the remainder of this work. However, we stress that the impact of this parameter on the analysis is negligibly small.

Furthermore, as discussed in [18, 19], α appears in various expressions quantifying the interactions between baryons leptons with the photons at recombination epoch.

Ultimately, the atomic energy levels of the Hydrogen atoms are shifted, leading to a delay or advance of recombination. This will impact all the interaction rates and thus, the behavior of the visibility function leading ultimately to a shift of the sound horizon at the last scattering surface, impacting the large ℓ values of the angular power spectrum of the cosmic microwave background [18, 20] and the value of the Hubble parameter at high redshift [19, 21, 22]. We self-consistently model this variation of the α fine-structure parameter using equation (10).

A minor influence on the redshift of reionization is also expected to be induced by a varying α . However, the dynamics of reionization is much less known, and the impact would be far less constrained by current data. For this reason, we will ignore it in the present study.

Last but not least, string theory is not a metric theory of gravity, implying that a violation of the Einstein equivalence principle is not only expected but indeed unavoidable at some level [6]. It can be shown that the Eötvos parameter η , quantifying deviations from the universality of free fall (UFF) and the Eddington parameter

γ (related to light deviation by massive objects, and constrained by the Cassini bound) are directly proportional to the square of the dilaton coupling to hadrons [10, 23]. At $z = 0$, one can derive bounds from general nuclear binding energy formulas

$$\eta \simeq 5.2 \times 10^{-5} \alpha_{h,0}^2, \quad (12a)$$

$$\gamma - 1 \simeq -2 \alpha_{h,0}^2. \quad (12b)$$

III. DATASETS

The runaway dilaton model can be constrained throughout the cosmic evolution using a wide range of local, astrophysical, and cosmological datasets, which we now enumerate.

Local constraints come from experiments on Earth laboratories or in low Earth orbit. Specifically, MICROSCOPE [24] provides constraints⁴ on η at $z = 0$

$$\eta = (-1.5 \pm 2.7) \times 10^{-15}. \quad (13)$$

Furthermore, [25] provides laboratory constraints on the drift rate $\dot{\alpha}/(\alpha_0 H)$ at $z = 0$ using experiments based on atomic clocks, constraining a variation of the fine-structure constant at current times as

$$\frac{1}{H_0} \left(\frac{\dot{\alpha}}{\alpha_0} \right)_{z=0} = (0.014 \pm 0.015) \times 10^{-6}. \quad (14)$$

Finally, the Oklo natural nuclear reactor [26] provides a geophysical constraint on $\Delta\alpha/\alpha_0$

$$\frac{\Delta\alpha}{\alpha_0}(z = 0.14) = (0.005 \pm 0.061) \times 10^{-6}. \quad (15)$$

Astrophysical constraints on α are provided by high-resolution spectroscopy of low-density absorption clouds along the line of sight of bright quasars, at low to intermediate redshifts ($z < 5$). We used the measurement described in [3] combined with recent measurements. All of them can be found in [27, 28] with an extra point coming from the recent ESPRESSO spectrograph measurement [29].

Finally, our cosmological data includes PLANCK constraints on CMB power-spectra, lensing [30, 31], large scale structures and baryon acoustic oscillation from the BOSS DR-12 galaxy survey [32]. In order to constrain the cosmological background evolution, we will also use the supernovae of type Ia (SNIa) likelihood associated to the PANTHEON dataset [33]. Finally, we also use $H(z)$ measurements coming from recent cosmic-clocks measurements [34].

⁴ The standard deviation value is obtained by adding quadratically the statistical and systematic errors of [24].

IV. RESULTS

We aim to obtain constraints on the runaway dilaton model free parameters over the whole cosmic history using the datasets presented in section III.

We use a modified version of the CLASS software [35] including the runaway dilaton field. The scalar field impact on background cosmology is computed by integrating the model equations to obtain $\phi(z)$. The code is also modified to consider the various impacts of a redshift dependent value of the fine-structure constant through the cosmic history. In particular, the computed $\Delta\alpha(z)/\alpha_0$ is given by equation (10).

In this work, we derive the constraints on the dilaton field simply for the case where the field is spatially homogeneous. However, we have also checked that for cases where the overall energy fraction of the dilaton is subdominant during most of the cosmic evolution, one does not obtain a significant impact of the dilaton field perturbations (when implementing the usual perturbed Klein Gordon equation, for example). As such, in these cases our results should generalize. Still, we leave a more detailed investigation of the dilaton perturbations for future work.

The likelihood analysis is done by sampling Monte Carlo Markov Chains (MCMC) with MONTEPYTHON [36, 37] directly coupled to the modified CLASS code. We consider the chains to be converged if, for all parameters, the Gelman-Rubin criterion satisfies $|R-1| < 0.05$. Plotting is done using the GETDIST software [38].

For every run, we sample over the standard cosmological parameters $\{\omega_b, \ln A_s, n_s, z_{\text{reio}}, H_0\}$, the dilaton parameters, and the nuisance parameters of the various likelihoods. The priors in all of these parameters are flat and unbounded. In order to remain concise, we will only display the contours for the dilaton parameters most of the time. Note that the values of ϕ_0 and ϕ'_0 are derived parameters and not sampled over. While not specified on the figures, their values are always expressed in units of $m_{\text{pl}}/\sqrt{4\pi}$.

A. Runaway dilaton and a cosmological constant

In this section we consider the cosmic evolution of a runaway dilaton model decoupled from the cosmological constant, which in this case is the only form of dark energy ($V = 0$). This is equivalent to a runaway dilaton with a constant potential $V = \Lambda$ and no cosmological constant. As such, only the dilaton couplings to baryons and/or dark matter are relevant here.

We display the 68% and 95% CL contours of the 2D marginalized posteriors for all combinations of parameters in fig. 3 and the corresponding 68% CL are detailed in Tab. I. One can witness a very strong correlation between $\alpha_{m,0}$ and today's value of the field ϕ_0 and its derivative ϕ'_0 , while such a correlation is mostly absent with $\alpha_{h,0}$. This is expected as the coupling to hadrons is

TABLE I: Best-fit values of the runaway dilaton parameters with associated 68% confidence levels (CL) in the case $V = 0$ (or $V = \Lambda$) and $\alpha_\Lambda = 0$.

Parameter	68% CL
$\alpha_{h,0}$	$(0.24^{+4.77}_{-4.57}) \times 10^{-6}$
$\alpha_{m,0}$	$(-1.33^{+1.92}_{-6.09}) \times 10^{-2}$
ϕ_0	$(1.5^{+4.0}_{-2.4}) \times 10^{-1}$
ϕ'_0	$(5.49^{+22.9}_{-7.82}) \times 10^{-3}$

highly constrained by local data as MICROSCOPE while the dark matter coupling, more loosely constrained by the cosmological dataset, has more freedom to accelerate the field toward late times. Compared to previous studies as [14] (which also include $\alpha_\Lambda \neq 0$), the field speed ϕ'_0 appears however to be more sharply constrained by one order of magnitude, indicating that $\alpha_{m,0}$ does not have an impact on the field evolution as strong as α_Λ (which here is fixed to 0).

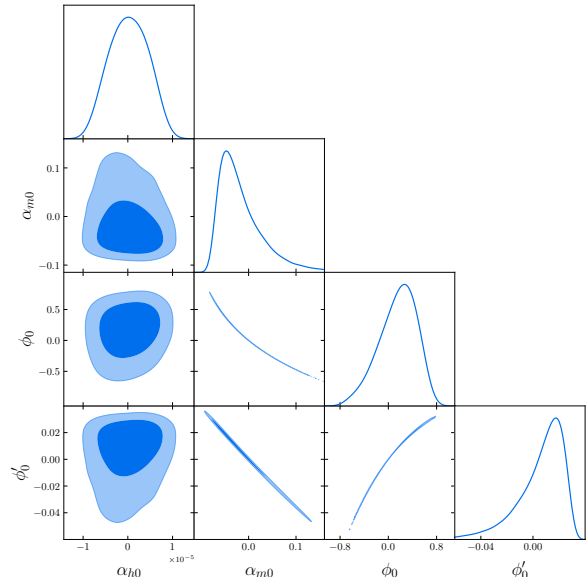


FIG. 3: Posteriors of the dilaton parameters with $\alpha_\Lambda = 0$ and a constant/zero potential.

B. Runaway dilaton and a constant coupling to dark energy

The latest results found in the literature (see e.g. [14]) consider the scenario in which ϕ can be coupled to Λ with a constant coupling. In low redshift studies, an extra prior on today's field speed was given by $|\phi'_0| = 0.0 \pm 0.1$, obtained from separate constraints in [39, 40]. This prior

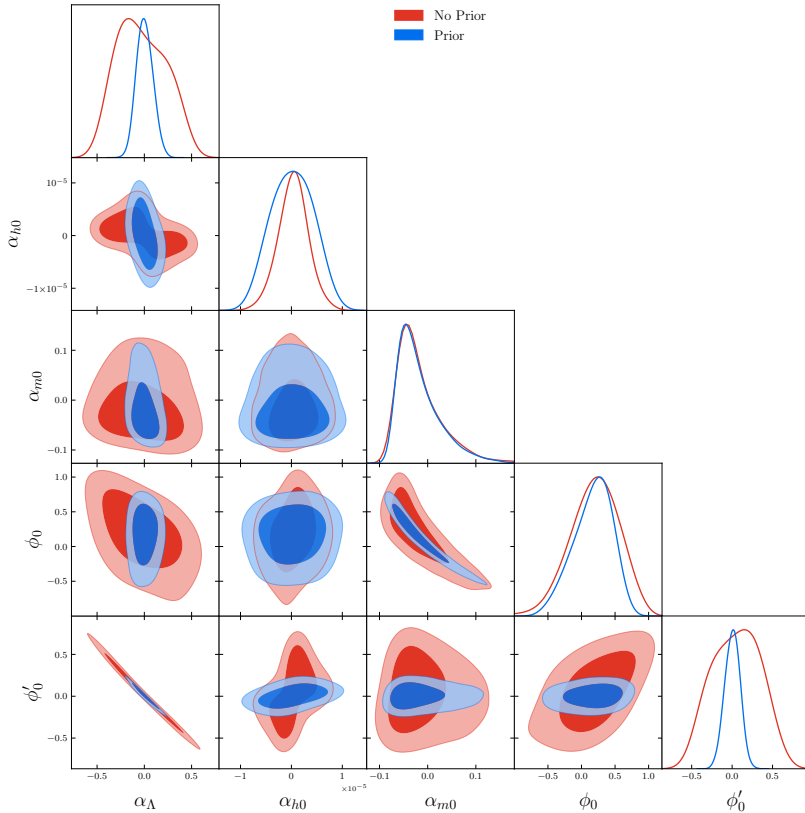


FIG. 4: Posteriors of the dilaton parameters with a constant coupling to dark energy α_Λ with an extra prior on ϕ'_0 (blue) and without it (red).

enables the simplification of the constraints coming from the probes of the cosmological background expansion and therefore provides the main (and effectively the only) constraint on today's field speed ϕ'_0 . However, using such a prior on today's field speed is in principle unjustified for a full cosmological study since it is derived from rough assumptions (such as matter domination in the current cosmological era), which can be superseded with our likelihood sets.

We show the results without this prior as the red contours in fig. 4, and the results with the prior on ϕ'_0 as blue contours. We further quantify the results in table II. These results provide for the first time a study of the full model including $\alpha_{m,0}$ without making any simplifying assumptions (which were called dark, field and matter coupling in the previous studies [12–14]). We find an improvement of the constraints on $\alpha_{h,0}$ by one order of magnitude compared to [14], solely due to the latest MICROSCOPE constraint. The constrains on the coupling to dark energy α_Λ are identical when using the prior, as they are an indirect consequence of this restriction set on the field speed, due to the strong degeneracy one can witness between the two parameters.

While α_m guides the field evolution in matter domination (and thus has a strong impact on the overall field offset ϕ_0) the impact of the dark energy coupling α_Λ is much stronger at late times (around dark energy domination), leading to a very tight degeneracy between α_Λ and the current field speed ϕ'_0 .

When leaving the prior, the contours are even more non-Gaussian, allowing for large values of α_Λ and hence of the field speed. Surprisingly, the coupling $\alpha_{h,0}$ ap-

TABLE II: Best-fit values of the runaway dilaton parameters with associated 68% confidence levels (CL) in the case $V = 0$ and $\alpha_\Lambda \neq 0$.

Parameter	Prior on ϕ'_0	No prior on ϕ'_0
$\alpha_{h,0}$	$ (-1.63^{+4.33}_{-4.71}) \times 10^{-6} $	$(0.21^{+2.97}_{-2.80}) \times 10^{-6}$
$\alpha_{m,0}$	$ (-1.70^{+2.08}_{-5.71}) \times 10^{-2} $	$(-1.39^{+2.65}_{-6.03}) \times 10^{-2}$
α_Λ	$ (0.50^{+8.94}_{-9.39}) \times 10^{-2} $	$((-0.16^{+2.34}_{-3.65}) \times 10^{-1}$
ϕ_0	$ (16.7^{+3.68}_{-2.43}) \times 10^{-1} $	$((17.5^{+4.25}_{-3.23}) \times 10^{-1}$
ϕ'_0	$ (0.20^{+9.97}_{-9.98}) \times 10^{-2} $	$((3.7^{+38.4}_{-31.0}) \times 10^{-2}$

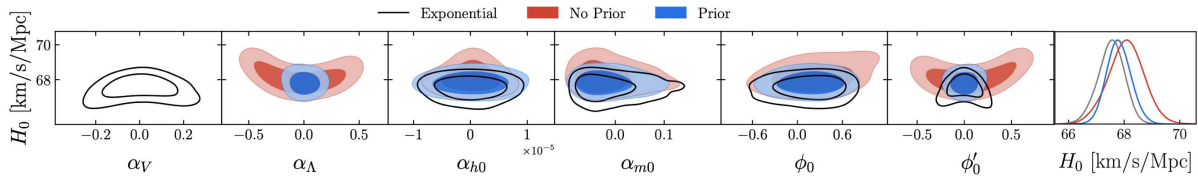


FIG. 5: Contour plots of H_0 and the dilaton parameters in the cases of an exponential potential (black) and a constant coupling to dark energy α_Λ with an extra prior on ϕ'_0 (blue) and without it (red).

pears to be ~ 2 times more constrained without providing any prior on ϕ'_0 , below what the MICROSCOPE bound (equation (13)) can constrain. This is a result from a Bayesian projection effect: The larger space of ϕ'_0 allowed also allows for a greater amount of models close to $\alpha_{h,0} \sim 0$ to be viable (due to the atomic clock likelihood constraining only the product $\alpha_{h,0}\phi'_0$, see equations (9) and (14)). This, in turn, explains the specific shape of the contour in the $(\phi'_0, \alpha_{h,0})$ space asking for the two parameters to have the same sign for their product to be positive, and tightens the posterior around $\alpha_{h,0}$ from the Bayesian marginalization.

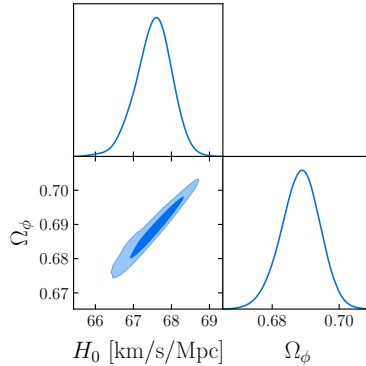


FIG. 6: Contour plot of Ω_ϕ and H_0 for the exponential potential scenario.

Since we do not have any potential in this case, the overall energy density of the field (equation (3)) is solely given by the kinetic energy of the field ($\Omega_\phi = \Omega_T$). Given that a large coupling to Λ is allowed ($|\alpha_\Lambda| \gg 0$), we find that the field strongly accelerates at late times, leading to $d\rho_\phi/d\ln a > 0$ (and large $|\phi'_0|$). This naturally allows for a higher H_0 due to the geometrical degeneracies in the CMB (compare e.g. with a model of dark energy equation of state with $w < -1$).⁵ The contour plots relating the dilaton parameters and H_0 are displayed in

⁵ The equation of state of the dilaton naturally always obeys $w_\phi > -1$ since $1 + w_\phi = 2\dot{\phi}^2/[\dot{\phi}^2 + V(\phi)] > 0$. However, since we have $d\rho/d\ln a > 0$ this is effectively equivalent to a decou-

fig. 5. We can observe that today's value of the Hubble parameter H_0 , is impacted quite strongly by high values of ϕ'_0 . Releasing the prior on ϕ'_0 naturally allows for higher H_0 values: $H_0 = 68.2^{+0.51}_{-0.65}$ km/s/Mpc instead of $H_0 = 67.8 \pm 0.43$ km/s/Mpc with the prior. These conclusions could be relevant in the context of the $\sim 4\sigma$ observational tension on the value of H_0 and the theoretical limitations of Λ as the standard source of dark energy (see e.g.,[41]). We observe, however, that (due to the atomic clock bound) this quintessence-like behavior of the dilaton field in this configuration is only allowed for smaller values of $\alpha_{h,0}$ and hence smaller violations of general relativity. A targeted and complete study on the role of the dilaton field in this regard remains for future work.

C. Exponential potential

We will now consider the case of an exponential shape for $V(\phi)$. In this case the runaway dilaton potential can explain all of the dark energy in the universe, providing that we add a constant term to V . The contours are shown in fig. 7, and the corresponding constraints are displayed in table III. As expected, we obtain a high value for $\Omega_\phi = 0.688 \pm 0.006$, showing a strong degeneracy with H_0 in fig. 6. This is expected from the measurement of the CMB sound horizon angle, which tightly constrains $\Omega_m h^3 \approx (1 - \Omega_\phi)h^3$. We also observe that this additional degree of freedom does not significantly impact the constraints on $\alpha_{h,0}$ or $\alpha_{m,0}$. In this scenario we find that H_0 cannot be increased, only decreased. Since the total field energy in this case is dominated by the potential, and one naturally finds $dV/d\ln a < 0$ (as long as $|\alpha_V| \gg 0$)⁶.

pled species with $w < -1$ since for such a species $d\rho/d\ln a = -3(\rho + P) = -3\rho(1 + w) > 0$. The point why such a behavior is preferable can be explained by looking at how late-time solutions to the Hubble tension manage to keep the angular diameter distance (and thus the sound horizon angle) constant. Since we can write $D_A(z_*) \approx \frac{1}{H_0} \int_0^{z_*} dz / \sqrt{\Omega_\phi(z) + \Omega_\Lambda + \Omega_m(1+z)^3}$, if we increase H_0 it is important to decrease the integrand and thus $\Omega_\phi(z)$ in order to keep $D_A(z_*)$ constant. Since $\Omega_\phi(z=0) = 1 - \Omega_m - \Omega_\Lambda$ is fixed, this can only happen if $d\Omega_\phi(z)/dz \propto d\rho_\phi(z)/dz \propto -d\rho_\phi(z)/d\ln a < 0$.

⁶ For a field rolling down its potential one naturally expects $dV/d\ln a < 0$, but this can also be confirmed by noticing that

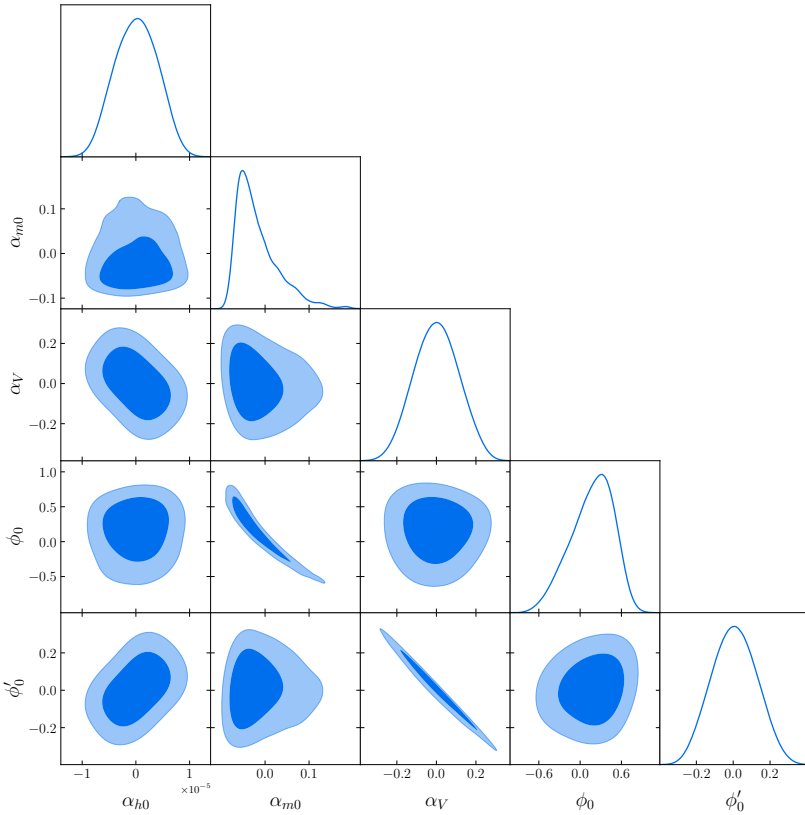


FIG. 7: Contour plots for the dilaton parameters in the exponential potential scenario.

Including both a coupling to a non-negligible cosmological constant and a runaway dilaton potential at the same time causes the parameter space to become extremely hard to sample efficiently. This is because the limit of $\Lambda \rightarrow 0$ (with the dilaton potential playing the role of dark energy) naturally allows α_Λ to diverge. At the same time, the limit of small Ω_ϕ and correspondingly small $V(\phi)$ also allows the dilaton potential parameters to diverge arbitrarily. As such, instead of imposing arbitrary priors on either the coupling parameters or the cosmological densities, we do not treat this case.

TABLE III: Best-fit values of the runaway dilaton parameters with associated 68% confidence levels (CL) for the exponential potential case.

Parameter	68 % CL
$\alpha_{h,0}$	$(0.01^{+4.22}_{-4.17}) \times 10^{-6}$
$\alpha_{m,0}$	$(-1.68^{+2.24}_{-5.78}) \times 10^{-2}$
α_V	$(0.04^{+1.12}_{-1.27}) \times 10^{-1}$
ϕ_0	$(1.64^{+3.82}_{-2.53}) \times 10^{-1}$
ϕ'_0	$(0.02^{+1.36}_{-1.26}) \times 10^{-1}$

V. DISCUSSION AND CONCLUSION

$dV/d\ln a = dV/d\phi \cdot \phi'$ and noticing that due to equation (5b) the field speed ϕ' naturally evolves in the opposite direction of $dV/d\phi$, i.e. $(\phi')' \propto -dV/d\phi$ as long as the Hubble drag and the other coupling terms are comparatively negligible, we also find in this case $d\rho/d\ln a < 0$ which (comparably to a dark energy model with $w > -1$) results in lower values of H_0 .

The runaway dilaton model provides a general and self-consistent framework to study the stability of fundamental constants, and the cosmological impact of their space-time variations. It also allows to probe credible models of string theories with existing data-sets. In this work, we obtained the first constraints on the complete parameter space of this model, considering its full cosmologi-

cal evolution with minimal assumptions on its couplings, updating and refining previous studies. To do so, we benefit from the synergy of multiple independent probes as cosmological, astrophysical, and laboratory datasets. In particular, a major lever arm is provided by the final data release of the MICROSCOPE experiment [24]. We explored three scenarios of increasing complexity, showing that order unity couplings (which would be natural in string theory) are ruled out in all cases.

While the possible field evolution is expected to be further constrained by the data of incoming wide cosmological surveys as *Euclid* [42], *DESI* [43], CMB *Stage-4* [44] or *LiteBIRD* [45], major restriction of its parameter space are expected to be provided by future experiments allowing to directly measure the value of the fine structure constant with an extreme precision, either in laboratory with nuclear clocks [46], in the nearby universe using spectroscopy [47], or in the primeval universe with spectral distortions of the CMB [48].

Runaway dilaton models (and, more widely, all scalar field induced varying constant models) can additionally play an important role in contemporary debates triggered by the recent discovery of the accelerated expansion of the universe [49, 50] and the nature of dark energy. As shown in [19, 21, 22, 51], a redshift dependence of α – or possibly of the electron mass m_e – can have a significant impact on recombination processes that could partially ease or solve the Hubble tension. Providing a suitable choice of couplings or potential, we discussed how the runaway dilaton field can act as dynamical dark energy and significantly impact the value of H_0 . Future studies will reveal if possible extensions of this model can fur-

ther ease cosmological tensions or if the framework is too restrictive to feasibly do so.

ACKNOWLEDGMENTS

L.V. would like to thank J. Aumont, A. Blanchard, B. Lamine, J. Lesgourgues and L. Montier who made this collaboration and this work possible by introducing the authors. Extra thanks also goes to S. Nesseris for interesting discussions on CLASS and MONTEPYTHON as well as C. M. J. Marques and P. Fayet for feedback on the latest stages of the draft. Computations were made on the Mardec cluster supported by the OCEVU Labex (ANR-11-LABX-0060) and the Excellence Initiative of Aix-Marseille University - A*MIDEX, part of the French “Investissements d’Avenir” program. LV would also like to thanks B. Carreres for several helps with the use of Mardec.

Nils Schöneberg acknowledges the support of the following Maria de Maetzu fellowship grant: Esto publicación es parte de la ayuda CEX2019-000918-M, finanziado por MCIN/AEI/10.13039/501100011033.

This work was financed by Portuguese funds through FCT - Fundação para a Ciência e a Tecnologia in the framework of the project 2022.04048.PTDC. JDJD is supported by an FCT fellowship, grant number SFRH/BD/150990/2021. C.J.M also acknowledges FCT and POCH/FSE (EC) support through Investigador FCT Contract 2021.01214.CEECIND/CP1658/CT0001.

-
- [1] CMS Collaboration, Observation of a new boson at a mass of 125 GeV with the CMS experiment at the LHC, *Physics Letters B* **716**, 30 (2012), arXiv:1207.7235 [hep-ex].
 - [2] Atlas Collaboration, Observation of a new particle in the search for the Standard Model Higgs boson with the ATLAS detector at the LHC, *Physics Letters B* **716**, 1 (2012), arXiv:1207.7214 [hep-ex].
 - [3] C. J. A. P. Martins, The status of varying constants: a review of the physics, searches and implications, *Reports on Progress in Physics* **80**, 126902 (2017), arXiv:1709.02923 [astro-ph.CO].
 - [4] S. Mukhi, String theory: a perspective over the last 25 years, *Classical and Quantum Gravity* **28**, 153001 (2011), arXiv:1110.2569 [physics.pop-ph].
 - [5] L. Susskind, The world as a hologram, *Journal of Mathematical Physics* **36**, 6377 (1995), arXiv:hep-th/9409089 [hep-th].
 - [6] C. M. Will, The Confrontation between General Relativity and Experiment, *Living Reviews in Relativity* **17**, 4 (2014), arXiv:1403.7377 [gr-qc].
 - [7] C. M. Will, *Theory and Experiment in Gravitational Physics (2nd edition)* (2017).
 - [8] T. Damour and A. Polyakov, The string dilation and a least coupling principle, *Nuclear Physics B* **423**, 532 (1994).
 - [9] T. Damour and K. Nordtvedt, General relativity as a cosmological attractor of tensor-scalar theories, *Phys. Rev. Lett.* **70**, 2217 (1993).
 - [10] T. Damour, F. Piazza, and G. Veneziano, Violations of the equivalence principle in a dilaton-runaway scenario, *Phys. Rev. D* **66**, 046007 (2002), arXiv:hep-th/0205111 [hep-th].
 - [11] M. Gasperini, F. Piazza, and G. Veneziano, Quintessence as a runaway dilaton, *Phys. Rev. D* **65**, 023508 (2001), arXiv:gr-qc/0108016 [gr-qc].
 - [12] C. Martins, P. Vielzeuf, M. Martinelli, E. Calabrese, and S. Pandolfi, Evolution of the fine-structure constant in runaway dilaton models, *Physics Letters B* **743**, 377 (2015).
 - [13] M. Martinelli, E. Calabrese, and C. J. A. P. Martins, E-ELT constraints on runaway dilaton scenarios, *J. Cosmology Astropart. Phys.* **2015**, 030 (2015), arXiv:1508.00765 [astro-ph.CO].
 - [14] C. Martins and L. Vacher, Astrophysical and local constraints on string theory: runaway dilaton models, *Physical Review D* **100**, 123514 (2019).
 - [15] L. Vacher, J. D. F. Dias, N. Schöneberg, C. J. A. P. Martins, S. Vinzl, S. Nesseris, G. Cañas-Herrera, and M. Martinelli, Constraints on extended Bekenstein models from

- cosmological, astrophysical, and local data, Phys. Rev. D **106**, 083522 (2022), arXiv:2207.03258 [astro-ph.CO].
- [16] R. J. Szabo, BUSSTEPP Lectures on String Theory, arXiv e-prints , hep-th/0207142 (2002), arXiv:hep-th/0207142 [astro-ph].
- [17] M. T. Clara and C. J. A. P. Martins, Primordial nucleosynthesis with varying fundamental constants. Improved constraints and a possible solution to the lithium problem, A&A **633**, L11 (2020), arXiv:2001.01787 [astro-ph.CO].
- [18] Planck Collaboration, Planck intermediate results. XXIV. Constraints on variations in fundamental constants, A&A **580**, A22 (2015), arXiv:1406.7482 [astro-ph.CO].
- [19] L. Hart and J. Chluba, New constraints on time-dependent variations of fundamental constants using Planck data, MNRAS **474**, 1850 (2018), arXiv:1705.03925 [astro-ph.CO].
- [20] S. Galli, C. J. A. P. Martins, A. Melchiorri, and E. Meneugoni, Testing the Variation of Fundamental Constants with the CMB, Astrophys. Space Sci. Proc. , 59 (2011).
- [21] L. Hart and J. Chluba, Varying fundamental constants principal component analysis: additional hints about the Hubble tension, MNRAS 10.1093/mnras/stab2777 (2021), arXiv:2107.12465 [astro-ph.CO].
- [22] N. Lee, Y. Ali-Haïmoud, N. Schöneberg, and V. Poulin, What it takes to solve the Hubble tension through modifications of cosmological recombination, arXiv e-prints , arXiv:2212.04494 (2022), arXiv:2212.04494 [astro-ph.CO].
- [23] T. Damour and J. F. Donoghue, FAST TRACK COMMUNICATION: Phenomenology of the equivalence principle with light scalars, Classical and Quantum Gravity **27**, 202001 (2010), arXiv:1007.2790 [gr-qc].
- [24] P. Touboul, G. Métris, M. Rodrigues, J. Bergé, A. Robert, Q. Baghi, Y. André, J. Bedouet, D. Boulanger, S. Bremer, P. Carle, R. Chhun, B. Christophe, V. Cipolla, T. Damour, P. Danto, L. Demange, H. Dittus, O. Dhuicque, P. Fayet, B. Foulon, P.-Y. Guidotti, D. Hagedorn, E. Hardy, P.-A. Huynh, P. Kayser, S. Lala, C. Lämmerzahl, V. Lebat, F. m. c. Liorzou, M. List, F. Löffler, I. Panet, M. Pernot-Borràs, L. Perraud, S. Pires, B. Pouilloux, P. Prieur, A. Rebray, S. Reynaud, B. Rievers, H. Selig, L. Serron, T. Sumner, N. Tanguy, P. Torresi, and P. Visser, *microscope* mission: Final results of the test of the equivalence principle, Phys. Rev. Lett. **129**, 121102 (2022).
- [25] R. Lange, N. Huntemann, J. M. Rahm, C. Sanner, H. Shao, B. Lipphardt, C. Tamm, S. Weyers, and E. Peik, Improved Limits for Violations of Local Position Invariance from Atomic Clock Comparisons, Phys. Rev. Lett. **126**, 011102 (2021), arXiv:2010.06620 [physics.atom-ph].
- [26] Y. V. Petrov, A. I. Nazarov, M. S. Onegin, V. Y. Petrov, and E. G. Sakhnovsky, Natural nuclear reactor at Oklo and variation of fundamental constants: Computation of neutronics of a fresh core, Phys. Rev. C **74**, 064610 (2006), arXiv:hep-ph/0506186 [hep-ph].
- [27] J. K. Webb, J. A. King, M. T. Murphy, V. V. Flambaum, R. F. Carswell, and M. B. Bainbridge, Indications of a Spatial Variation of the Fine Structure Constant, Phys. Rev. Lett. **107**, 191101 (2011), arXiv:1008.3907 [astro-ph.CO].
- [28] M. T. Murphy and K. L. Cooksey, Subaru Telescope limits on cosmological variations in the fine-structure constant, Monthly Notices of the Royal Astronomical Society **471**, 4930 (2017), <https://academic.oup.com/mnras/article-pdf/471/4/4930/19650209/stx1949.pdf>.
- [29] M. T. Murphy, P. Molara, A. C. O. Leite, G. Cupani, S. Cristiani, V. D'Odorico, R. Génova Santos, C. J. A. P. Martins, D. Milaković, N. J. Nunes, T. M. Schmidt, F. A. Pepe, R. Rebolo, N. C. Santos, S. G. Sousa, M.-R. Zapatero Osorio, M. Amate, V. Adibekyan, Y. Alibert, C. A. Prieto, V. Baldini, W. Benz, F. Bouchy, A. Cabral, H. Dekker, P. Di Marcantonio, D. Ehrenreich, P. Figueira, J. I. González Hernández, M. Landoni, C. Lovis, G. Lo Curto, A. Manescau, D. Mégevand, A. Mehner, G. Micela, L. Pasquini, E. Poretti, M. Riva, A. Sozzetti, A. S. Mascareño, S. Udry, and F. Zerbini, Fundamental physics with ESPRESSO: Precise limit on variations in the fine-structure constant towards the bright quasar HE 0515–4414, A&A **658**, A123 (2022), arXiv:2112.05819 [astro-ph.CO].
- [30] N. Aghanim, Y. Akrami, F. Arroja, M. Ashdown, J. Aumont, C. Baccigalupi, M. Ballardini, A. J. Banday, R. B. Barreiro, and et al., Planck2018 results, A&A **641**, A1 (2020).
- [31] Planck Collaboration, Planck 2018 results. V. CMB power spectra and likelihoods, A&A **641**, A5 (2020), arXiv:1907.12875 [astro-ph.CO].
- [32] The B.O.S.S. collaboration, The clustering of galaxies in the completed SDSS-III Baryon Oscillation Spectroscopic Survey: cosmological analysis of the DR12 galaxy sample, MNRAS **470**, 2617 (2017), arXiv:1607.03155 [astro-ph.CO].
- [33] A. G. Riess, S. A. Rodney, D. M. Scolnic, D. L. Shafer, L.-G. Strolger, H. C. Ferguson, M. Postman, O. Graur, D. Maoz, S. W. Jha, B. Mobasher, S. Casertano, B. Hayden, A. Molino, J. Hjorth, P. M. Garnavich, D. O. Jones, R. P. Kirshner, A. M. Koekemoer, N. A. Grogan, G. Brammer, S. Hemmati, M. Dickinson, P. M. Challis, S. Wolff, K. I. Clubb, A. V. Filippenko, H. Nayyeri, V. U, D. C. Koo, S. M. Faber, D. Kocevski, L. Bradley, and D. Coe, Type Ia Supernova Distances at Redshift >1.5 from the Hubble Space Telescope Multi-cycle Treasury Programs: The Early Expansion Rate, Astrophys. J. **853**, 126 (2018), arXiv:1710.00844 [astro-ph.CO].
- [34] M. Moresco, L. Amati, L. Amendola, S. Birrer, J. P. Blakeslee, M. Cantiello, A. Cimatti, J. Darling, M. Della Valle, M. Fishbach, C. Grillo, N. Hamaus, D. Holz, L. Izzo, R. Jimenez, E. Lusso, M. Meneghetti, E. Piedipalumbo, A. Pisani, A. Pourtsidou, L. Pozzetti, M. Quaratin, G. Risaliti, P. Rosati, and L. Verde, Unveiling the Universe with Emerging Cosmological Probes, arXiv e-prints , arXiv:2201.07241 (2022), arXiv:2201.07241 [astro-ph.CO].
- [35] J. Lesgourgues, The cosmic linear anisotropy solving system (class) i: Overview (2011), arXiv:1104.2932 [astro-ph.IM].
- [36] B. Audren, J. Lesgourgues, K. Benabed, and S. Prunet, Conservative constraints on early cosmology with MONTE PYTHON, J. Cosmology Astropart. Phys. **2013**, 001 (2013), arXiv:1210.7183 [astro-ph.CO].
- [37] T. Brinckmann and J. Lesgourgues, MontePython 3: Boosted MCMC sampler and other features, Physics of the Dark Universe **24**, 100260 (2019), arXiv:1804.07261 [astro-ph.CO].
- [38] A. Lewis, GetDist: a Python package for analysing Monte

- Carlo samples, arXiv e-prints , arXiv:1910.13970 (2019), arXiv:1910.13970 [astro-ph.IM].
- [39] D. B. Thomas, M. Kopp, and C. Skordis, Constraining the Properties of Dark Matter with Observations of the Cosmic Microwave Background, *Astrophys. J.* **830**, 155 (2016), arXiv:1601.05097 [astro-ph.CO].
- [40] I. Tutzusaus, B. Lamine, A. Blanchard, A. Dupays, Y. Rousset, and Y. Zolnierowski, Dark sectors of the Universe: A Euclid survey approach, *Phys. Rev. D* **94**, 123515 (2016), arXiv:1607.08016 [astro-ph.CO].
- [41] J. Martin, Everything you always wanted to know about the cosmological constant problem (but were afraid to ask), *Comptes Rendus Physique* **13**, 566 (2012), arXiv:1205.3365 [astro-ph.CO].
- [42] M. Martinelli, C. J. A. P. Martins, S. Nesseris, I. Tutzusaus, A. Blanchard, S. Camera, C. Carbone, S. Casas, V. Pettorino, Z. Sakr, V. Yankelevich, D. Sapone, A. Amara, N. Auricchio, C. Bodendorf, D. Bonino, E. Branchini, V. Capobianco, J. Carretero, M. Castellano, S. Cavuoti, A. Cimatti, R. Cledassou, L. Coccione, A. Costille, H. Degaudenzi, M. Douspis, F. Dubath, S. Dusini, A. Ealet, S. Ferriol, M. Frailis, E. Franceschi, B. Garilli, C. Giocoli, A. Grazian, F. Grupp, S. V. H. Haugan, W. Holmes, F. Hormuth, K. Jahnke, A. Kiessling, M. Kümmel, M. Kunz, H. Kurki-Suonio, S. Ligori, P. B. Lilje, I. Lloro, O. Mansutti, O. Marggraf, K. Markovic, R. Massey, M. Meneghetti, G. Meylan, L. Moscardini, S. M. Niemi, C. Padilla, S. Paltani, F. Pasian, K. Pedersen, S. Pires, M. Poncet, L. Popa, F. Raison, R. Rebolo, J. Rhodes, M. Roncarelli, E. Rossetti, R. Saglia, A. Secroun, G. Seidel, S. Serrano, C. Sirignano, G. Sirri, J. L. Starck, D. Tavagnacco, A. N. Taylor, I. Tereno, R. Toledo-Moreo, L. Valenziano, Y. Wang, G. Zamorani, J. Zoubian, M. Baldi, M. Brescia, G. Congedo, L. Conversi, Y. Copin, G. Fabbian, R. Farinelli, E. Medinaceli, S. Mei, G. Polenta, E. Romelli, and T. Vassallo, Euclid: Constraining dark energy coupled to electromagnetism using astrophysical and laboratory data, *A&A* **654**, A148 (2021), arXiv:2105.09746 [astro-ph.CO].
- [43] DESI Collaboration, The DESI Experiment Part I: Science, Targeting, and Survey Design, arXiv e-prints , arXiv:1611.00036 (2016), arXiv:1611.00036 [astro-ph.IM].
- [44] CMB-S4 Collaboration, CMB-S4 Science Case, Reference Design, and Project Plan, arXiv e-prints , arXiv:1907.04473 (2019), arXiv:1907.04473 [astro-ph.IM].
- [45] LiteBIRD Collaboration, Probing Cosmic Inflation with the LiteBIRD Cosmic Microwave Background Polarization Survey, *Progress of Theoretical and Experimental Physics* 10.1093/ptep/ptac150 (2022), ptac150, <https://academic.oup.com/ptep/advance-article-pdf/doi/10.1093/ptep/ptac150/47465454/ptac150.pdf>.
- [46] P. Fadeev, J. C. Berengut, and V. V. Flambaum, Sensitivity of ^{229}Th nuclear clock transition to variation of the fine-structure constant, *Phys. Rev. A* **102**, 052833 (2020), arXiv:2007.00408 [physics.atom-ph].
- [47] J. Liske, G. Bono, J. Cepa, et al., *Top Level Requirements For ELT-HIRES*, Tech. Rep. (Document ESO 204697 Version 1, 2014).
- [48] L. Hart and J. Chluba, Using the cosmological recombination radiation to probe early dark energy and fundamental constant variations, *MNRAS* **519**, 3664 (2023), arXiv:2209.12290 [astro-ph.CO].
- [49] A. G. Riess, A. V. Filippenko, P. Challis, A. Clocchiatti, A. Diercks, P. M. Garnavich, R. L. Gilliland, C. J. Hogan, S. Jha, R. P. Kirshner, B. Leibundgut, M. M. Phillips, D. Reiss, B. P. Schmidt, R. A. Schommer, R. C. Smith, J. Spyromilio, C. Stubbs, N. B. Suntzeff, and J. Tonry, Observational Evidence from Supernovae for an Accelerating Universe and a Cosmological Constant, *AJ* **116**, 1009 (1998), arXiv:astro-ph/9805201 [astro-ph].
- [50] S. Perlmutter, G. Aldering, G. Goldhaber, R. A. Knop, P. Nugent, P. G. Castro, S. Deustua, S. Fabbro, A. Goobar, D. E. Groom, I. M. Hook, A. G. Kim, M. Y. Kim, J. C. Lee, N. J. Nunes, R. Pain, C. R. Pennypacker, R. Quimby, C. Lidman, R. S. Ellis, M. Irwin, R. G. McMahon, P. Ruiz-Lapuente, N. Walton, B. Schaefer, B. J. Boyle, A. V. Filippenko, T. Matheson, A. S. Fruchter, N. Panagia, H. J. M. Newberg, W. J. Couch, and T. S. C. Project, Measurements of Ω and Λ from 42 High-Redshift Supernovae, *Astrophys. J.* **517**, 565 (1999), arXiv:astro-ph/9812133 [astro-ph].
- [51] N. Schöneberg, G. F. Abellán, A. Pérez Sánchez, S. J. Witte, V. Poulin, and J. Lesgourgues, The H_0 Olympics: A fair ranking of proposed models, arXiv e-prints , arXiv:2107.10291 (2021), arXiv:2107.10291 [astro-ph.CO].

